BEHAVIOUR OF SMALL GROUPS OF GRANULAR COLUMNS IN CLAY

Thesis submitted by

David Hope BSc(Hons) MSc FGS

for the Degree of Doctor of Philosophy

Department of Civil Engineering,
University of Birmingham,
P.O. Box 363,
Birmingham B15 2TT.

July, 1988

SYNOPSIS

The results of a laboratory investigation into the behaviour of small groups of up to five granular columns, in soft clay, loaded by various foundation configurations under rapid undrained conditions is presented. Columns with a constant layer length to diameter ratio in both floating and end-bearing conditions are considered. Electronic instrumentation was developed to record boundary stresses and displacements and radiographic techniques were employed to measure internal displacements and strains in the columns and clay.

Extensive use of interactive mainframe and mini computers was made in collecting, storing and processing the laboratory data.

The improvement in bearing capacity and reduction in settlement was found to be strongly dependent on the relative column and clay areas in contact with a foundation. The column end-bearing condition was also a contributory factor.

The mechanism of column and clay deformation was observed as being dependent on the boundary conditions. Column yield occurred as a general shear failure or a local shear failure depending on the relative sizes of the clay and column areas.

Laboratory results showed that direct analogy with conventional piles or pile groups cannot be made. An empirical relationship for estimating the improvement in bearing capacity and settlement is proposed.

CONTENTS

CHAPTER 3 - RADIOGRAPHY

CHAPTER 4 - GENERAL EQUIPMENT

CHAPTER FIVE - INSTRUMENTATION

CHAPTER SEVEN - RADIOGRAPHIC ANALYSIS

CHAPTER EIGHT - DATA PROCESSING

CHAPTER TEN - TEST PREPARATION AND PROCEDURES

CHAPTER ELEVEN - CORRECTIONS, CONSTANTS AND EXPOSURE

DEDICATION

To Jo, my Mother and the

memory of my Father.

CHAPTER 1

VIBROREPLACEMENT

1.1 INTRODUCTION

Vibroreplacement has been used in the United Kingdom for over twenty years as a means of improving predominantly cohesive ground materials of poor engineering quality, on which structural foundations and ground slabs have to be constructed. The operating techniques have been well documented by many authors, notably Watt et al (1967), Greenwood (1970, 1972), and Bauman and Bauer (1974).

A vibrating poker, or 'vibroflot', with air or water jets, and suspended from a crane, is used to form a vertical hole. Spoil is removed by the air or water flush, as the vibroflot penetrates, and is subsequently replaced by granular backfill compacted to form a dense granular column.

1.2 OBJECTS OF THE PROCESS

The aim is to achieve economically an increase in bearing capacity in weak cohesive media (natural or fill material), and a reduction of total and differential settlements at working loads.

1.3 REASONS FOR AND SCOPE OF THE STUDY

Typical grid patterns for granular columns sustaining various types of applied loads are shown in Figure 1.1. In the case of large areas of uniformly distributed loading (such as storage tanks, embankments or ground slabs), the columns are constructed in some regular array. Near the centre of a large group, any column and an associated surrounding block of soil may be treated approximately as a radially symmetric element subject to one-dimensional strain. This is the basis of design proposed by several researchers.

The analysis for line and point loads is more complicated and it has received less attention in the literature. This aspect is important as the performance of isolated structural foundations will influence the performance of the building as a whole. Settlement characteristics

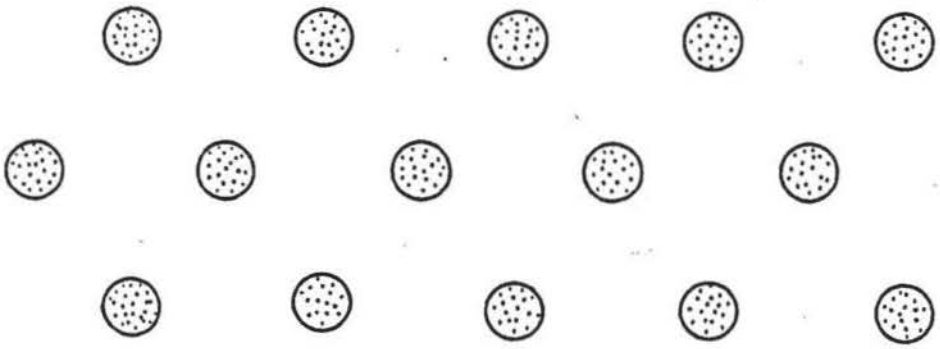

(a) Large areas of uniformly distributed loads.

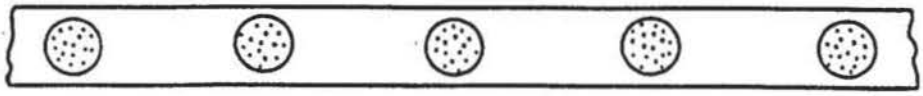

(b) Line load

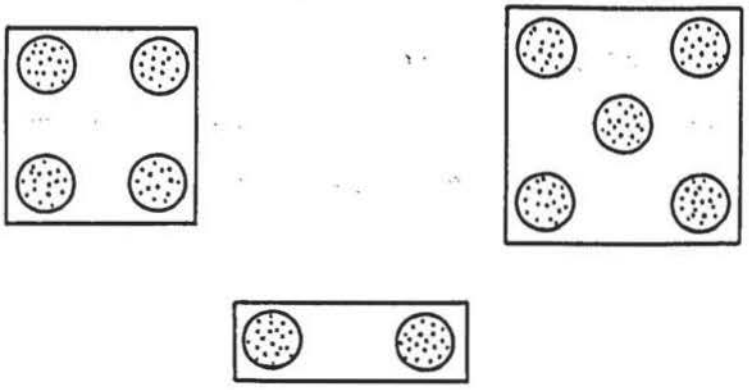

(c) Point loads

Typical examples of grid patterns of granular columns.

FIGURE 1.1

will be more critical than for ground slabs or embankments, since excessive deformation will cause structural damage. Therefore, the behaviour of small groups of granular columns supporting structural loads was considered to be an important aspect for study.

The scope of the study was designed as an initial step towards understanding small group behaviour by determining general trends and failure modes from small scale laboratory studies and relating the results to various analyses. The work was also aimed at defining a basis for further research. In the laboratory, granular columns of fixed length in floating and end-bearing conditions were formed in clay and deformed under rapid undrained conditions by various model scale foundation configurations.

1.4 PREVIOUS STUDIES

A single isolated granular column is the basic unit of any group and various authors have presented methods of analysis to predict its behaviour. The methods have been concerned with ultimate bearing capacity (Greenwood, 1970; Greenwood, 1972; Jones, 1972; Thorburn, 1975; Hughes and Withers, 1974), settlement (Hughes et al, 1975; Brown et al , 1979) or predicting the entire load-settlement response to failure (Hughes et. al, 1975; Balaam et al, 1976; Rowe et al, 1977).

A number of authors (Greenwood, 1972; Bauman and Bauer, 1974; Wong, 1975; Priebe, 1976; Brauns, 1978; Billam, 1981; Balaam and Booker, 1981) have extended their studies to large arrays of columns subject to uniformly distributed loads. Line loads have been considered by Thorburn and MacVicar (1968), Greenwood (1970 and 1972), Madhav and Vitkar (1978) and Priebe (1976).

1.5 BEARING CAPACITY OF SINGLE COLUMNS

Brauns (1978) suggested three possible failure modes for a single isolated granular column, illustrated in Figure 1.2, as being radial bulging, shearing of the column or a 'rigid' pile action. Watt et al (1967) had earlier considered a column to act as either a slightly flexible friction pile restrained by the passive resistance of the surrounding soil as the granular material bulged

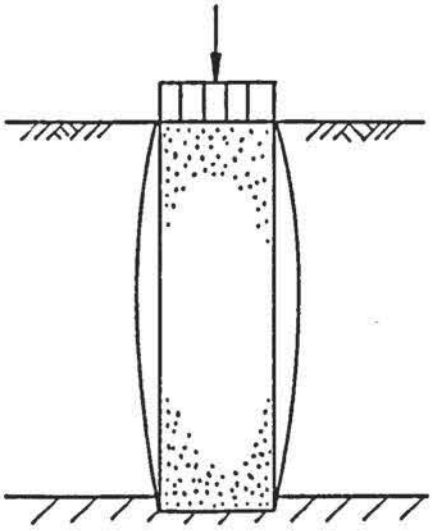

(a) Bulging

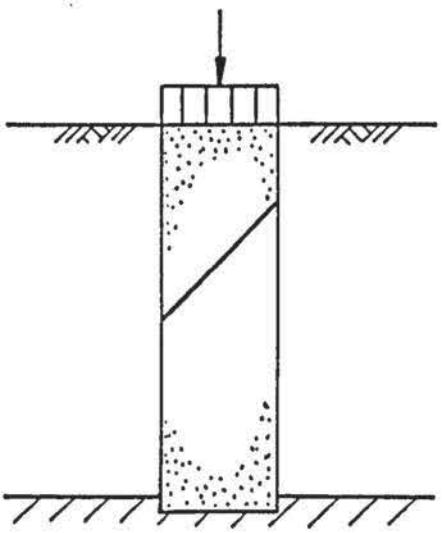

(b) Column shear

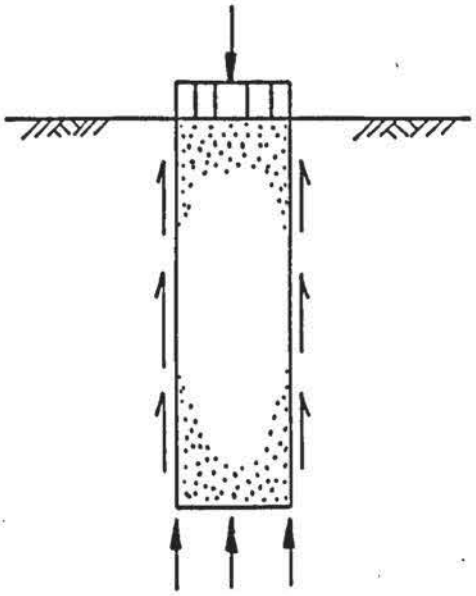

(c) Rigid pile

Possible modes of failure of a single isolated granular column under rapid loading (after Brauns, 1978).

FIGURE 1.2

laterally underload, or as a kind of shear pin providing an increase in the average shearing resistance along a possible slip plane. The belief was largely that columns acted in a bulging mode.

This philosophy was adopted by the Cementation Company as the basis for design, being later supported by model tests carried out by Dullage (1969). Greenwood (1970) outlined the resulting design procedure, describing it as "as primitive approach giving conservative results". The theory of Bell (1915) was used to determine the passive resistance of the ground to the laterally expanding column such that for a uniform clay with undrained cohesion c_u and unit weight γ, the passive resistance σ_p is given by:

$$\sigma_p = \gamma.z.K_p + 2\,c_u\sqrt{K_p} \qquad (1.1)$$

$$= \gamma.z + 2\,c_u \quad (\text{for } c_u > 0;\ \phi_u = 0)$$

where z is the depth below ground level and K_p is Rankine's coefficient of passive pressure for the clay. By assuming the column material to have yielded, the vertical stress on the column σ_{vc} is a principal stress. For a column material with an effective angle of internal friction ϕ', Eqn. 1.1. becomes:

$$\sigma_{vc} = \sigma_p \,.\, K_{pc} \qquad (1.2)$$

where

$$K_{pc} = (1 + \sin\phi')/(1 - \sin\phi')$$

The Bell analysis was not modified for radial strain.

A notable contribution was made by Hughes and Withers (1974) in reporting the results of experiments using model granular (sand) columns in clay. Stress-displacement characteristics, using a model foundation equal to the column diameter, were measured together with internal displacements of the column and clay. The latter was achieved by taking successive radiographs of lead-shot markers, set in the central vertical plane of the column and clay. It was found that if the column was of sufficient length to prevent a rigid-pile mode failure (in their case four column diameters), a column fails by axi-symmetric bulging near its top, shown in Figure 1.3. The depth to the position of maximum bulging was found to be about one column diameter, which

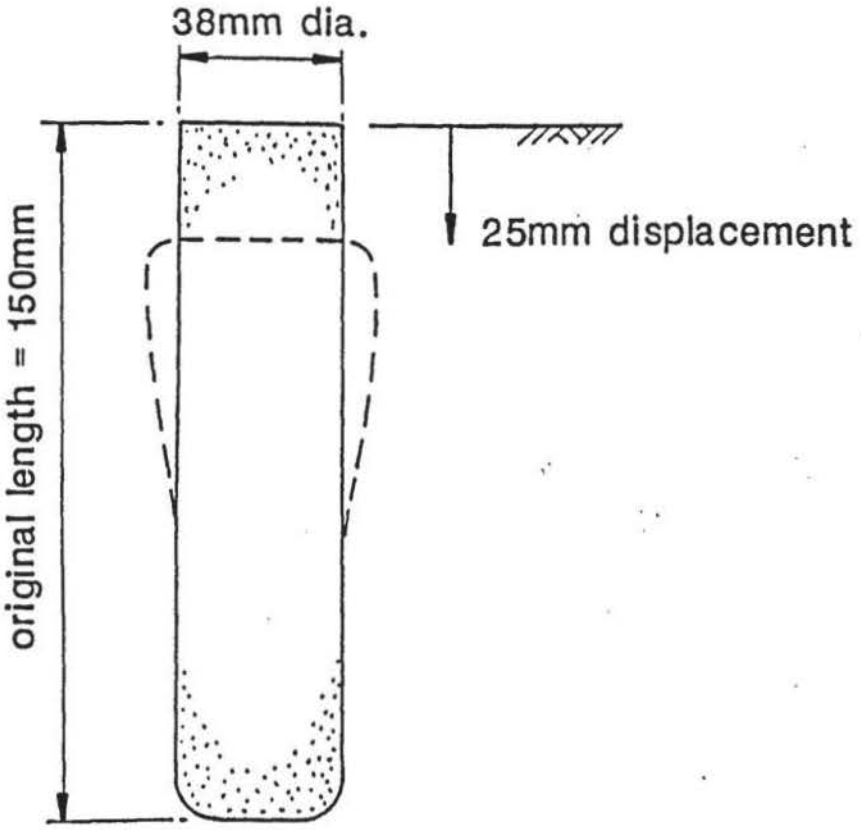

Axi-symmetric bulging at the top of a granular column (after Hughes and Withers, 1974).

FIGURE 1.3

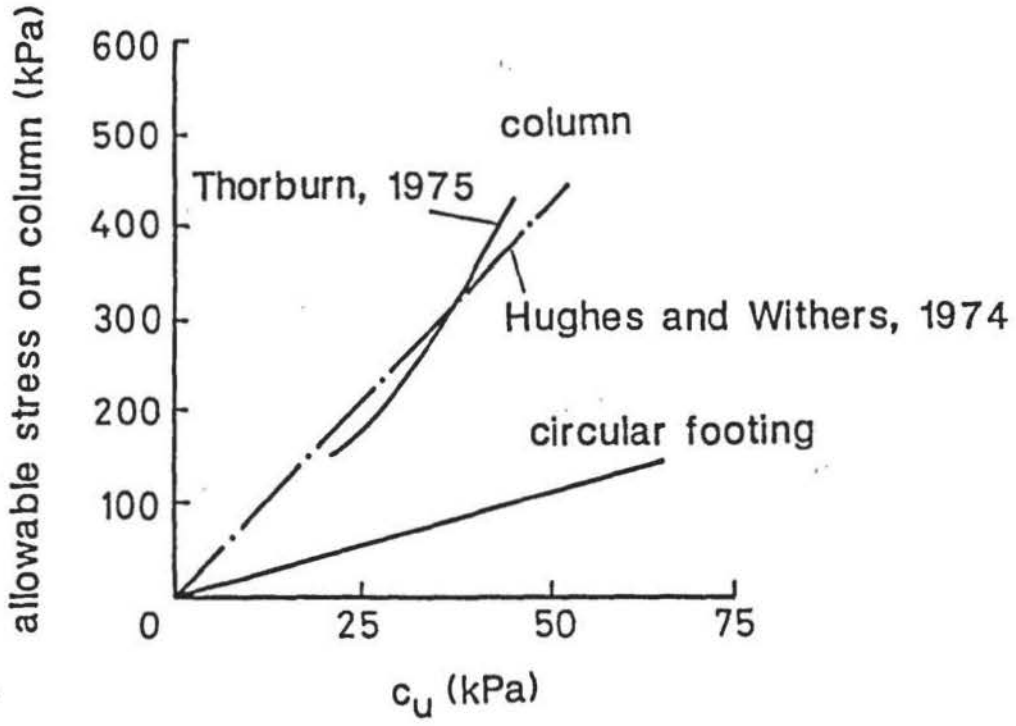

Comparison of allowable stresses on single granular columns (after Thorburn, 1975).

FIGURE 1.4

broadly agreed with one to one-and-a-half the column diameter reported by Dullage (1969) and Williams (1969) in earlier model scale experiments.

Observations of the limits of radial expansion at ultimate load suggested that columns would act independently when placed more than two-and-a-half diameters apart. The ulitmate load carrying capacity of a column was found to be governed by the maximum radial reaction of the clay around the bulging zone. Dullage (1969) had also reported earlier that column bearing capacity increased with increasing density of the column material.

In their analysis, the condition was idealized as one of failure by considering the expansion of a cylindrical cavity in the clay, as in a pressuremeter test. An expression derived by Gibson and Anderson (1961) to determine the limiting radial stress σ_{rl} at the boundary of a cylindrical cavtiy, in an elasto-plastic material, was simplified on the basis of many undrained pressuremeter field tests (Wroth and Hughes, 1973) to:

$$\sigma_{rl} = \sigma'_{ro} + u + 4\,c_u \qquad (1.3)$$

where u is the pore water pressure and σ_{ro}' is the effective in-situ lateral stress.

If the granular material in the bulging region at the top end of the column has yielded, then:

$$\sigma'_{vc} = \frac{(1 + \sin\phi')}{(1 - \sin\phi')} \cdot \sigma'_r \qquad (1.4)$$

where

ϕ' is the angle of internal friction of the column material under drained conditions.

σ_{vc}' is the effective vertical stress at the top of the column (a principal stress).

σ_r' is the effective radial stress at the column boundary.

By equating Eqn's 1.3 and 1.4, the ultimate vertical stress that the column can carry in the bulging mode is:

$$\sigma'_{vc} = K_{pc}\,(\sigma_{ro} + 4\,c_u) \qquad (1.5)$$

where

$$K_{pc} = \frac{(1 + \sin \phi')}{(1 - \sin \phi')}$$

It is evident from Eqn. 1.5 that σ_{vc}' is strongly dependent upon the magnitude of the initial (or at rest) horizontal stress in the soil.

The critical length L_c of a column required to prevent rigid-pile mode failure was determined from the side shear resistance and end-bearing force:

$$P = c_u A_l + N_c . c_u A_c \qquad (1.6)$$

where

P is the ultimate column load.

N_c is the appropriate bearing capacity coefficient (taken as 9).

A_l is the surface area $\pi D L_c$ of the column of diameter D.

A_c is the column cross-sectional area $\pi D^2/4$.

This suggests that a column length greater than L_c would not increase the load carrying capacity.

The ultimate σ'_{vc}/c_u value of 22 obtained experimentally by Hughes and Withers compared favourably with the calculated value of 25.2. The latter, however, was determined using undrained parameters whilst the tests were done under drained conditions, by allowing sufficient time for excess pore water pressures to dissipate after each loading stage.

Although a number of idealisations were made in proposing their analysis, the method has considerable value. In practice, however, the determination of the in-situ lateral stress and c_u value are more problematic.

Thorburn and MacVicar (1968) also considered a bulging mode of deformation and they developed a semi-empirical approach to predict the load carrying capacity which was presented by Thorburn (1975) for general use in preliminary design. Figure 1.4 compares the allowable vertical stress on a column using Eqn. 1.5 and a factor of safety of 3, with those of Thorburn. The comparison shows close agreement between the two curves, which when compared with the

calculated allowable stress on a circular footing shows a bearing capactiy increase of about 4 (i.e. σ_{vc}/σ_v footing $\approx$ 4).

Hughes et al (1975) described the loading of a full scale isolated granular column to verify the theoretical work of Hughes and Withers (1974). Prediction of ultimate load was found to be excellent providing the in-situ lateral stress and column diameter were accurately determined.

By comparison, the ultimate load determined by Bell's theory (Eqn. 1.1) was roughly 40% less than that obtained using the Hughes and Withers approach. The field test took about 30 minutes and was, therefore, considered to have been essentially undrained.

In field tests undertaken by Jones (1972), bulging was found to have a significant effect on load carrying capacity, with over 50% of the axial load being transferred from the column to the clay within a depth of one column diameter. This behaviour was also noted by Brown et al (1979). Jones suggested that prevention of bulging in weak surface soils, by casing or grouting the upper portion of the column, may substantially increase bearing capacity. A similar effect, however, could be achieved by founding at deeper levels below the ground surface where lateral resistance due to overburden (and in some cases soil shear strength) is greater.

Another approach, similar to one used by Steinfield (1953), was adopted by Brauns (1978) by considering a column shear mode. The mechanism is detailed in Figure 1.5 and the soil surrounding the column was considered as entirely cohesive ($\phi_u = 0$) and weightless. The resulting expression for the ultimate vertical stress on the column is :

$$\sigma_{vc} = \left[\frac{2}{\sin 2\delta}\right] \left[1 + \frac{\tan \delta_s}{\tan \delta}\right] c_u.K_{pc} \qquad (1.7)$$

where

δ_s is $(45^o + \phi'/2)$

δ is the angle to the horizontal of the shear surface of the truncated cone of clay.

with magnitude of δ being found, by trial and error, from the relationship:

$$\tan \delta (\tan^2 \delta - 1) = 2 \tan \delta_s \qquad (1.8)$$

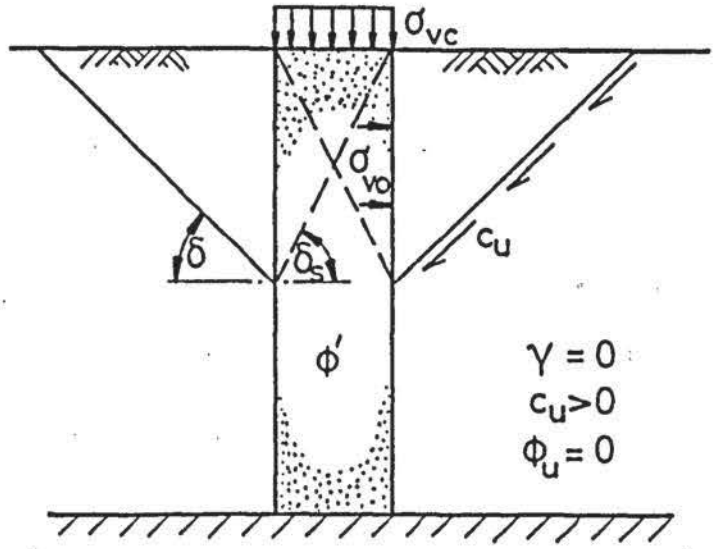

Mechanism for column shear failure mode (after Brauns, 1978).

FIGURE 1.5

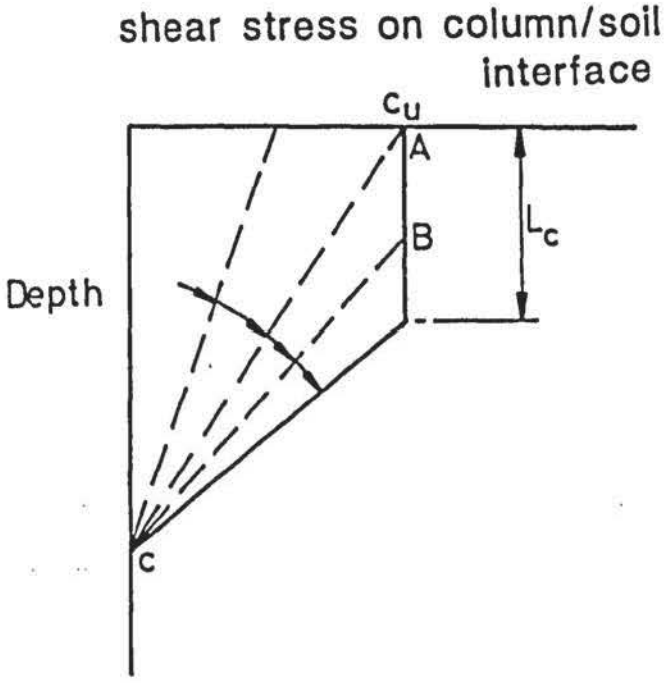

Idealised build up of shaft friction on a single granular column (after Hughes et al, 1975)

FIGURE 1.6

There is, however, no supporting evidence, from either laboratory or field tests, that this mode of failure occurs.

1.6 SETTLEMENT OF SINGLE COLUMNS

Because the vibroreplacement process is more often applied in practice to reduce potential settlement, methods of settlement prediction are of primary importance.

By assuming the radial expansion of a column to occur at constant volume (i.e. no dilation) and K_{pc} having a constant value during loading, Hughes et al (1975) also outlined a way of predicting settlement for a single column. It was noted that whilst these assumptions were not strictly correct, in practice the inaccuracy was found to be small when compared with the accuracy of establishing the soil and column parameters.

In the method the column is divided into n layers of thickness H, and its compression is calculated from the equation:

$$\delta = 2H.\frac{\delta r}{r} \qquad (1.9)$$

where $\delta r/r$ is the radial strain in the layer derived from pressuremeter curves for the surrounding soil of radial stress σ_r versus radial strain. The radial stress σ_{rc} at the column perimeter was taken as:

$$\sigma_{rc} = \sigma_r = \sigma_{vz}\, K_{pc} \qquad (1.10)$$

where σ_{vz} is the calculated vertical stress in the column layer at depth z. Total settlement ρ at the top of the column was found by summation:

$$\rho = \delta_1 + \delta_2 + \delta_3 \ ..... \ \delta_n \qquad (1.11)$$

The influence of the column diameter and side shear were found to be critical. Settlement was overestimated if side shear was neglected since the growth of the column-soil shear zone directly influences the distribution of vertical stress within the column. Referring to Figure 1.6, it was assumed that side shear increased to a maximum value of c_u, at the top, with the applied load. With the progressive increase of load the shear would reach the maximum value and decrease

linearly with depth (points ABC in Figure 1.6). At failure, it was taken that the full shear strength would be mobilised over the critical depth L_c.

In the calculation of column diameter, at depth z, it was assumed the column could not bulge unless the in-situ lateral stress was exceeded. This assumption was justified on the basis of results from pressuremeter tests. Using these assumptions an excellent correlation with the observed settlement, beyond the working load range, was obtained.

Based on the results of a parametric finite element study using hyperbolic stress-strain curves for the column and soil materials, Brown et al (1979) suggested undrained settlement ρ of a single column of diameter D up to working loads could be approxmated by the equation:

$$\rho = \sigma_{vc} D/ (C. \tan \phi' c_u/\sigma') \qquad (1.12)$$

where σ_{vc} is the applied vertical stress on the column

C is the empirical settlement coeficient (C = 70 MPa for undrained loading).

ϕ' is the effective angle of internal friction of the column material.

c_u is the soil undrained cohesion.

σ' is the effective overburden stress.

Using finite difference analyses, based on linear elastic theory, in a study of compressible conventional piles (e.g. concrete, steel) Mattes and Poulos (1969) derived an expression for the settlement ρ at the top of a single compressible pile in a semi-infinite mass subject to an axial load P as:

$$\rho = \frac{P}{E_s L} . I_p \qquad (1.13)$$

where E_s is Youngs modulus of the soil ($E_s = E_u$ in the undrained state).

L is the pile length.

I_p is the displacement influence factor related to the relative stiffnesses of the pile and soil.

The authors showed a major proportion of the long-term settlement occurred as immediate (undrained) settlement, particularly when pile-soil slip was allowed.

Although the analysis was not specifically devised for use with granular columns, Balaam and Poulos (1978) regarded the method as suitable for preliminary predictions.

1.7 LOAD-SETTLEMENT RESPONSE

The analyses of Hughes and Withers (1974), Hughes et al (1975) and Mattes and Poulos (1969) can be applied in predicting load-settlement response of a single granular column. The first method does require an accurate knowledge of radial stress-strain characteristics of the soil, which the authors suggest may only be obtained using the Cambridge type pressuremeter. This factor, restricts the general applicability of the method.

Details given by Hughes et al (1975) of the ground conditions and column parameters were used by Balaam and Poulos (1978) for inclusion in a finite element study for load-settlement prediction of a single column. Both the column and soil were treated as elasto-plastic materials. The analysis was originally devised by Balaam et al (1976) and extended by Rowe et al (1977) to include adhesive-frictional and frictional column-soil slip together with column dilation when slip occurs. Results from the finite element analysis are compared with those obtained from the methods of Hughes et al and Mattes and Poulos, and the observed field settlements in Figure 1.7. Calculated load and settlement are also tabulated in Figure 1.8, with the former including results from the Thorburn (1975) and Greenwood (1970) approaches.

The results emphasise the importance of column-soil slip in load-settlement prediction. Up to working loads (one third of ultimate), the finite element analysis gives excellent correlation whilst that of Mattes and Poulos marginally underestimates settlement. The method of Hughes et al is poor since no settlement is indicated until working loads are exceeded. Beyond this range, however, the Mattes and Poulos approach severely underestimates observed settlement, while that of Hughes, et al shows a better correlation. The conventional pile analysis by the former places greater emphasis on vertical pile movement in contributing to settlement than the effects from radial expansion. The latter authors assume settlement is due to lateral bulging only. This suggests that in the early stages of loading a single granular column the settlement behaviour is related to the

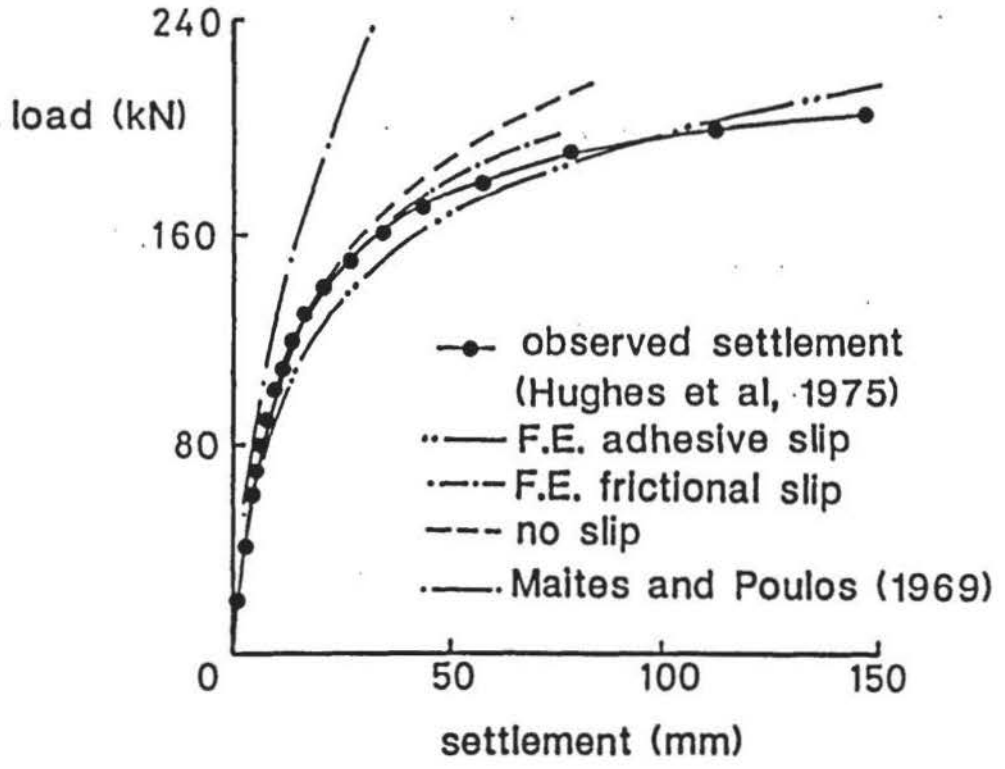

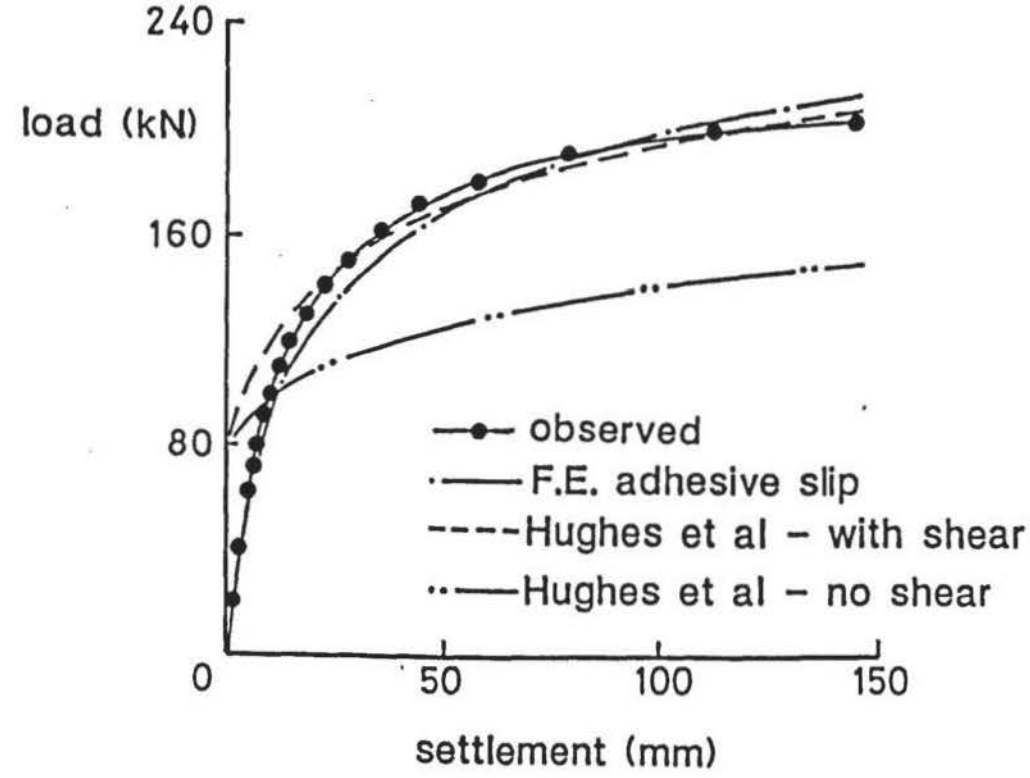

Comparisons of finite element analyses, Mattes and Poulos (1969) and Hughes et al (1975) (after Balaam and Poulos, 1978).

FIGURE 1.7

Method	Load (kN) at settlement of 100 mm	Remarks
Thorburn	193	F of S = 3 taken
Hughes and Withers	142 197	No allowance for shear. With allowance for shear.
Greenwood	154	σ_p taken at 2 m depth
Finite element	120 201 214 234	No granular column Adhesive slip Frictional slip No slip
Measured	200	

(a) Calculated and measured loads at 100 mm settlement (after Balaam and Poulos (1978).

Method	Settlement at load of 70 kN (mm)	Remarks
Mattes & Poulos	4.7	
Hughes et al	0	
Finite element	10.7 7.0 7.0 6.0	No granular Adhesive slip Frictional slip No slip
Measured	6	

(b) Calculated and measured settlements at 70 kN load

Comparison of calculated loads and settlements (after Balaam and Poulos, 1978).

FIGURE 1.8

vertical movement needed to mobilise shaft resistance, and the bulging mode becomes the predominant influence thereafter.

Close agreement was achieved with ultimate load prediction using the analyses of Thorburn, Hughes and Withers and the finite element methods. The latter also largely supported the bulging mode of failure by predicting the development and advance of progressive axi-symmetric yielding within the column and soil.

1.8 LARGE ARRAYS OF COLUMNS

Although columns in a large array may be spaced at sufficient distance to enable them to act independently of each other (Hughes and Withers suggested 2.5 column diameters apart) the application of a uniformly distributed load q over the whole area will induce stress in the columns σ_{vc} and surrounding soil σ_{vc}, as illustrated in Figure 1.9. The arrangement will also induce practically equal displacement of the columns and soil (Greenwood, 1972; Pilot, 1977; Vautrain, 1978; Balaam and Booker, 1981). This condition substantially modifies the column-soil shear stress distribution from that of a single isolated column. Field studies reported by Goughnour and Bayuk (1979b) showed that peripheral column shear stress remains low (0.3 c_u - 0.25 c_u).

Balaam and Poulos (1978) question whether the bulging mode is justified where a foundation, or ground slab, also applies pressure to the soil surrounding a column because the induced confining stress may alter the failure mechanism. A direct analogy with the triaxial compression test was made by Poteur (1973) by considering the columns and soil to be in a limiting state of equilibrium, with the maximum confining pressure of a soil cylinder ($c_u > 0$; $\phi_u = 0$) being equal to:

$$\sigma_{rl} = 2\ c_u + \sigma_{vs} \qquad (1.14)$$

This also corresponded to an earlier passive pressure approach by Greenwood (1970).

In the case of a single isolated column, $\sigma_{vs} = 0$ and $\sigma_{rl} = 2\ c_u$, which gives the limit bearing stress of the column as:

$$\sigma_{vc} = K_{pc}\ (\sigma_{ro} + 2\,c_u) \qquad (1.15)$$

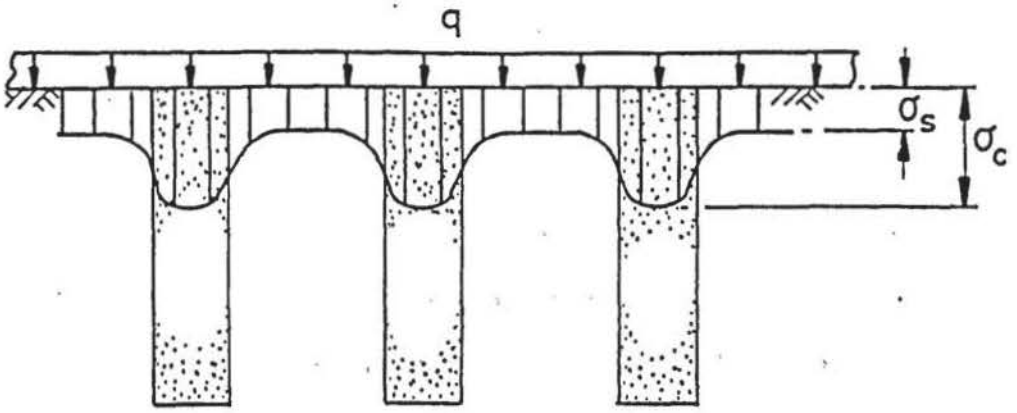

Application of uniformly distributed load q inducing column stresses σ_{vc} and soil stresses σ_{vs}.

FIGURE 1.9

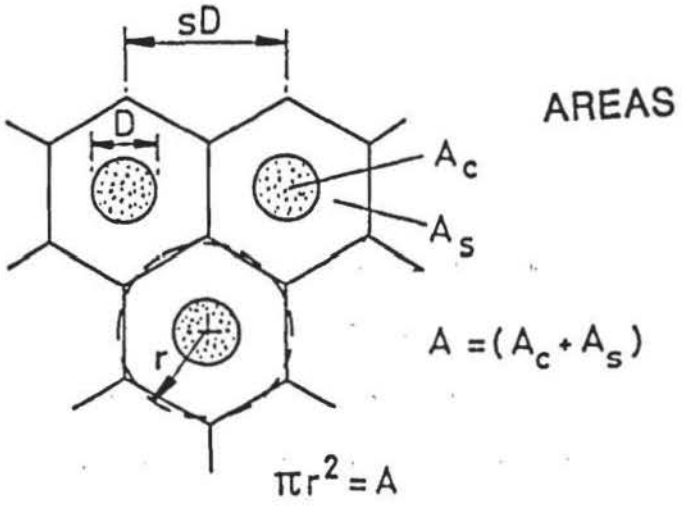

Areas of a unit cell in a large array.

FIGURE 1.10

where σ_{ro} is the in-situ lateral stress.

Comparison with Eqn. 1.5, of Hughes and Withers (1974) suggests that a complete analogy with the pressuremeter is unsupported.

Results from finite element methods and laboratory studies reported by Aboshi et al (1979) have shown failure of a composite material to be compressive, similar to triaxial compression, with yielding starting at depth and developing upwards.

The design approach by Greenwood (1970) and Brauns (1978) was to regard the applied uniform pressure q as increasing the lateral restraint to the columns by an amount $q.K_p$ (K_p = 1 when $c_u > 0$, $\phi_u = 0$) and for the columns to support the entire unit load, over area A:

$$qA = \sigma_{vc} . A \qquad (1.16)$$

Eqn. 1.2 was modified by Greenwood to account for the increased confining pressure:

$$\sigma_{vc} = (\sigma_p + q) K_{pc} \qquad (1.17)$$

with Eqn. 1.7 and 1.8, of Brauns becoming :

$$\sigma_{vc} = \left[q + \frac{2}{\sin 2\delta} \right] \left[1 + \frac{\tan \delta_s}{\tan \delta} \right] c_u . K_{pc} \qquad (1.18)$$

and

$$\frac{q}{2c_u} \tan \delta_s = - \left[\frac{\tan \delta + \tan \delta_s}{\tan 2\delta} + \frac{\tan \delta_s}{\sin 2\delta} \right] \qquad (1.19)$$

respectively.

Greenwood (1970) found the contribution of the applied pressure q to the lateral restraint was generally significantly greater than that due to the soil strength or in-situ lateral stresses. Consequently, the limiting load capacity of the column was governed by local shear failure in the soil or by column failure in the rigid pile mode. Greenwood (1970) and Nahrgang (1976) noted that columns at the periphery of an array undergo asymmetrical bulging due to the smaller lateral restraint in the unloaded area. The latter author also suggested that movement of soft soil away from the loaded area may also cause some lateral shift of the peripheral columns. In the case of a rigid foundation the problem is aggravated by high contact pressures occurring at the edge

(Greenwood, 1970; Tanimoto, 1973; Lubking et al, 1976). Greenwood (1970) proposed closer spacing of peripheral columns and for their bearing capacity be taken as a single isolated column.

Other methods of analysis have considered the relative distribution of q between the columns and surrounding soil, the latter being taken as isotropic and homogeneous. In the literature considered, the principle of superposition has been assumed by all the authors to apply to the composite material, such that:

$$qA = \sigma_{vc} A_c + \sigma_{vs} A_s \qquad (1.20)$$

and for the columns and soil to undergo equal vertical displacement.

1.8.1 Replacement Ratio

The relative sizes of the original column area A_c and soil area A_s of a unit cell in a large array, shown in Figure 1.10, have been shown to have a significant influence on the magnitudes and distribution of σ_{vc} and σ_{vs} (Greenwood, 1972; Bauman and Bauer, 1974; Wong, 1973; Goughnour and Bayuk, 1979a; Balaam and Booker, 1981). Aboshi et al (1979) defined the ratio:

$$a_c = A_c/(A_c + A_s) \qquad (1.21)$$

as the replacement ratio. The total area $A = (A_C + A_S)$ of a hexagonal unit cell is usually idealised by most authors as circular, having a radius r to give an area equal to A, for analytical simplicity. In terms of the replacement ratio a_C, Eqn. 1.20 becomes:

$$q = \sigma_{vc} a_c + \sigma_{vs} (1 - a_c) \qquad (1.22)$$

1.8.2 Stress Concentration

Greenwood (1972) suggested $\sigma_{vs} = f(q)$ and using the relationships described the following equation may be derived for a cohesive soil ($\phi_u = 0$):

$$\sigma_{vs} = xq = \frac{q - a_c\,(\gamma.z.K_{pc} + 2c_u\sqrt{K_{pc}})}{\left[(1-a_c) + a_c.K_{pc}\right]} \qquad (1.23)$$

after solving for the coefficient x, σ_{vs} can be determined and σ_{vc} found from Eqn. 1.22. The analysis, however, pays no regard to the column-soil stiffnesses. The ratio of the total vertical stress taken by the column σ_{vc} and the soil σ_{vs} at the surface has been defined by Aboshi et al (1979) as the stress concentration ratio n:

$$n = \sigma_{vc}/\sigma_{vs} \tag{1.24}$$

which in conjunction with Eqn. 1.23 gives the relationships for σ_{vc} and σ_{vs} as:

$$\sigma_{vc} = nq/[1+(n-1)\, a_c] = \mu_c\, q \tag{1.25}$$

$$\sigma_{vs} = q/[1+(n-1)\, a_c] = \mu_s\, q \tag{1.26}$$

where μ_c and μ_s were defined as the ratio of stresses on the column and soil, respectively. In reporting the results from field tests, Vautrain (1978) obtained values of n in the range of 2-3.

Bauman and Bauer (1979) derived an expression for n using elastic theory, which for a cohesive soil ($\phi_u = 0$) becomes:

$$n = \frac{1}{2\frac{E_s}{E_c} \cdot K_c \cdot \ln\left[\frac{2b}{D}\right]} + \frac{1}{K_c} \tag{1.27}$$

where b is $\sqrt{(A/\pi)}$

D is the column diameter

E_S is Young's modulus for the soil.

E_C is Young's modulus for the column.

K_C takes a value between the at-rest and active pressure coefficient $(1-\sin\phi')/(1+\sin\phi')$ of the column material.

Also using elastic theory, Priebe (1976) developed a relationship for n as:

$$n = 1 + a_c\left[\frac{0.5 + f}{K_{ac}\, f} - 1\right] \tag{1.28}$$

where K_{ac} is the active earth pressure coefficient for the column material $(1-\sin\phi')/(1+\sin\phi')$ and f is:

$$\frac{1-\nu^2}{1-\nu-2\nu^2}\cdot\frac{(1-2\nu)(1-a_c)}{1-2\nu+a_c} \qquad (1.29)$$

ν is Poisson's ratio (a value of $\nu = 1/3$ was suggested as suitable in consideration of the accuracy limitations contained in the assumptions made in deriving Eqn. 1.29).

The analysis allows for the elastic expansion of the column. For values of $a_c = 0.5$ to 0.25, corresponding values of n obtained from Eqns. 1.27 and 1.28 are in the range 4 to 2, respectively.

1.8.3 Settlement

Since the vertical displacement of the columns and soil are almost the same, Greenwood (1972) considered overall settlement could be estimated by conventional means from the average stress on the soil σ_{vs} between the columns. This method, however, precludes any stiffening effect offered by the columns. Bauman and Bauer (1974) adopted the elastic approach where immediate settlement ρ is obtained from:

$$\rho = \frac{D}{E_s}\cdot\sigma_{vs} \qquad (1.30)$$

where D is the column diameter

E_s is the soil Young's modulus

σ_{vs} is obtained from Eqns. 1.27 and 1.26.

By assuming no lateral expansion to occur at working stresses, Billam (1981) considered the overall effect of the columns and soil in terms of a settlement coefficient m, this being the ratio of settlement with columns ρ and without columns ρ_o such that:

$$m = 1/\left[R_m.a_c + (1 - a_c)\right] \qquad (1.31)$$

where R_m is either the ratio of the coefficients of compressibility or Young's moduli for the column and soil (i.e. $m_v$soil/m_v column or E_c/E_s).

An alternative approach was proposed by Wong (1975) in predicting column loads for settlements which were termed small (25 mm), medium (50mm) and large (100-200 mm). It was argued that in the initial stages of loading a column behaved as bin or silo, with horizontal stress rapidly decreasing with depth, which mobilised a small proportion of the maximum passive resistance of the soil. With increasing settlement bulging of the column increases, which is aided by dilatancy of the column material, the greatest effect being at the surface. As settlement progressed further, full mobilsation of the lateral soil resistance is achieved. The effect of radial yield is to transfer greater load down the length of the column.

For purely cohesive soil ($\phi_u = 0$), equating column-soil horizontal stresses at the surface for small settlements gave:

$$\sigma_{vc} = (\sigma_{vs} + 2\,c_u)/K_{ac} \qquad (1.32)$$

where σ_{vs} is equal to the uniformly applied pressure q.

For medium settlements, equating horizontal stress over a column length of 1.5D from the surface:

$$\sigma_{vc} = \left[(\sigma_{vs} + 2\,c_u) + 3\,D.\gamma\right] / (1 - 3D/L) \qquad (1.33)$$

where L is the total length of a column of diameter D.

For large settlements, considering horizontal stresses over the total column length:

$$\sigma_{vc} = 2\left[(\sigma_{vs} + 2\,c_u = 6D) + 6D.\gamma(1 - 3D)\right] / K_{ac} \qquad (1.34)$$

To avoid local shear failure of soil due to shear stress exceeding c_u, limits on the value of σ_{vs} were suggested by Wong to be πc_u, $1.5\pi c_u$ and $3\pi c_u$ for small, medium and large

settlements, respectively. The value of K_{ac} for small settlement, in which negligible vertical shear stresses at the boundary would enable the vertical and horizontal stresses to be taken as principal stresses, was taken as $(1-\sin\phi')/(1+\sin\phi')$.

For large settlements, where considerable re-orientation of the principal planes would have occurred, $K_{ac} = (1 - \sin^2 \phi')/(1+ \sin^2 \phi')$ with an average of the two values being taken for medium settlement.

Good agreement was obtained when calculated values were compared with observed load-settlement characteristics in twelve case histories.

1.9 SMALL GROUPS OF COLUMNS

Small groups of columns may be considered as a special case of a large array. Greenwood (1972) considered the bearing pressure applied by a small foundation will not be as uniform as over a widely loaded area and also its effect will diminish rapidly with depth. The principle of superposition may, therefore, not be applicable. The effects on peripheral columns, previously referred to, would broadly apply to all columns in a small group.

In the case of a line load (strip foundation), Greenwood (1970) suggests that the discontinuity of the pressure applied by the foundaton to the soil is of little consequence to the ultimate bearing capacity of a column. This view is supported by Thorburn and MacVicar (1968). Indeed, close spacing of columns may cause them to act as a granular trench which lends support to Greenwood's passive earth pressure approach. Carrying this idea further, Madhav and Vitkar (1978) have presented a parametric study of bearing capacity factors for a strip foundation on a granular trench in clay, based on the general shear failure mechanism shown in Figure 1.11. The analogy is with a plane-strain variation of a granular column with the ultimate vertical stress q_{ult} expressed in the form:

$$q_{ult} = c_u N_c + (\gamma B/2) N_\gamma + D.\gamma.N_q \qquad (1.35)$$

Use of the equation shows a potential increase in bearing capacity by a factor of 2.5-3.

Greenwood (1972) and Wong (1973) describe the results of a full scale field test undertaken to study the contact pressure distribution between two columns and the soil. Figure

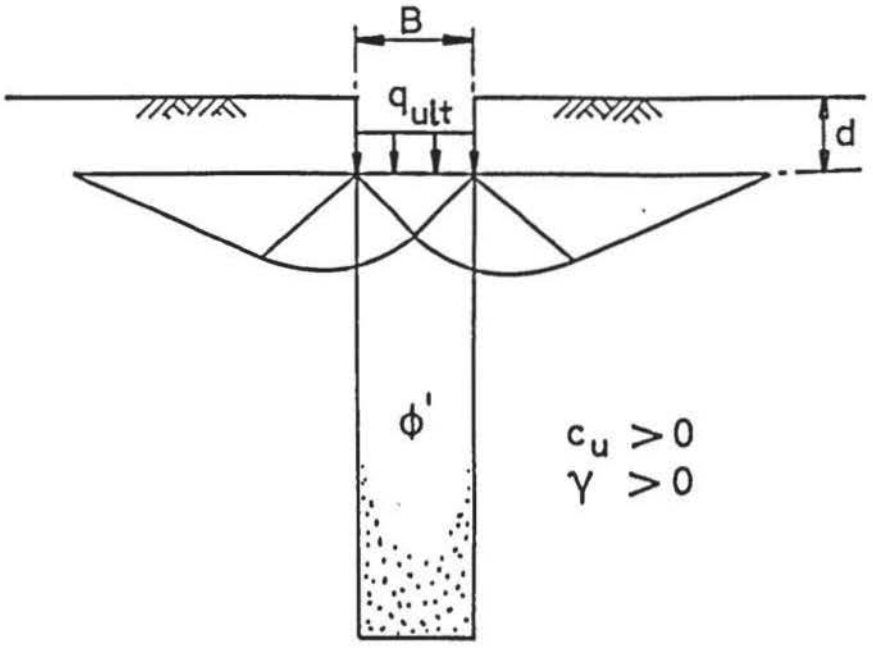

General shear failure mode of a granular trench (after Madhar and Vitkar, 1978).

FIGURE 1.11

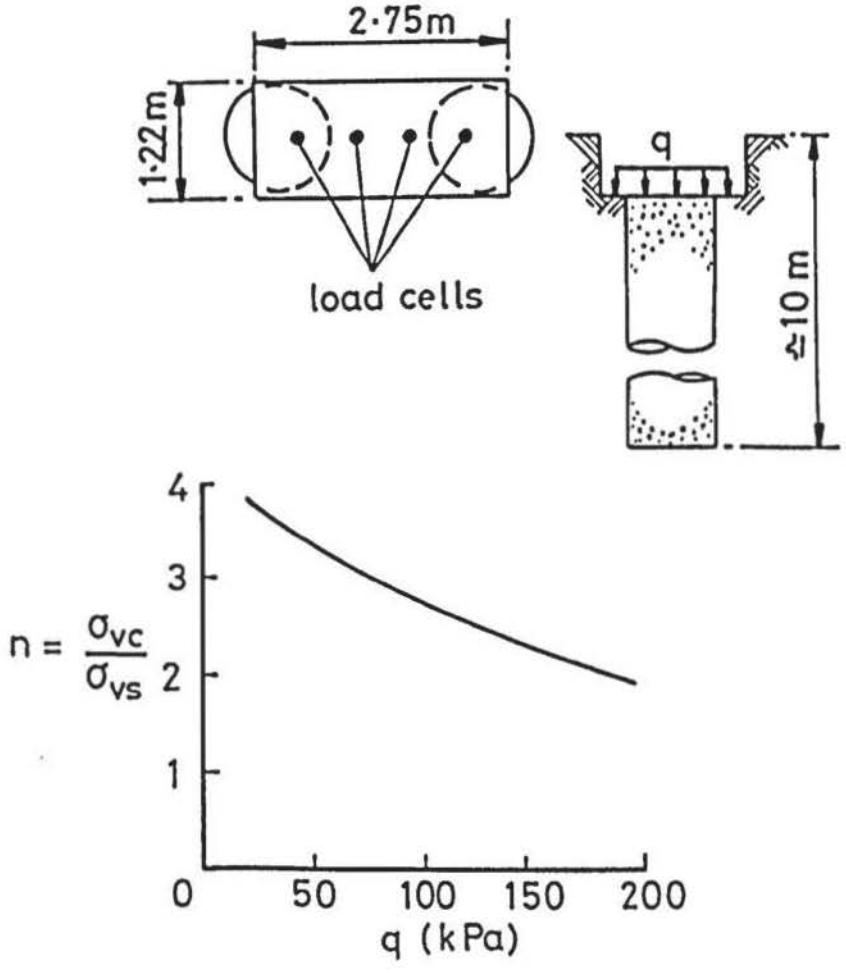

Contact stress distribution beneath a rectangular footing (after Greenwood, 1972).

FIGURE 1.12

1.12 illustrates the method and shows the behaviour of a pre-cast concrete footing containing pressure transducers loading the columns constructed in a sandy silt-sized industrial waste. The results show the soil to take an increasing share of the applied pressure q, with the contact stress becoming more uniform with higher pressures. It is to be noted, however, that the sandy silt may have been somewhat densified under the action of the vibroflot. This effect would be to reduce the stress concentration factor n.

The results of small scale laboratory tests, using five 50 mm diameter granular (sand) columns in an oil-kneaded clay loaded by a circular plate, are given by Aboshi et al (1979). The variation of n with loading intensity q, at depths of one and four column diameters, are shown in Figure 1.13. The general trend of n decreasing with q is similar to that reported by both Greenwood and Wong, with higher values of n being recorded at depth. Aboshi et al showed the magnitude of n to be limited by the relationship:

$$n \leq \frac{(1 + \sin\phi')}{(1 - \sin\phi')} \cdot (1 + 2\, c_u/\sigma_{v_s}) \qquad (1.36)$$

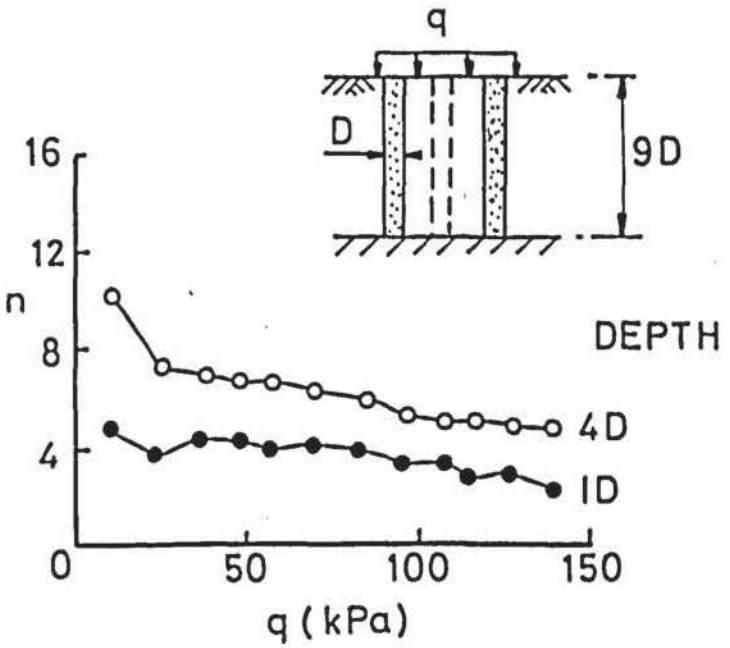

Variation of n with q from model tests (after Aboshi et al, 1979).

FIGURE 1.13

CHAPTER 2

MATERIALS

2.1 INTRODUCTION

Reduced scale laboratory tests required the selection of a suitable granular material for the columns and a cohesive material in which they were to be formed. The latter proved more problematic in terms of achieving the desired repeatability and testing time.

2.2 GRANULAR MATERIAL

Leighton Buzzard sand was chosen as the material for the columns. This was because the particle size and grading were suitable with reference to forming high density samples by pouring techniques, for the tests, and because of the wide experience of its use in soil mechanics.

2.2.1 Specification

The sand is a rounded quartz material with a mean roundness of 0.5 and mean sphericity of 0.84 (Wadell, 1933). Values of the maximum and minimum void ratio (e) obtained by the methods of Kolbuszewski (1948a) were 0.79 and 0.49, respectively. Hope (1979) obtained a value of 2.66 for the specific gravity (G_S) of the material.

2.2.2 Grading

The sand was graded between B.S. sieve Nos. 14 and 25, with 60-65% passing the No. 18 sieve, using an 'Endicott' electro-mechanical shaker and about 2 kg of air-dried ungraded material each time. Each batch was shaken for a period of 45 minutes. The grading procedure, based on recommendations given by Suen (1982), removed contaminant debris and ensured consistency in the grain size distribution. After grading, the sand was stored in a container.

2.2.3 Shear Strength Tests

The shear strength of a sand, with a given mineral composition and grading, has been found to be significantly affected by the nature of the applied boundary stresses and deformation conditions. Cornforth (1964) has demonstrated that the effective angle of shearing resistance (ϕ') from triaxial plane-strain tests exceeds the angle obtained from conventional triaxial tests by as much as 4^{o} for very dense sand specimens (e = 0.52 to 0.54). Comparisons have also been made between the value of ϕ' from both the triaxial and direct shear apparatus. Taylor (1939) found values of ϕ' from the former were generally less (by about 2^{o}) than the latter, particularly for dense samples. It is important, therefore, to use a method of testing 'elemental' sand samples that best characterises the likely stress-strain environment to which the main body of sand will be subject.

Triaxial compression equipment was considered the most appropriate means to determine stress-strain parameters of the sand used to form the columns, because of their axi-symmetric form.

2.2.4 Triaxial Tests

Drained, strain controlled, compression tests with volume change measurements were performed on, nominally 38 mm diameter and 76 mm high, air-dried samples of the graded sand using standard laboratory equipment supplied by Wykeham Farrance Limited. The samples had an initial mean void ratio (e_o) of 0.54 and were formed by a pouring technique using the same equipment which formed the granular columns and described later in Section 4.10.8. The tests were carried out at a range of cell pressures (σ'_3) in accordance with the procedures outlined by Bishop and Henkel (1962). Corrections were applied to account for the effects of the rubber membrane on the strength of the contained sand. Since the shear strength of sand in triaxial compression is practically insensitive to the rate of strain for the range of confining pressures used (Whitman and Healy, 1963), a convenient rate of vertical compression of 2.5 mm/min. was adopted.

2.2.5 Relevant Characteristics

Selected results from the triaxial tests are shown in Figures 2.1 to 2.4 in terms of effective stress.

2.3 COHESIVE MEDIUM

2.3.1 Fundamental Considerations

Vibroreplacement is a technique of forming dense granular columns in predominently cohesive soils. The method is used in cohesive materials of low shear strength or high compressibility such as normally and lightly over-consolidated clays or fills. A prime concern in laboratory soil model testing is for conditions that are homogeneous and repeatable.

Wet clay soils do not easily meet these requirements and so a compromise has often been adopted in other model testing research.

2.3.2 Remoulded Clays

Numerous researchers have made use of remoulded clays for laboratory investigations into the behaviour of shallow foundations (e.g. Meigh, 1950; Meyerhof, 1951); piled foundations (e.g. Whitaker, 1960; Saffery and Tate, 1961); granular columns (e.g. Dullage, 1969; Dodd, 1979).

The process of remoulding involves mechanically re-mixing clay samples with water to obtain a desired consistency and to subsequently knead or compact the mixture into a container for testing purposes. Clay samples have been obtained directly from natural deposits (London Clay has been popular) or indirectly, in a dry form, from that processed for industrial use (e.g. Kaolin, Ball clays, Bentonites).

In the present work, remoulded clays gave a number of distinct disadvantages. After remoulding, the shear strength increases with time and any disturbance causes a decrease in the strength gained. This phenomenon of thixotropy has been studied with a number of clay types by Seed and Chan (1959). London Clay used by Saffery and Tate (1961) for laboratory model pile group studies showed an undrained strength increase of 12% in two days with a further 2% increase two days later.

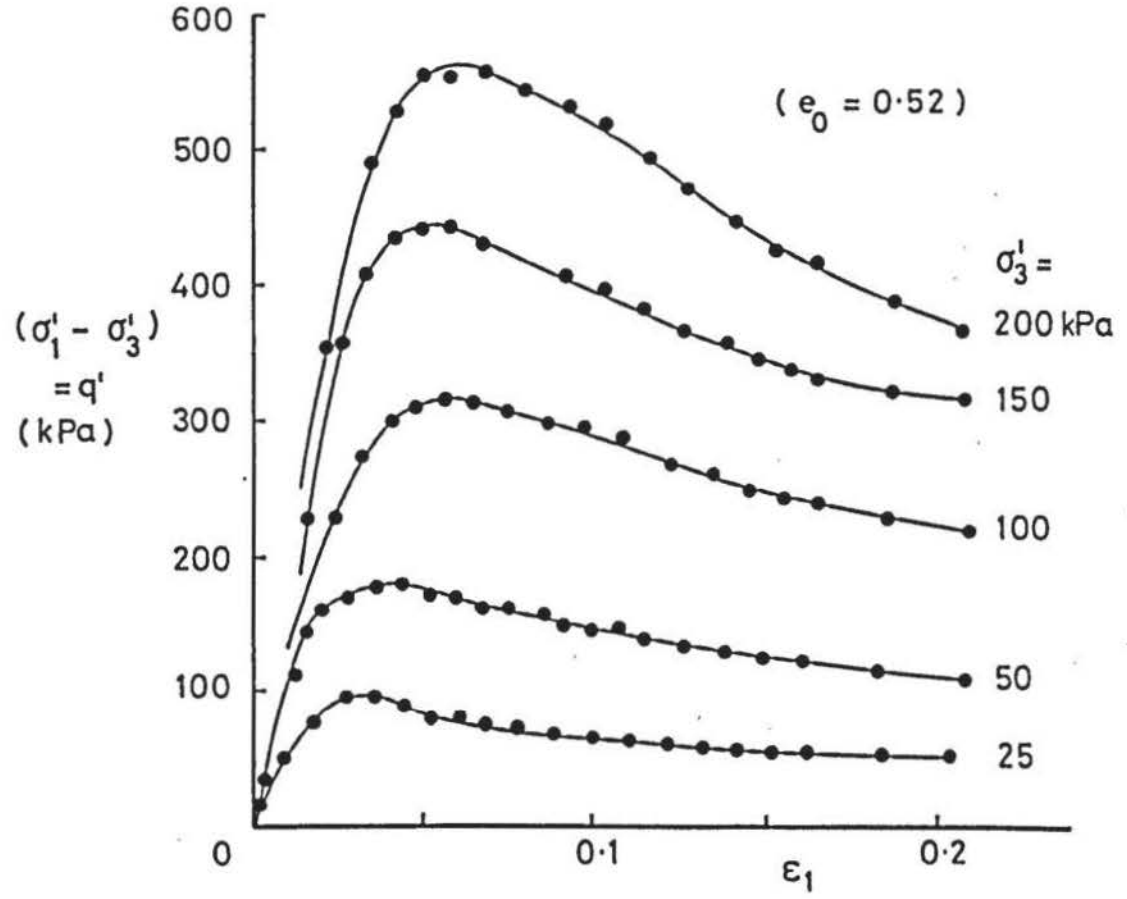

Stress-strain characteristics of air-dry Leighton-Buzzard sand obtained from triaxial compression tests at different cell pressures.

FIGURE 2.1(a)

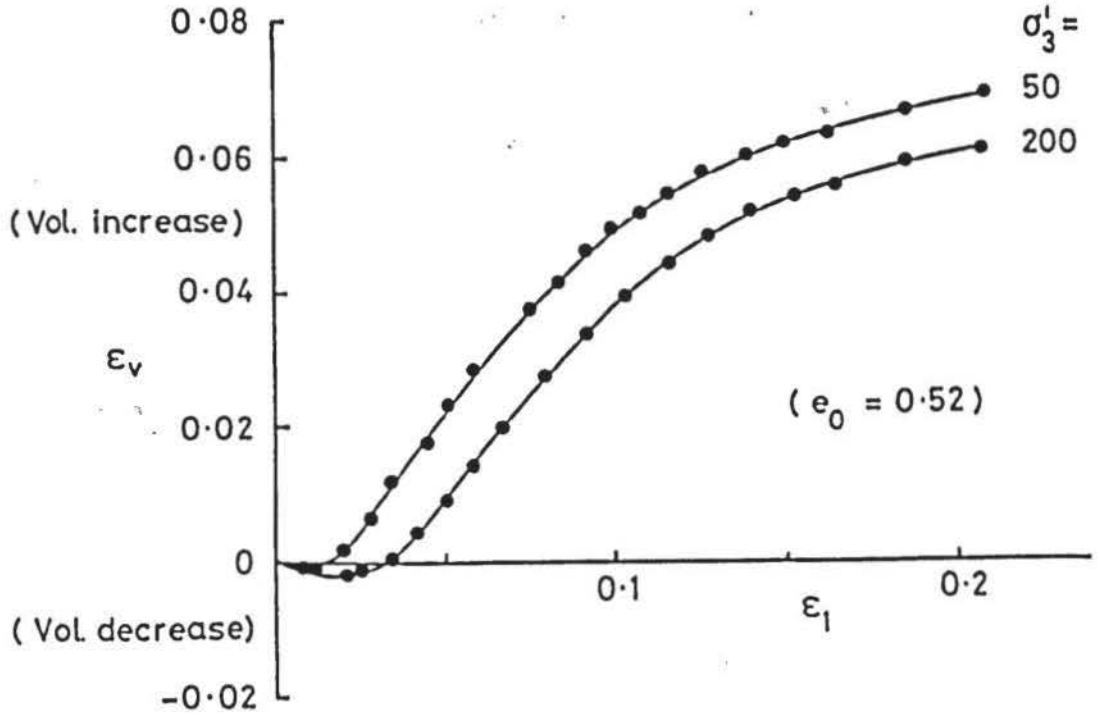

Examples of volumetric strain behaviour

FIGURE 2.1(b)

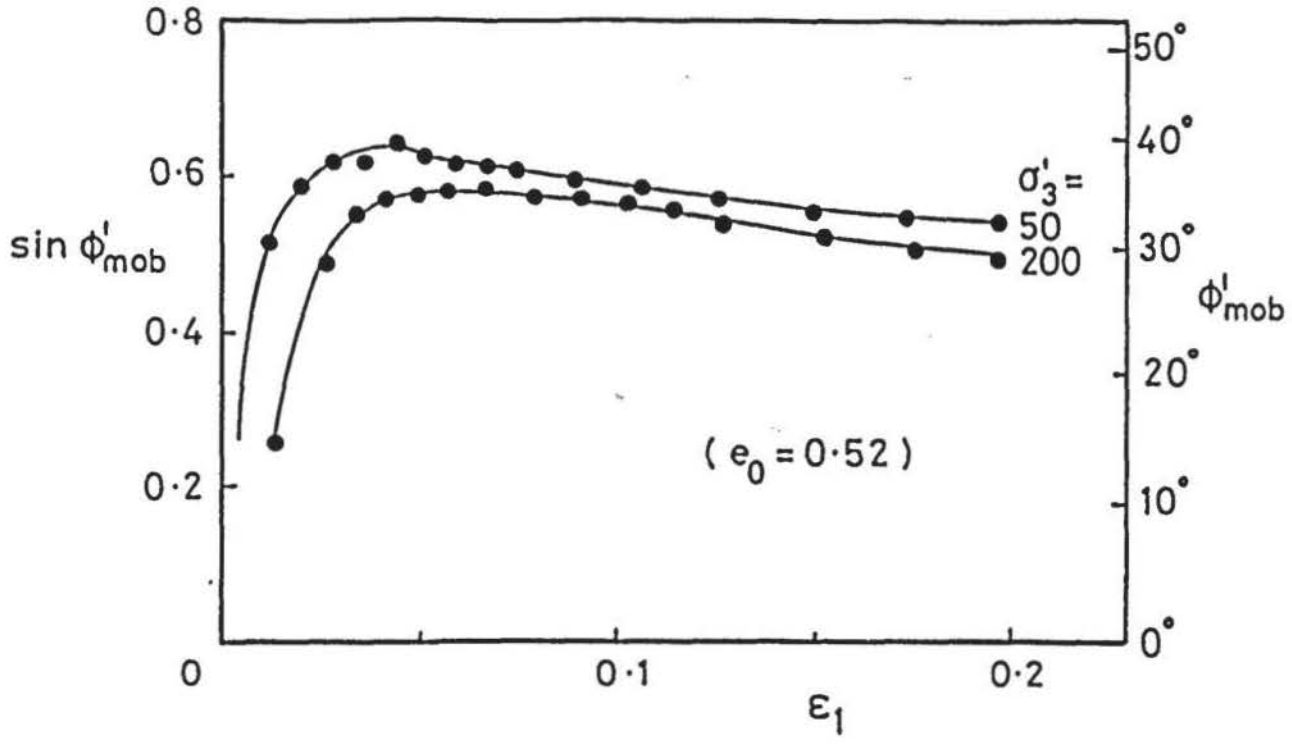

Examples of mobilisation of shearing resistance with increasing strain and confining pressure.

FIGURE 2.2

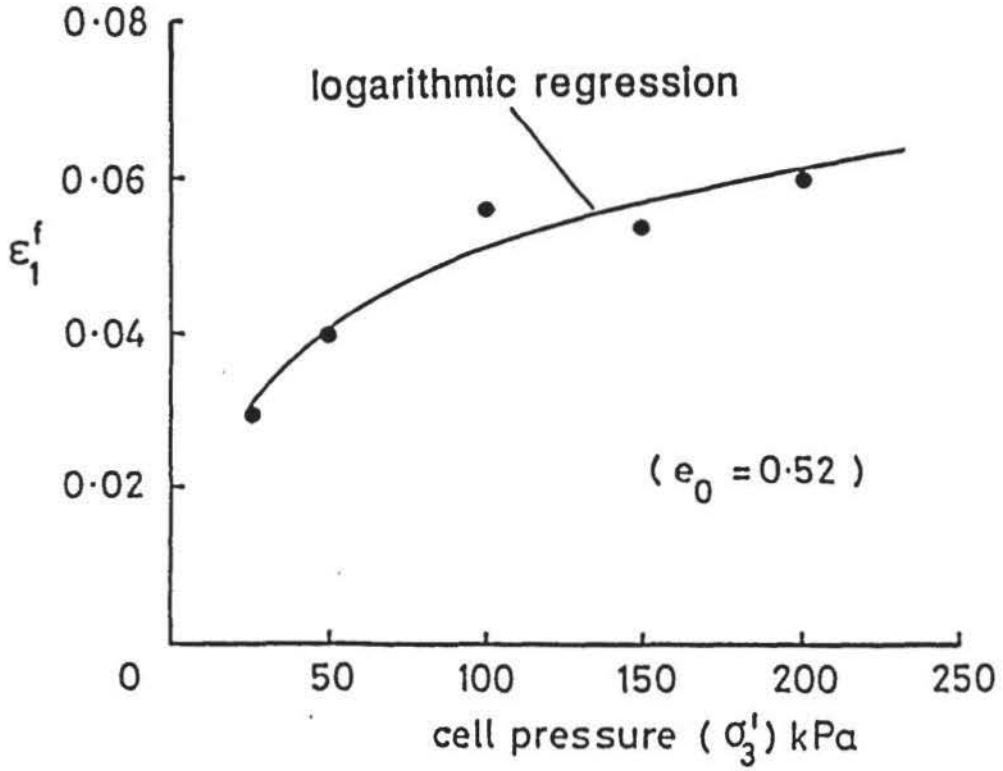

Variation of strain at which peak strength occurs with respect to confining pressure.

FIGURE 2.3

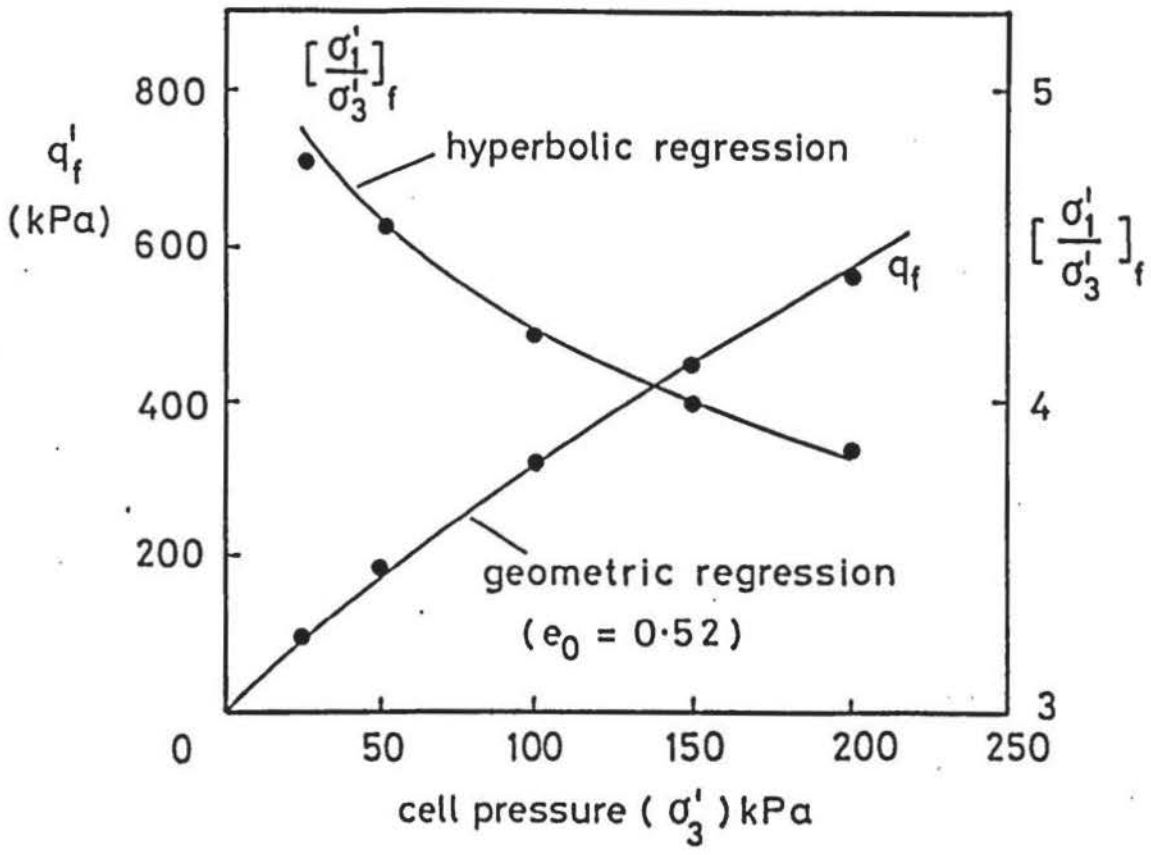

Variation of peak strength and peak principal stress ratio with confining pressure.

FIGURE 2.4

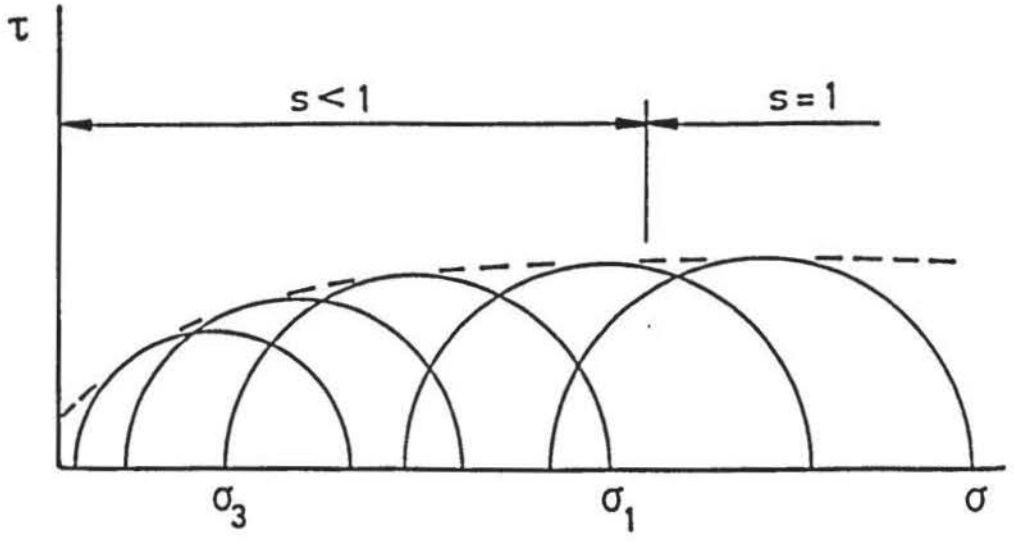

Typical quick-undrained multi-stage triaxial test results on initially partly saturated clay.

FIGURE 2.5

It has been common practice, therefore, to allow a period of 4-7 days to elapse after remoulding and installation of the model. This causes considerable delays in testing. Remoulding also results in a partly saturated soil. The undrained shear strength is affected by the effective stresses present in the soil skeleton and consequently it increases with confining pressure. This is illustrated in Figure 2.5. In recognition of this, Meigh (1950) and Meyerhof (1951) used unconfined compression test results to give an 'index strength' by assuming $\phi_u = 0$. However, a mass of remoulded clay after being left for a period of time, when subject to deformation, will develop latent non-uniformities as a result of the varying degrees of disturbance experienced throughout the material.

A wet clay surface is also subject to hardening through evaporation of the pore water. Since the literature indicates granular columns derive a significant part of their initial strength from soil near the surface, some way of adequately preventing moisture loss would be necessary.

2.3.3 Vacuum Extrusion

There can also be severe inhomogeneity in immediately remoulded soils due to uneven moisture distribution. Coyle and Shiffert (1968) used vacuum extrusion equipment to produce remoulded soils with small moisture content variations and high degrees of saturation. A minimum curing time after extrusion of a few days was still necessary to allow for thixotropy. Such equipment is costly and was not available for the author's use.

2.3.4 Saturated Clays

Saturated clays are an ideal medium as far as homogeneity and repeatability are concerned. They are obtained by remoulding clay at about twice its liquid limit and then subjecting it to compression until consolidation achieves the desired moisture content and shear strength. The process is not easily achieved in practice. This is illustrated by the following extract from Lewin and Burland (1970), describing the preparation of 36 mm x 75 mm triaxial samples, viz:

> "..... the oven-dried powder (clay) was mixed with a measured quantity of de-aired distilled water to a water content approaching twice the liquid limit. It was stirred intermittently for half an hour and then transferred to a bumping

apparatus where it was drawn through 1 mm jets under a section of 30 kPa and at the same time bumped once a second.

Bumping was continued for two hours since it was observed that, even after passing through the jets, the slurry still contained a few very small bubbles ..... The slurry was spooned in a 3.8 cm diameter Perspex mould with drained pistons at each end. After filling the 10 cm long mould, the outer cylinder was raised a few centimetres so that it acted like a floating ring oedometer with consolidation taking place symmetrically about the centre plane.

Three successive piston loads, corresponding to stresses of 12, 25 and 50 kPa ..... were applied at two hourly intervals. The final load was left for two days.....a check was made on the water content profile at this stage and showed that the samples had a moisture content that was 1.5% wetter at the middle than at the ends....."

The preparation of larger samples requires equipment capable of applying large loads and takes substantially longer since consolidation time is proportional to the square of the drainage path taken by the pore-water. For samples of the size and shear strength required for the present investigation the complete process would take between 2-3 weeks (James, 1980).

Further practical difficulties arise in foundation behaviour studies needing normally consolidated samples since release of the consolidation pressure results in a state of over-consolidation and induces negative pore-water pressures. This may be overcome using equipment that allows testing while maintaining an ambient stress level on the sample equal to the final consolidation pressure. Such specialist equipment was used by Hughes and Withers (1974) and is described by Burland and Roscoe (1969).

2.3.5 Synthetic Materials

Because of the significant practical disadvantages of clay-water materials, attention was given to using a synthetic cohesive substance. The most suitable was found to be a Bentonite/glycerine.

2.4 GLYBEN

2.4.1 Background

For reasons similar to those just described, Mayfield (1963) used a sodium bentonite (Fulbent 150) and glycerine mixture, termed glyben. Its shear strength decreased with increasing glycerine content and undrained triaxial test results showed almost fully saturated cohesive properties (i.e. $c_u > 0$; $\phi_u \approx 0$). The material exhibited no thixotropic properties of significance and over a period of about one and a half years maintained a relatively constant shear strength. Glyben with a mean value of c_u of 43 kPa was used and gave an estimated standard deviation (s) of 2.9 kPa over this period. Insensitivity to handling and low volatility of the pore fluid enabled the material to be re-used and allowed a higher number of tests to be performed. The surface of glyben samples was found, by Mayfield, to be slightly hygroscopic because the glycerine slowly absorbed atmospheric moisture.

Glyben has also been used successfully by Davie and Sutherland (1977).

2.4.2 Specification

After some preliminary tests, glyben was adopted for use in the laboratory investigation. It was prepared from constituents with the following specification, viz:

Wyoming (Sodium) Bentonite

98.7% passing B.S. No. 100 sieve

81.3% passing B.S. No. 200 sieve

60.9% passing B.S. No. 300 sieve.

The material had a specific gravity (G_s) of 2.5 and was obtained in 50 kg sealed bags.

Glycerine

Food solvent glycerol B.P. to B.S. 26521/5 (1965), was obtained in 5 gallon drums. It had a viscosity of 1495 Ns/m^2 and $G_s = 1.26$. Glycerine with the same batch number was used throughout the laboratory programme.

2.4.3. Mixing and Storage

For small samples, glyben was mixed thoroughly by hand in a 600 ml plastic beaker using a spatula. Larger samples were mixed in an 11 litre capacity electric mixer or a 56 litre capacity concrete mixer, depending on the volume required. Machine mixing took about 1 hour. Bentonite was added to de-aired glycerine and after mixing, placed in a vacuum chamber for 2 hours under a vacuum of 635 mm of mercury. It was then stored in polythene bags kept in a sealed metal container with moisture absorbing silica-gel.

2.4.4. Triaxial Tests

Since the main laboratory programme was concerned with conditions of rapid loading, quick-undrained tests were chosen to obtain shear strength parameters and characteristics. It was concluded from initial pilot tests that the most consistent results were obtained using standard triaxial compression equipment. Corrections described by Bishop and Henkel (1962) were made for the effect of the rubber membrane.

2.4.5 Sample Preparation

Triaxial samples (nominally 36 mm x 76 mm) were prepared in a cylindrical split former. Its internal surface was treated with resin-based molybdenum disulphide and oven cured. This, together with a light dusting of talc, gave an effective non-stick surface.

Glyben was kneaded and hand-rolled into a cylindrical shape (nominally 34 mm x 100 mm), inserted into the mould and squeezed at opposite ends to fill the mould. After trimming each end with a spatula the sample former was then removed, and Perspex end caps, a rubber membrane, and 0-rings were fitted. A new sample was used for each test.

2.4.6 Glycerine Content

By analogy with moisture content, glycerine content was defined as, viz:

$$\text{glycerine content } (m_g) = \frac{\text{mass of glycerine}}{\text{mass of bentonite}} \qquad (2.1)$$

Stress-strain characteristics at varying values of m_g were obtained from the triaxial compression tests and are shown in Figure 2.6, together with the relationship between peak stress (q_f) and m_g.

For the range of glycerine contents used (0.55 - 1.0) the glyben exhibited strain-hardening characteristics with q_f occurring at strains of about 20%. It was found that q_f decreased in direct proportion to an increase in m_g.

2.4.7 Effects of Confining Pressure

The effects of the cell pressure (σ_3) on glyben samples (m_g = 0.8 to 0.95) is shown in Figure 2.7. This confirmed that the shear strength was unaffected by the confining pressure within the limits given. For this range $c_u = 0.5\, q_f$.

2.4.8 Choice of Consistency

On the basis of shear strength and particularly workability, glyben with $m_g = 0.95$ was adopted as the suitable consistency for the laboratory test programme.

2.4.9 Temperature Effects

Although unmentioned by Mayfield (1963) or Davie and Sutherland (1977), the shear strength of glyben was found to be strongly dependent upon its temperature. Triaxial samples (m_g = 0.95) with Perspex end caps, and no membrane, were warmed in an oven or cooled in a refrigerator and then tested in unconfined compression. Two calibrated thermocouples were placed in the samples at the start of each test to monitor temperature. The arrangement is shown in Figure 2.8. The average sample temperature (t) measured at location 1 ($t = t_1$) and location 2 ($t = t_2$) were recorded at the start and the end of the test:

$$\text{start of test } t_o = 0.5\,(t_1 + t_2)_o$$

$$\text{end of test } t_e = 0.5\,(t_1 + t_2)_e$$

Average temperature change of sample during test:

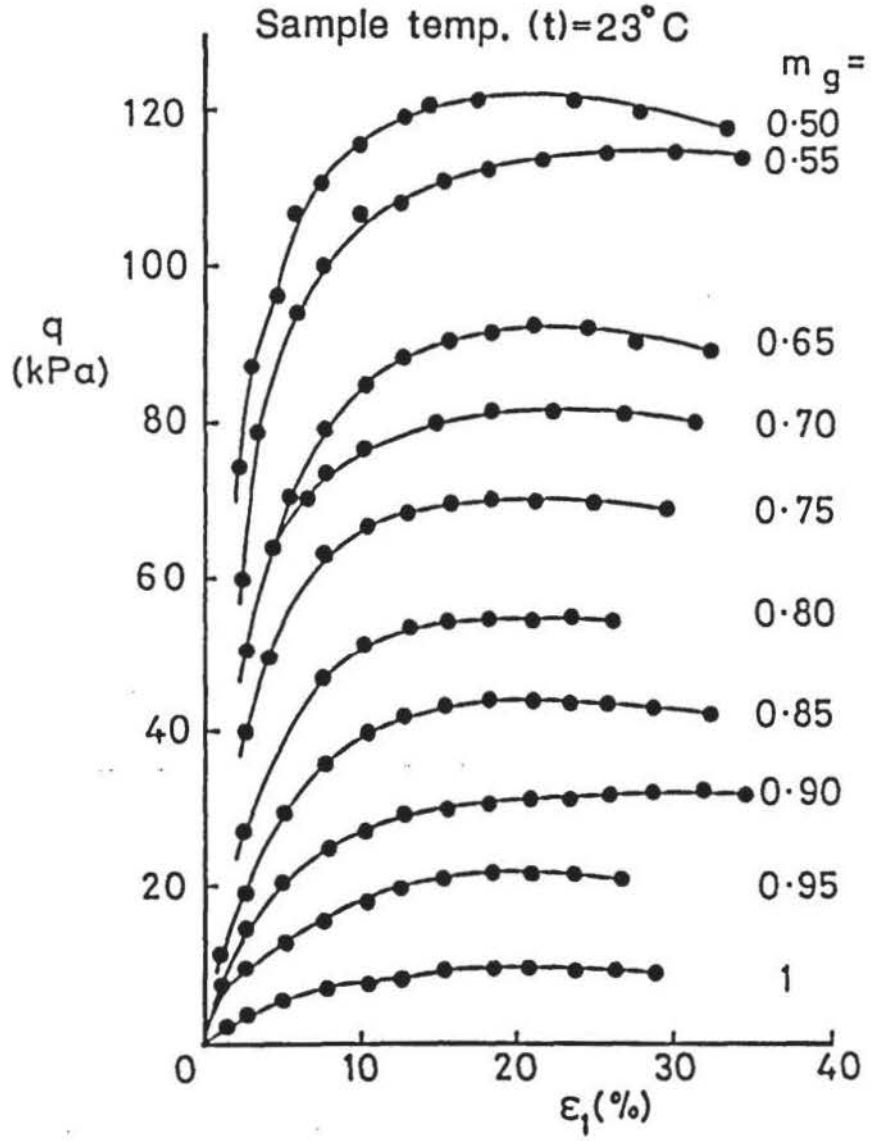

Quick-undrained triaxial stress-strain characteristics of glyben.

FIGURE 2.6(a)

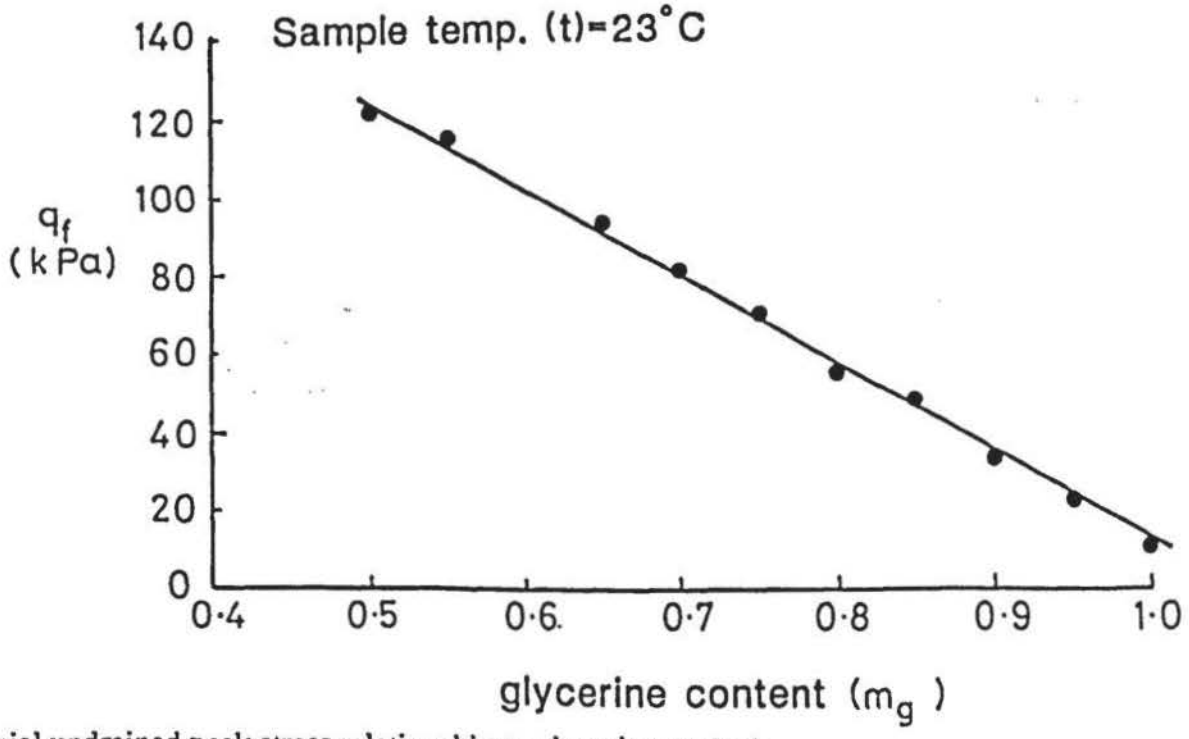

Triaxial undrained peak stress relationship to glycerine content.

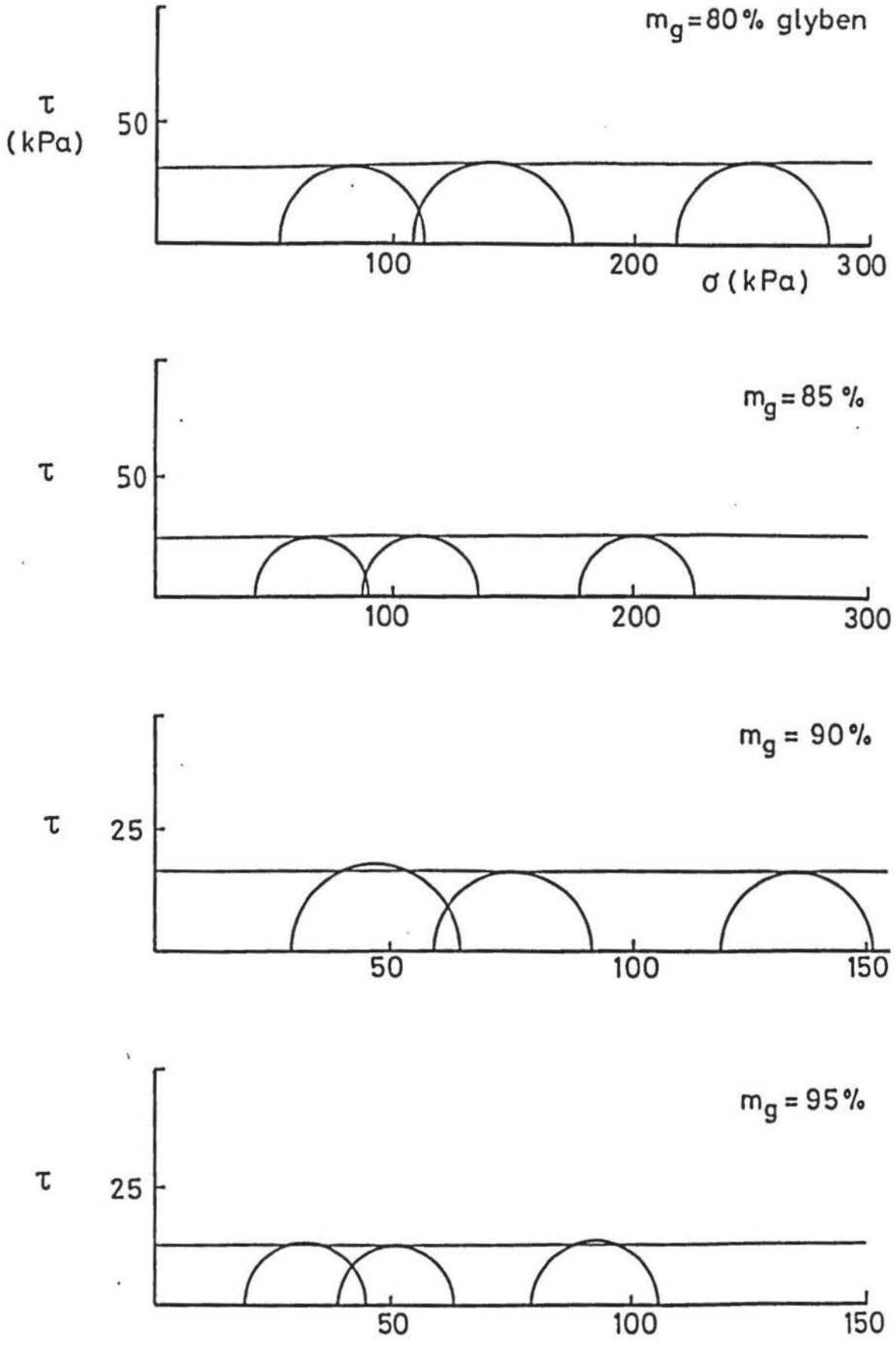

Effects of confining pressure on the undrained shear strength of glyben.

FIGURE 2.7

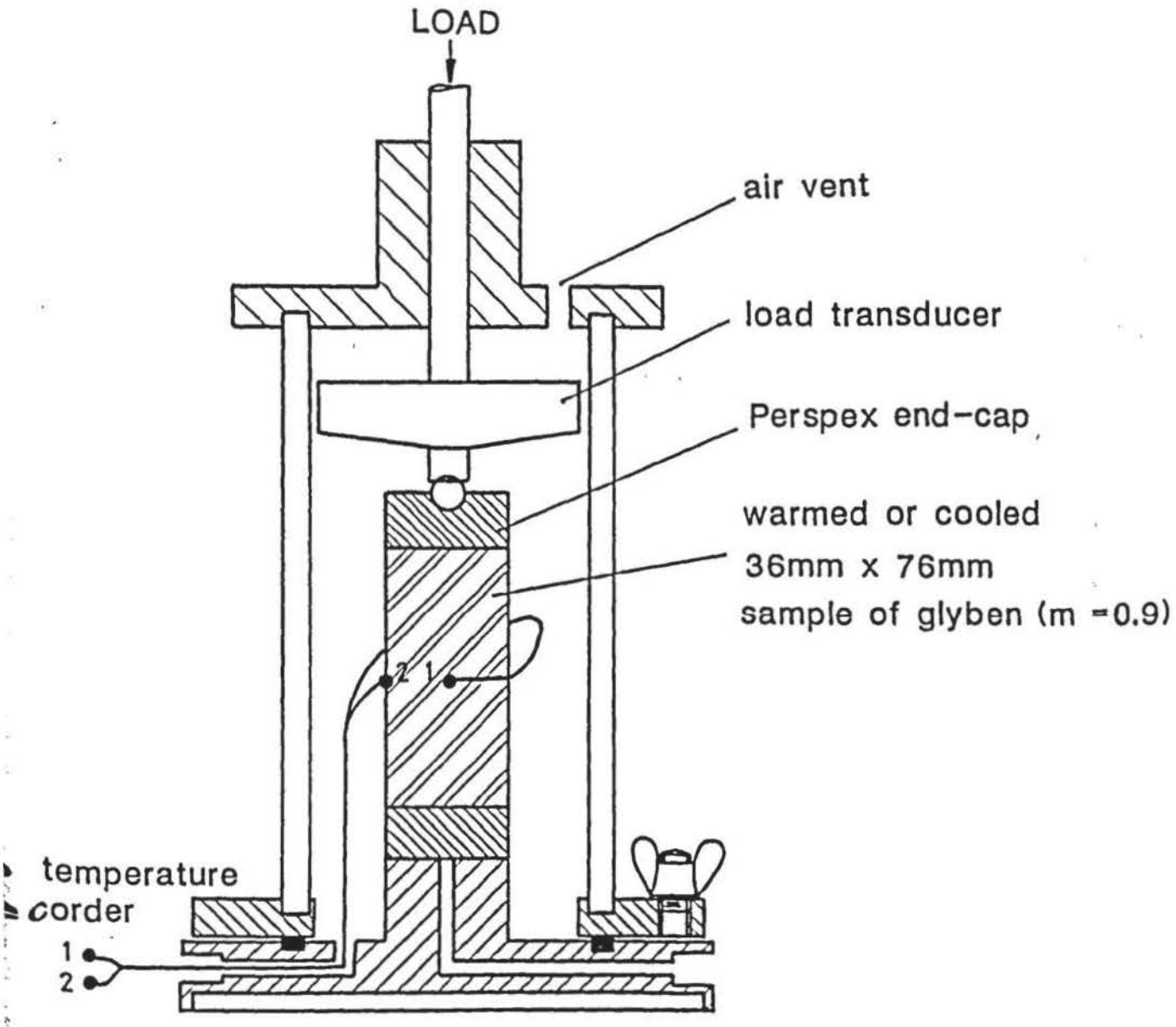

Positioning of two thermocouples in a sample for unconfined compression testing using the triaxial apparatus.

FIGURE 2.8

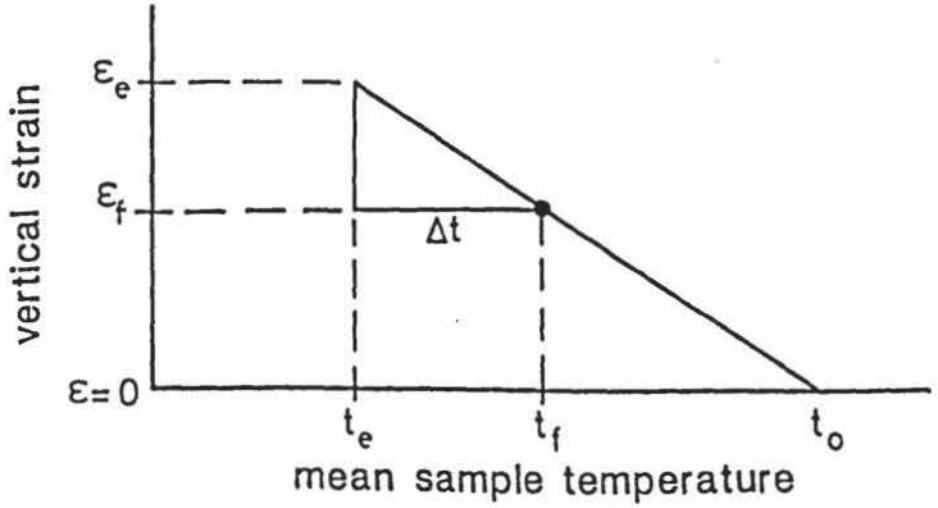

Assumed linear relationship between vertical strain and mean sample temperature.

FIGURE 2.9

$$\Delta t = (t_o - t_e) \qquad (2.2)$$

By assuming Δt occurred in direct proportion to test duration, the average sample temperature (t_f) when peak strength was reached could be determined. Since the rate of loading the sample was constant, then Δt is also proportional to the vertical strain (ε). For a sample cooler than ambient, the assumed relationship is shown in Figure 2.9. By similar triangles:

$$t_f = \Delta t\, \varepsilon_f/\varepsilon_e + t_o \qquad (2.3)$$

For reasons given in Chapter 11.0, a standard temperature of 23°C was adopted to give a reference undrained cohesion (c_u^{23}) to which the undrained cohesion (c_u^t) at any temperature (t) could be determined. The relationship obtained from the laboratory test results is shown in Figure 2.10. A logarithmic regression curve was obtained, giving the equation:

$$c_u^t = c_u^{23}\,(2.615 - 0.515 \ln (t)^o\,C) \qquad (2.4)$$

The relationships shown previously in Figure 2.6 were temperature corrected (to 23°C) using Eqn. 2.4.

2.4.10 Rate of Compression

A further feature unmentioned by Mayfield or Davie and Sutherland was the significant effect of the rate of shearing on the shear strength of glyben. Using triaxial compression tests, glyben samples were subject to constant compression rates of 0.25, 2.5 and 53 mm/minute. For reference purposes a standard rate of 2.5 mm/minute was adopted from which the standard undrained cohesion (c_{us}) was obtained after correction for temperature. Expressing the change in strength (Δc_u) as a percentage of c_{us} and the compression rates as rates of strain, the relationship shown in Figure 2.11 was obtained. For comparison, the characteristics of London Clay using data from Taylor (1943), Northey (1950) and Meigh (1950) are also shown.

From Figure 2.11, it can be deduced, for glyben ($m_g = 0.95$, t = 23°C):

$$\Delta c_u = c_{us}\,[0.067 \log (\varepsilon^r/\varepsilon_s^r)] \qquad (2.5)$$

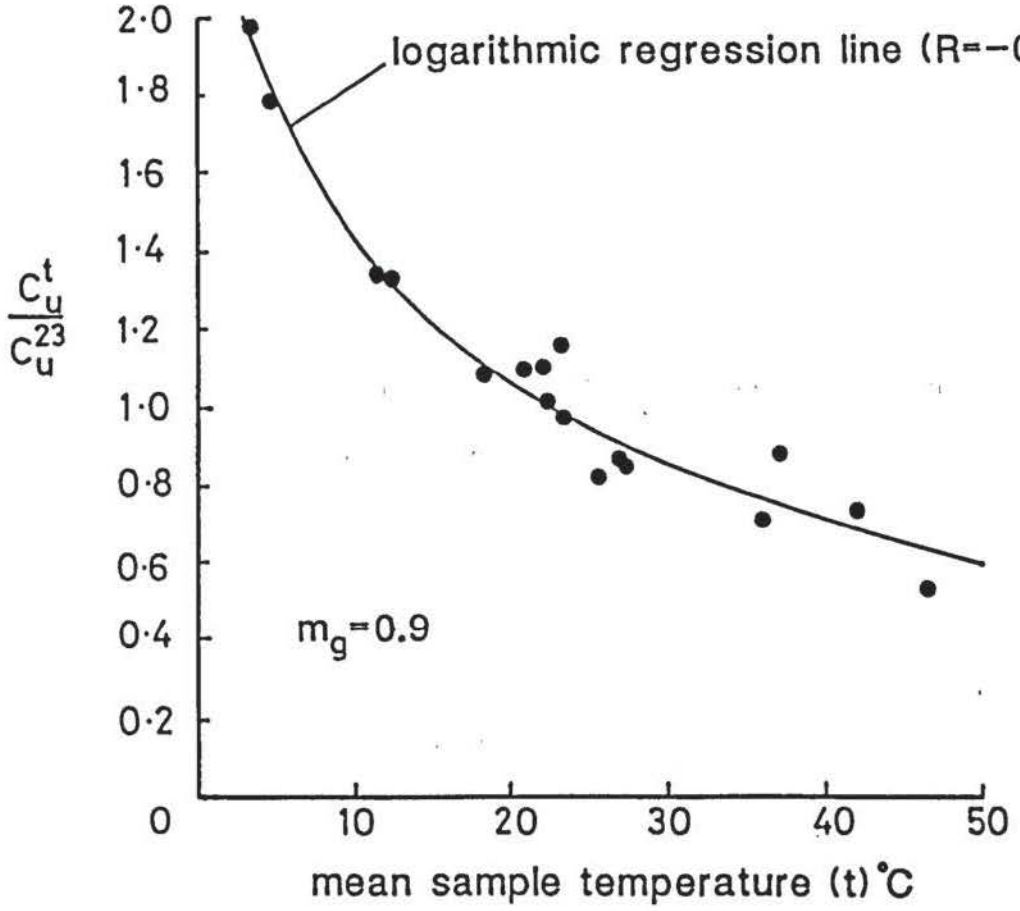

Relative change in undrained cohesion from unconfined compression of glyben with a change in material temperature.

FIGURE 2.10

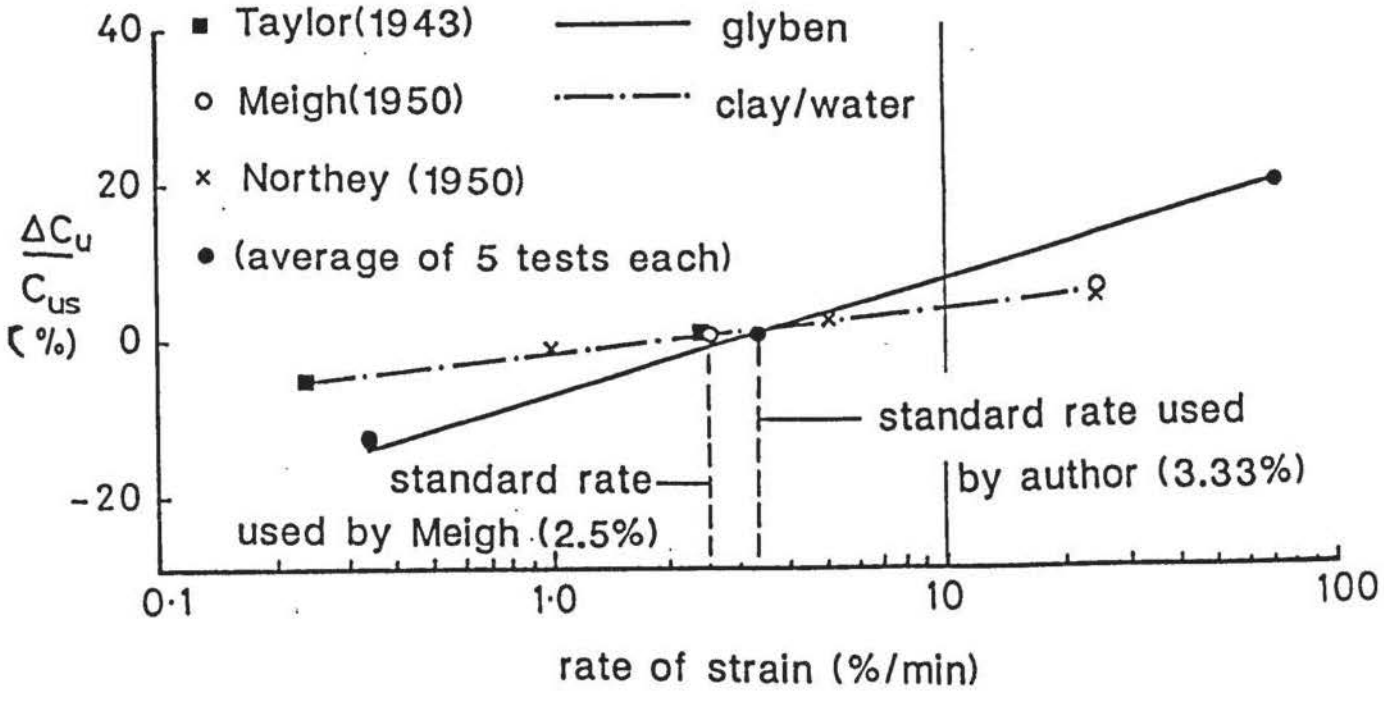

Effect of rate of compressive strain on the undrained cohesion of glyben in the triaxial test.

where ε^r is the actual rate of strain and ε_s^r is the standard rate of strain. The deviation of Eqn. 2.5 is given in Appendix A. The implications of this in the laboratory test programme are discussed in Chapter 11.0.

2.4.11 Thixotropy

Mayfield (1963) found glyben exhibited no significant thixotropic properties. This was confirmed by the author from the results of triaxial tests performed on samples of various 'ages', for the m_g range 0.5 to 1.0.

2.4.12 Pressuremeter Tests

Labrue (1981) investigated stress-strain characteristics of glyben ($m_g = 0.95$) with a small scale 'Menard' type pressuremeter. The material gave a mean value of shear strength of 11.93 kPa, with s = 1.04 kPa, over a period of about 3 months. The equipment and test programme, used by Labrue, was designed by the author.

Labrue concluded the characteristics were those of a saturated, normally consolidated clay.

2.4.13 Conclusion

Glyben may be used to simulate a saturated clay in the sense that the material is almost frictionless (i.e. $\phi_u = 0$). This does not imply, however, that $\nu = 0.5$. Different strengths can be obtained by varying the glycerine content. The material is insensitive to handling since there are no significant thixotropic effects. There is negligible evaporation. These properties permitted repeated tests using the same batch of material and allowed a greater number of tests to be performed.

2.4.14 Terminology

From this point on, glyben will be referred to as clay. References to clay/water soils will be referred to as wet clay.

CHAPTER 3

RADIOGRAPHY

3.1 INTRODUCTION

A radiographic technique was developed and selectively used in an attempt to monitor internal displacements and strains which had occurred at various stages of compression of the granular columns and clay, when subject to a number of varying foundation configurations. The Chapter outlines basic criteria and considerations for implementing the technique and for equipment design.

3.2 PRINCIPLE

In principle, the method was one of recording on a radiograph the images formed by X-rays of a plane regular array of lead-shot markers embedded in the clay/granular columns, as illustrated in Figure 3.1. By making successive radiographs during progressive deformation it is possible to establish, by comparison, incremental displacements of the markers and by analysis, the soil strains.

3.3 HISTORICAL

The first application of X-radiography and lead-shot markers to soil mechanics is attributed to Gerber (1929) who used the method to determine overall displacements within a soil mass at failure. The process was later improved by Davis and Woodward (1949) which enabled differentiation between pre- and post- failure conditions. Roscoe et al (1963) outlined a procedure for obtaining incremental strains throughout a soil mass during plane strain or under conditions of radial symmetry, from displacements occurring in a co-planar regular array of lead-shot markers. This latter method has been extensively developed and used by Cambridge researchers and is well documented, particularly by James (1965), Coumoulos (1967), Bransby (1968), Lord (1969), James (1973a), James (1973b) and Cuckson (1975).

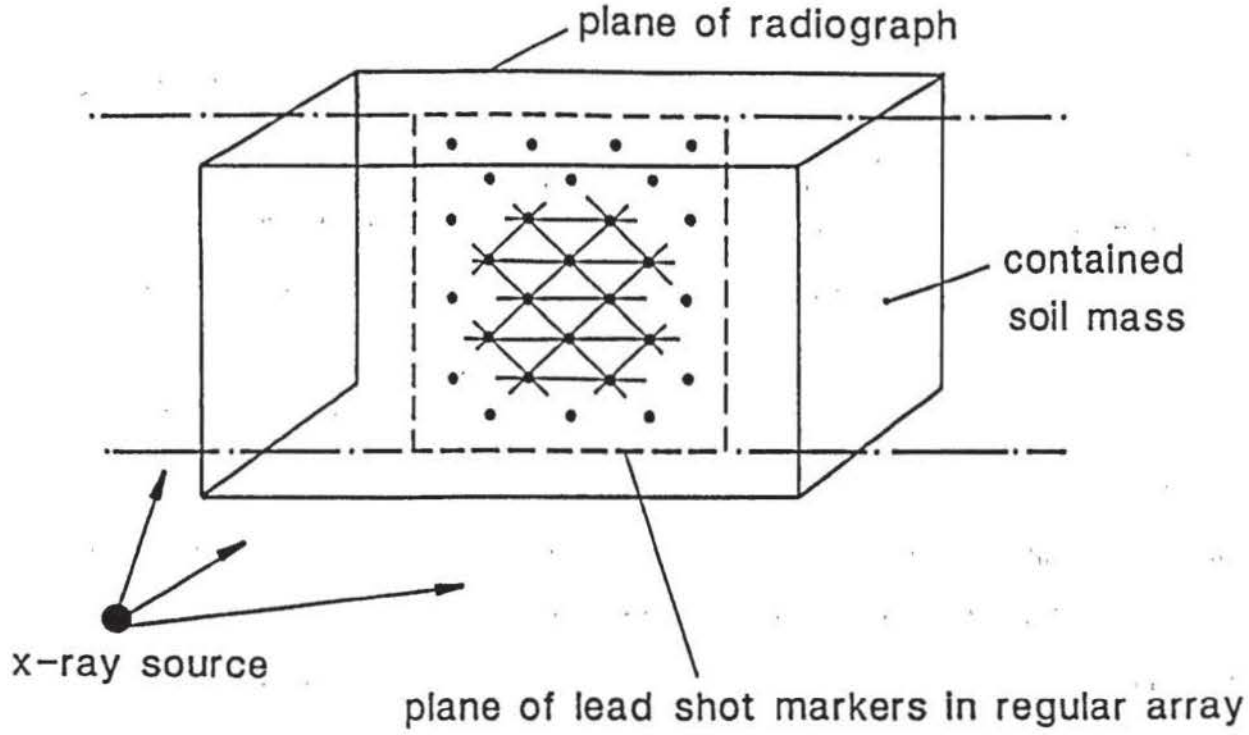

Principle of the radiographic technique used in soil mechanics.

FIGURE 3.1

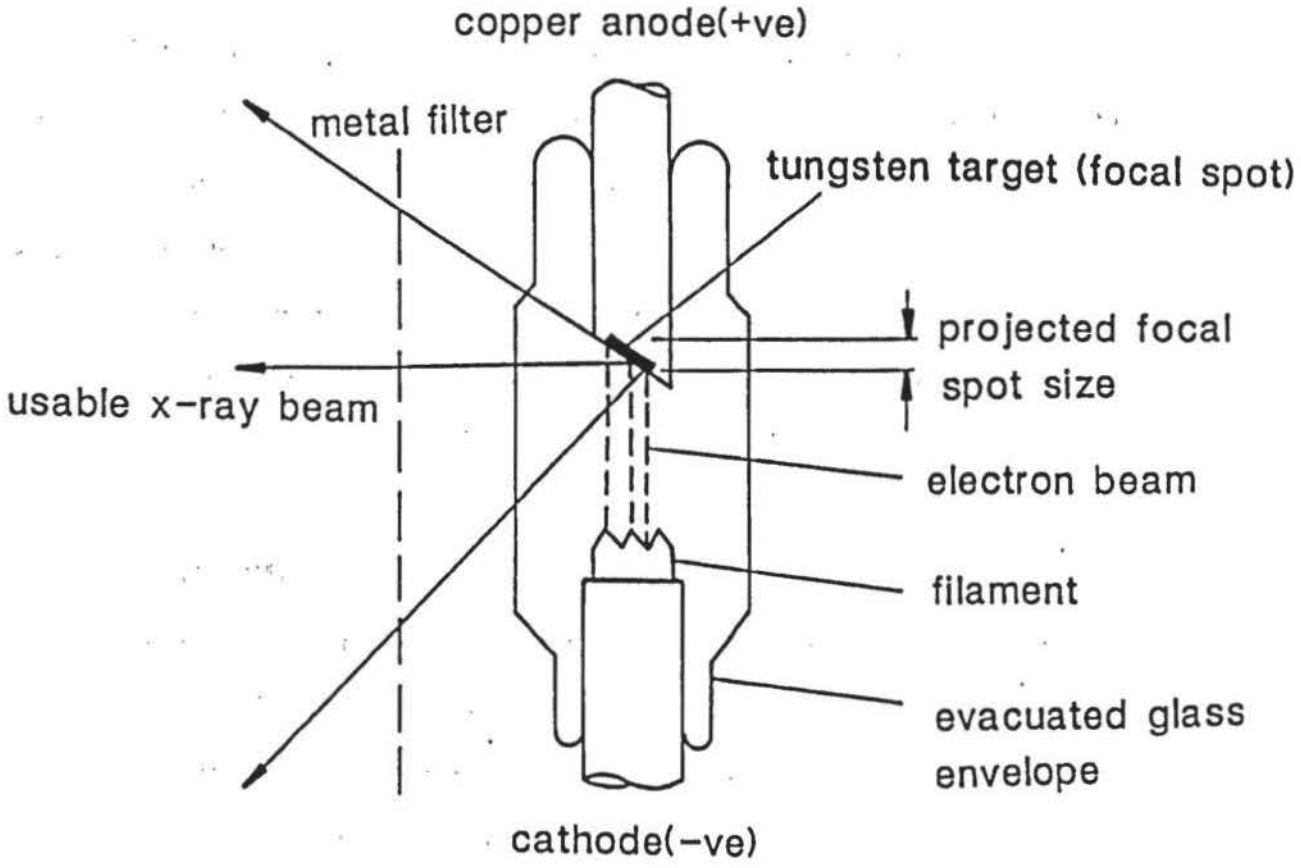

Diagramatic representation of an X-ray tube (after Kodak, 1980).

FIGURE 3.2

3.4 X-RAY GENERATION

The principal features of an X-ray tube are shown diagramatically in Figure 3.2. X-rays are generated when a stream of electrons from a heated cathodic filament are accelerated in a vacuum by a high constant voltage difference and strike a tungsten metal target.

3.5 NATURE OF X-RAYS

X-rays are a form of electromagnetic radiation and travel at the same speed as light and obey most of its 'laws'. X-radiation is emitted as a continuous spectrum with the wavelength distribution dependent on the magnitude of the applied voltage (expressed in kV), as illustrated by Figure 3.3. The radiation intensity increases with increasing kV and also with increasing current (expressed in mA), but the latter has no effect on the wavelength spectrum. The ability of X-rays to penetrate materials increases with decreasing wavelengths and is independent of their intensity.

3.6 X-RAY IMAGE

When radiated, the soil and lead-shot markers will absorb differing proportions of the X-rays. Their degree of absorbtion varies as $e^{\alpha t}$, where α is the absorbtion coefficient and t is its thickness. The absorption coefficient depends upon material density and atomic weight, the higher their values the less permeable is the material to X-rays. The resulting pattern of emergent radiation intensities produces the X-ray image.

Since lead is more than six-times as dense as an engineering soil, and has an atomic weight over seven times greater than the soil minerals, it is an ideal cost-effective choice for a 'marker' material.

3.7 RADIOGRAPHS

Radiographs are the result of recording X-ray images on an X-ray sensitive photographic film. Kodak 'Industrex C' was used which was available in sheet form, individually packed in sealed envelopes. Industrex C is a high constrast, fine grained direct X-ray film requiring a minimum exposure time. Kodak Industrex film bases are 0.18 mm thick, pliable blue-tinted transparent plastic 'Estar' material coated each side with X-ray sensitive emulsion.

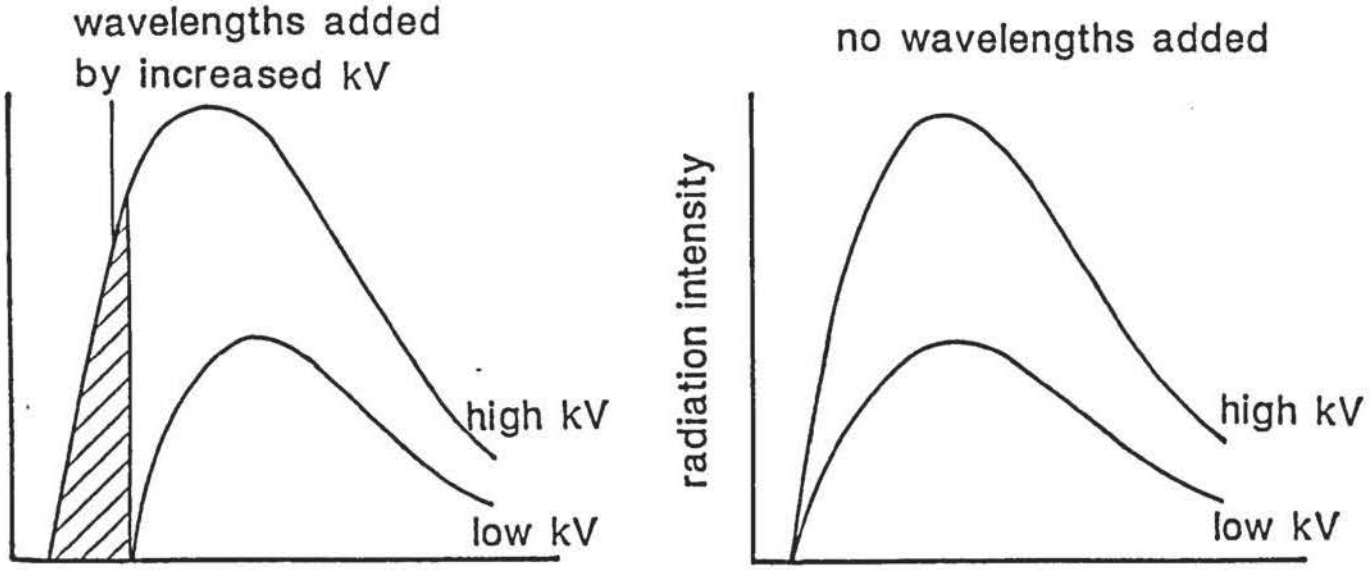

Curves illustrating the effect of a change in voltage or current on the composition and intensity of X-rays (after Kodak, 1980).

FIGURE 3.3

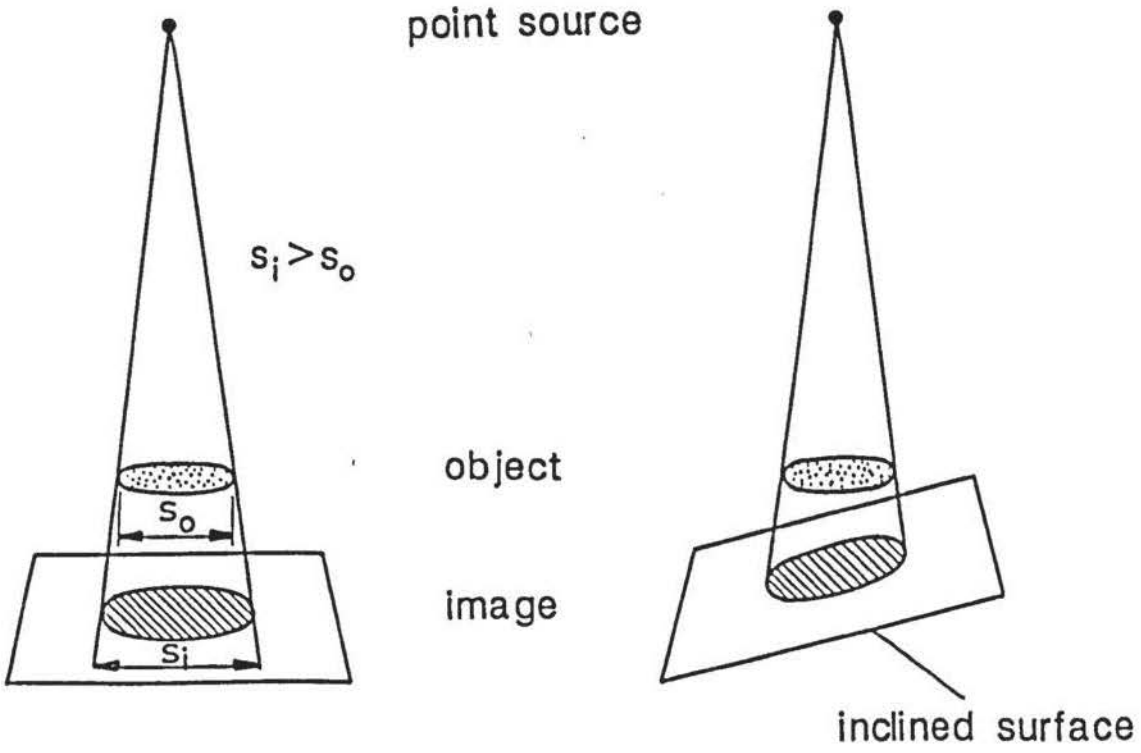

Illustrating of some general geometric principles of image formation (after Kodak, 1980).

FIGURE 3.4

'Estar' gives a high dimensional stability. Radiographic film is more sensitive to light than X-rays and so when in use was enclosed in a light proof cassette which was highly permeable to X-rays. The film was transferred from its sealed envelopes to the cassette in a photographic darkroom.

3.8 FILM PROCESSING

The radiographs were processed in accordance with the manufacturers specification by the Department's Photographic Section.

3.9 RADIOGRAPHIC QUALITY

Displacement of the lead-shot markers is a measure of the change in the x-y co-ordinates of their images on successive radiographs. The co-ordinates were linearly measured (Section 6.3) from an origin which was common to all the radiographs. It was of fundamental importance to achieve an adequate visual radiographic quality by way of contrast and definition between the marker images and the soil 'background'. Integrity of the marker images was also a primary requirement.

3.9.1 Contrast

In consideration of the nature of X-rays (Section 3.5), maximising contrast (or differences of optical density) between marker images and the soil background clearly requires the use of low kilovoltages to avoid over production of short wavelengths that would otherwise have too great a penetrating power.

Increasing development time of the radiographic film, at a reduced temperature, can enhance contrast. This procedure was not adopted because this increased contrast is achieved at the cost of poorer image definition.

3.9.2 Definition

Image definition (or sharpness) and integrity is dependent on spatial relations of the X-ray source, object (soil and lead-shot) and film. It is apparent from Figure 3.4, that the image

cast by an object using a point source will show some enlargement. The image shape will also differ from that of the object if their planes are not parallel, or if the source is not perpendicular to the central axis of the object.

In practice the target or focal spot of an X-ray tube is not a point source, but is of finite size. This results in the image boundary having a penumbra (p), shown by Figure 3.5, whose size depends upon the focal spot (f), the focus-to-film distance (d_i) and the object-to-film distance (d). The larger the penumbra the poorer the definition. From similar triangles, it is easily shown that:

$$\text{penumbra (p)} = \frac{f.d}{(d_i - d)} \qquad (3.1)$$

To obtain marker images with minimal distortion and high definition, these geometric considerations lead to five general rules for overall implementation of the technique and for the design and construction of equipment, viz:

1. Focal spot size (f) to be as small as operational conditions allow.
2. Focus-to-film distance (d_i) to be a maximum.
3. Lead-shot marker-to-film distance (d) to be a minimum.
4. Ideally, the radiation should be directed perpendicularly to the film surface. (Because the beam is conical this could only be approximated in practice).
5. The planes of the markers and film should be parallel to each other.

James (1973a) recommends, for visual purposes, the penumbra (p), of the lead-shot markers, should not exceed 0.25 mm. Thus, by substitution in Eqn. 3.1, the focus-to-film distance (d_i) has to be:

$$d_i \geq 4\, d\, (f + 0.5) \qquad (3.2)$$

for dimensions in mm.

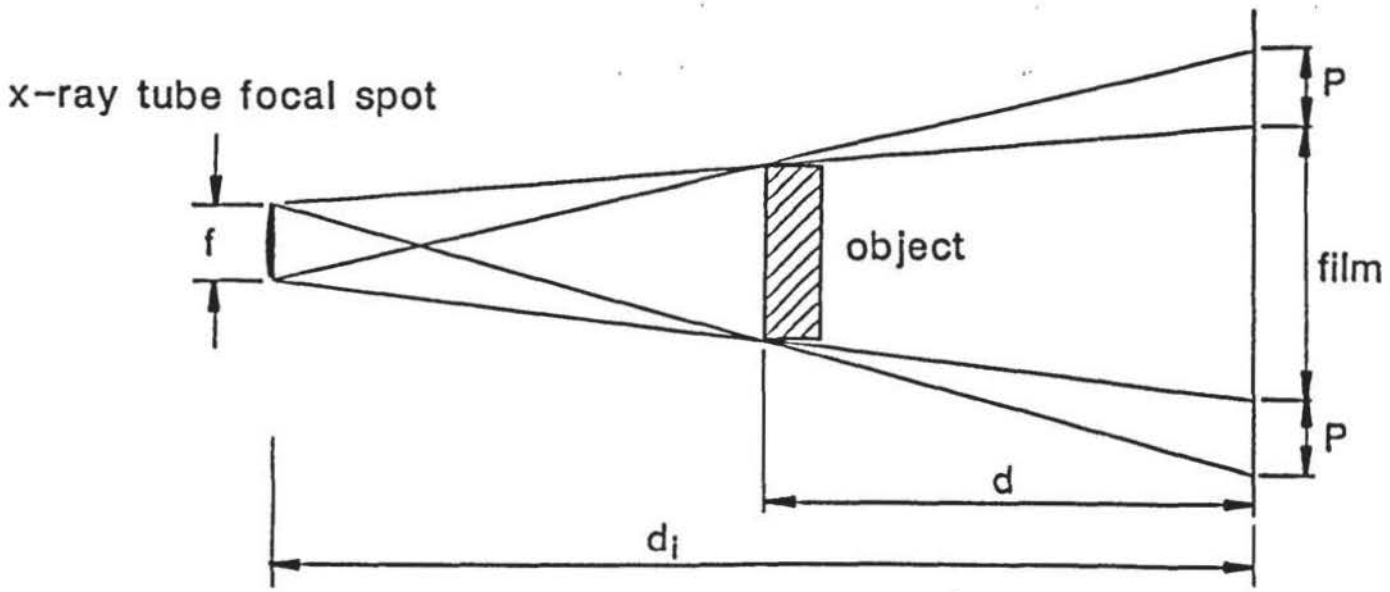

Formation of a penumbra around a radiograph image through the effect of the focal spot size (after Kodak, 1980).

FIGURE 3.5

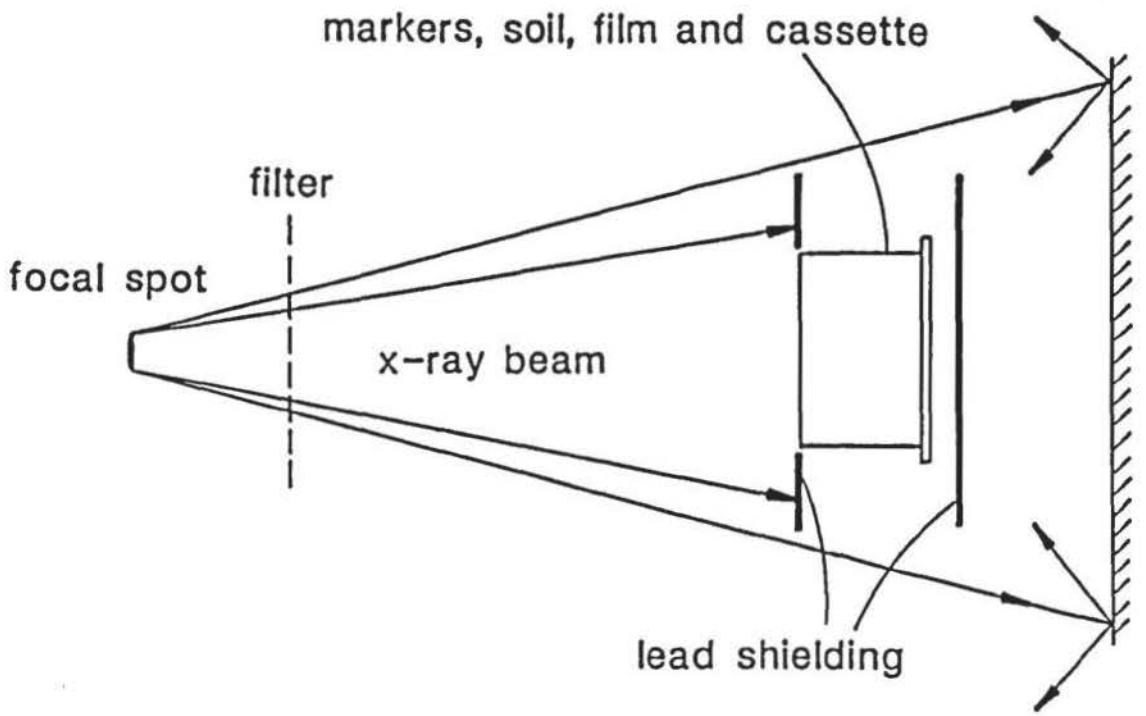

Control of scattered radiation with lead shielding and a metal filter (after Kodak, 1980).

FIGURE 3.6

3.9.3 Scattered Radiation

A light beam directed onto the wall of a room will illuminate all the other surfaces to some degree through scattering of the primary light beam. X-rays also behave in the same manner. In practice, 60% (or more) of the total radiation reaching the film may be scattered, which seriously impares the radiographic quality.

Traditionally, scatter is controlled by using lead shielding in a manner shown in Figure 3.6. Thin metal filters, positioned at the X-ray tube, were also used to harden the radiation by removing lower energy wavelengths and reduce scatter to within acceptable limits.

3.10 EXPOSURE

Since the radiographs were taken immediately after a loading increment, it was necessary to minimise exposure time to prevent any 'creep' of the markers causing distortion of their image. The main factors influencing exposure time are:

1. Tube kV
2. Tube current (i.e. radiation intensity).
3. Film speed.
4. Focus-to-film distance (d_i).
5. Absorption coefficient of the soil and the walls of its container.

Higher values of items 1 to 3 and smaller magnitudes of items 4 and 5 reduce exposure time. By convention, exposure (E) is given as:

$$E = \text{tube current} \times \text{exposure time} \qquad (3.3)$$

with units of mA.min or mA.sec. X-ray film obeys the reciprocity law, so an exposure of 4 minutes at 1.5 mA should produce the same results as 1.5 minutes at 4mA. The table in Figure 3.7, from James (1973a), gives a number of typical exposures of various samples of sand and clay soils used by Cambridge researchers. Lead-shot markers nominally 2.5 mm diameter were generally used, which gave an acceptable image quality. The Industrex D film was withdrawn by Kodak in 1979. It had the same overall properties as Industrx C, but was 1.8 times faster.

SAMPLE	Focus-to-film distance (d_i) (mm)	Tube kV	Exposure (mA.min)	
			Industrex D*	Industrex C+
60 mm dense sand	1500	85	50	90
100 mm dense sand	1500	80	90	162
150 mm dense sand + 30 mm of glass	1500	140	75	135
190 mm dense sand + 35 mm of glass	1500	150	120	216
150 mm clay + 40 mm glass	1500	130	50	90

* withdrawn by Kodak in 1979.

\+ included by the Author. (Industrex D is 1.8 times faster than C).

Some typical exposures used by Cambridge researchers (from James, 1973a).

FIGURE 3.7.

PROPERTIES	Plywood	Alumin.	Glass	Perspex	Steel
α (@150 kV) cm^{-1}	0.116	0.36	0.5	0.25	1.6
E kPa	12.4	68.9	73.8	3.4	206.8
coef.linear expn. 10^{-6}/°C	18.0	22.0	9.8	80.0	11.0
$A = \alpha/E^{1/3}$ kPa/cm^{-3}	0.137	0.255	0.349	0.613	0.9
Tensile strength. MPa	49.4	308.9	92.7*	61.4	308.9
Spec. gravity	0.6	2.8	2.6	1.2	7.8
Coef. of friction	-	0.15	0.08	-	0.15
Surface quality	v.soft	hard.	v.hard	soft	hard

* based on 1% chance of failure.

Physical properties of some soil container materials (from James, 1965).

FIGURE 3.8

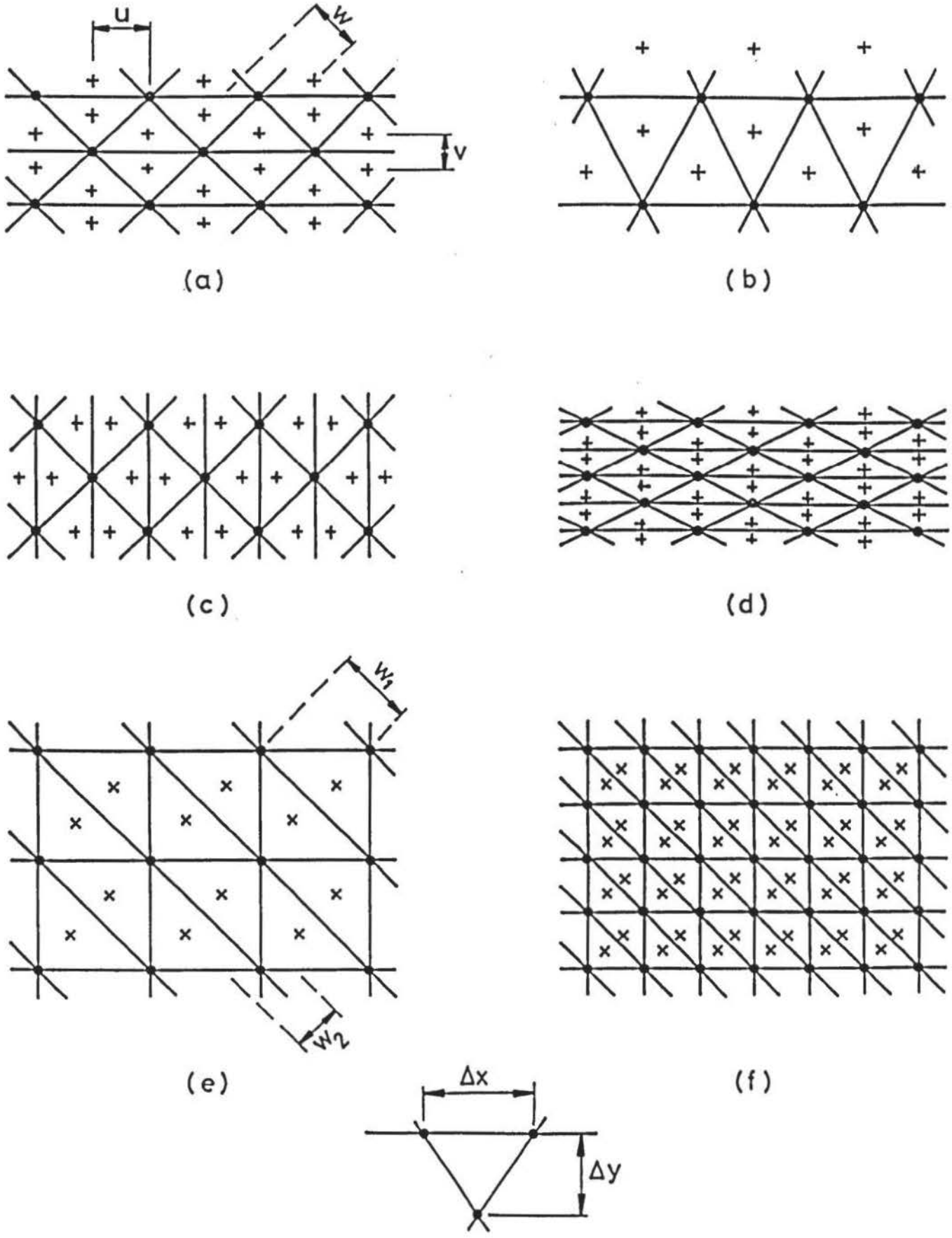

Some possible triangular configurations of lead-shot (after Lord, 1969).

FIGURE 3.9

Configuration	Δx (inches)	Δy (inches)	Error in derived strain* $\Delta\varepsilon_y$	Error in derived strain* $\Delta\varepsilon_x$	No. of Shot+	Max. distance between centroids (inches) v	u	w
a	1	0.5	0.001	0.002	768	0.33	0.5	0.47
b	1.	1	0.001	0.001	384	0.66	0.5	0.6
c	1	0.5	0.002	0.001	768	0.5	0.33	0.47
d	1	0.25	0.002	0.002	1536	0.25	0.33	0.3
e	1	1	0.001	0.001	384	0.67	0.67	0.71/0.47
f	0.5	0.5	0.002	1536		0.33	0.33	0.23/0.35

* based upon displacement measurement errors of each point of ± 0.0005"

\+ Coverage of lead-shot in traingular configurations (after Lord, 1969).

Coverage of lead-shot in triangular configurations (after Lord, 1969)

FIGURE 3.10

3.10.1 Cassette

In practice, it was found that the five factors influencing exposure were largely fixed by the previous considerations concerning radiographic quality together with the operating conditions and equipment. This gave an unacceptably long exposure time. A solution was provided by use of a Kodak X-Omatic cassette which incorporated ultra-fine grained intensifying screens. The screens emit electrons when struck by X-rays which results in an increase in intensification of the radiographic image for energy levels greater than about 110 kV. Exposure times were reduced about fivefold with no noticeable depreciation in contrast or definition.

3.11 SOIL CONTAINER MATERIALS.

It was important for the soil container material to be both structurally stiff and transparent as possible to X-rays. This aspect was studied by James (1965) who considered a number of materials for use in soil container construction. The properties of these materials are tabulated in Figure 3.8. James proposed that a suitable container material should have a low absorption coefficient (α) and since "for a given stiffness the thickness of a plate of given size varies as $1/(E)^{1/3}$" - where E is Young's Modulus - then a material with a low value of $A = \alpha/(E)^{1/3}$ is required. He concluded that glass gave a suitable overall compromise.

3.12 LEAD-SHOT

Various geometries for lead-shot networks have been considered by Lord (1969) and are shown in Figures 3.9 and 3.10. From mathematical analysis considerations, the accuracy of strain patterns derived from displacement of the lead-shot will be greater as the mesh size is reduced. This conflicts with a number of practical requirements, viz:

1. Lead-shot markers need to be at sufficient distance from each other so as not to have any effect on the soil.
2. Centroids of the network element should be regularly spaced.
3. The number of markers should be restricted to minimise co-ordinate measuring time.

The errors in derived strains also increase as the mesh size is reduced.

Lord concluded that configurations (a) and (c), shown in Figure 3.9, were the most uniform and offered an acceptable compromise in coverage.

Configuration (a) was adopted by the author, using a grid size of $\Delta x = 20$ mm and $\Delta y = 10$ mm, and lead-shot of 2.5 mm nominal diameter.

3.13 PLACEMENT OF LEAD-SHOT

To allow placing of the lead-shot in the central plane of the clay, the container was constructed in two equal sections. Using a template, the lead-shot was positioned on the clay surface of one section and then the two halves brought together and secured. The validity of the technique and the equipment necessary for its implementation are discussed later, in Chapters 12 and 4 respectively.

CHAPTER 4

GENERAL EQUIPMENT

4.1 INTRODUCTION

Items of laboratory equipment were designed and constructed to contain the clay, form the granular columns and to implement the X-ray technique. Equipment design was based on using two existing compression testing machines and that X-radiation facilities were sited some distance from the Department's laboratories, at the University's Radiation Centre. The latter consideration implied transportability of the relevant items of equipment.

4.2 COMPRESSION MACHINE A

Compression machine 'A' was an existing strain controlled Wykeham Farrance 5000 kgf loading capacity unit. It had a stepless speed range, under electronic control, from 0.0005 to 5 mm/min. with a maximum upward travel of 100 mm. The overall dimensions are shown in Figure 4.1.

4.3 SOIL CONTAINER A

Clay container 'A' was specifically designed for application of the X-ray technique in association with compression machine A, since the latter's compact size and 103 kg mass made it sufficiently portable for transportation to and from the Radiation Centre as required.

4.3.1 Design and Construction

In order to give adequate lateral restraint to the clay during testing, the container was designed for a high overall stiffness. To allow placement of the lead-shot markers in the central plane of the clay, the container was constructed in two halves. These were positioned and secured together with the aid of four steel dowel locating pins and nine 5 mm diameter by 280 mm long steel bolts with butterfly-nuts, respectively.

The side walls and base were made from 36 mm thick marine plywood, coated with

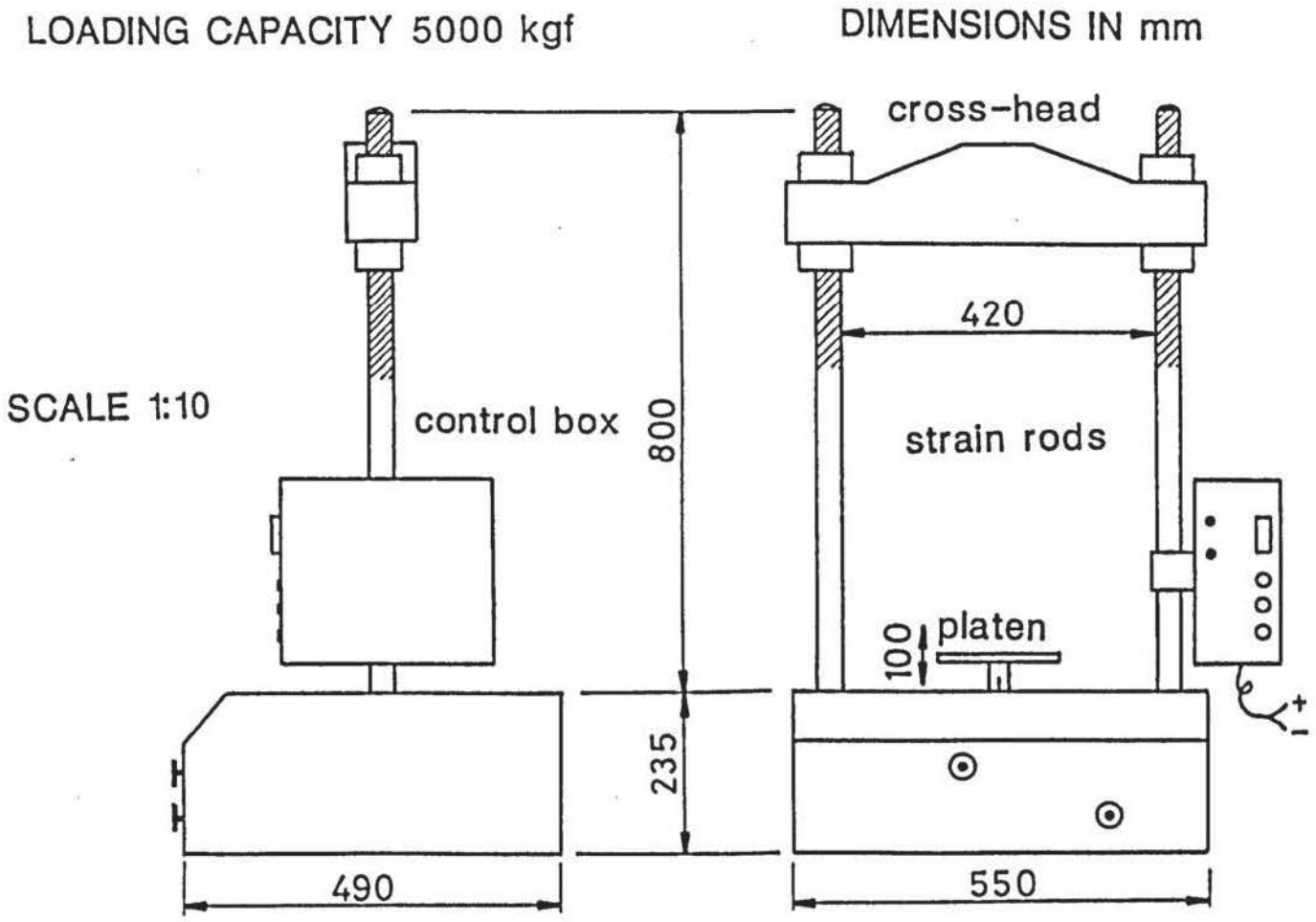

Overall dimensions of compression machine A.

FIGURE 4.1

polyurethane sealant. The side walls were secured to the base in a 5 mm deep groove with expoxy resin and 5 mm diameter by 345 mm long steel bolts. Lead-free glass, 10 mm thick, was used for the front and rear faces which were seated in 5 mm deep grooves with epoxy resin, in the sidewalls and base. Glass was used in preference to the marine plywood for the container walls parallel to the plane of the radiographic film in view of the conclusion by James (1965) (Section 3.11) and also since the latter material is subject to density variations which, at that stage, were feared may cause spurious radiographic images.

Details of the container are shown in Figure 4.2 and Plate 4.1. The internal width and breadth were approximately 30% larger than those of the container used by Hughes and Withers (1974), the depth being about the same.

4.3.2. Pressure Transducer

A 25 mm diameter hole was made in the rear glass face to accommodate a horizontal soil-boundary stress transducer. The hole was located with regard to the position of maximum dilation of a single model-scale granular column reported by Dullage (1969) as occurring at about one to one and a half column diameters below the initial clay surface level. This observation was also supported by results obtained by Williams (1969) and Hughes and Withers (1974). Details of the transducer and the method of fixing are described in Section 5.5.6. Provision was made for the removal of the transducer during radiographic work (to eliminate its shadow), the hole being filled by a Perspex plug.

4.3.3 Radiographic Axes

Radiographic x-y axes were defined on the rear glass face by 1 mm wide grooves. These can be seen in plate 4.1. Lead markers set in epoxy resin were used to identify the axes origin and fiducial positions. The latter were some 150 mm from the origin position.

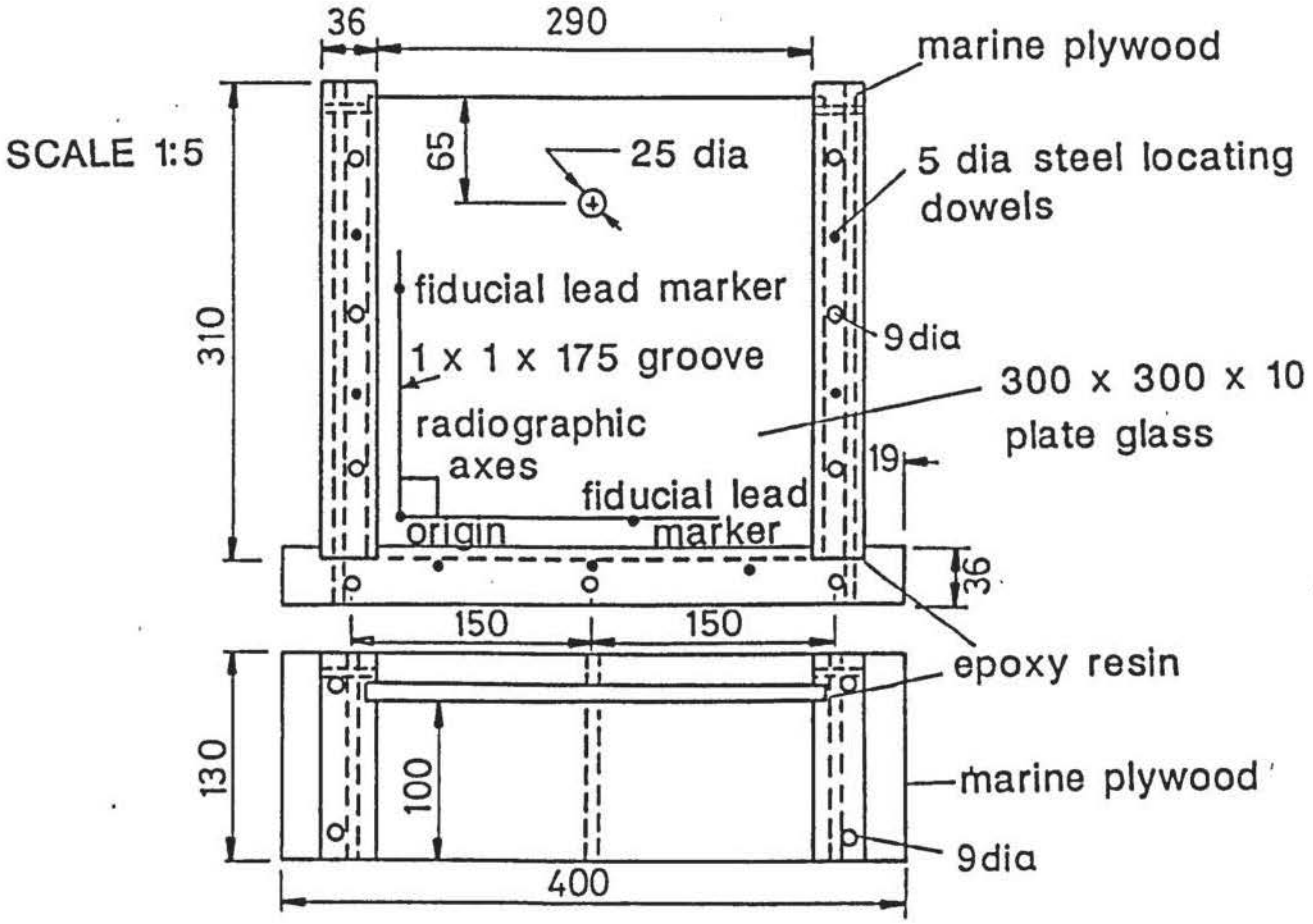

Constructional details of container A.

FIGURE 4.2

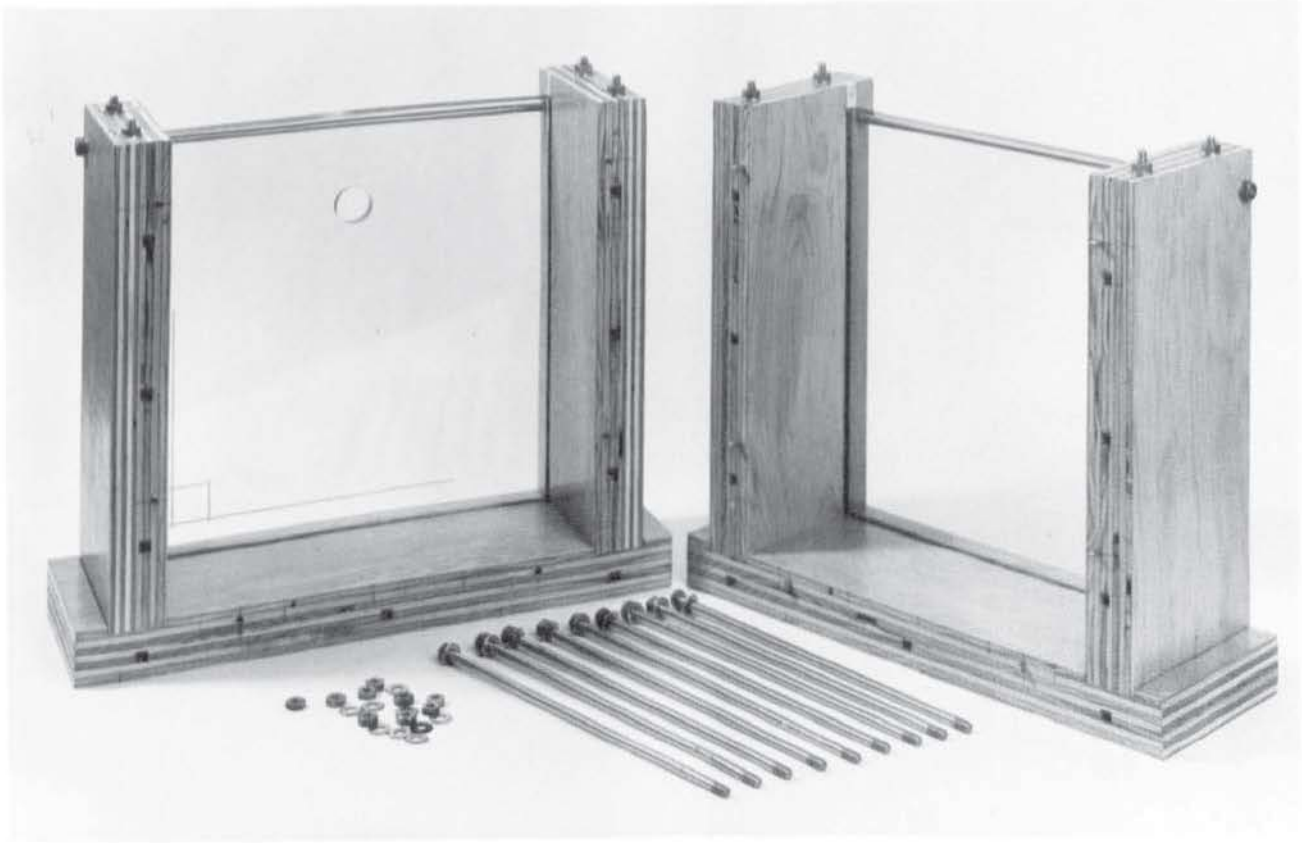

Soil Container A.

PLATE 4.1

4.3.4 Cassette Location

Two aluminium angle brackets and a wood batton were securely attached to the rear of the container by screws and epoxy resin to ensure consistent positioning of the cassette containing the radiographic film. The cassette was held in place by four wood wedges, shown in Plate 4.2.

4.3.5 Securing to Platen

A metal bar and two bolts were made to clamp the container to the platen of the compression machine during radiographic work. The general arrangement is shown in Figure 4.3. This prevented any rotation of the film plane between taking successive radiographs and eliminated a potential source of error in the radiographic analysis (Section 7.11.3).

4.4 COMPRESSION MACHINE B

Compression machine 'B' was a strain controlled clockhouse Engineering A21, 50 000 kgf capacity unit. A dual-gear reduction system gave loading speeds from between 0.0018 to 6.1 mm/minute, with a maximum upward platen travel of 120 mm. The overall dimensions are given in Figure 4.4.

4.5 CONTAINER B

Clay container 'B' was designed for use in conjunction with compression machine B and to accommodate a configuration of up to five granular columns.

4.5.1 Design and Construction

The walls and base was made from 20 mm thick marine plywood, butt-jointed and secured by screws and epoxy resin. To enhance the overall stiffness, of the container, it was lined with a fine aggregate concrete (40 MPa at 28 days) to a thickness of 15 mm. The concrete surface was given a trowelled finish, which after sanding was coated with an epoxy resin sealant. Details of the container are shown in Figure 4.5 and Plate 4.3.

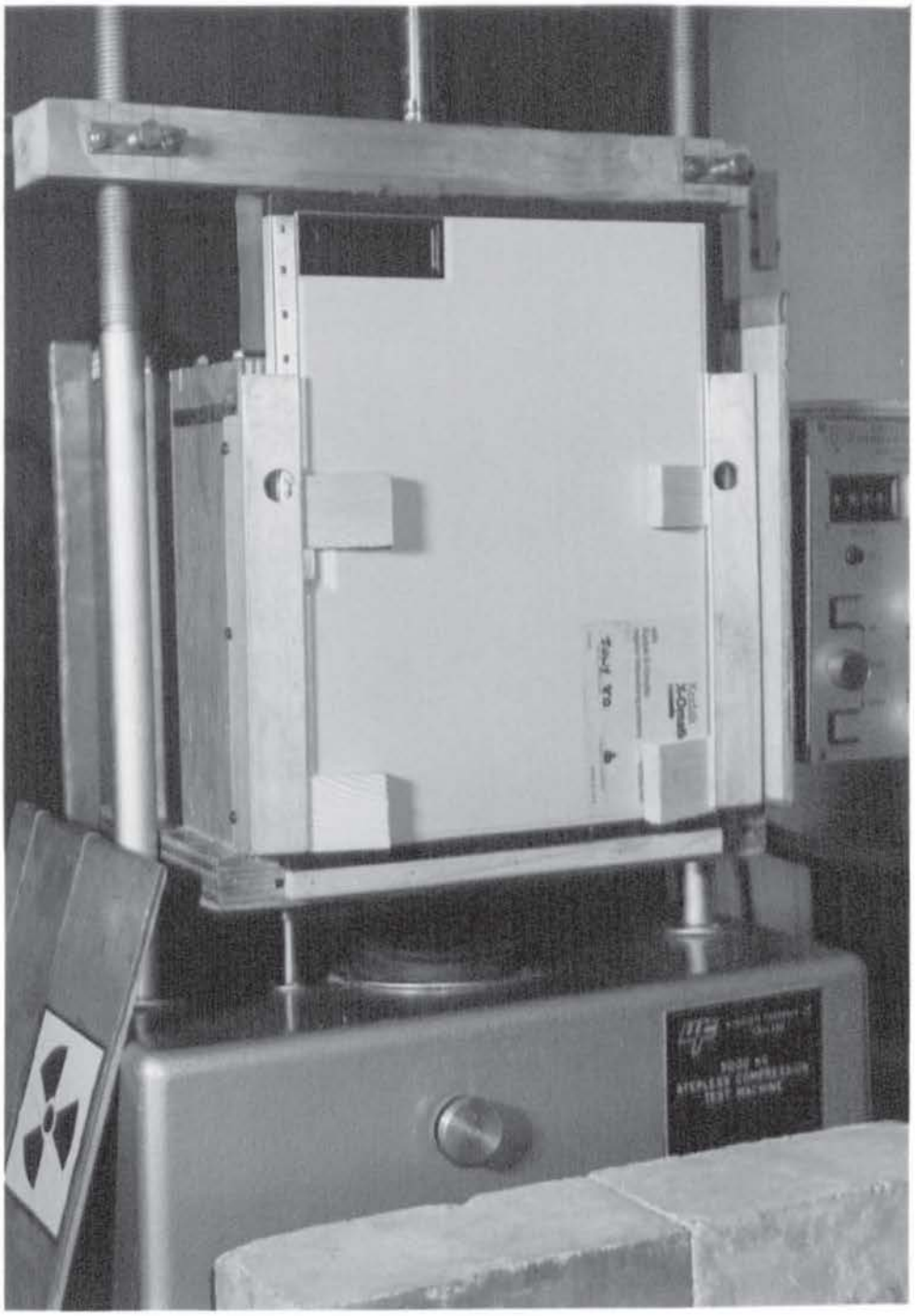

Location of X-ray cassette.

PLATE 4.2

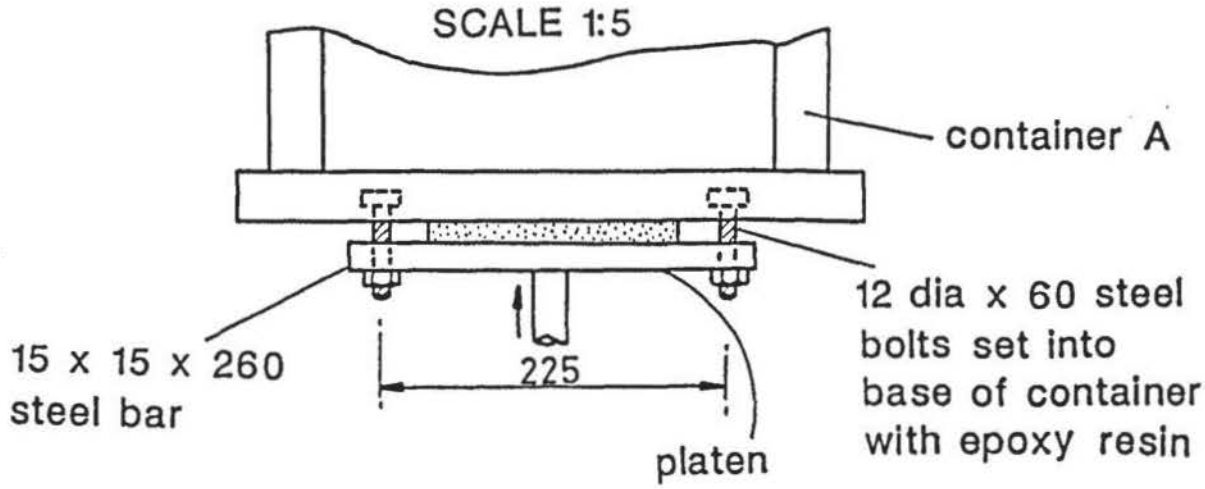

Details of securing container A to platen during radiographic work.

FIGURE 4.3

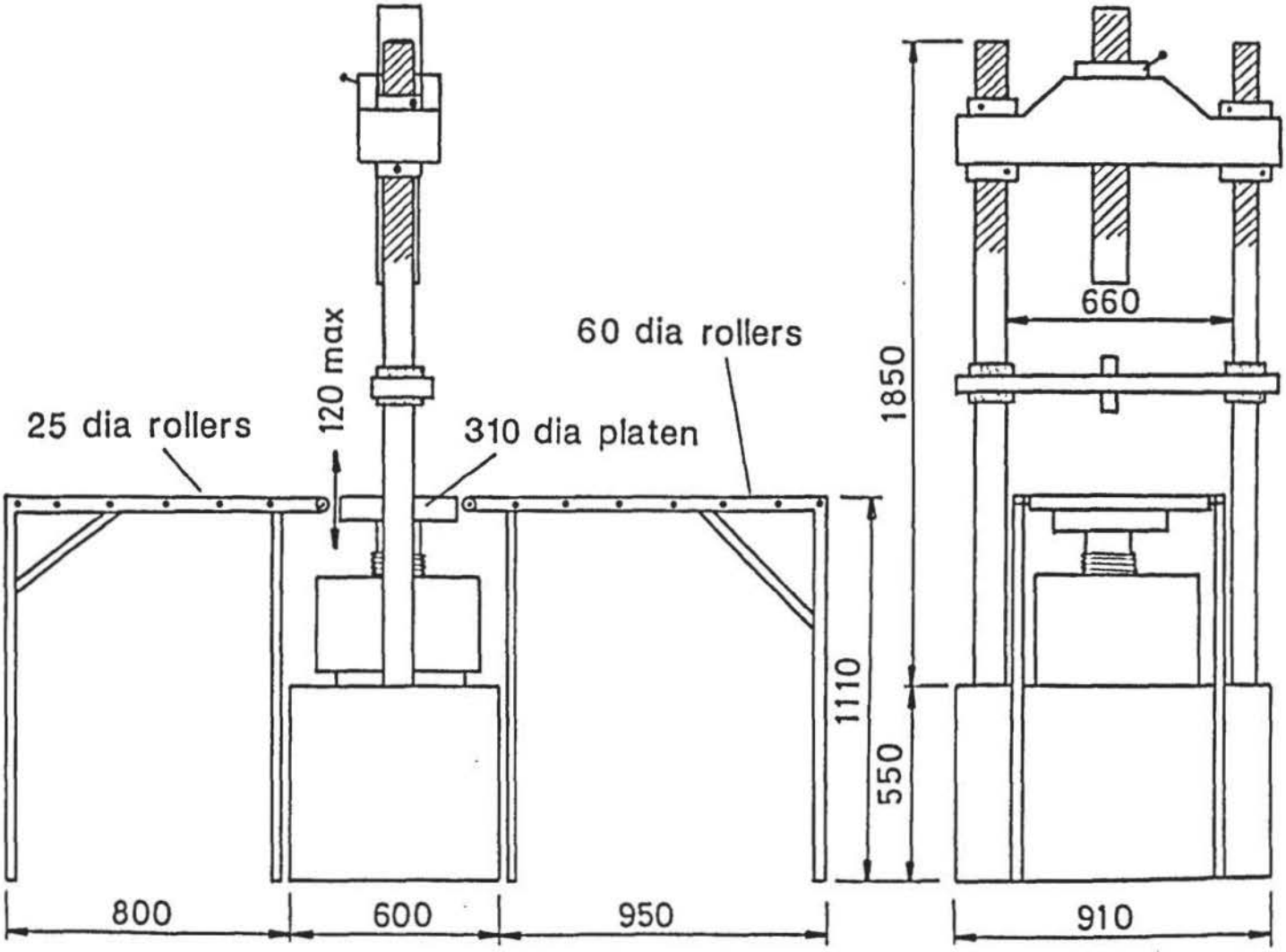

Overall dimensions and arrangement of compression machine B.

FIGURE 4.4

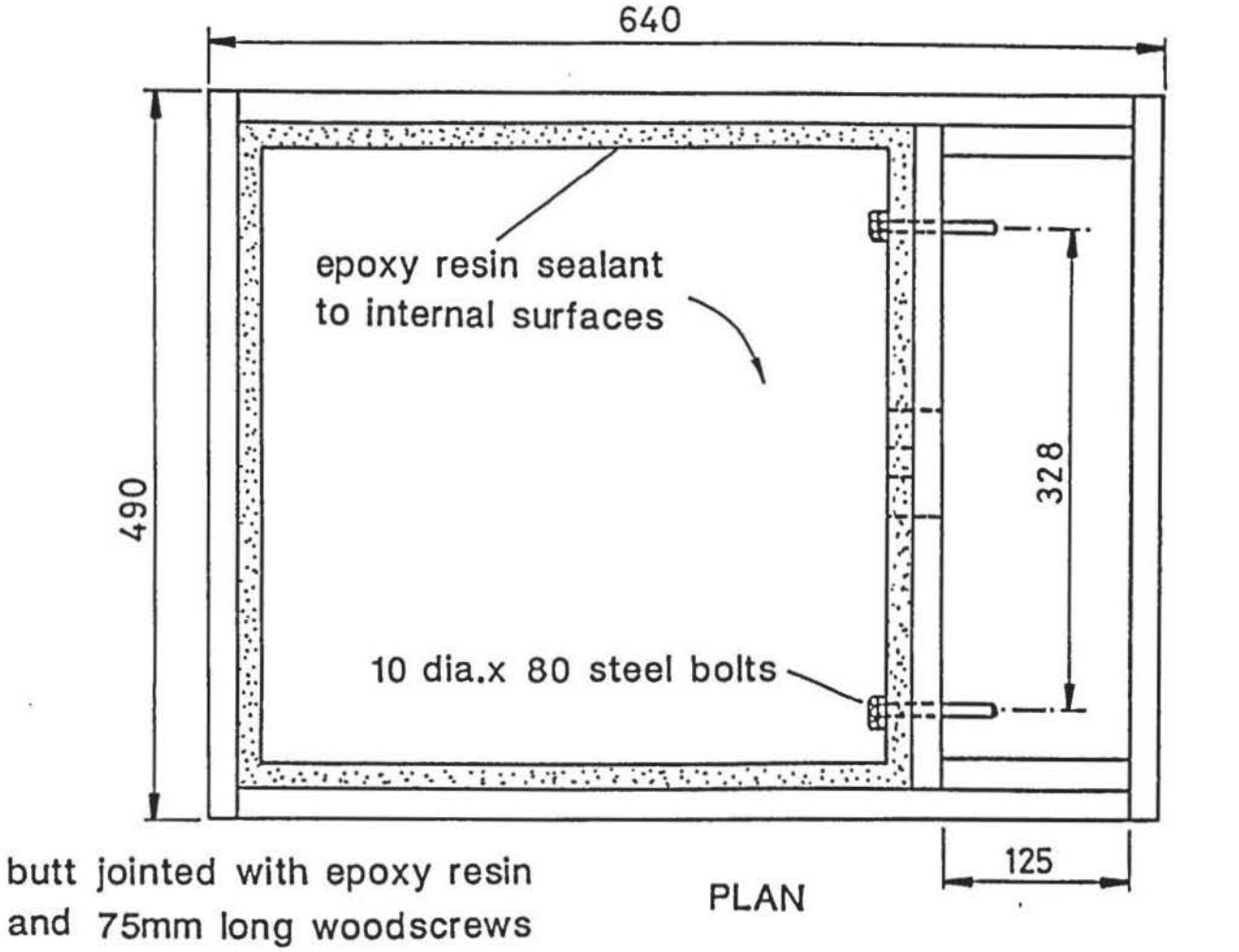

Constructional details of container B.

FIGURE 4.5

Soil Container B.

PLATE 4.3

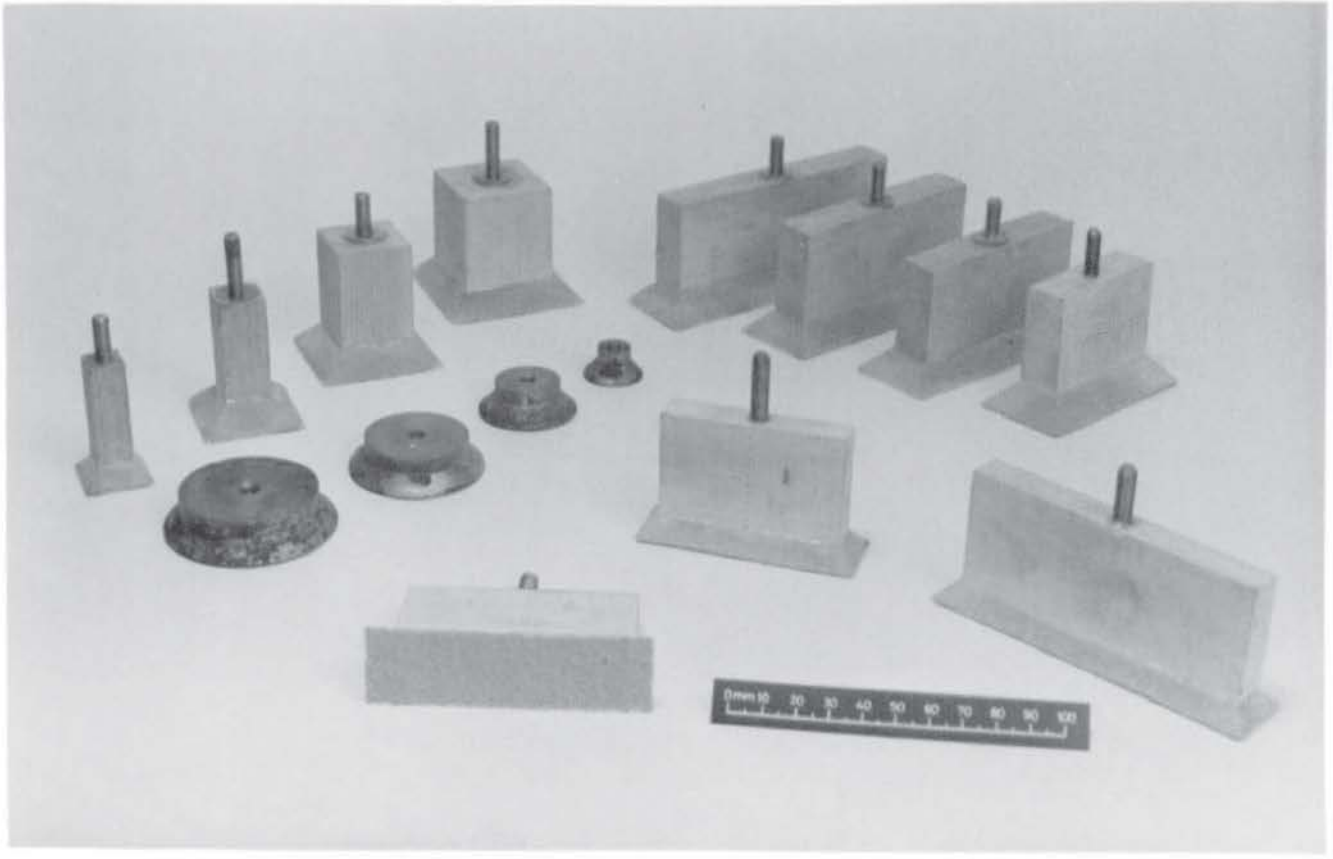

Selection of model foundations.

PLATE 4.4

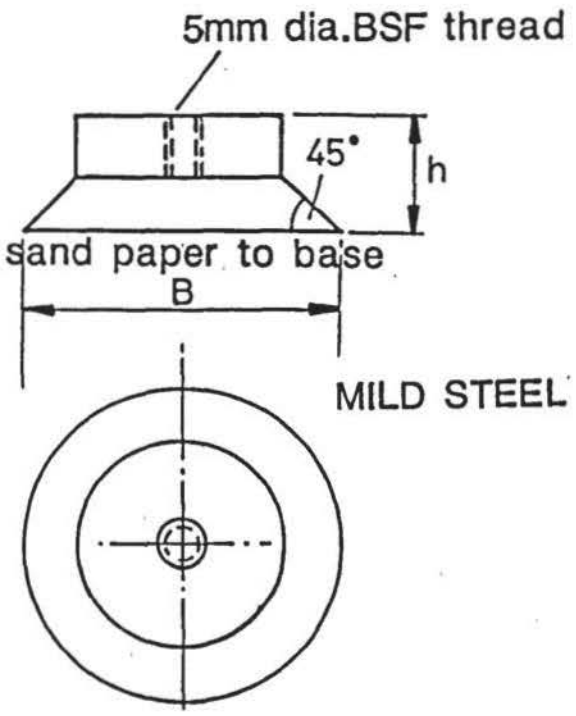

circular

B (mm)	H
25	12
38·1	12
50	12
60	12

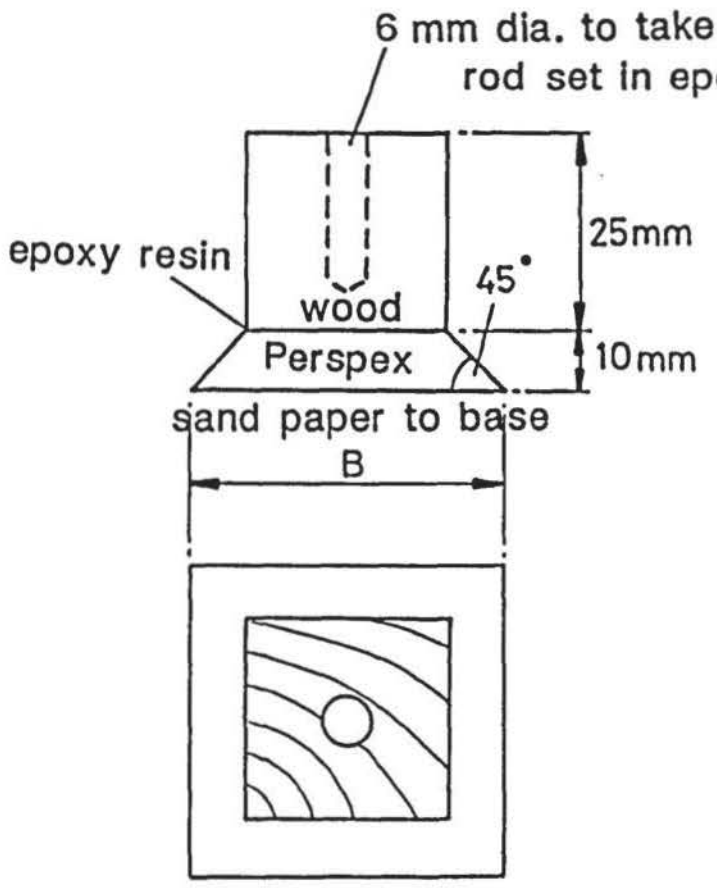

square

B(mm)
25
38·1
50
60

Constructional details of foundations (circular and square).

FIGURE 4.6

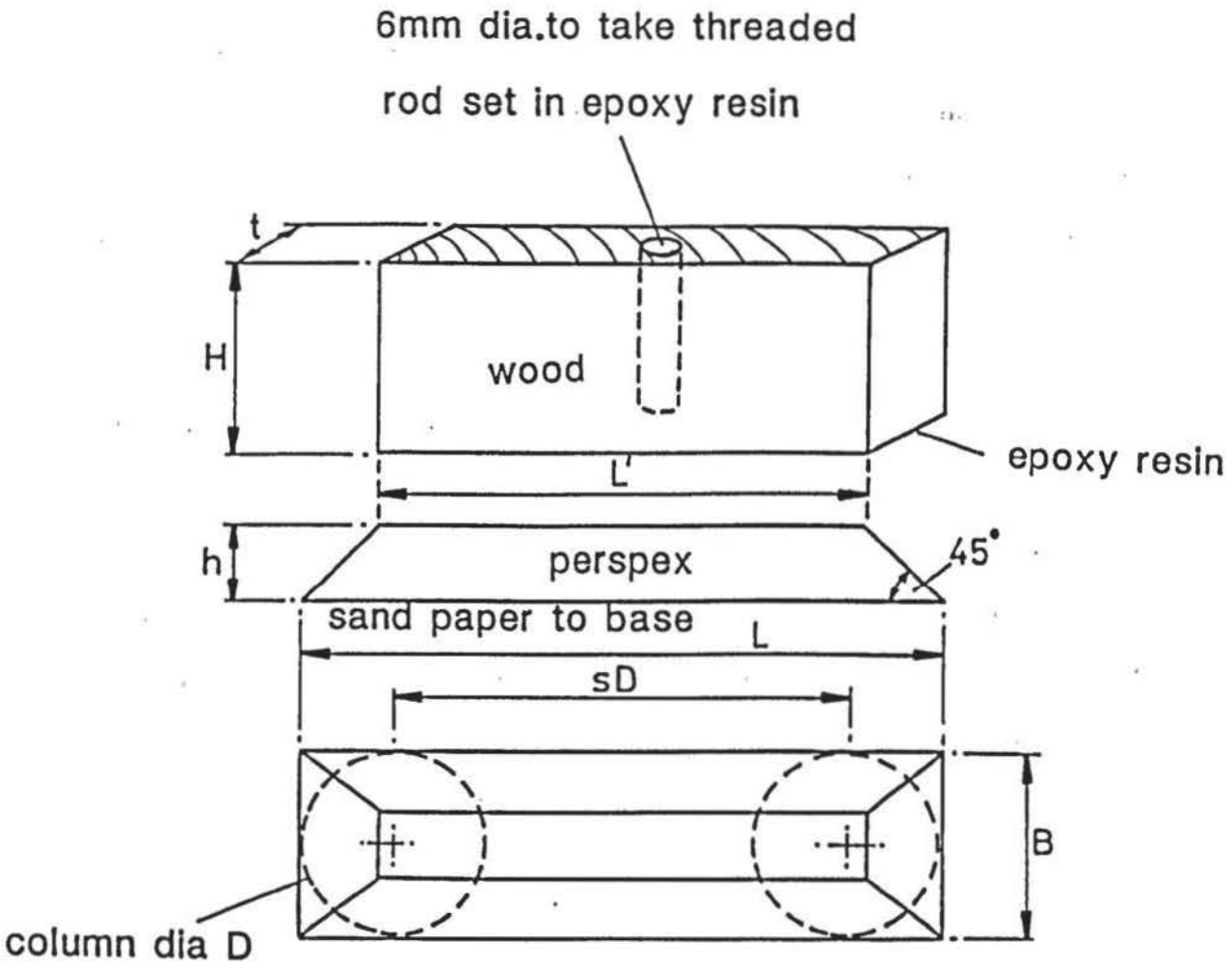

B	PERSPEX s (mm)	L	h	WOOD H	L'	t
38.1	1	76.2	10	40	56	18
25.0	1	76.2	6	40	64	13
38.1	1.25	85.7	10	40	65	18
25.0	1.25	85.7	6	40	74	13
38.1	1.5	95.3	10	40	75	18
38.1	1.75	104.8	10	40	85	18
38.1	2	114.3	10	40	94	13
25.0	2	114.3	6	40	102	18
38.1	2.5	133.4	10	40	113	18
38.1	3	152.4	10	60	132	18
25.0	3	152.4	6	60	140	13
38.1	4	190.5	10	60	170	18
25.0	4	190.5	6	60	178	13

Constructional details of model foundations (Rectangular)

FIGURE 4.7

4.5.2 Pressure Transducer

In one of the container walls a 26 mm diameter hole was made to positon the horizontal soil-boundary stress transducer. As with container A, its position was located with reference to the position of maximum column dilation. Securing details are described in Section 5.5.6.

4.6 MODEL FOUNDATIONS

Model foundations with various geometries were constructed from either mild steel or, mainly, wood bonded to machined Perspex bases. The edges of all foundation bases were chamfered to eliminate side shear and their undersides made 'rough' by the bonding of coarse grade sand paper. Threaded steel rod, 5 mm diameter, seated centrally in the top of the foundations enabled their connection to a vertical loading tube. A selection of foundations are shown in Plate 4.4, together with constructional details in Figures 4.6 and 4.7.

4.7 LINEAR BEARING

The vertical loading tube was manufactured from case hardened steel tubing (25 mm diam. x 200 mm long) which was positioned in a low-friction linear bearing held in a cross-bar located between the vertical strain rods of the particular compression machine used.

4.8 LOAD MEASUREMENTS

Load measurement was by way of an electronic load transducer situated at the top of the loading tube and reacting against the compression machines' cross-head. The transducers are later described in Section 5.4.

4.9 DISPLACEMENT MEASUREMENTS

Since all the compression tests were strain controlled, displacement of the foundation relative to the initial soil level was obtained by a linear electronic displacement transducer, attached to the cross-bar, measuring upward movement of the container top.

The overall arrangement of a container, foundation, loading tube, linear bearing, load transducer, cross-bar and displacement trransducer is shown in Figure 4.8.

4.10 GRANULAR COLUMNS

In engineering practice, a vibroflot or vibrating poker is used to make a dense granular column by first using it to create a vertical bore, in the ground, and then to densify the granular infill material. Methods were sought to produce the same end result at a laboratory scale under controlled conditions.

4.10.1 Column Size

The results of preliminary tests indicated that a 38.1 mm column diameter gave a suitable compromise between a minimum size to restrict boundary effects of the containers and a maximum size to allow workability and practical measurement of column dilation at various loading stages. Difficulties with the latter had been experienced by Dodd (1979), although it may have been that the column densities achieved were less than the critical void ratio of the granular material used.

4.10.2 Vibroflot

Initially, consideration was given to directly simulating the vibroreplacement process at laboratory scale. Metzger and Koerner (1975) describes the construction of a $^1/_{60}$ scale vibroflot used in laboratory studies to densify granular soils. For the present study, however, the method was considered unsuitable for a number of reasons, viz:

(a) The column diameter and length would be difficult, if not impractical, to control. Hughes et al (1975) have shown the critical nature of column diameter in load-settlement prediction analysis.

(b) Densification, to a given void ratio, of the sand column would not be uniform within a given column or consistent for a number of columns.

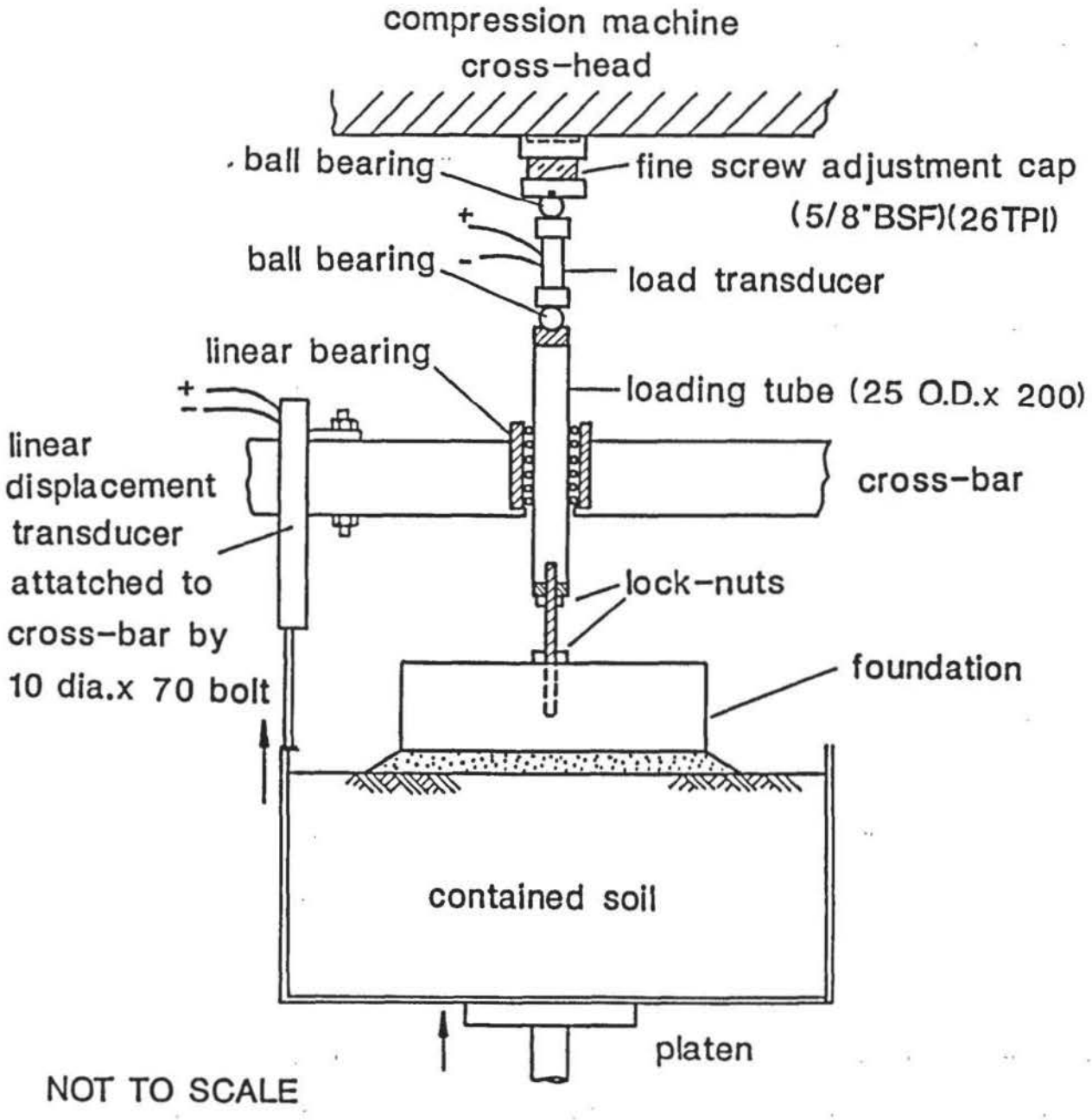

Illustration of the overall arrangement of container, foundation, loading tube, linear-bearing, load and displacement transducers and cross-bar.

FIGURE 4.8

(c) Vibrating pokers give off significant quantities of heat which would affect the shear strength of the clay.

(d) The manufacture and development of a model vibroflot would be unnecessarily time consuming.

As a result, alternative methods were sought to make the column void and dense sand column.

4.10.3 Column Void

By the process of trial and error, the most successful method of forming a clean cylindrical void in the clay was found to be by the initial use of an auger and final trimming with the aid of a steel tube with machined cutting edges.

4.10.4 Auger

The auger was a modified woodworking auger 38 mm diameter. This was held by a 'bit' which was attached to a 25 mm outside diameter steel tube with a T-bar at the top. The assembly was designed to fit into the linear bearing so that it would give accurate vertical alignment whilst allowing rotation by means of the T-bar.

4.10.5 Tubes

Steel tubes 300 mm long and 38.1 mm outside diameter were given cutting edges, shown in Figure 4.9. The external surface of each tube was also coated with a low friction material to prevent adhesion to the clay.

4.10.6 Templates

To ensure the correct positioning of the column voids with respect to the container walls and each other, templates were made from 5 mm thick Perspex for both container types and all the various column configurations. Use of the template and auger to position and make the

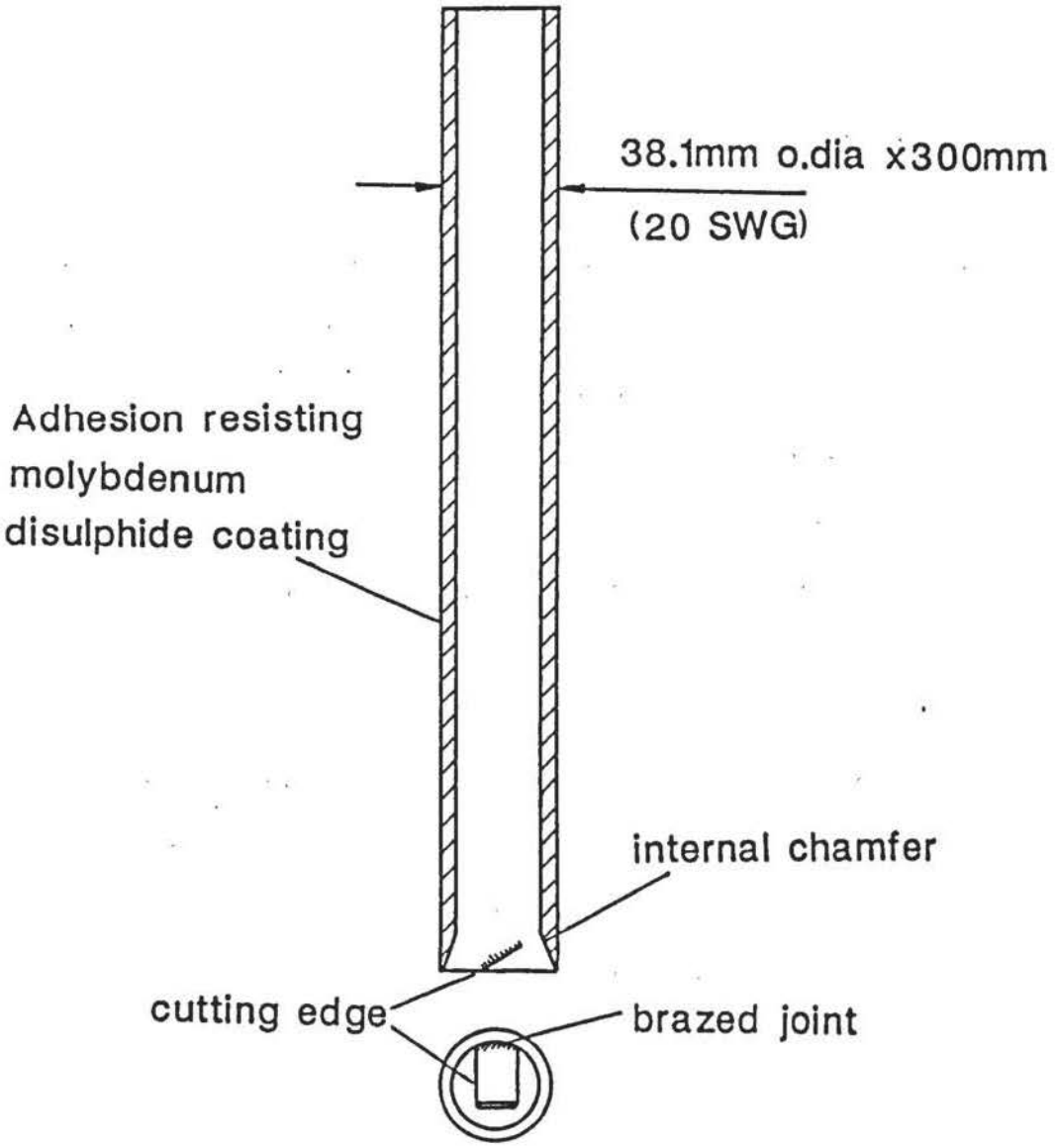

Diagram of steel tube used to complete column void after augering.

FIGURE 4.9

column voids is illustrated in Figure 4.10.

4.10.7 Sand Deposition

The columns were formed by pouring the sand into the void from a hopper. This method was adopted since James (1965) had concluded, from radiographic density tests, that for a given container the pouring technique was the most likely to give consistent and uniform samples.

Kolbuszewski (1948a) had shown sand samples formed by rapid pouring through air resulted in less dense samples than those obtained by slow pouring. After further experimental work, Kolbuszewski (1948b) concluded that a high velocity of fall, through several hundred centimetres height in air, gave a dense sample with a low intensity of deposition and more loose samples as the intensity of deposition was increased. This effect was explained that with high velocities of fall sufficient energy was available to achieve dense packing. When accompanied by a low intensity of deposition the sand grains behaved almost as individuals which enabled them to be forced into positions of relatively close packing.

Kolbuszewski (1958) gave data for Leighton Buzzard sand, from which the curves in Figure 4.11 are derived in metric form. It is evident that provided the height of drop exceeds 600 mm, then the resulting density of the sand for practical purposes is controlled by selecting a mass flow rate. James (1965) also correlated mean void ratio of Leighton Buzzard sand, using a 600 mm x 600 mm container, with the ratio of the hopper flow area to the surface area of the container, shown in Figure 4.12.

4.10.8 Sand Hopper

A sand hopper was found in an existing item of laboratory equipment which consisted of a Kilner jar with its base removed and fitted with a conical nozzle onto the end of which could be screwed caps having different sized apparatus, shown in Plate 4.5. The caps were modified to attach a tube made from Polythene fixed to three cylindrical Perspex formers with plastic hose-clips, shown by Plate 4.6. A Perspex slide is also shown, which was used to shut off the sand flow. The Polythene tube fixed the height of drop to 1 m and prevented spillage of the poured sand. The hopper jar was suspended inside a 115 mm internal diameter Perspex tube by pulleys,

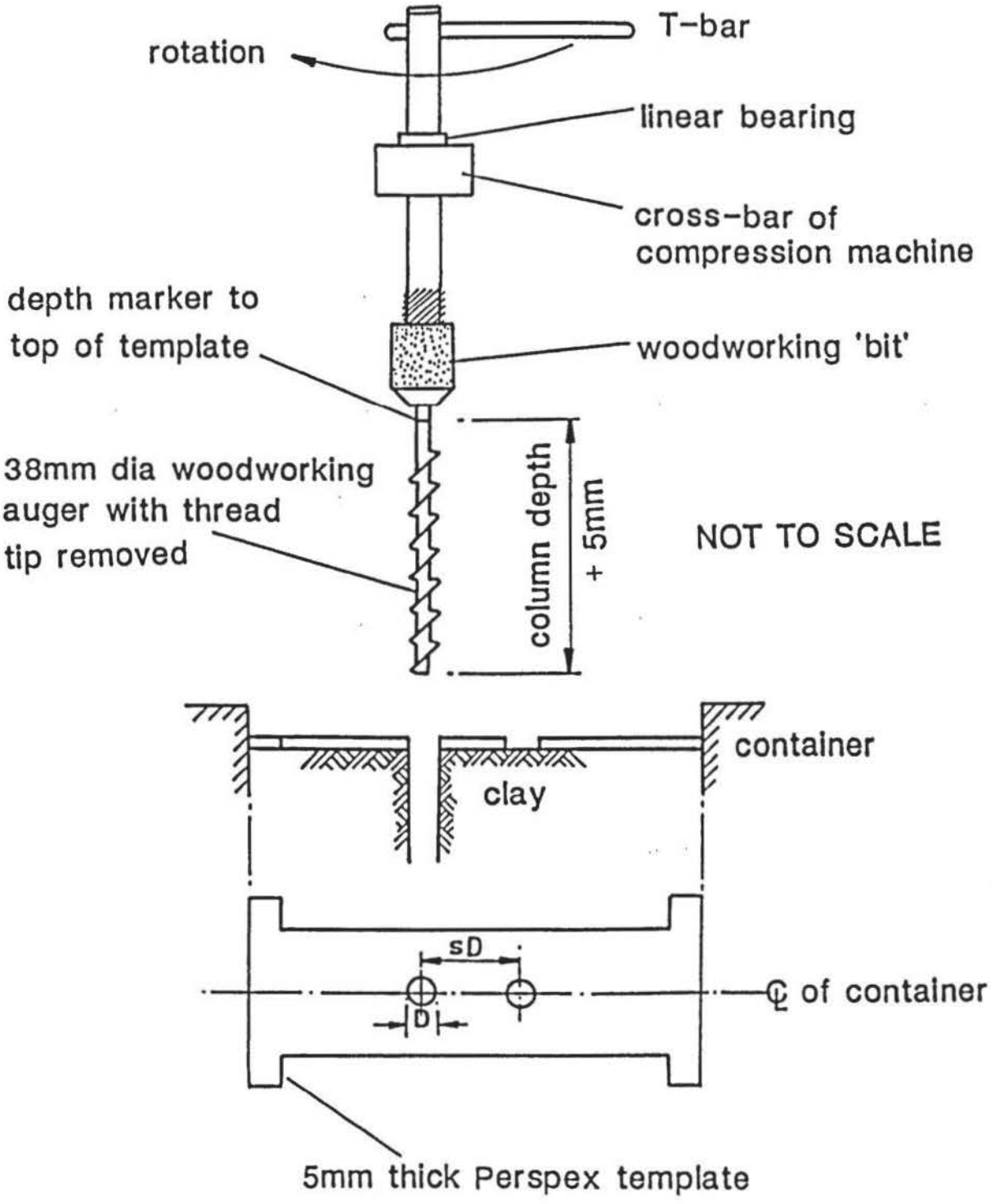

Illustrating use of the template and auger to position and make column voids.

FIGURE 4.10

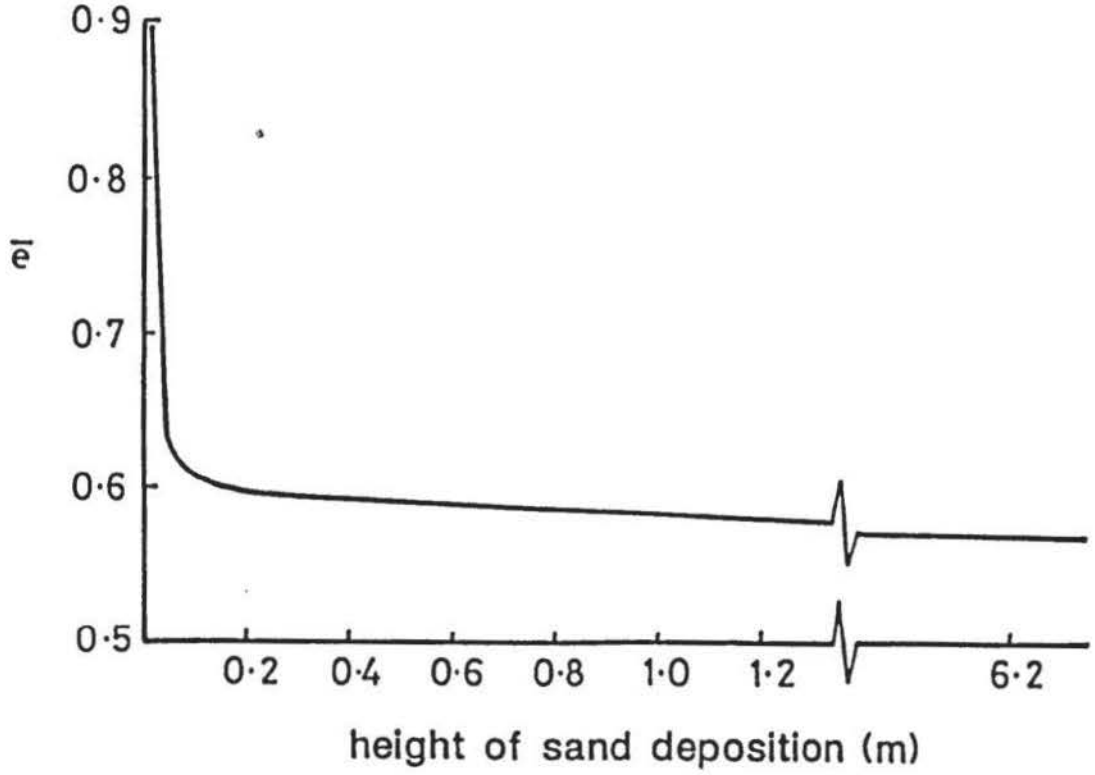

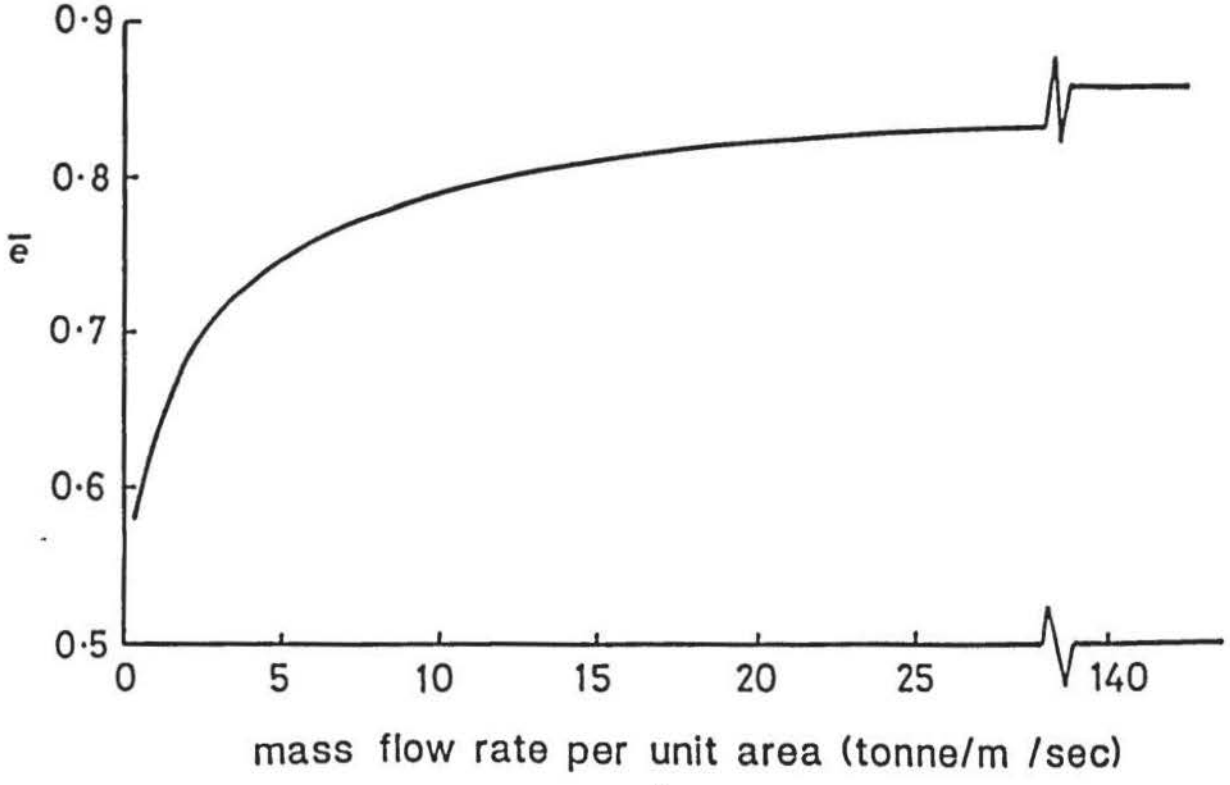

Variation of mean void ratio with height of drop and mass flow rate per unit area of hopper of poured Leighton Buzzard sand (after Kolbuszewski, 1958).

FIGURE 4.11

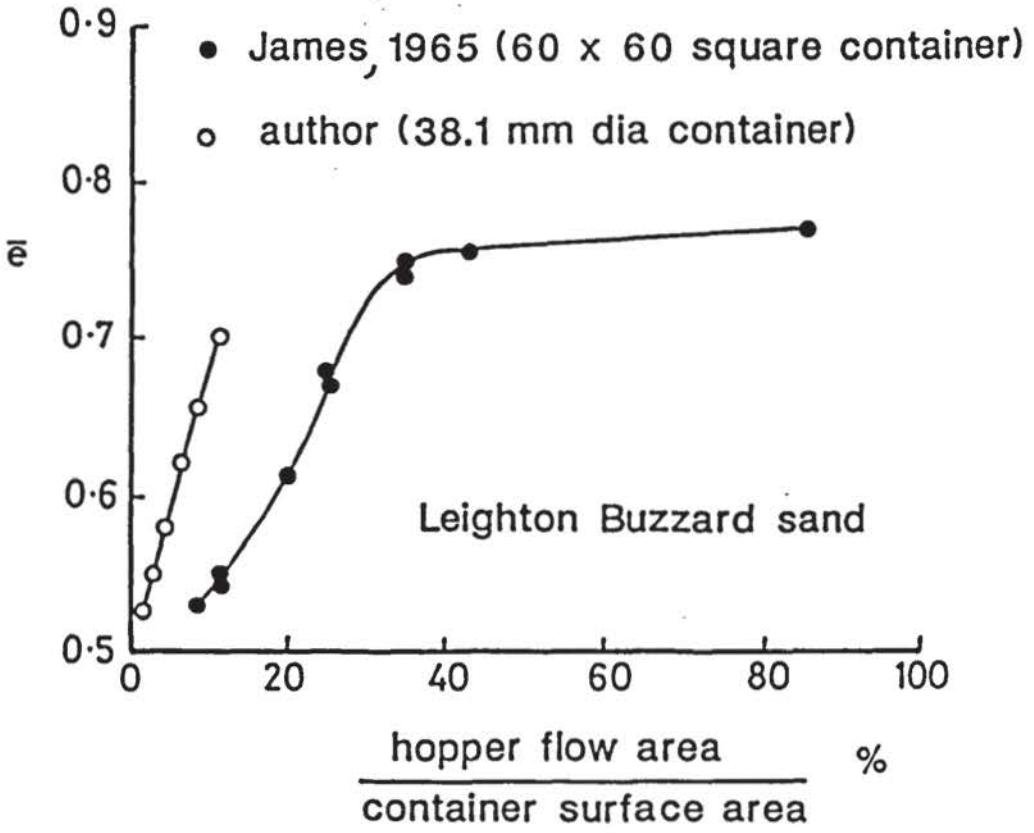

Variation of mean void ratio for Leighton Buzzard sand with the ratio of hopper flow area of surface area of container (after James, 1965).

FIGURE 4.12

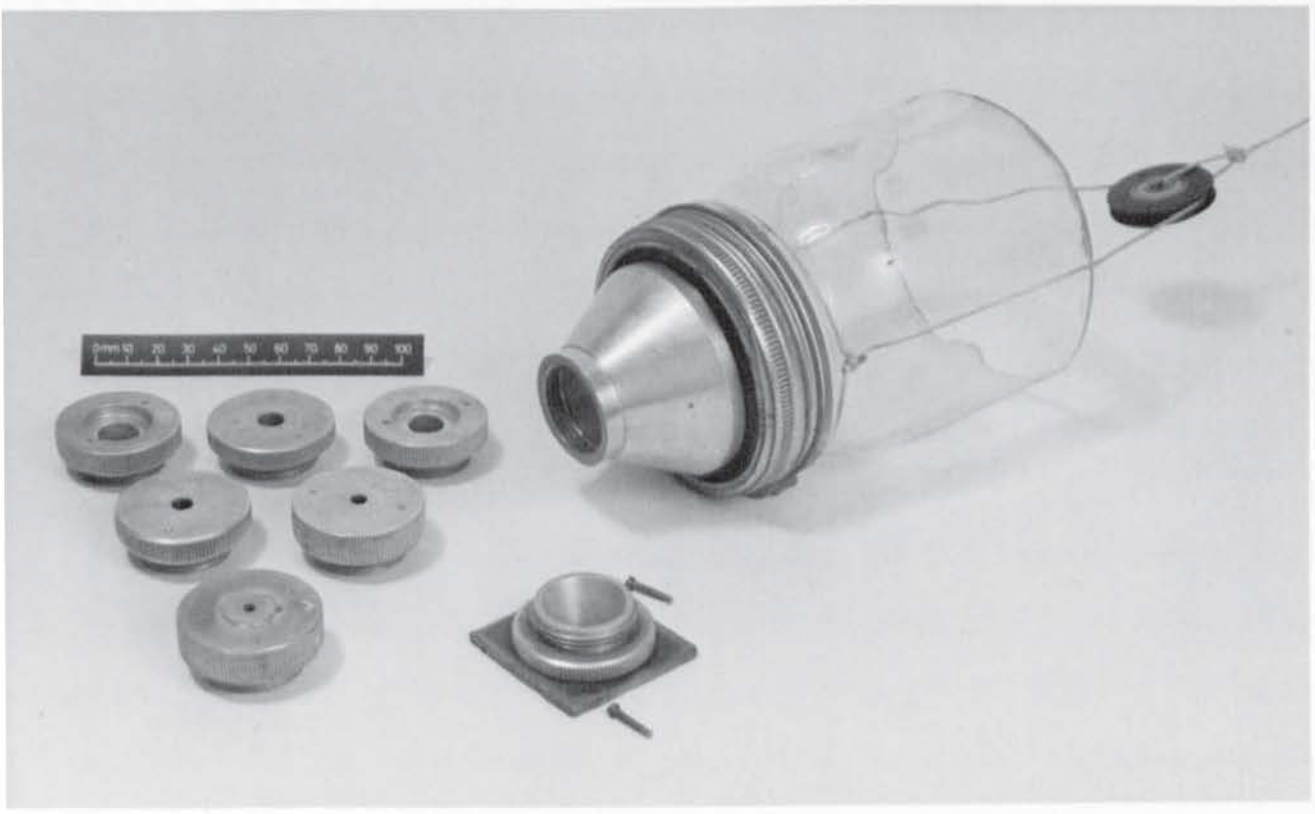

Sand hopper jar with a range of appertures.

PLATE 4.5

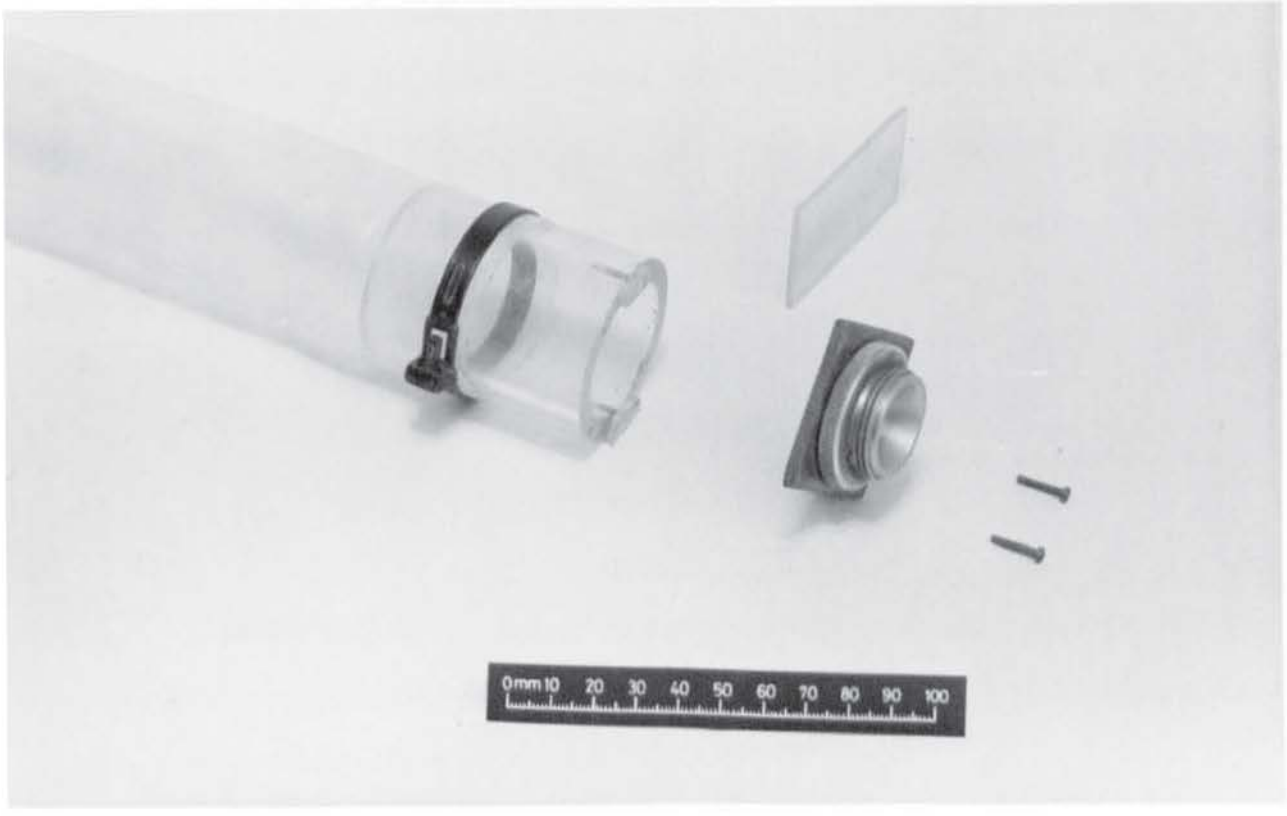

Showing attachment of polythene tube and perspex former to hopper apperture.

PLATE 4.6

shown in Plate 4.7, to ensure vertical alignment and allow adjustment of height to suit the clay container being used. The whole assembly was held in a frame made from 40 mm x 40 mm Dexion angle. Provision was made for lateral movement of the hopper to allow positioning over the clay container. Overall dimensions of the frame and the general mode of operation of the assembly is illustrated in Figure 4.13. Plates 4.8 and 4.9 show the hopper and frame in use with containers A and B, respectively.

4.10.9 Pouring Characteristics

Using a 38.1 mm internal diameter by 150 mm long metal tube, the pouring characteristics were obtained using 0.4 kg batches of the Leighton Buzzard sand poured from a series of cap aperture between 11/64 inch (4.366 mm) and $^1/_2$ inch (12.7 mm) diameter from the fixed height of 1 m. The results are tabulated in Figure 4.14. The 4.366 mm (11/64 inch) diameter cap aperture was the smallest that could be used without clogging of the sand particles, for the sand grading used. This apperture was used to form the columns in the laboratory programme since it produced the densest samples.

In order to establish an objective measure of the consistency in producing the columns, a statistical approach was used. Using the values of mean void ratio (e) obtained from twenty samples prepared in the metal tube, using the 4.366 mm apperture, the average mean void ratio (e_{av}) and estimated standard deviation (s) were determined as 0.5266 and 0.0018, respectively. The results gave a normal distribution curve and so the 99.73% (i.e. near certainty) confidence limits are :

$$0.5266 \pm 3\,s$$

giving $$0.5266 \pm (3 \times 0.0018)$$

$$= 0.5266 \pm 0.0054$$

or $$\underline{0.5266 \pm 1.03\%}$$

The results of all the pouring characteristic tests are shown graphically in Figure 4.15. For comparative purposes the e vs. ratio of hopper flow area to container area, obtained, have been added to those of James (1965) in Figure 4.12.

Suspended hopper assembly and perspex guide tube.

PLATE 4.7

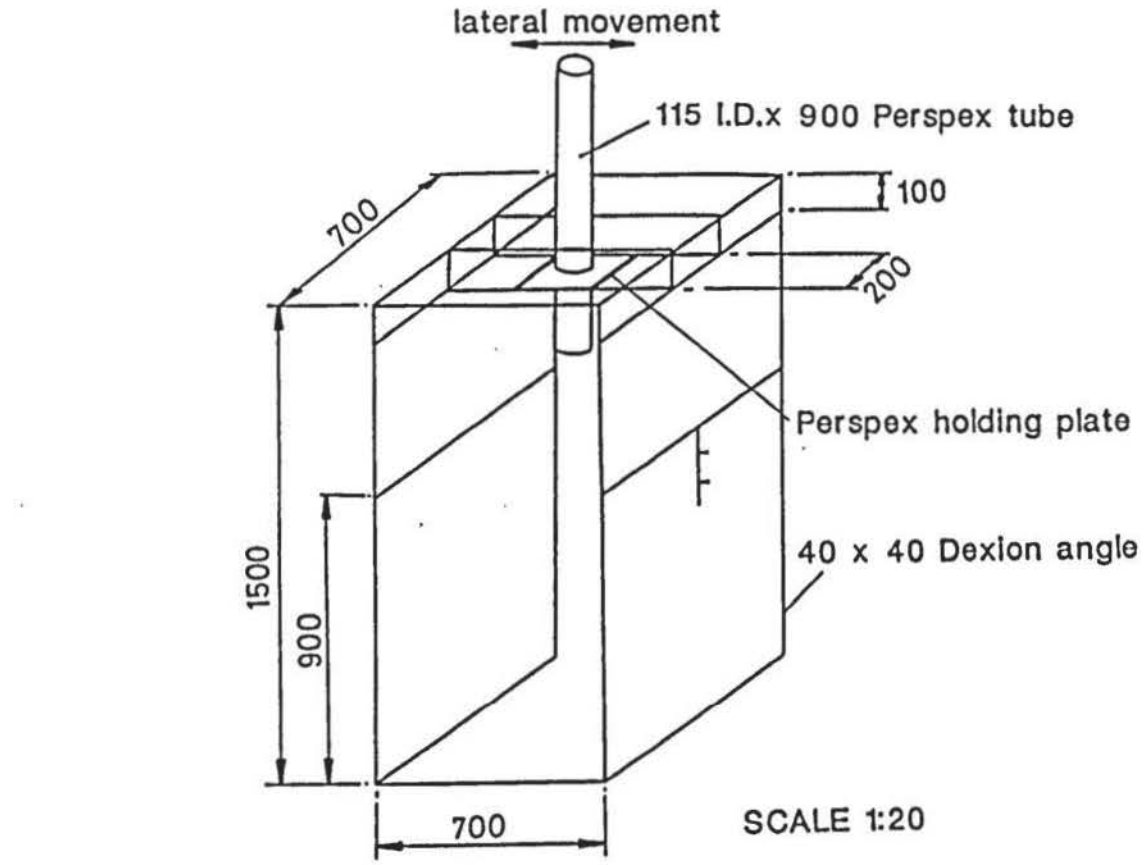

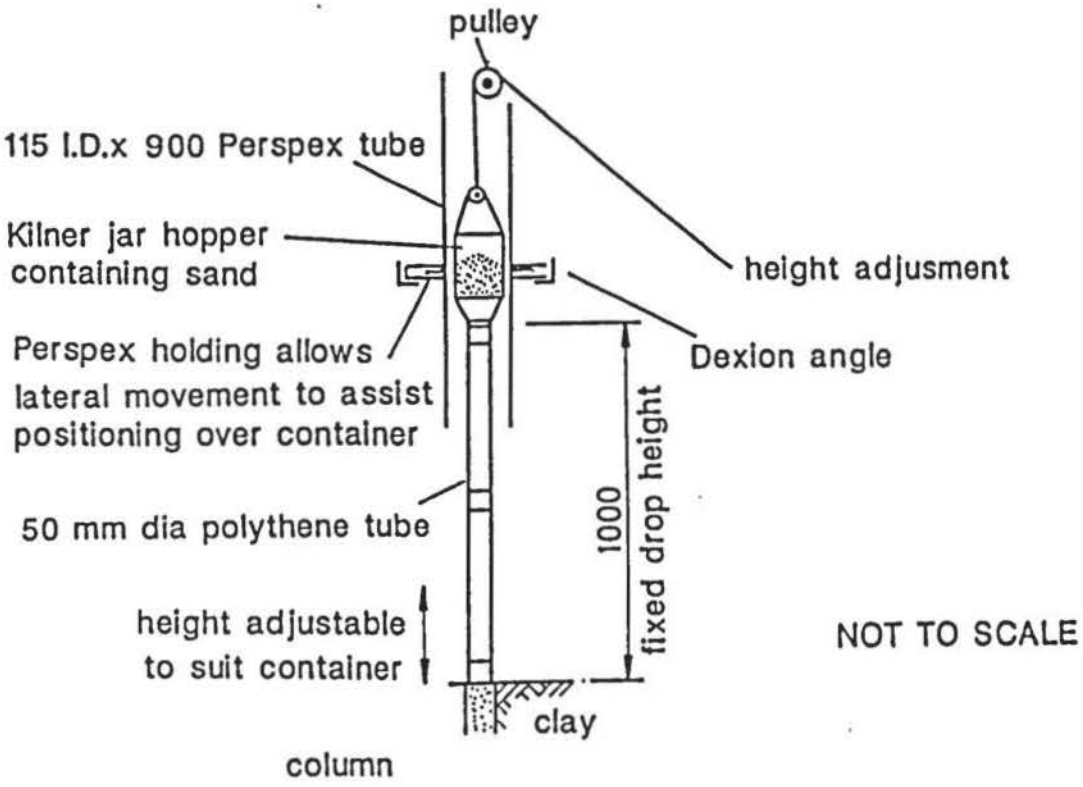

Overall dimensions of sand hopper rame and mode of operation of the assembly.

FIGURE 4.13

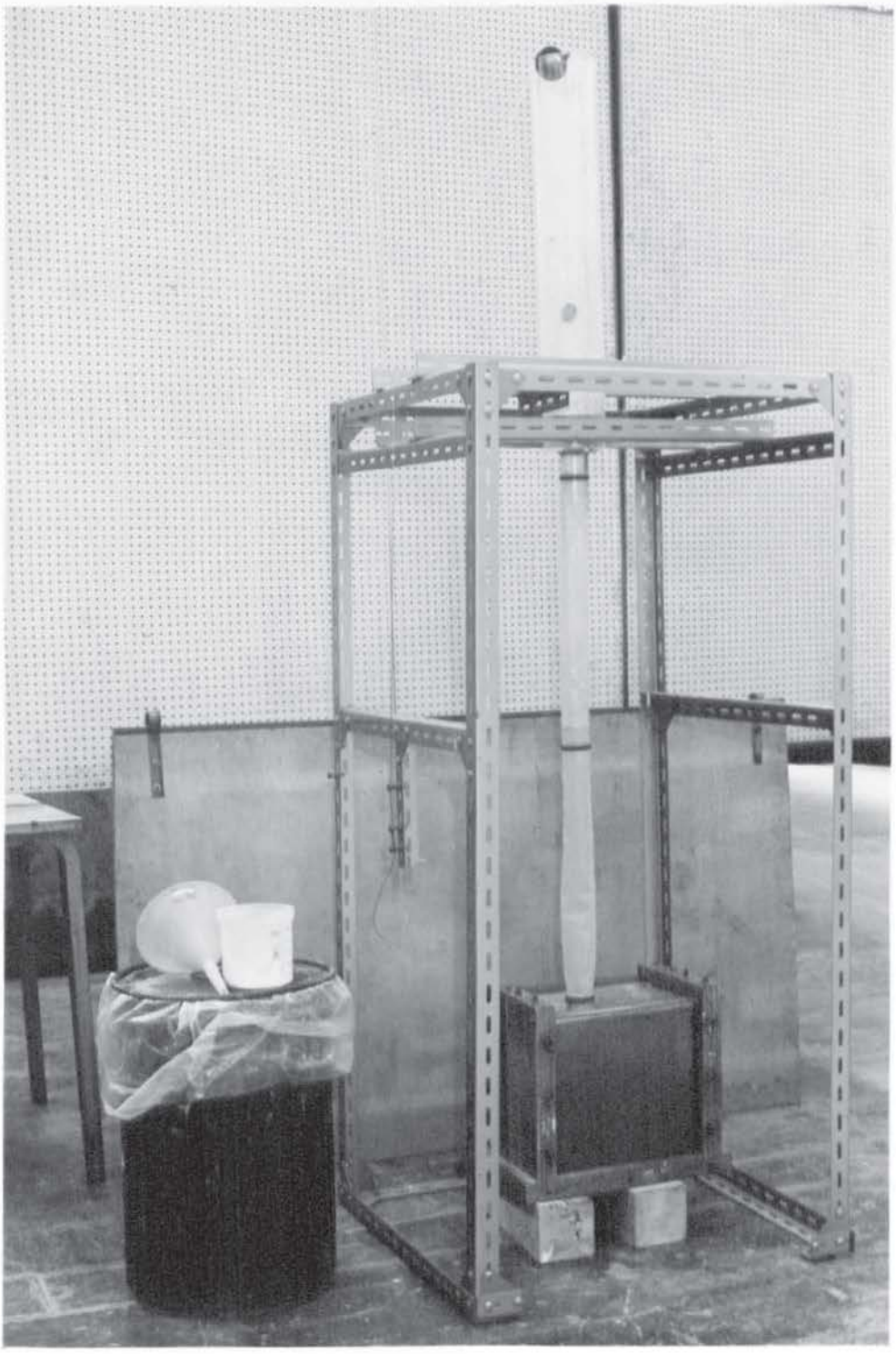

Hopper and frame over container A.

PLATE 4.8

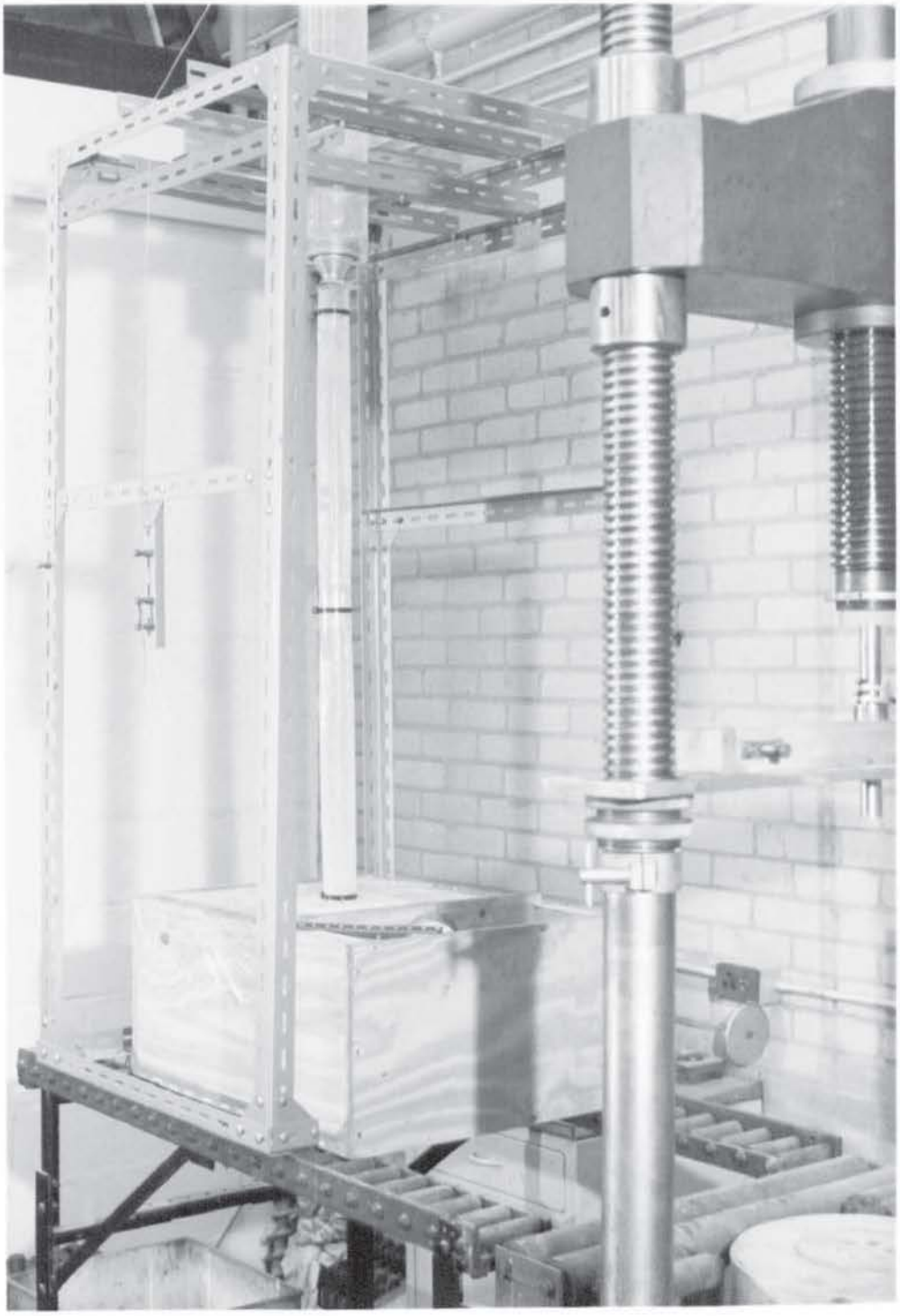

Hopper and frame over container B.

PLATE 4.9

Hopper Flow Diameter		Area	Mass of sand	Time	e	(1)	(2)
inch	mm	mm^2	g	sec.		$kg/m^2/s$	%
*11/64	4.366	14.969	400	200	0.525	111.34	1.32
3/16	4.763	17.814	400	155	0.530	144.87	1.57
1/4	6.350	31.669	400	62	0.549	203.72	2.80
5/16	7.938	49.483	400	34.5	0.582	234.31	4.37
7/16	11.113	96.987	400	14.5	0.656	284.43	8.57
1/2	12.70	126.677	400	9.5	0.703	332.38	11.20

(1) Mass flow rate per unit area

(2) hopper flow area/container surface area normal to flow.
(38.1 mm diameter x 150 mm container).

* smallest diameter possible without clogging.

Table of test results using various hopper flow apparatus.

FIGURE 4.14

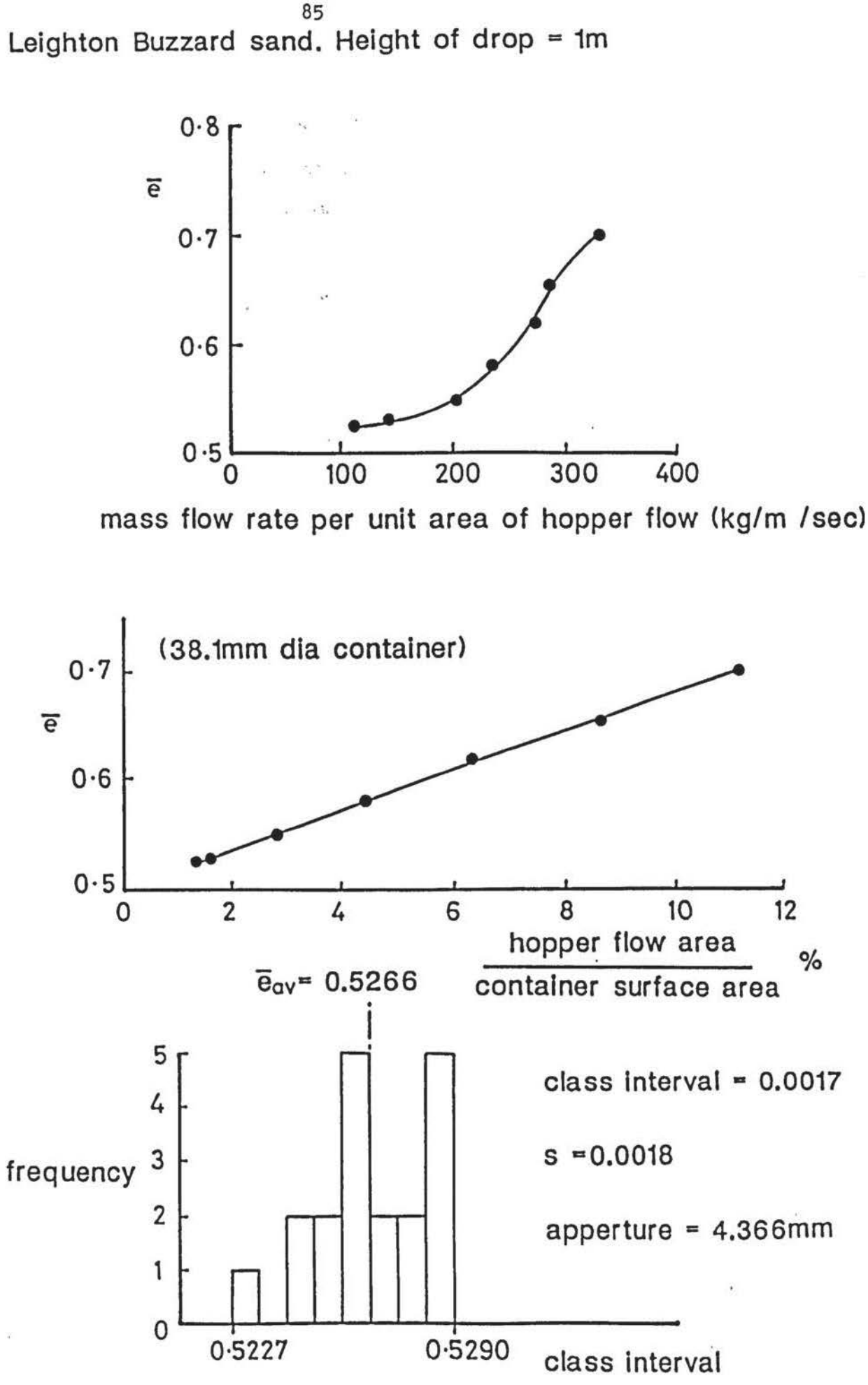

Pouring characteristics of hopper using Leighton Buzzard sand and 38.1 mm diam. x 150 mm deep container.

FIGURE 4.15

For all the tests, after deposition of the sand into the tube the surplus sand (heaped at the surface) was removed by a thin metal spatula. This method showed more consistent results than the vacuum method described by Cole (1967) and Hope (1979).

4.11 RADIOGRAPHIC EQUIPMENT

4.11.1 X-ray Set.

The X-ray set was a circulating oil-cooled Pantak constant potential industrial radiography unit which had been modified to reduce output fluctuations by stabilising the mains supply and tube current. Both voltage and current were continuously variable up to a maximum of 300 kV and 12 mA. The standard focal spot size was 4 mm x 4 mm. An automatic timer and exposure shutter allowed the voltage and current to be set before exposure.

The tube-sheld was cantilevered from a steel column which incorporated a millimetre scale, via a Minilift winding mechanism to give accurate height adjustment to within ± 1 mm. The tube-shield was used locked in the horizontal position, shown in plate 4.10.

4.11.2 Sheilding

To minimise the adverse effects of scattered radiation on radiograph quality, the clay container and cassette were shielded by double thickness of 2 mm lead sheet mounted on hardboard. Examples of the shielding may be seen in plate 4.10.

4.11.3 Lead-Shot

Lead-shot obtained direct from the manufacturer was of 2.5 mm nominal diameter. Grading analysis showed a size range varying between > 2.79 and < 2.41. The diameters of the lead-shot used were restricted to the range 2.41 mm to 2.67 mm. Because some of the shots were not spherical, a tolerance was applied by rejecting those which pursued an irregular path when rolled down a slightly sloping flat surface.

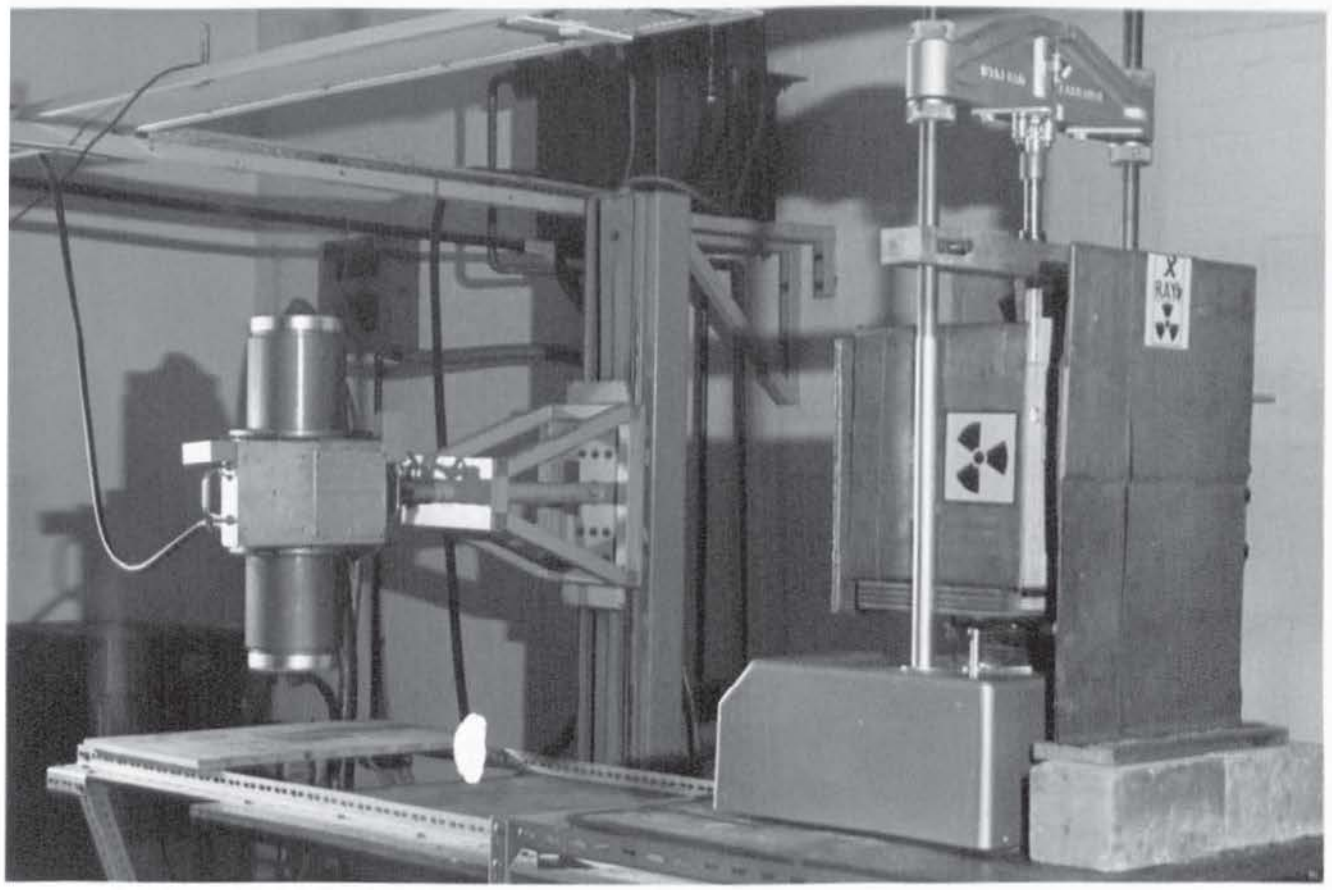

X-ray set and lead-shielding.

PLATE 4.10

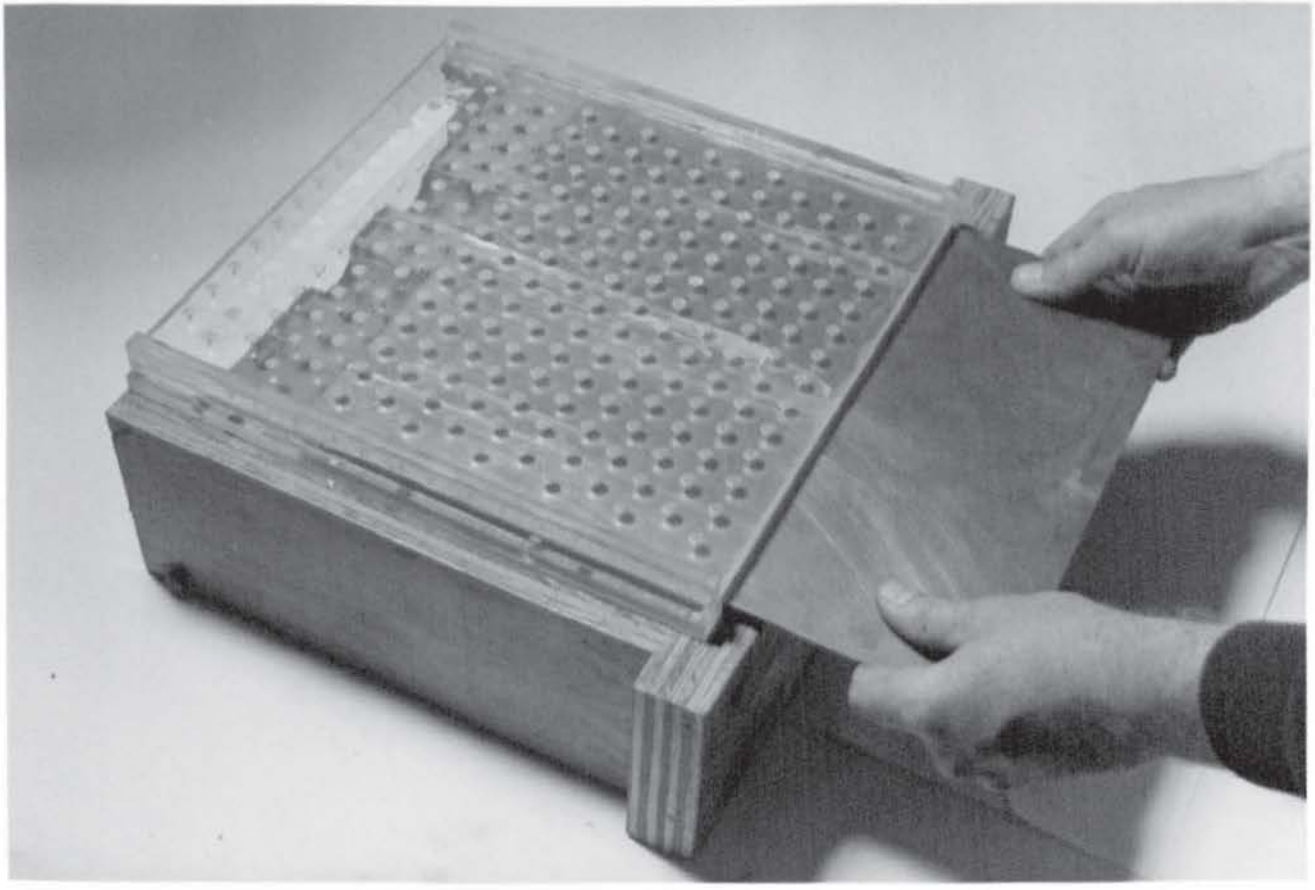

Lead-shot template.

PLATE 4.11

4.11.4 Lead-Shot Templates

Positioning of the lead-shot onto the vertical surface of the clay was achieved by using a template. This was fabricated from 10 mm thick Perspex sheet, the general details of which are shown in Figure 4.16. After drilling 2.75 mm diameter holes in the desired array, these were countersunk to allow ease of inserting the lead-shot. Strips of Perspex were bonded to the sides of the sheet and given 5 mm diameter holes at positions coincident with the steel dowels set into one of the halves of container A. The strips were also positioned to give a continuous slot into which a 3 mm thick steel sheet could be inserted. This arrangement allowed all the shot to be placed into the template and then for it to be correctly located and positioned on the container when the latter was laid horizontally. By withdrawing the steel sheet, the lead shot would drop under their own weight onto the clay surface beneath. The template is shown in Plate 4.11.

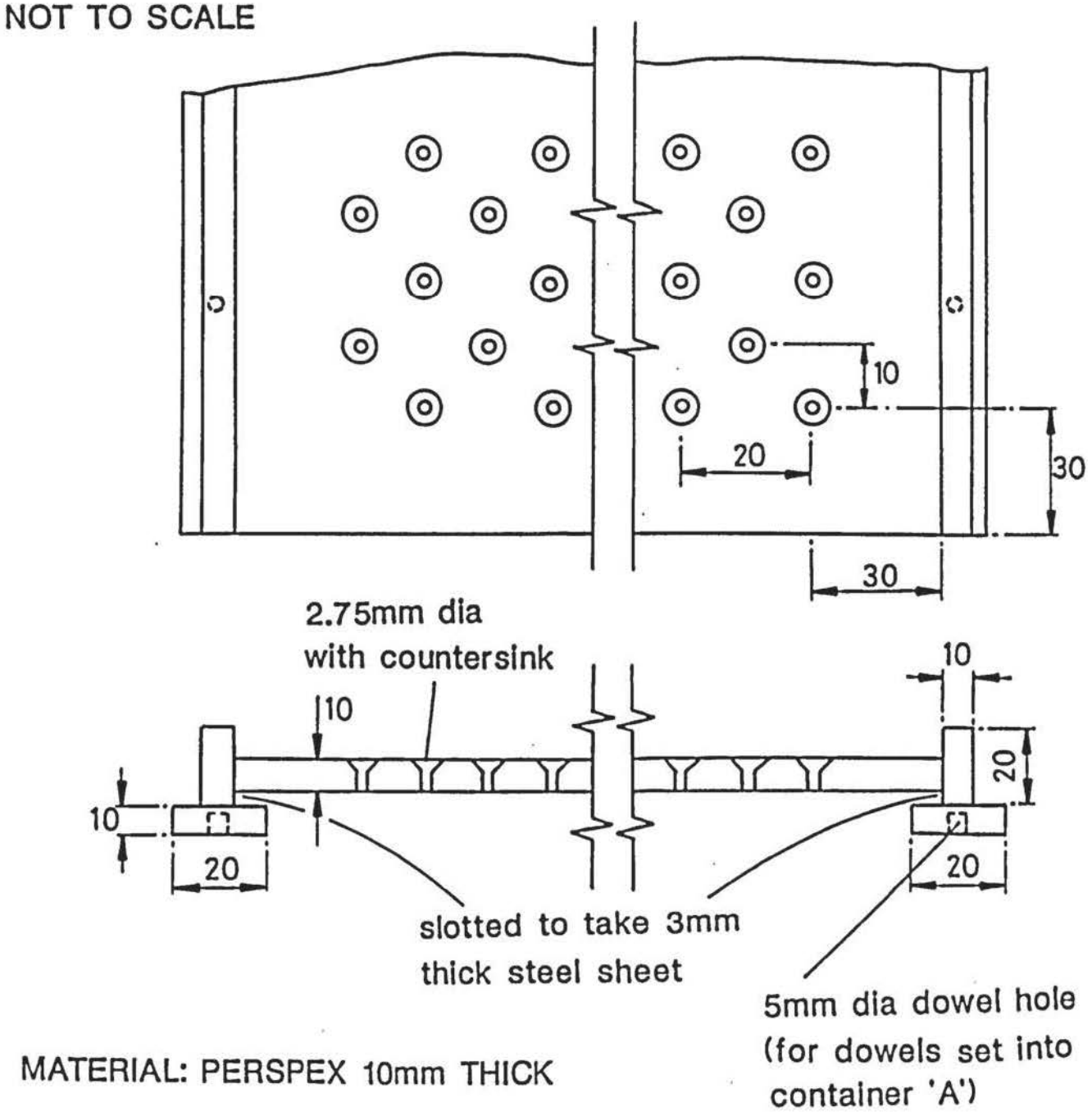

General details of Perspex template for placing lead-shot.

FIGURE 4.16

CHAPTER 5

INSTRUMENTATION

5.1 INTRODUCTION

Electronic transducers were used to measure load, displacement and boundary stresses in the laboratory experimental work. They allowed simultaneous recording of multiple measurements to be made by automatic data-collection equipment in a form suitable for computer processing.

Commercially manufactured transducers were used for triaxial compression test and displacement measurement applications. Foundation load and soil boundary stress transducers, however, were purpose-designed by the author and fabricated by the Department's Electronic Section.

5.2 TRANSDUCER DESIGN PRELIMINARIES

5.2.1 Basic Principle.

The transducers designed by the author featured a basic conformation comprising an 'elastic' structural element with bonded electrical foil resistance gauges connected in a Wheatstone Bridge circuit, shown in Figure 5.1(a). A change in resistance of the gauges results from deformation of the element, due to an applied load (L), which produces a proportional response in the circuit output voltage (V_o) as illustrated in Figure 5.1(b). The overall sensitivity is the ratio of the amount by which the output voltage changes to the change in applied load, or stress.

A comprehensive review of soil mechanics instrumentation by Hanna (1973), indicated that load and stress transducers of this pattern are the most popular. A survey of the literature suggests this popularity is a result of versatility, cost and reliability.

5.2.2 Bridge Circuits

Four foil resistance gauges were used to form all the transducer bridge circuits. The arrangement practically eliminates output voltages induced by thermal straining of the structural

A : active gauge

D : dummy gauge

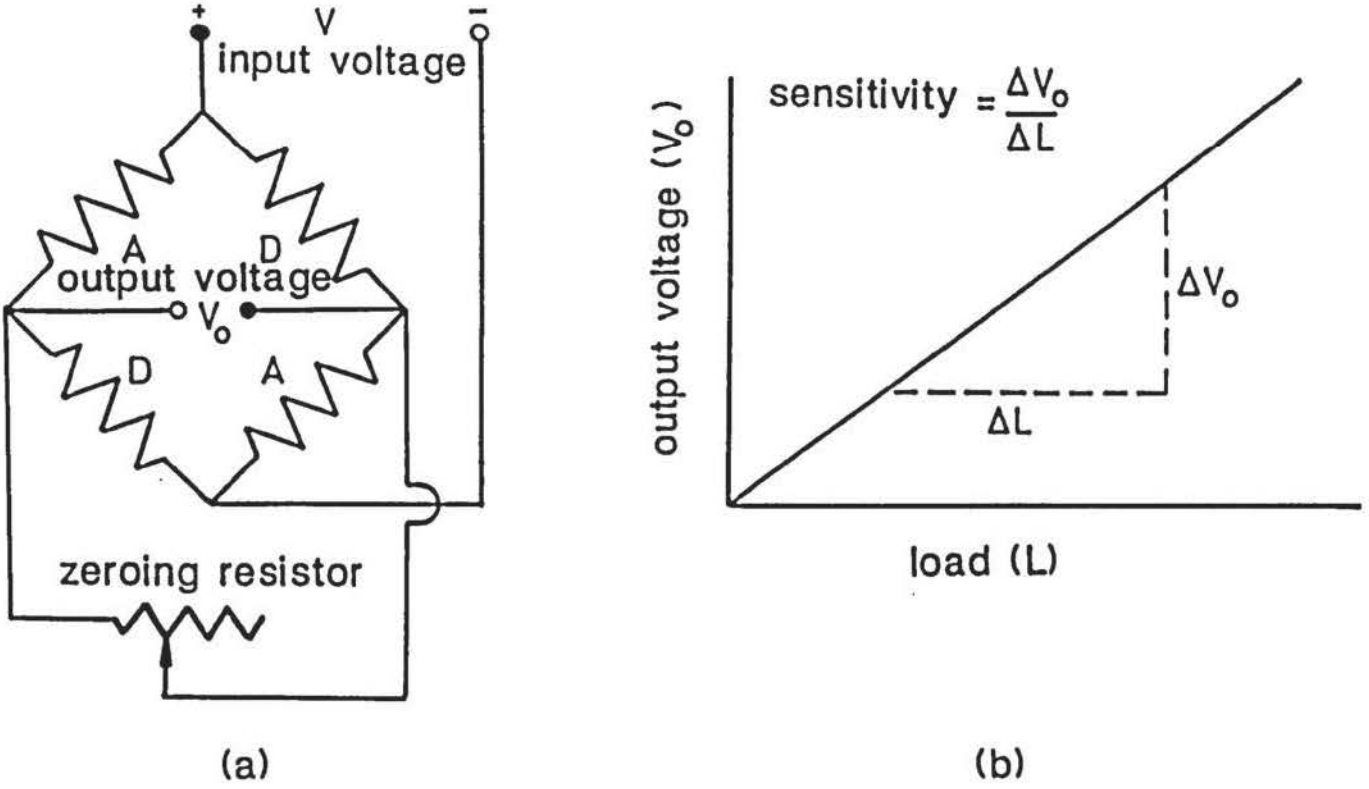

Wheatstone bridge circuit formed by four foil gauges and desired output voltage response to load.

FIGURE 5.1

element and temperature changes directly affecting the specific resistance of the gauge material. Although adequate temperature compensation may be achieved with just two gauges, it has the inconvenience of needing external resistances to complete the circuit. A two gauge bridge is also less sensitive than a four gauge one. In practice, a zero adjusting resistance (shown in Figure 5.1(a)) is necessary to correct the initial circuit imbalance attributable to gauge manufacturing tolerances and possible length variations of circuit wiring. Murray and Stein (1958) have shown that zero adjusting resistances greater than 4kΩ cannot cause any appreciable change in the output voltage during adjustment.

5.2.3 Structural Element

The transducer element must be rigid enough for its stress-strain characteristics to be linear over the operating range and for its structural stresses, over that range, to induce negligible creep or hysteresis effects. Trollope and Currie (1960) emphasised the critical effect of element stiffness in the measurement of soil boundary and in-situ stresses, particularly in the case of sands. Insufficient stiffness causes significant errors in measurement due to stress redistribution at the measuring face.

5.2.4 Sensitivity

For accuracy and convenience, the sensitivity needs to be kept to a constant value which is high enough to give a desired measurement range. Providing structural linearity is achieved by suitable choice of the element material and geometry, then the objective becomes one of maximising the change in the bridge output voltage (ΔV_o). From an analysis by Murray and Stein (1958), for a strain gauge bridge circuit, it can be shown that :

$$\Delta V_o \propto F V \varepsilon \qquad (5.1)$$

where F is the gauge strain sensitivity factor, V is the bridge input voltage and ε is the strain in the element at the gauge position(s).

For foil gauges the strain sensitivity is fairly low (typically F = 2.1), so in order to maximise ΔV_o the bridge input voltage and strain need to be as high as possible. However, criteria

influencing the design and performance of the structural element place a severe restriction on the latter, particularly in the case of soil boundary-stress transducers.

5.2.5 Bridge Input Voltage

The bridge input voltage is also limited by the largest current that can flow through a resistance gauge without causing adverse heating effects. These are characterised by greater drift of the ouptut voltage from its low-current value. Where heat dissipation from the gauge exceeds the heat sink capabilities at its position of attachment to the element, physical damage occurs.

Whitaker (1963) used two gauges in series in each arm of a load transducer full-bridge circuit. This doubled the resistance in each arm and halved the current through the gauges, allowing the input voltage (and hence the sensitivity) to be doubled in restoring the maximum current flow. Burland (1967) immersed whole transducers in silicone oil to overcome charring of small foil gauges, bonded to extremely thin structural webs, when voltages larger than those allowable were applied.

5.2.6 Range Limitations

As a result of the constraints imposed by the element stiffness, gauge strain sensitivity and input voltage, transducers invariably suffer practical limitations in range with typical peak output voltage changes of a few hundred micro-volts. In soil mechanics terms, this can mean that transducers designed for maximum sensitivity up to 'working-load' may be structurally inadequate (i.e. exceeding the linear range) to sustain stresses at failure. Conversely, transducers designed to adequately accommodate 'failure loads' may not give reliable measurement significantly below 'working-load' levels. In practice a design compromise can be adopted or a given test repeated using two transducers to cover the desired stress or load range.

Also, with such small voltages, difficulties are compounded by the risk of spurious electrical signals occurring with monitoring equipment causing erroneous measurment.

5.2.7 Semi-Conductors

Semi-conductor gauges have been tried previously (e.g. Dunn and Billam, 1966) since they have a strain sensitivity factor 50-60 times that of foil gauges (i.e. F = 105-125), but their cost is substantially greater. Semi-conductor gauges have large temperature coefficients and because their resistance change is so large it is necessary to supply them from a constant current source to eliminate non-linearities, and temperature effects, through changes in power consumption (Bransby, 1973). They also have smaller specific areas than comparable foil gauges which increase the stress in the bonding material holding the gauge to the element, and reduces the heat sink capacity.

5.2.8 Amplification

There was a conspicuous absence in geotechnical literature of reference to the use of electrical amplifiers, although their merits offer a solution to the incompatibilities of practical transducer design. Attention was given to the use of micro-electronic amplifiers to give substantial increases in transducer output voltages, and hence sensitivity . Unlike semi-conductors, amplifiers can be re-used so the initial capital costs can be spread over their working life.

Micro-electronic components are manufacturerd to extremely fine tolerances, requiring very small electrical currents. This leads to high stability and negligible contributory errors.

5.3 AMPLIFIER

5.3.1 Basic Principle

In principle, an amplifier increases the strength of a signal fed into it by obtaining the power to do so from another source. If the input signal used is the output voltage (ΔV_o) from a transducer bridge circuit, then:

$$\Delta V_o^{amp} = G.\Delta V_o \qquad (5.2)$$

where ΔV_o^{amp} is the amplified bridge output voltage and G is defined as the amplifier gain.

5.3.2 Advantages

The use of a transducer amplifier offers a number of distinct advantages:

(a) The high amplification (or gain) allows some over-design in the stiffness of the structural element. Thus, both the element and gauge bonding materials operate much below their yield stresses, so reducing errors due to zero-drift, creep and hysteresis. The transducer will also be robust and should introduce significantly less error in soil stress measurement.

(b) The bridge circuit may operate at a reduced proportion of its maximum supply voltage, preventing adverse heating effects of the foil gauges and bonding material.

(c) The occurrence of spurious signals present in the monitoring equipment (generally of the order of micro-volts) will be negligible in comparison with the magnitude of the output voltage (ΔV_0^{amp}).

5.3.3 Description

The amplifier used was a hybrid integrated circuit (SGA 100 module, manufactured by CIL Electronics Limited, Worthing) with added circuitry to give:

(a) Adjustment of the bridge circuit supply voltage.

(b) Zeroing the bridge circuit.

(c) Adjustment of gain.

A circuit diagram, including the bridge network, is given in Figure 5.2 and a complete amplifier unit is shown in Plate 5.1.

The SGA 100 module was 33 mm x 20 mm x 12 mm and was mounted directly on a printed circuit board. It contained all the circuit elements to both power the transducer bridge network and amplify its output. The module was operated with ± 12 volt DC supply applied to pins 22 and 24.

5.3.4 Specification

A full specification of the SGA 100 module is given in Appendix B. The total cost (1983) of the SGA module, printed circuit board and associated components was about £38.

5.3.5 Error Magnification

It may be considered that amplification of transducer output would also magnify intrinsic errors by the same degree. This is not the case. Whilst that proportion of the bridge output voltage change not generated directly by the applied load (or stress) is similarly amplified, its proportionality to the true signal remains unchanged:

$$\Delta V_o = \Delta V_\sigma + \Delta V_e \qquad (5.3)$$

where ΔV_e is the change in output voltage generated by causes other than the applied load, or stress. Using Eqn. 5.2 and substituting Eqn. 5.3:

$$\Delta V_o^{amp} = G.\Delta V_o = G\,(\Delta V_\sigma + \Delta V_e)$$

then

$$\text{error} = \frac{G.\Delta V_e}{\Delta V_o^{amp}}$$

giving

$$\text{error } \% = \frac{\Delta V_e}{\Delta V_o} \times 100 \qquad (5.4)$$

Thus, the percentage error will remain constant with gain.

5.3.6 Effects of Power Supply

Changes of a few volts in the amplifier supply voltages ($\pm V_s$) were found to have little or no effect on the magnitude of the bridge supply voltage (V). The amplifier gain, however, was found to be sensitive to such changes, particularly when the supply voltages changed by equal and opposite amounts (e.g. V_s = + 12.010 and - 11.990 volts). As a result, it was important to maintain the stability of the amplifier voltages to prevent fluctuations in gain introducing errors in measurement.

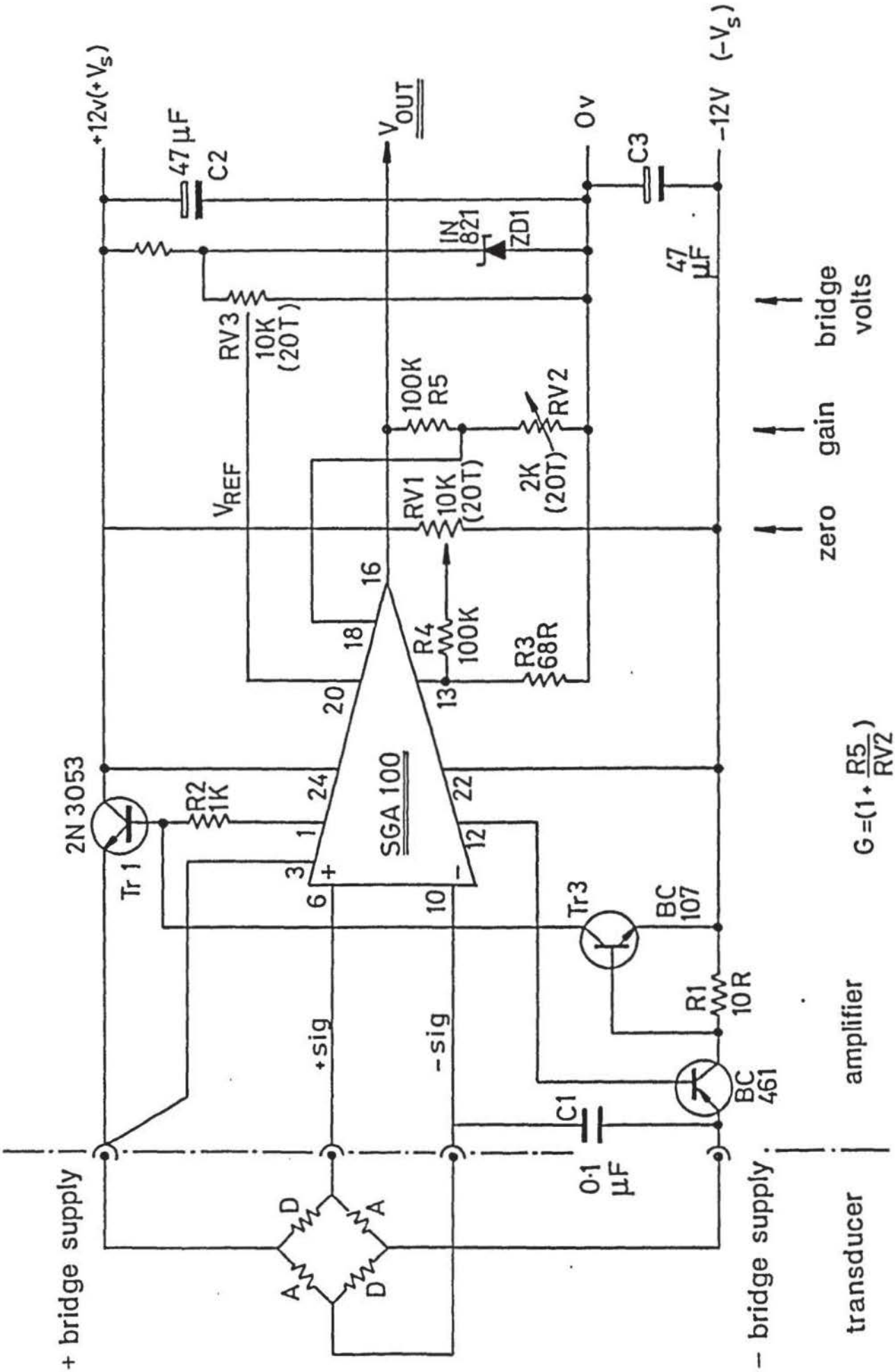

Amplifier-unit circuit diagram including the bridge network.

FIGURE 5.2

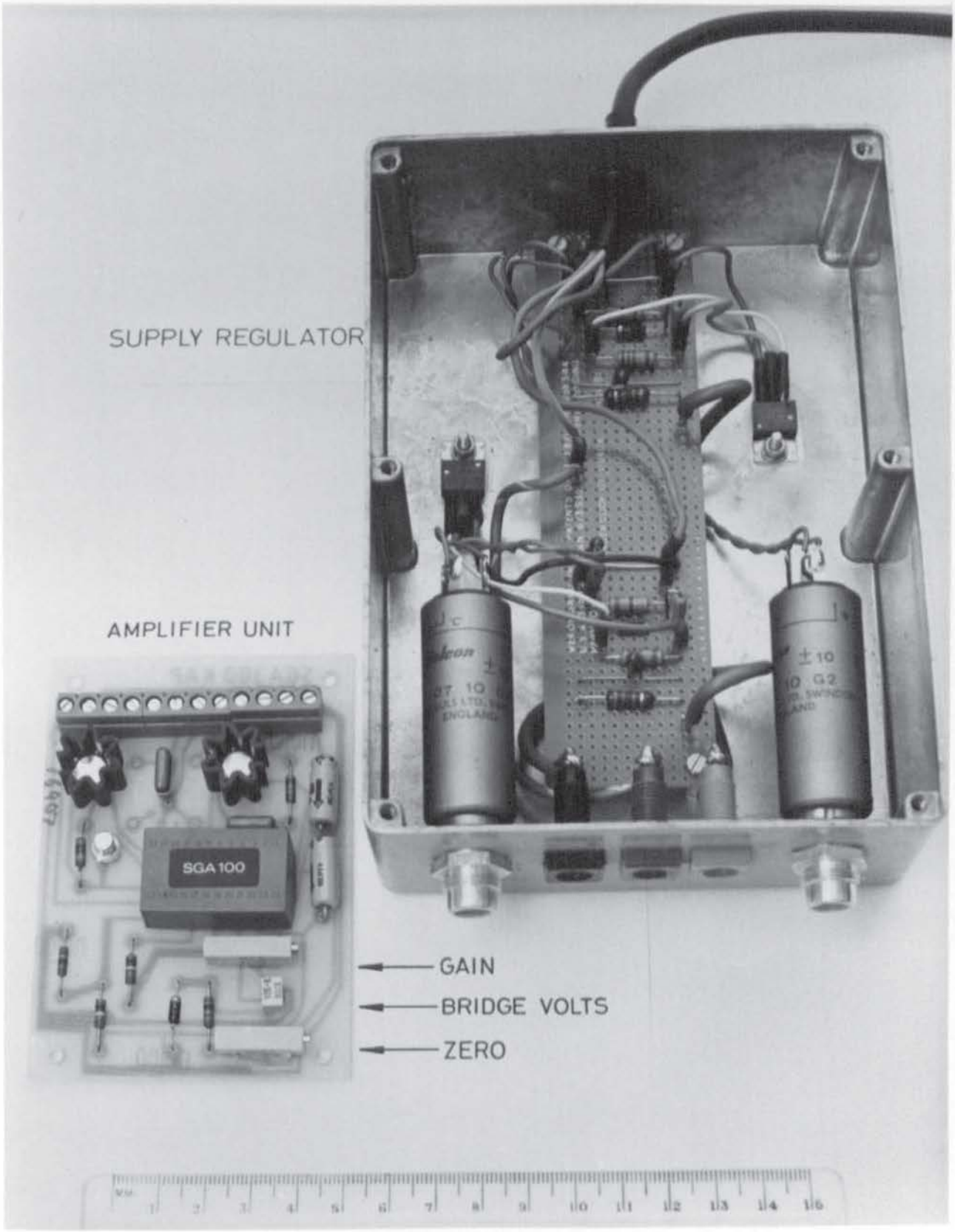

Single amplifier unit and power supply regulator.

PLATE 5.1

5.3.7 Power Supply Regulator

A simple but reliable circuit, illustrated in Figure 5.3, proved capable of providing the amplifier with a highly stabilised DC supply. The variable resistor (RV1), allowed the outputs to be set to ± 12v and the stability was such that this value was maintained to within ± 1mV. The supply regulator is shown in Plate 5.1 and the cost (1983) of components was about £8.

5.3.8 Multi-Channel Amplifier

To cater for simultaneous amplification of output from a number of transducers, a multi-channel amplifier was constructed using seven amplifier units connected in the way shown by the circuit wiring diagram in Figure 5.4. They were installed in a metal cabinet, the details of which may be seen in Plate 5.2.

Transducer output voltages were received by seven 5-pin DIN sockets. These were located at the front of the cabinet, as were holes through which a small screwdriver could reach the variable resistances to zero any initial imbalance and set the bridge input voltage and amplifier gain, to the required values, for each channel. The bridge input voltrage could be set precisely using the leads shown on the extreme right of Plate 5.2, connected to a high impedence voltmeter. A value of 4 volts DC was used for all the transducers.

5.3.9 Micro-Electronics

It is to be noted that the micro-electronic components used during the laboratory programme were largely 'state-of-the-art' at that time. Since then, signficiant changes may have occurred in respect of specifications and costs.

5.4 LOAD TRANSDUCERS

Two load transducers (LC1 and LC2) were used to measure the model foundation loads. LC1 and LC2 are shown to the left and right, respectively, of Plate 5.3. Transducer LC2 was loaned from the Department's Structures Laboratory, where it had been designed and constructed by a member of its technical staff.

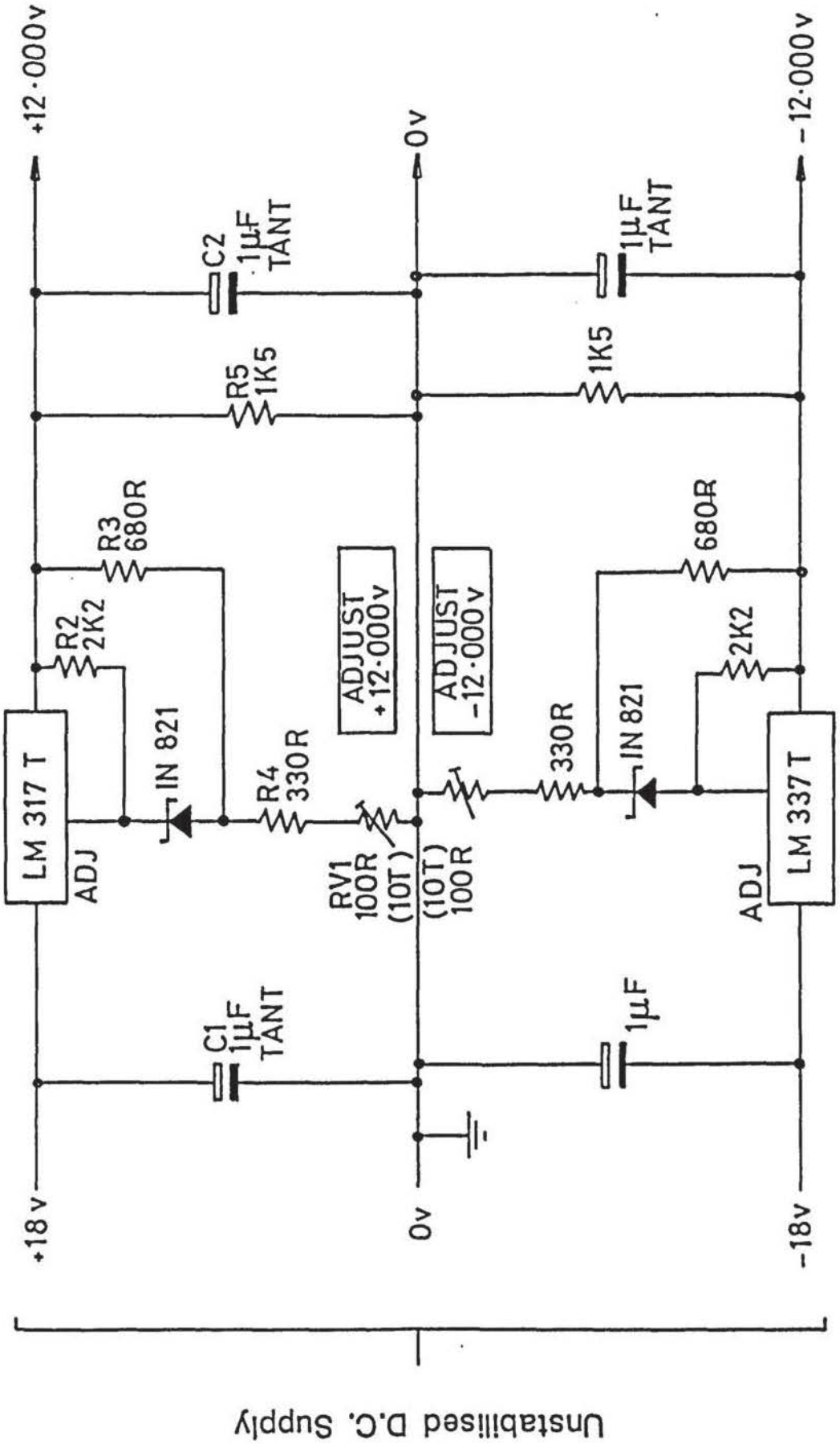

Power-supply regulator circuit diagram.

FIGURE 5.3

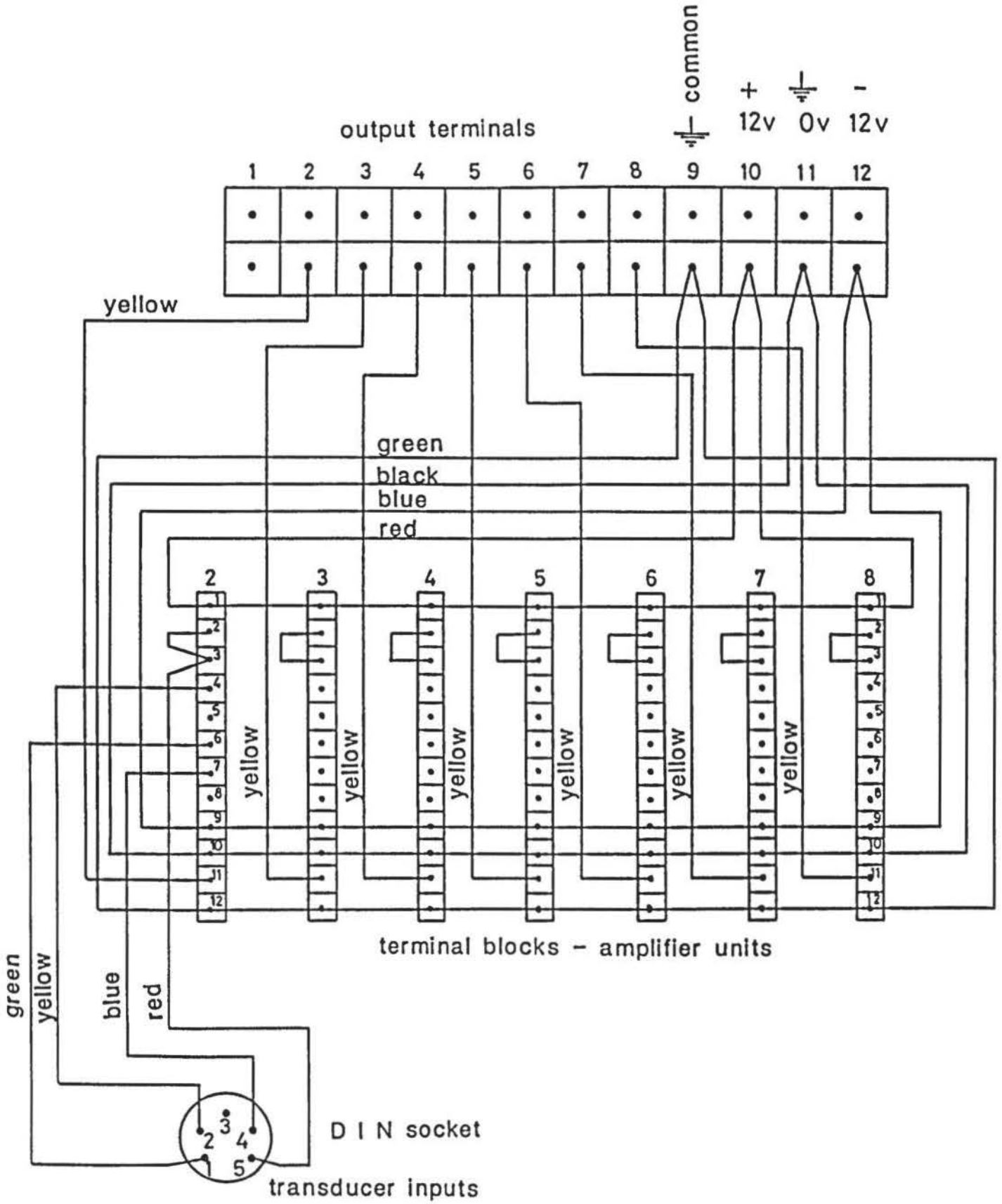

Circuit diagram for seven channel transducer amplifier.

FIGURE 5.4

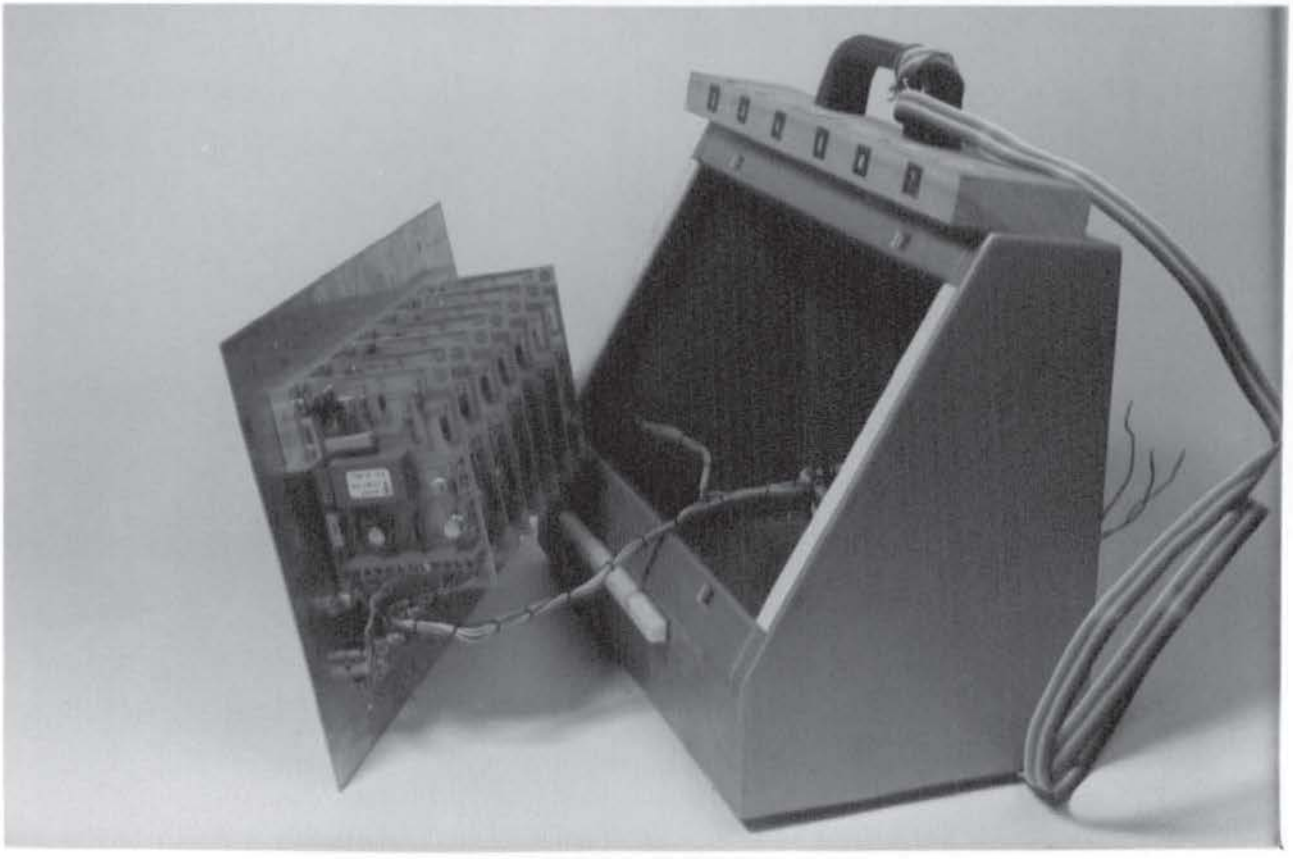

Multi-channel amplifier with power supply regulator

PLATE 5.2

Load transducers LC1 (left), LC2 (right), diaphragm transducer, and two fine-screw adjustment caps.

PLATE 5.3

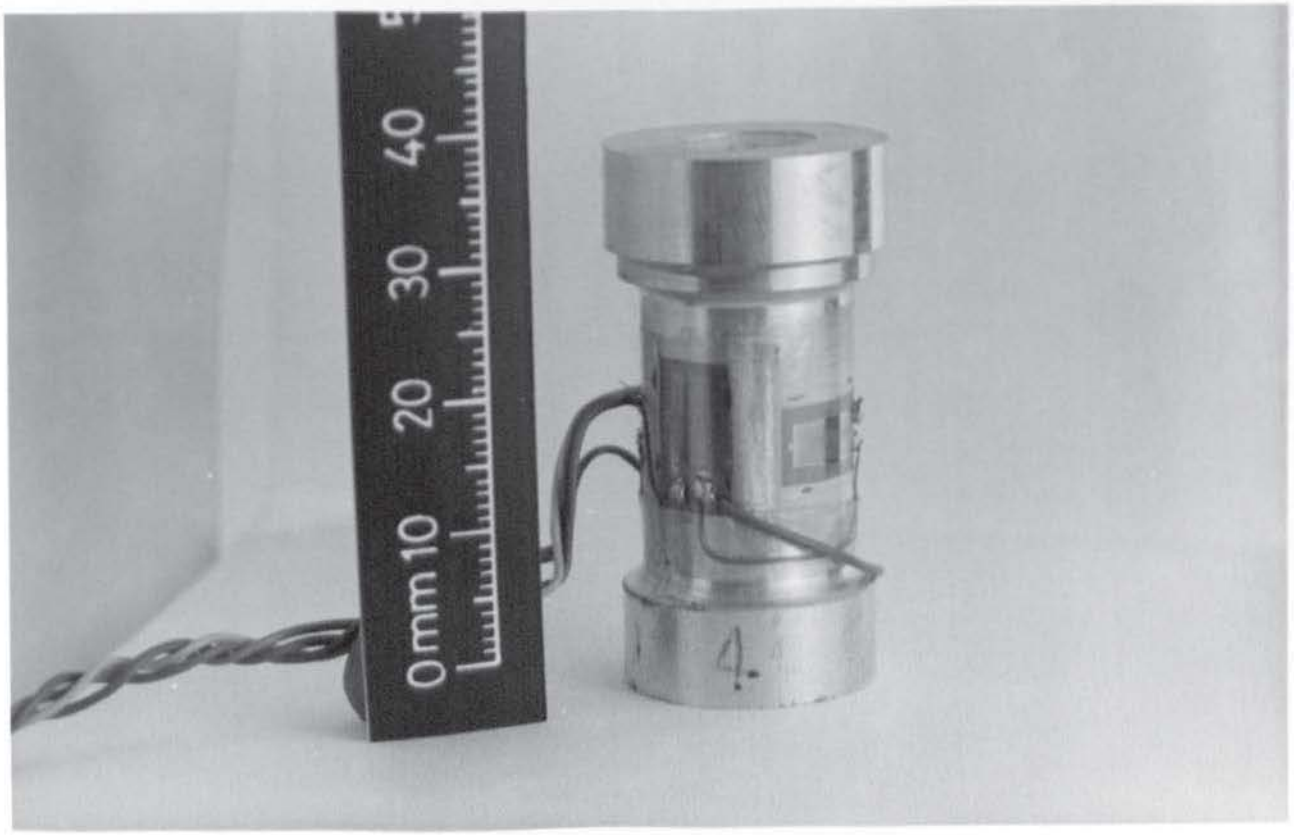

Details of foil gauges and wiring to LC1.

PLATE 5.4

5.4.1 Description

Both transducers were similar to a design adopted by Whitaker (1963). The structural element was essentially a thin walled cylinder, closed at each end by a rigid cap. The caps had a conical recess to seat a ball-bearing through which vertically concentric loading was applied. Four foil resistance gauges were bonded to the cylindrical element and connected in a bridge circuit, shown in Figures 5.5(a) and (b). Two active gauges (R1 and R3) lay with their longitidinal axes in the direction of the applied load with two dummy, or passive, gauges (R2 and R4) positioned at right angles to them.

5.4.2 Design and Construction

The element for LC1 was machined from a solid bar of aluminium alloy (HE15TB) which had a 0.2% proof stress of 255 MPa and a Young's Modulus of 74 GPa. Figure 5.6 shows the details of the element which gave a maximum working load of 2.5 kN. The structural stresses imparted by this load amount to about $^2/_3$ of the proof stress.

The foil gauges (type 8/350/P/C-23) and bonding agent (TT300 cement) were manufactured by Tinsley Telcon Limited. Transducer LC2 had been similarly constructed using a mild steel element and type 3/250/P/C-1 foil gauges.

5.4.3 Electrical

Short lengths of enamelled tinned copper wire (SWG 46) were soldered to the foil gauge terminals forming the bridge circuit. Cable of low electrical resistance was used for the input and output leads, which ended in a 5-pin DIN plug for direct connection to the amplifier. Transducer LC1 is shown in Plate 5.4 after completion and prior to the fixing of a proctective polythene film, using PVC tape, to the cylindrical body.

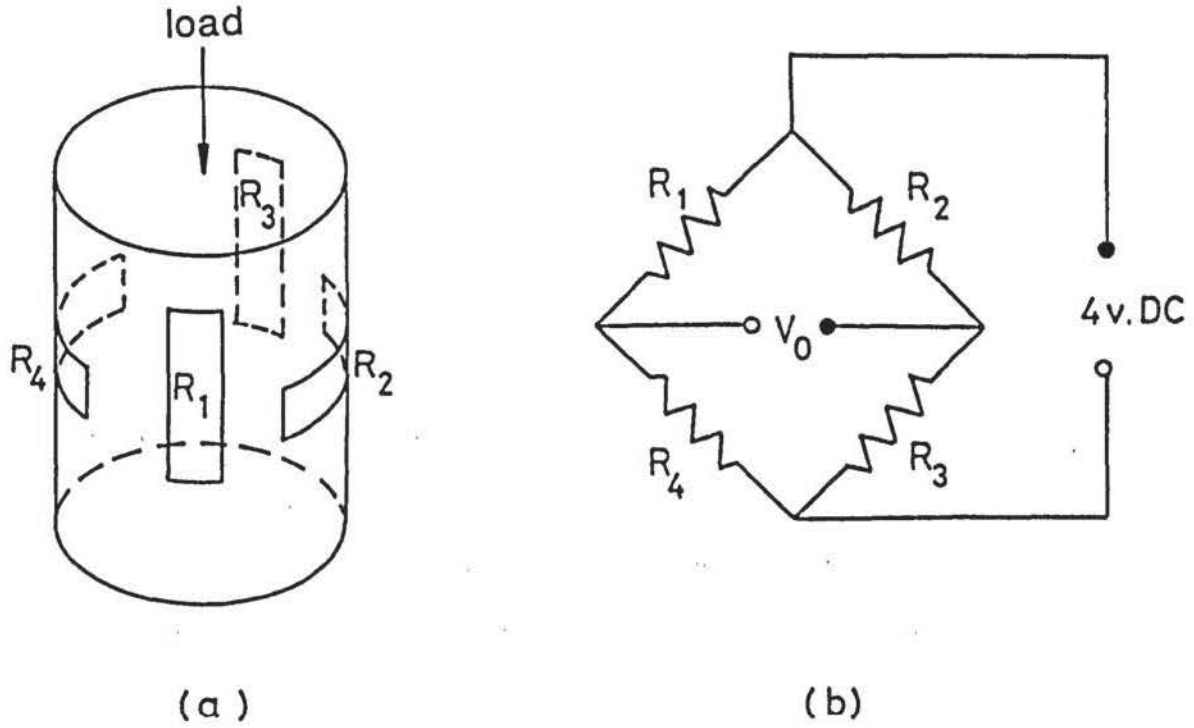

Positioning of foil gauges on cylindrical element and the corresponding bridge circuit.

FIGURE 5.5

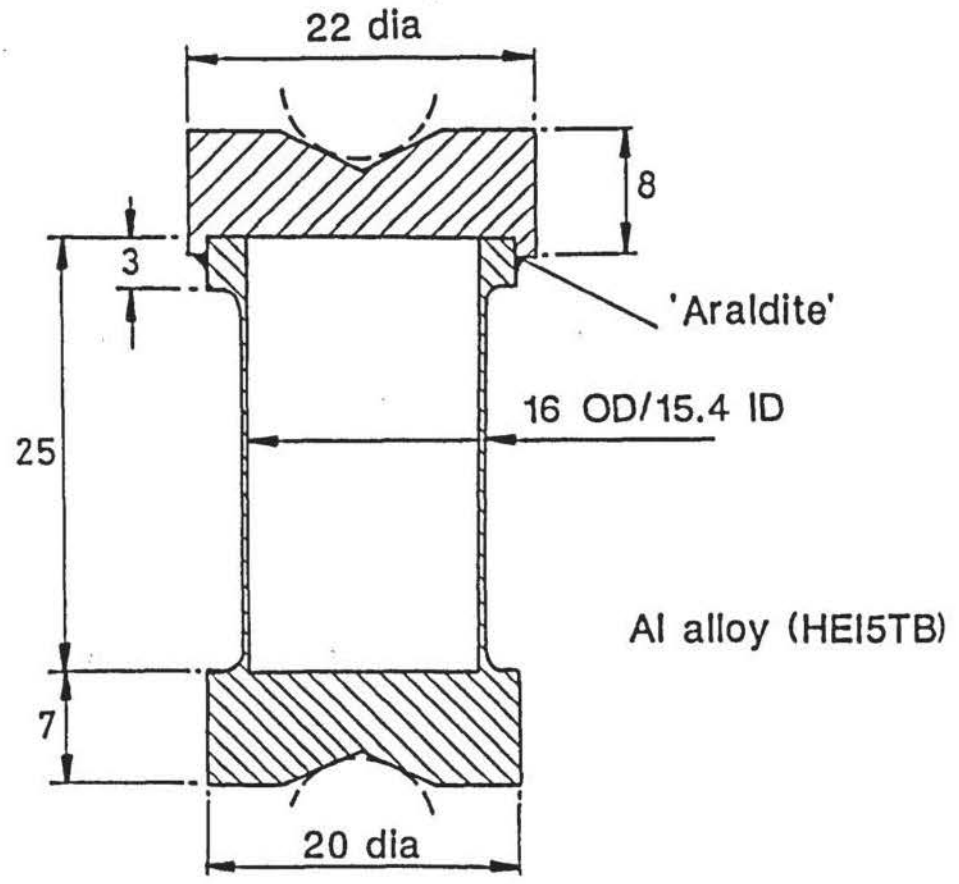

Structural element details of load transducer LC1.

FIGURE 5.6

5.4.4 Calibration

Calibration was undertaken using a Bishop-type rear-loading oedometer. The transducers were positioned between 14 mm diameter ball-bearings by an arrangement shown in Figure 5.7.

Relative vertical alignment was checked with a spirit level. After zeroing the bridge circuit and adjusting the amplifier gain by a suitable amount, loads were applied in increments to a maximum of 1.87 kN and 6.18 kN for LC1 and LC2, respectively. To minimise the effects of possible small variations in the actual mass of the loading weights, calibration was repeated eight times using the same weights in different orders and taking the mean of the results.

5.4.5 Characteristics

The mean values of the amplified transducer output voltages (V_o^{amp}) were plotted against the applied calibration loads. A best-fit line was determined from linear regression analysis, giving a correlation coefficient (R) of almost unity. The results are shown in Figures 5.8 and 5.9. From the equation of a straight line:

$$V_o^{amp} = B \times load + A$$

$$\text{hence load} = \frac{(V_o^{amp} - A)}{B} \qquad (5.5)$$

where B is the sensitivity and A is the voltage output under no load. Since it was normal practice to zero the transducer bridge circuit prior to loading, Eqn. 5.5 became:

$$load = \frac{V_o^{amp}}{sensitivity} \qquad (5.6)$$

5.5 HORIZONTAL STRESS TRANSDUCER

5.5.1. Type

The transducer operated on the principle, shown in Figure 5.10, of a structural diaphragm element which deflects under pressure from an adjacent soil. Strain gauges are generally attached at positions on the diaphragm where tensile and compressive strains occur. This

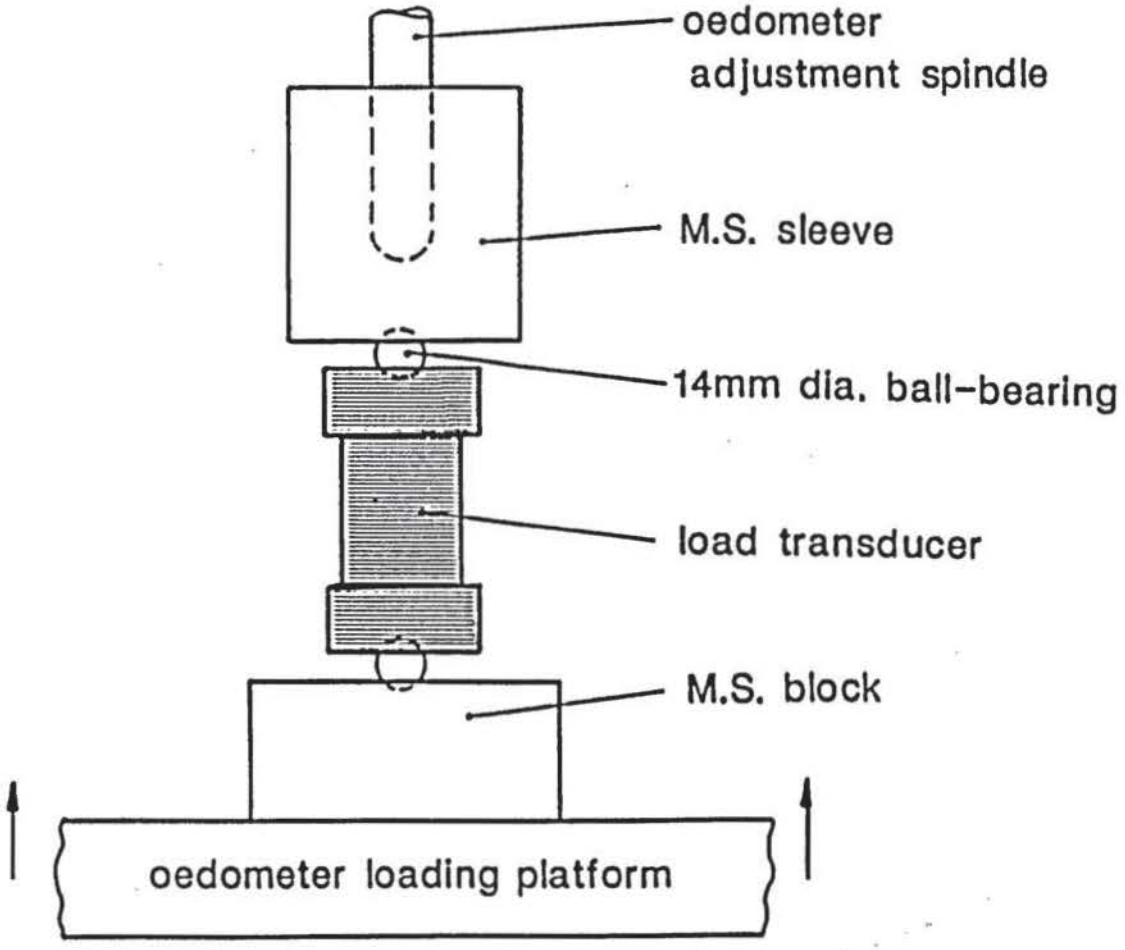

Positioning of load transducer for calibration in a Bishop-type oedometer.

FIGURE 5.7

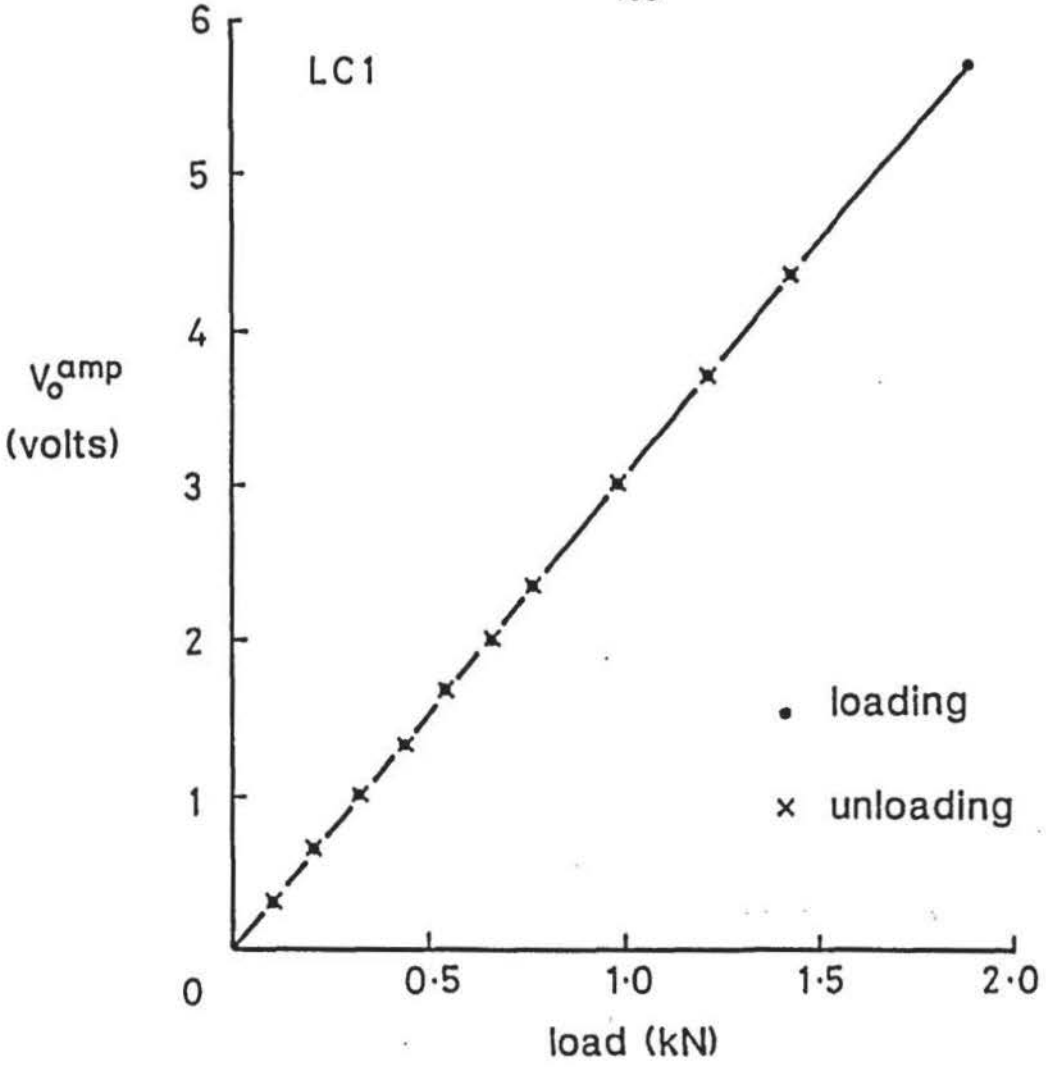

Calibration of load transducer LC1.

FIGURE 5.8

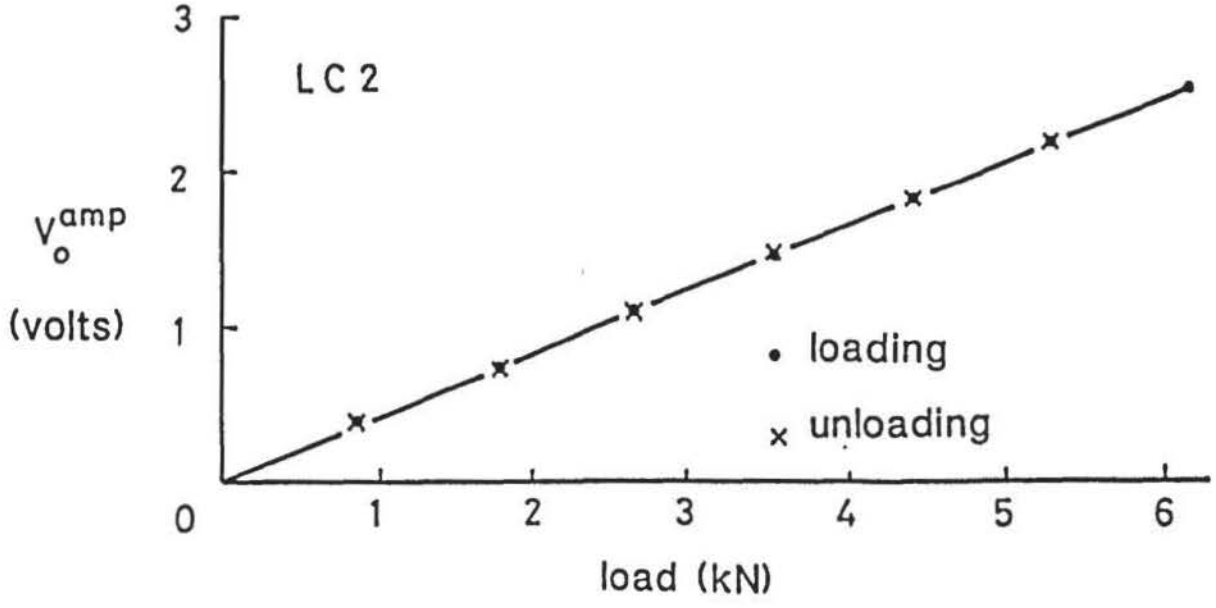

Calibration of load transducer LC2.

FIGURE 5.9

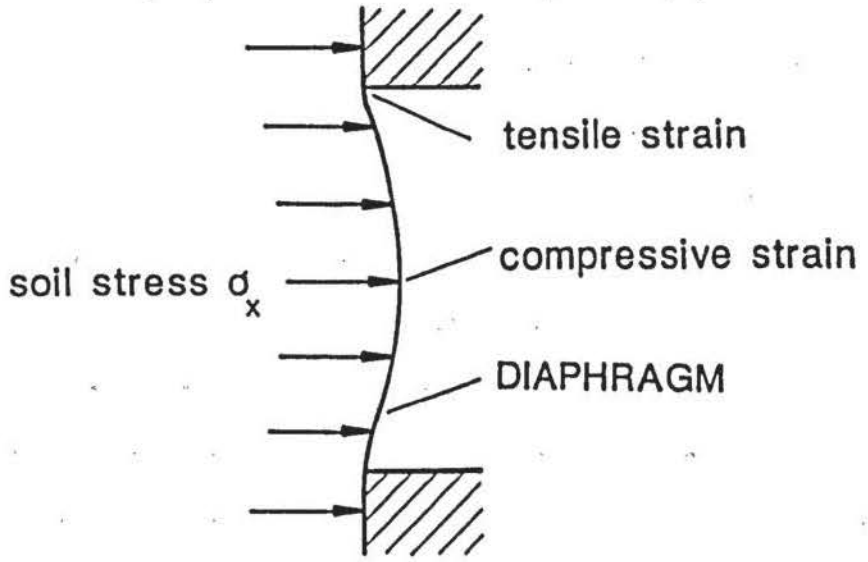

Deflection of a diaphragm element from stress in an adjacent soil.

FIGURE 5.10

type of transducer is widely used and examples may be found in Plantema (1953), Redshaw (1954), Trollope and Currie (1960), Burn (1963), Dunn and Billam (1966), Brown (1971), Wong (1973), Sherif (1975) and many others. Its most signficiant advantage is that it can be easily and cheaply constructed. There is no evidence to show that shear stresses acting across the diaphragm would unduly affect measurement of the normal stress component (Suen, 1982).

5.5.2 Influencing Factors

The main factors influencing the successful performance of diaphragm transducers are reported on the basis of theoretical work by Taylor (1947), Monfore (1950), Kallstenius and Bergau (1956), Tory and Sparrow (1967) and from experimental work by Trollope and Lee (1961) and Peattie and Sparrow (1955). A summary of these findings is given by Selig and Vey (1965) and Dunn and Billam (1966). The main factors are concerned with the relative flexibility and size of the diaphragm to the soil compressibility and particle size.

Mention has been made previously (Section 5.2.3) of the emphasis placed on providing a high relative element stiffness to avoid significant stress redistribution at the measuring face. From theoretical considerations, Thomas and Ward (1969) estimated the probable error in pressure registration of a diaphragm transducer for a range of diaphragm to soil stiffness ratios. The relationship is reproduced in Figure 5.11. It is evident that the penalty of a 'soft' diaphragm is a rapidly changing error whilst for very stiff diaphragms there is a more constant error of over-registration.

The effect of soil grain size has been considered by Kallstenius and Bergau (1956). They proposed that a circular transducer which is required to have errors of less than 3%, caused by random positioning of the soil grains, should be of sufficient size to be in contact with at least 60 grain diameters. A disadvantage in the use of a diaphragm element with particulate media is that the applied pressure and diaphragm strain relationship is not reversible on unloading. Figure 5.12 gives a typical example of this phenomenon, which is severely aggravated by coarse grained soils (i.e. sand). It is thought that this behaviour is a result of the reversal of soil-diaphragm stiffness interaction and the modification of the soil grain structure (and hence particle-diaphragm contact) as a result of the prior loading.

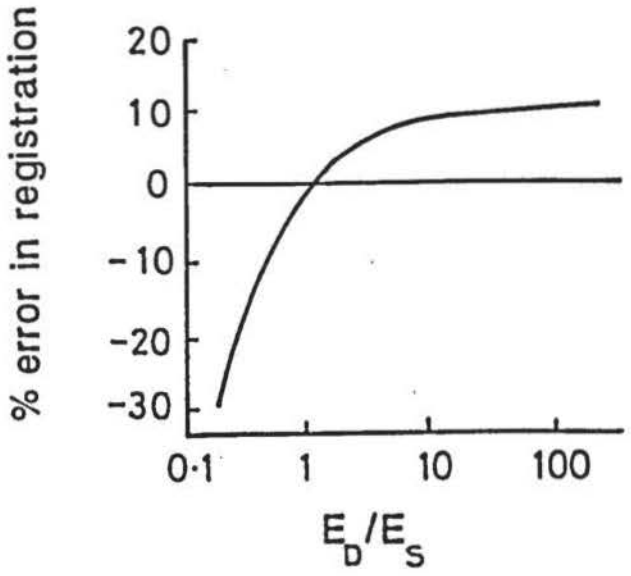

Error in transducer pressure registration vs. ratio of diaghragm stiffness to soil stiffness (after Thomas and Ward, 1969).

FIGURE 5.11

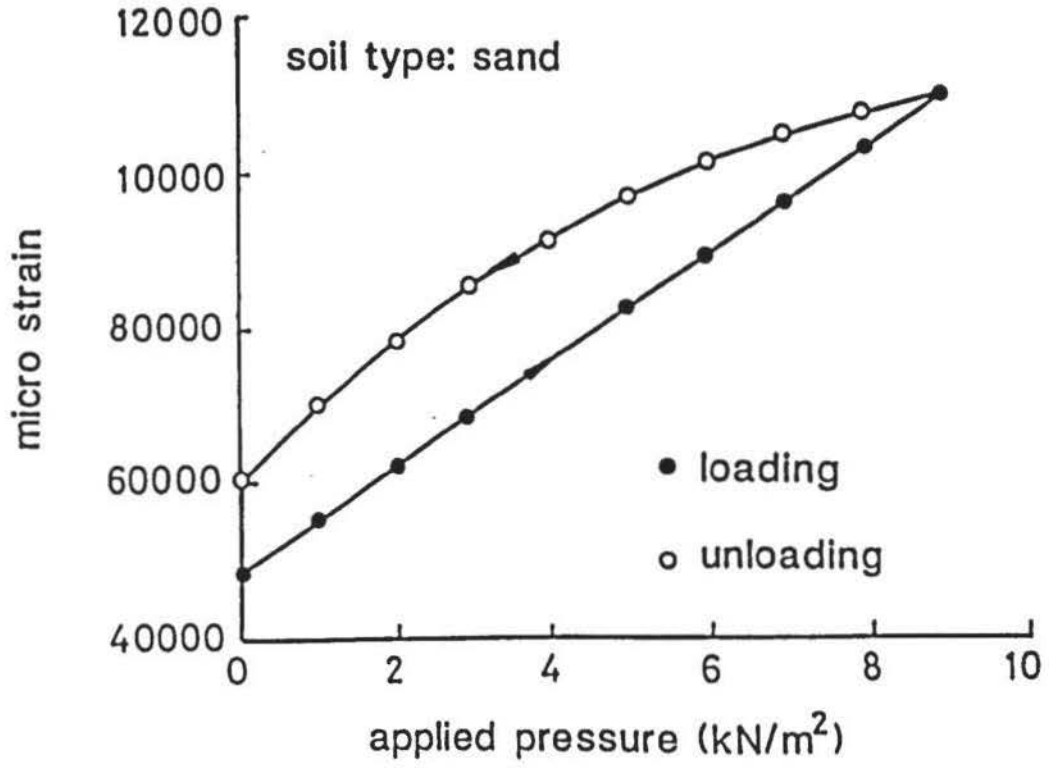

Typical sand calibration for a diaphragm pressure transducer (after Sherif, 1975).

FIGURE 5.12

From overall considerations, diaphragm transducers appear better suited for work with clay soils of low compressibility, particularly if their dimensions are required to be relatively small, which is often the case in laboratory studies.

5.5.3 Strain Gauge Configuration

The use and positioning of a single element strain gauge on a circular diaphragm has received attention by previous researchers (e.g. Billam, 1965; Dunn and Billam, 1966; Brown, 1971 and Wong, 1974) since the introduction of the purpose designed four-element foil gauge by Redshaw (1954), shown in Figure 5.13. The various single element configurations were designed to give an acceptable compromise between cost, measurement accuracy and sensitivity. The most recent findings, by Wong (1974), indicate that to minimise errors, gauges should be positioned at the diaphragm edge only and be kept as far away from the centre as possible. In effect, the suggestion may be satisfied using a Redshaw type gauge with the two centre elements disconnected.

An existing Redshaw diaphragm (type RED/20/240/P/C - 17) with a copper nickel alloy element was used.

5.5.4 Design and Construction

The structural element consisted of a beryllium copper diaphragm bonded to an alluminium ring. The dimensions were such that when fixed to the container wall the face was flush with the inside surface. The properties of beryllium copper made it a suitable material for both a pressure sensitive diaphragm element (especially when subject to cyclic stressing) and compatibility with the Redshaw gauge available. It had a 0.2% proof stress of 170 kPa and a Young's modulus of 130 kPa. Details of the transducer are given in Figure 5.14.

The diaphragm was designed to withstand a maximum pressure of 30 kPa with a corresponding recommended (Taylor, 1947) effective diameter to central deflection of over 2000. The diaphram effective diameter was 20 mm and its thickness was 0.35 mm. The diaphragm was bonded to the aluminium ring by a heat curing epoxy resin.

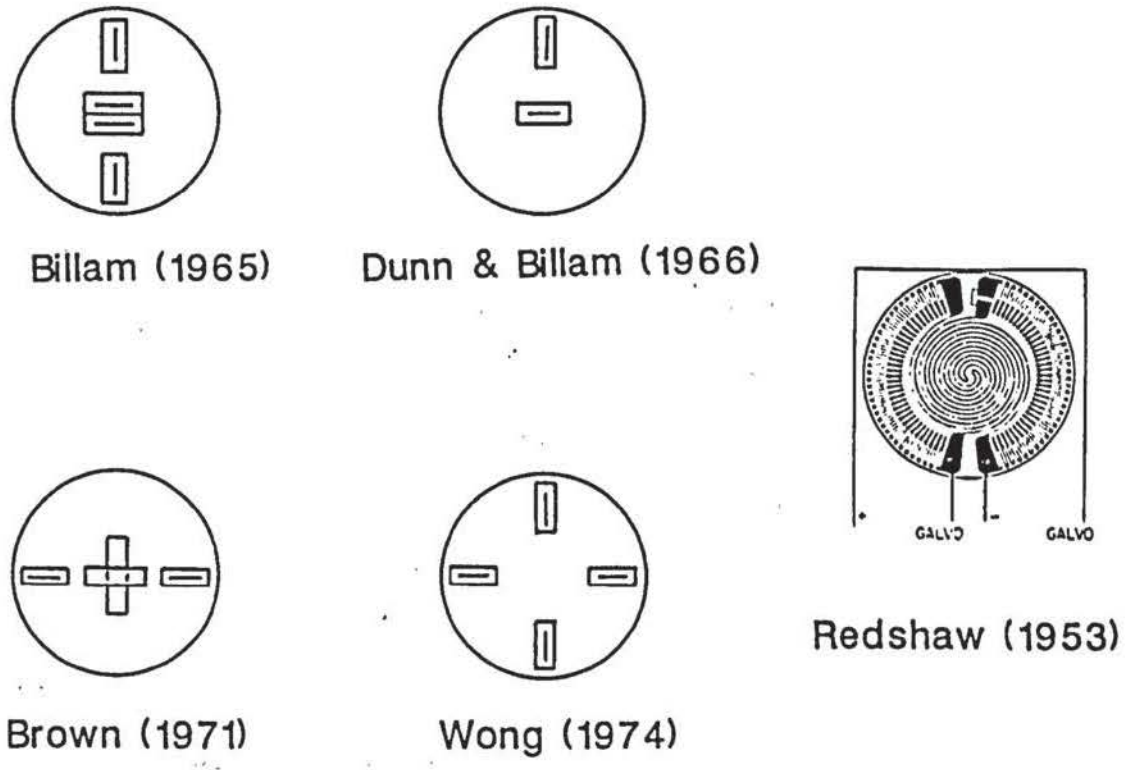

Examples of strain gauge configurations on circular diaphragms.

FIGURE 5.13

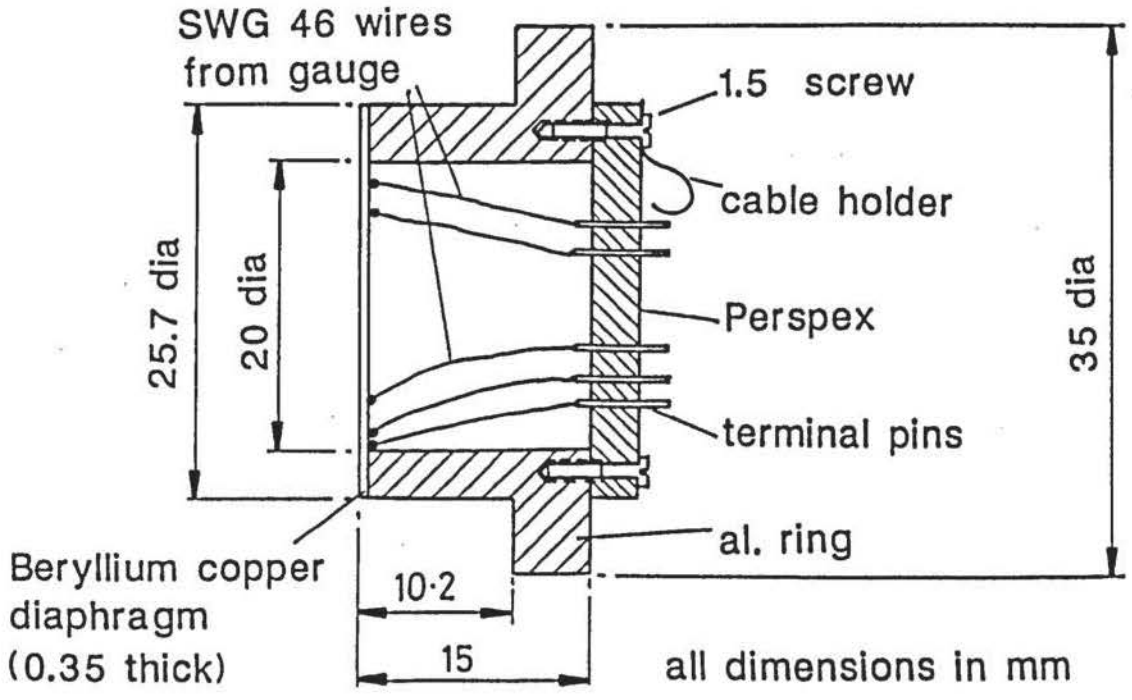

Horizontal stress diaphragm transducer details.

FIGURE 5.14

A 25 mm diameter, 3 mm thick, Perspex protective cover was fixed to the rear of the ring by screws. The outer surface of the assembly was coated with lacquer to prevent oxidation of the metals by the glycerine present in the clay.

5.5.5 Electrical

It was considered prudent to assess the behaviour of the transducer prior to the irreversible disconnection of the central elements of the gauge. Short lengths of copper wire (SWG 46) were soldered between the gauge terminals and terminal pins situated in the Perspex cover. Low resistance wiring was attached to these pins by female connectors and were terminated in a 5-pin DIN plug, for connection to the amplifer. The completed transducer is shown centrally in Plate 5.3.

5.5.6 Positioning on Soil Containers

The transducer was secured to the wall of each container with a steel bar and aluminium cap, detailed in Figure 5.15 and Plate 5.5.

5.5.7 Pressure Chamber

A pressure chamber similar to a design by Sherif (1975) was made from mild steel for calibration purposes. Details of the container are shown in Figure 5.16 and Plate 5.6. It had a 220 mm diameter, 15 mm thick, top plate (A) through which fluid pressure could be applied and an 18 mm thick baase plate (B). A vent was also provided in the base plate to release pore air pressure that might develop during calibration with soils. An annular ring (C) of 150 mm internal diameter, 15 mm thick and 25 mm in height, was seated on rubber 0-rings in the plates. The assembly was held together with four 8 mm diameter bolts.

To allow fixing of the transducer to the base plate, a Kaffir-D industrial plaster was poured into its conical opening after positing the moulds and 6 mm threaded rod shown in Figure 5.17. After the mixture had hardened, the moulds were removed giving the result pictured in Plate 5.7. The physical properties of Kaffir-D are given in Appendix C. The transducer was secured to the pressure chamber in the same way as the container, shown in Plate 5.8, using the mild steel bar

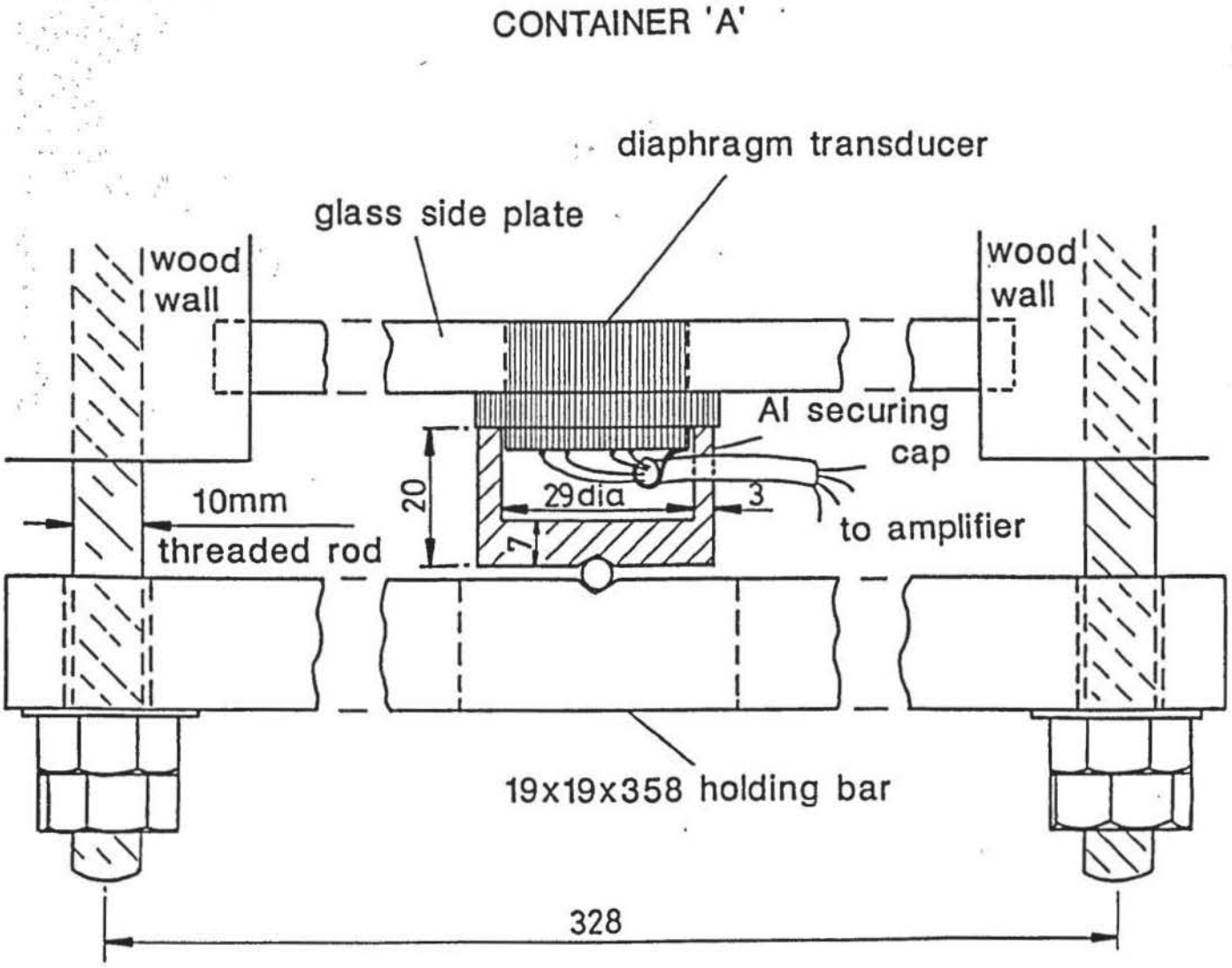

Details of securing diaphragm transducer to glass wall of container A.

FIGURE 5.15

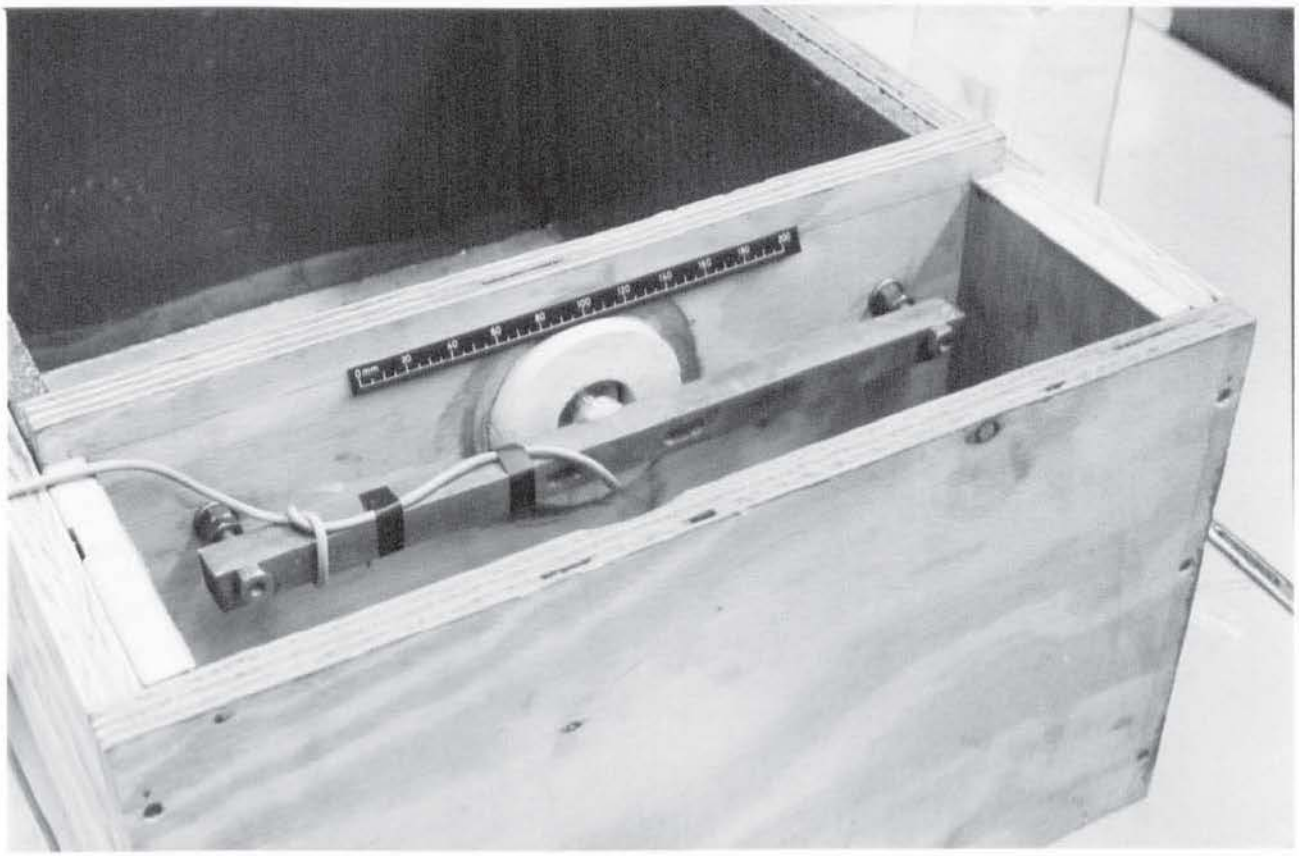

Positioning of diaphragm transducer in container B.

PLATE 5.5

Diaphragm transducer calibration chamber.

PLATE 5.6

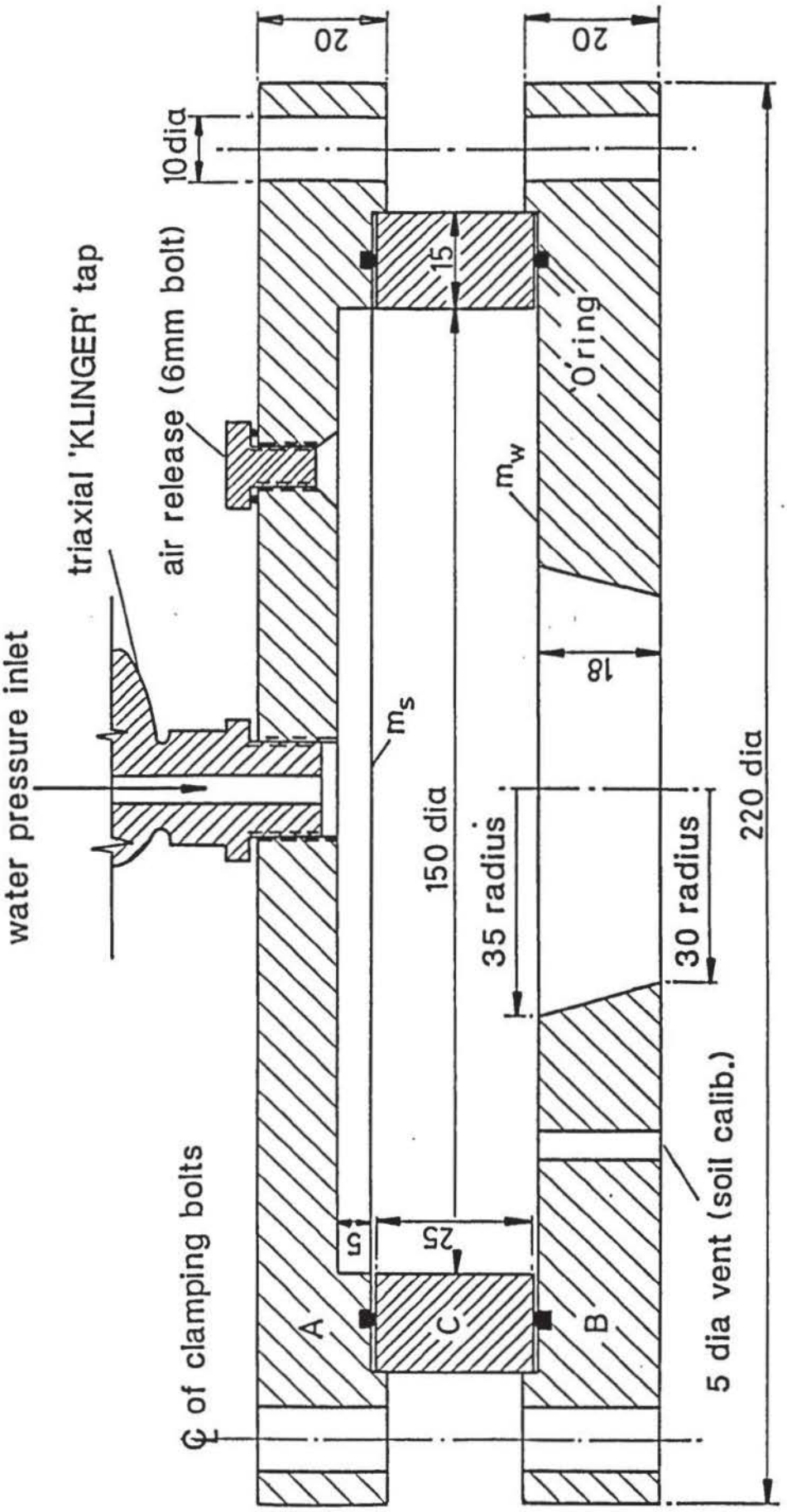

m_s rubber membrane – soil calibration only

m_w rubber membrane – water calibration only

A top plate

B base plate

C annular ring

Details of pressure chamber for calibration using water or soil.

FIGURE 5.16

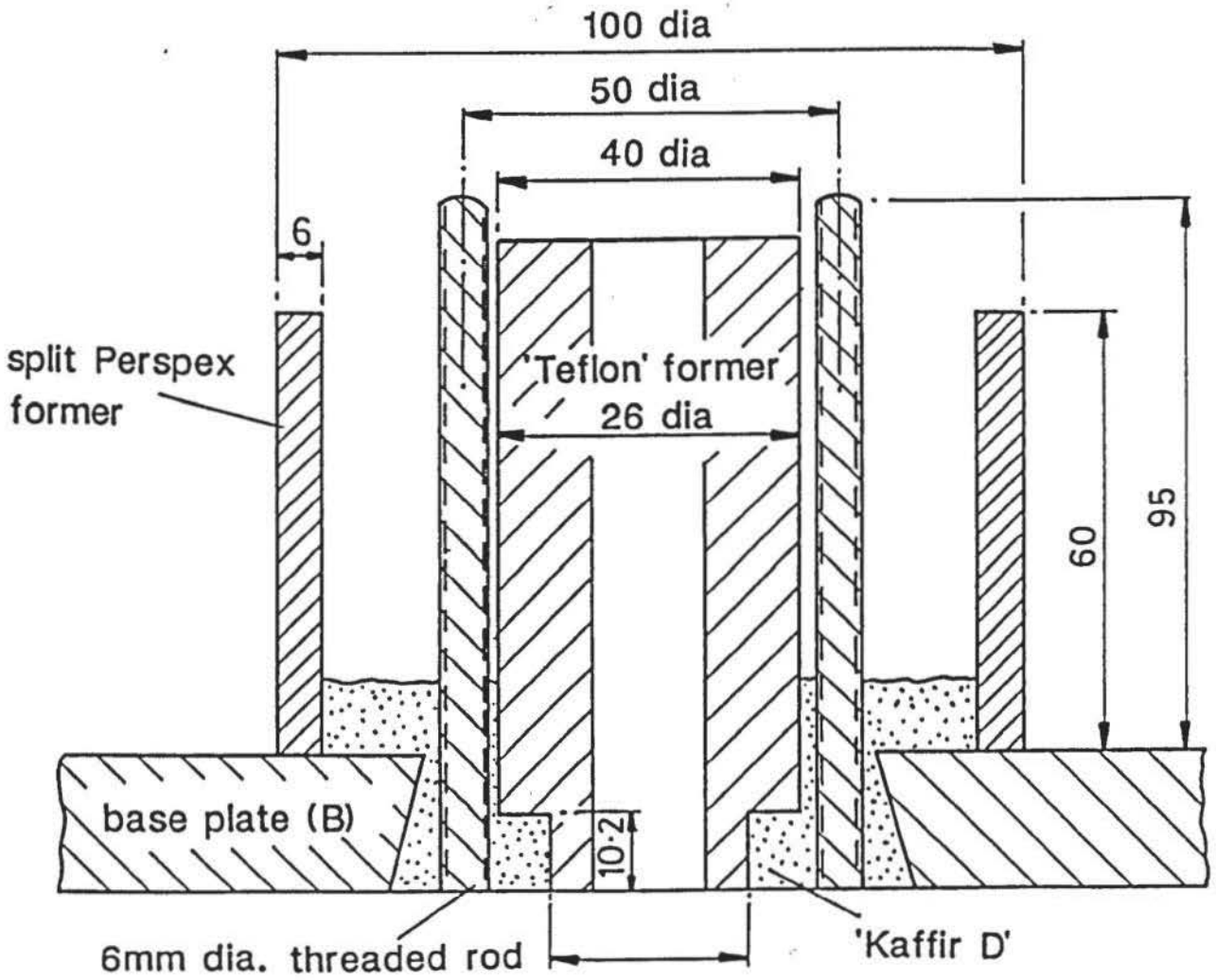

Details and positioning of moulds and threaded rod in pressure chamber base plate.

FIGURE 5.17

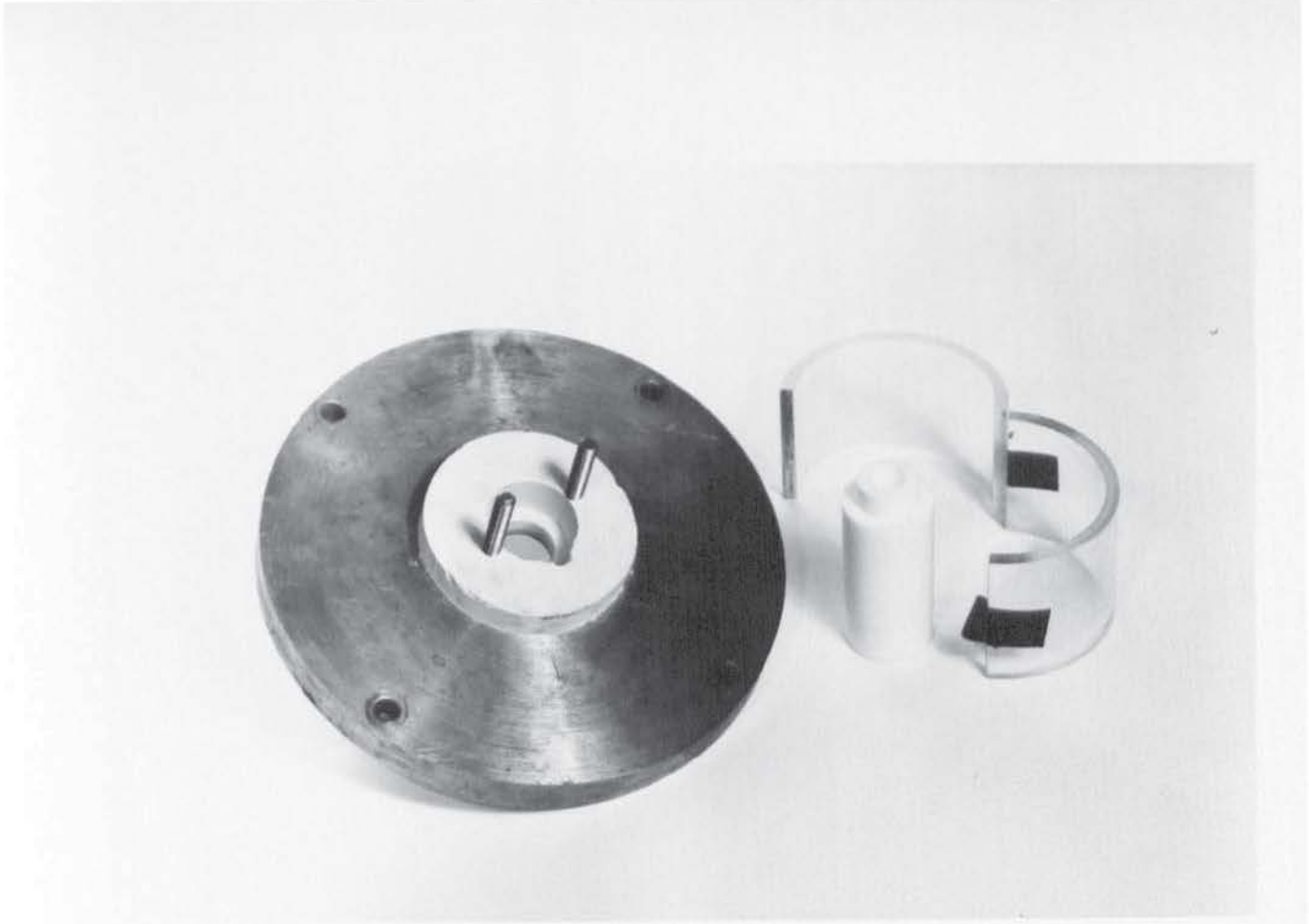

Formation of seat for transducer in base plate of calibration chamber.

PLATE 5.7

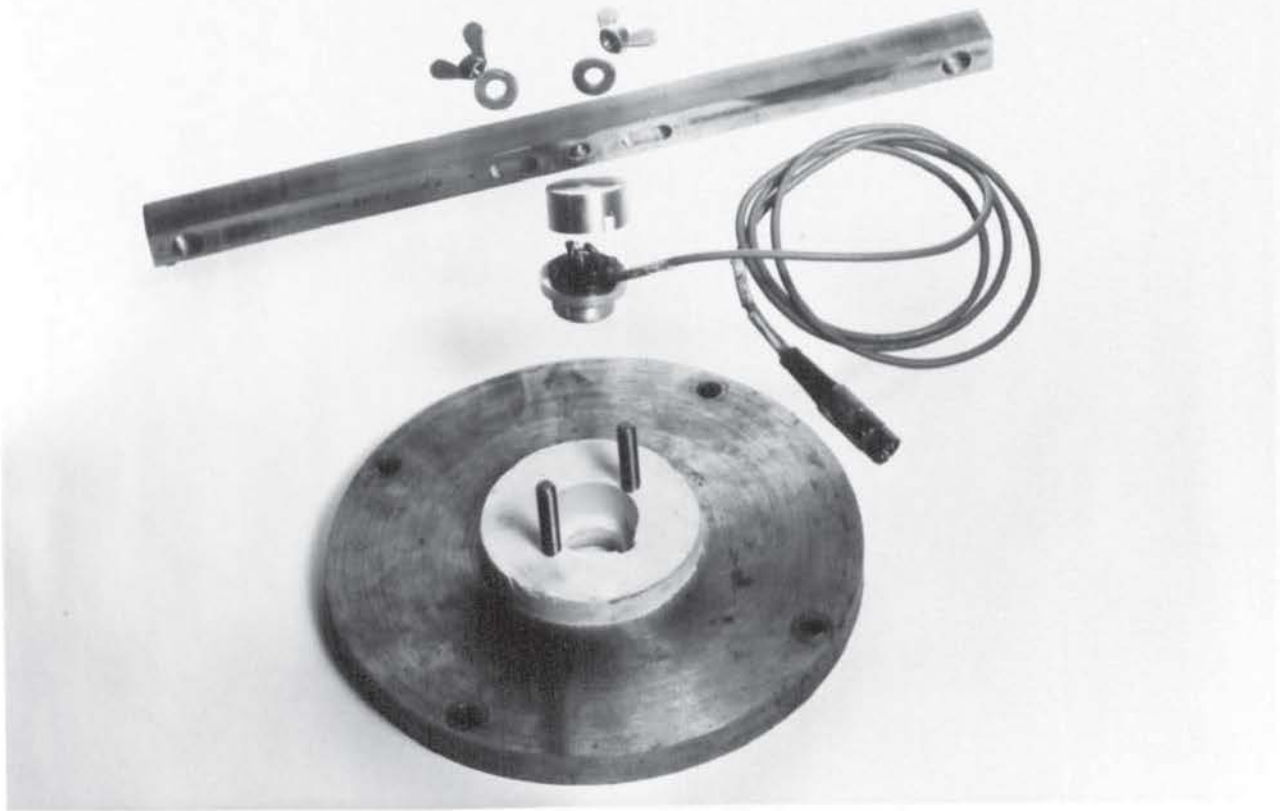

Location of diaphragm transducer to calibration chamber base plate.

PLATE 5.8

Continuation Page.....

and alluminium cap referred to in Section 5.5.6.

5.5.8 Water Calibration

For reference purposes, the transducer was calibrated under fluid pressure.

After placing a rubber membrane on a lightly silicone greased inside surface of the base plate, the pressure chamber was assembled and filled with water. Pressure increments were applied from the mercury manometer arrangement illustrated in Figure 5.18. After connection to the amplifier, and prior to its attachment to the pressure chamber the transducer bridge circuit was adjusted to zero and the gain was set to give a suitable output voltage. Pressure increments were applied in 2.54 kPa stages to a maximum of 28 kPa and then similarly released. Calibration was repeated five times and the mean taken.

5.5.9 Clay Calibration

The transducer was to measure the in-situ lateral stresses in the clay, at the container wall. The clay was to be subjected to several applications of loading and accordingly the transducer would experience cyclic stressing. The calibration process reflected these operating conditions.

With the annular ring (C) seated in the base plate (B) and a small piece of air-permeable fabric covering the pore-air vent, clay was kneaded into the enclosed space. Using a straight edge, the material was trimmed flush with top of the ring after which a rubber membrane was placed over the surface. The top plate (A) was brought into position and the four clamping bolts secured. After connection to the mercury manometor, the upper portion of the pressure chamber was filled with water. In the same way as the fluid calibration, pressure increments were applied in stages of 2.54 kPa up to a maximum of 28 kPa and then unloaded. This represented one cycle of loading. Calibration was done at 1, 5 and 15 cycles of loading. The whole procedure was repeated three times and the mean taken.

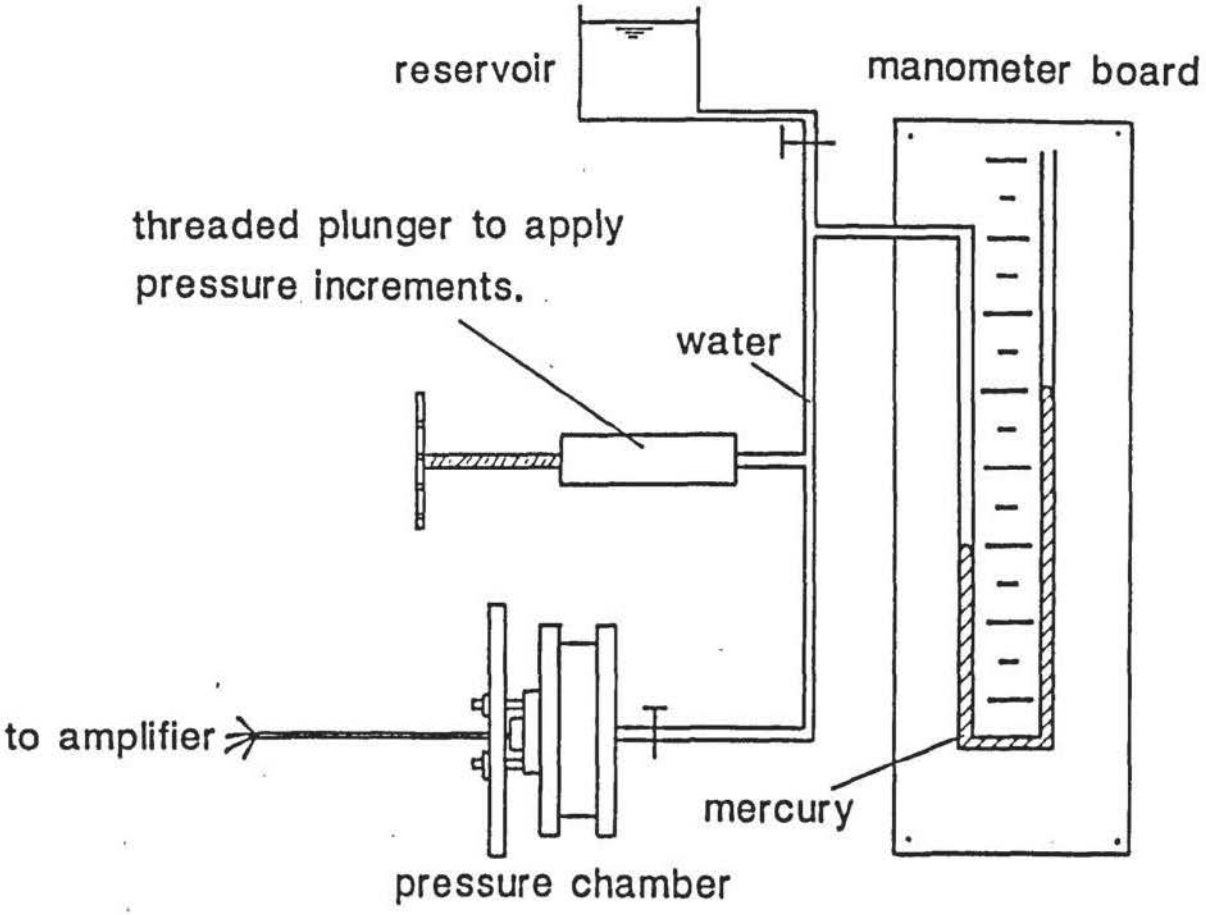

Diagramatic layout of arrangement for pressure calibration using a mercury manometer.

FIGURE 5.18

5.5.10 Characteristics

The water calibration curve, in Figure 5.19, was obtained from a linear regression on loading (R = 0.9989). Results from the clay calibration for the 1st and 15th loading cycles are shown in Figure 5.20. It is evident that there is a change in the loading correlation between the two cycles and that the loading characteristics are not reciprocal during unloading. The latter may be anticipated from previous comments in Section 5.5.2. Using regression analysis on all three cycles, a linear correlation on loading was obtained (R = 0.9992). For unloading, a best line of fit was achieved with a quadratic equation in the form:

$$\text{pressure} = D(V_o^{amp})^2 + E.V_o^{amp} + F \qquad (5.7)$$

where D, E and F are the calibration coefficients.

The calibration characteristics were considered sufficiently satisfactory not to warrant the further development of disconnecting the central gauge element.

5.6 FOUNDATION CONTACT STRESS TRANSDUCERS

Transducers were designed and constructed to be embedded in some of the model foundations to determine the average stresses at the interface with the columns and the clay.

5.6.1 Operations Requirements

Foundation contact stresses were investigated with a number of column configurations and spacings. For reasons of cost, versatility and expendiency, the transducers were designed to be precast en bloc with the foundation, using Kaffir-D as the casting material, and were subject to the following operational requirements:

(a) To allow stress measurement at the contact surface with the columns (i.e. sand) and clay during one cycle of loading.

(b) To be self-contained and suitably protected against contamination by the casting material.

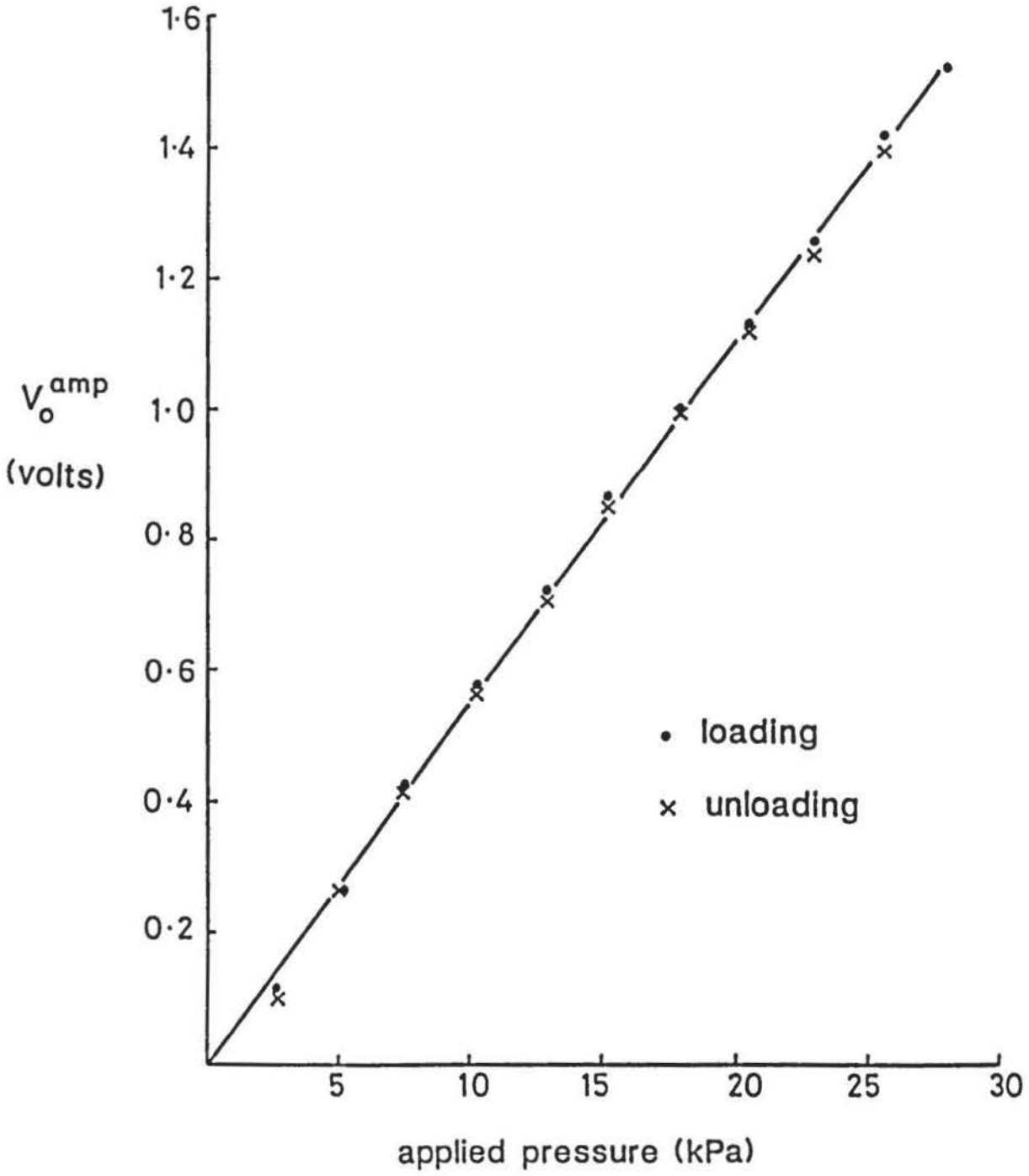

Calibration of the diaphragm transducer using fluid pressure.

FIGURE 5.19

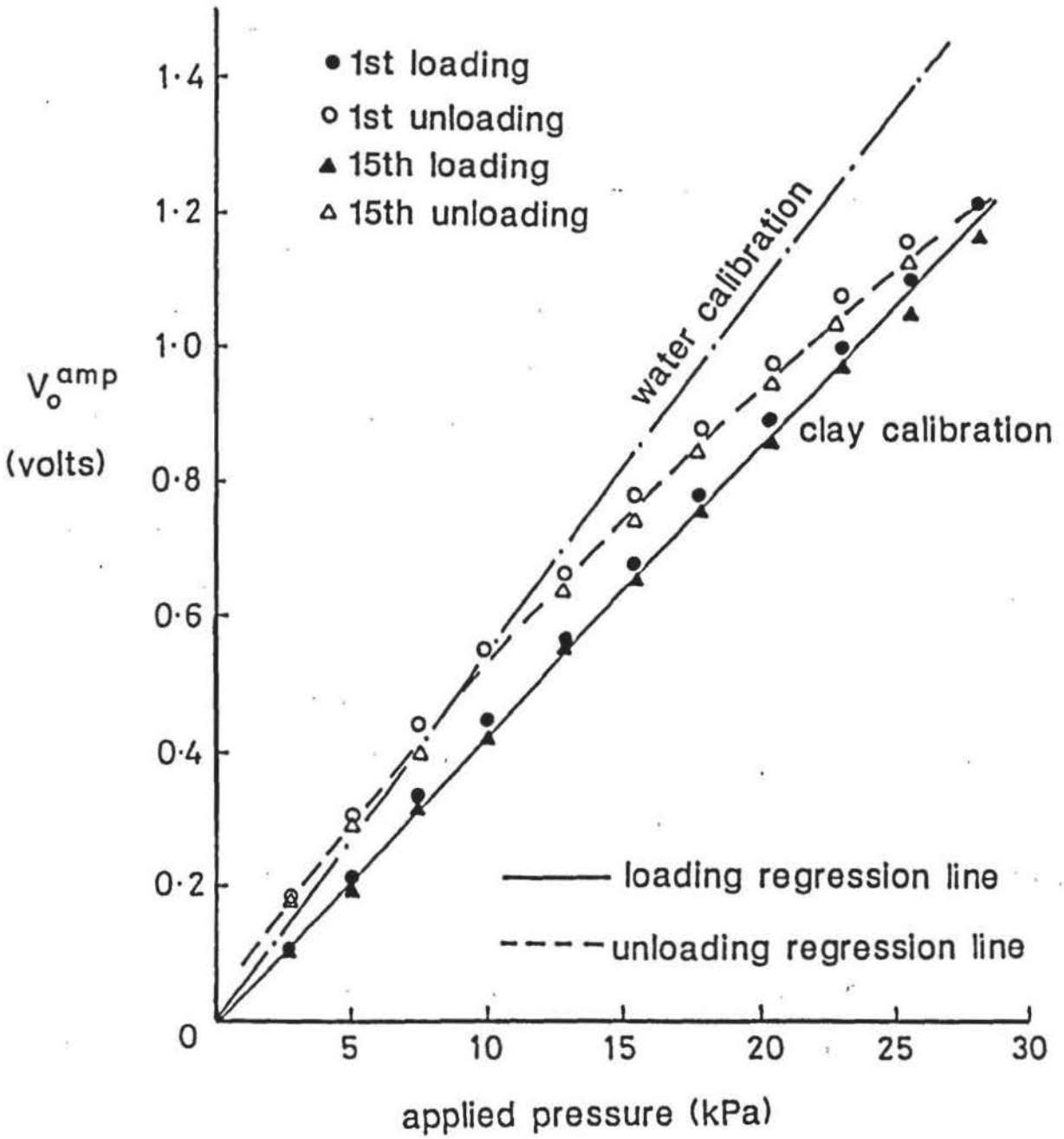

Calibration of the diaphragm transducer using fluid pressure.

FIGURE 5.20

(c) To be as small as possible, whilst complying with the needs of measurement accuracy.

(d) To be self-securing when the foundation is cast and yet be easy removable for re-use.

(e) To be cheap and easily constructed.

5.6.2 Normal and Shear Stresses

Roscoe and Schofield (1956), Roscoe (1957) and Schofield (1961) considered that the measurement of normal pressure distribution at a foundation face without measurement of shear stress results in a significant deficiency in the understanding of the overall behaviour. Also, since non-uniform pressure distributions can occur beneath foundations, eccentricity of normal loadng on a transducer face is likely. An earth pressure transducer measuring shear stresses, normal load and its eccentricity was described by Arthur and Roscoe (1961), which has been used and further developed by Cambridge researchers - notably Stroud (1971). This transducer is commonly termed the Cambridge Load Cell (abbreviated CLC). Referring to Figure 5.21, the CLC has a rigid measuring face and the normal load is resisted by strain-gauged vertical webbs. Shear load is measured by other webs parallel to the measuring face.

The CLC structural elements are machined from a solid block of aluminium alloy to which twenty-four foil gauges are attached to form three bridge circuits. The circuitry is sufficiently intricate, especially in small elements, to warrant the use of specially formulated printed circuit boards.

The facilities and expertise needed to construct this type of transducer were not available to the author. The cost of commerically available CLC's was also prohibitive.

5.6.3. Type

To simplify manufacture, Suen (1982) built six CLC's from fabricated components. There were many difficulties (Suen, 1981), in achieving an acceptable performance. It was considered that the practical problems and cost that would be incurred in the development and construction of a transducer of this type to meet the author's requirements (particularly

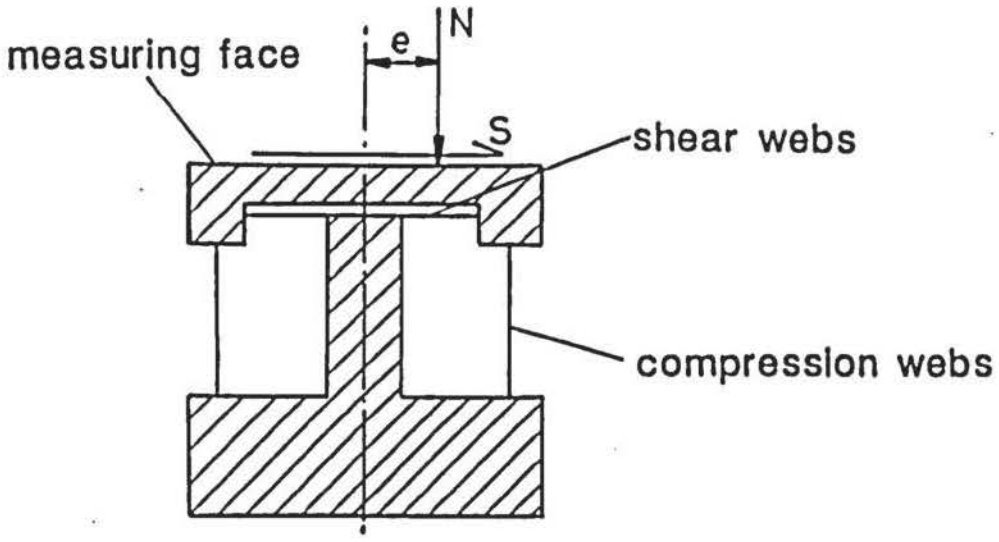

Cross-section of a Stroud-type CLC showing normal load, shear load and eccentricity of normal load (after Stroud, 1971).

FIGURE 5.21.

dimensionally) were too formidable to be pursued.

A simplified piston-type transducer, measuring normal load only, was adopted as it avoided the condition of soil arching, particularly in the case of sands. Suen (1982) also reported that piston-type transducers could be calibrated independently of the soil by using weights.

5.6.4 Description

Details of the clay transducer (type C) and larger granular column transducer (type S) are given in Figure 5.22. Their structural elements were similar to the load transducer LC1, previously described in Section 5.4.1. They have a thin-walled active cylindrical shell positioned between a rigid annular top and a stepped base block, the latter including the stress measuring face. The elements were housed in a protective PTFE casing fitted with a top-cap, bedded on epoxy resin, to give vertical restraint to the assembly as a whole. An outlet was also provided for the electrical wiring when the transducer was encasted with the foundation.

5.6.5 Design and Construction

The structural elements and caps were machined from a solid bar of HE15TB alluminium alloy. The wall thickness of the active cylinders were dictated by robustness in handling, which resulted in a decreased sensitivity. This was, however, adequately compensated by amplification. Mention has been made previously, in Section 5.5.2, of the minimum diameter of the transducer measuring face relative to the soil grain size. The d_{50} grain size of the graded Leighton Buzzard sand required a minimum base block diameter of about 36mm. A diameter of 29.7 mm was actually used. This was the result of a necessary compromise between model size and the diameter theoretically indicated by the soil grading. Bransby (1973), however, considered the statistical calculations of Kallstenius and Bergau (on which the base block diameter was based) to be excessively conservative.

The step in the base block had a 0.15 mm diameter clearance from the inside wall of the PTFE casing. This clearance, dictated by the smallest particle size, was to avoid jamming. To prevent the ingress of finer soil particles, a circular shaped membrane of 'Cling-Film' was put over the contact face of the transducer assembly and was held in place by Dunlop L107 adhesive,

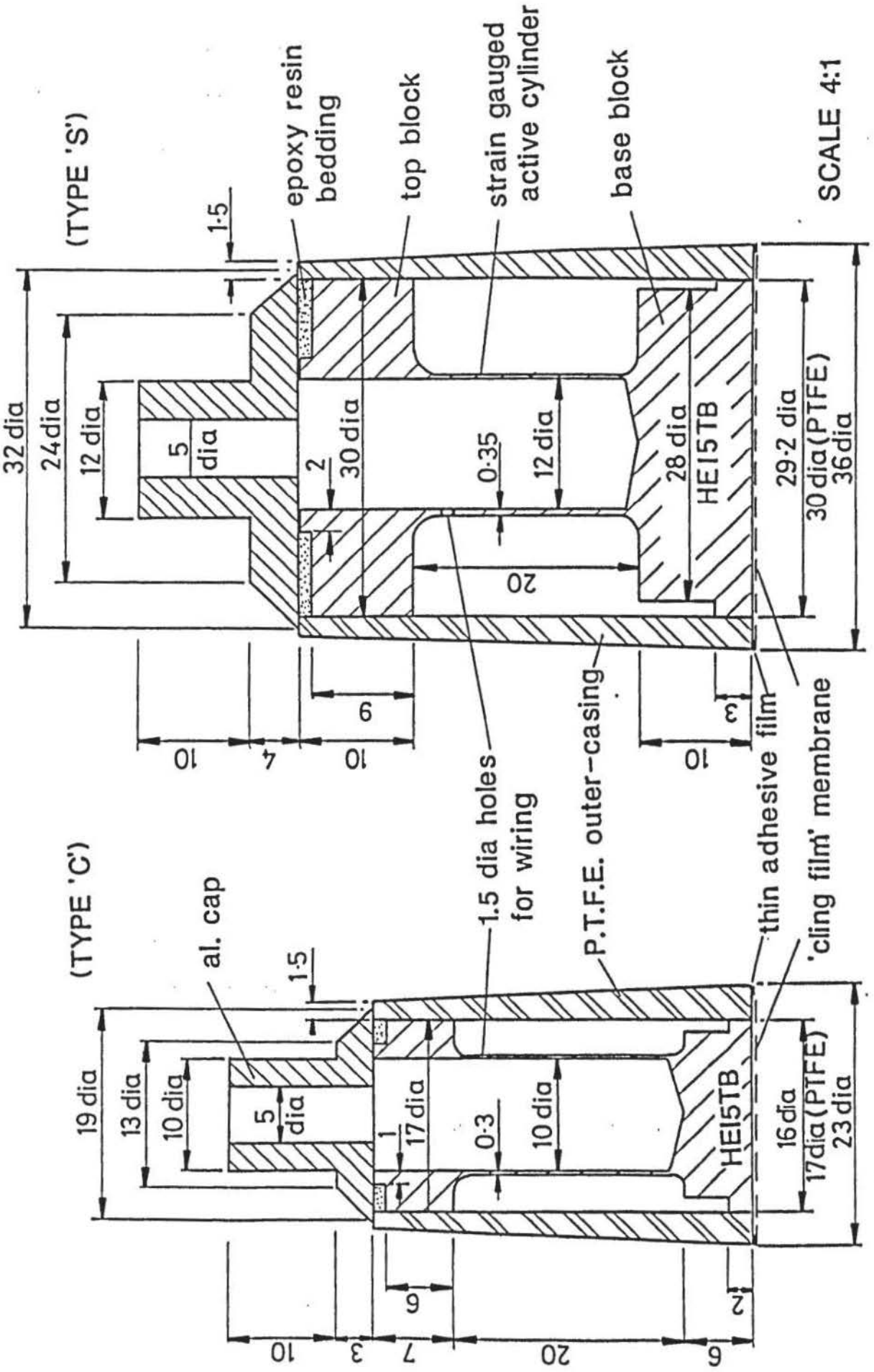

Details of contact stress transducers for clay and granular columns.

FIGURE 5.22

smeared lightly at the circumference of the PTFE casing. The physical characteristics of PTFE and the tape applied to the outer surface of the casing, ensured debonding of the assembly, from the foundation, for re-use.

Four foil resistance gauges were bonded to each of the outer surfaces of the active cylinders in a pattern shown in Figure 5.5. To avoid shear stresses at the measuring face unduly affecting the transducer output voltage, care was taken to ensure each pair of complimentary gauges (i.e. R1, R3 and R2, R4) were diametrically opposed and equidistant from the base block.

Three transducers of each type were constructed.

5.6.6 Electrical

Lengths of SWG46 copper wire were soldered to the foil gauge terminals to form the bridge circuit. Insulated cable of low resistance was used for the input and output leads which were given access to the gauges through two 1.5 mm diameter holes made in the walls of the active cylinders. Epoxy resin cemented the cable at the hole position. The cable was connected to the amplifier by a four-way bus-bar, shown in Plate 5.3. Examples of the completed transducers are given in Plate 5.9.

5.6.7 Static Weight Calibration

Using the arrangement illustrated by Figure 5.23, the transducers were calibrated with static weights. Increments were applied to a maximum of 200 N (type S) and 40 N (type C) which corresponded to normal pressures of 288 kPa and 91 kPa, respectively. The calibrations were repeated five times and the mean taken. Using a dial gauge, the maximum vertical deflection of the transducer was also obtained.

Although piston-type transducers are normally calibrated by static weights only, it was considered prudent to compare these calibrations to those with fluid pressure and with the clay and sand, under conditions as close to those in the laboratory tests.

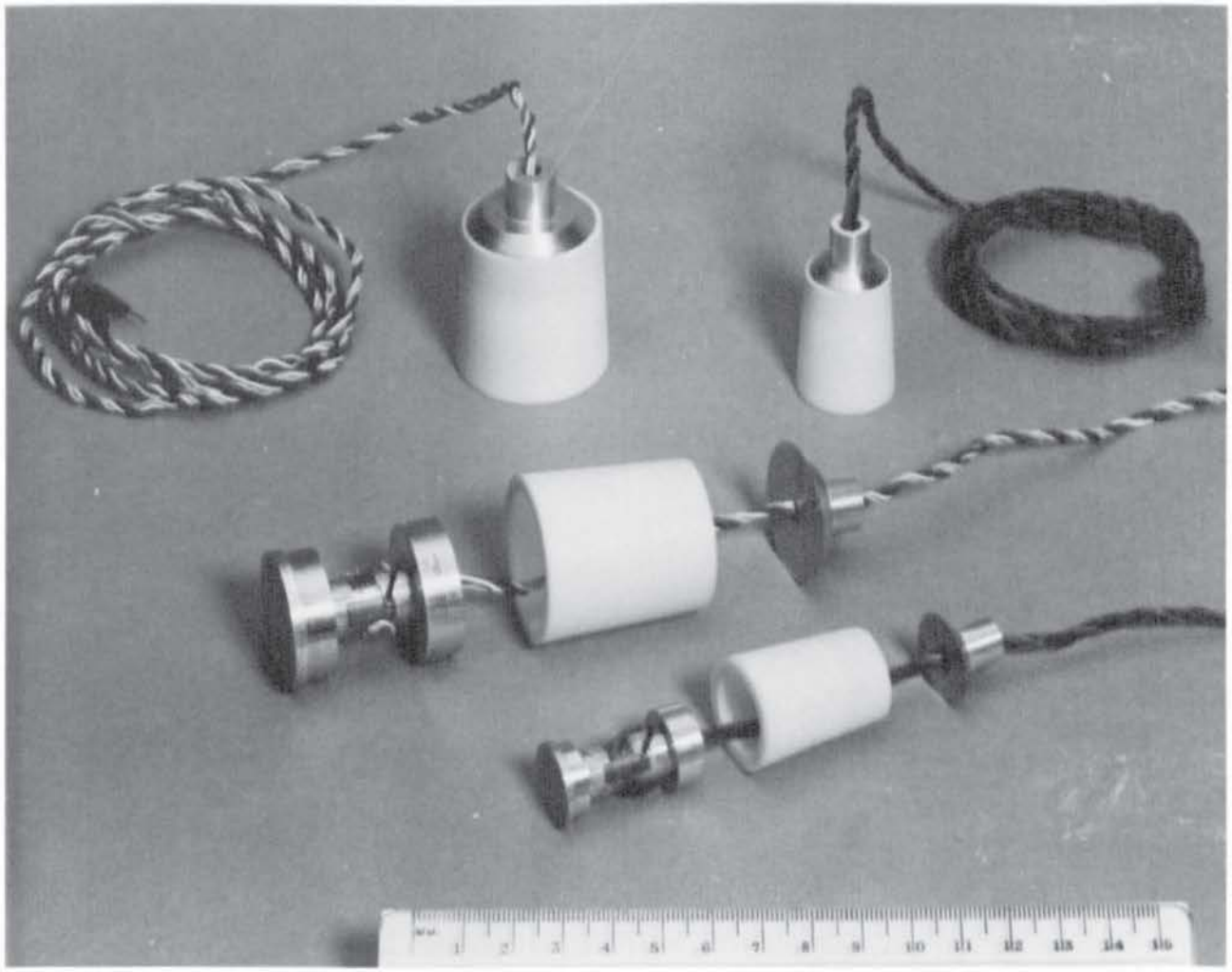

Type C (clay) and Type S (sand) contact pressure transducers.

PLATE 5.9

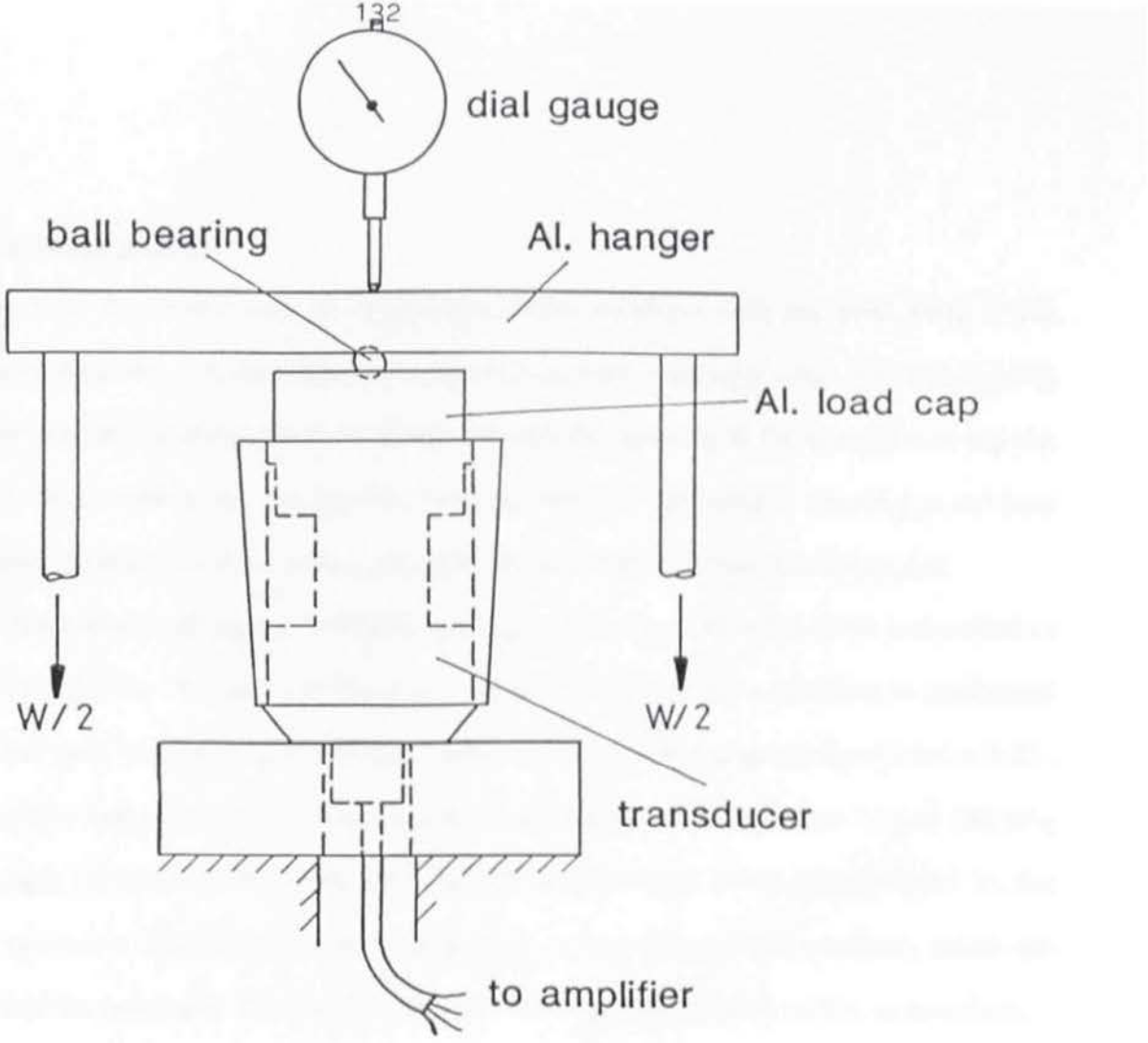

Diagramatic arrangement showing calibration of foundation pressure transuducers using static weights and deflection measurement.

FIGURE 5.23

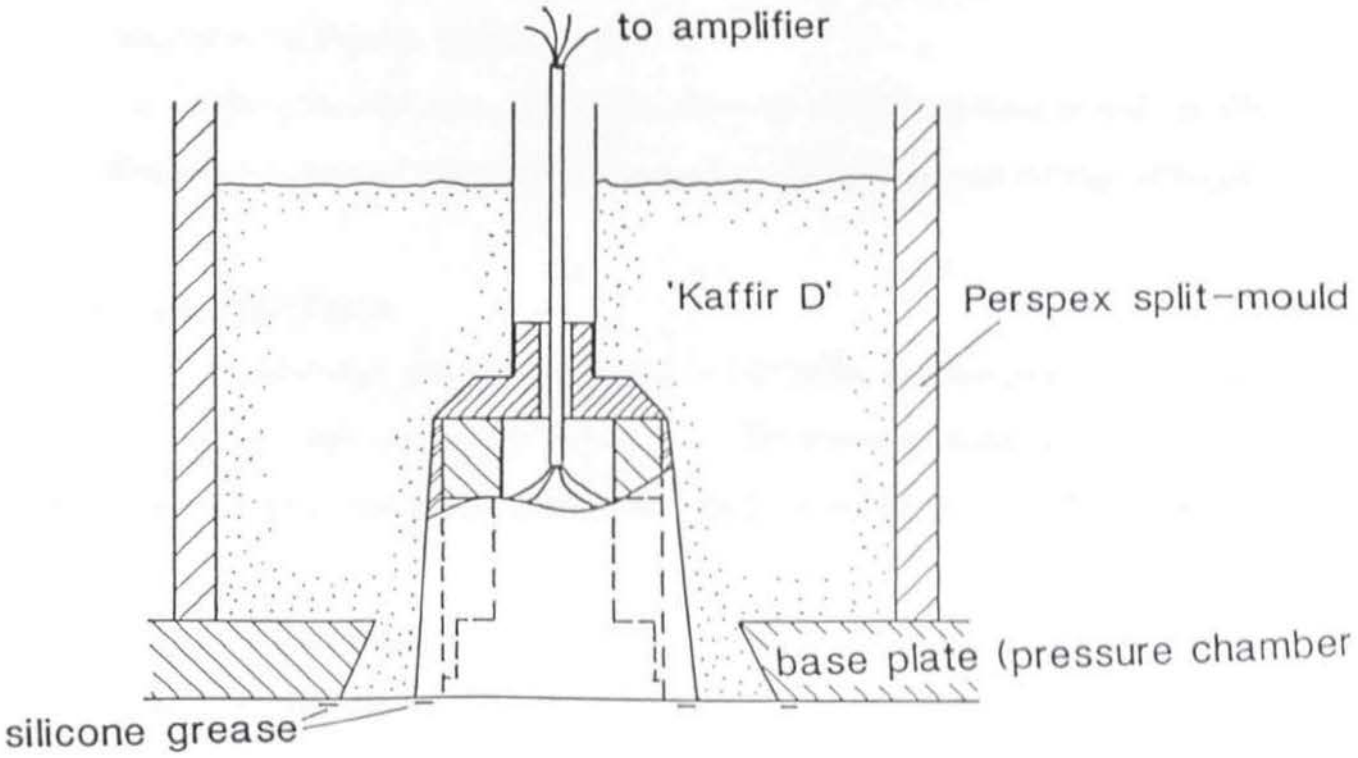

Diagramatic illustration of casting transducer into base plate, of pressure chamber, for calibration purposes.

5.6.8 Water Calibration

Plate 5.10 shows the way the transducers were encastre with the base plate of the calibration pressure chamber. A tube made from paper (computer hardcopy waste was ideal) using a metal-bar former and sellotape extended vertically through the opening in the transducer's top cap (see also Figure 5.24) to form a conduit for the electrical wiring. The conical opening in the base plate was big enough to allow all three type C transducers to be cast and calibrated together.

One hour after making the Kaffir-D casting, the pressure chamber was assembled as described in Section 5.5.8. Because of the higher pressures involved, a previously calibrated Bourdon gauge was used to pressurise the system, which is shown diagramatically in Figure 5.25.

Pressures were applied in increments to maximums of 300 kPa (type S) and 160 kPa (type C). Although the transducers were intended for single cycle loading conditions in the experimental programme, the pressures were unloaded incrementally and readings taken for calibration characteristic purposes. The calibrations were repeated five times and the mean taken.

5.6.9 Clay Calibration

Because, at the calibration stage, it was conceivable that the type S transducers may also be used with the clay, both types were calibrated using the same method described in Section 5.5.9, but connected to the Bourdon gauge system.

One cycle of pressure was applied to a maximum of 200 kPa (type S) and 160 kPa (type C). Calibration was repeated three times (with excellent repeatability) and the mean obtained.

5.6.10 Sand Calibration

Type C transducers were calibrated with the Leighton Buzzard sand. To simulate operational conditions a 'sand column' was formed in the clay contained in the pressure chamber using the cutting tube and sand hopper previously referred to in Sections 4.10.5 and 4.10.8, respectively.

The overall layout is shown in Figure 5.26. Prior to placing the membrane over the surface of the clay and sand column, the clay and later the sand were levelled with a thin straight

Contact pressure transducers and accessories for casting into calibration base plate.

PLATE 5.10

Linear displacement transducers.

PLATE 5.11

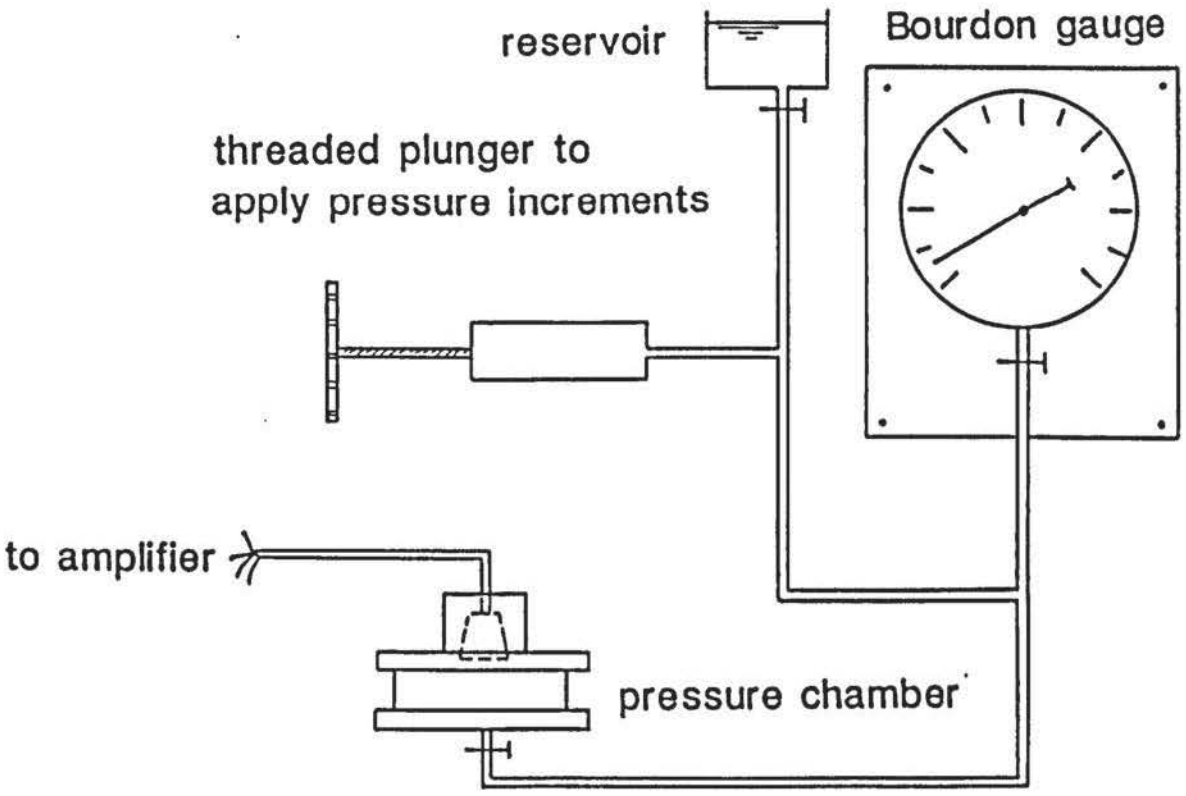

Diagramatic layout of arrangement for pressure calibration using a Bourdon gauge.

FIGURE 5.25

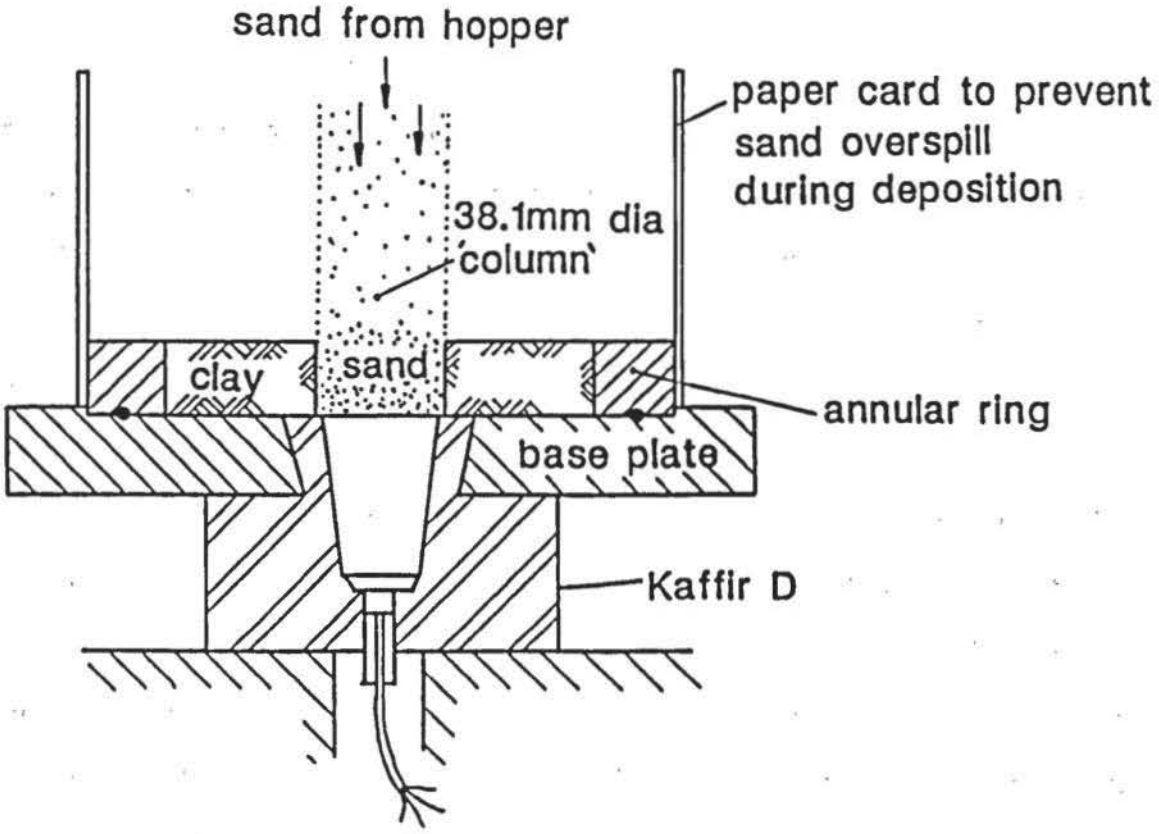

Diagramatic arrangement showing formation of sand column in clay contained in the pressure chamber, for type C transducer calibration.

FIGURE 5.26

edge.

One cycle of pressure was applied in increments to a maximum of 300 kPa. This was repeated three times and the mean taken.

5.6.11 Characteristics

Typical calibration characteristics of type S transducers are shown in Figures 5.27 to 5.30. A true elastic correlation was obtained from static weight calibration. A linear regression gave the best line of fit for the fluid, clay and sand calibration results for loading only. For unloading, a quadratic regression of the same form of Eqn. 5.7 was found the most suitable. This dispartity was more evident from calibration results using clay and, particularly, the sand. These characteristics were also evident with type C transducers.

For comparative purposes, the calibration loading regression curves were drawn on the same axes and are shown in Figure 5.31 (type S) and Figure 5.32 (type C).

It is evident that transducer sensitivity was dependent upon the medium transmitting thrust to the measuring face. Static weights and water gave conjugate sensitivities, whilst those using clay and sand were generally about 7% and 20% less, respectively.

A prominent factor in considering reasons for this was in the particulate nature of the soils. Initially, it was suspected that soil particles along with the protective'Cling-Film' membrane were ingressing into the 0.15 mm annular gap, between the base block and PTFE casing, to produce a jamming effect. This, however, seemed unlikely since the sand, although giving the greater loss in sensitivity, had particle sizes at least about four times larger than the annular gap. Close inspection, after a number of calibrations, showed no evidence of soil ingression.

The ratio of the measuring face diameter to the vertical deflection, at the maximum static calibration loads, was 1.07 (type S) and 1.19 (type C) times greater than that recommended by the U.S. Waterway Experiment Station (1944) for diaphragm type transducers. This indicated that the transducer elements were sufficiently stiff to prevent significant stress redistribution at the measuring face. On this basis it was considered likely that sensitivity variations between the clay and sand calibrations, relative to those using static-weights and water pressure, were due to the properties of the respective soil structures preventing the transfer of the applied pressures to the

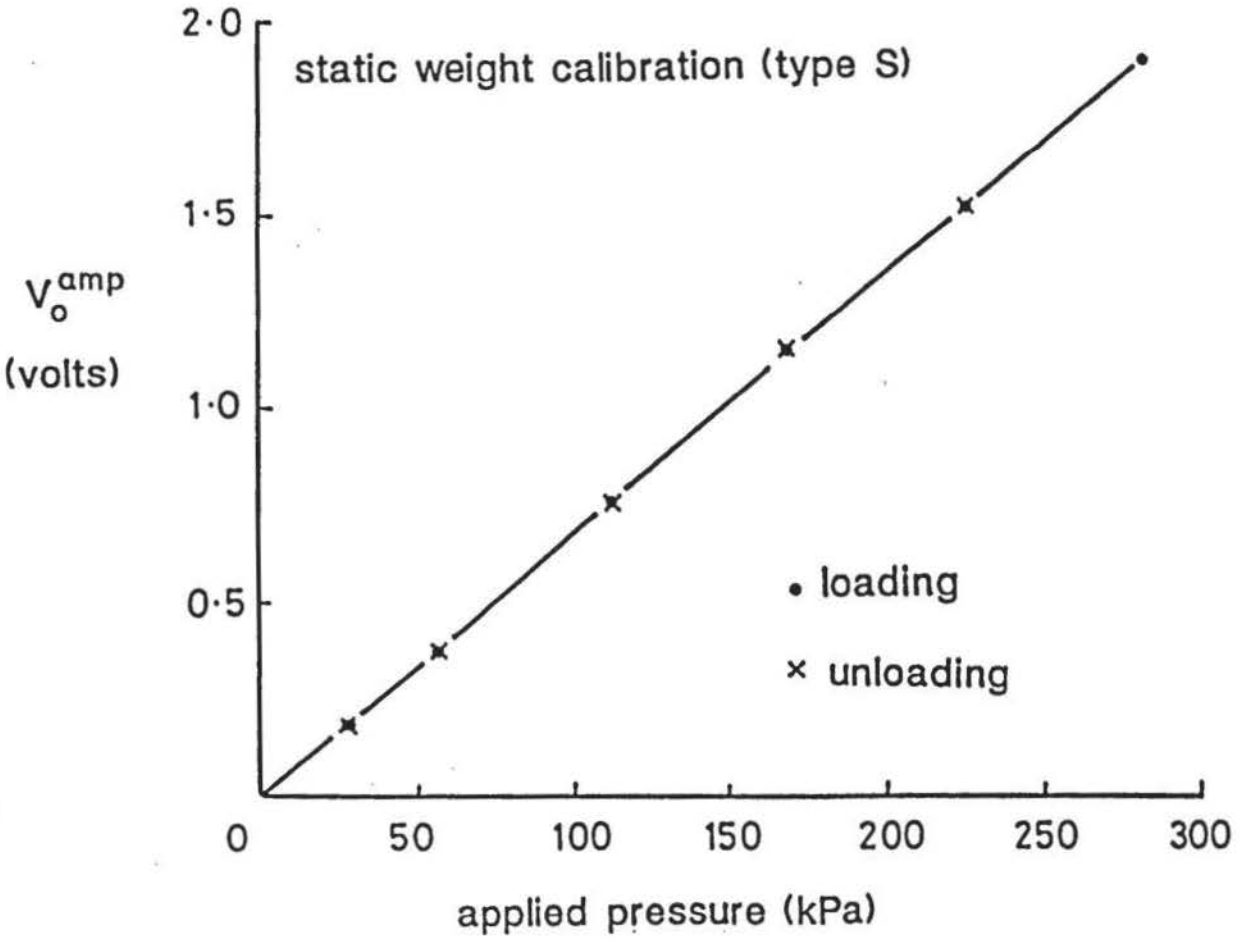

Typical calibration curve for type S transducer using static weights.

FIGURE 5.27

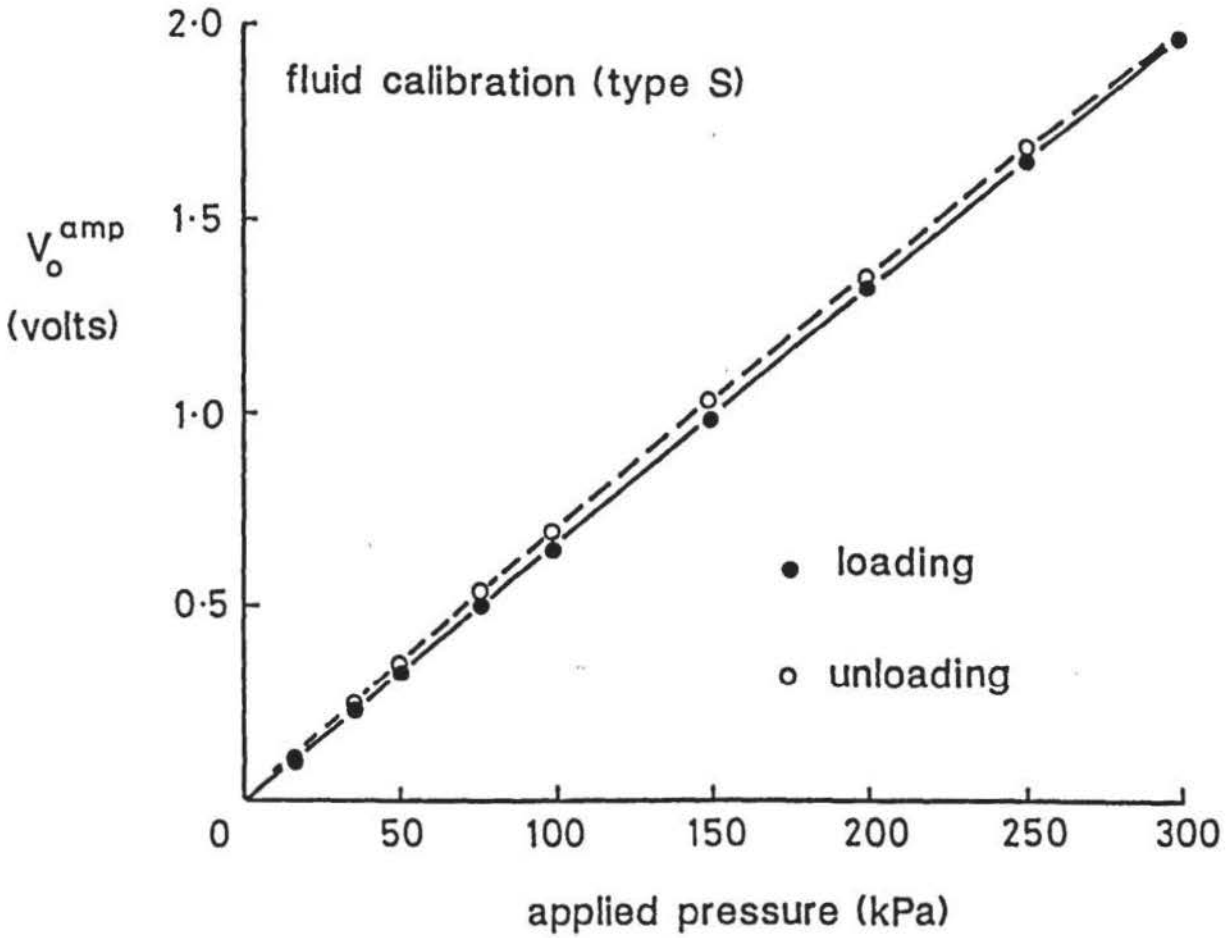

Typical fluid calibration curve for type S transducer.

FIGURE 5.28

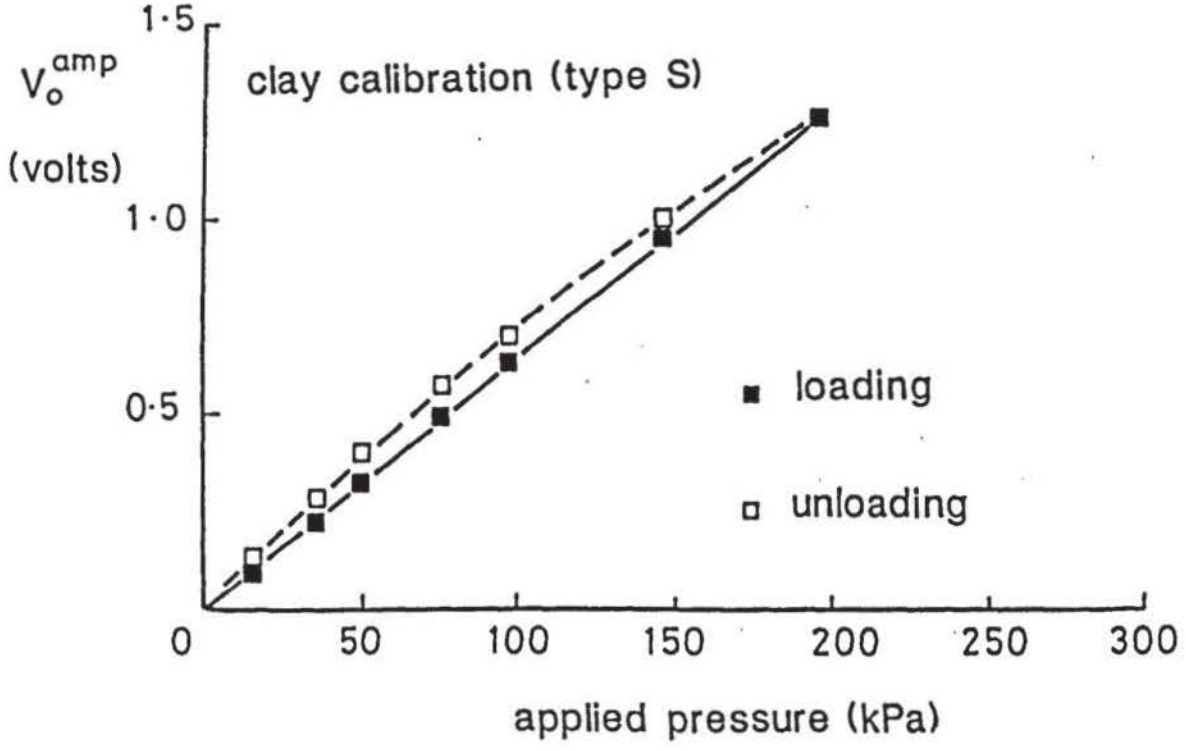

Typical clay calibration curve for type S transducer.

FIGURE 5.29

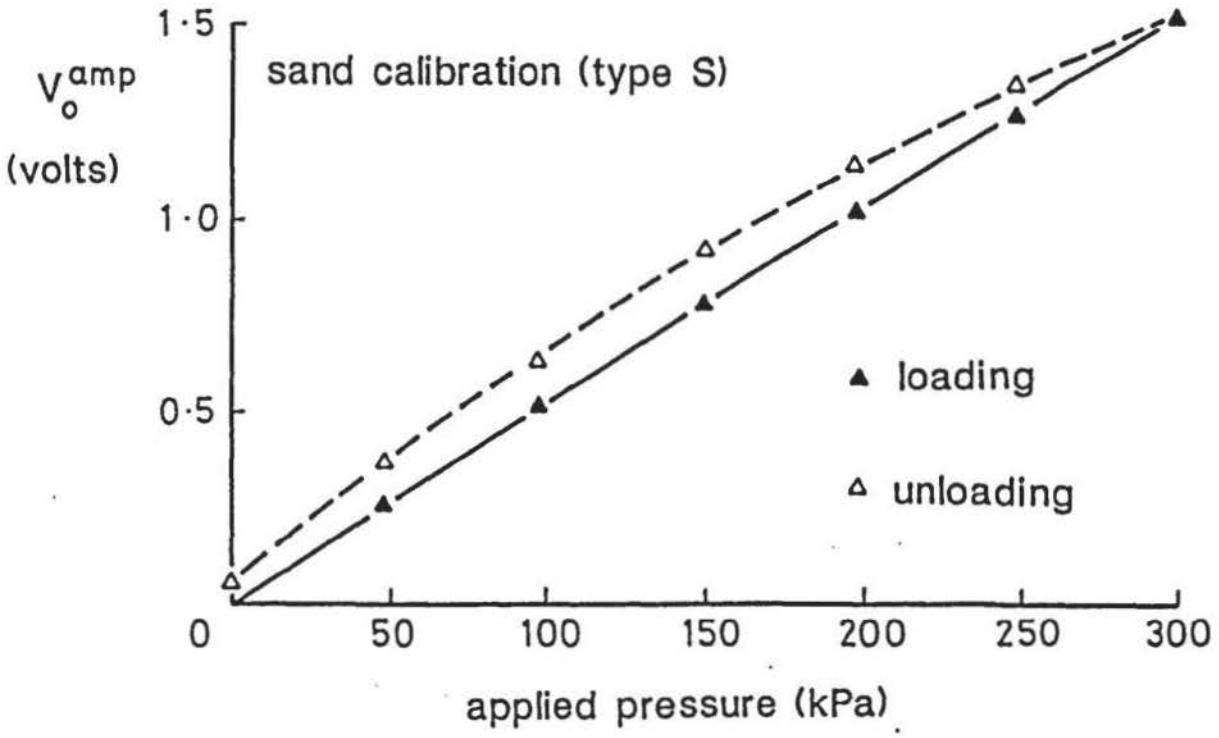

Typical sand calibration curve for type S transducer.

FIGURE 5.30

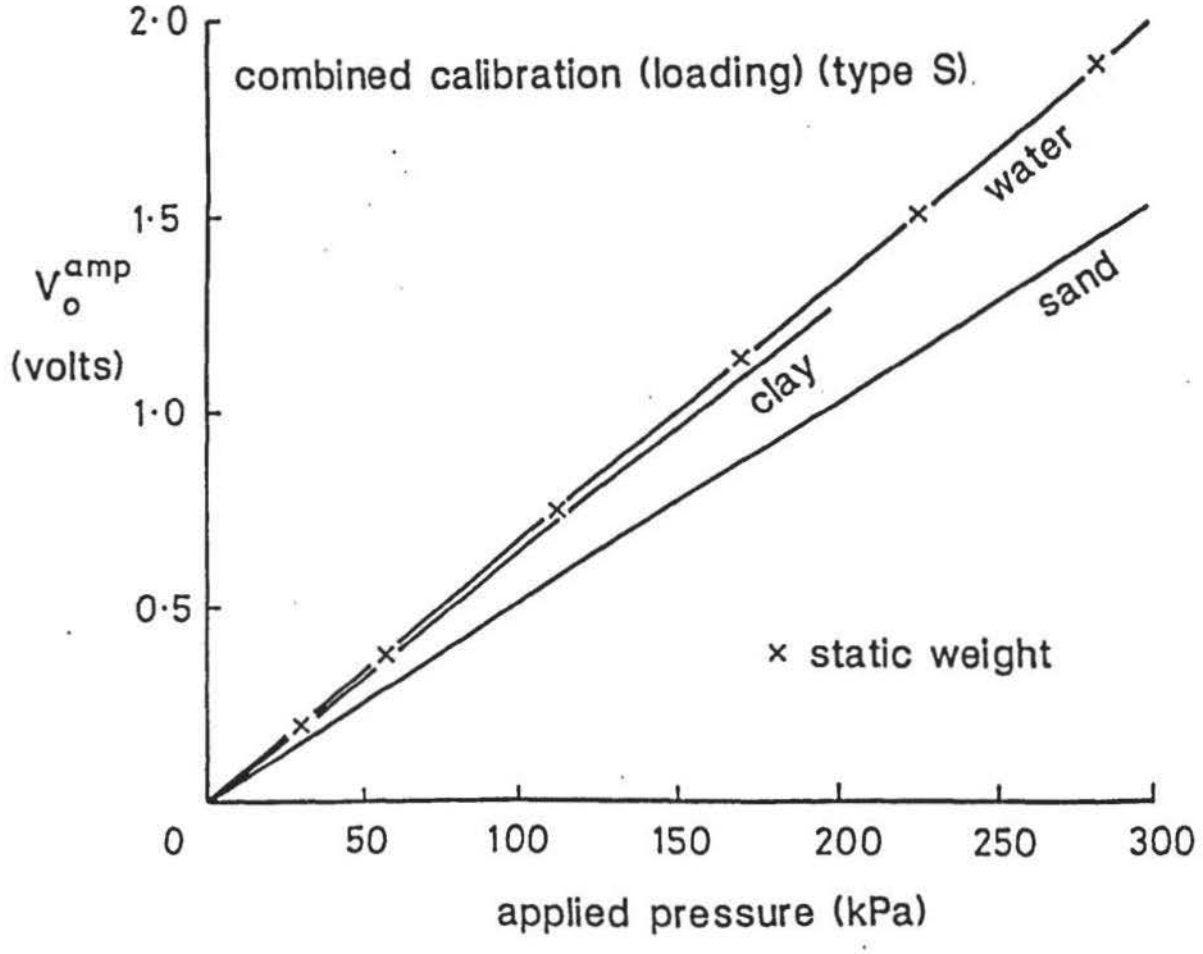

Comparison of the calibration (loading) regression curves for a typical type S transducer.

FIGURE 5.31

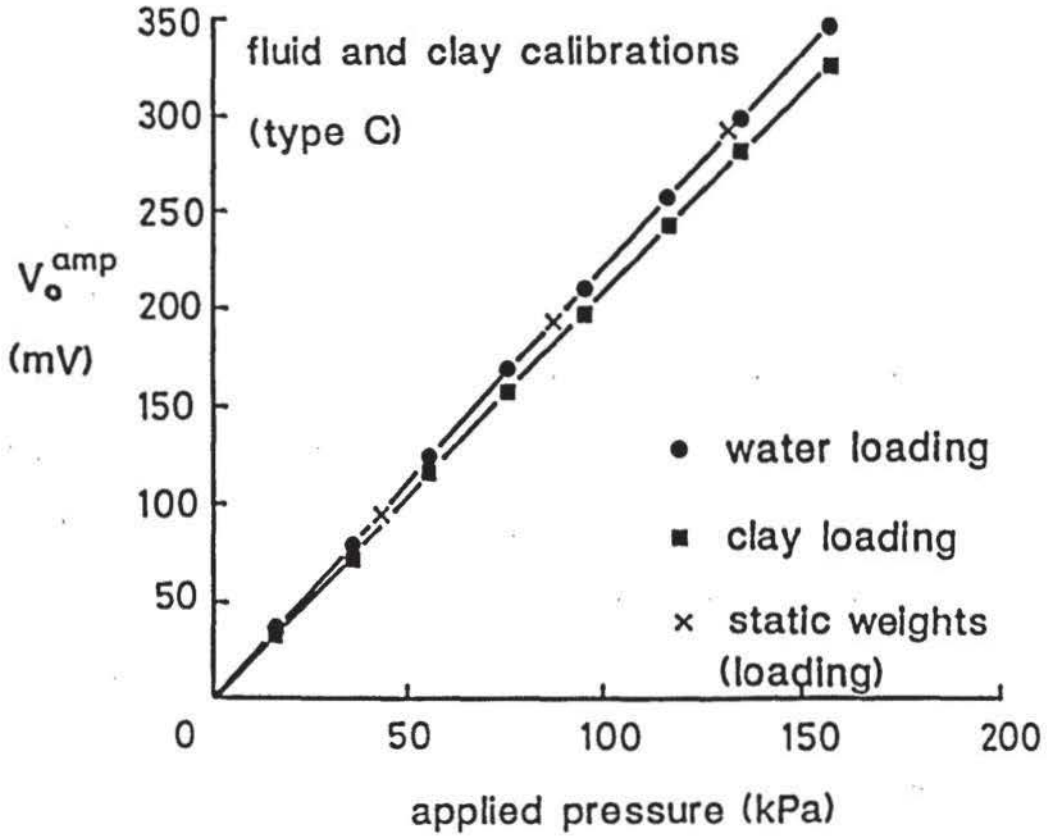

Typical loading calibration curve for type C transducer under fluid pressure and clay.

FIGURE 5.32

measuring face. The shear strength of sand depends on the applied pressure. Shear strength enables some of the applied pressure to be dispersed laterally, thus relieving pressure on the measuring face. The 'column' of sand, used in the calibration would have been restrained vertically by the surrounding clay, in the undrained state. This vertical restraint would have been approximately constant, so a linear calibration would be expected.

In the case of the clay calibration, the clay shear strength was independent of applied pressure and had a value significantly less than the sand. Correspondingly, lateral dispersion of pressure would have been less and a greater proportion of the applied pressure would register at the measuring face. Since water has no shear strength, the pressure at the measuring face was equal to the pressure applied.

5.6.12 Effects of Shear Stress

Figure 5.33(a) illustrates the method used to determine the effects of shear stress at the measuring face. Worst-case results for type S and type C transducers are shown in Figure 5.33(b) as magnitudes of erroneous output voltages (V_o^{amp}) produced by shear stress acting at right angles to the longitudinal axes of the active strain gauges and parallel to the dummy gauge axes. It is evident that V_o^{amp} is greatest in the former case. The effects were due to constructional variations in diametric alignment and positioning between the strain gauges. Using previously determined values of $c_u = 11.35$ kPa, $\phi' = 40^o$ and the normal pressure $q_f^{col} \approx 250$ kPa at failure of a granular column, the maximum theoretical shear stress (τ_{max}) that could occur at the measuring face of the transducer in practice was:

$$\text{clay}: \quad \tau_{max} = c_u = 11.35 \text{ kPa}$$

$$\text{sand}: \quad \tau_{max} = q_f^{col} \tan\phi' \approx 209 \text{ kPa}$$

The active case results, from Figure 5.33(b) for transducer types C and S were used to give the maximum fictitious normal stresses (i.e. V_o^{amp} x calibration sensitivity) and were plotted against shear stress τ in relation to τ_{max} for the clay and sand, shown by Figure 5.34.

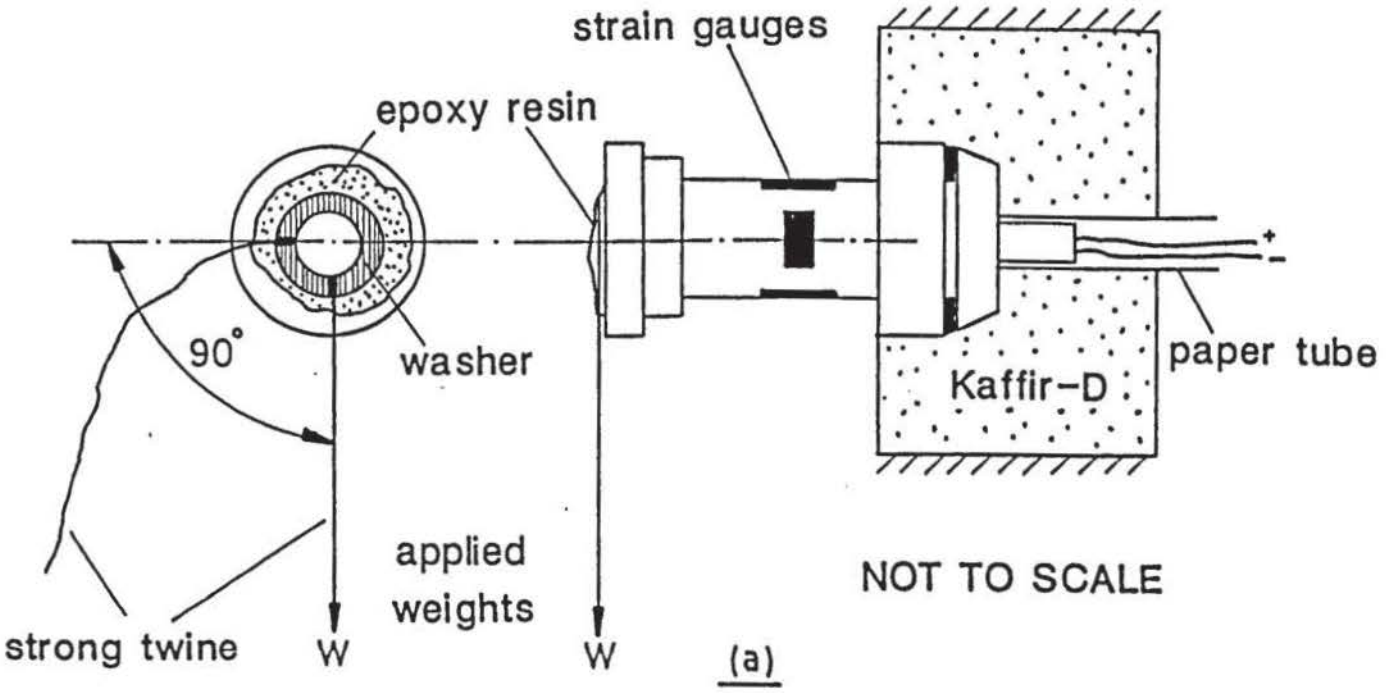

(a)

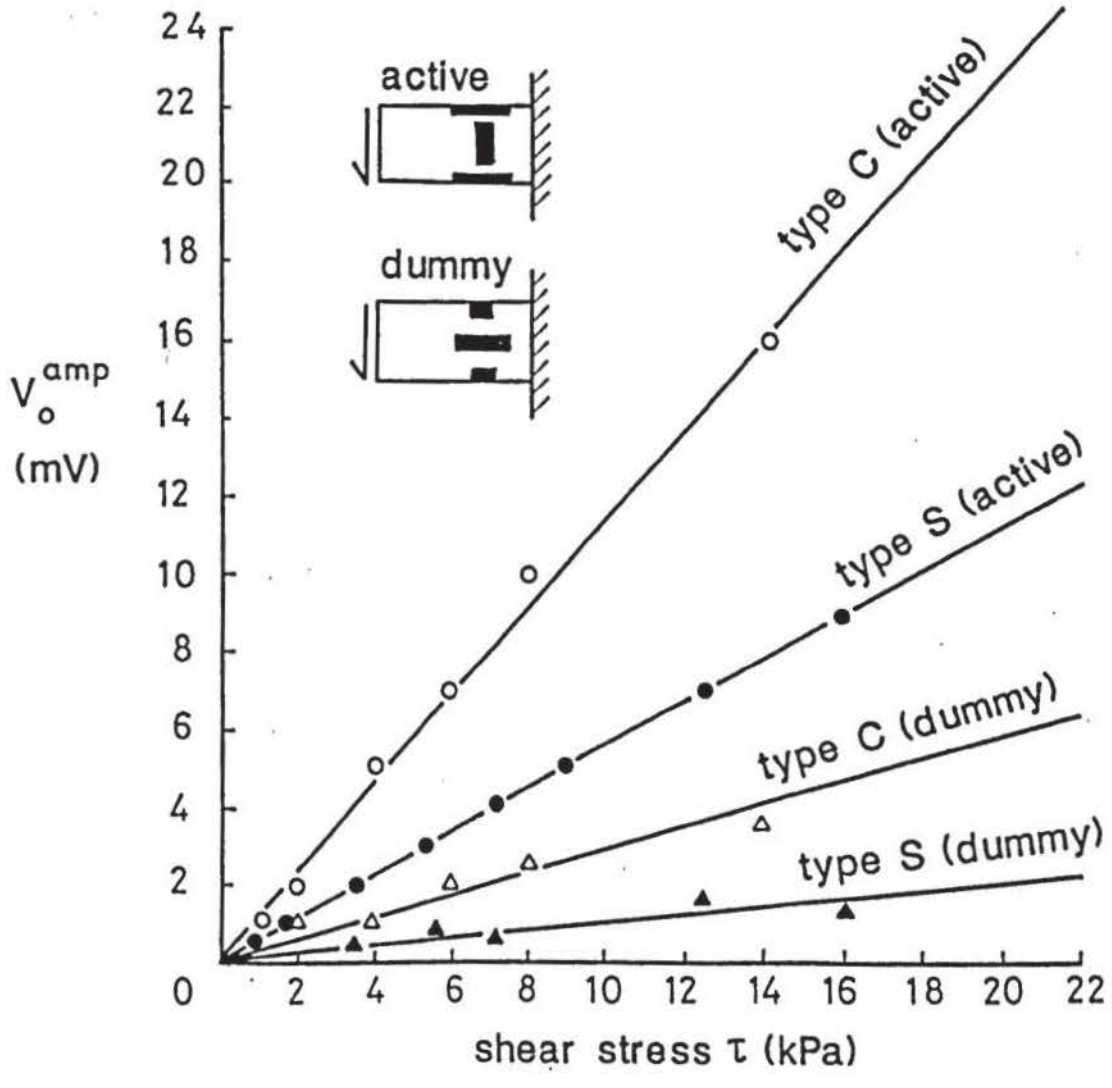

(b)

Arrangement to determine the effects of shear stress.

FIGURE 5.33

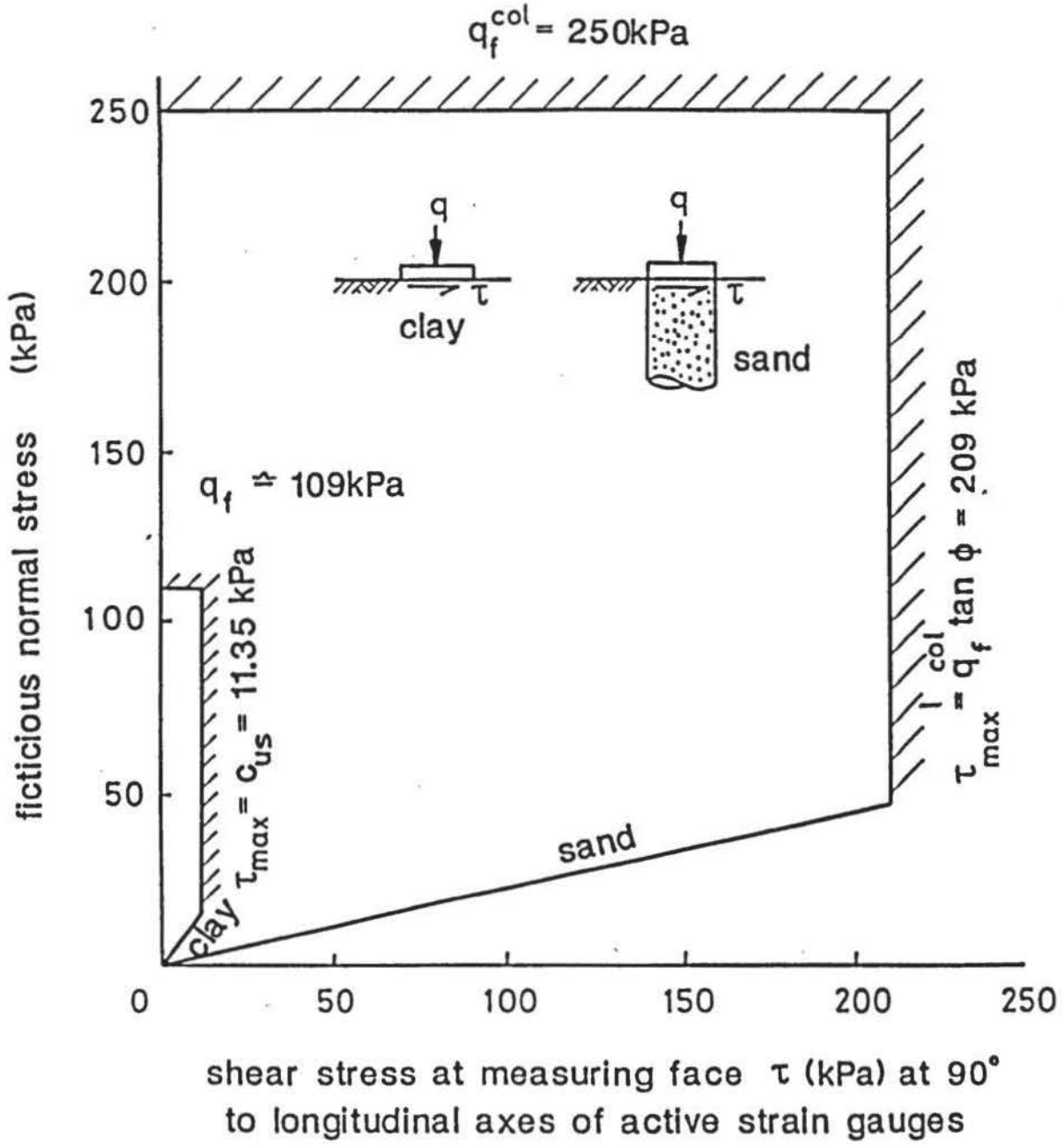

Fictitious normal stress through development of shear stress.

FIGURE 5.34

The potential error is a maximum, and assumes full development of the shear strength, of the contacting material, at the measuring face and for it to act wholly in one direction at 90° to the longitudinal axes of the active strain gauges.

In practice, the probability of all these factors occurring simultaneously was considered to be of the order of 5% of the total number of readings during the given test.

5.6.13 Casting Foundations

The transducers were incorporated into the model foundations by casting them in Kaffir-D using Perspex base templates and wood shuttering. The procedure is shown in Plates 5.12 to 5.16, and a schedule of the base template specifications are given in Figure 5.35 and 5.36. Constructional details, showing the means of connecting the foundation to the loading tube, are shown in Figure 5.37.

Removal of the transducers from the foundation, after completion of testing, was by way of applying a small pressure to their alluminium top-caps via a metal rod inserted down the electrical wiring conduits.

5.7 DISPLACEMENT TRANSDUCERS

Two existing transducers, manufactured by Wykeham Farrance Limited, were used to measure small (transducer LT1) and large (transducer LT2) linear displacements. These can be seen to the right and left of Plate 5.11. LT1 and LT2 were fed from stabilised DC supplies of 12 v and 24 v, respectively. Their output voltages were large enough not to need amplification.

The transducers were calibrated with the aid of their integral dial gauges. The mean of three calibrations is shown in Figure 5.38 and linear correlations obtained.

5.8 TRIAXIAL COMPRESSION TEST TRANSDUCERS

The load transducer was of the Imperial College design, for use inside a trixial cell. It had a maximum load capacity of 450 Kgf. The cell-pressure transducer was of Bell and Howell manufacture with an operating range of 0 - 1000 kPa. Both transducers were supplied by Wykeham Farrance Limited.

Mandrels for making holes, in foundation bases, to site pressure transducers.

PLATE 5.12

Selection of Perspex foundation base templates and a completed foundation.

PLATE 5.13

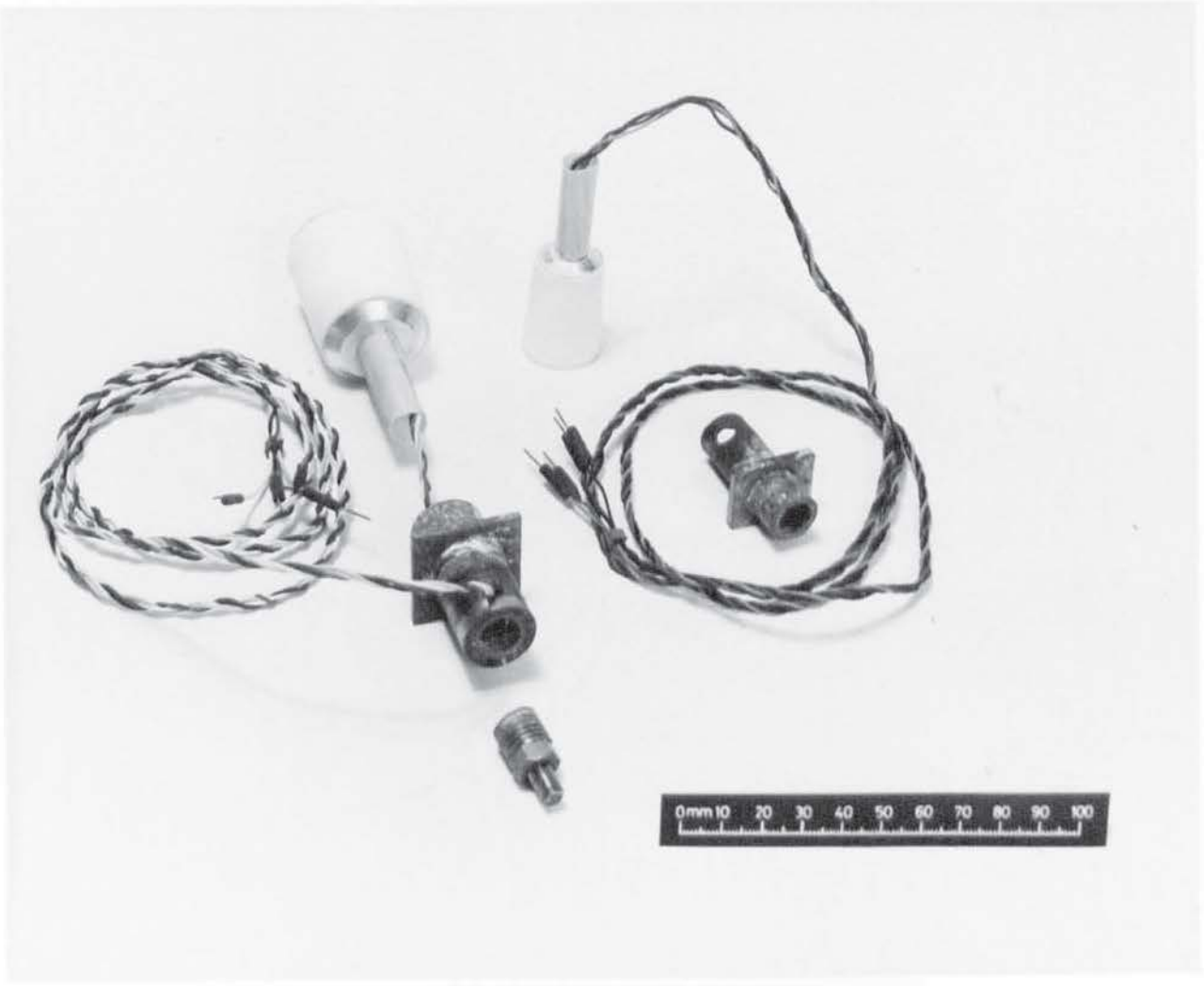

Connectors, for type C and type S transducers, to attach completed foundation to loading tube.

PLATE 5.14

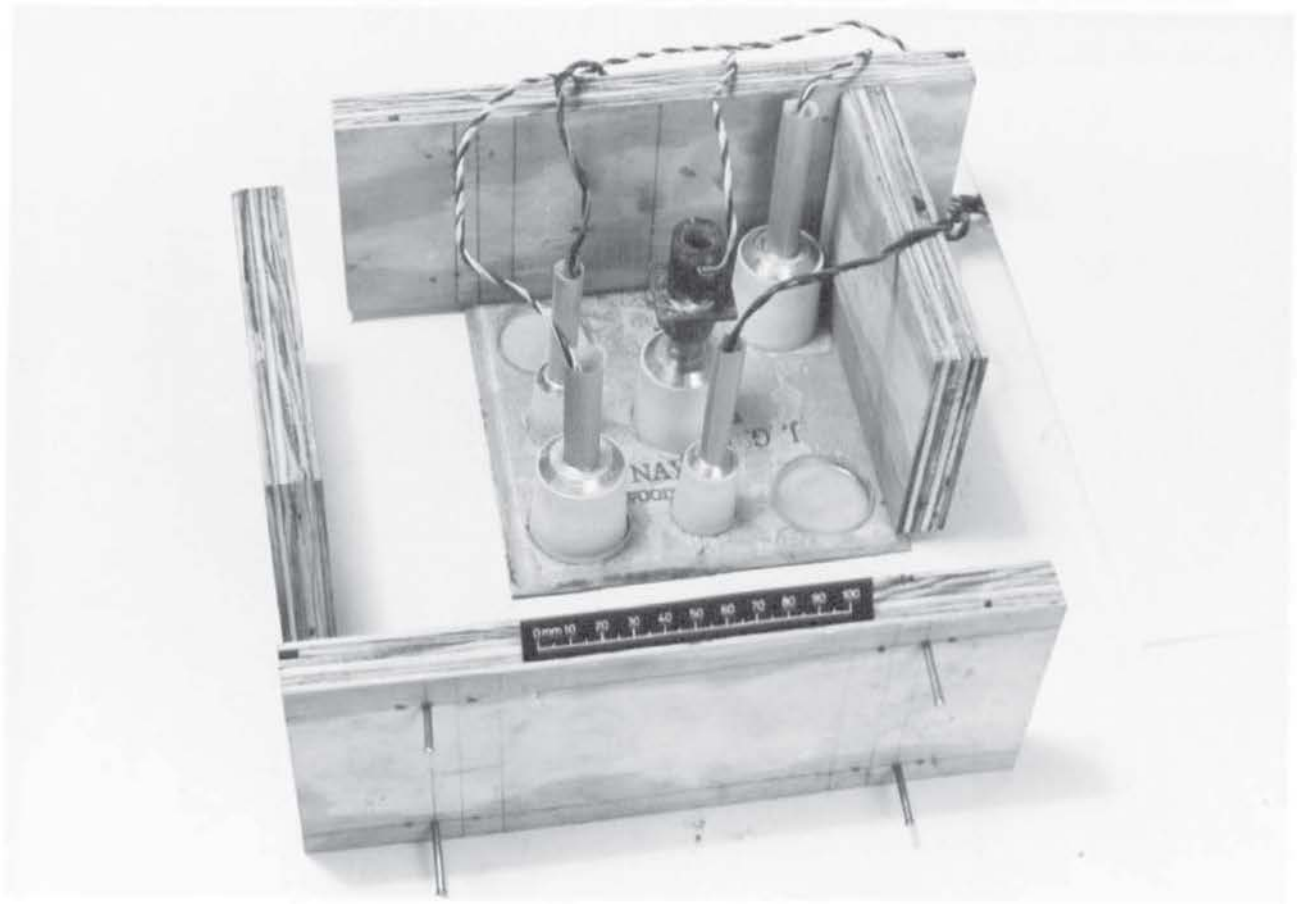

Shuttering to base template incorporating type S and type C transducers.

PLATE 5.15

Underside of completed foundation

PLATE 5.16

Perspex

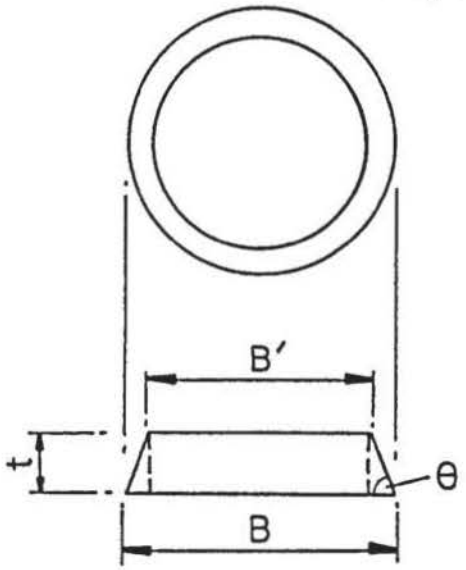

B	B′ (mm)	t	θ (degrees)
50	40	10	63
60	40	10	45

circular

Perspex

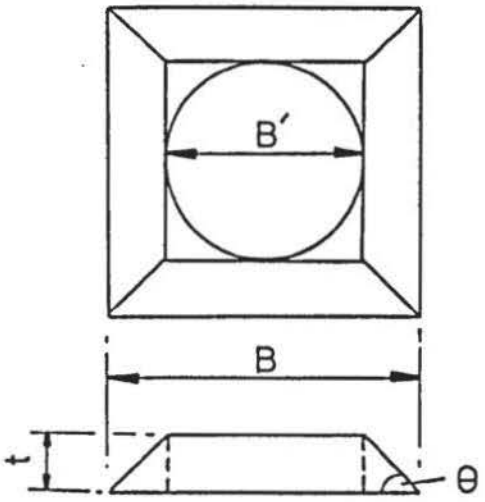

B	B′ (mm)	t	θ (degrees)
60	40	10	45

square

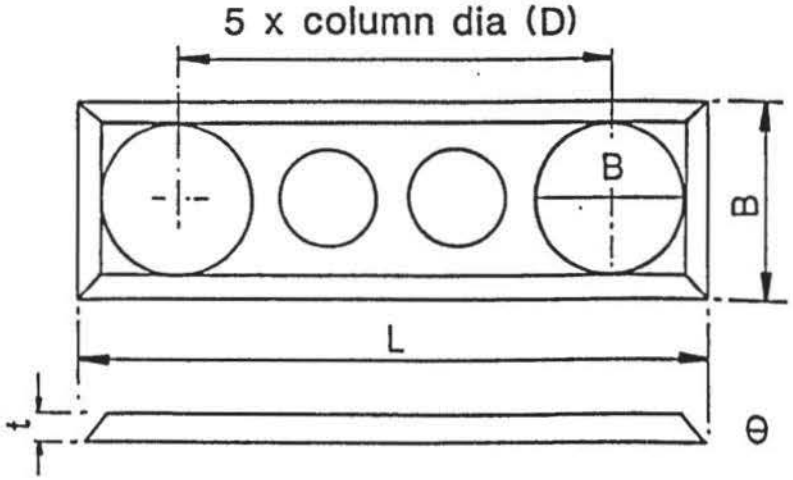

B	B′ (mm)	L	sD	t (mm)	θ (deg)
50	38	116	1·75D	6	45
50	38	145	2·5D	6	45
50	38	164	3·0D	6	45

rectangular

Base-plate specifications for pressure transducers located in circular, square and rectangular foundations.

FIGURE 5.35

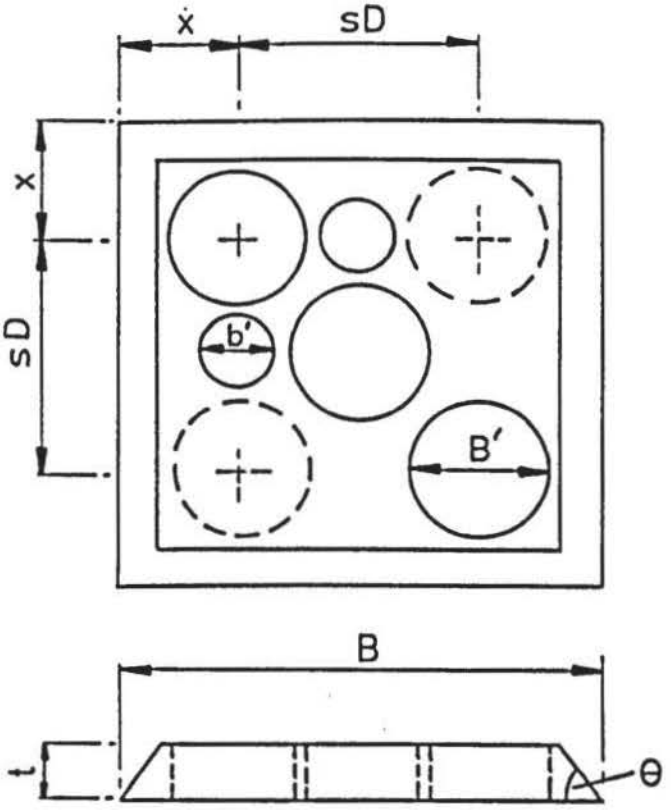

B	B′	b′	t	0	x	sD
	(mm)			(degrees)	(mm)	
125	36	23	6	45	29	1·75D
153	36	23	6	45	29	2·5D
172	36	23	6	45	29	3D

rectangular – multiple columns

Base-plate specification for pressure transducers located in square foundation (multiple columns).

FIGURE 5.36

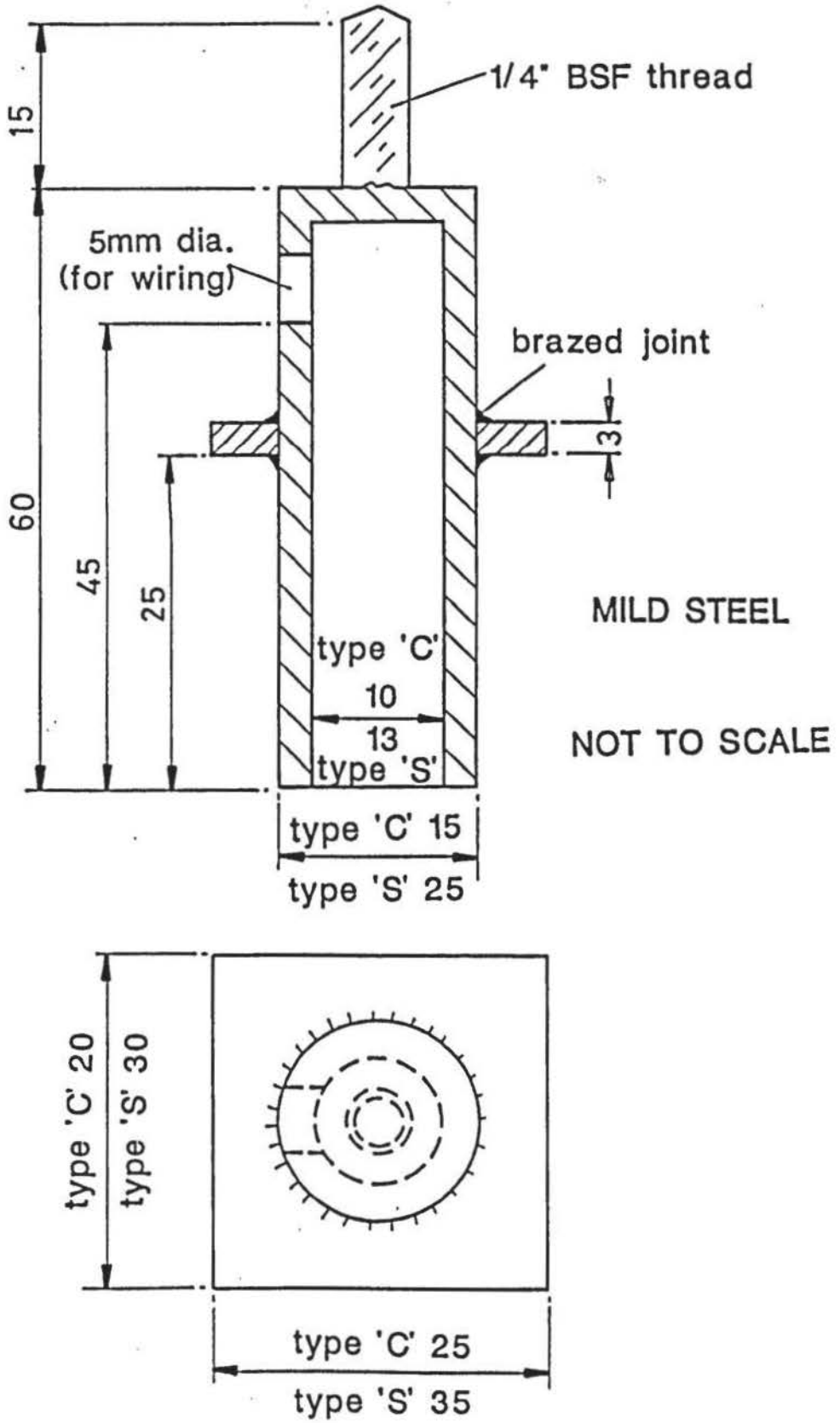

Constructional details of connecting instrumented foundation to loading tube.

FIGURE 5.37

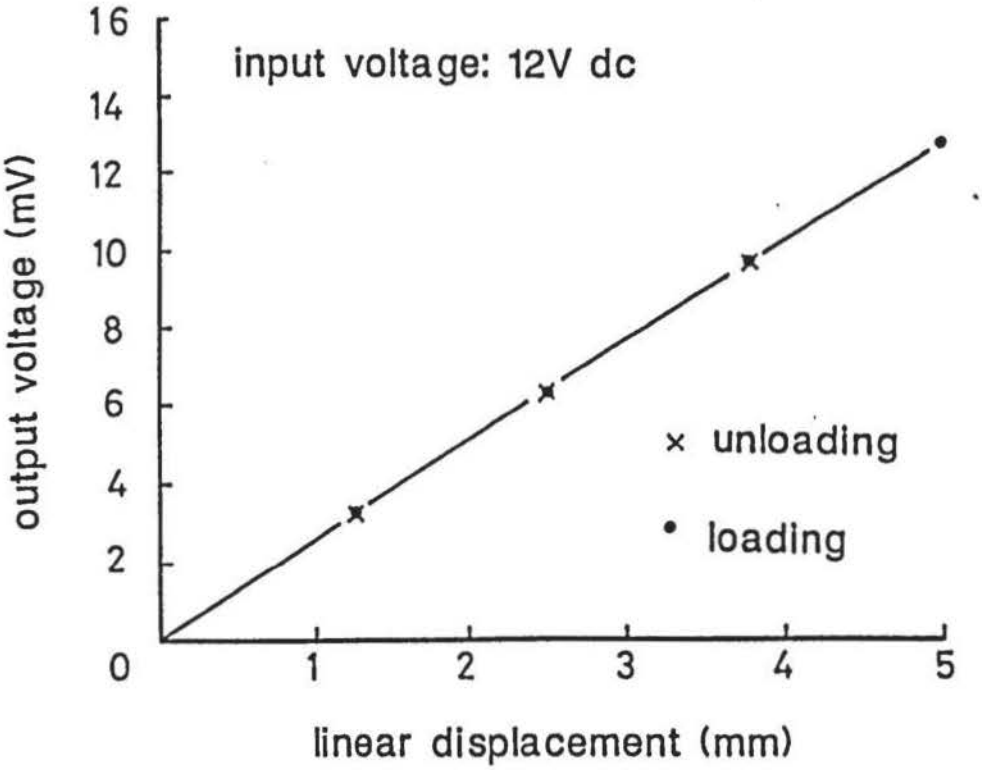

Calibration of linear displacement transducer LT1.

FIGURE 5.38a

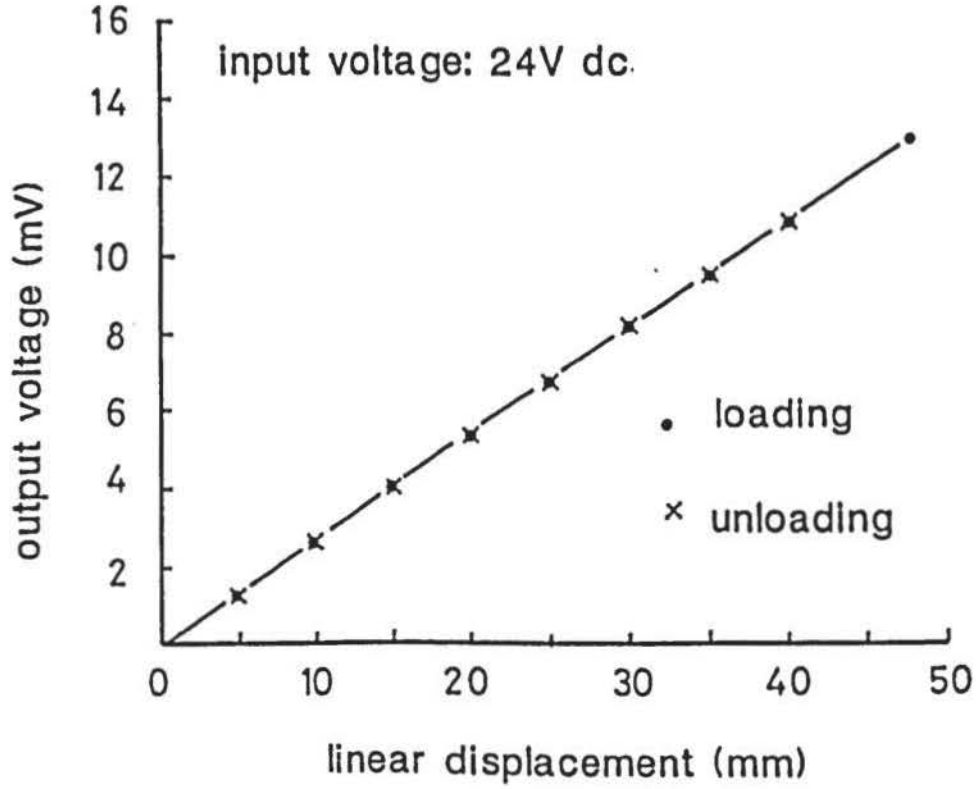

Calibration of linear displacement transducer LT2.

FIGURE 5.38b

The load and pressure transducers were operated independently of the amplifier unit at input voltages of 8.5 v and 10v DC, respectively. The load transducer was calibrated under static loading to a maximum of 270 N. The pressure was calibrated in-situ with a pre-calibrated Bourdon gauge. The results of the mean of three calibrations are given in Figure 5.39 and 5.40.

5.9 STRAIN GAUGES

All strain gauges used were manufactured by Tinsley Telcon Limited. The gauges were attached to the elements in the strictest accordance with the manufacturers specification. This operation was always performed by a technician experienced with the procedure.

5.10 STRAIN CYCLING

After construction, all the load and stress transducers were loaded to their maximum calibration load, or pressure, at least twenty five times. This strain cycled the structural element, strain gauges and bonding material to remove hystersis effects.

5.11 TEMPERATURE EFFECTS

All the made transducers were checked for temperature sensitivity by placing them, wrapped in a rubber membrane, in water and allowing them to cool. For the temperature range 18°C to 30°C, changes in output voltage were negligible (i.e. less than 1%).

5.12 CALIBRATION STABILITY

Re-calibration of the transducers was done at the end of the laboratory experimental programme. It was found that the calibration constants for the load and pressure transducers differed by less than 1% and 3% (clay) to 5% (sand), respectively. During the course of the experimental work, loads and pressures did not exceed those applied during calibration.

5.13 ZERO DRIFT

Lord (1969) examined the drift variation of Cambridge Load Cells (CLC), used in his experimental work, over 2 hour (short-term) and 8 hour (long-term) periods. It was concluded that

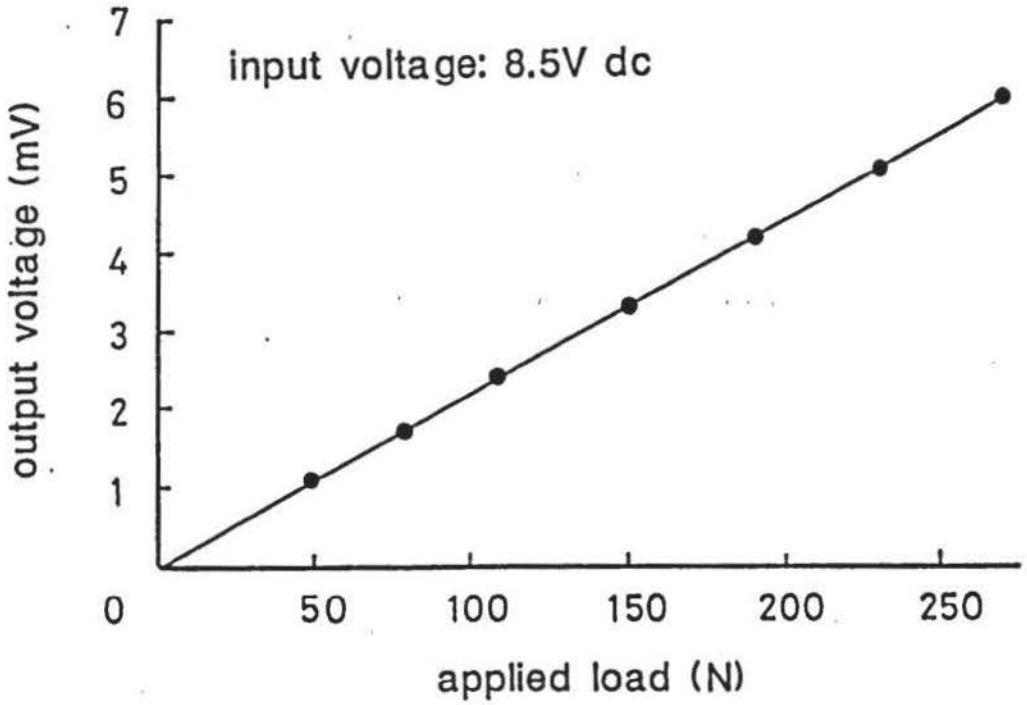

Calibration of triaxial load transducer.

FIGURE 5.39

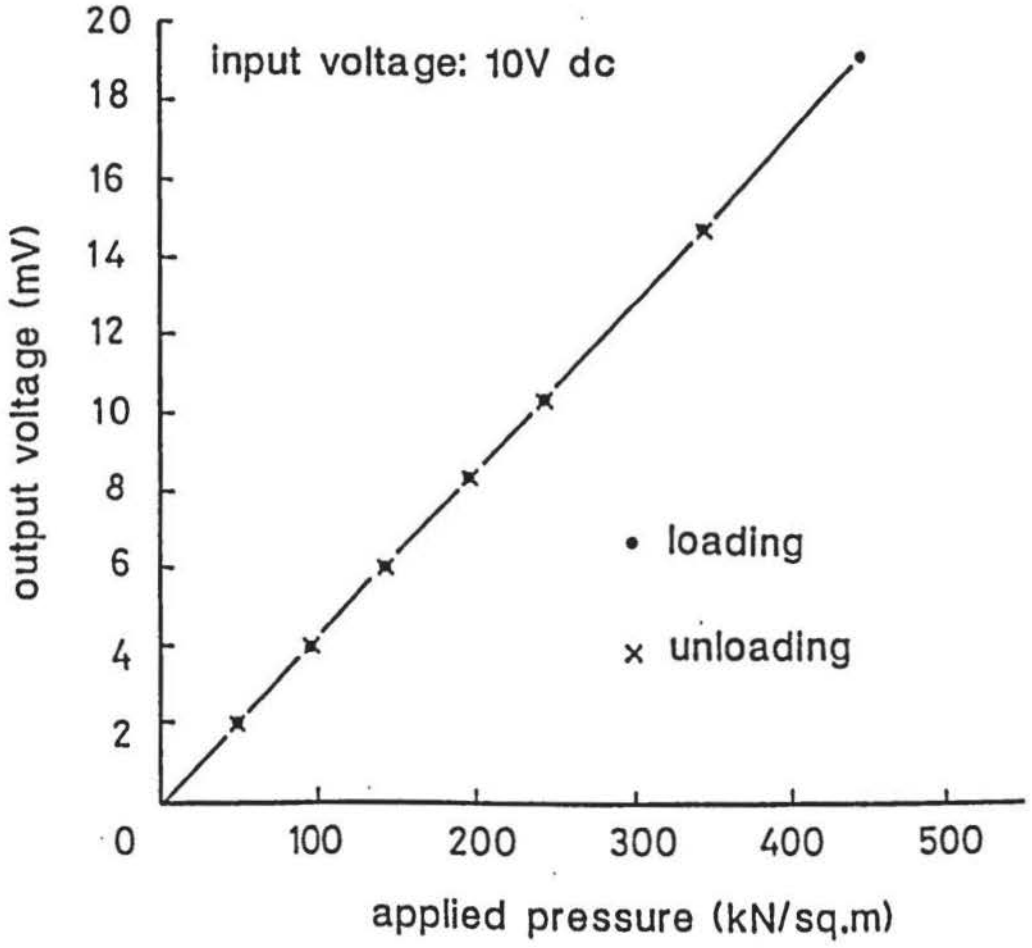

Calibration of triaxial hydrostatic pressure transducer.

FIGURE 5.40

the drift consisted of two components. A random amplitude fluctuation, varying according to the particular CLC, superimposed on a periodic fluctuation of a similar amplitude. The extremes of the short-term fluctuations were found to be about half those of the long-term.

Lord suggested that the mean error in a transducer circuit was likely to be equal to the square root of the sum of the squares of individual maximum errors. If all the transducer circuit errors are assumed to occur simultaneously, the maximum likely recording error in stress can be derived using the transducer calibration constants. Typical results for the made transducers are shown in Figure 5.41.

The relative size of the error will depend upon the magnitude of the stress level measured. Low stress gives high error. The recording errors quoted, however, are maximum values, and Lord considered their occurrence to be of the order of 5% of the total number of readings taken during a given test.

In the author's case, test duration was 20 minutes on average.

5.14 WARM UP PERIOD

A one hour 'warm-up' period was always allowed for all the electronic and electrical equipment prior to data recording.

	A	B	C	$D = \sqrt{A^2+B^2+C^2}$	D x Calibration Constant
Transducer	Short-Term Drift (mV)	Long-Term Drift (mV)	Calibration Deviation (mV)	Mean Error in Circuit (mV)	Recording Error (kPa)
LC1 (load)	6	17	6	19	2.5*
Diaphragm (clay)	18	40	28	52	1.3
Type S (sand)	11	18	10	23	4.4
Type C (clay)	1	3	3	4	2
Lord (1969)** (CLC)	0.02	0.05	0.03	0.06	1.4

* 38.1 mm diameter foundations

** Un-amplified output.

Accuracy of results from transducer measurements.

FIGURE 5.41

CHAPTER 6

DATA RECORDING

6.1 INTRODUCTION

Electronic data-collecting systems were used to transfer and record the transducer outputs and to digitise the x-y co-ordinates of the lead-shot images, from successive radiographs, in a correlated and coded form for direct processing by computer. The Chapter describes and verifies the systems used.

6.2 TRANSDUCER OUTPUT

Output from the transducers, during calibration and in the laboratory tests, was recorded by punched paper-tape via a data transfer unit. A flow chart illustrating the process is shown in Figure 6.1.

6.2.1 Data Transfer Unit

The data transfer unit (DTU) was a Solartron modular data-collecting system which incorporated a Solartron A210 series digital voltmeter (DVM), for monitoring purposes.

Digital data from each transducer (i.e. voltage output) was transferred through four head-unit input modules to a recording unit in a serial-by-character form, with channel number identification and an output scale code number, e.g.:

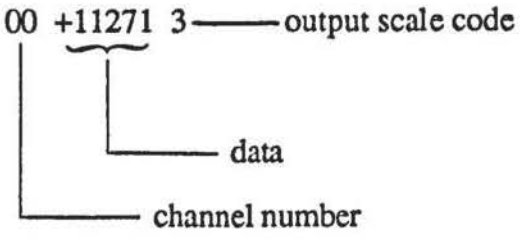

Interpolation of the output scale codes is shown in the Table in Figure 6.2.

Data transfer was set at preselected time intervals using a built-in timing control.

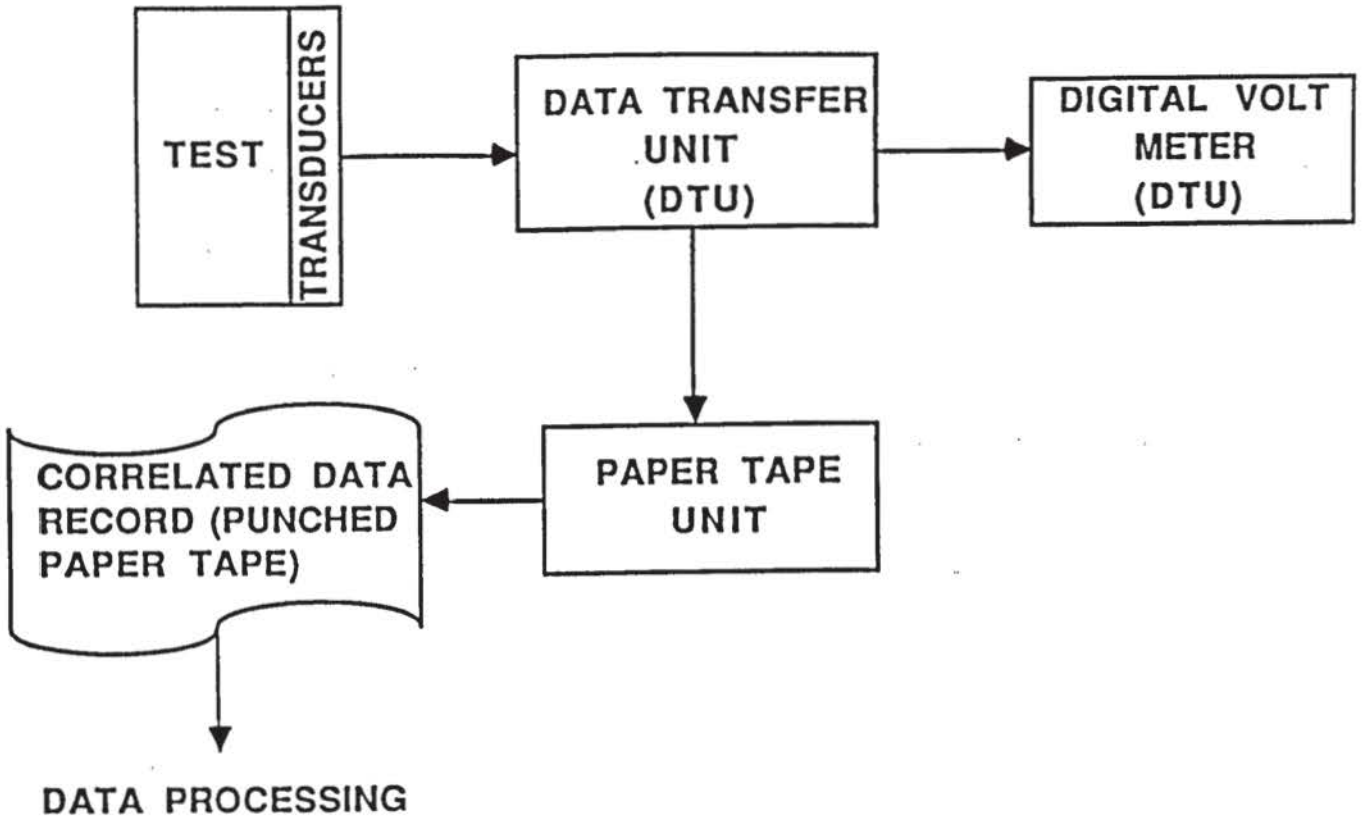

Data recording flow chart for compression tests.

FIGURE 6.1

Data output scale code	Magnitude of data output	Conversion to mV
1	mV + 100	x 100
2	mV + 10	x 10
3	mV	x 1
4	mV x 10	+ 10
5	mV x 100	+ 100
6	mV x 1000	+ 1000

Table of data - output scale codes.

FIGURE 6.2

6.2.2 Paper Tape Unit

The DTU recording device was a Facit 4070 compact paper-tape punch unit which gave eight tracks of punching.

6.2.3 Paper Tape Code

Characters were punched one to a line across a 25.4 mm wide paper-tape at a density of ten per 25.4 mm, of length. Each character was represented by 8 one's (hole) or zero (no hole) to conform to the 8-bit ASCII code, an example of which is given in Figure 6.3(a). The appearance of an ecoded piece of paper-tape is shown in Figure 6.3(b).

6.2.4 Assembly

Connection of the transducers to the DTU and peripherals is shown by the wiring diagram in Figure 6.4, and the complete arrangement is pictured in use during laboratory testing, in Plates 6.1.

6.3 LEAD-SHOT IMAGES

An electronic digitiser was used to identify the position of each individual lead-shot image (on successive radiographs) by x-y co-ordinates measured at their centroids, from a common origin, to produce a correlated record.

6.3.1 Digitiser A

Because of their overall optical density, radiographs have to be back-lit for normal viewing purposes. A digitiser (Tracey Reader) with this facility was available in the Department of Chemical Engineering. It consisted of an opaque back-lit sloping glass surface traversed by a hand-operated cursor with cross-wires, one of which was adjustable in inclination. The operation of the cursor and cross-wires is shown in Figure 6.5. The position of coincidence of the cross-wires identified the measurement point. Output from the machine was in the form of pairs of integers corresponding to the x-y co-ordinates of the points which were recorded on ASCII coded punched-tape.

Alphanumeric Character	8-bit ASCII code 7	6	5	4	3	2	1	0	Bit number
0	0	0	1	1	0	0	0	0	
1	1	0	1	1	0	0	0	1	
2	1	0	1	1	0	0	1	0	
3	0	0	1	1	0	0	1	1	
4	1	0	1	1	0	1	0	0	
5	0	0	1	1	0	1	0	1	
6	0	0	1	1	0	1	1	0	
7	1	0	1	1	0	1	1	1	
8	1	0	1	1	1	0	0	0	
9	0	0	1	1	1	0	0	1	
A	0	1	0	0	0	0	0	1	
B	0	1	0	0	0	0	1	0	
C	1	1	0	0	0	0	1	1	
D	0	1	0	0	0	1	0	0	
E	1	1	0	0	0	1	0	1	
F	1	1	0	0	0	1	1	0	
G	0	1	0	0	0	1	1	1	
H	0	1	0	0	1	0	0	0	

A selection of ASCII 8-bit codes. (after Lippiatt, 1979)

FIGURE 6.3(a)

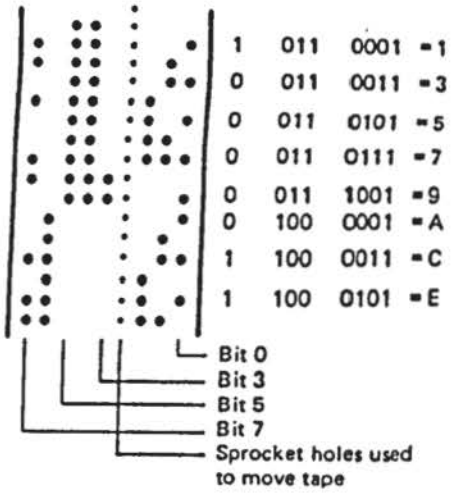

Punched paper tape showing examples of ASCII encoded characters. (after Lippiatt, 1979)

FIGURE 6.3(b)

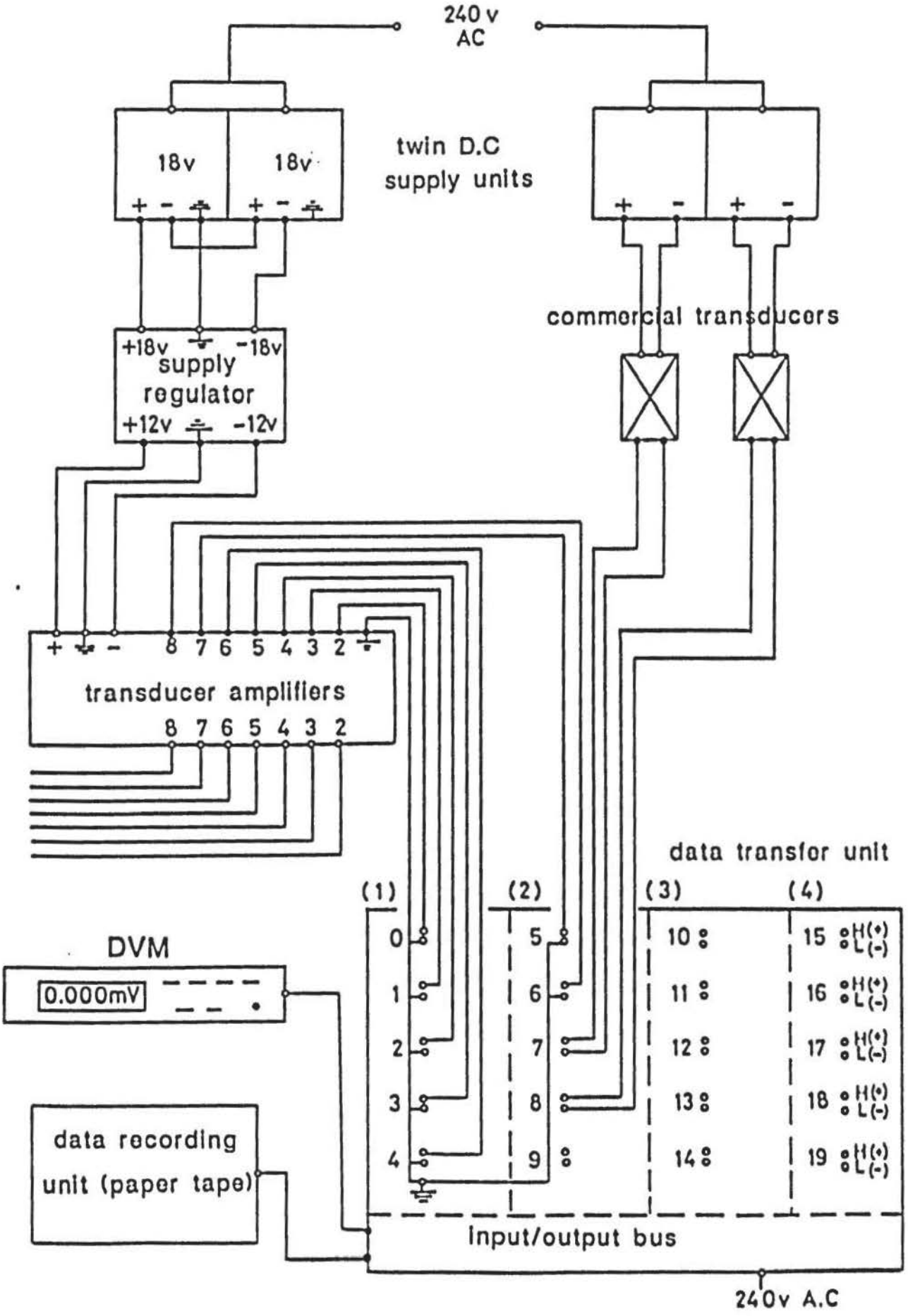

Wiring diagram for test transducers, data transfer unit and peripherals.

FIGURE 6.4

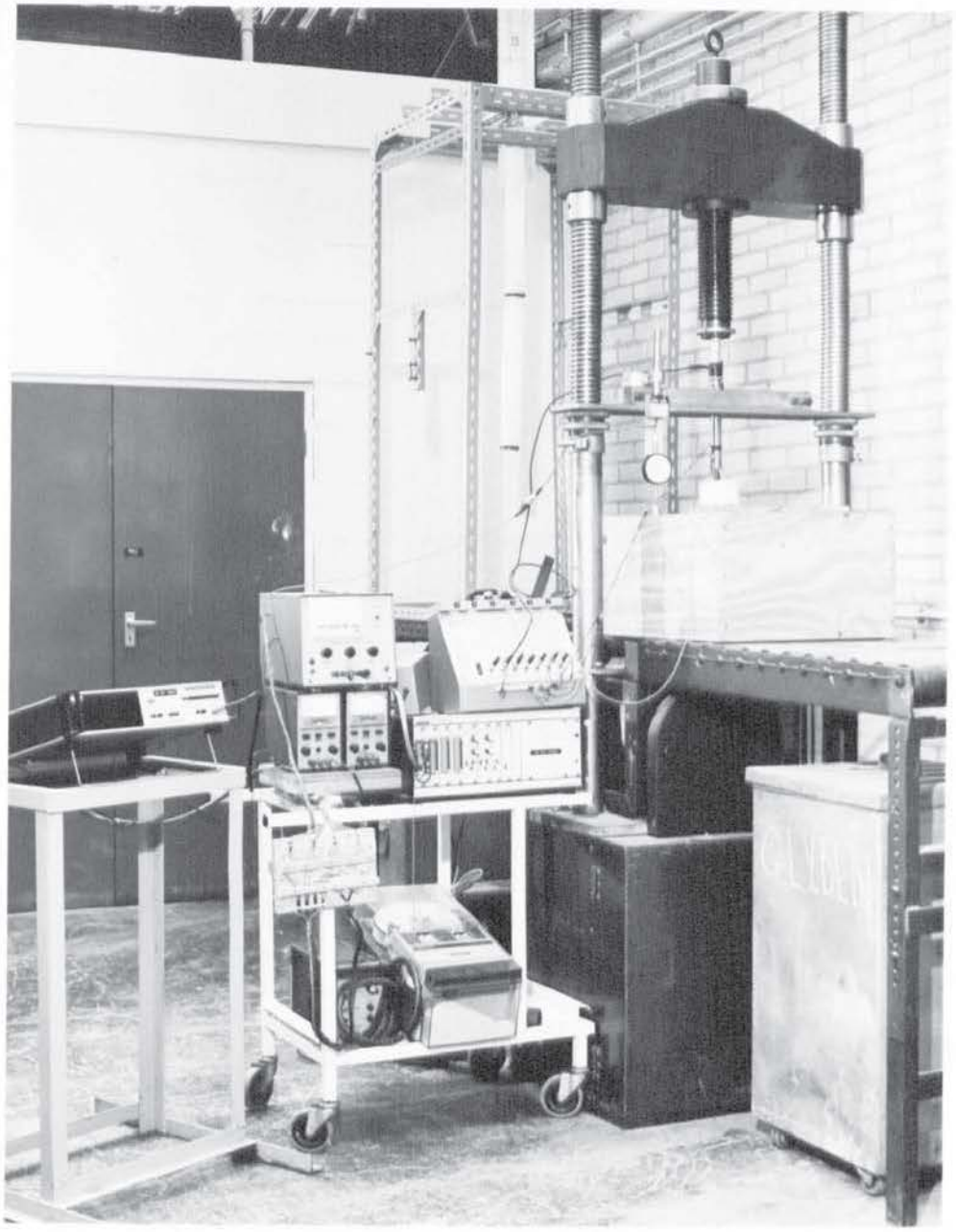

Data recording equipment.

PLATE 6.1

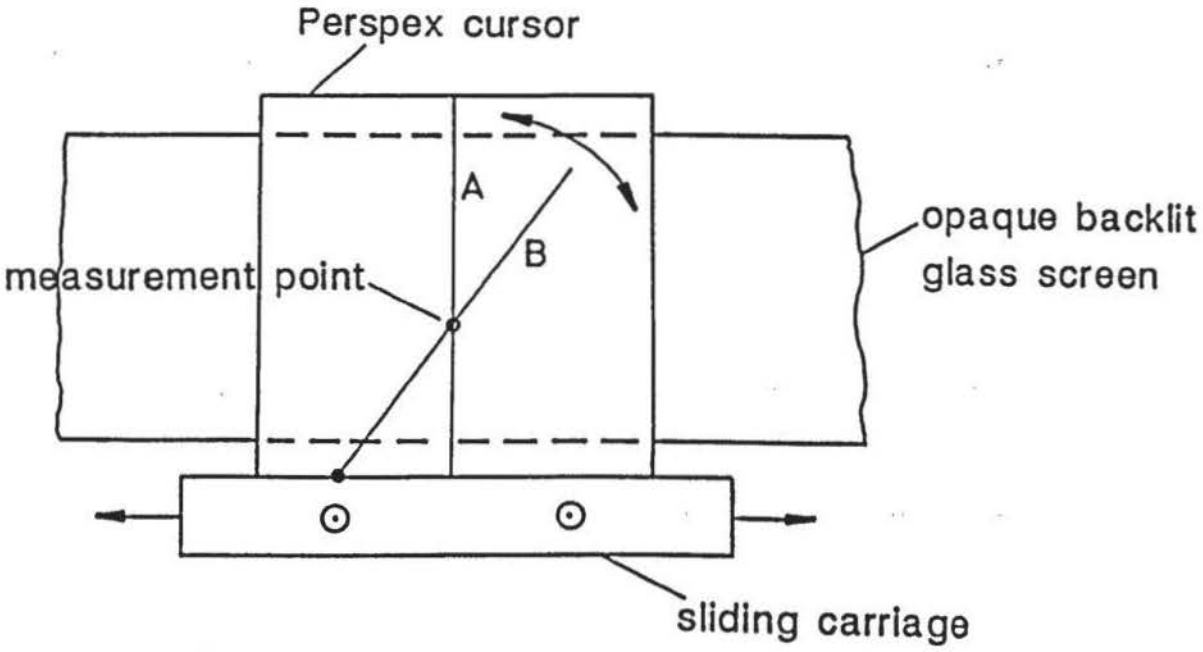

Digitiser A: Operation of cursor and cross-wires.

FIGURE 6.5

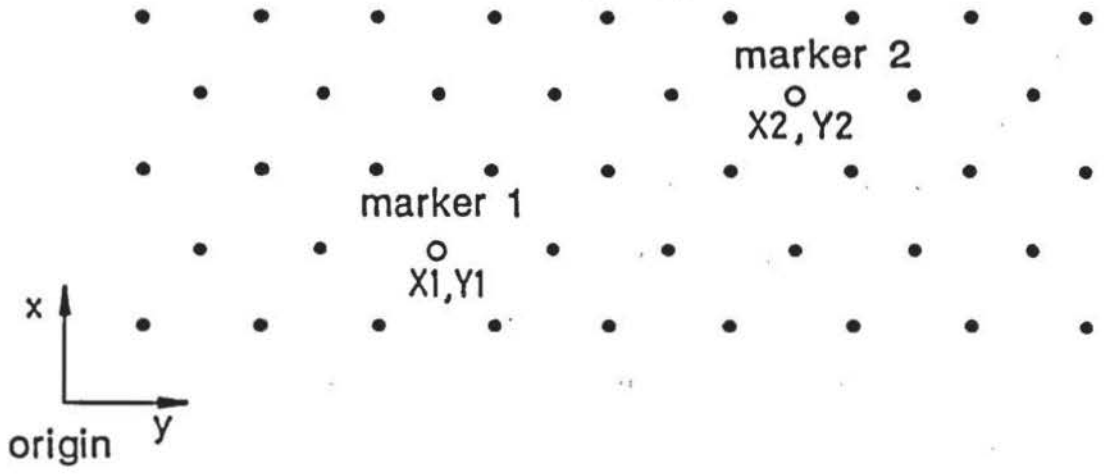

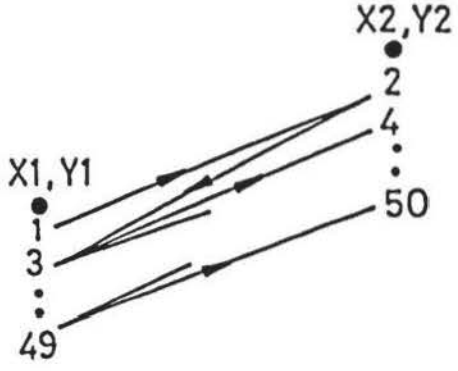

Digitising sequence of test markers.

FIGURE 6.6

The manufacturer's (University Computing Company) specification gave the machine resolution as better than 0.06 mm with an accuracy of 0.05% and repeatability of ± 0.09 mm, approximately.

6.3.2 Measurement Accuracy

The accuracy and repeatability in positioning the cross-hairs at the centroid of a lead-shot image, by eye, is dependent upon the experience of a given operator until some peak level in skill is reached. Thereafter, variations in operator accuracy are dependent on physiological factors (Lord, 1969).

To assess the combined operator/machine characteristics, the radiographic images of two lead-shot were chosen from a regular array as test markers (Figure 6.6). The two markers were digitised fifty times each in the sequence shown also in Figure 6.6. To minimise the risk of bias through visual conditioning, the positions of other randomly selected 'dummy' lead-shot images were digitised between each successive measurement of the test markers. The method was based on that described by Lord (1969). Using the results obtained, four histograms were drawn (Figure 6.7) and the estimated means (x, y) and estimated standard deviation (s) of each ordinate calculated. It is apparent that for marker 1, the position of the mean lies outside the class interval at which the maximum frequency occurs. Also, there is a much greater variation from the mean by the y-ordinates. The latter may be explained by the operation of the digitiser cursor (Figure 6.5 refers). The y-ordinate was determined by rotating the reference line B until its inclination was such that it intersected line A, at the measurement point. This inclination of the reference line caused difficulty with visual alignment and is illustrated by Figure 6.8.

The digitiser also suffered from uneven backlighting, a cramped operator position and noise from the paper-punching unit (a Teletype). This led to rapid operator fatigue and performance deterioration.

6.3.3 Digitiser B

An alternative was provided by a new digitiser installation at the University's Computer Centre. It was an active flat-bed, tablet type digitiser with an active area of 915 mm x

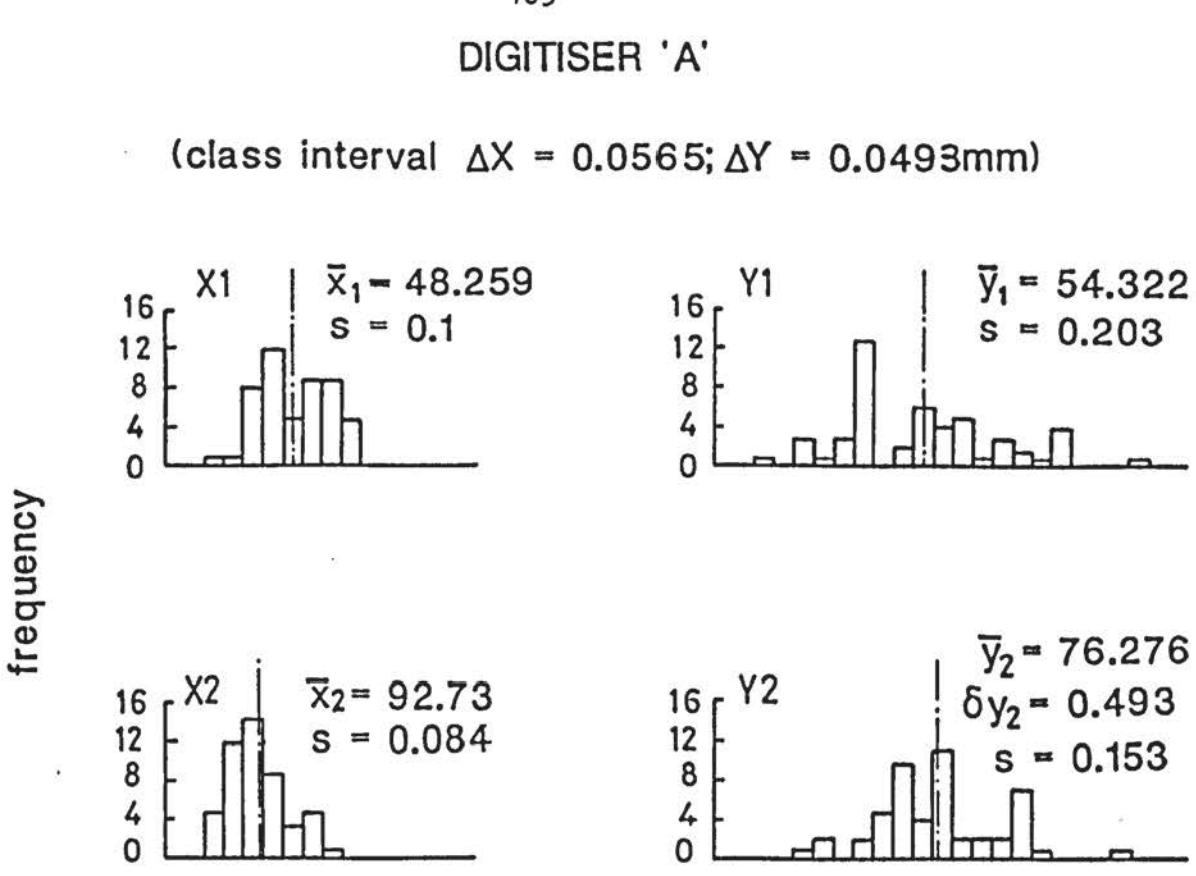

Digitiser A: Histograms and statistical data from test markers.

FIGURE 6.7

Showing difficulty in visual positioning of cross-wires over a lead-shot image centroid due to inclination.

FIGURE 6.8

1220 mm. The x-y co-ordinates were determined by the position of very fine cruciform cross-hairs set in a detached movable cursor. The digitiser was linked to a DEC 2050 mainframe, via a Heath micro-system, which enabled the x-y co-ordinates to be stored in a file structure ready for computer processing.

6.3.4 Output format

The x-y co-ordinates were output as integers representing thousands of an inch from the bottom left hand corner of the digitiser (i.e. the digitiser origin). Using identifier buttons on the cursor, the co-ordinate format was as follows:

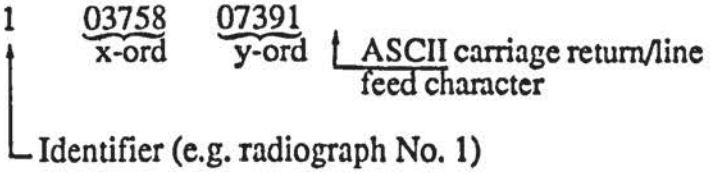

6.3.5 Radiographic Prints

Because digitiser B lacked a back-lit surface, photographic prints were made from the radiographs. The prints had an Estar base which preserved the dimensional stability of the lead-shot images. The copying of radiographs is not unusual; Bransby (1968) and Lord (1969), for example, re-photographed radiographs to reduce their overall dimensions by a quarter due to size limitations imposed by their digitising equipment.

There was some advantage in taking prints. Using processing and 'burning-in' techniques, contrast quality was enhanced, particularly in those areas of the radiographs which had been impaired by scattered radiation.

Each set of radiographs taken during a given test were printed and processed at the same time by the Department's Photograhpic Section.

6.3.6 Measurement Accuracy

Assessment of the operator/machine accuracy, for digitiser B, was done as described in Section 6.3.2. The co-ordinates were measured from the digitiser origin and converted to mm. The resulting histograms together with the co-ordinates estimated means and estimated standard

deviations (s) are shown in Figure 6.9. The slightly higher value of s obtained for the x_1 ordinate was attributed to some ovality of the lead-shot image. By comparing the histograms and estimated standard deviations obtained from both digitisers, it was apparent that the performance of digitsier B was more satisfactory. On this basis, it was adopted for use.

6.3.7 Confidence Limits

The overall estimated standard deviation for a single measurement of the x-y co-ordinates of a lead-shot image is given by:

$$(s)_{x,y} = \sqrt{\left\{ \left[(s)^2_{x1} + (s)^2_{y1} + (s)^2_{x2} + (s)^2_{y2} \right] / 4 \right\}}$$

$$= \pm 0.0461 \text{ mm}$$

The measurements of each of the four ordinates (X1, Y1, X2, Y2) gave a normal distribution curve and so the 99.73% confidence limits (i.e. near certainty) were, viz:

$$x, y \pm 3\,(s)_{x,y}$$

giving $x, y \pm 0.1468$ mm

For comparative purposes, accuracies achieved by other researchers using various types of measuring equipment are shown in the table in Figure 6.10.

6.3.8 Coincidence of axes

Because it was not possible to obtain exact coincidence of the radiographic print and digitiser origin, provision was made to allow a print to be placed at any orientation on the digitiser bed. By digitising the images of the radiographic origin and a fiducial marker, their co-ordinates were used as references points to transform all the lead-shot co-ordinates, on the same radiograph, at the data processing stage.

Measurement accuracy of the reference co-ordinates was essential since they affected all the following co-ordinates. To minimise this potential error source, both the origin and fiducial marker were digitised five times and their means obtained, prior to digitising the lead-shot images. Averaging the measurement of five readings reduced the estimated standard error of the mean by

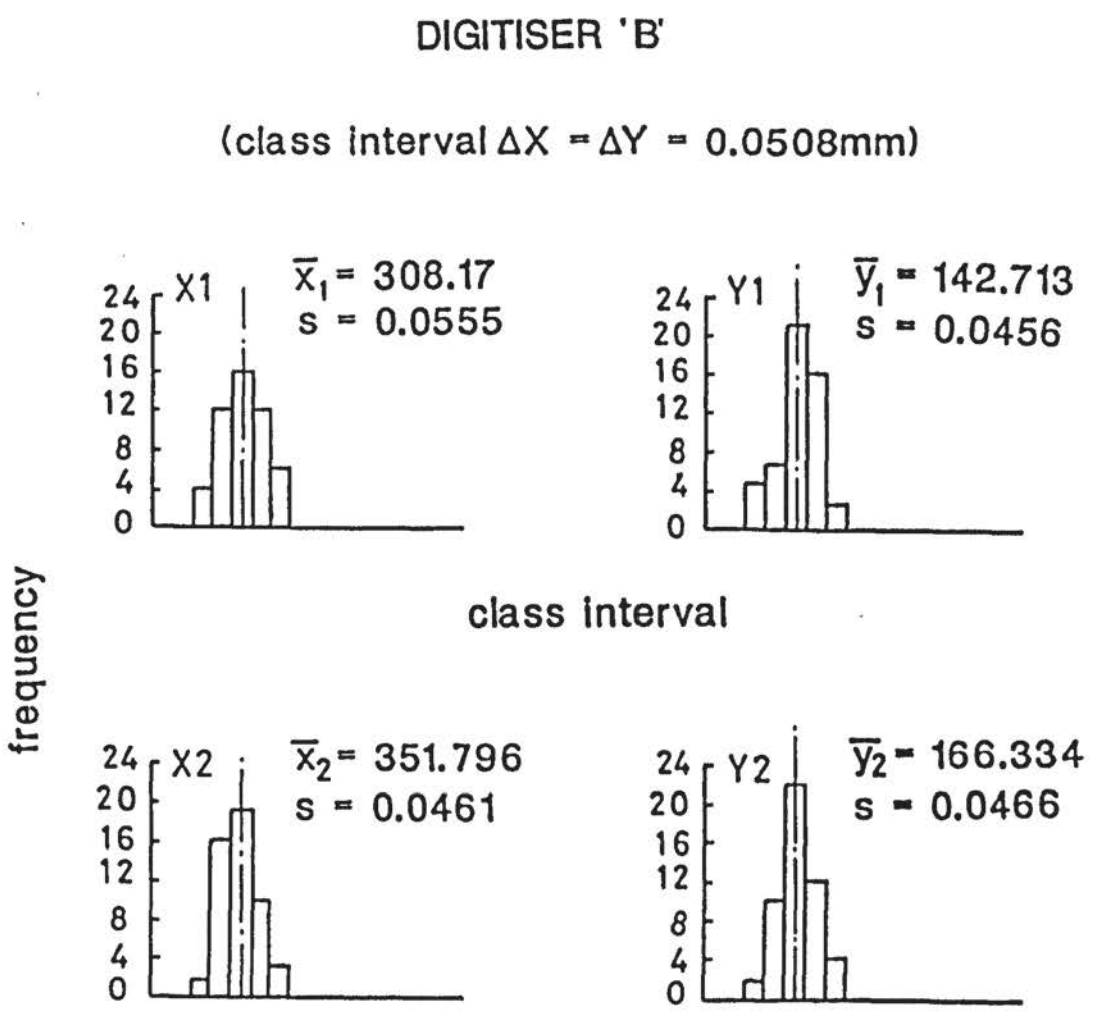

Digitiser B: Histograms and statistical data from test markers.

FIGURE 6.9

Researcher	Measurement Method	Accuracy spread (mm)	s (mm)	*99.73% confidence limits (mm)
Roscoe et al (1963)	orthogonal disp meter.	±0.0254		
James (1965)	orthogonal disp. meter		±0.0159	±0.0476
Burland (1967)	+CLARA		±0.0254	±0.0762
Bassett (1968)	CLARA		±0.0203	±0.0610
Lord (1969)	CLARA			
High Contrast			±0.0178	±0.0533
Low Contrast			±0.036	±0.107
‡Author	flat bed digitiser		±0.0461	±0.1468

‡ 20.20 vision/machine accuracy ± 0.0254 mm.

* assumes normal distribution curve

+ CLARA was a semi-automatic Moire Fringe co-ord. measuring system. It featured a computer programmed orbiting routine to locate lead-shot image centroid, see James (1973b).

Comparison of accuracy achieved with other researchers in the measurement of the positions of lead-shot images.

FIGURE. 6.10

more than 50%, i.e.

$$(s)_{\bar{x},\bar{y}} = (s)_{x,y} / \sqrt{N}$$

where N is the number of readings.

thus: $(s)_{\bar{x},\bar{y}} = \pm 0.0461/\sqrt{5}$

$= \pm 0.0206$ mm

The mean origin and fiducial marker co-ordinates headed the data file created from each radiograph.

6.3.9 Digitising Sequence

For the purposes of identification and comparison in computation, each lead-shot image was assigned a node number which was common to every radiograph taken during the same test. The method is illustrated by Figure 6.11. A matt surface finish of the radiographic prints allowed the use of a pencil for the numbering process.

The node numbers also constituted the digitising sequence. Thus, for any radiograph from the same test, the first pair of lead-shot co-ordinates corresponds to node 1, the second pair to node 2 and the nth pair to node n.

6.3.10 Files

Each computer stored data file contained the digitised data from all the radiographs taken during any one test. An example of the format is shown in Figure 6.12.

6.3.11 Fixing of Radiographs

The radiographs (digitiser A) and radiographic prints (digitiser B) were fixed to the digitising surface by adhesive tape. A rubber faced roller was used to ensure that they were held flat and in contact with the supporting surface without causing any undue distortion through stretching.

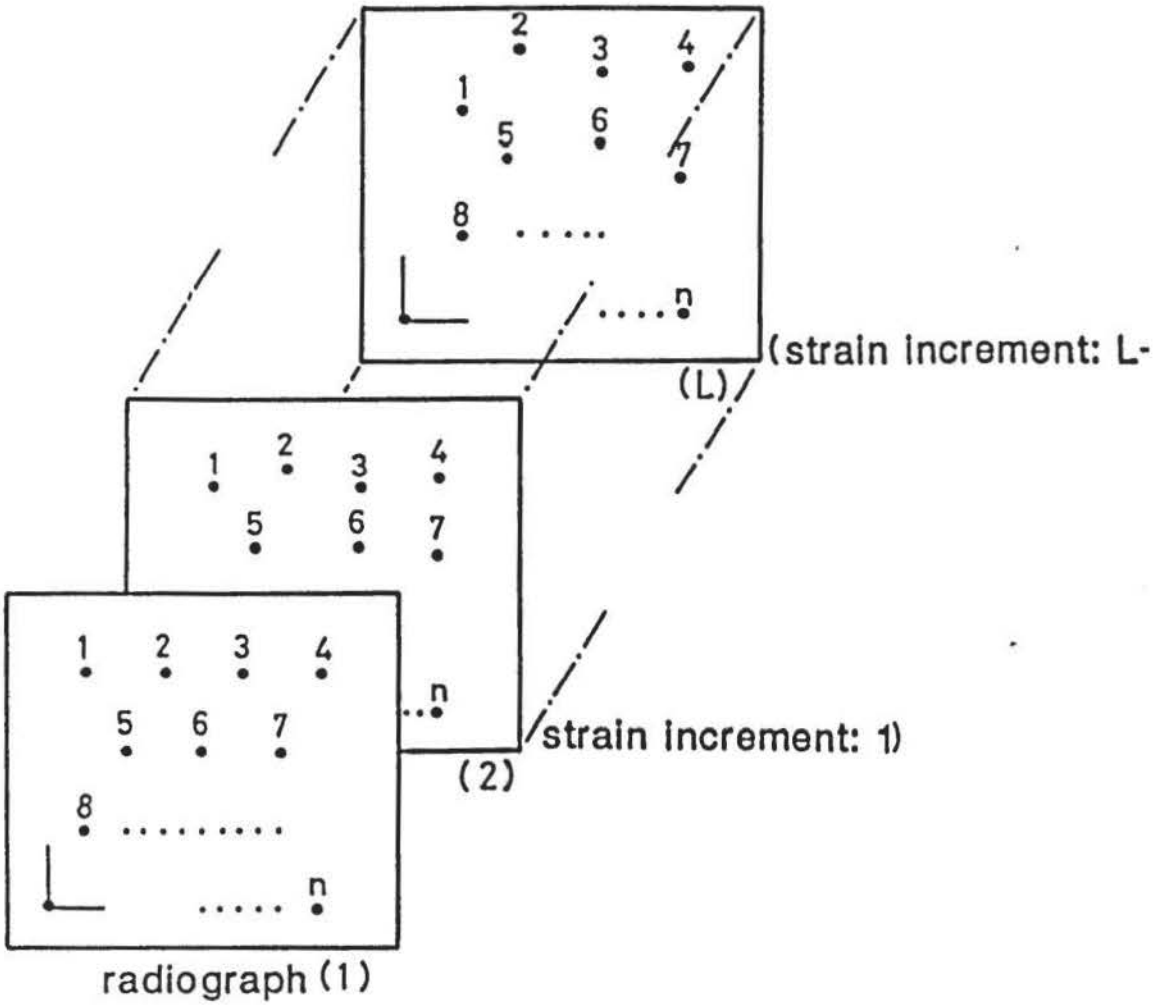

Identificaton of lead-shot images by node numbers (digitising sequence).

FIGURE 6.11

digitised co-ordinates

Radiograph no.	x						y					
1	2	1	4	5	6	0	2	0	0	7	radiograph (1) origin*	
1	2	1	0	1	5	1	1	1	4	7	"	fiducial point*
1	1	6	4	1	7	1	1	7	8	3	node	1
1	1	7	3	1	1	1	1	8	5	4		2
1	1	8	1	4	5	1	1	9	1	7		3
.										.		.
.										.		.
.										.		.
1	1	6	4	0	1	0	5	5	1	5		n
2	2	1	1	6	9	0	1	3	1	7	radiograph (2) origin*	
2	2	0	7	3	2	1	0	4	7	6	"	fiducial point*
2	1	6	2	2	0	1	0	9	4	5	node	1
2	1	7	0	4	7	1	1	1	6	9		2
2	1	7	8	7	4	1	1	2	2	0		3
.										.		.
.										.		.
.										.		.
2	1	6	1	1	6	0	4	8	2	6		n
.										.		.
.										.		.
.										.		.
.										.		.
L	2	1	6	5	3	0	1	1	9	5	radiograph (L) origin*	
L	2	1	5	3	6	0	5	5	9	0	"	fiducial point*
L	1	6	9	5	2	1	0	9	8	0	node	1
L	1	7	7	5	5	1	1	1	8	1		2
L	1	8	5	8	2	1	1	2	2	5		3
.										.		.
.										.		.
.										.		.
L	1	6	7	1	2	0	4	7	1	6		n

* mean of 5 values

Digitised co-ordinates from a number of radiographs (taken during any one test) making a single data file.

FIGURE 6.12

CHAPTER 7

RADIOGRAPHIC ANALYSIS

7.1 INTRODUCTION

Displacement of the lead-shot, at each loading stage, was found from the change in their x-y co-ordinates obtained from successive radiographs. Strains were obtained by further analyses. This Chapter describes the analytical procedures used together with the assumptions made.

7.2 ANALYSIS

Arthur (1962) and Roscoe et al (1963) described a method to calculate strains from the displacements at the four corners of a diamond shaped element. The method's accuracy depended upon the geometry changes being small during distortion of the element. The use of triangular elements over which two-dimensional strain is assumed uniform, overcame this restriction. The analysis became a computational analogue of the finite element method.

7.3 ASSUMPTIONS

The displacement and strain calculations were based upon the assumptions given by Arthur (1962), James (1965) and Bransby (1968), viz:

(a) Displacements of the lead-shot represent displacements of the corners of the soil element they define.

(b) The behaviour of the elements are unaffected by the presence of the lead-shot.

(c) The shot lie and remain in a single vertical plane to which the calculated strains apply.

(d) There are negligible effects on the calculated results through geometry changes of the system.

(e) Each element of the network strains uniformly and, as corollary:

  (i) each calculated strain refers to the strain at the element centroid.

  (ii) the strain pattern throughout the soil mass at the instant at which the radiograph is

taken is the same as the strain pattern recorded by the lead shot image on the radiograph.

7.4 VALIDITY

Lord (1969) concluded that "the veracity of these assumptions is difficult to prove and they may be gross over simplifications". Uniformity of strain within an element (even for practical purposes) is suspect unless it is proportionally small. It was considered more realistic to consider calculated strain to represent an average value for the element.

The true position within the element at which this average value occurs would depend upon the manner in which any non-uniformity is distributed. Therefore, the positioning of an average value of strain at an element's centroid is an approximation or an 'index' strain.

7.5 TRIANGULAR ELEMENT

To define two-dimensional strains within an element (i,j,k in Figure 7.1(a)) two arbitary mathematical functions, in terms of the x-y co-ordinates, were used. There were two displacements at each shot of node position, shown by Figure 7.1(b) at i,j,k. For displacements u(x-direction) and v(y-direction), the simplest functions (Zienkiewicz, 1977) are:

$$u = a + bx + cy$$
$$v = d + ex + fy \qquad (7.1)$$

7.6 DISPLACEMENTS

Displacements (u,v) of the shot were obtained by direct subtraction of their initial and deformed state co-ordinates. Denoting these co-ordinates by subscripts 1 and 2, respectively, then:

$$u = x_2 - x_1$$
$$v = y_2 - y_1 \qquad (7.2)$$

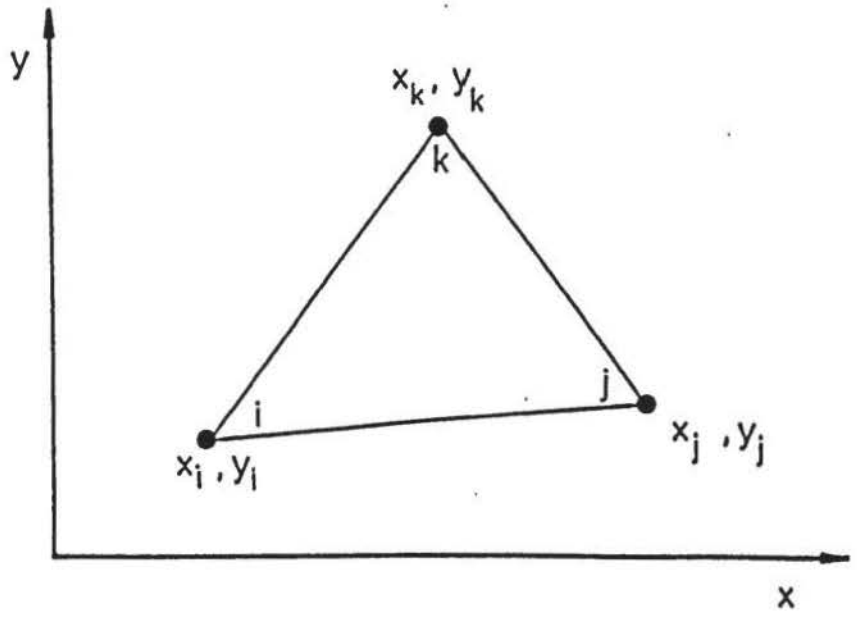

Triangular element related to x-y co-ordinates.

FIGURE 7.1(a)

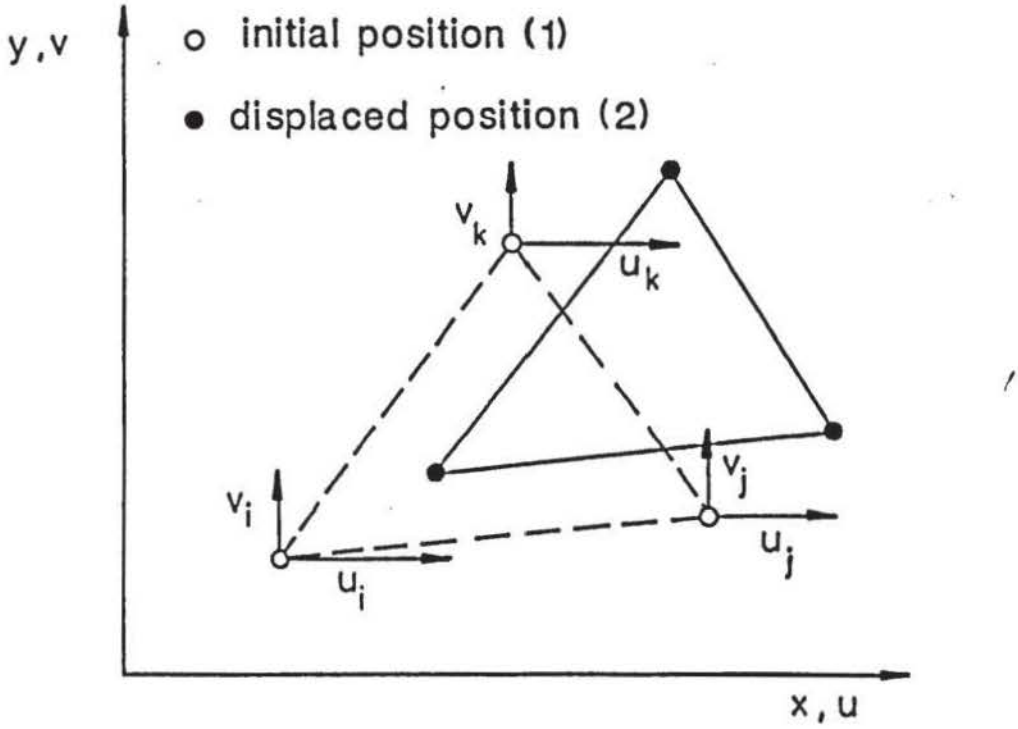

Initial and displaced element positions.

FIGURE 7.1(b)

7.7 STRAINS

Using the soil mechanics sign convention of positive for compressive strain, the two-dimensional strains were derived from Eqn. 7.1 as follows (Zienkiewicz, 1977):

$$\delta\varepsilon_x = -\frac{\partial u}{\partial x} = -b$$

$$\delta\varepsilon_y = -\frac{\partial v}{\partial y} = -f \qquad (7.3)$$

$$\delta\gamma_{xy} = -\frac{\partial v}{\partial x} - \frac{\partial u}{\partial y} = -e - c$$

where $\partial\varepsilon_x$ and $\partial\varepsilon_y$ are strain increments in the x and y directions, respectively, and $\partial\gamma_{xy}$ is the engineering shear strain increment. Putting Eqn. (7.3) in matrix form:

$$\begin{bmatrix} \partial\varepsilon_x \\ \partial\varepsilon_y \\ \partial\gamma_{xy} \end{bmatrix} = \begin{bmatrix} 0 & -1 & 0 & 0 & 0 & 0 \\ 0 & 0 & 0 & 0 & 0 & -1 \\ 0 & 0 & -1 & 0 & -1 & 0 \end{bmatrix} \begin{bmatrix} a \\ b \\ c \\ d \\ e \\ f \end{bmatrix}$$

that is: $$\{\varepsilon\} = [A]\{\alpha\} \qquad (7.4)$$

Applying Eqn. (7.1) to the three corners of the element i,j,k, in its initial state and expressing the result in matrix form gives:

$$\begin{bmatrix} u_i \\ u_j \\ u_k \\ v_i \\ v_j \\ v_k \end{bmatrix} = \begin{bmatrix} 1 & x_i & y_i & 0 & 0 & 0 \\ 1 & x_j & y_j & 0 & 0 & 0 \\ 1 & x_k & y_k & 0 & 0 & 0 \\ 0 & 0 & 0 & 1 & x_i & y_i \\ 0 & 0 & 0 & 1 & x_j & y_j \\ 0 & 0 & 0 & 1 & x_k & y_k \end{bmatrix} \begin{bmatrix} a \\ b \\ c \\ d \\ e \\ f \end{bmatrix}$$

that is: $$\{\Delta\} = [B]\{\alpha\} \qquad (7.5)$$

Transposing Eqn. (7.5) gives:

$$\{k\} = [B]^{-1} \{\Delta\}$$

and substituting in Eqn. (7.4):

$$\{\varepsilon\} = [A] [B]^{-1} \{\Delta\}$$

$$= [Z] \{\Delta\} \qquad (7.6)$$

After mathematical manipulation, the final form of Eqn. (7.6) becomes:

$$\begin{bmatrix} \delta\varepsilon_x \\ \delta\varepsilon_y \\ \delta\varepsilon_{xy} \end{bmatrix} = \frac{1}{C} \begin{bmatrix} Z_{1,1} & Z_{1,2} & Z_{1,3} & 0 & 0 & 0 \\ 0 & 0 & 0 & Z_{2,4} & Z_{2,5} & Z_{2,6} \\ Z_{3,1} & Z_{3,2} & Z_{3,3} & Z_{3,4} & Z_{3,5} & Z_{3,6} \end{bmatrix} \begin{bmatrix} u_i \\ u_j \\ u_k \\ v_i \\ v_j \\ v_k \end{bmatrix}$$

where

$$Z_{1,1} = Z_{3,4} = (y_k - y_i) \qquad Z_{3,1} = Z_{2,4} = (x_j - x_k)$$

$$Z_{1,2} = Z_{3,5} = (y_i - y_k) \qquad Z_{3,2} = Z_{2,5} = (x_k - x_i)$$

$$Z_{1,3} = Z_{3,6} = (y_j - y_i) \qquad Z_{3,3} = Z_{2,6} = (x_i - x_j)$$

and

$$C = (x_i y_k - x_k y_i) - (x_i y_k - x_i y_j) + (x_k y_i - x_j y_j)$$

$\{\varepsilon\}$ was termed the strain increment matrix,

[Z] the incremental shape matrix and $\{\Delta\}$ the displacement increment matrix.

7.8 PRINCIPAL STRAIN VECTORS

When the basic x-y strain increments were established, the magnitudes and relative positions of the principal strain increments ($\delta\varepsilon_1$ and $\delta\varepsilon_3$) together with their directions in the physical plane were found. Using the Mohr's circle (of strain increment) construction shown in Fgiure 7.2(a), it can be shown that:

$$\begin{matrix}\delta\varepsilon_1 \\ \\ \delta\varepsilon_3\end{matrix} = 0.5\,(\delta\varepsilon_x + \delta\varepsilon_y) \pm 0.5\,\sqrt{[(\delta\varepsilon_x - \delta\varepsilon_y)^2 + \delta\gamma_{xy}{}^2]} \qquad (7.7)$$

$$\alpha = 0.5 \arctan\left[\frac{\delta\gamma_{xy}}{(\delta\varepsilon_x - \delta\varepsilon_y)}\right] \qquad (7.8)$$

where α is the inclination of the major principal strain increment ($\delta\varepsilon_1$) to the horizontal physical plane, shown in Figure 7.2(b). The angle α was taken as positive in the anti-clockwise direction. The relationship given by Eqn. (7.8) did not give solutions in the range 0 to 2π and had to be expressed in component form. The derivation and application of the components are given in Appendix D.

7.9 ZERO EXTENSION

The points A and B shown on the Mohr's circle (Figure 7.2(a)) represent planes at which the net linear strains are zero. These planes of zero extension are where potential discontinuities in the material may occur. Their directions lie at β and λ to the horizontal physical plane (Figure 7.2(b)) and were calculated using the angle of dilation ν (after Hansen, 1958), where:

$$\sin\nu = -\frac{\delta\varepsilon_v}{\delta\varepsilon_m} = -\frac{(\delta\varepsilon_x + \delta\varepsilon_y)}{\sqrt{[(\delta\varepsilon_x - \delta\varepsilon_y)^2 + \delta\gamma_{xy}^2}} \qquad (7.9)$$

$\delta\varepsilon_v$ and γ_m were the areal (or plane volumetric) strain and maximum engineering strain increments, respectively. The sign convention of negative for volumetric expansion was used. Hence, when $\delta\varepsilon_v > 0$ then $\nu > 0$ and conversely, when $\delta\varepsilon_v < 0$ then $\nu < 0$. From the Mohr's circle geometry (Figure 7.2(a)):

$$B\,c\,A = 180^o + 2\,\nu$$

$$B\,c\,D = D\,c\,A = \frac{B\,c\,A}{2} = 90^o - \nu$$

A,B represent planes of zero extn.

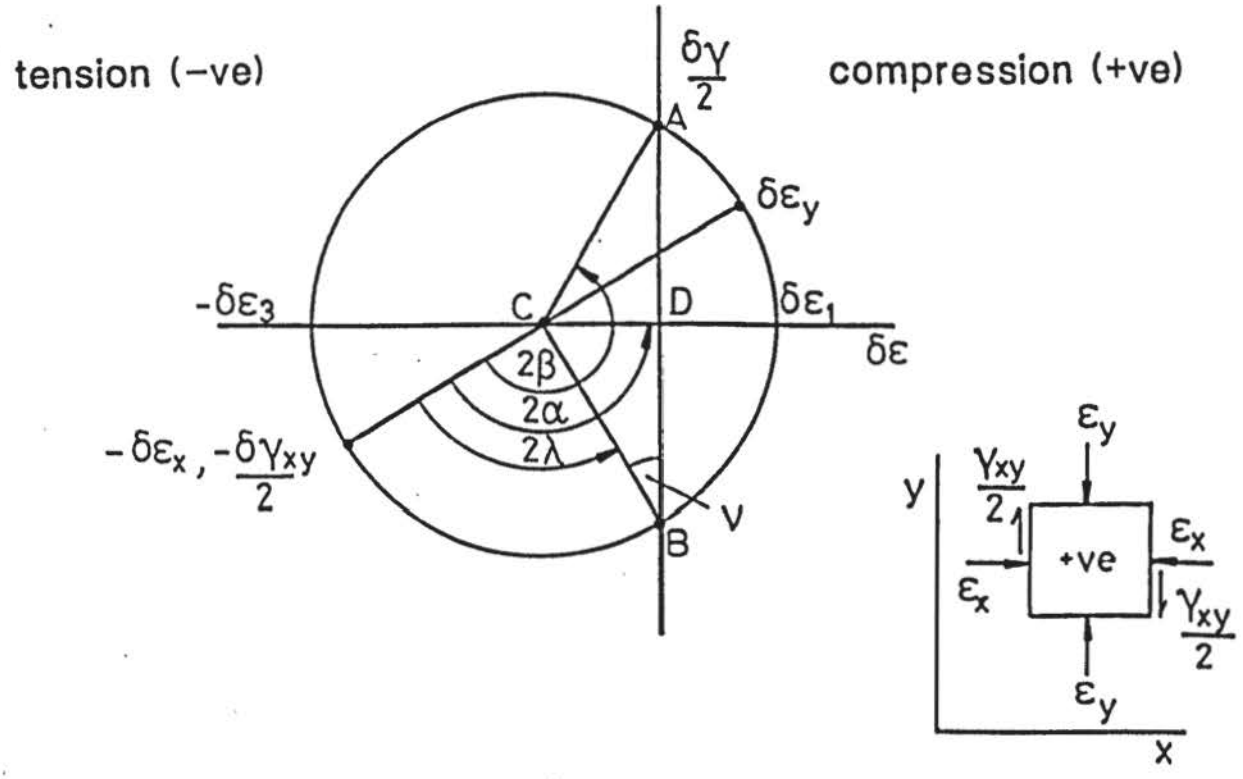

Mohr's circle of strain increment.

FIGURE 7.2(a)

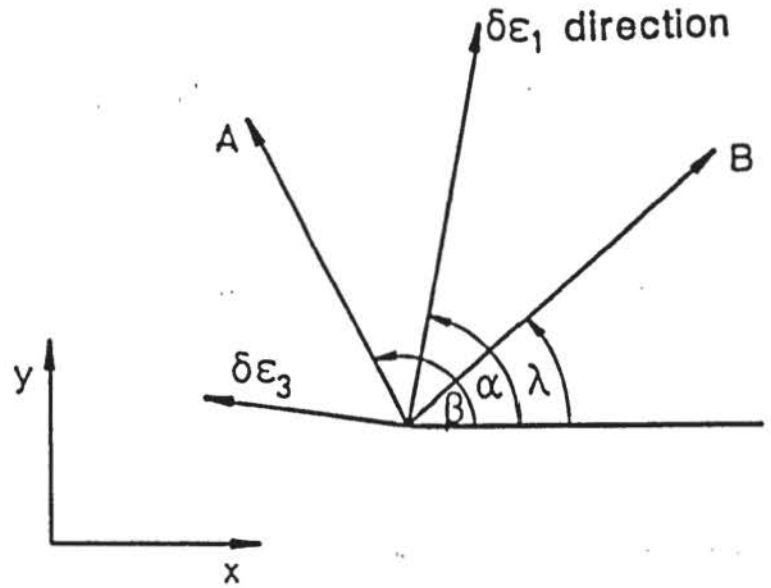

Resulting principal strain increment and zero extension directions in the physical plane.

FIGURE 7.2(b)

$$\text{then} \qquad \frac{2\beta}{2\lambda} = 2\alpha \pm (90^\circ - \nu)$$

which in the physical plane becomes:

$$\frac{\beta}{\lambda} = \alpha \pm (45^\circ - \nu/2) \qquad (7.10)$$

In some cases of the Mohr's circle of construction, $\beta = \beta - 180^\circ$ and/or $\lambda = \lambda - 180^\circ$. But since the planes of zero extension are not vectors (i.e. they only have direction) it is of no matter in the physical plane, so Eqn. (7.10) is valid for all the possible Mohr circle configurations.

When $\delta\varepsilon_v > \delta\gamma_m$, there are no planes of zero extension.

7.10 CUMULATIVE STRAINS

Cumulative x-y strains were obtained by summation of the incremental strains:

$$\varepsilon_x = \Sigma\, \delta\varepsilon_x$$

$$\varepsilon_y = \Sigma\, \delta\varepsilon_y \qquad (7.11)$$

$$\gamma_{xy} = \Sigma\, \delta\gamma_{xy}$$

from which the principal strains, angle of dilation and relevant directions were calculated.

7.11 ERRORS

There were a number of factors which introduced error in determining displacement of the shot and in the strain calculations.

7.11.1 Radiographic Film

Dimensional changes of the radiographic film and prints may occur through the effects of processing, temperature and humidity changes, and 'ageing'. The practical significance of these effects were discussed by Lord (1969). The Kodak Estar base is specifically designed to give dimensional stability of the highest order. The films and prints were processed and stored in the

same room where the temperature was generally within ± 2°C of the test and digitising environments. Films from any one test were processed, printed and later digitised together. All the film and prints used were taken from the same batch, thereby ensuring uniformity of their emulsions and base thicknesses.

7.11.2 Equipment

Geometric distortion of the test equipment during testing may cause movement of the attached fiducial and origin markers. Due regard was paid to this aspect during the design and construction of the author's equipment, which has been discussed in Sections 3.16 and 4.3.

7.11.3 Cassette and X-ray Set

Error due to the relative movements between the film and X-ray set, between successive exposures, were detailed by Roscoe et al (1963). Attention at the design stage ensured that the cassette could be re-positioned and secured to the clay container without signficant change. Also, because the dimensions of individual cassettes vary slightly, the same cassette was used throughout.

After each loading increment, the clay container and cassette were raised vertically by the compression machine platten. This caused a parallel, relative movement between the film plane and the X-ray source. Whilst no error is caused by the lead-shot which all occur in the same plane, the origin and fiducial markers lie in a different plane.

Using the Minilift mechanism, the X-ray set was raised the same vertical distance travelled by the cassette prior to exposure. However, the vertical column incorporating the Minilift and supporting the X-ray set was found to be out of vertical alignment by about 5 mm over a height of 2500 mm. This meant a 20 mm vertical movement caused the X-ray set to move forward along the beam-axis by 0.04 mm.

A table in Figure 7.3 gives an indication of the expected magnitudes and relative significance of the fictitious strains from these sources using the spatial dimensions of the X-ray set, lead-shot and film planes, and by assuming some reasonable magnitudes of erroneous movements.

X-ray source to shot plane distance	d_o = 1977 mm
Shot-plane to film-plane distance	d = 133.5 mm
grid size	s(x-direction) = 20 mm s(y-direction) = 10 m m
maximum x and y co-ordinates	x,y = 300 mm
forward movement of X-ray set	δd_o = +0.004 mm
assumed forward/backward movement of film	δd = ±0.2 mm
assumed rotation error of cassette	$\delta\theta$ = ± 10^{-2} radians

Type of Movement	(mm) Fictitious displacements		Fictitious Strains		
A. X-ray set along beam axis	-0.00002	-0.00001	-0.000001	0.000001	0.000001
B. Film along beam axis	±0.002	±0.001	±0.0001	±0.0001	±0.0001
C. Film rotation	-	-	0.0028	±0.0014	±0.0004

A. $\delta(\delta u, \delta v) = -(d.s.\,\delta d_o)/d_o^2$

B. $\delta(\delta u, \delta v) = (s.\delta d)/d_o$

C. $\delta(\delta t_x) = (2x.\delta\theta)/(d_o + d)$

$\delta(\delta t_y) = (\delta(\delta e_x)/2$

$\delta(\delta\theta_{xy}) = (y.\delta\theta)/4\,(d_o + d)$

equations derived by

Roscoe et al (1963)

Expected maximum errors in displacement and strains through relative movement of the X-ray set and cassette using equations derived by Roscoe et al (1963).

FIGURE. 7.3

7.11.4 Lead-Shot Plane

Error incurred through departures of the lead-shot from the plane of the array was also considered by Roscoe et al (1963). Out of plane positioning of the shot may occur during either its placement or during deformation.

Placement errors of up to 0.64 mm, out-of-plane, were found by Roscoe et al to contribute negligible errors in the derived strains (i.e. less than 1% for a 25 mm grid). In the author's case, the method used in placing the shot assured the out-of-plane placement errors were kept within the same order of magnitude.

7.11.5 Measurement

The accuracy of measuring the co-ordinates of a single lead-shot image has been discussed in Section 6.3.6. Error from this source is propagated when transforming the digitised coordinates to the radiograph axes, since the origin and fiducial marker co-ordinates are also in error. This is repeated when the co-ordinates obtained from the successive radiograph are also transformed. After the two sets of co-ordinates are subtracted to obtain the displacements, these errors become compounded.

For this reason, measurement inaccuracies form a significant proportion of the overall errors incurred in practice.

7.11.6 Overall Accuracy

It would be complex to determine analytically the overall effect that all the sources of error, so far mentioned had on the magnitudes of displacements and derived strains. To preserve the integrity of the results, however, it was considered essential that some overall assessment be made.

During one test, two radiographs were taken after the final strain increment. They were processed, printed, 'digitised' and the apparent displacement and strains calculated. If no inaccuracies existed then the displacements and strains would have been zero.

The magnitude of the apparent displacements and strains were a direct measurement of the effect of all the prevailing error sources.

The results are compared with those of other researchers (who used the same method), in the Table shown in Figure 7.4. James (1973b) estimated the average overall accuracy of strain measurement achieved by a variety of Cambridge researchers was probably of the order of ± 0.3%. In the case of the author, accuracies of about ± 1% were generally achieved.

7.11.7 True Co-ordinates

Because the lead-shot network was at some distance from the radiograph, its image did not have the same dimensions as the actual network. The effect is illustrated in Figure 7.5. This shows the dimensional magnification varies with the relative position within the array and of the X-ray set. In a similar manner, the displacements were also magnified

From geometric considerations, Stroud (1971) devised a method to obtain the true x-y co-ordinates of the lead-shot images. The method, described in Appendix E was used in the data processing stages.

7.11.8 Large Strain

The definitions given by Eqns. 7.3 apply strictly to very small magnitudes of strain, Case and Chilver (1975) in their consideration of structural materials (e.g. concrete and steel) suggest that such strains are of the order of 0.1%. Investigation of strain phenomena in plastic engineering soils is concerned with strains of a much larger order, particularly in the laboratory. As a result, 'infinitesimal' strain theory underestimates actual strain. Cole (1967) adopted an empirical procedure as an analysis correction for large strains in strain calculations. This involved calculating ε_x, ε_y and γ_{xy} strains using the initial-state co-ordinates, then repeating the procedure with the deformed-state co-ordinates and obtaining the average values.

Representing the initial and deformed state co-ordinates by subscripts 1 and 2, respectively, then from Eqn. (7.6):

Researcher	Estimated standard deviation (s)				
	Displacement (mm)		Strain		
	u	v	ε_x	ε_y	γ_{xy}
*Bransby (1968) 25 mm grid length	-	-	0.0031	0.0021	0.002
Hambly (1969) 6 mm gauge length 10 mm gauge length	-	-	0.0034	0.0039	0.002
author 10 mm gauge length (y-dir) 20 mm gauge length (x-dir)	0.116	0.108	0.0083	0.0108	0.008

*radiographs re-photographed to 1/4 scale

Table of estimated standard deviations of apparent displacements and strains from two radiographs taken of the same array of lead-shot.

FIGURE. 7.4

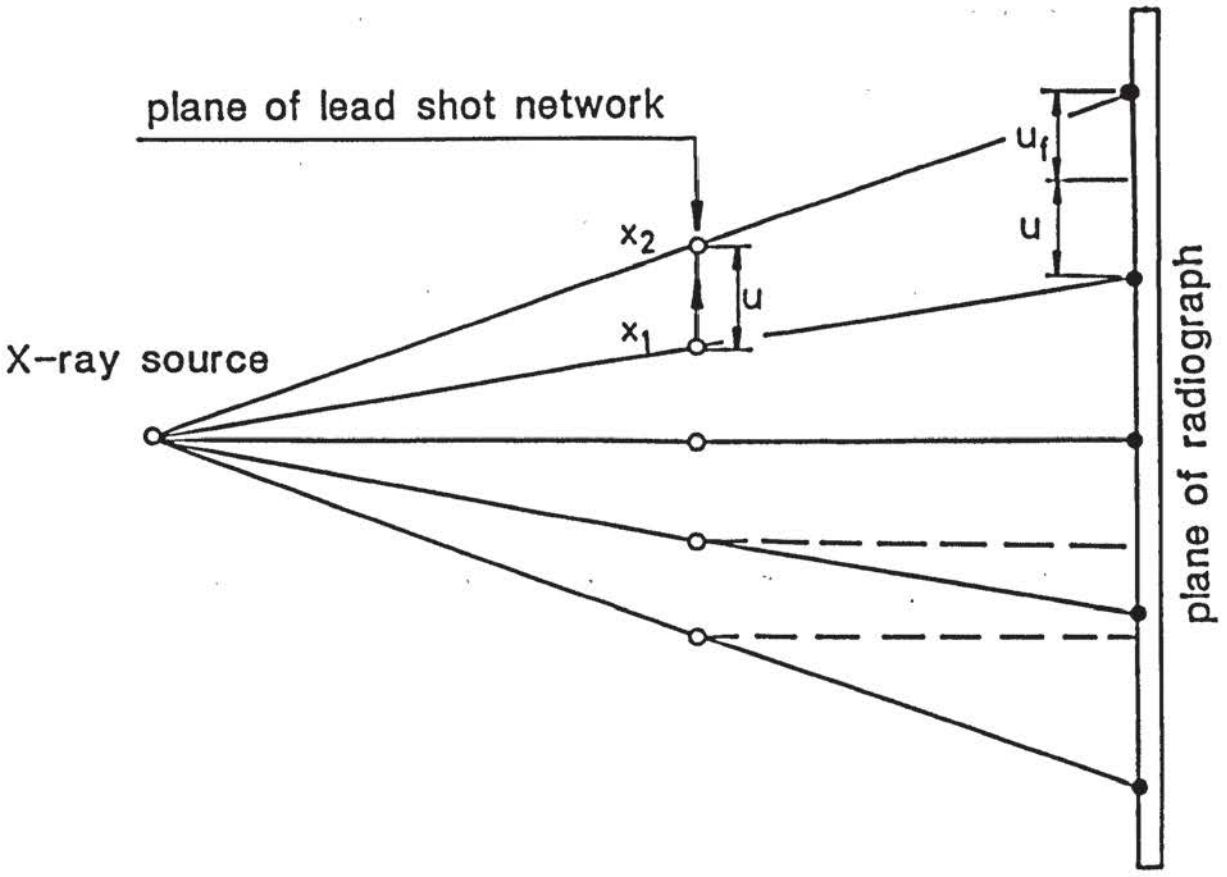

Relative positions of shot images to actual positions and X-ray source.

FIGURE 7.5

$$\{\varepsilon\}_1 = [Z]_1 \{\Delta\}$$

$$\{\varepsilon\}_2 = [Z]_2 \{\Delta\}$$

hence $$\{\varepsilon_{av}\} = (\{\varepsilon\}_1 + \{\varepsilon\}_2)/2 \qquad (7.12)$$

Using the avearge values for ε_x, ε_y and γ_{xy}, the principal strains, angle of dilation and the relevant directions were obtained.

Using the triangular element subject to the deformation increments shown in Figure 7.6, incremental small strains ε_o and average strains ε_{av} were calculated for comparative purposes and are shown plotted against each other in Figure 7.7. Although, it is apparent that Cole's procedure is strongly corrective from strain levels of about 20% it is evident that the method is valid whether displacements or strains are large or small.

Natural strain and Green's stress tensor also serve similar functions as general definitions of strain. From their respective equations given in Appendix F, incremental strains were calculated and plotted against ε_{av}, as shown in Figure 7.8. It can be seen that Cole's method is more corrective from strain levels of about 55%.

On the basis of its proven use, the Cole procedure was used in the computational process.

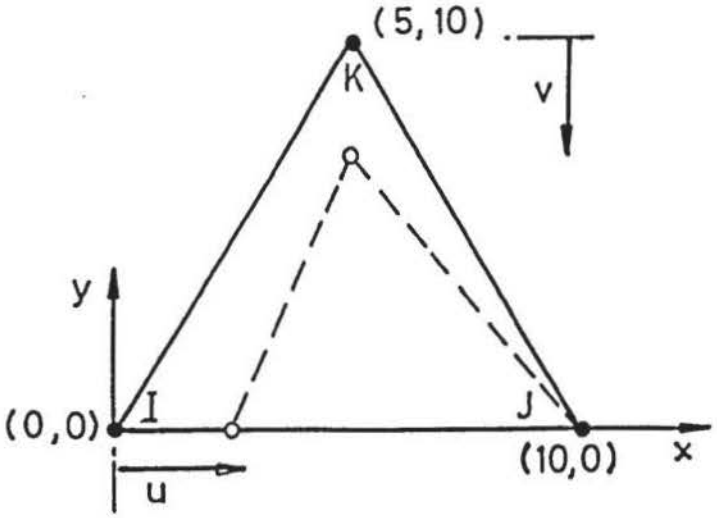

u	v
0·001	-0·0015
0·01	-0·015
0·1	-0·15
1·0	-1·5
2·0	-3·0
3·0	-4·5
4·0	-6·0
5·0	-7·5

Displacements at nodes I and K of a triangular element.

FIGURE 7.6

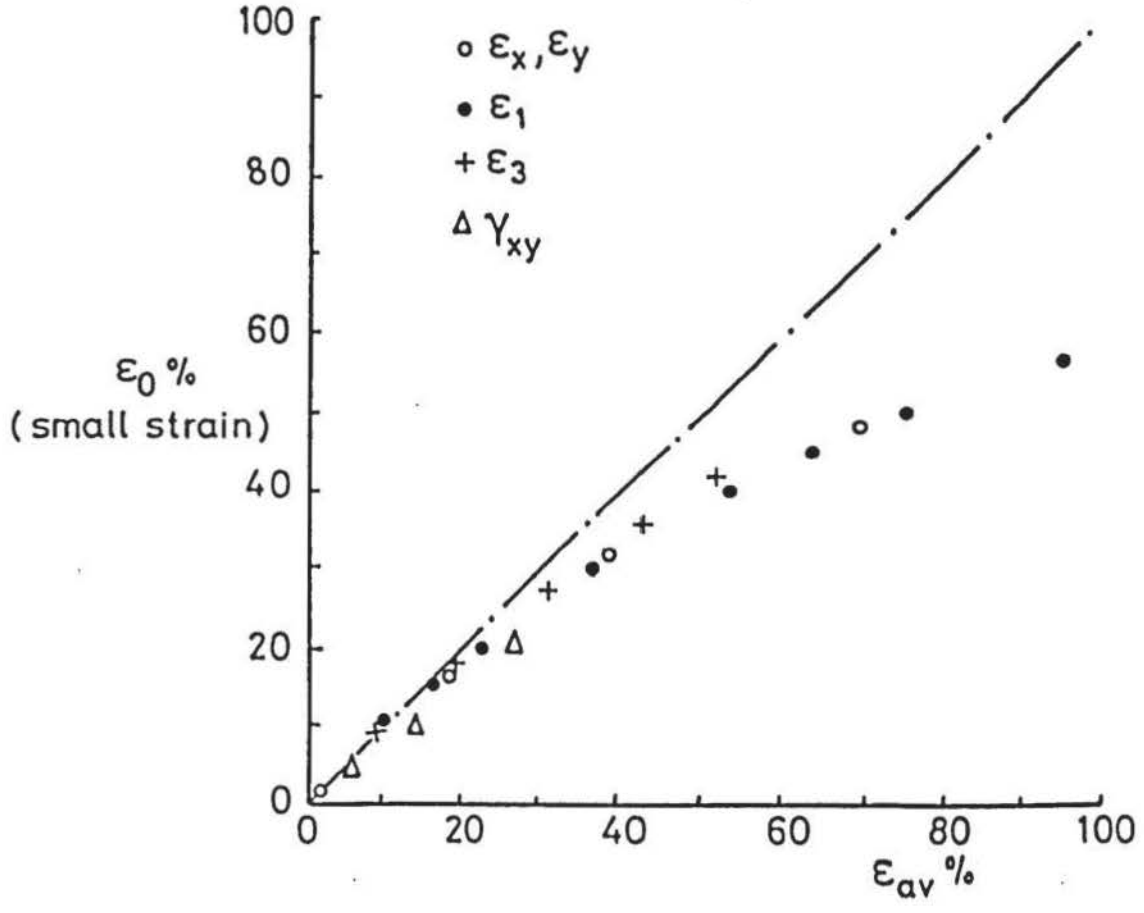

Variation of small strain with average strain.

FIGURE 7.7

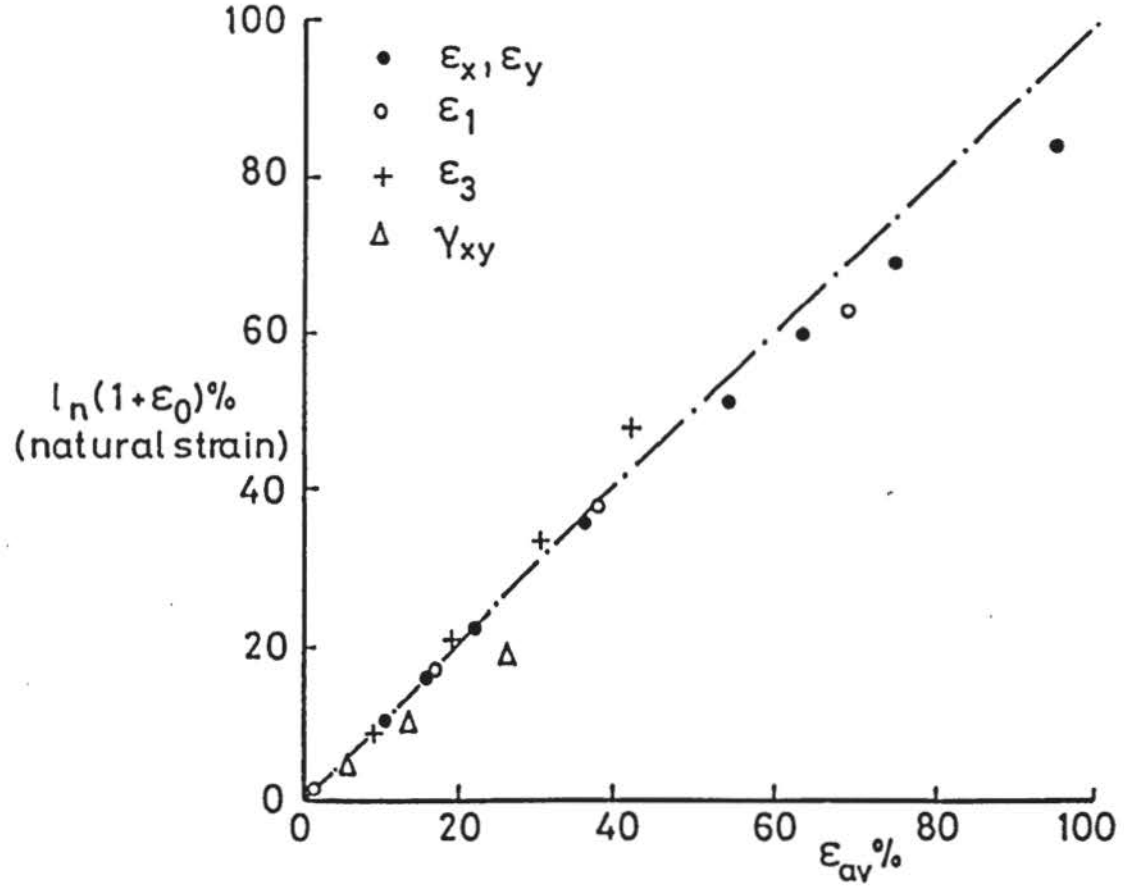

Variation of natural strain with average strain.

FIGURE 7.8(a)

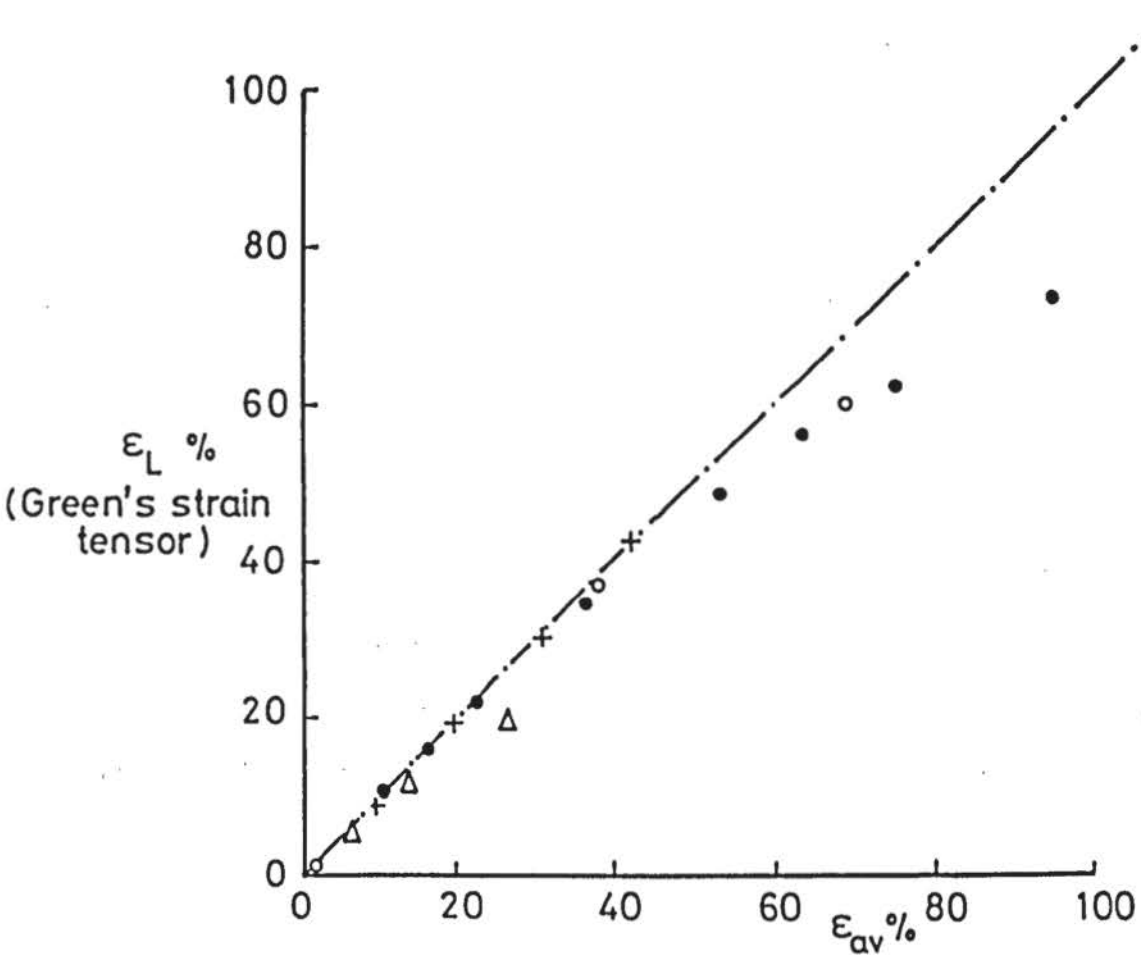

Variation of large strain (Green's stress tensor) with average strain.

FIGURE 7.8(b)

CHAPTER 8

DATA PROCESSING

8.1 INTRODUCTION

To cater for the quantities of experimental data produced, computers were used for its permanent storage and subsequent processing. A mini-computer, in the Department, was used to handle the recorded transducer data and a mainframe dealt with the digital information taken from the radiographs.

8.2 TRANSDUCER DATA

8.2.1 System

The Departmental Computer was initially a DEC PDP-11/34 and later a DEC 11/750 VAX. The systems gave interactive time-sharing facilities via a number of Televideo visual display units (VDU's) and other peripheral devices, shown schematically in Figure 8.1.

8.2.2 Paper Tape Reader

The coded punched paper-tape was read and decoded by a fast paper-tape reader (constructed by the Department's Electronics Section) connected to the PDP-11/VAX. The decoded data was kept on magnetic disk in a designated file structure.

8.2.3 Files

Data files were checked for spurious characters that may have been introduced during the decoding process or in the initial punching of the tape. Test identification numbers and appropriate data constants (e.g. calibration constants, column diameter, footing width, temperature, etc.) were also appended to the beginning of each file in a format corresponding to the requirements of the particular computer program and test conditions.

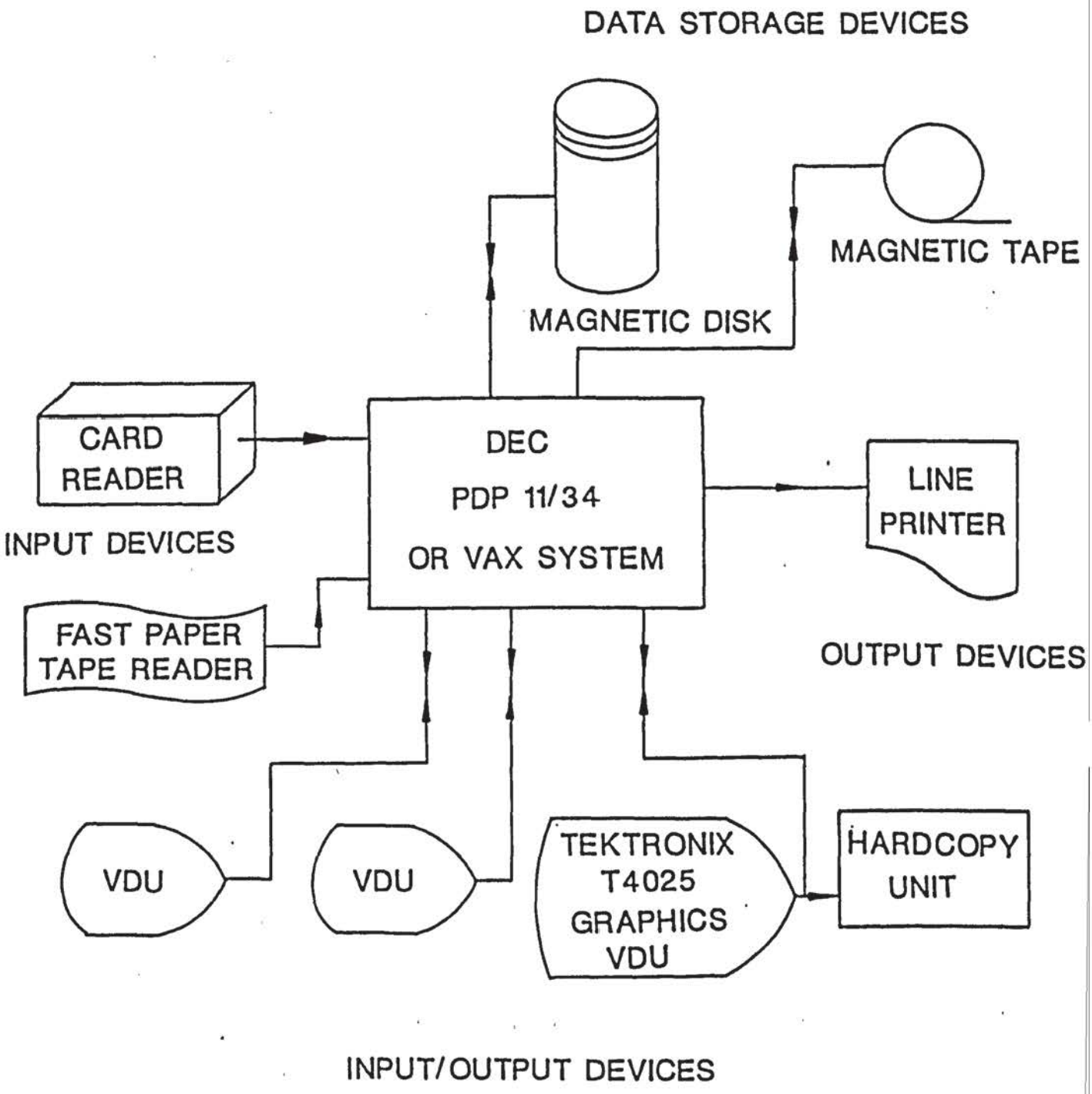

Departmental mini-computer and arrangement of available peripherals.

FIGURE 8.1

8.2.4 Programming

Computer programs were written by the author using FORTRAN 77. All programs were checked by 'de-bugging' software and by comparison to at least one set of results obtained by manual calculation.

8.2.5 Alphanumerics

It was found useful to use alphanumeric characters in test identification numbers and to allow for comments (e.g. "shear plane observed at 10 mm compression") to be included in the data file, and for these to appear on the ouput.

Unlike BASIC, FORTRAN was not found to be well disposed in handling alphanumerics. It is perhaps worthy of note that the routine given in Appendix G allows reading and writing of alphanumeric strings. The routine may not, however, work with all FORTRAN compilers.

8.2.6 Results Output

All the programs were written with interactive prompts to give options for directing the computed numerical results files to the VDU, the line-printer (for hardcopy) and/or a graphical display unit. The latter was a Tektronix T4025 graphics VDU supported by general purpose graph-plotting software. This facility was useful for rapidly comparing graphical relationships between a number of variables. An electrostatic type hardcopy device linked to the Tektronix VDU did not give graphical quality suitable for analytical purposes. Formal graphical relationships, when established, were therefore done by hand.

8.3 RADIOGRAPHIC DATA

8.3.1 DEC 2050

The direct transfer of data from the digitiser to a DEC 2050 mainframe has been outlined in Section 6.3.3. The DEC 2050, administered by the University's Computer Centre, gave interactive time-sharing facilities via the Departmental Tektronics VDU. NAG Library, GINO graphics routines and other software aids were available.

8.3.2 Processing

The strain analysis (outlined in Chapter 7) applies to a single element. An array of lead-shot defines many elements. The data processing involved uniquely identifying each triangular element, by allocating a 'node' number at each lead-shot position, and applying iterative computation to obtain the displacement and strain vectors.

8.3.3 Element Identification

Each element of an array of lead-shot, used in a particular test, was given an element number in the same way as the nodes. The correlation of each element m with the node numbers nI(m), nJ(m) and nK(m) defining it was achieved by producing a table similar to the example shown in Figure 8.2. Where large numbers of elements are concerned (about 200 was typical in the author's case) producing identification tables for a data file is best achieved using a computer program.

By considering the structural geometry of a regular triangular array the procedure described in Appendix H was adopted.

8.3.4 Computational Procedure

The computational procedure is shown by the program flow chart in Figure 8.3.

8.3.5 Unit Conversion

The digitised co-ordinates were 5-digit integers for each ordinate (See Section 6.3.4) which represented thousandths of an inch. The co-ordinates were converted to millimetres.

8.3.6 Co-ordinate Transformation

The digitised co-ordinates (x_d, y_d) were measured with respect to the digitiser axes (Section 6.3.4) and were obtained with the radiographic prints at any orientation on the digitiser bed, shown in Figure 8.4.

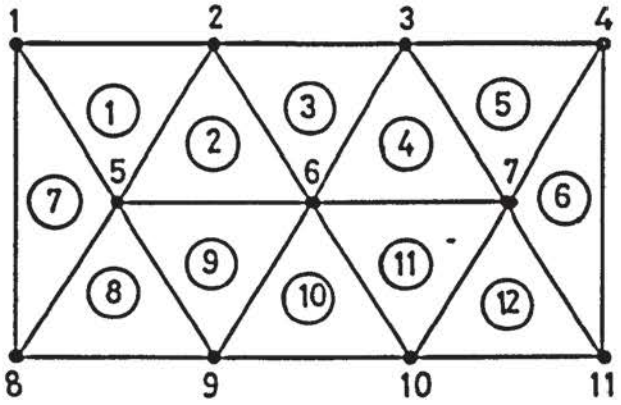

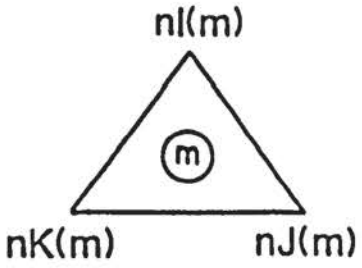

element (m)

Element no.	Node no.		
m	nI(m)	nJ(m)	nK(m)
1	1	2	5
2	2	6	5
3	2	3	6
4	3	6	7
5	3	4	7
6	4	11	7
7	1	5	8
8	5	9	8
9	5	6	9
10	6	10	9
11	6	7	10
12	7	11	10

An example of element identification using an array of 11 nodes and 12 elements.

FIGURE 8.2

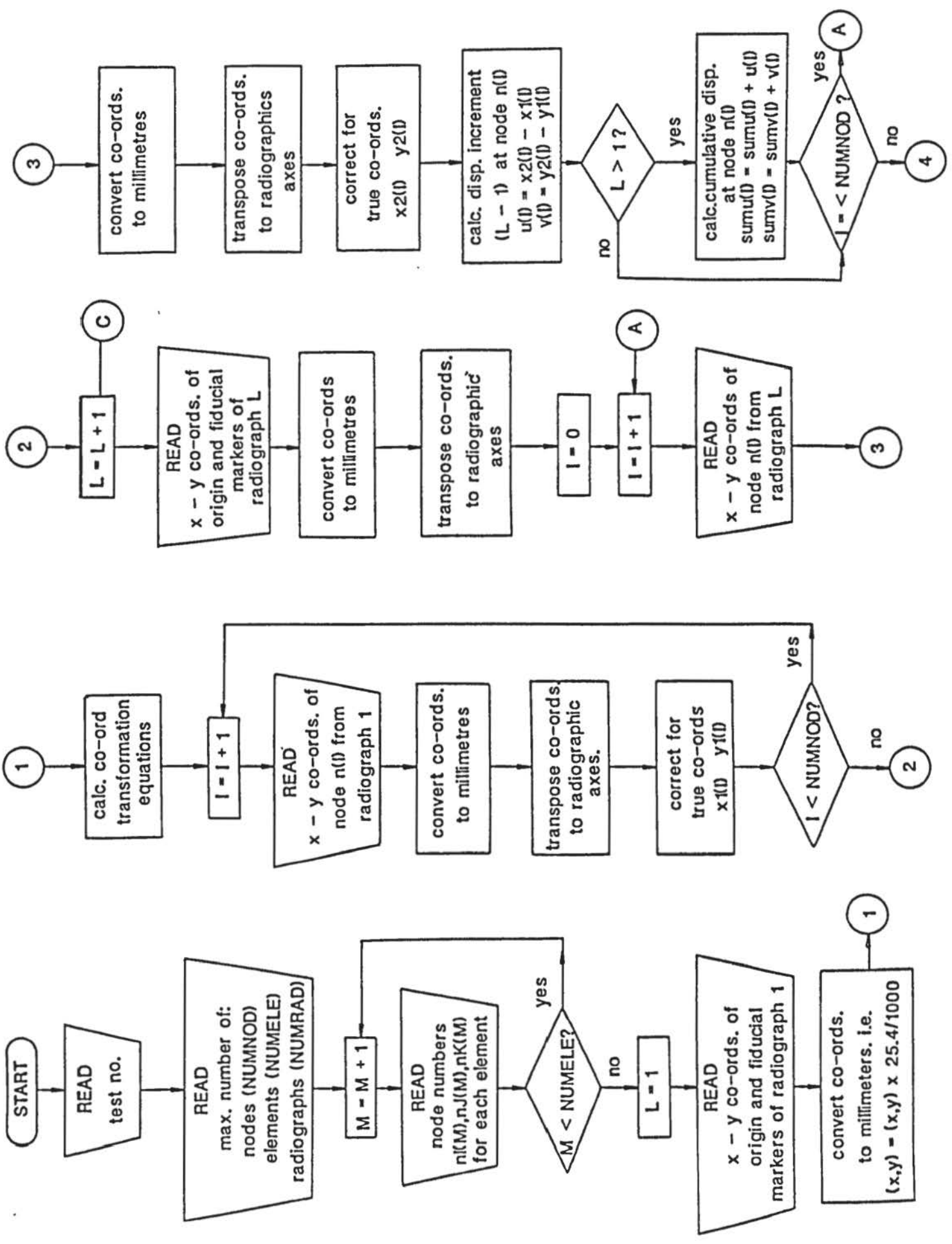

Computer program flow chart for radiographic analysis.

FIGURE 8.3

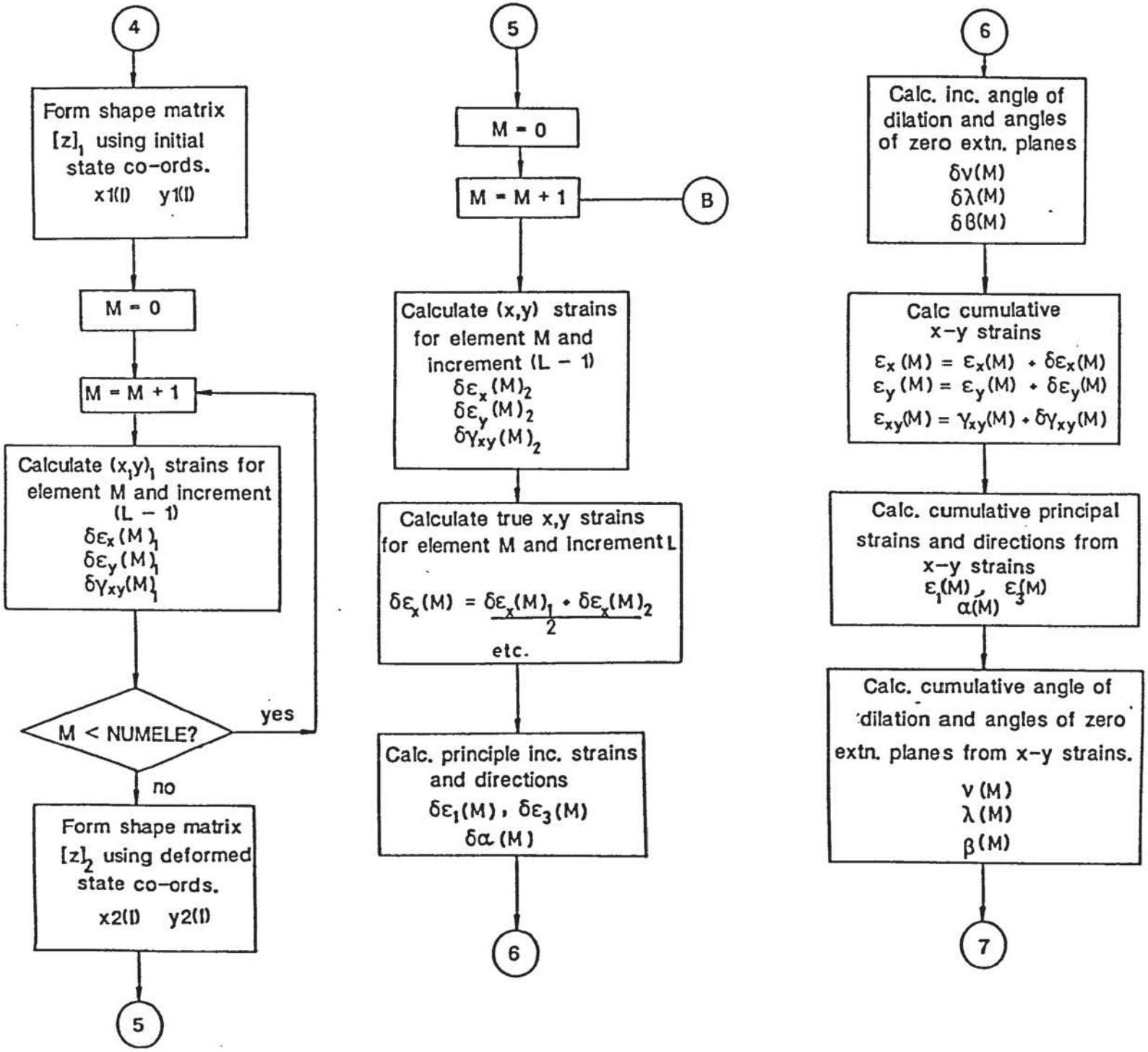
4
Form shape matrix [z]1 using initial state co-ords. x1(I) y1(I)
M = 0
M = M + 1
Calculate (x,y)1 strains for element M and increment (L − 1)
δεx(M)1
δεy(M)1
δγxy(M)1
M < NUMELE?
yes
no
Form shape matrix [z]2 using deformed state co-ords. x2(I) y2(I)
5
5
M = 0
M = M + 1
B
Calculate (x,y) strains for element M and increment (L − 1)
δεx(M)2
δεy(M)2
δγxy(M)2
Calculate true x,y strains for element M and increment L
δεx(M) = (δεx(M)1 + δεx(M)2) / 2
etc.
Calc. principle inc. strains and directions
δε1(M), δε3(M)
δα(M)
6
6
Calc. inc. angle of dilation and angles of zero extn. planes
δν(M)
δλ(M)
δβ(M)
Calc cumulative x−y strains
εx(M) = εx(M) + δεx(M)
εy(M) = εy(M) + δεy(M)
εxy(M) = γxy(M) + δγxy(M)
Calc. cumulative principal strains and directions from x−y strains
ε1(M), ε3(M)
α(M)
Calc. cumulative angle of dilation and angles of zero extn. planes from x−y strains.
ν(M)
λ(M)
β(M)
7

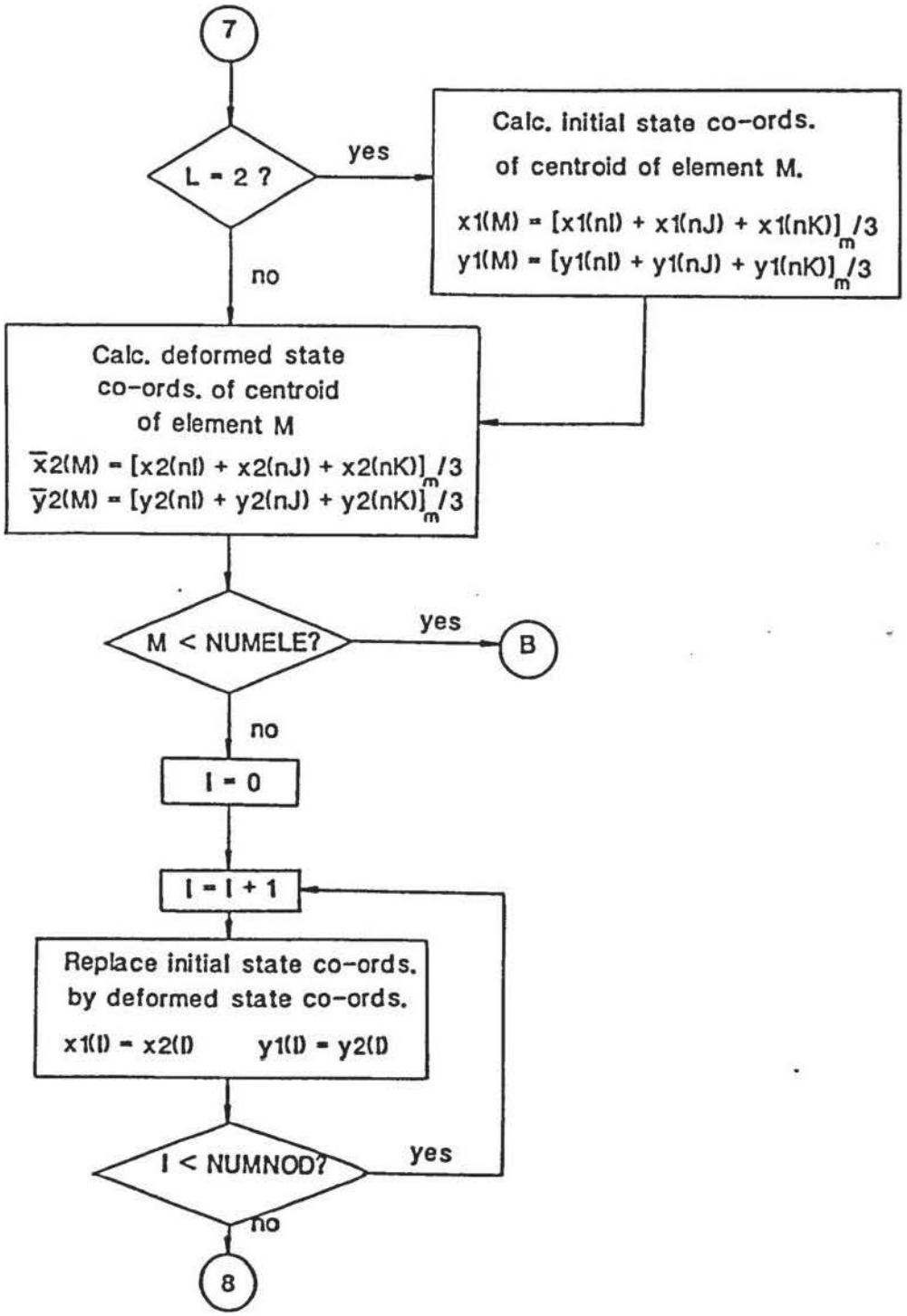
7
L = 2 ?
yes
no
Calc. initial state co-ords.
of centroid of element M.
x1(M) = [x1(nI) + x1(nJ) + x1(nK)]m /3
y1(M) = [y1(nI) + y1(nJ) + y1(nK)]m /3
Calc. deformed state
co-ords. of centroid
of element M
x̄2(M) = [x2(nI) + x2(nJ) + x2(nK)]m /3
ȳ2(M) = [y2(nI) + y2(nJ) + y2(nK)]m /3
M < NUMELE?
yes
B
no
I = 0
I = I + 1
Replace initial state co-ords.
by deformed state co-ords.
x1(I) = x2(I) y1(I) = y2(I)
I < NUMNOD?
yes
no
8

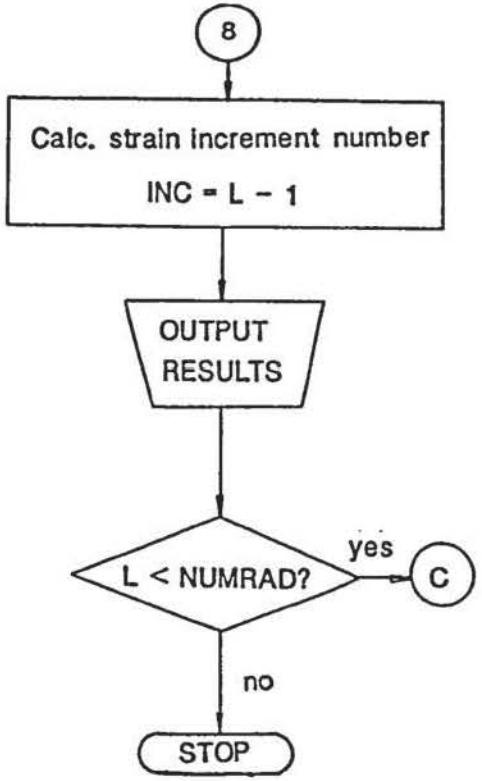
8
Calc. strain increment number
INC = L - 1
OUTPUT
RESULTS
L < NUMRAD?
yes
C
no
STOP

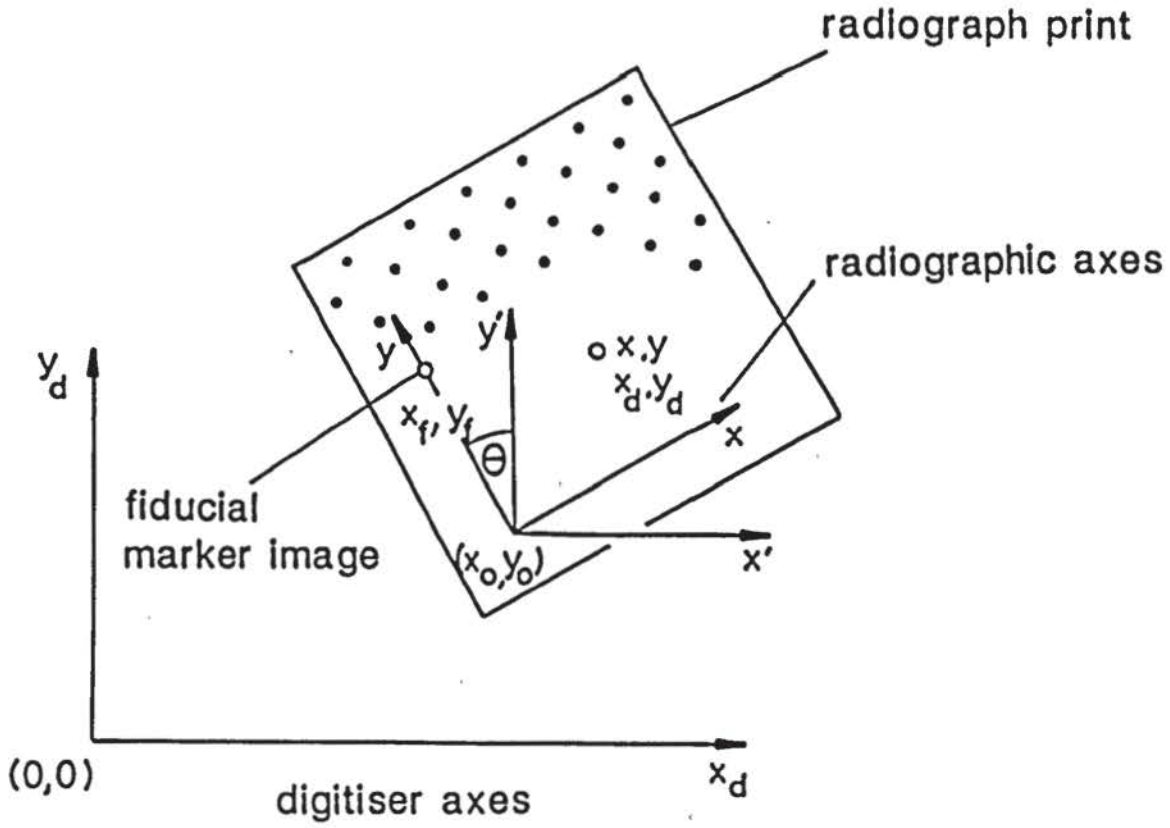

Positioning of radiograph print at any orientation on the digitiser bed.

FIGURE 8.4

The co-ordinates were transformed to the radiographic axes, havng co-ordinates (x_o, y_o). Referring to Figure 8.4, the transformation equations are:

$$x = (x_d - x_o)\cos\theta + (y_d - y_o)\sin\theta$$
$$y = (y_d - y_o)\cos\theta + (x_d - x_o)\sin\theta \qquad (8.1)$$

where angle θ was obtained using the digitised co-ordinates of the fiducial marker (x_f, y_f), thus:

$$\tan\theta = \left|(x_f - x_o)/(y_f - y_o)\right| \qquad (8.2)$$

8.3.7 True Co-ordinates

Using the relationships established from the method described in Appendix E, from the previous chapter, the true x-y co-ordinates of the lead-shot were determined.

8.3.8 Results Output

To minimise computer storage requirements, the results of computation were output at the end of each increment in numerical and/or graphical form.

8.3.9 Results Presentation

Using interactive prompts, in the program, the results could be directed to a line printer (numerical results), the Tektronix VDU (numerical and/or graphical) or to a Hewlett-Packard 722 OT flat-bed graph plotter. The process is illustrated in Figure 8.5. Examples of the presentation of numerical results, using the line printer, are given in Appendix I.

8.3.10 Graphical Output

The Tektronix VDU was used mostly for checking purposes prior to obtaining graphical hardcopy.

It was also useful to output graphically the node and element numbers and positions shown in Figure 8.6. By comparison to the numbering on the radiographic prints, a check could be made to ensure the input data had been read in the correct sequence.

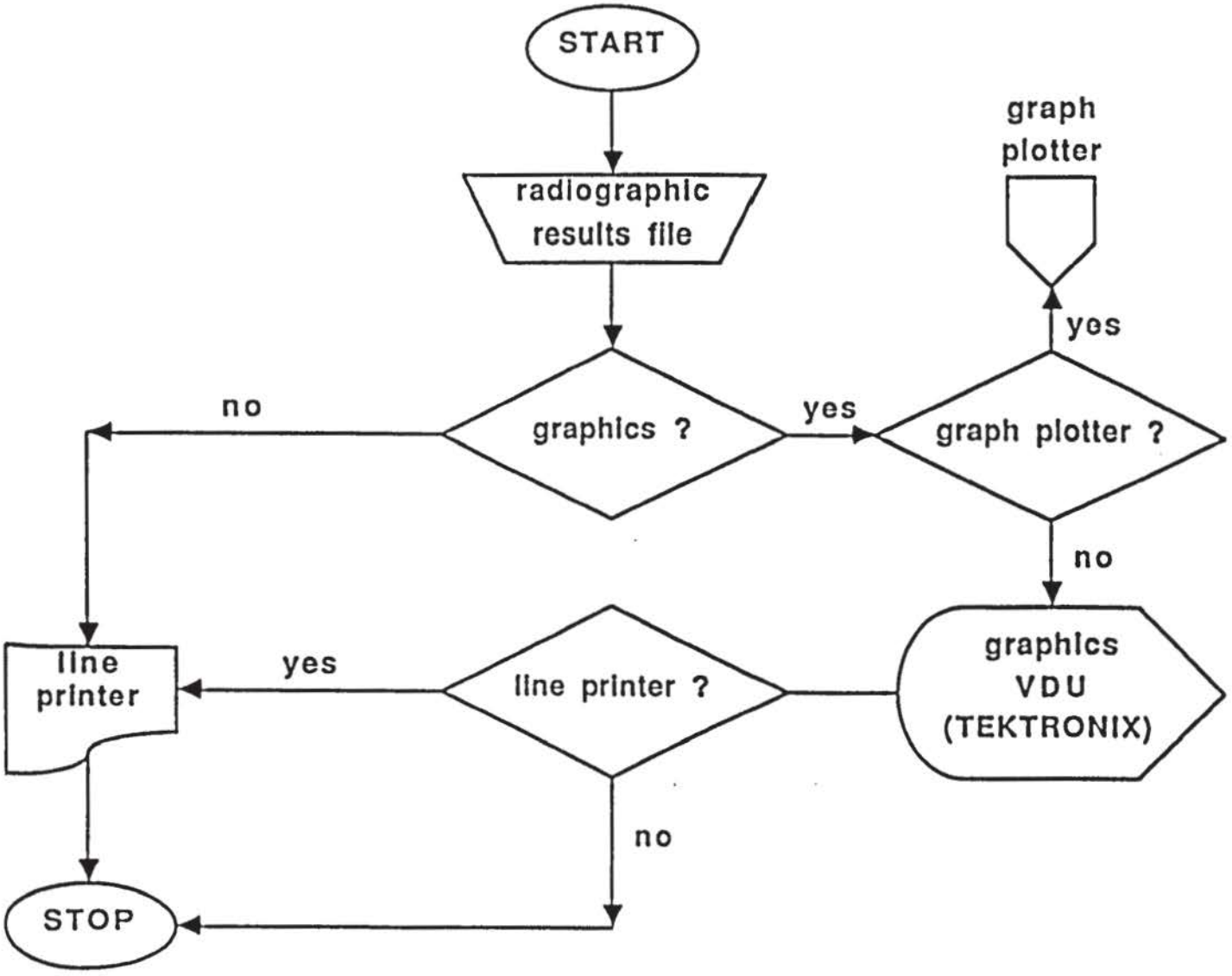

Device options for outputing results from radiographic analyses.

FIGURE 8.5

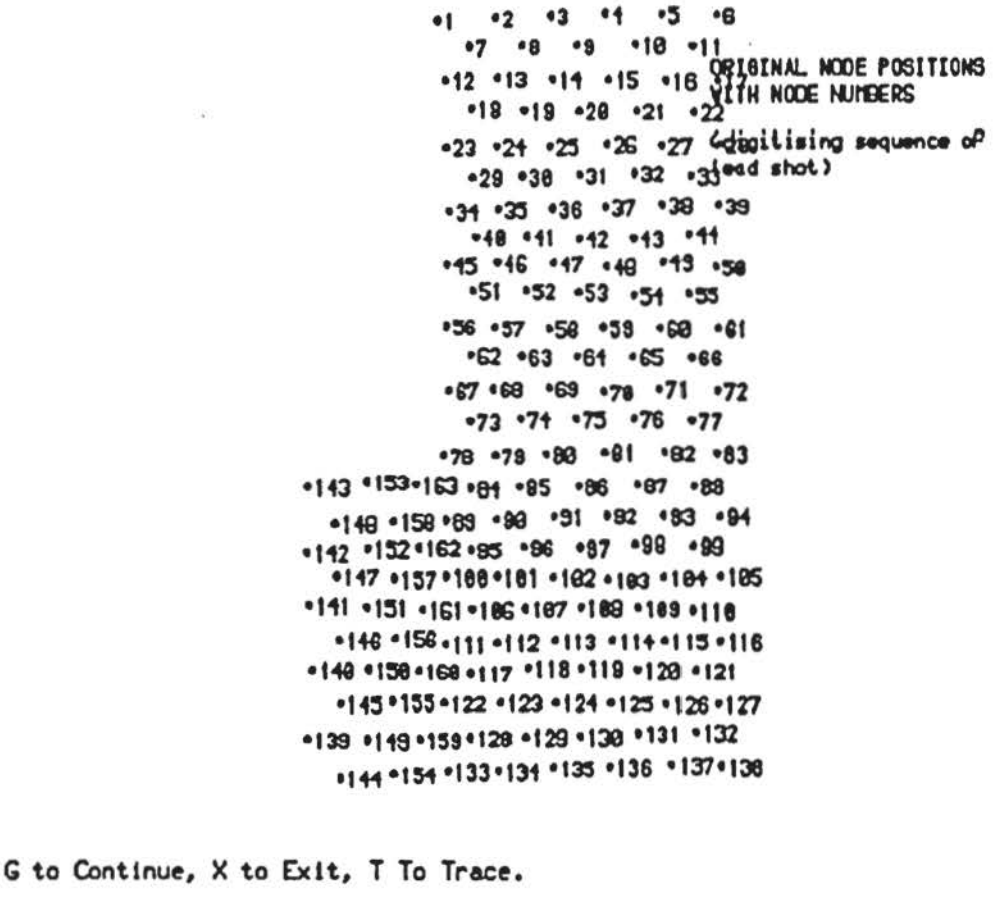

Graphical output showing node numbers.

FIGURE 8.6(a)

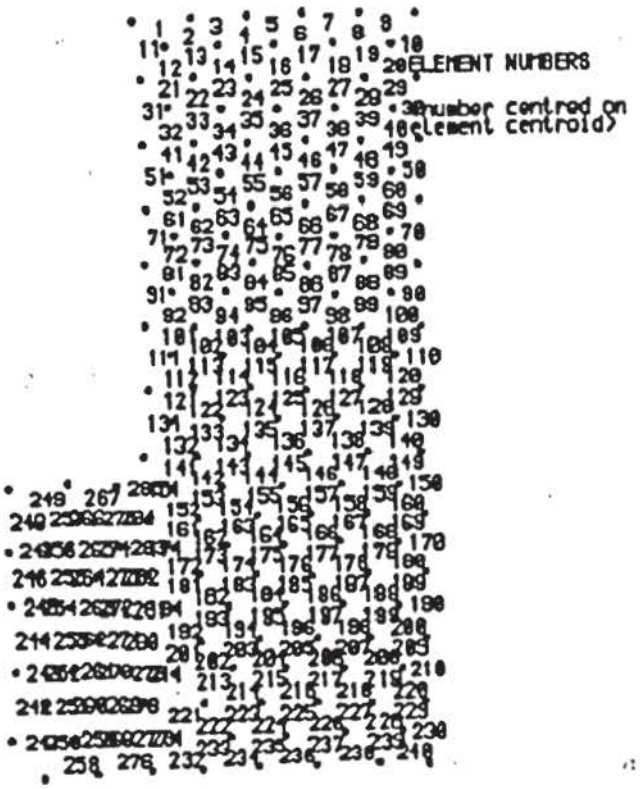

Type G to Continue, X to Exit, T To Trace.
*_

Graphical ouptut showing element numbers.

FIGURE 8.6(b)

8.3.10.1 Displacement

Graphical representation of displacement was by straight lines, the length of which were proportional to its magnitude. The lines were drawn from the initial positions of the lead-shot to their deformed positions.

8.3.10.2 Strain

Strain was also represented by straight lines, with the magnitude defined by line length. Tensile strains were coloured red. The mid-point of each line was positioned at the centroid of the element to which it referred. The centroids of the deformed elements were used in recognition of assumption (e) in Section 7.3.

8.3.10.3 Zero Extension

Planes of zero extension were represented by short dashed-lines at the angle calculated to the horizontal. They were positioned at the centroid of the deformed element to which they referred.

8.3.10.4 Hardware Limitations

Because of limitations in the graph-plotting hardware and drawing pen thickness, a displacement or strain represented by a line less than about 0.5 mm would always be drawn with a minimum length of 0.5 mm. Computers are capable of holding very small numbers, some of which in the practical sense are zero. In the case of displacement and strain, such numbers would be represented by a line length of 0.5 mm.

To overcome this practical difficulty, strains or displacements represented by lines of 0.5 mm or less were omitted in the drawing process.

8.3.11 Programming

Programs were written in FORTRAN 77 and used GINO-F graphics routines. For ease in development and de-bugging, programs were written in modular form and kept in a file library which allowed linking of the modules as required.

All programs were checked by de-bugging software and by at least one set of results obtained from manual calculation.

CHAPTER 9

TEST PROGRAMME

9.1 INTRODUCTION

The main laboratory test programme was concerned with the measurement of boundary stress-displacement conditions and internal displacements when single and small groups of granular columns, in various configuartions, were subjected to loading by the model foundations in floating and end-bearing conditions. The tests were strain controlled and the rate of vertical compression was designed to give rapid undrained conditions. The model foundations were considered rigid and rough faced. The same column size was used for all the tests carried out.

9.2 COLUMN SIZE

A column size of 38.1 mm nominal diameter and 150 mm in length was chosen for the test programme. Reasons for the former dimension have been previously discussed in Section 4.10.1. The latter was assessed from the minimum length to prevent early pile-mode failure and the depth to the base of the container to effectively allow a floating condition. Calculations are given in Appendix J and the suitability of the column length was confirmed by preliminary tests. The overall column dimensions also corresponded to those used by Hughes and Withers (1974) which allowed some direct comparisons to be made.

9.3 COMPRESSION TESTS

Using the various sizes of circular, square and rectangular model foundations, compression tests were performed on single and groups of up to 5 No. granular columns in container B. Column spacing was related to the column diameter (D). Some of the model foundations incorporated the contact pressure transducers. A schedule of tests, and the measurements taken, are given in Figure 9.1 to 9.7. For comparative purposes, prior to each column compression test, a compression test using the appropriate model foundation was

Measurements

Load (p)
Settlement (ρ)
Horizontal stress (σ_x)
Soil temperature (t^oC)

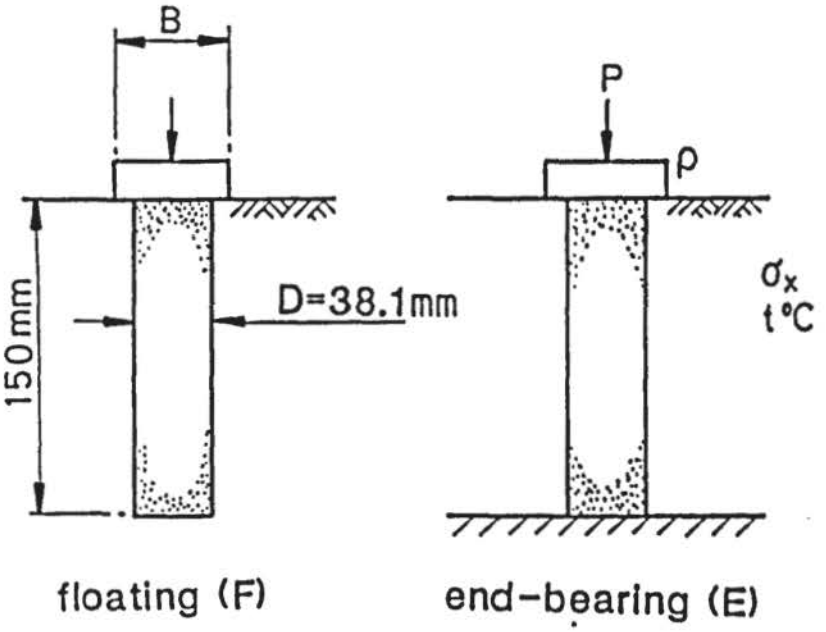

Foundation	B(mm)	Test Number (F)	(E)
Circular	24.28	C1	C1E
	38.02	C2	C2E
	49.84	C3	C3E
	60.02	C4	C4E
Square	24.76	SQ1	SQ1E
	38.52	SQ2	SQ2E
	49.44	SQ3	SQ3E
	60.70	SQ4	SQ4E

CONTAINER B

Schedule of compression tests for circular and square foundations on single granular columns.

FIGURE 9.1

Measurements

Load (p)
Settlement (ρ)
Horizontal stress (σ_x)
Average vertical
Pressure on Col. (σ'_{vc})
Soil temperature (t^oC)

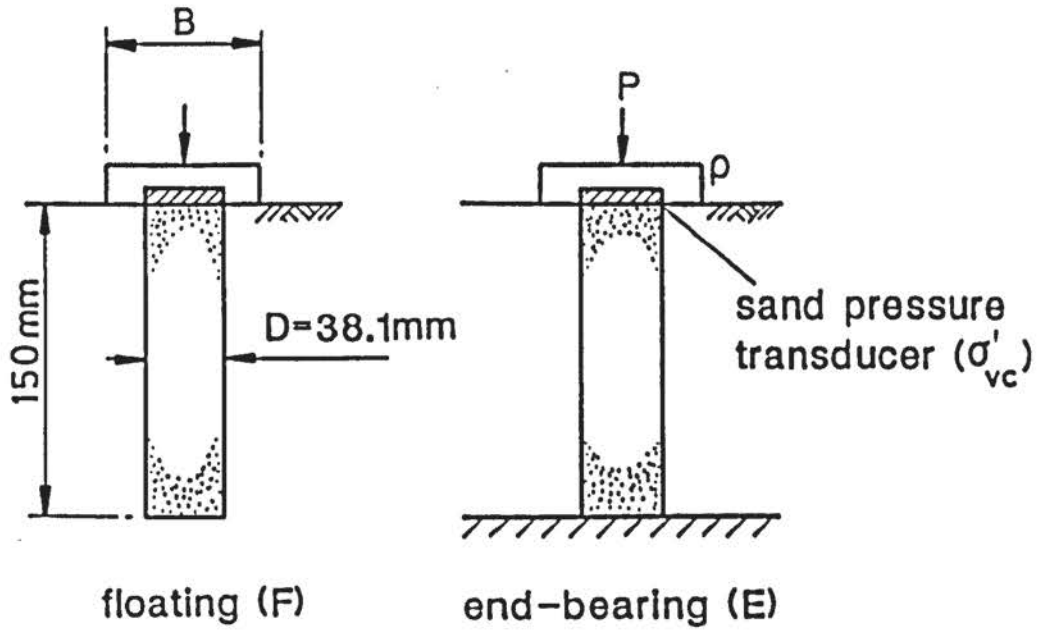

Foundation with Sand Pressure Transducer	B(mm)	Test Number (F)	(E)
Circular	50.0	PC1	PC1E
	60.0	PC2	PC2E
Square	60.18	PSQ1	PSQ1E

CONTAINER B

Schedule of compression tests for circular and square foundations, with a sand pressure transducer, on single granular columns.

FIGURE 9.2

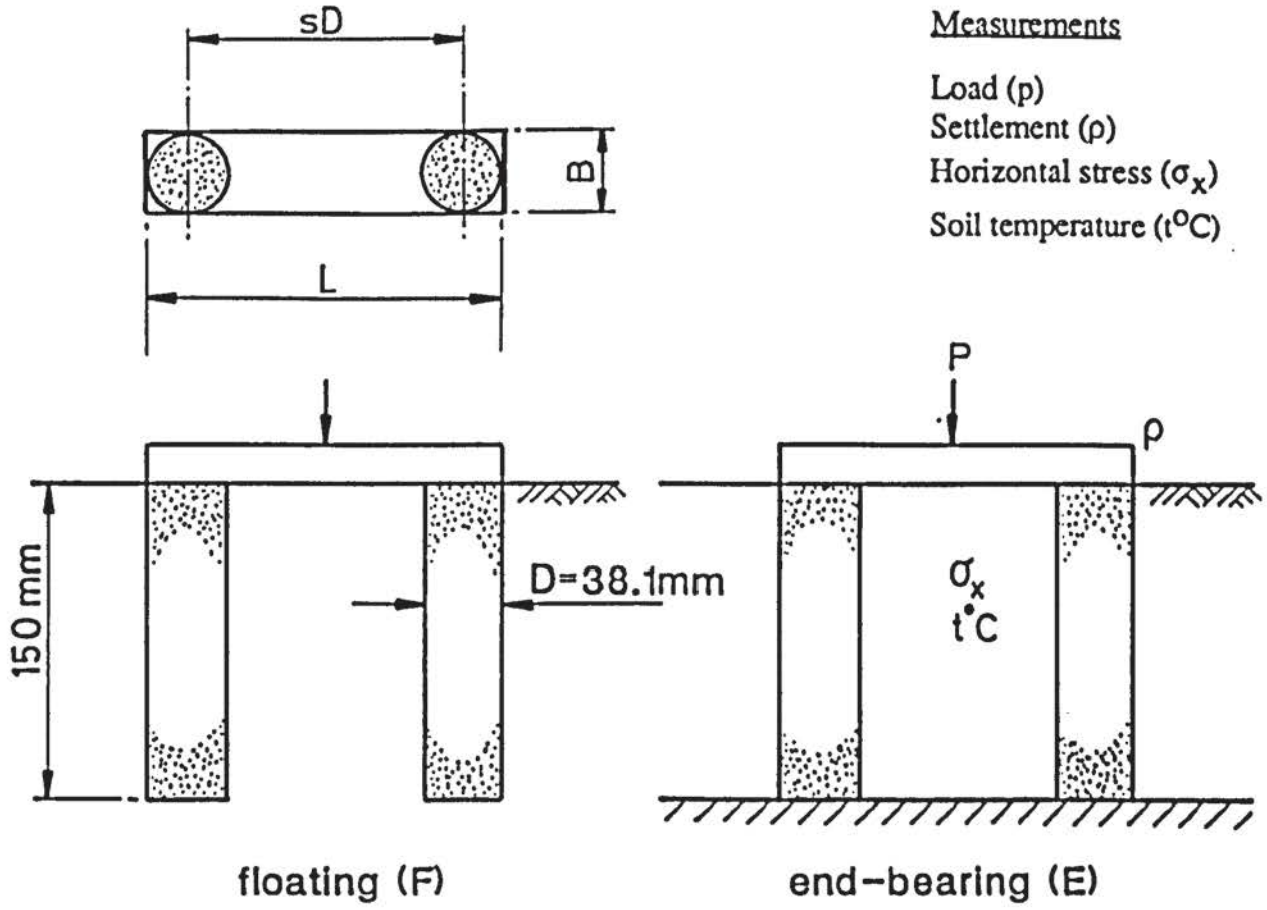

Foundation	B(mm)	L(mm)	s	Test Number (F)	(E)
Rectangular	38.10	152.20	0*	R	RE
	38.10	85.88	1	RO	ROE
	38.10	85.88	1.25	R1	R1E
	38.16	95.20	1.5	R2	R2E
	38.20	105.08	1.75	R3	R3E
	38.10	113.90	2	R4	R4E
	38.24	132.90	2.5	R5	R5E
	38.10	152.20	3	R6	R6E
	38.10	189.70	4	R7	R7E

*s=0 (single column at centre-line of foundation).

CONTAINER B

Schedule of compression tests for rectangular foundations on pairs of granular columns.

FIGURE 9.3

Measurements

Load (p)
Settlement (ρ)
Horizontal stress (σ_x)
Soil temperature (t^oC)

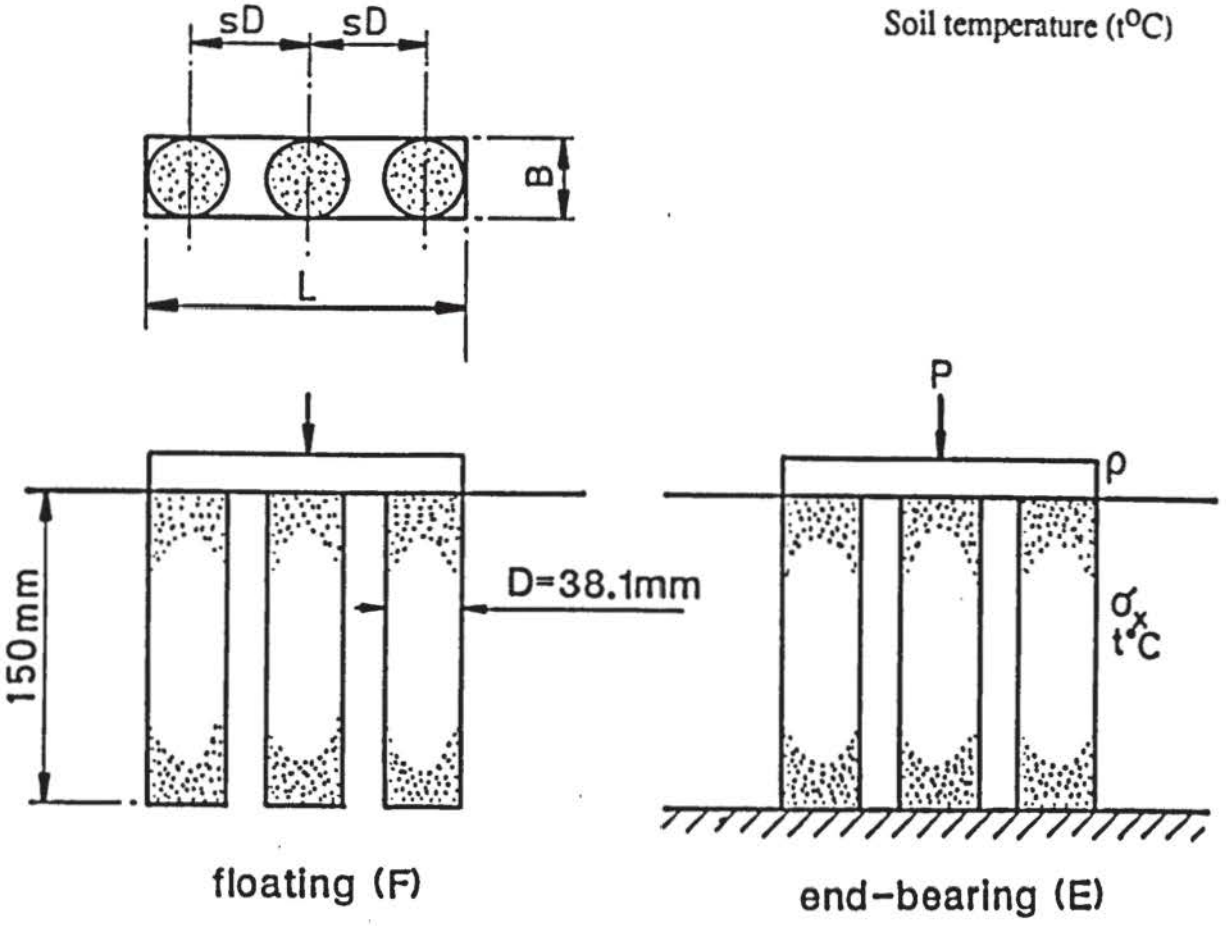

Foundation	B(mm)	L(mm)	s	Test Number F	E
Rectangular	38.10	152.20	1.5	R8	R8E

CONTAINER B

Schedule of compression tests for a rectangular foundation on three granular columns.

FIGURE 9.4

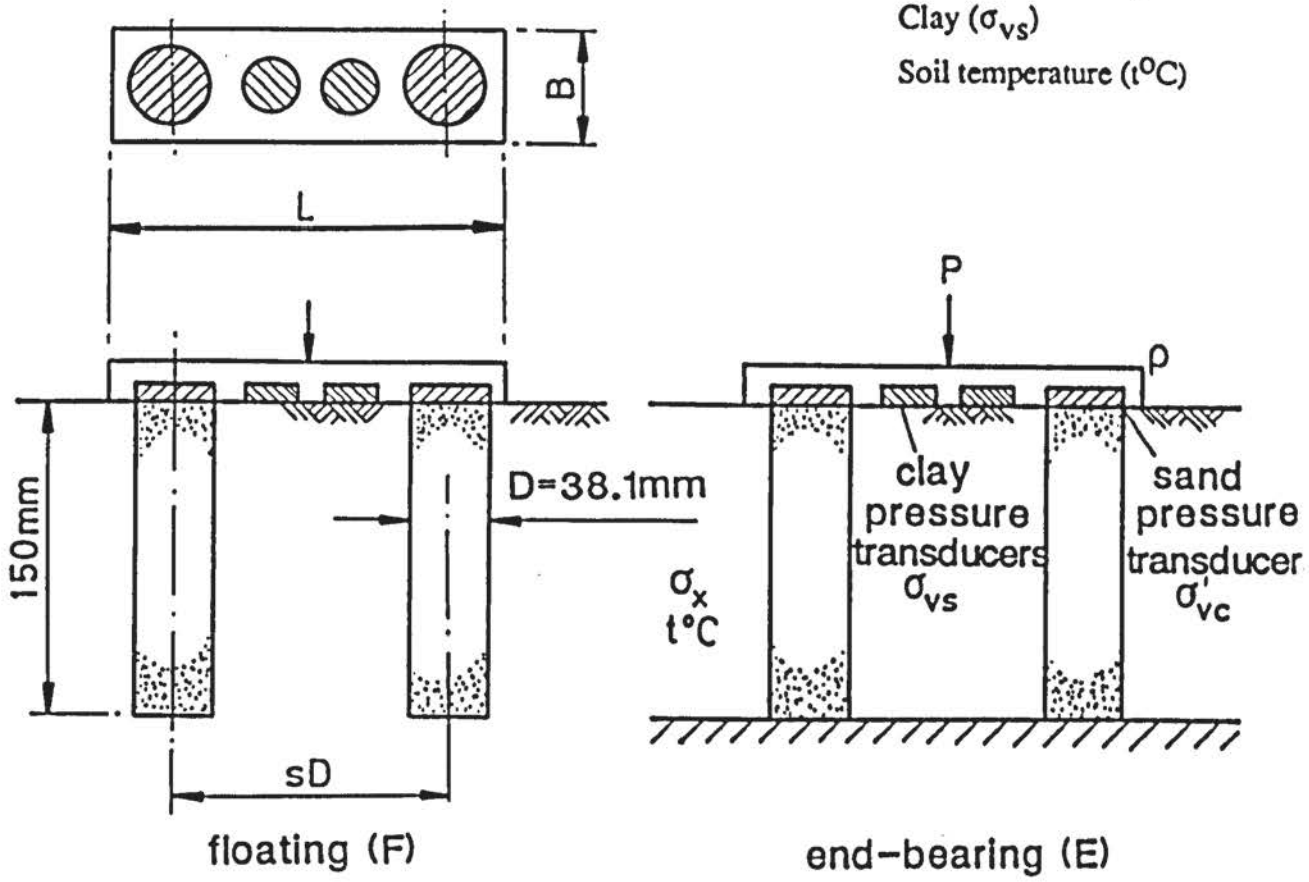

Foundation with clay and sand pressure transducers	B(mm)	L(mm)	s	Test Numbers (F)	(E)
Rectangular	50.0	115.7	1.75	PR1	PR1E
	49.6	145.0	2.5	PR2	PR2E
	49.8	164.0	3	PR3	PR3E

CONTAINER B

Schedule of compression tests for rectangular foundations, with sand and clay pressure transducers, on pairs of granular columns.

FIGURE 9.5

Measurements

Load (p)
Settlement (ρ)
Horizontal stress (σ_x)
Soil temperature (t^oC)

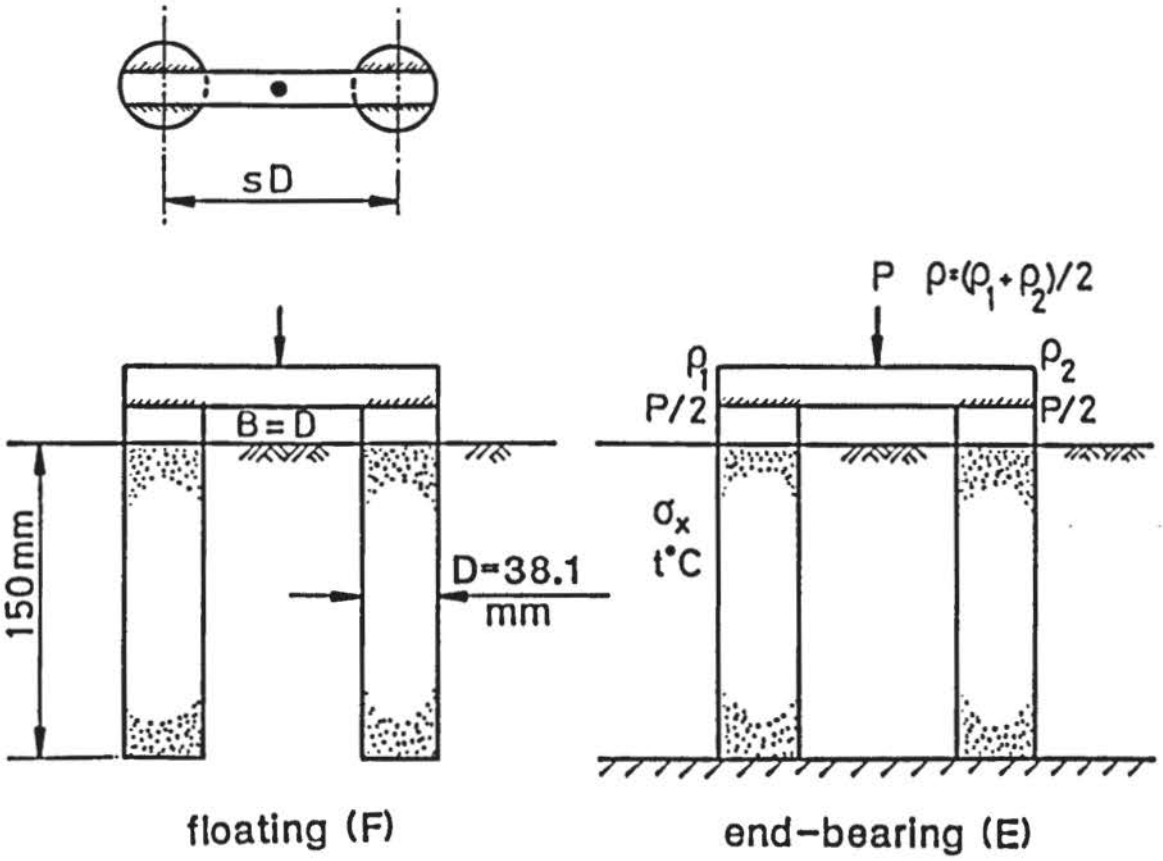

Foundation	s	Test Number (F)	(E)
2 circular isolated (rigidly secured to cross-beam)	1.25	TC1	TC1E
	1.5	TC2E	TC2E
	3	TC4	TC4E

CONTAINER B

Schedule of compression tests for two isolated foundations on granular columns.

FIGURE 9.6

Measurements

Load (p)
Settlement (ρ)
Horizontal stress (σ_x)
Average vertical
Pressure: Col. (σ'_{vc})
Clay (σ_{vs})
Soil temperature (t°C)

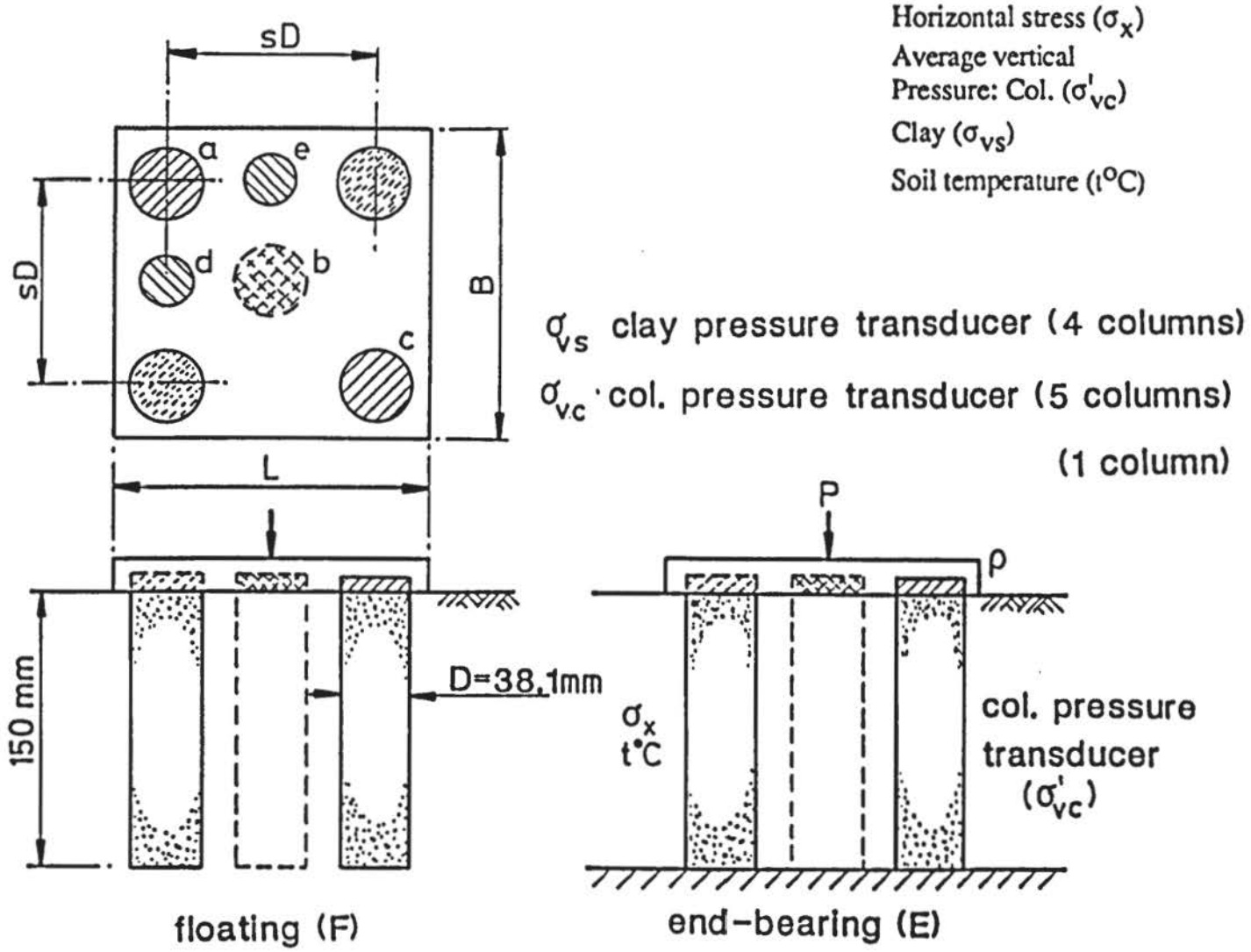

Foundation with clay and sand pressure transducers	B(mm)	L(mm)	s	Measuring Transducer σ_{vs}	Measuring Transducer σ_{vc}	Test Number (F)	Test Number (E)
5 columns (one at each corner + one at centre)	125.3	125.3	1.75	a,b,c	d,e	PSQ3	PSQ3E
	152.5	152.5	2.5	a,b,c	d,e	PSQ4	PSQ4E
	172.5	172.5	3	a,b,c	d,e	PSQ5	PSQ5E
4 columns (one at each corner)	125.3	125.3	1.75	a,c	b,d,e	PSQ7	PSQ7E
	152.5	152.5	2.5	a,c	b,d,e	PSQ8	PSQ8E
	172.5	172.5	3	a,c	b,d,e	PSQ9	PSQ9E
1 column (at centre)	152.5	152.5	-	b	a,c d,e	PSQ10	PSQ10E

CONTAINER B.
Schedule of compression tests for square foundations, with sand and clay pressure transducers, on 1 to 5 No. columns.

FIGURE 9.7

performed on the clay only.

9.4 INTERACTION TESTS

The vertical deflection of an unloaded 38.1 mm diameter model foundation, situated on (a) the clay surface and (b) a granular column, was measured when an adjacent column was loaded by a foundation of the same diameter. Tests were made at various spacings related to the column diameter and the test schedule is given in Figure 9.8.

9.5 RADIOGRAPHIC TESTS

The schedule of radiographic tests is given in Figure 9.9. In each test, radiographs were taken at increments of ρ/B (ratio of foundation displacement ρ to foundation width B) of 0, 0.2, 0.66 and 1.5.

For comparative purposes, respective compression and interaction tests were also performed using container A.

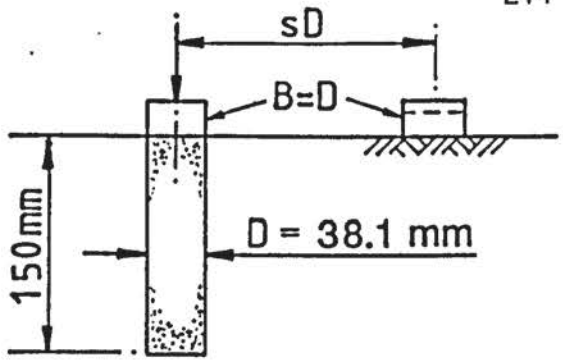

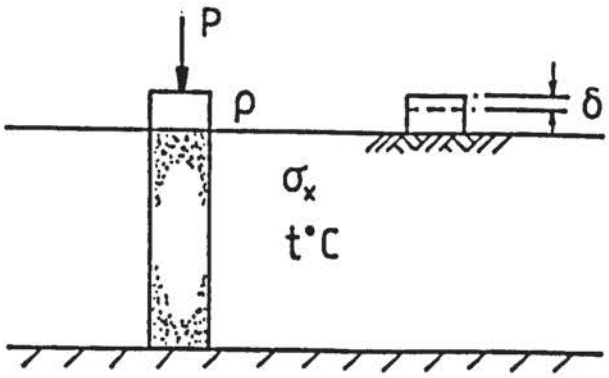

floating (F) end-bearing (E)

Foundation	s	Test Numbers (F)	(E)
Circular	1.25	IC1	IC1E
(one on each	1.5	IC2	IC2E
column)	2	IC3	IC3E
	2.5	IC4	IC4E
	3	IC5	IC5E

Measurements

Load (P)
Settlement (ρ)
Horizontal stress (σ_x)
Vertical deflection (δ)
Soil temperature (t^oC)

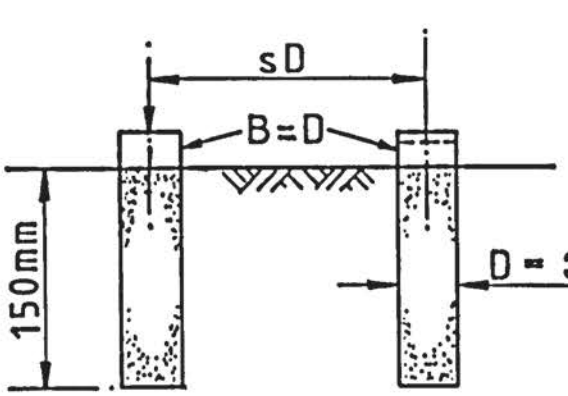

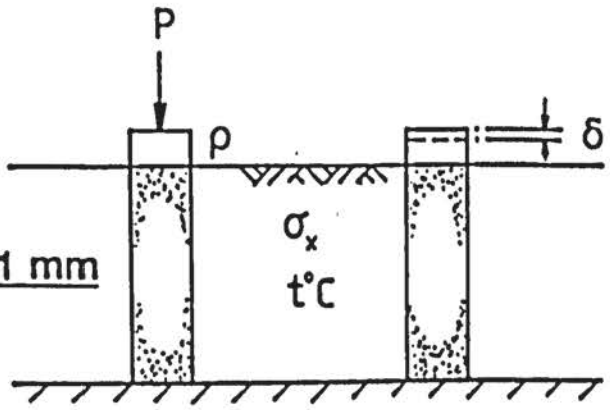

floating (F) end-bearing (E)

Foundation	s	Test Numbers (F)	(E)
Circular	1.25	IC1	IC1E
(one on each	1.5	IC2	IC2E
column)	2	IC3	IC3E
	2.5	IC4	IC4E
	3	IC5	IC5E

Measurements

Load (P)
Settlement (ρ)
Horizontal stress (σ_x)
Vertical deflection (δ)
Soil temperature (t^oC)

CONTAINER B

Schedule of compression interaction tests to determine vertical deflection of a foundation at distance sD from a column.

FIGURE 9.8

RADIOGRAPHS TAKEN AT ρ/B = 0, 0.2, 0.66 and 1.5 FOR ALL TESTS

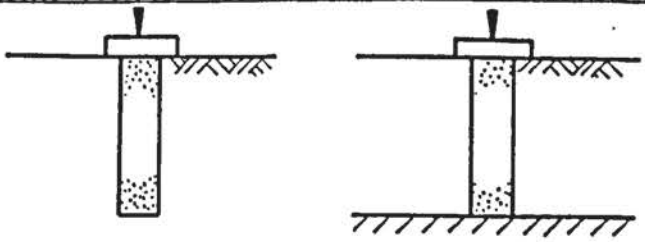

(F) (E)

Foundation	B	Test Numbers (Container A) Radiographic (F)	(E)	Compression (F)	(E)
Circular	38.02	XC2	XC2E	AC1	AC1E
	66.02	XC4	XC4E	AC4	AC4E

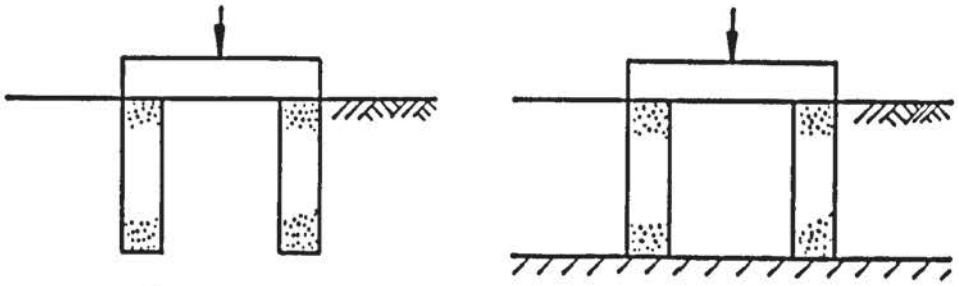

(F) (E)

Foundation	B(mm)	L(mm)	s	Test Numbers (Container A) Radiographic (F)	(E)	Compression (F)	(E)
Rectangular	38.16	95.2	1.5	XR2	XR2E	AR2	AR2E
	38.10	152.2	3	XR6	XR6E	AR6	AR6

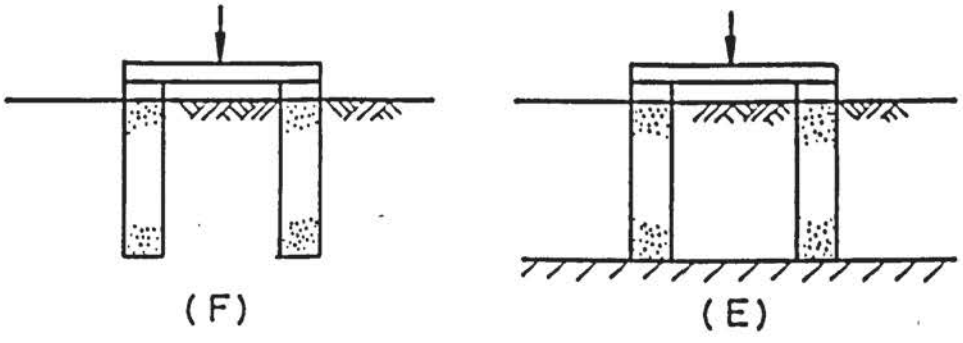

(F) (E)

Foundation	s	Test Numbers (Container A) Radiograph (F)	(E)	Compression (F)	(E)
2 Circular Isolated	1.5	XTC2	XTC2E	ATC2	ATC2E

Schedule of radiographic and compression tests for Container A.

FIGURE 9.9

CHAPTER 10

TEST PREPARATION AND PROCEDURES

10.1 INTRODUCTION

This chapter describes the preparation stages and procedures undertaken during the laboratory programme to achieve acceptable levels of accuracy and repeatability. The methods used were established and developed from preliminary laboratory work.

10.2 FILLING CONTAINERS

Lumps of clay, each about 150 g, were successively placed and kneaded in the containers, taking care not to trap large air voids or to overstress the horizontal pressure transducer. Container A was filled completely and then the two halves were separated using a cheese-wire cutter.

10.3 LEVELLING SURFACES

After filling, the clay surfaces were levelled with a machined Perspex or steel straight-edge, and covered with a protective 'Cling-Film' preventing moisture absorption by the glycerine. An example of the levelling process is shown in Plate 10.1.

10.4 FORMING VOID

With the appropriate Perspex template positioned on the levelled clay surface, the container was manoeuvered beneath the auger and the initial void formed. This was repeated for the number of voids required. An example is shown in Plate 10.2.

The voids were completed using the cutting tubes in conjunction with a small spirit level to maintain verticality. The tube was left in place while the adjacent void was prepared, so as to maintain the bore diameter. Tape was fixed to the cutting cylinders as a depth marker, shown in Plate 10.3. On completion each tube was carefully removed.

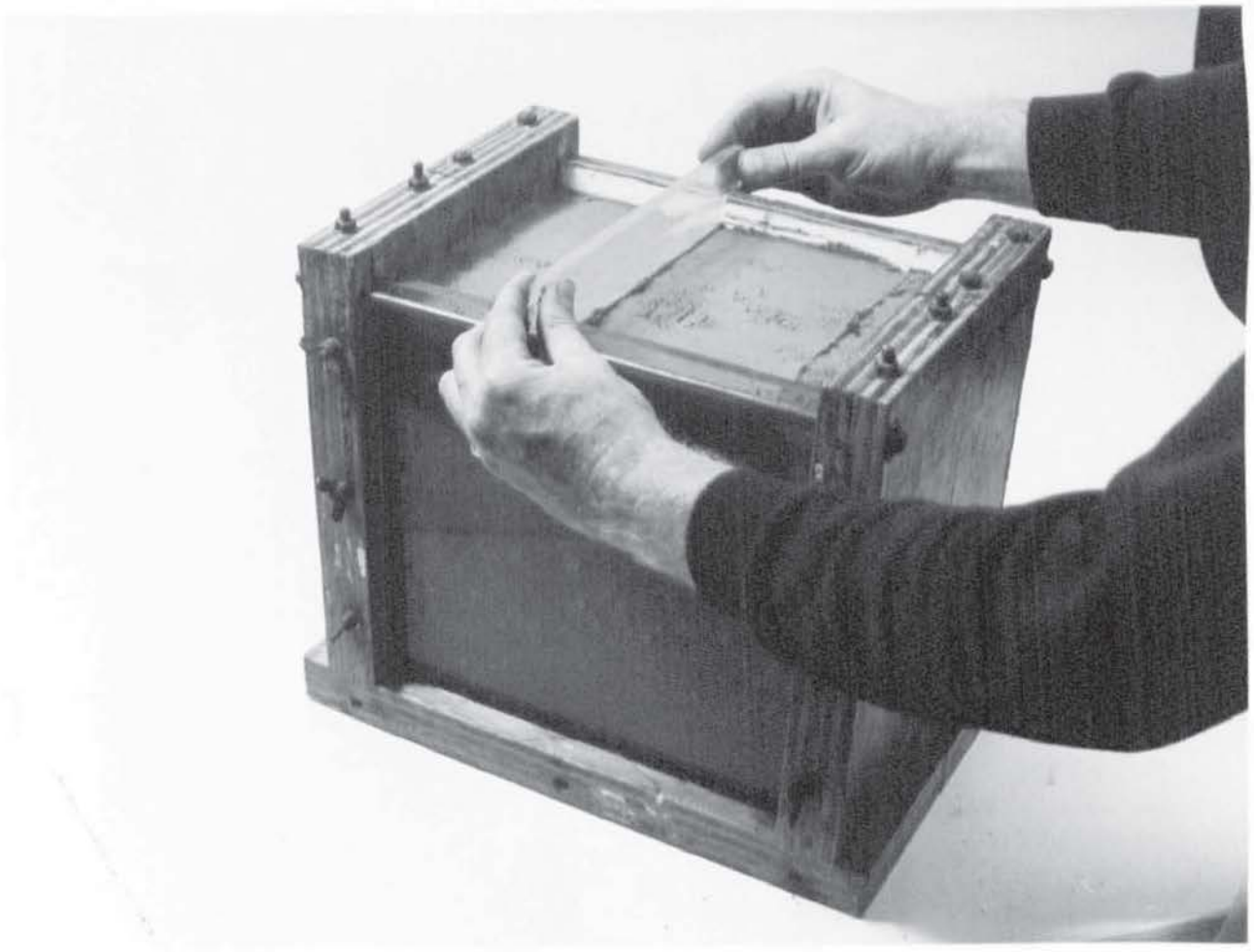

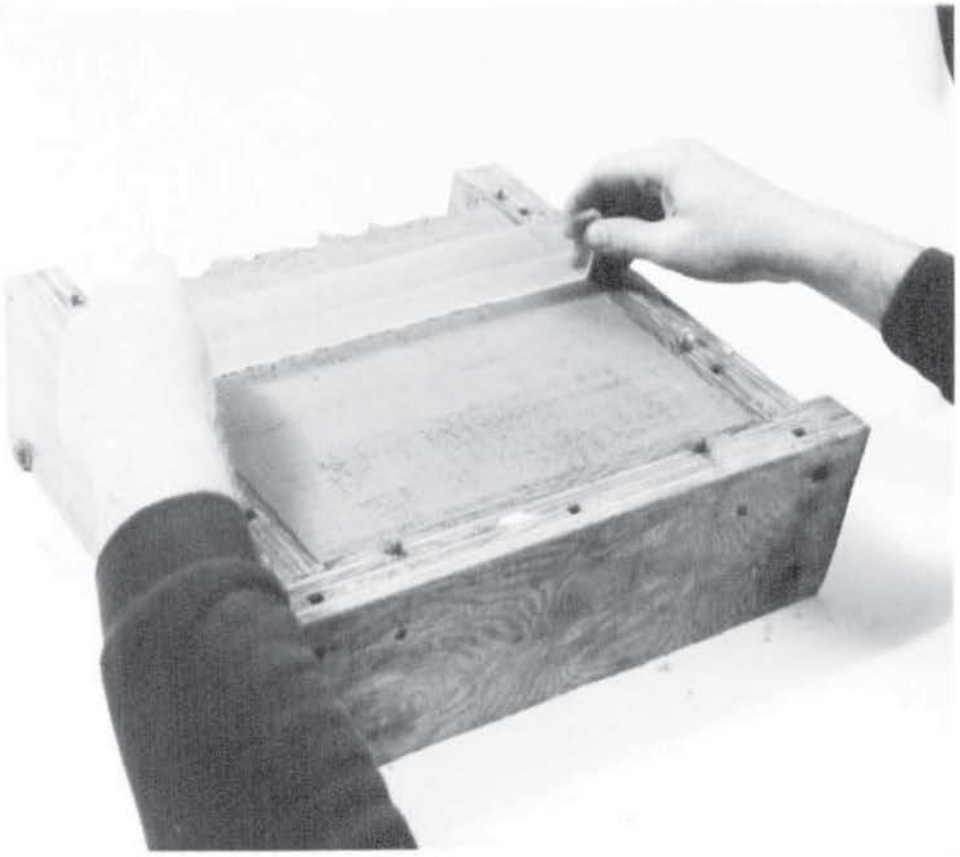

Levelling clay surface.

PLATE 10.1

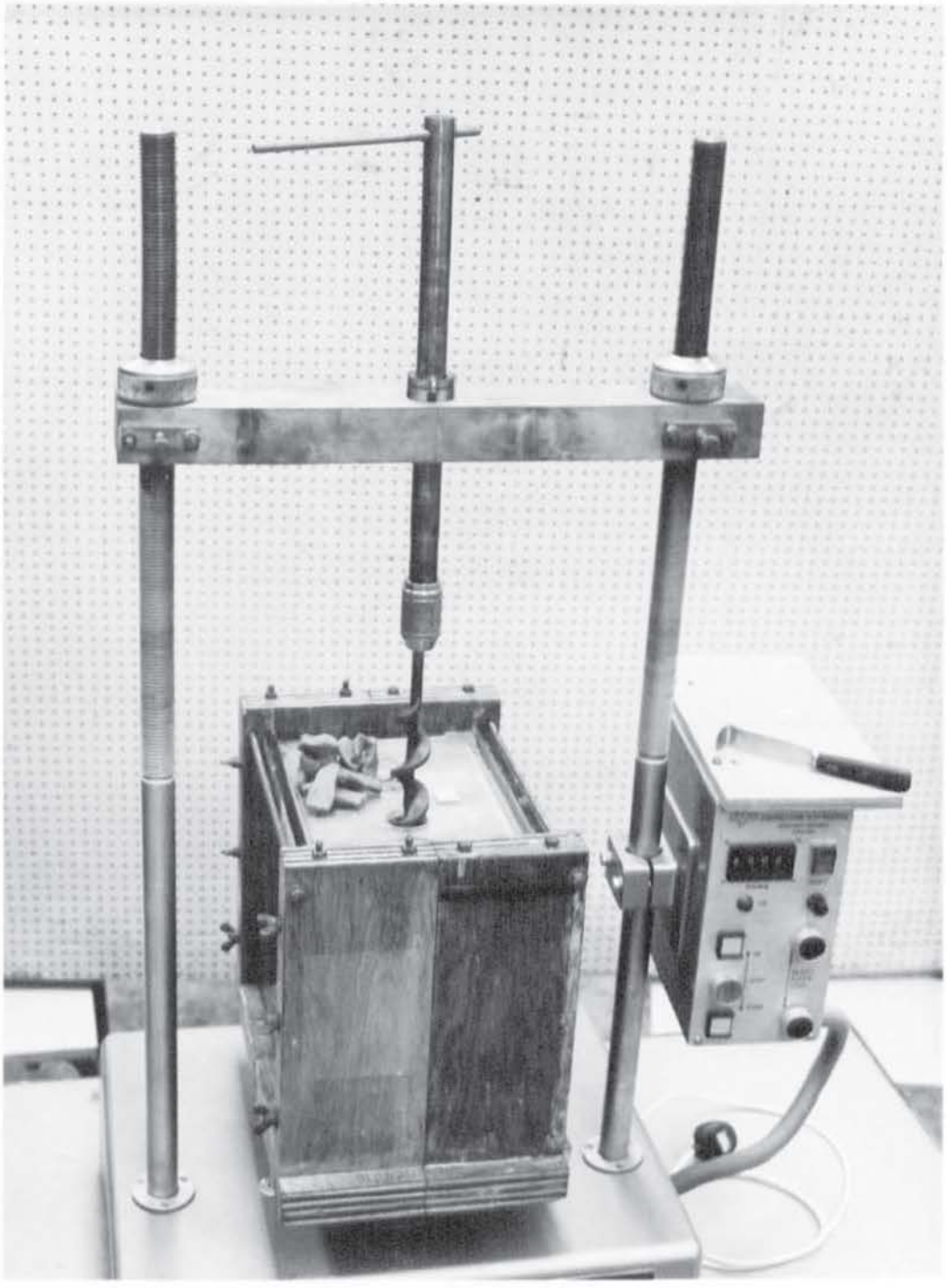

Forming column void with auger.

PLATE 10.2

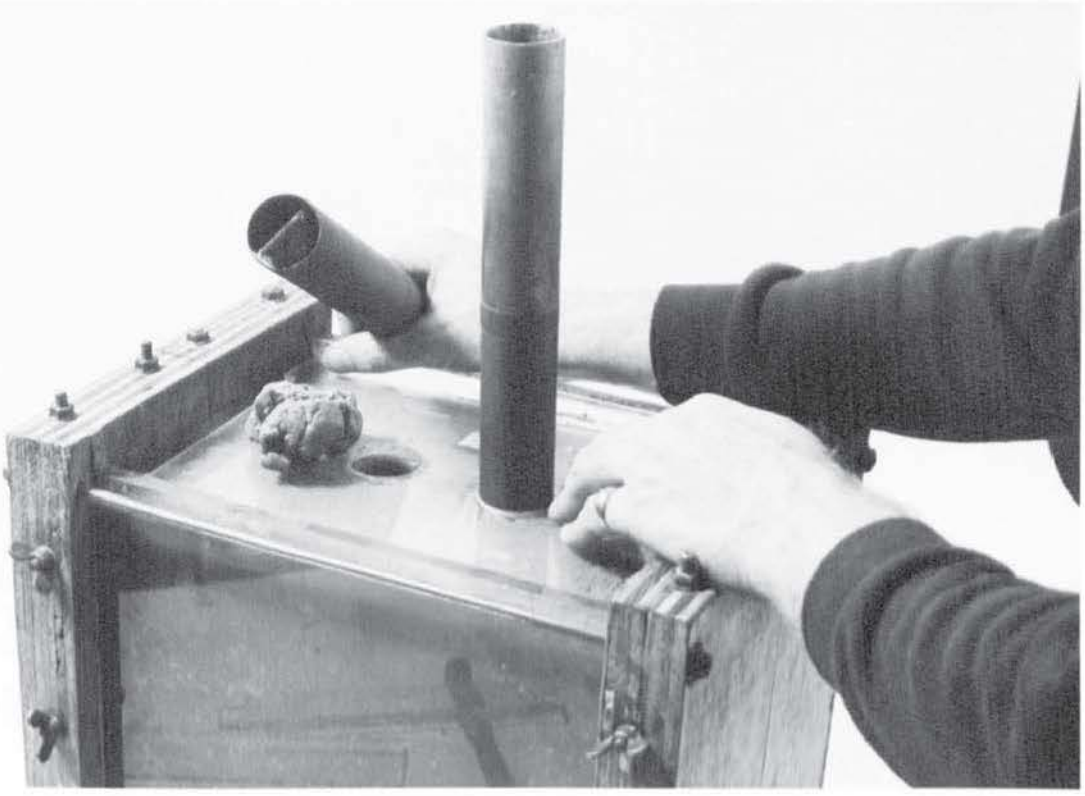

Completing column void using cutting tubes.

PLATE 10.3

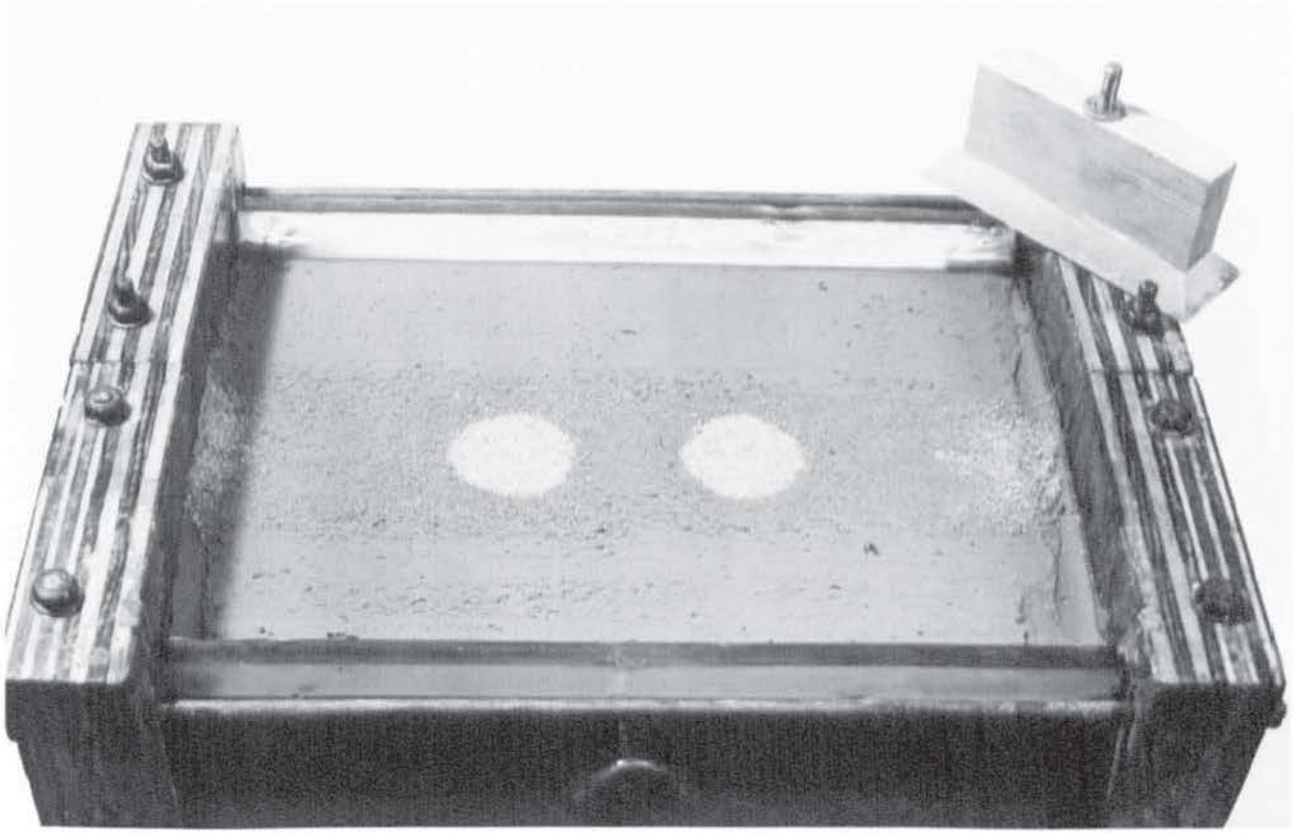

Level surface.

PLATE 10.4

During use of the auger or cutting tubes, any associated heave of the clay could generally be countered by applying hand pressure to the template in order to maintain a level clay surface. Sometimes, however, the surface needed to be re-levelled by gently skimming it with the straight-edge and re-using the cutting tubes. An iterative procedure was often necessary to achieve the desired result. This operation was critical to ensure uniform contact of the model foundations and clay surface.

10.5 FILLING VOID

After positioning the container beneath the sand hopper (shown previously in Plates 4.8 and 4.9) the voids were filled to about 5 mm above the clay surface. Levelling was achieved by a thin straight edge (a converted spatula) carefully drawn over the surface to give the result shown in Plate 10.4. This method was found more effective than using vacuum techniques.

10.6 SAND REMOVAL

After testing, the sand was removed by vacuum using equipment described by Hope (1979).

10.7 REPLACEMENT OF CLAY

After the removal of sand-contaminated surfaces using a spatula, the clay was replaced with stored material from the same batch.

10.8 HORIZONTAL STRESS

As expected, the horizontal stress (σ_x) in the clay was found to increase as a result of the clay replacement and column forming process. It was found, however, that the stress level would relax to a nominally average value within a period of 20-30 minutes. Tests were not undertaken until at least 30 minutes after the columns had been formed or until the stress level had stabilised to about its nominal value.

10.9 POSITIONING CONTAINERS

The containers were positioned with respect to the centre line of the loading tube by means of a Perspex template. The centre line was common to the templates used to form the column voids.

10.10 INITIAL TRANSDUCER READINGS

All transducer bridges were balanced prior to taking their initial zero readings. The bridge circuit of the horizontal stress transducer was balanced prior to installation into the container to eliminate stress changes caused by fixing. After installation, the initial zero reading was taken before filling the container with clay.

Initial zero readings of the load transducers were taken when they were in a free-standing unloaded position. After their assembly onto the top of the loading tube, the model foundation was gently brought into contact with the soil surface and any vertical play was taken up by the fine-screw cap adjuster, shown previously in Figure 4.6. At this time a secondary (initial load) reading was taken simultaneously with the initial zero reading of the displacement transducer(s).

The contact pressure transducers had their initial zero-load readings taken when the foundation containing them had been attached to the loading tube, prior to contact with the soil surface.

10.11 PLACEMENT OF LEAD-SHOT

To ensure a level surface on which to place the lead-shot the two halves of container A were separated after the column voids had been made and the two vertical surfaces for each half levelled. This caused some distortion of the surfaces in the horizontal plane and to the column voids, so the two halves were re-assembled and the levelling and void making procedure repeated. This process was iterated until the required result was obtained.

Using the Perspex template, the lead-shot was dropped onto the surface of one of the container halves as shown by Plate 10.5. The other half was then carefully repositioned, using the

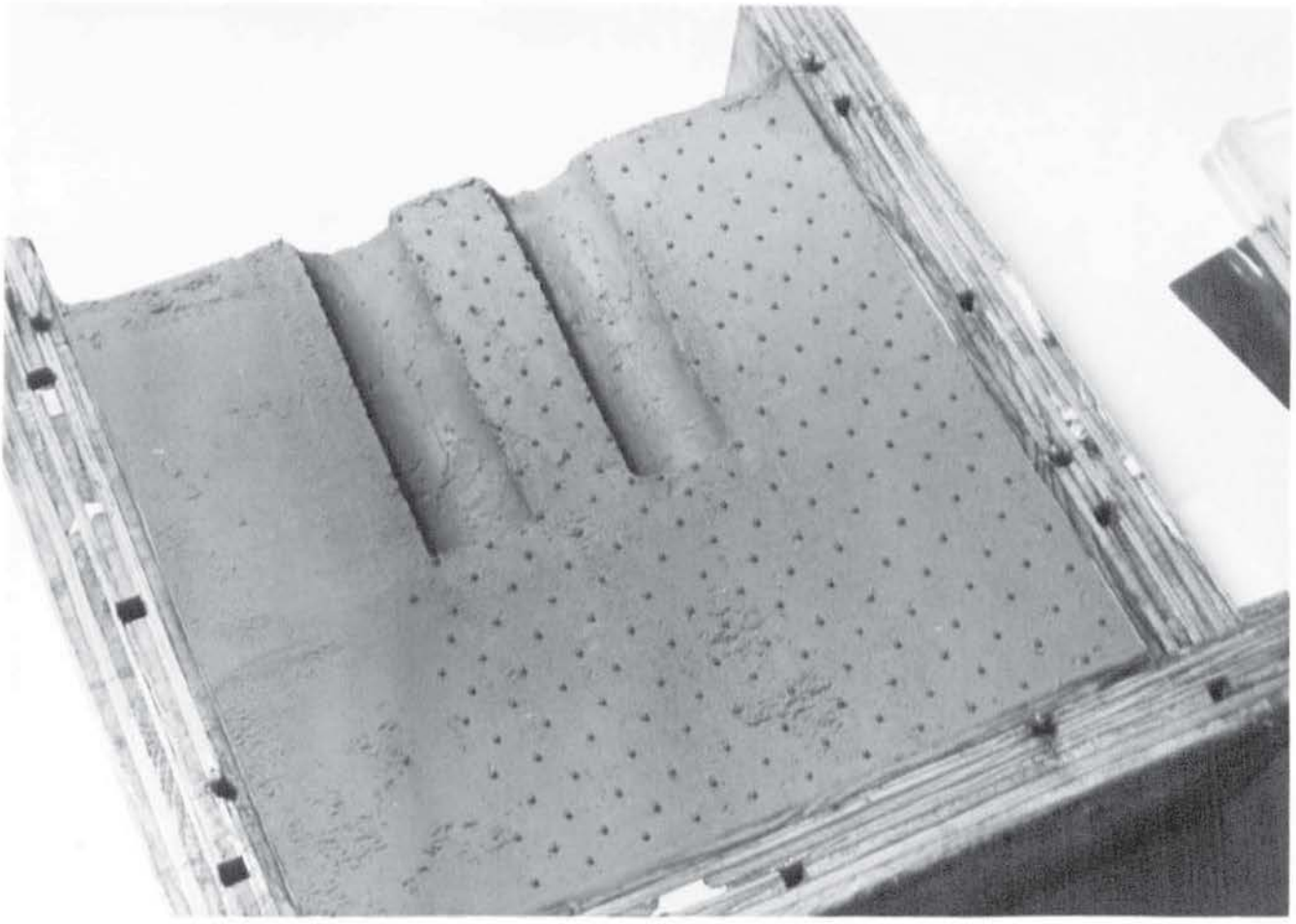

Placement of lead-shot.

PLATE 10.5

metal dowels, and the assembly secured.

Lead-shot was positioned in the granular column by filling the column void in stages as shown in Figure 10.1. The last two lead-shot were placed after careful final trimming of the sand surface level with that of the clay.

10.12 RADIOGRAPHY

With container A securely clamped to the platen of the compression machine (shown previously by Figure 4.3), the assembly was positioned and maintained at a constant distance from the X-ray set. Using surveying equipment, the film and shot planes were aligned as close to 90^{o} as possible to the X-ray beam axis. The height of the X-ray set was adjusted, using the Minilift, to position the beam axis central to the plane of the lead-shot. A radiograph was taken prior to loading the soil surface. When the required displacement increment was reached the compression machine was stopped and a radiograph was taken after the X-ray set had been raised by an amount corresponding to the upward movement of the platen.

10.13 TEMPERATURE READINGS

Temperature readings from four calibrated thermocouples were taken at the start and end of each test and the mean taken. Two of the thermocouples were positioned about 50 mm below the clay surface, at opposite ends of the container, with the other two approximately 200 mm below surface level. When the average temperature difference between any two thermocouples exceed $\pm 2^{o}C$ (corresponding to $c_u \pm 5\%$) the test was abandoned.

10.14 LINEAR BEARING

The linear bearing was lubricated often with a light machine oil, which contained a friction reducing additive (Molyslip).

Time taken to fill column void with sand from hopper = 3.5 minutes (average of 3 Tests)

Therefore: 150 mm height in 3.5 minutes.

= 10 mm height in 14 seconds.

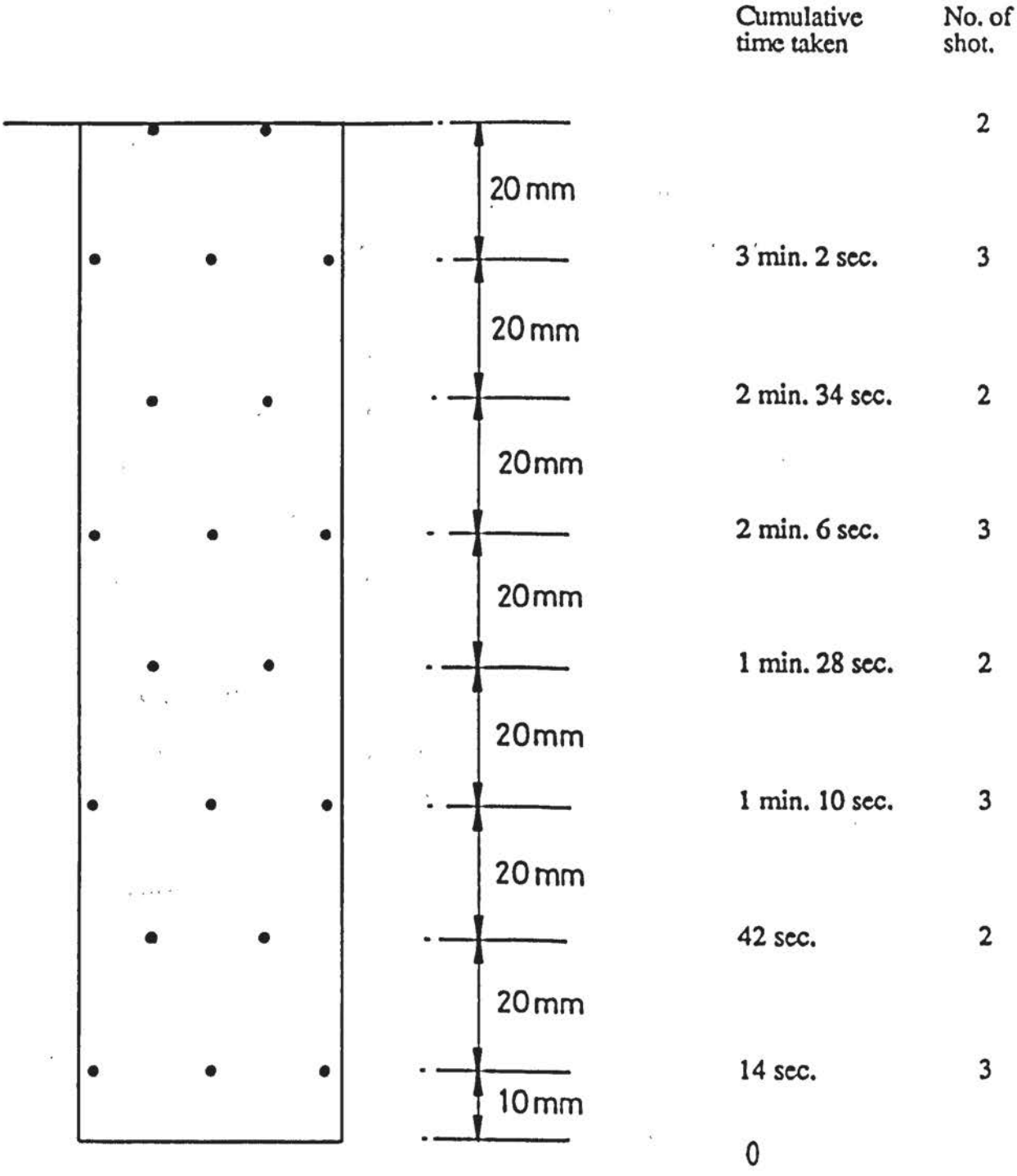

Placing of lead-shot in the column by staged filling.

FIGURE. 10.1

CHAPTER 11

CORRECTIONS, CONSTANTS AND EXPOSURE

11.1 INTRODUCTION

This Chapter describes the nature and application of corrections and constants used during the analyses of the compression tests and the determination of the radiographic exposure.

11.2 STANDARD TEMPERATURE

The mean temperature of the clay during the laboratory programme was 23.6°C with an estimated standard deviation (s) of 0.9°C. The X-ray room temperature was controlled and the clay temperature during the radiographic work was recorded as 23 ± 0.1°C. On this basis 23°C was adopted as for standard clay strength (c_{us}).

11.3 STANDARD CLAY STRENGTH

During the main laboratory programme (about 18 months), quick-undrained triaxial tests (σ_3 = 25 kPa, rate = 2.5 mm/min.) were regularly performed on samples of the clay used, and showed the material to maintain a mean value of c_{us} of 11.35 kPa (corrected to 23°C) with s = 0.42 kPa.

11.4 HORIZONTAL STRESS

The mean initial horizontal stress (σ_{xo}) measured in the clay from all the tests during the laboratory programme was 5.1 kPa with s = 1.85 kPa.

11.5 MINIMUM RATE OF TEST

During small scale foundation tests in remoulded wet clay, Meigh (1950) found that the ratio:

$$\frac{\text{average bearing pressure at failure}}{\text{undrained cohesion}} = \frac{q_f}{c_u}$$

increased with a slow rate of penetration, as shown in Figure 11.1(a). Meigh considered this increase was due to consolidation, with the variations of individual foundations being accounted for by differing lengths of the pore-water drainage path. The effect is emphasised by the graph in Figure 11.1(b) which brought q_f/c_u for all the sizes onto one curve. It was concluded that a test rate x foundation diameter greater than 0.2 inch^2/minute was needed to avoid consolidation effects.

Tests were carried out using the author's clay and a 25 mm diameter foundation. The results shown in Figure 11.1(c), indicated a minimum rate of penetration (R) x foundation width (B) of 50 mm^2/minute was required to avoid consolidation effects. The smallest magnitude of B used in the laboratory test programme was 25 mm. This corresponded to a minimum test rate of 2 mm/minute, which compares with 5.16 mm/minute (for B = 25 mm) obtained by Meigh for the wet clay. This result is not unexpected since glycerine is more viscous than water and so would offer greater resistance to expulsion from the soil pores.

A normal test rate of 5 mm/minute was chosen, which gave the R x B range shown in Figure 11.1(c), for the foundation sizes used.

11.6 VISCOSITY CORRECTION

The effect of the rate of shearing on the shear strength of clay has been shown in Section 2.4.10. This aspect is also displayed by all the test results in Figure 11.1, whereby the resistance of the clay to penetration by the foundation increases with the rate of penetration. Meigh (1950) used a correction for his foundation load test results to allow for what was termed "viscous effects".

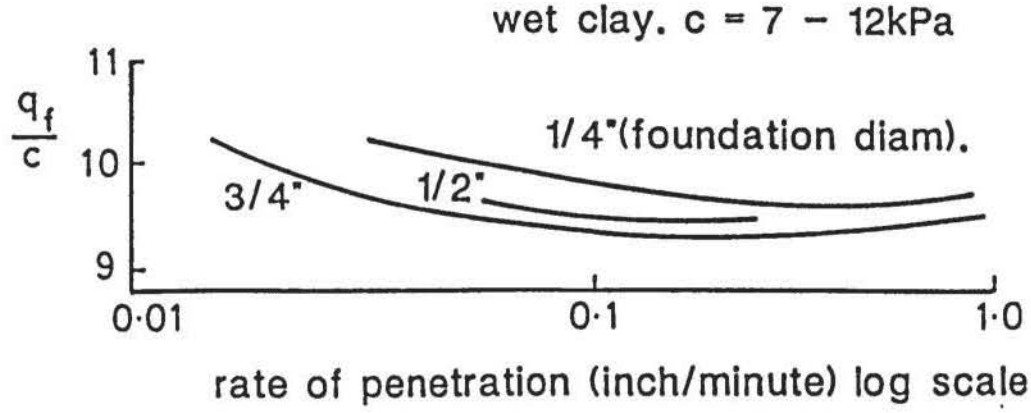

Variation of q_f/c with log rate of penetration of various sized foundations (after Meigh, 1950).

FIGURE 11.1(a)

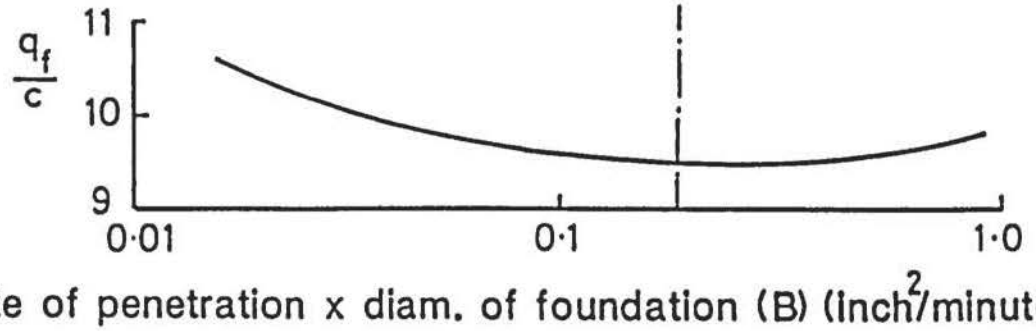

Variations of q_f/c with log rate of penetration x diameter of foundation for various sizes (after Meigh, 1950).

FIGURE 11.1(b)

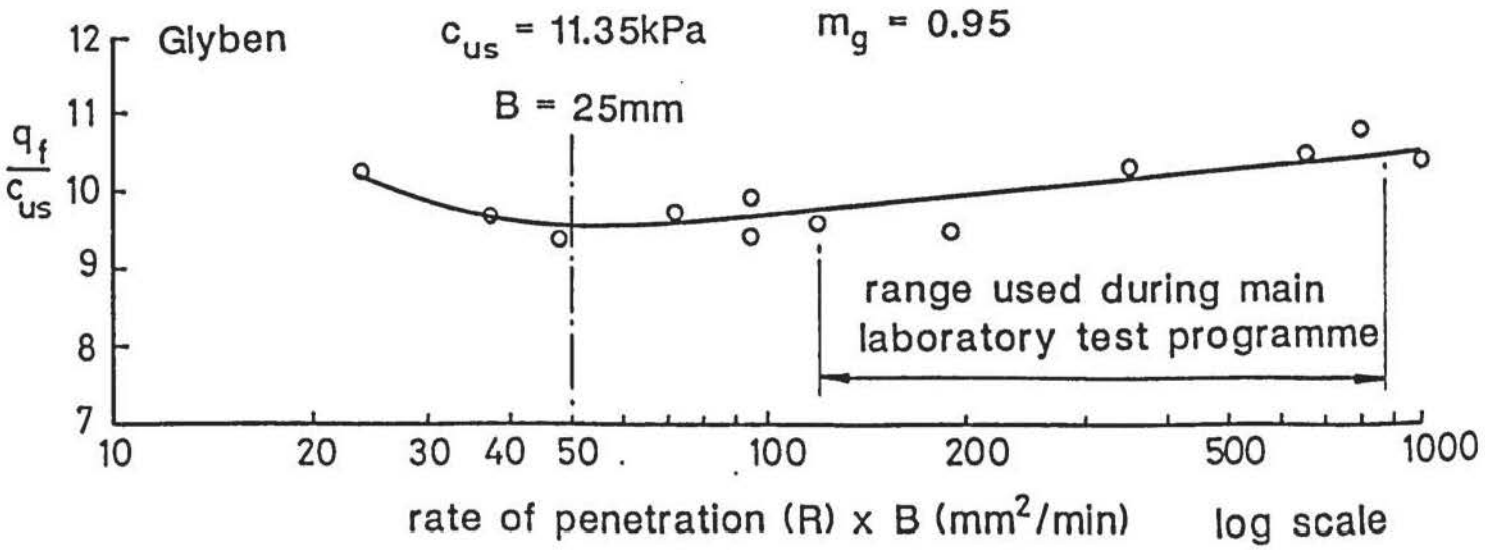

Variation of q_f/c_{us} with log rate of penetration x foundation width for glyben.

FIGURE 11.1(c)

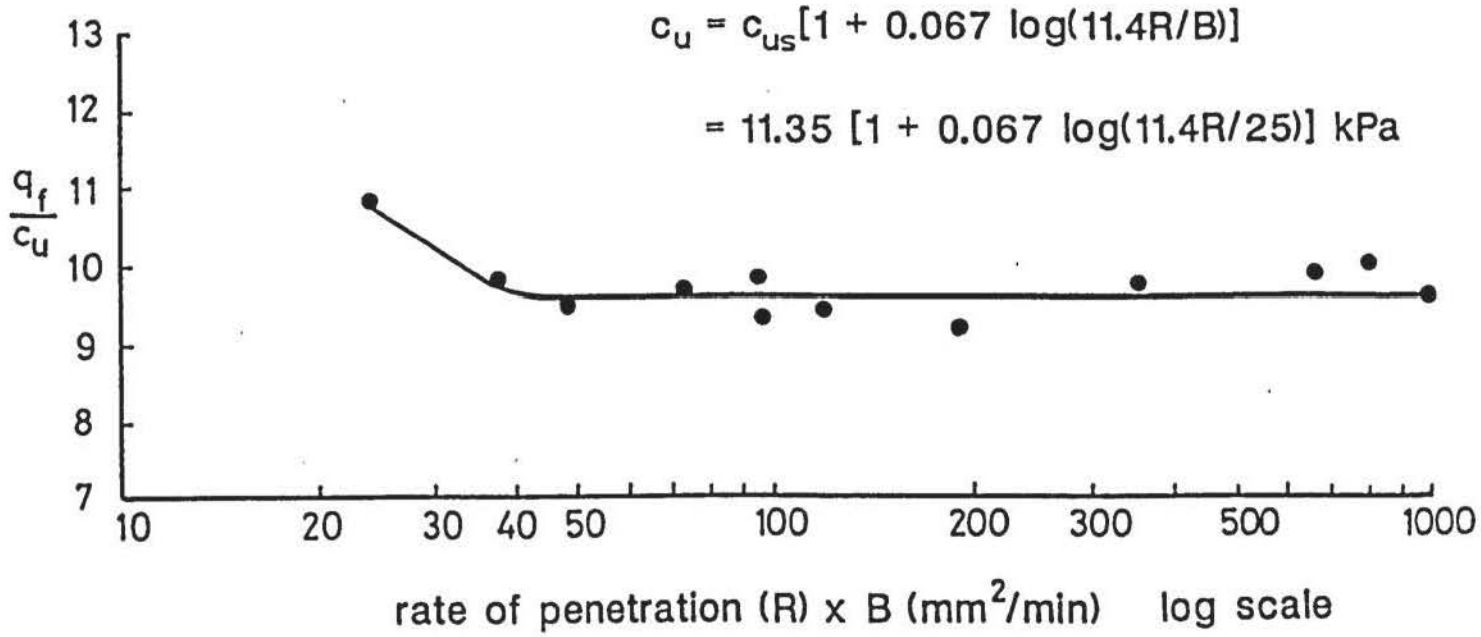

Corrected variation of q_f/c_u with R x B from Figure 11.1(c).

FIGURE 11.2

Foundation System	UNCORRECTED q/c_u @ ρ/B = 0.5		@ ult		CORRECTED q/c_u @ ρ/B = 0.5		@ ult	
	R(mm/min)				R(mm/min)			
1 column (D=38.1)	s	52.8	s	52.8	s	52.8	s	52.8
B = 25 mm diam.	15.5	16.0	27.4	28.4	15.1	14.6	26.8	26.0
38	15.7	17.5	21.6	23.1	15.5	16.2	21.4	21.4
50	12.7	14.2	17.4	20.1	12.7	13.2	17.3	18.7
60	11.6	12.7	15.5	17.1	11.6	11.9	15.4	16.0
2 column B=38mm sD = 2.5D	10.6	11.9	14.1	15.0	10.5	11.0	13.9	13.9
sD = 1.25D	12.6	13.6	17.3	18.5	12.5	12.6	17.1	17.2

Viscosity corrections when applied to granular columns.

FIGURE 11.3

It was necessary to decide which rate of foundation loading corresponded to the standard rate of strain used in the triaxial test to enable the conjugate c_u to be determined. The correction is derived in Appendix K and is of the form:

$$c_u = c_{us} [1 + 0.067 \log (11.4 R/B)] \qquad (11.1)$$

By applying this correction to the results shown in Figure 11.1(c), the curve in Figure 11.2 was produced.

The correction was found to be valid whether or not the granular columns were present. Tests with single and double columns were carried at rates of 5 and 52.8% mm/minute. The results are tabulated in Figure 11.3.

11.7 APPLICATON OF CORRECTIONS

In any test with a clay temperature (t), a foundation (of width B) applied an average pressure (q) at a rate of penetration (R). Using Eqns. 2.4 and 11.1, the standard clay strength (c_{us} = 11.35 kPa) was corrected for temperature and viscosity effects to give the compression test in-situ strength c_u. This enabled the ratio q/c_u to be determined. It was assumed that values of this ratio would be the same at any temperature t for a given penetration rate, so :

$$\left[\frac{q}{c_u}\right]_R^{t^\circ C} = \left[\frac{q}{c_u}\right]_R^{23^\circ C} \qquad (11.2)$$

Hence, by only correcting the in-situ clay strength c_u for viscosity effects (Eqn. 10.1), values of q for a clay strength (c_{us}) at the standard temperature of 23°C could be determined:

$$q^{23^\circ C} = \left[\frac{q}{c_u}\right]^{t^\circ c} x\, c_{us} \qquad (11.3)$$

Since the magnitude of the horizontal stress (σ_x) is some function of the magnitude of q,

that is $\sigma_x = f(q)$

the values of the ratio σ_x/q were also taken to be the same at any temperature t for a given penetration rate:

$$\left[\frac{\sigma_x}{q}\right]^{t^\circ C} = \left[\frac{\sigma_x}{q}\right]^{23^\circ C}$$

giving:

$$\sigma_x^{23^\circ C} = \left[\frac{\sigma_x}{q}\right]^{t^\circ C} \times q^{23^\circ C} \qquad (11.4)$$

as a first approximation.

11.8 RADIOGRAPHY

11.8.1 Focus-To-Film Distance

Using a focal spot size (f) of 4 mm x 4 mm, and having determined the lead-shot-to film distance (d) as 133.5 mm, Eqn. 3.2 gave a minimum focus-to-film distance (d_i) of 2403 mm to restrict penumbral unsharpness of the lead-shot images. For operational reasons, however, the acutal distance was set to 2110.5 mm. Although this increased the penumbra by 0.02 mm (Eqn. 3.1), the effect was found to be insignificant in practice.

11.8.2 Exposure

The film speed, focus-to-film distance, absorption coefficient of the soil and container and the tube current (12 mA) were constants. The radiographic quality was dependent upon an optimum combination of the X-ray tube kV and time of irradiation. Because intensifying screens, were used, energy levels of over 110 kV were necessary. By a process of trial and error, an exposure of 24 mA minutes at 130 kV with a 0.1 mm copper filter was found to be suitable.

11.8.3 Lead-Shielding

During the radiographic work it was found that lead-shielding placed at the sides and on the top of the container impaired the radiographic contrast. This was seemingly due to the

internal scattering of radiation. They were subsequently discarded.

11.9 ORIGIN CORRECTION

When a model foundation was brought into contact with the clay or column/clay surface, and the vertical play taken up by the fine adjustment cap, a small bedding pressure was induced. This produced q/c_u values of up to 0.5 when $\rho = 0$.

During graphical plotting of the results an origin correction was applied which generally followed the procedure used in the oedometer test.

CHAPTER 12

RESULTS AND DISCUSSION

12.1 INTRODUCTION

This Chapter presents the results of the laboratory compression tests and radiographic work, mainly in graphical form. The order of presentation is in increasing complexity of column-soil-foundation behaviour beginning with a single isolated column in floating and end-bearing conditions, and ending with a small group of up to five columns loaded by a rigid square foundation. The end-bearing case is analogous to a shallow clay layer overlying an incompressible stratum, which in the laboratory consisted of a concrete plinth placed in the bottom of the clay containers.

A single isolated column is the basic unit of any group and the behaviour of floating and end-bearing columns is given in this study to provide a reference for comparison with numbers of columns in various configurations and subject to more complex boundary conditions.

References made to ultimate stress, or load, are intended to relate to the condition at which a peak load is reached through the strain-controlled deformation used in the tests. Working stress, or load, is defined as one-third of ultimate and implies a factor of safety of 3.

12.2 REPEATABILITY

Examples of results from a number of compression tests performed at different times on both the clay only and on a single isolated granular column, using a 38 mm nominal diameter model foundation, are shown in Figure 12.1. The variation of the applied average foundation pressure q divided by the undrained cohesion of the clay c_u is plotted against settlement ρ expressed as a proportion of the foundation width B.

Providing that the strictest care was taken at the preparation stages and with the experimental procedure, repeatability was of a high order.

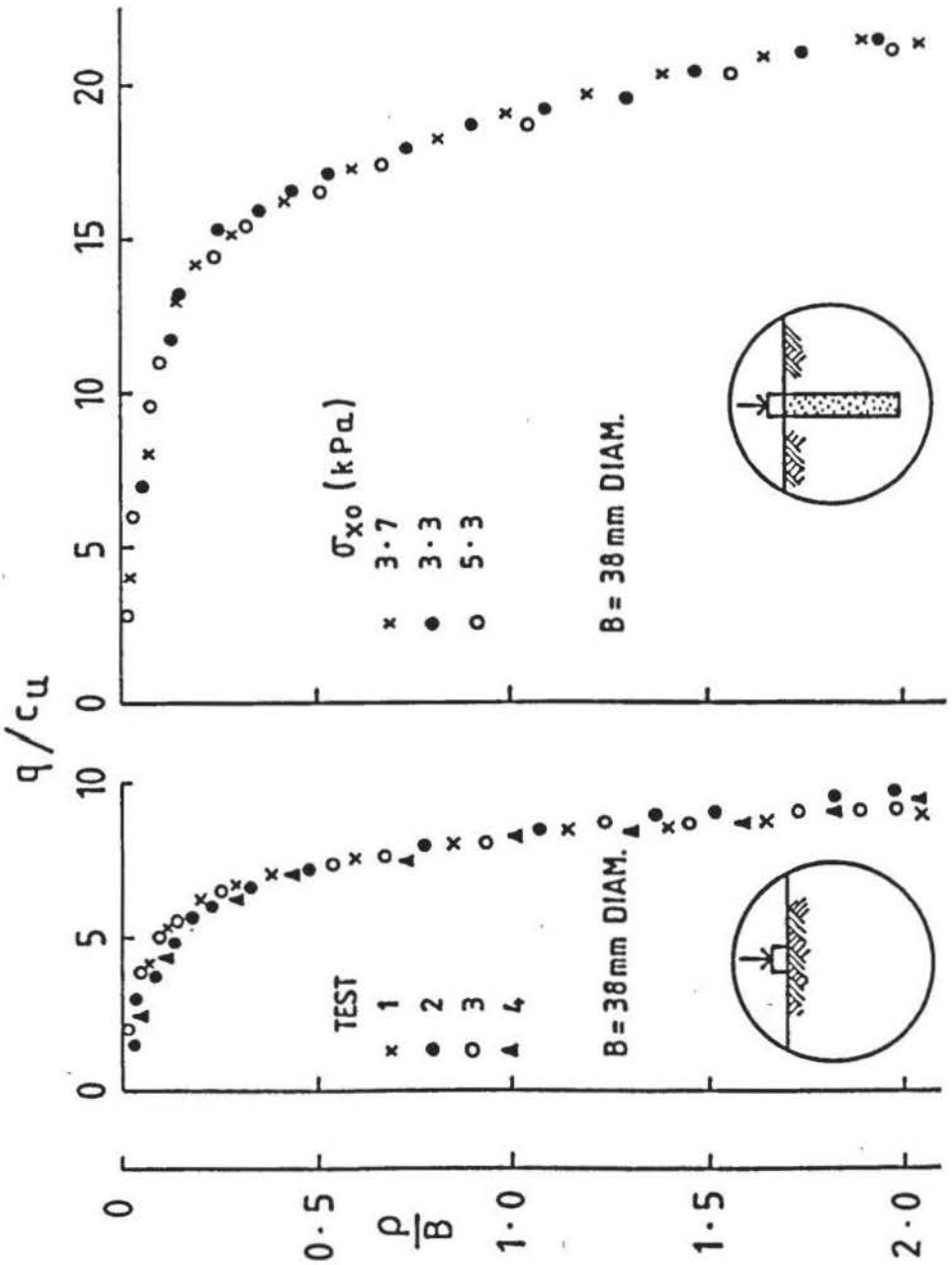

Examples of the repeatability of foundation compression tests on clay and on a single column performed at different times.

FIGURE 12.1

12.3 SINGLE COLUMNS

12.3.1 Boundary stresses and settlement

Typical boundary stress-settlement characteristics of a single isolated column in floating (F) and end-bearing (E) conditions loaded by a rigid model foundation nominally the same diameter as the column (Test Nos. C2 and C2E) are shown in Figure 12.2, as the variation of q/c_u with ρ/B. For comparison, curves for the same foundation on the clay only, without a column, are also given.

The increase in horizontal stress ($\Delta\sigma_x$), above the initial horizontal stress (σ_{xo}), divided by the applied average foundation pressure is also plotted against ρ/B. As with all the compression tests, horizontal stress in the clay was measured at the container boundary 1.57D below the initial-clay surface. Because the foundation applying the pressure moved downwards relative to the fixed measurement point, the $\Delta\sigma_x/q$ curve is analogous to 'influence lines' in structural mechanics.

The F column shows an ultimate q/c_u value of 21.5 occurring at $\rho/B \approx 2.25$ with the working stress value of $q/c_u \approx 7.5$ at $\rho/B \approx 0.05$. The E column, however, gives no ultimate condition, with q/c_u continuously increasing with ρ/B. By definition, a working stress cannot be directly obtained from this case but for the purposes of this study the working stresses (or loads) derived from the F columns will also apply to the E columns.

The original horizontal stress σ_{xo} (when $q/c_u = 0$) was 5.1 kPa and 4 kPa for the F and E columns, respectively. The $\Delta\sigma_x/q$ characteristics are similar for both cases and have a common maximum of about 4%, with this occurring nearer the surface for the F column when $\rho/B \approx 0.3$. This suggests that the capacity of the columns to transfer vertical load laterally reaches a peak at or before this stage of deformation and decreases thereafter.

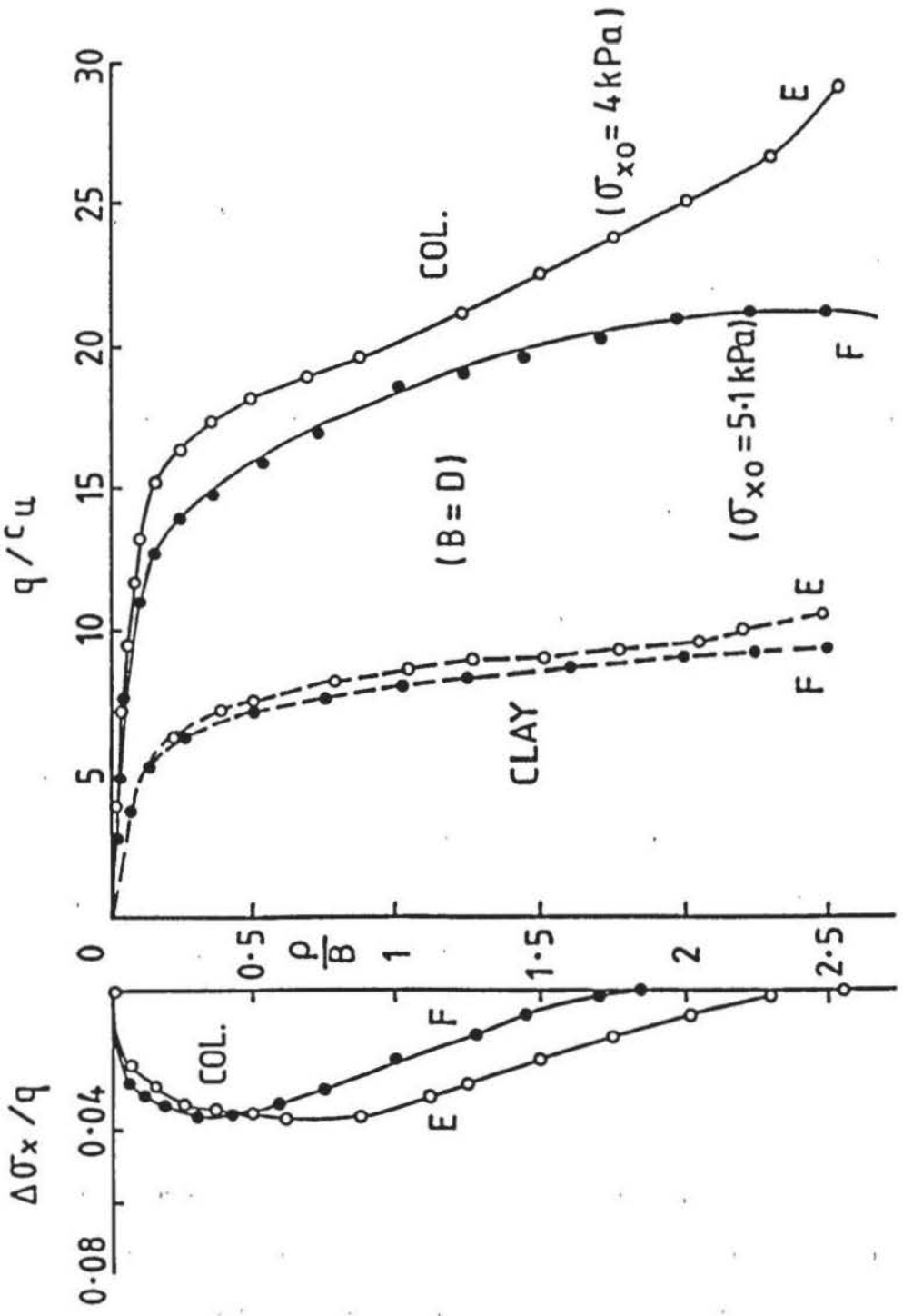

Typical variation of vertical stress q/c_u and horizontal stress $\Delta\sigma_x/q$ against settlement ρ/B for a foundation (B=D) on clay and on a single isolated column in floating (F) and end-bearing (E) conditions.

FIGURE 12.2

The E column sustains greater applied pressure, for the same settlement, than the F column. Conversely, for the same bearing pressure, settlement at the top of the column is less. The effect becomes increasingly prominent beyond working stress. The improved bearing capacity and settlement characteristics of the E column are emphasised by the variation of the bearing pressure of the E column q_E divided by the bearing pressure of the F column q_F at conjugate values of ρ/B, shown by Figure 12.3. Similarly, the settlement of the E column ρ_E divided by the settlement of the F columns ρ_F is plotted against conjugate of q/c_u. At small settlements within the working stress range ($\rho/B = 0 - 0.2$) the E column typically sustains 18% to 25% greater applied pressure which decreases to about 14% at $\rho/B \approx 0.6$ and remains roughly constant to $\rho/B \approx 1.5$, after which point the relative increase in bearing capacity begins to increase as the F column approaches its ultimate bearing capacity.

Settlement of the E columns (ρ_E) is 60% to 70% of the F column (ρ_F) up to about half the ultimate bearing capacity of the latter, after which there is a decrease (i.e. an improvement) to a minimum value of 35% of ρ_F at $q/c_u = 1.55$. Beyond this point, the settlement of the E column relative to the F column returns to its original level.

These effects are only apparent because similar characteristics are also produced by the foundation on the clay only, and they are attributable to the proximity of the container bottom in the E case modifying the foundation failure mechanism (e.g. Button, 1953; Reddy and Srinivasan, 1967).

12.3.2 Improvement

Improvement in the bearing capacity and settlement characteristics offered by a granular column is a measure of its increased performance relative to the bearing capacity and settlement characteristics of the clay under the same boundary conditions. This defines the bearing capacity improvement coefficient I_q as :

$$I_q = q_{COL}/q_{CLAY} \qquad (12.1)$$

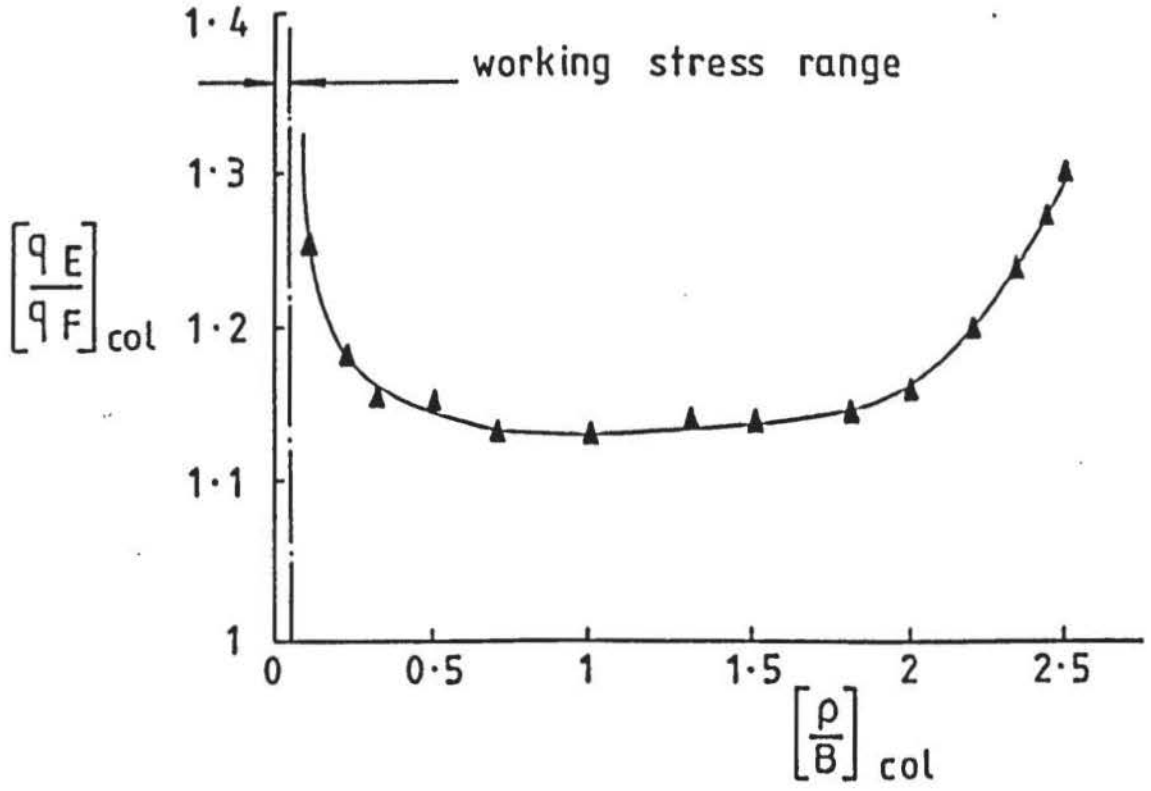

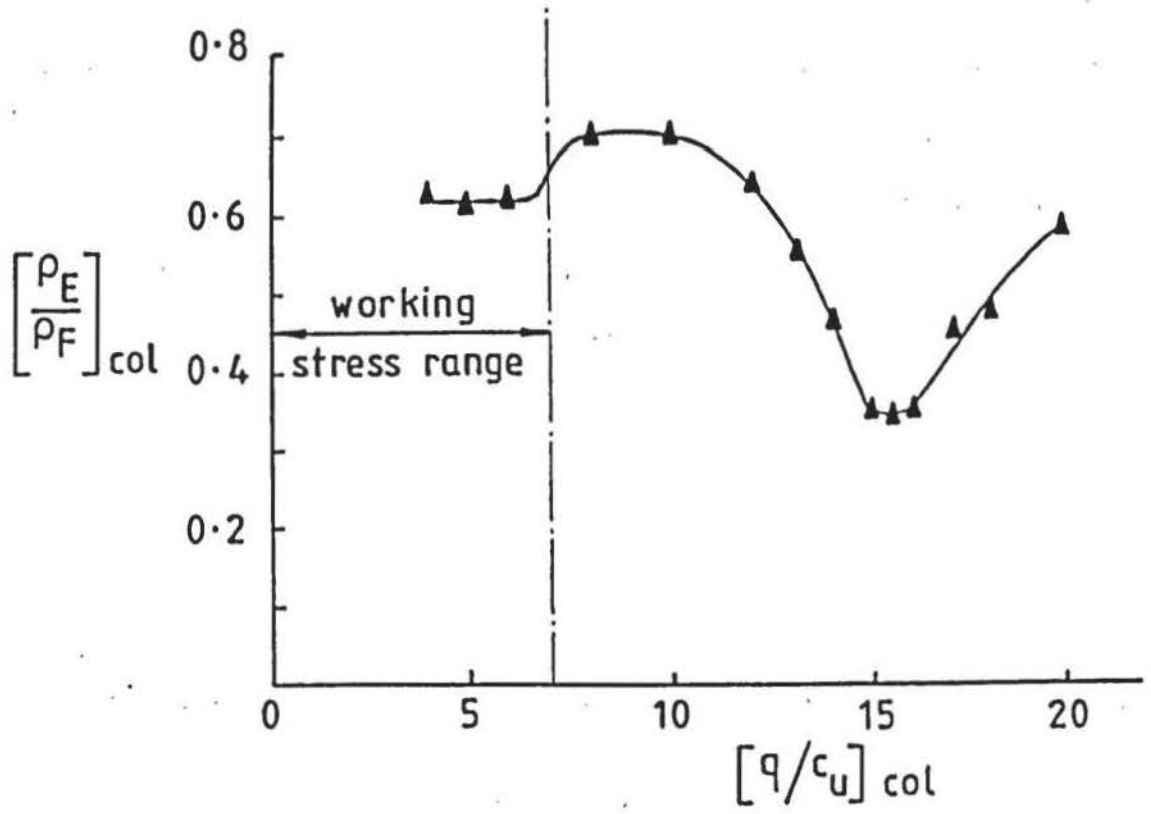

Typical apparent improved bearing capacity and settlement characteristics of E column relative to the F column.

FIGURE 12.3

where q_{COL} and q_{CLAY} are taken at the same value of ρ/B.

This relationship is analogeous to the stress concentration ratio $n = \sigma_{VC}/\sigma_{VS}$, defined by Equation 1.24. Because the vertical soil stress σ_{VS} is a measure of the vertical stress applied to clay between columns in a group, its interaction within the group may make $\sigma_{VS} \neq q_{CLAY}$.

Settlement improvement has been defined by Billam (1976), in Eqn. 1.31, as the settlement coefficient m :

$$m = \rho_{COL}/\rho_{CLAY} \qquad (12.2)$$

where ρ_{COL} and ρ_{CLAY} are taken at the same value of q/c_u.

The variation of I_q with ρ/B and m with q/c_u are shown in Figure 12.4a and 12.4b, respectively.

Significant improvements in bearing capacity and settlement are indicated, although they are both strongly dependent upon the applied pressure level. More potential improvement is offered by the E column and both cases show peak improvements of 125% (F) and 150% (E) which occur at ρ/B = 0.2 and 0.15, respectively, after which they reduce to roughly constant levels. Within the working stress range, however, improvement is restricted to 80% (F) and 125% (E). The shapes of the curves are similar to the triaxial stress-strain characteristics of the sand forming the columns, shown previously in Figure 2.1a.

Over the working stress range, where in practice settlement will be of most concern, a linear relationship between m and q/c_u is shown in Figure 12.4b. Improvement is in the range 40% to 90% and increases with bearing pressure.

12.3.3 Column yield

The comparison between the I_q - ρ/B curves and those of the triaxial stress-strain characteristics of the sand in conjunction with the peak values of $\Delta\sigma_x/q$ suggest yield of the column. By re-plotting q/c_u against ρ/B on a larger scale for the F and E columns using more of

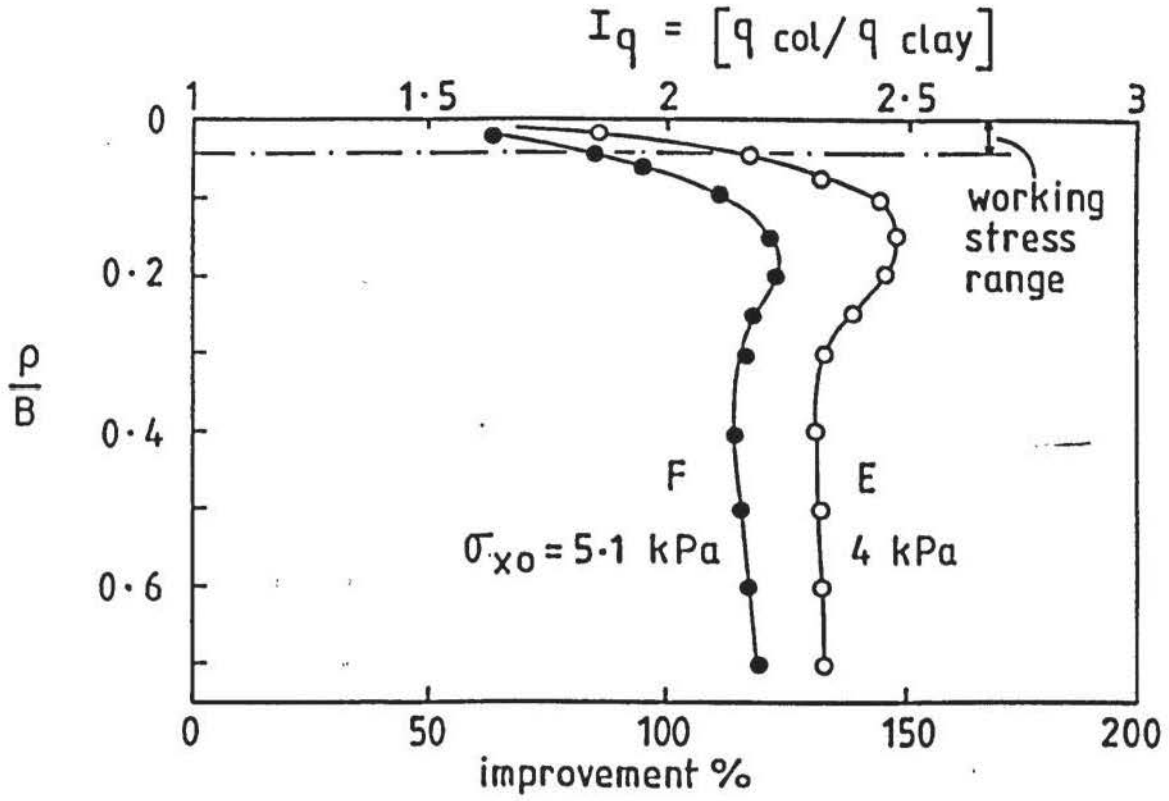

Typical bearing capacity improvement curves for a single isolated column in F and E conditions.

FIGURE 12.4a

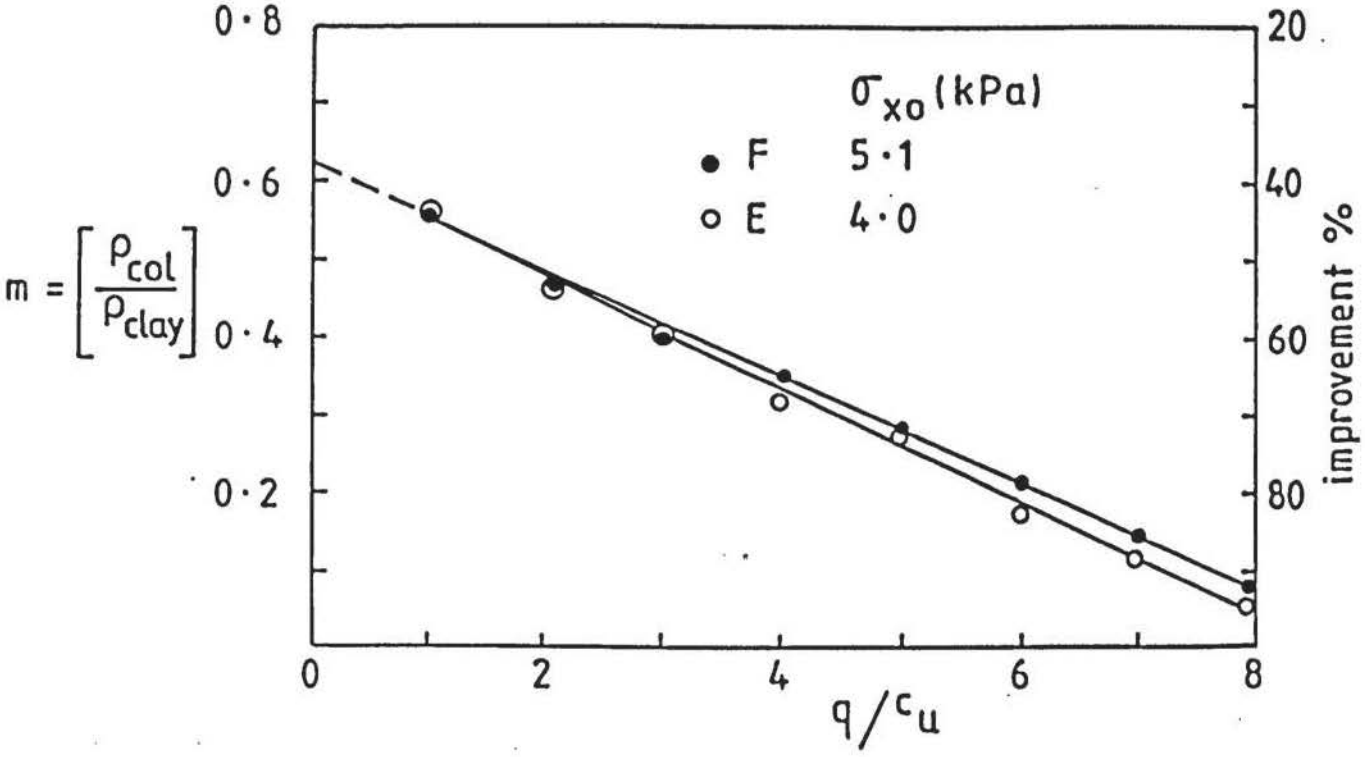

Typical settlement curve for a single isolated column in F and E conditions.

FIGURE 12.4b

the recorded measurements, the result shown in Figure 12.5 was obtained. Yield plateau are evident for both cases, occurring between ρ/B = 0.2 - 0.25 (F) and 0./2 - 0.3 (E), being more pronounced in the E case. These stages of deformation concur with those of peak $\Delta\sigma_x/q$ (accounting for stress-lag in the clay), I_q and ρ_E/ρ_F. After yield, the vertical pressure increases with vertical deformation.

In large-scale field tests, Vautrain (1978) observed the same effect of column yield which leads to a significant increase in the rate and magnitude of settlement. For structural loads this situation would be unacceptable, but because the yield stresses are about twice the working stress this phenomenon is not a critical one in this instance.

The yield stresses q/c_u = 13.5 (F) and 16 (E) are those at which plastic flow has been initiated and the stress-settlement behaviour stems from the non-homogeneous deformation which begins at the foundation-column interface and propagates through the column and clay materials.

12.3.4 Column-Clay Distortion

Using the format established by Hughes and Withers (1974) in expressing the results of their radiographs, Figure 12.6 shows the pattern of radial and vertical distortion at vertical displacements of ρ/B = 0.2, 0.66 and 1.5, for F and E columns. Vertical displacement ρ/B = 0.2 corresponds to the position of column yield, with the latter two at stages of progressive shear failure.

Vertical displacement (v) was measured from the radiographic images of lead-shot positioned nominally at the centre of the column and the radial distortion u/r_o was obtained from the displacement (u), along the horizontal x-axis, of lead-shot at the column boundary divided by the initial column radius, r_o. The variations of v and u/r_o are shown against column depth Z divided by the initial column diameter D.

There is considerable vertical and lateral distortion, with the latter commensurate with bulging of the column at the top and rapidly reducing with depth. For the same vertical displacement, radial distortions of the E column are about 20% greater than for the F column. The

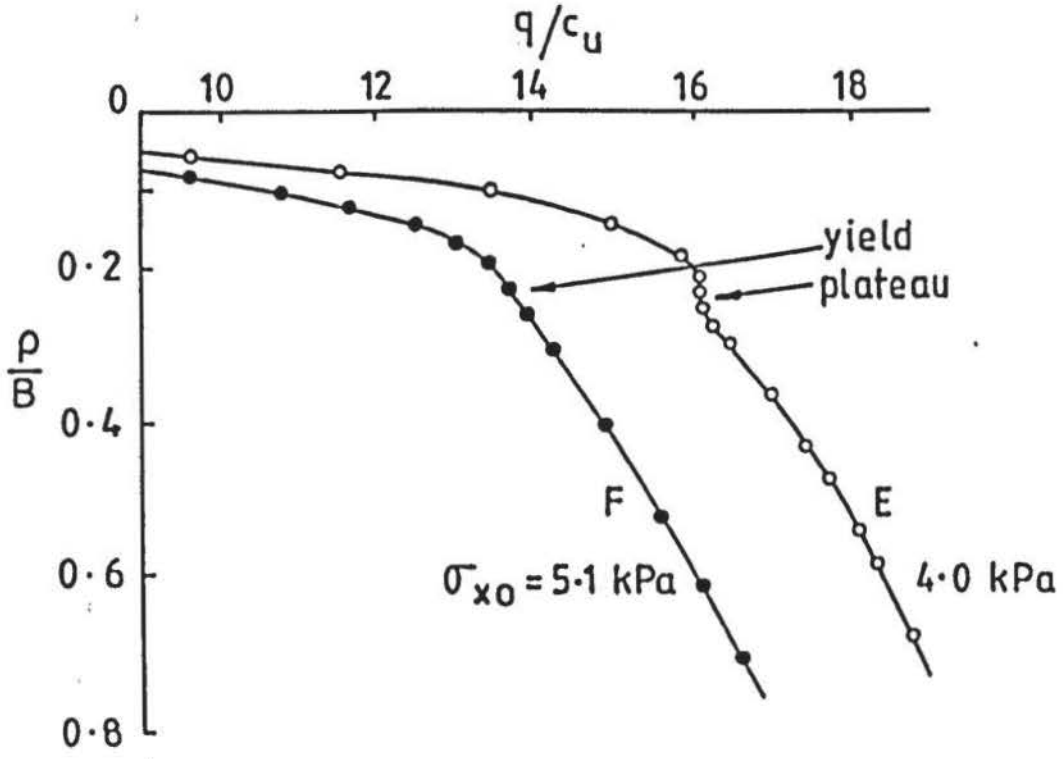

Typical yield plateau for F and E columns.

FIGURE 12.5

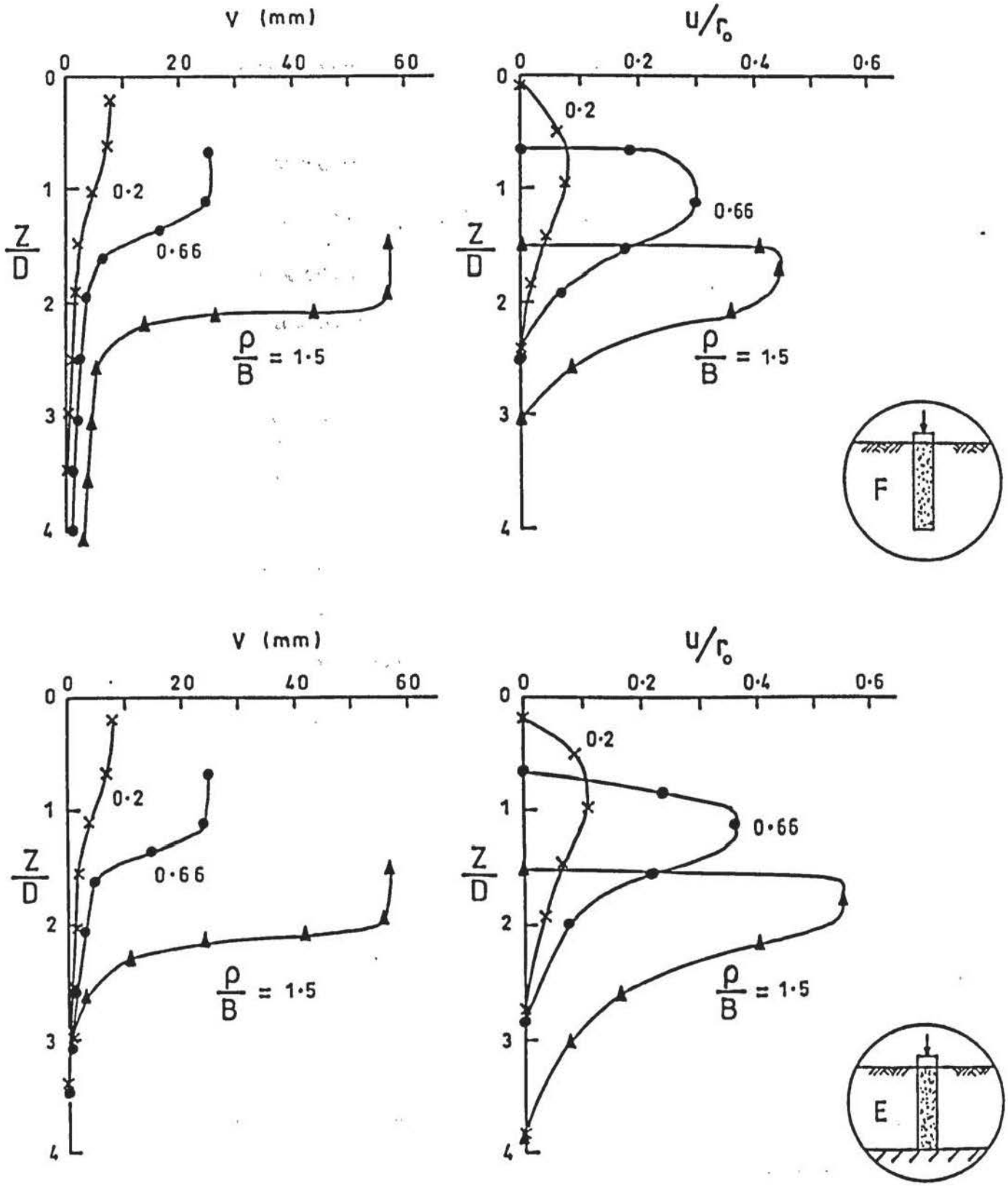

Vertical and lateral distortion of F and E columns at three stages of vertical deformation.

FIGURE 12.6

depth influenced is also larger with the former. At column yield, a 2.5D (F) and 3.8D (E) length of column is affected.

The magnitude and pattern of vertical displacement down the centre of the columns are similar, but from $\rho/B = 0.66$ displacement down the full length of the F column occurs with movement at the column toe when $\rho/B = 1.5$. This indicates that the ultimate vertical stress shown by the F column occurs through rigid-pile failure mode.

To consider the relative vertical movements within the columns and the adjacent clay, displacements of lead-shot, at the positions shown in Figure 12.7, divided by the foundation diameter B are shown with respect to z/D, for vertical column deformations $\rho/B = 0.2$, 0.66 and 1.5, in Figure 12.8. The types of line used to represent the lead-shot positions with a curve are shown in Figure 12.7. For clarity, the horizontal v/B scale has been exaggerated.

In the top-third portion of the columns, substantial deformations occur both within the columns and at the column-soil boundaries. The magnitudes of these deformations are similar for both column cases except that rigid-pile action is shown in the F case when $\rho/B \geq 0.66$. Strain reversal is exhibited by the E column at $\rho/B = 1.5$.

At column yield ($\rho/B = 0.2$) distortion or slip at the top of the column is greater between the column and clay than within the column. However, as ρ/B increases, greater vertical distortions occur within the columns than at the column soil boundaries.

Inspection of the clay surface in the column-void after completion of a test showed it to be impregnated by sand particles to about 1-2 grain diameters, and no evidence of slip or a slickensided shear surface was found below the level of the foundation. This indicates that the relative vertical distortions at the column-clay surface beneath the foundation, are largely due to shear strain with increasing shear strains occuring within the column as vertical displacement proceeds.

This also shows that direct comparison with conventional (non-particulate) piles is not valid.

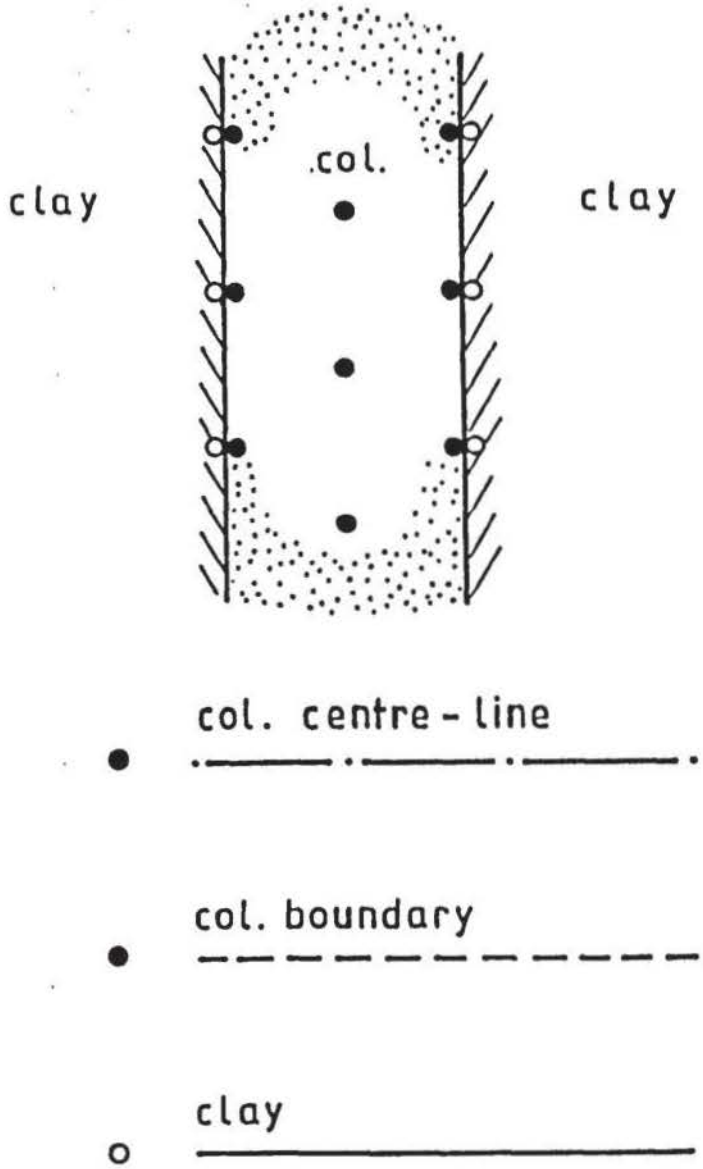

Types of line used to represent lead-shot positions in the columns and clay.

FIGURE 12.7

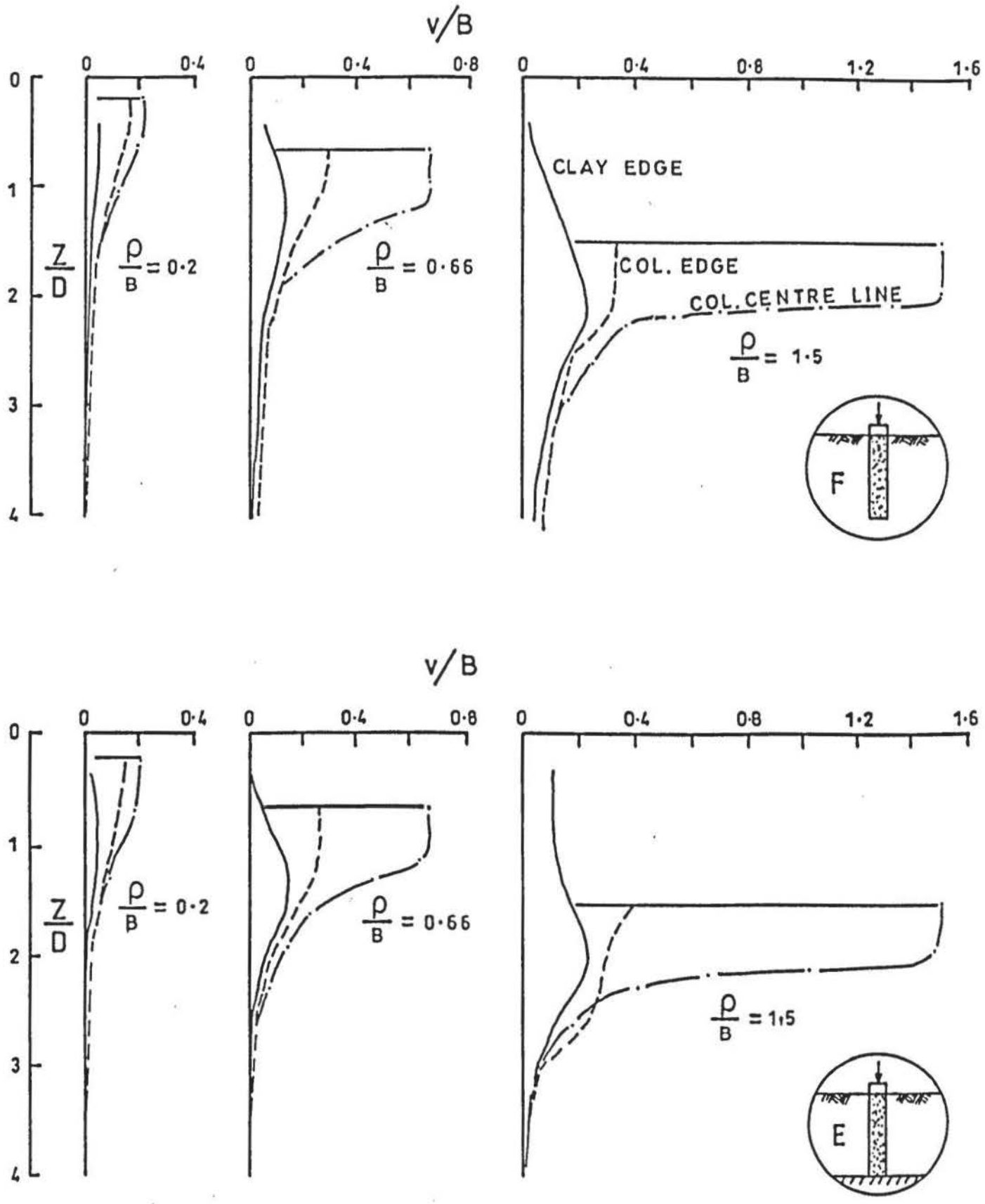

Relative vertical distortions within F and E columns and at column-clay boundary.

FIGURE 12.8

12.3.5 Comparison

In Figure 12.9 and 12.10, a direct comparison of the results with those of Hughes and Withers (1974) is made. Ultimate values of q/c_u are almost the same, although this occurs through different design criteria shown in Appendix J. In the author's case considerably greater applied vertical displacement for the same q/c_u was needed due to the high plasticity of the clay. The maganitude of these dispalcements is not unique to glyben, since the displacements recorded by Dodd (1979) using remoulded wet clay (Ball clay) were of the same order.

For roughly the same ρ/B, the magnitude and distribution of u/r_o and v against z/D are the same, except in the author's case a greater length of column is affected by vertical displacement. The peak increase in lateral stress recorded by Hughes and Withers was almost half that of the author's.

It is considered that the excellent correlation between the radiographic results establishes the validity and usefulness of the author's radiographic technique and laboratory procedures.

The yield plateau observed in the author's experiments prompted a closer examination of Hughes and Withers stress-settlement curve. It may be noticed that their curve has been drawn as a best-fit line through the measurement points lying between $\rho/B = 0$ to 0.1. The curve was re-drawn through the exact position of each of these points, shown in Figure 12.11. This revealed a yield plateau at $\rho/B \approx 0.02$ and $q/c_u \approx 9.5$, which lay just beyond their working stress range.

12.3.6 Clay displacement fields

Displacement trajectories of the clay surrounding the columns are shown in Figures 12.12 to 12.14 on a 1:2 scale for $\rho/B = 0.2$, 0.66 and 1.5 which corresponds to strain increment numbers 1,2 and 3. The u-v displacement vectors are cumulative at each increment and are shown relative to the initial position of the lead-shot. For clarity, displacement was increased by a factor

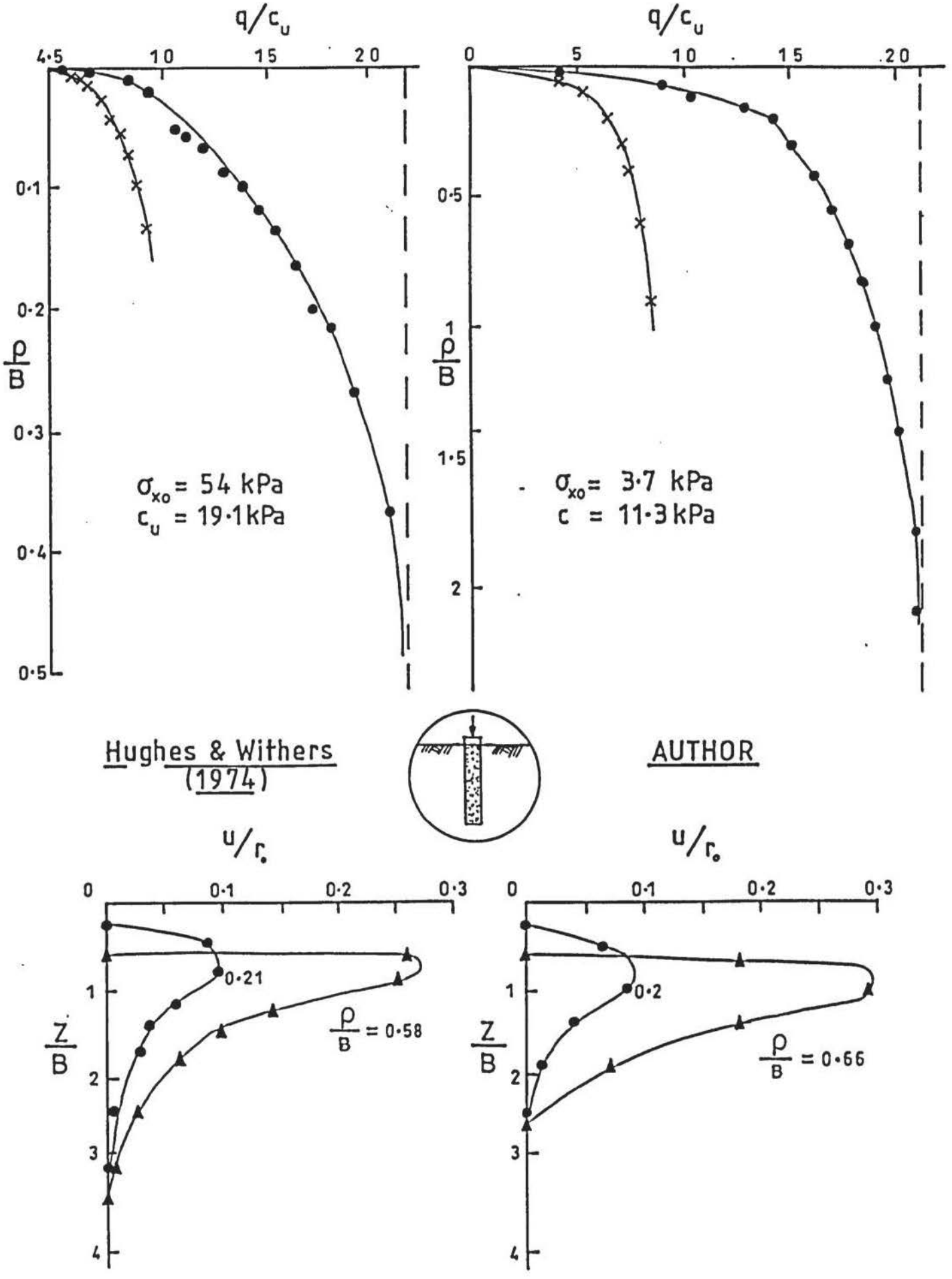

Comparison of stress-settlement and lateral distortion of a single isolated column with the results of Hughes and Withers (1974).

FIGURE 12.9

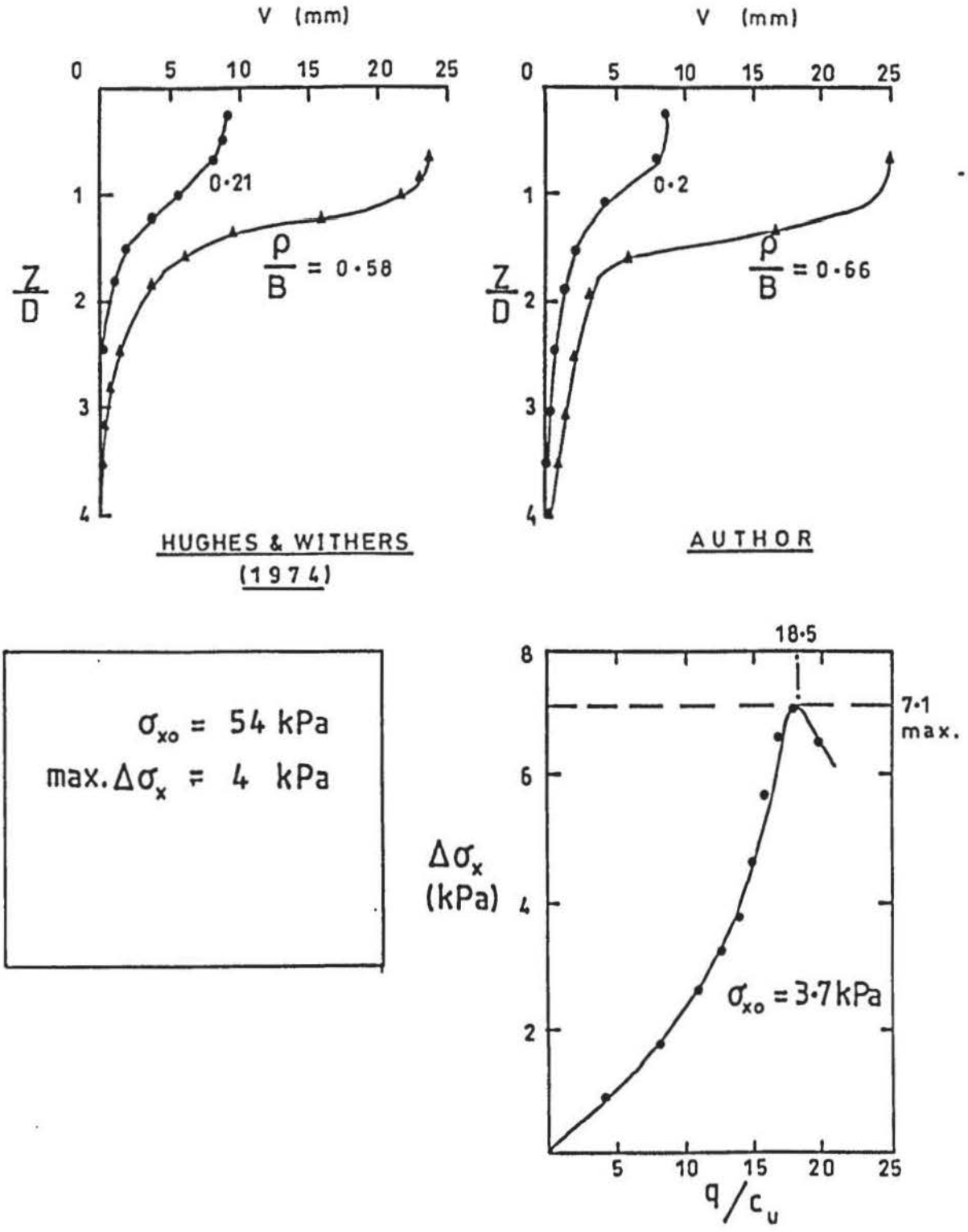

Comparison of vertical displacement and horizontal stress with the results of Hughes and Withers (1974).

FIGURE 12.10

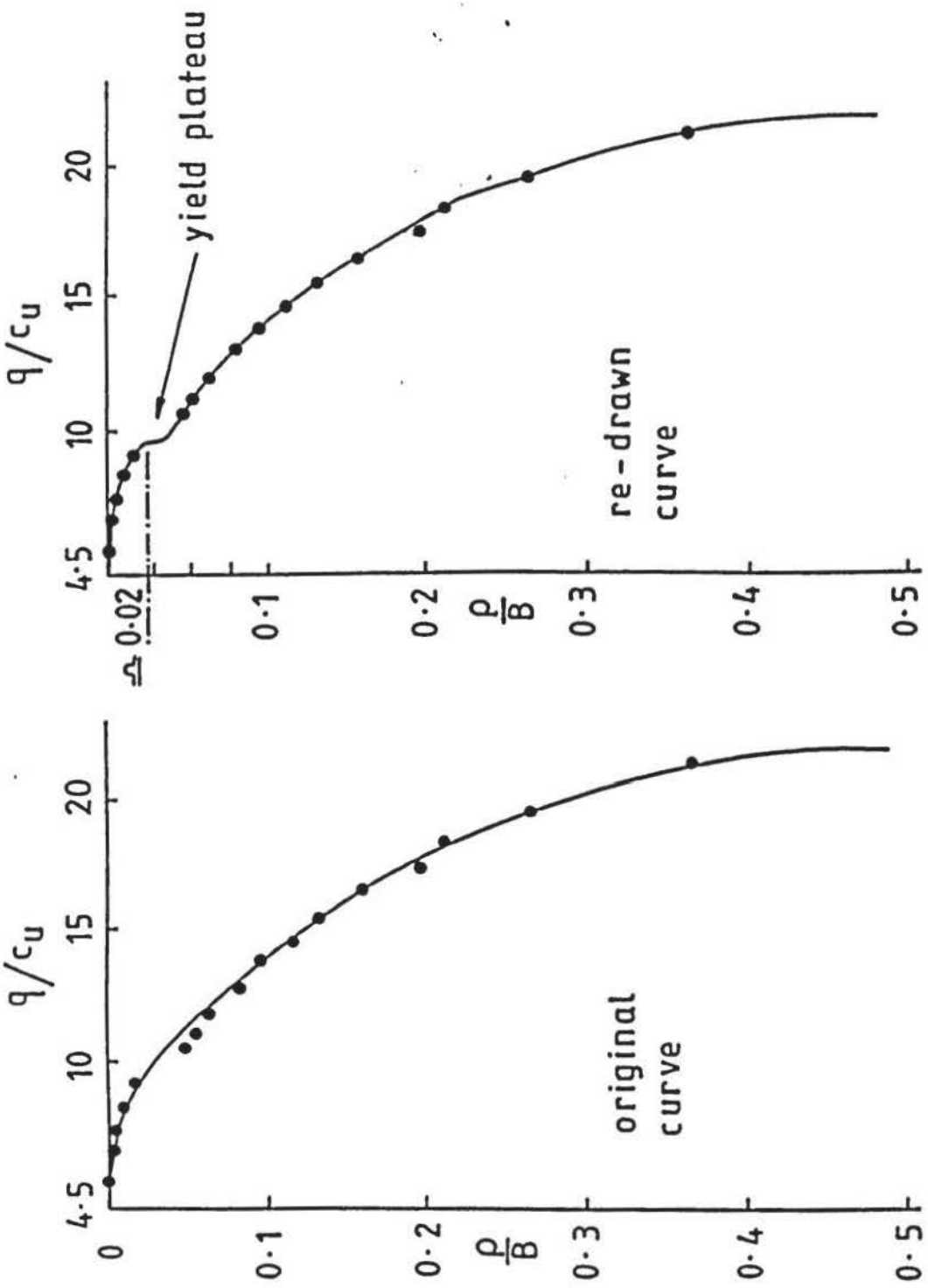

Re-drawn curve of results from Hughes and Withers (1974).

FIGURE 12.11

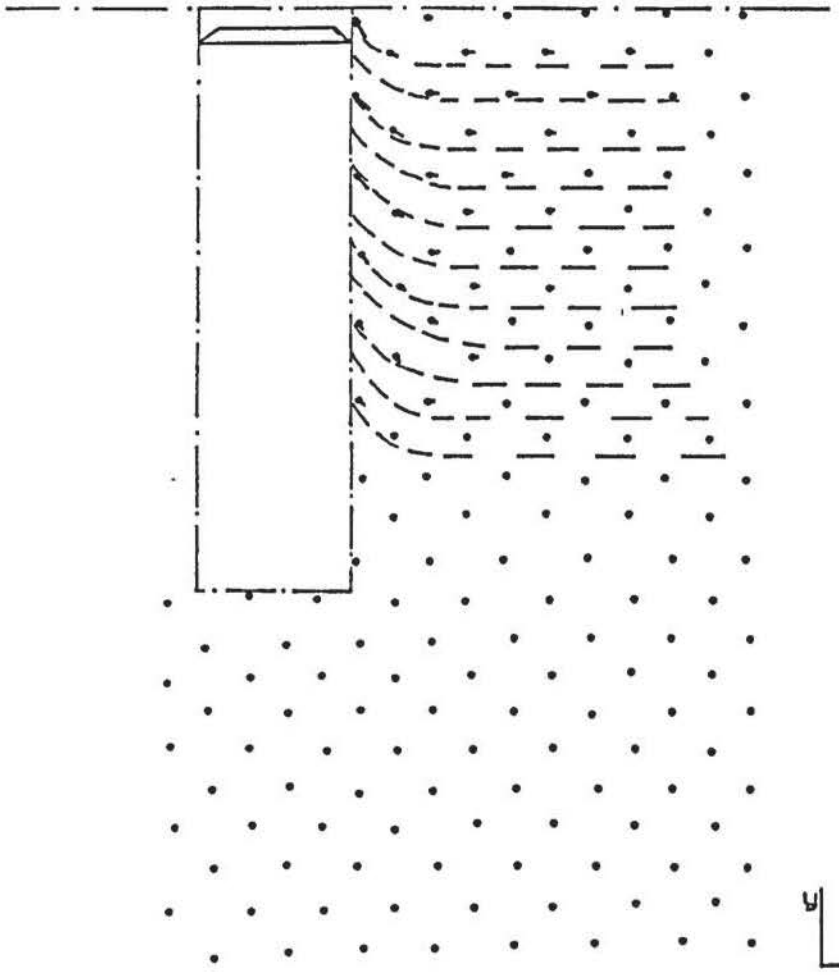

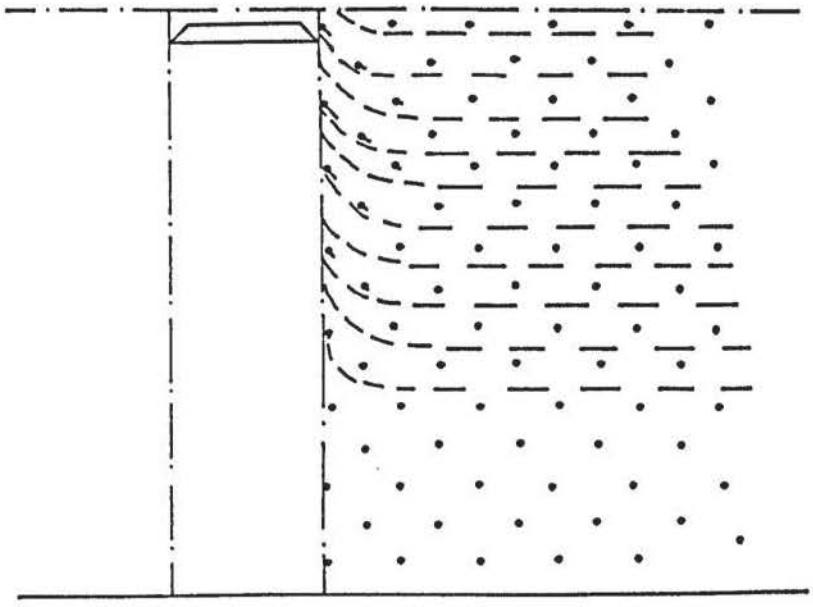

Clay displacement fields at ρ/B = 0.2 for F and E columns.

FIGURE 12.12

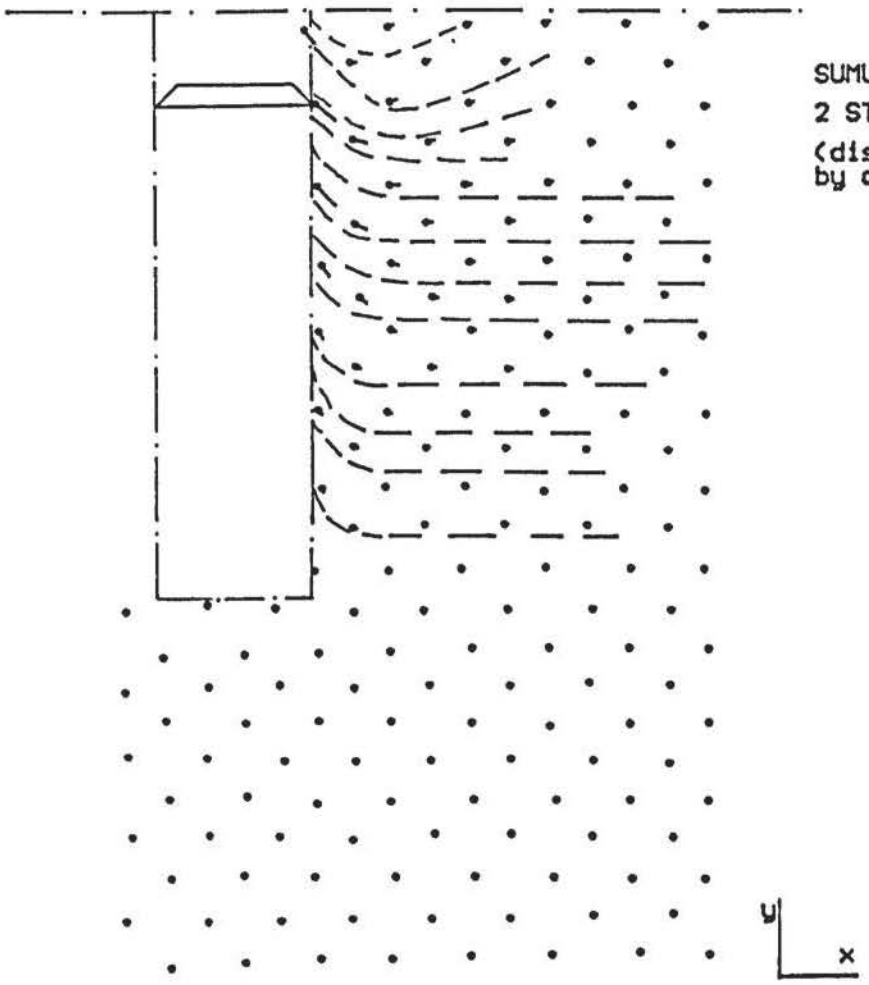

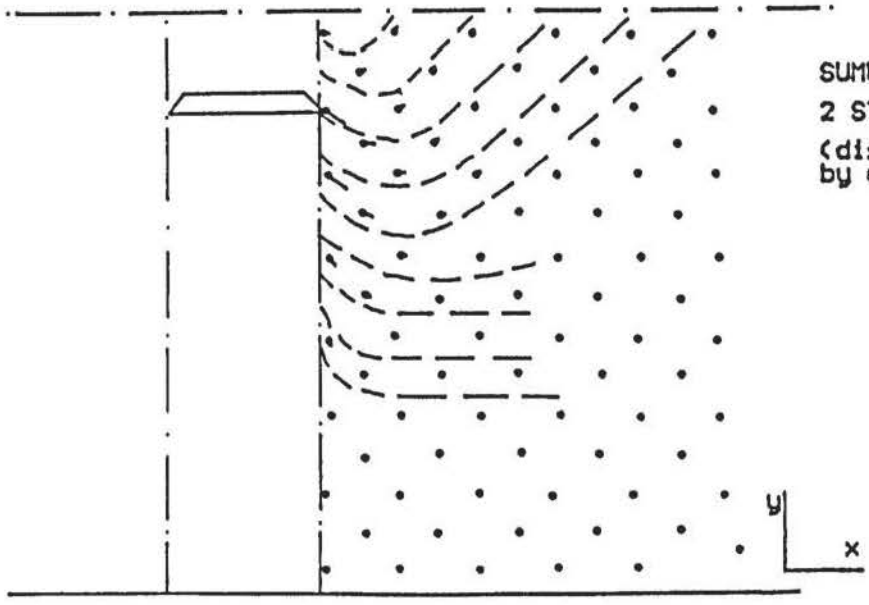

Clay displacement fields at $\rho/B = 0.66$ for F and E columns.

FIGURE 12.13

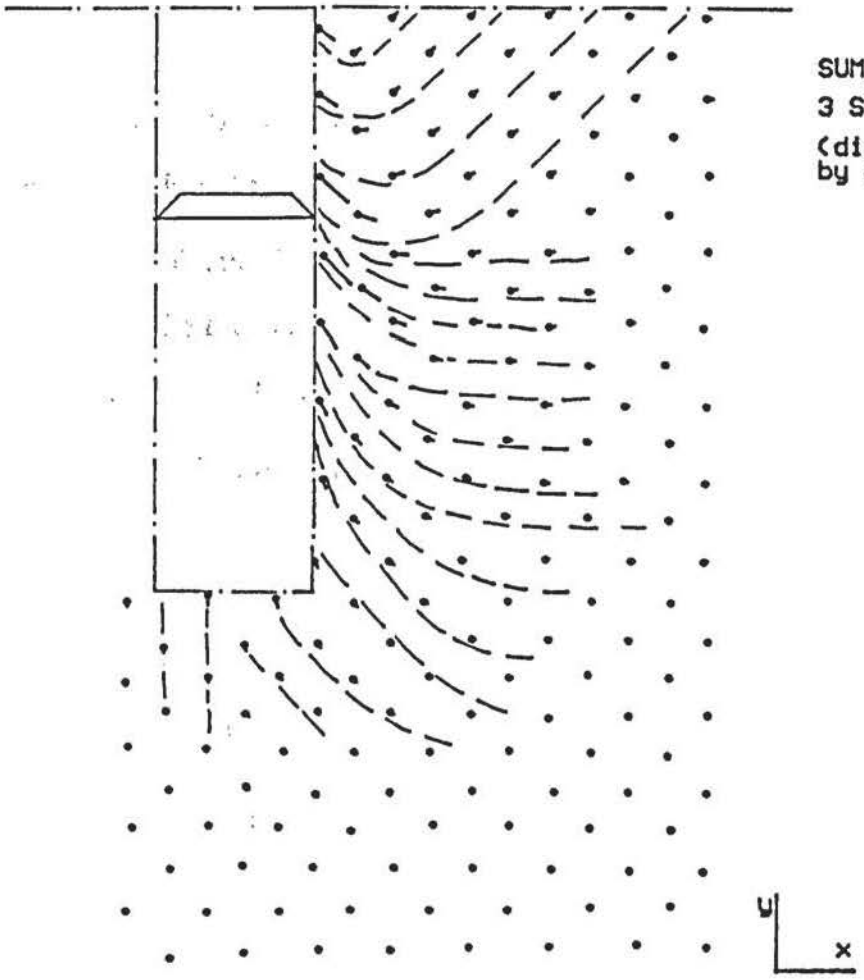

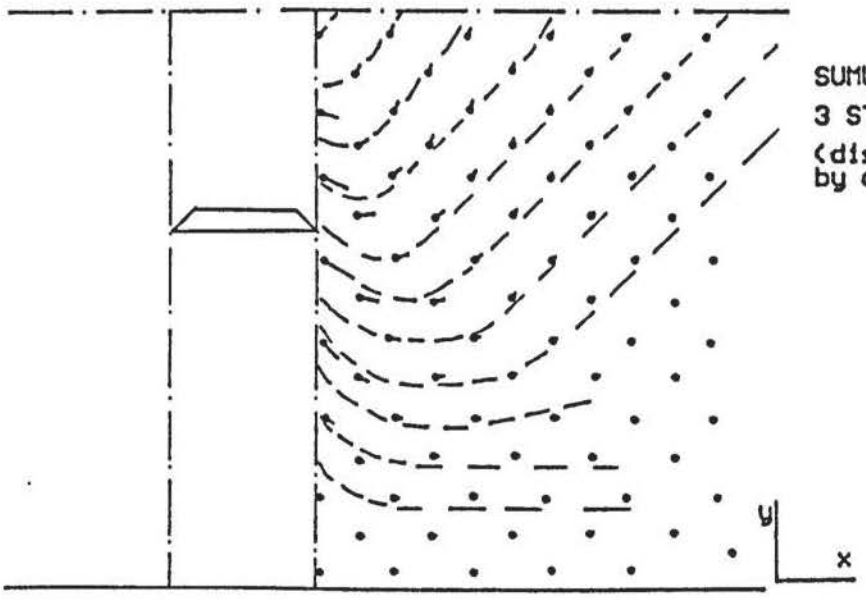

Clay displacement fields at ρ/B = 1.5 for F and E columns.

FIGURE 12.14

of 2 for the first increment.

At column yield ($\rho/B = 0.2$) the displacement trajectories are at 45^o to the horizontal immediately adjacent to the F and E columns, and then they curve to become horizontal within about 0.5D of the perimeter. When $\rho/B = 0.66$, the trajectory pattern is the same for the F column but changes significantly for the E column with previously horizontal trajectories that were sloping at 45^o to the surface of the clay. This suggests that at this stage of vertical displacement, the mechanism of bearing capacity is different for each column. At $\rho/B = 1.5$ the condition is further exaggerated.

12.3.7 Strain Analyses

The strain analysis described in Chapter 7.0 uses triangular plane strain elements where the major (ε_1) and minor (ε_3) principal strains lie in the x-y plane with the intermediate principal strain perpendicular to it. Single columns, however, are axi-symmetric and their corresponding strain behaviour is three-dimensional. As the column bulges circumferential strains are induced which has led to analogy with the pressuremeter, as illustrated by Figure 12.15. With this analogy, the strain analysis is treated as two-dimensional in the x-y plane with the horizonal radial strain ε_{rx} and circumferential strain ε_θ being treated as ε_1 and ε_3 respectively (Baguelin et al, 1978). In the real situation, the element shown in Figure 12.15 is subject to shear strains acting in the x-y plane which orientates any principal planes with respect to the horizontal (ε_x) and vertical (ε_y) strains.

So, if the two-dimensional section used by the author is to be valid, the major and minor principal strains must lie in the x-y plane with ε_θ being the intermediate strain (ε_2).

Using the triangular elements defined by the lead-shot in the clay within a distance of about 2.7 r_o of the centre-line of the column (where r_o was the initial column radius) analyses were performed to determine ε_1 and ε_3 in the x-y plane and ε_θ in the x-z plane. Referring to Figure

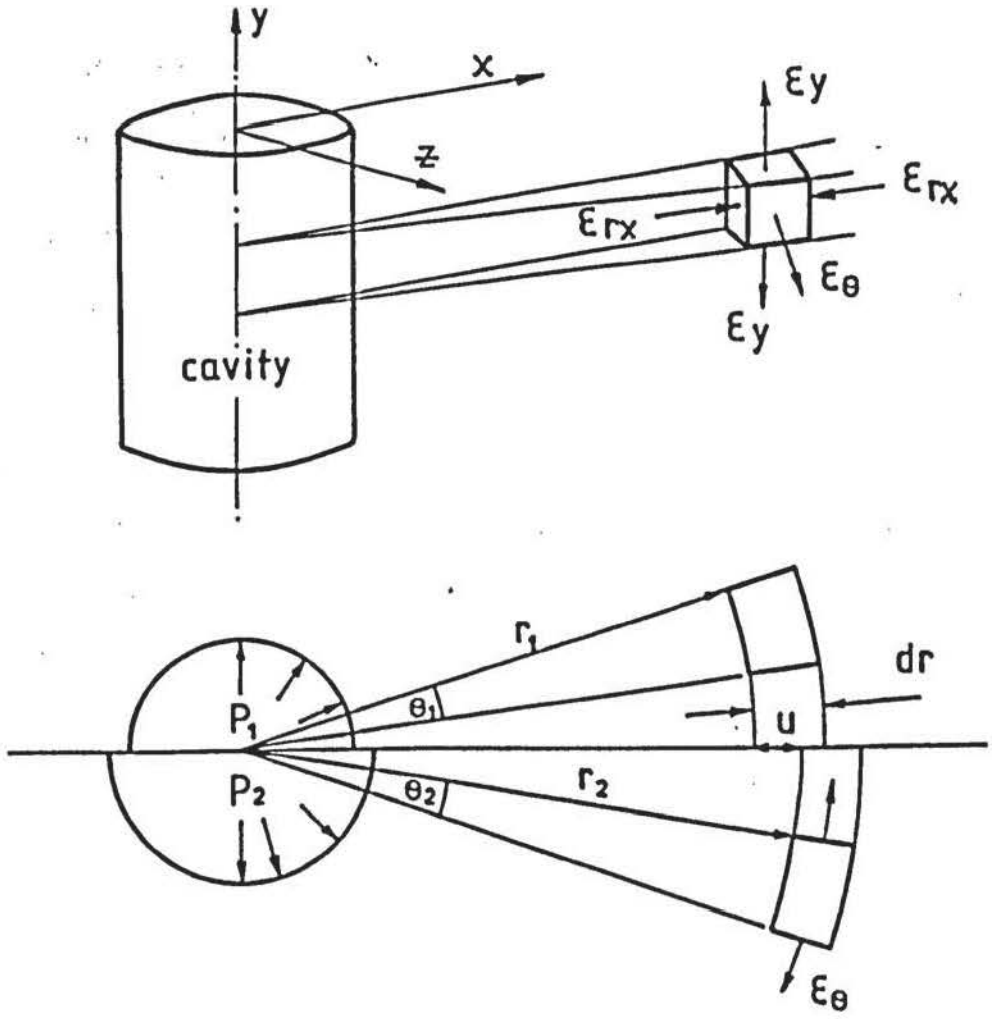

Strains induced by the expansion of a cylindrical cavity of infinite length in a weightless, isotropic, homogeneous and infinite mass (pressuremeter analogy).

FIGURE 12.15

12.15 and considering the adopted method for large strains, ε_θ was calculated from:

$$\varepsilon_\theta = 0.5 \left(\frac{u}{r_1} + \frac{u}{r_2}\right) \qquad (12.3)$$

where u is the displacement of a lead-shot, of a triangular element, nearest to the column boundary.

r_1 is the initial distance of the lead-shot from the centre-line of the column.

r_2 is $r_1 + u$.

Typical results of the analyses are tabulated in Figure 2.16 and show that, despite some small deviations immediately adjacent to the position of maximum lateral deformation of the column, ε_θ is an intermediate principal stress.

It was concluded that the two-dimensional section was valid for practical purposes and this allowed direct comparison with strains obtained with asymmetric boundary conditions.

12.3.8 Column-soil strains

The development of internal strains within an isolated granular column, and the surrounding clay, in F and E conditions are presented in Figures 12.17 to 12.22 for applied vertical displacements of $\rho/B = 0.2$, 0.66 and 1.5, which correspond to strain increment numbers 1, 2 and 3 respectively. Strains ε_x, ε_y, ε_1, ε_3 and γ_{xy} are represented by straight lines where 1 mm represents a strain of 7%. The original print has been reduced from A3 to A4 size for presentation purposes and so the strain magnitudes will need to be correspondingly reduced. Tensile strain is shown in red. The original column and clay surface positions are shown by dash-dot lines and the position of the foundation, at the particular strain increment is drawn in with a solid line. Due to symmetry and to reduce the number of lead-shot to be digitised, strains and zero extension lines are shown in just over one-half of the clay and in the opposite half of the column. The latter was also for reasons of clarity.

At strain increment no. 1, ($\rho/B = 0.2$) which approximately corresponds to column yield, in Figure 12.17, ε_x in the F columns are wholly tensile and occur in the upper half of the

[TEST No.: XC2E $\rho/B = y/D = 0.66$]

$B = D$

POSITION OF ELEMENT CENTROID		CALCULATED STRAINS (%)		
x/r_o	y/D	$\varepsilon_1(x\text{-}y)$	$\varepsilon_\theta(x\text{-}z)$	$\varepsilon_3(x\text{-}y)$
1.19	0.38	+20.1	-21.0	-22.2
2.1	0.50	+5.1	-2.1	-2.1
2.62	0.58	+5.1	-2.2	-4.9
	0.66			
1.24	0.85	+20.7	-20.1	-22.5
1.65	0.74	+14.1	-8.9	-9.0
2.10	0.81	+59.7	-5.0	-6.0
2.62	0.74	+4.1	-2.0	-2.0
1.23	1.01	+35.8	[-10.8]	-19.0
1.66	1.07	+9.0	-7.8	-8.0
2.14	0.97	+6.1	[4.9]	-3.7
2.65	1.06	+4.0	-2.0	-2.0
1.19	1.37	+16.0	-5.0	-13.0
1.67	1.25	+13.9	[-7.8]	-5.8
2.16	1.34	+4.3	[-2.9]	-2.5
1.17	1.54	+17.0	-5.0	-8.0
1.64	1.62	+5.0	-3.2	-5.0
2.14	1.52	+5.0	-3.0	-3.0
1.11	1.90	+5.9	-2.1	-8.1
1.6	1.79	+5.0	-3.2	-3.9
1.09	2.07	+10.0	-2.1	-3.0

x = distance of element centroid form column centre-line.

r_o = initial column radius.

y = distance of element centroid form column centre-line.

D = initial column diameter.

1) Planes to which the strains relate are shown within ().

2) Values of $\varepsilon_\theta < \varepsilon_3$ shown within [].

Table of principal strains derived from elements in the clay defined by the lead-shot

FIGURE 12.16

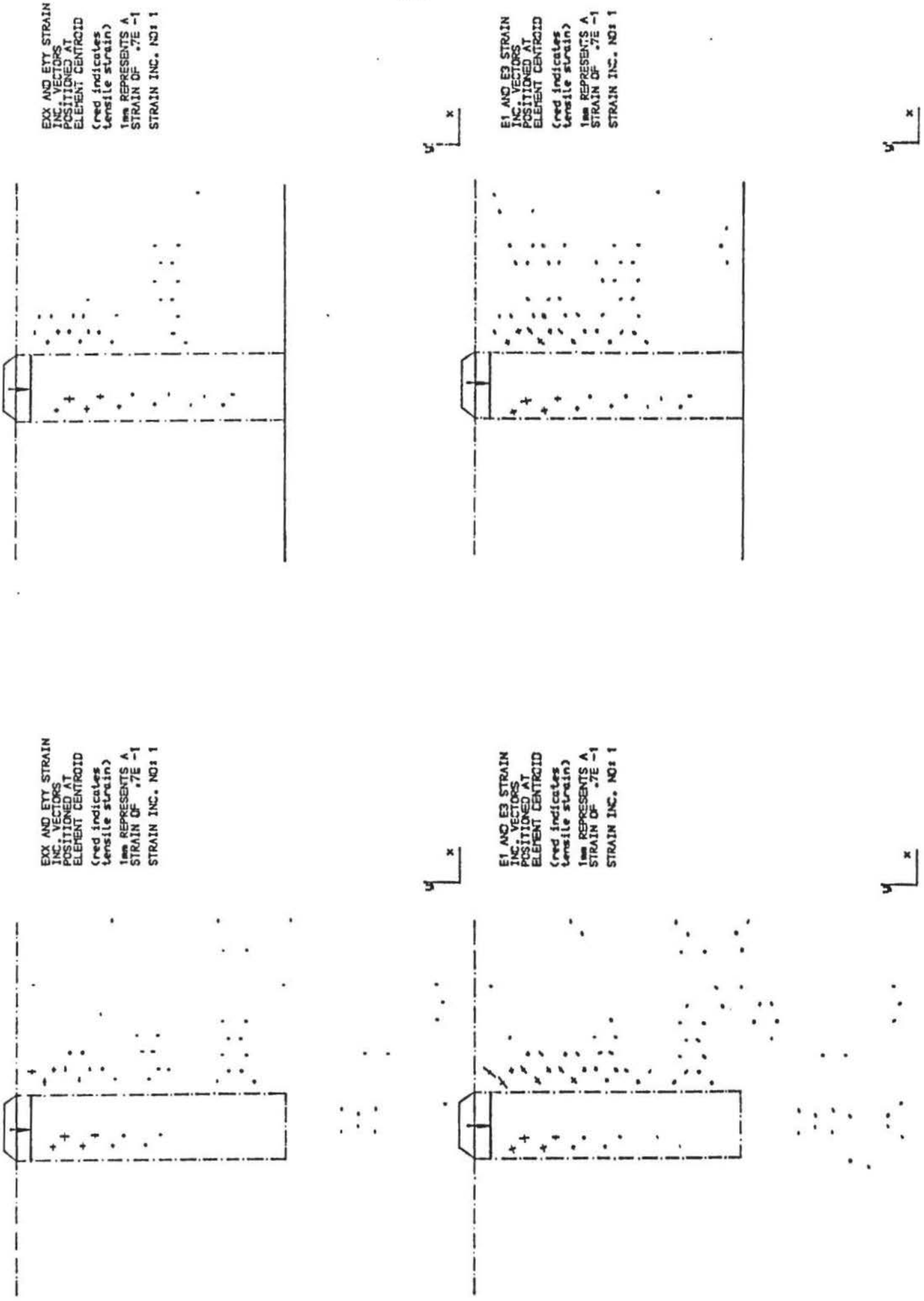

ε_x and ε_y, ε_1 and ε_3 vectors for F and E columns at $\rho/B = 0.2$.

FIGURE 12.17

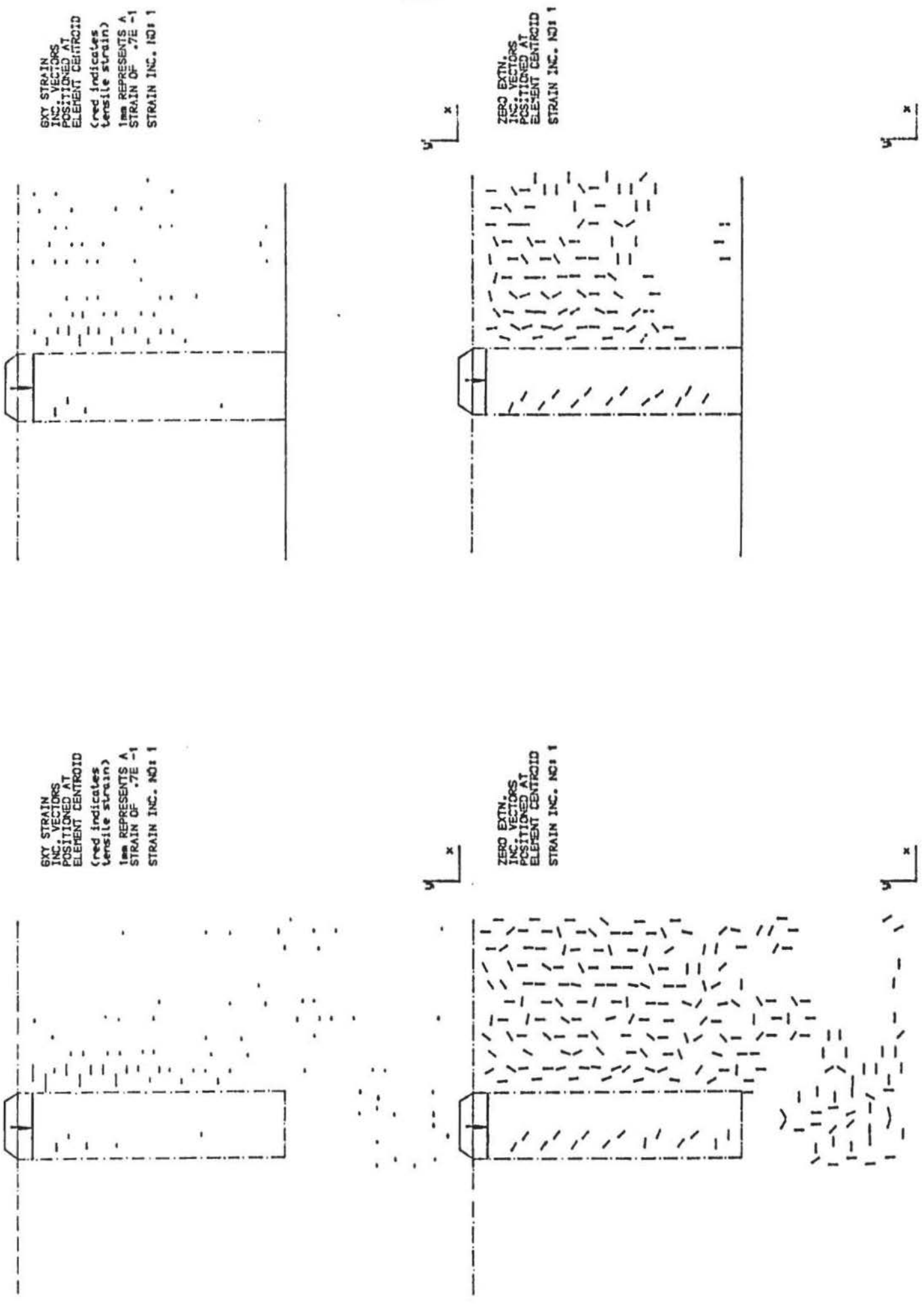

γ_{xy} and zero extension lines for F and E columns at $\rho/B = 0.2$.

FIGURE 12.18

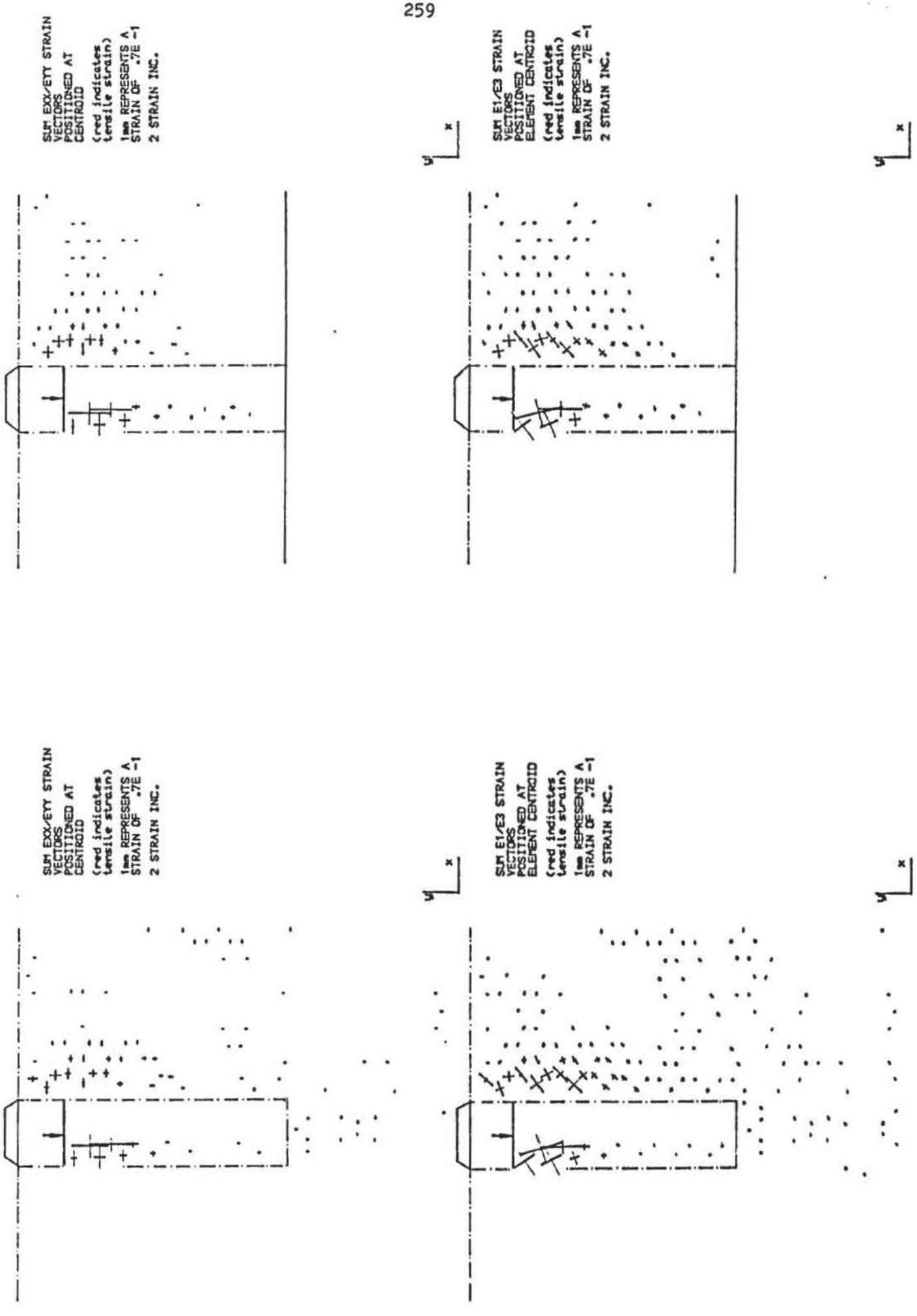

ε_x and ε_y, ε_1 and ε_3 vectors for F and E columns at $\rho/B = 0.66$.

FIGURE 12.19

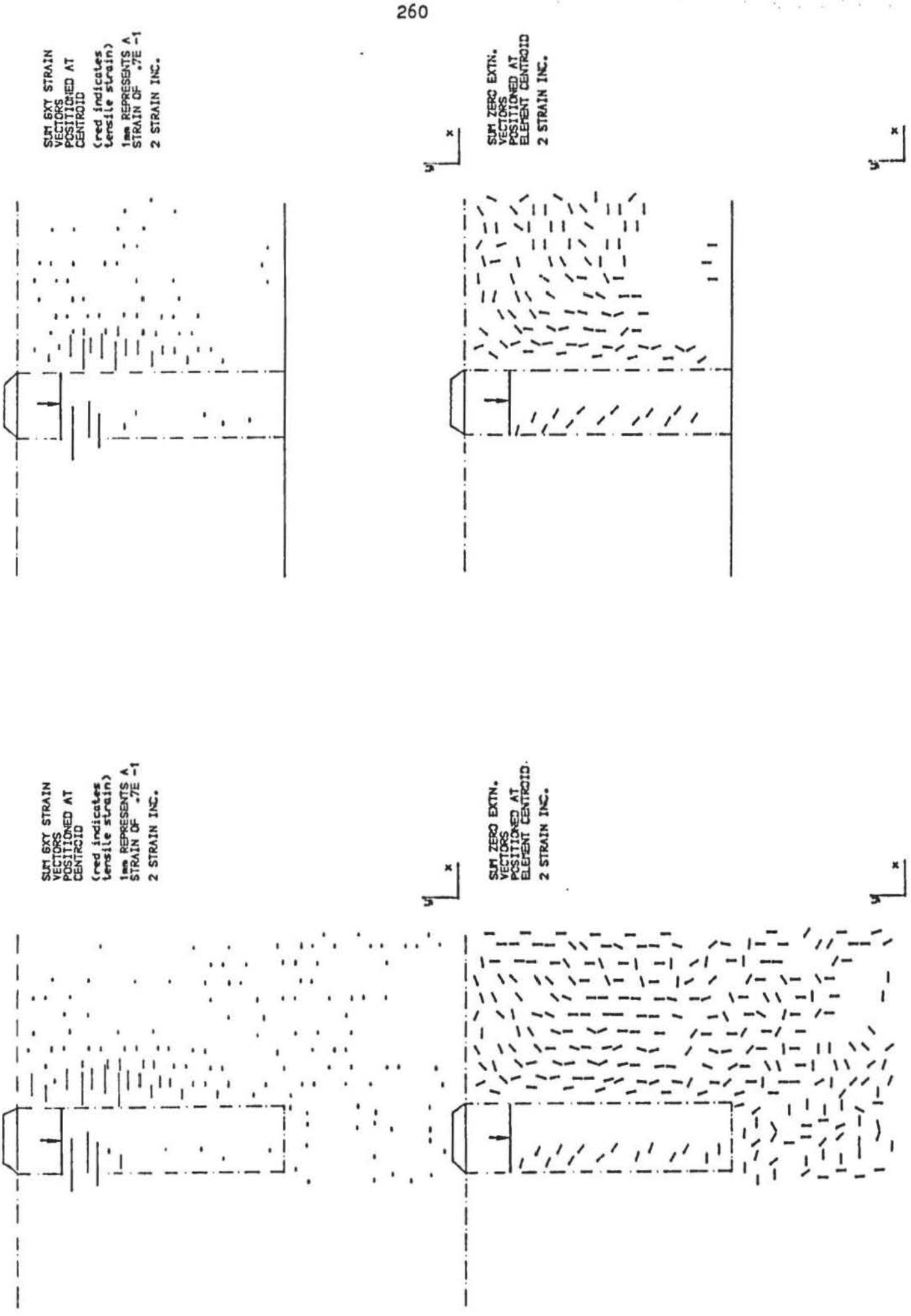

γ_{xy} and zero extension lines for F and E columns at $\rho/B = 0.66$.

FIGURE 12.20

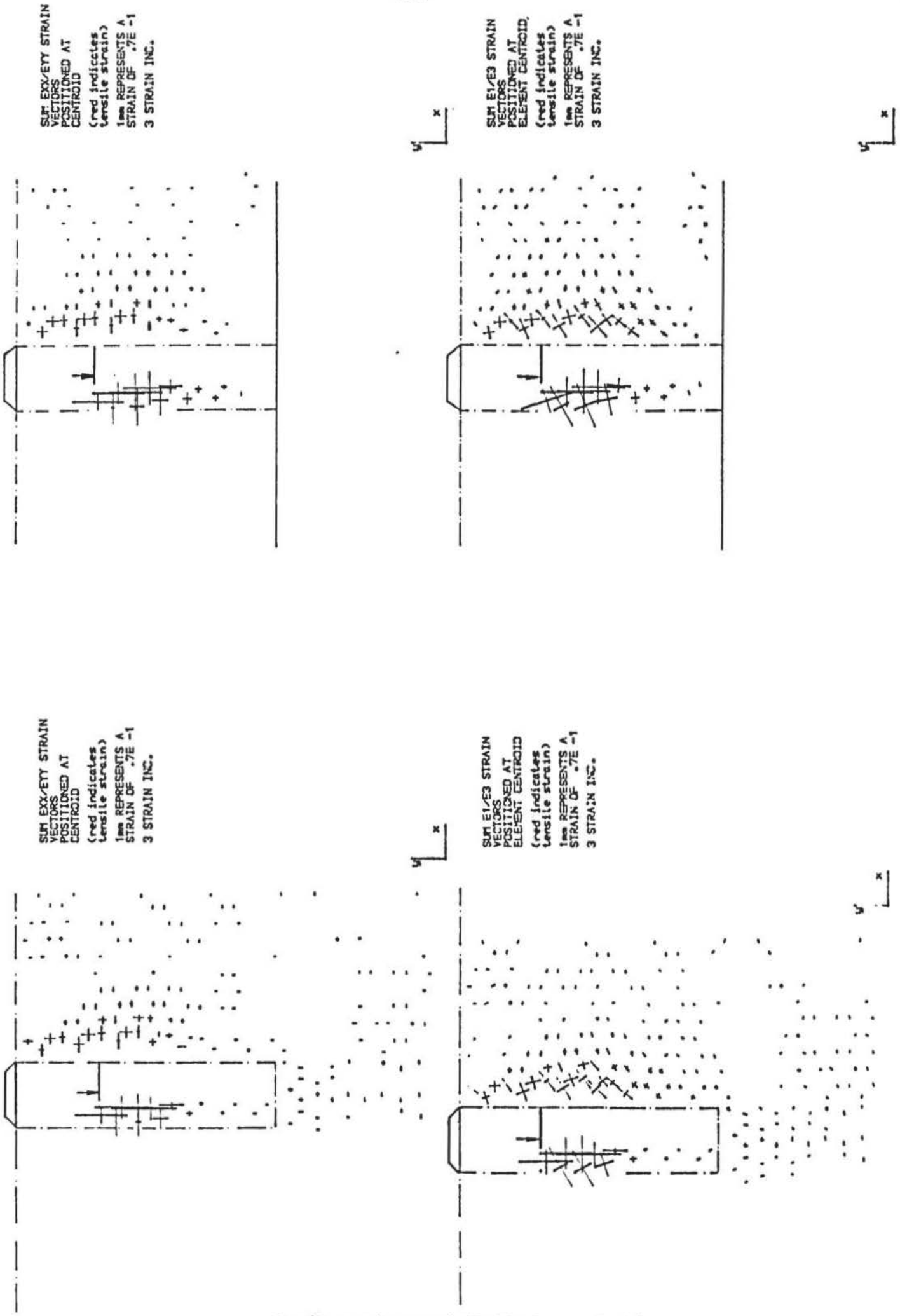

ε_x and ε_y, ε_1 and ε_3 vectors for F and E columns at $\rho/B = 1.5$.

FIGURE 12.21

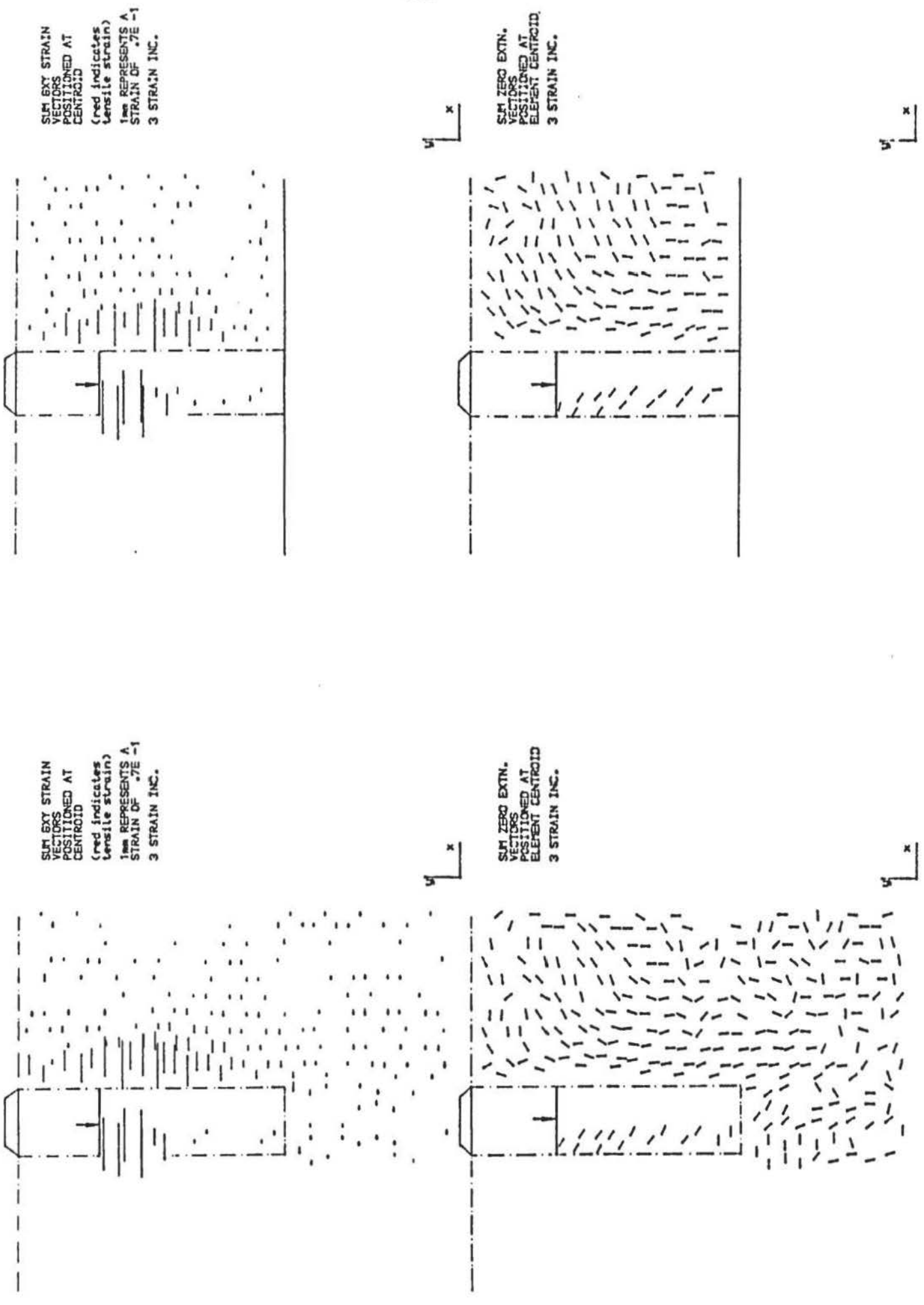

γ_{xy} and zero extension lines for F and E columns at $\rho/B = 1.5$.

FIGURE 12.22

column while in the clay ε_x are compressive with their influence extending about 1.0D laterally from the column centre-line. ε_y are compressive in the column and are tensile in the zone of clay affected. The pattern is the same for the E columns except a greater depth of column is subject to strain, but to a lesser depth in the clay. Orientations of the principal strains for both the E and F columns are similar. In the column, orientation is concentrated near the top and toward the column perimeter due to the shear strains caused by relative vertical disortion of the column material shown in Figure 12.8. In the clay, a greater degree of orientation of the principal strains is indicated with ε_1 at about 45^o to the horizontal. This means that γ_{xy} is at a maximum. The ε_1 are compressive and ε_3 are tensile.

In Figure 12.18, engineering shear strains (γ_{xy}) are shown to have developed to about three-quarters of the column length in the F case and about two-thirds in the E case. Within the column, however, γ_{xy} is less and occurs to about one-third and one-quarter of the column length in the F and E cases respectively. This concurs with the vertical distortions shown in Figure 12.8.

The remaining two-strain increments at $\rho/B = 0.66$ and 1.5 show exaggerated patterns of those just described and the effects of a rigid-pile failure mode at the last strain increment ($\rho/B = 1.5$).

In summary, ε_y within the columns are similar but a greater depth of column is affected in the E case. In the clay ε_y and γ_{xy} occur in a larger zone in the E case.

Settlement is the sum of the vertical and shear strains, assuming immediate settlements are equal, such that:

$$\rho = \left[\Sigma \varepsilon_y + \Sigma \gamma_{xy} \right] \qquad (12.4)$$

In the F case, $\Sigma\varepsilon_y$ and $\Sigma\ 0.5\ \gamma_{xy}$ are larger which accounts for the higher settlements than were observed with the E case.

12.3.9 Zero extension

Zero extension lines are shown in Figures 12.18 to 12.20 and 12.22 for the three strain increments. These lines represent planes of zero nett strain and indicate a well defined zone of plastic deformation. They also indicate potential slip surfaces.

At the first strain increment slip planes are shown within the column, at about 46 - 48° to the horizontal, and near vertical in the clay adjacent to the column. Further strain increments show the progressive lateral development of vertical slip planes within the clay.

By plotting the trajectories of zero extension and principal compressive strain, Figure 12.23, it is apparent that considerable plastic deformation has occurred at the first strain increment within both the column and the clay.

12.4 TWO COLUMNS

12.4.1 Stress-settlement characteristics

When two columns were loaded simultaneously at 1.25D apart, centre-to-centre (Test Nos. TC1 and TC1E) there was little difference in the stress-settlement characteristics, shown in Figure 12.24, from those of a single column. Yield plateau were evident and were similar to those shown in Figure 12.5. Within the limits of experimental repeatability, the variations of I_q with ρ/B and m with q/c_u were also found to vary insignificantly from those of a single column (Figure 12.4 a and b). The peak $\Delta\sigma_x/q$ for E and F conditions increased more than two-fold above that of a single column, which suggests superposition.

By comparing the q_E/q_F and ρ_E/ρ_F relationships with those for a single column in Figure 12.25, it is apparent that sufficient interaction occurs beyond the working-stress range either to reduce the bearing capacity and settlement of the E column, or increase those of the F column, or give a combination of both. Within the working stress range, differences in these characteristics are negligible.

Settlement behaviour is clarified by the relationships shown in Figure 12.26, where the settlement at 1.25D ($\rho_{1.25}$) divided by the settlement of a single column (ρ) is plotted against

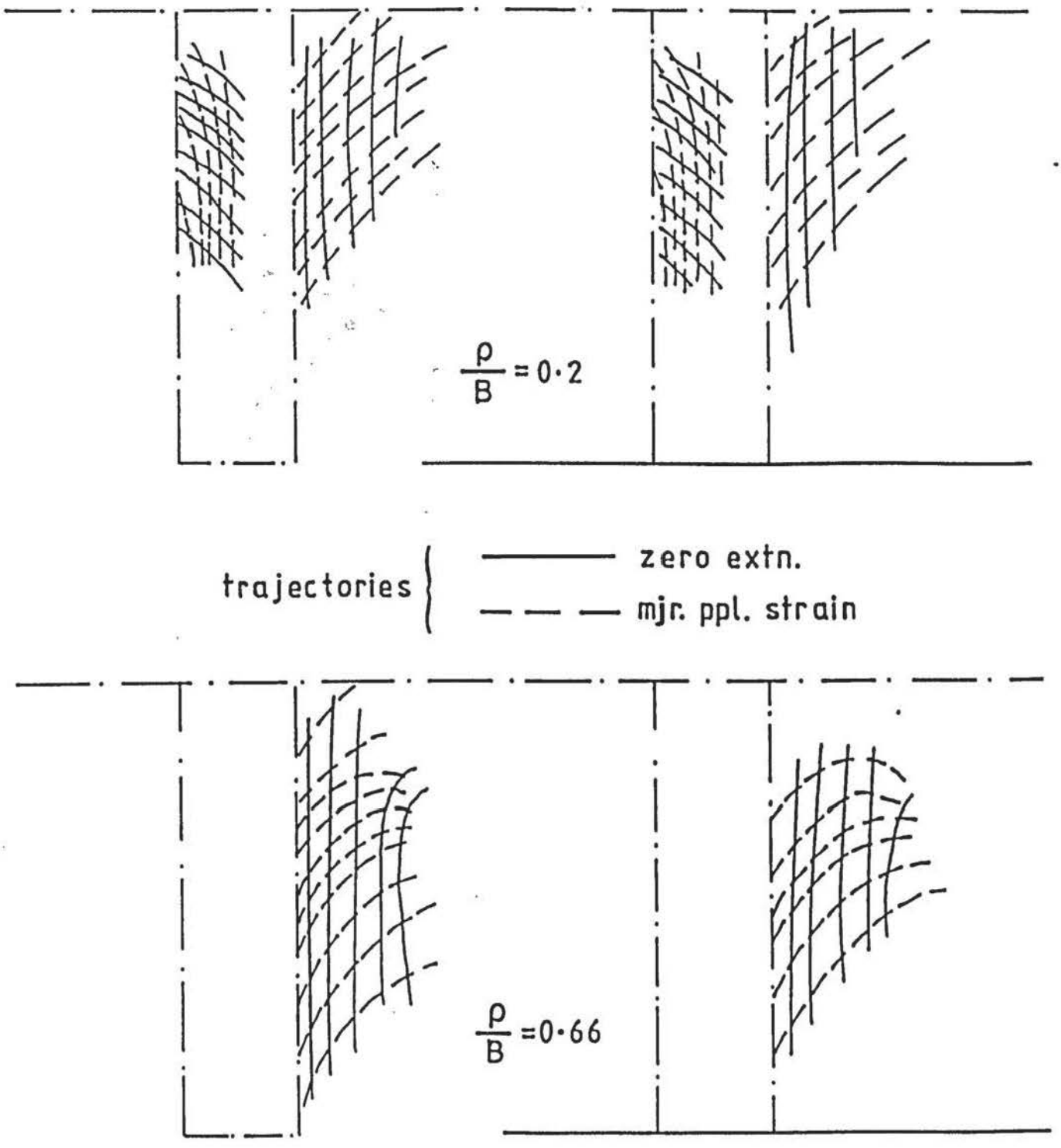

Trajectories of zero extension and principal compressive strains at ρ/B = 0.2 and 0.66 for F and E columns.

FIGURE 12.23

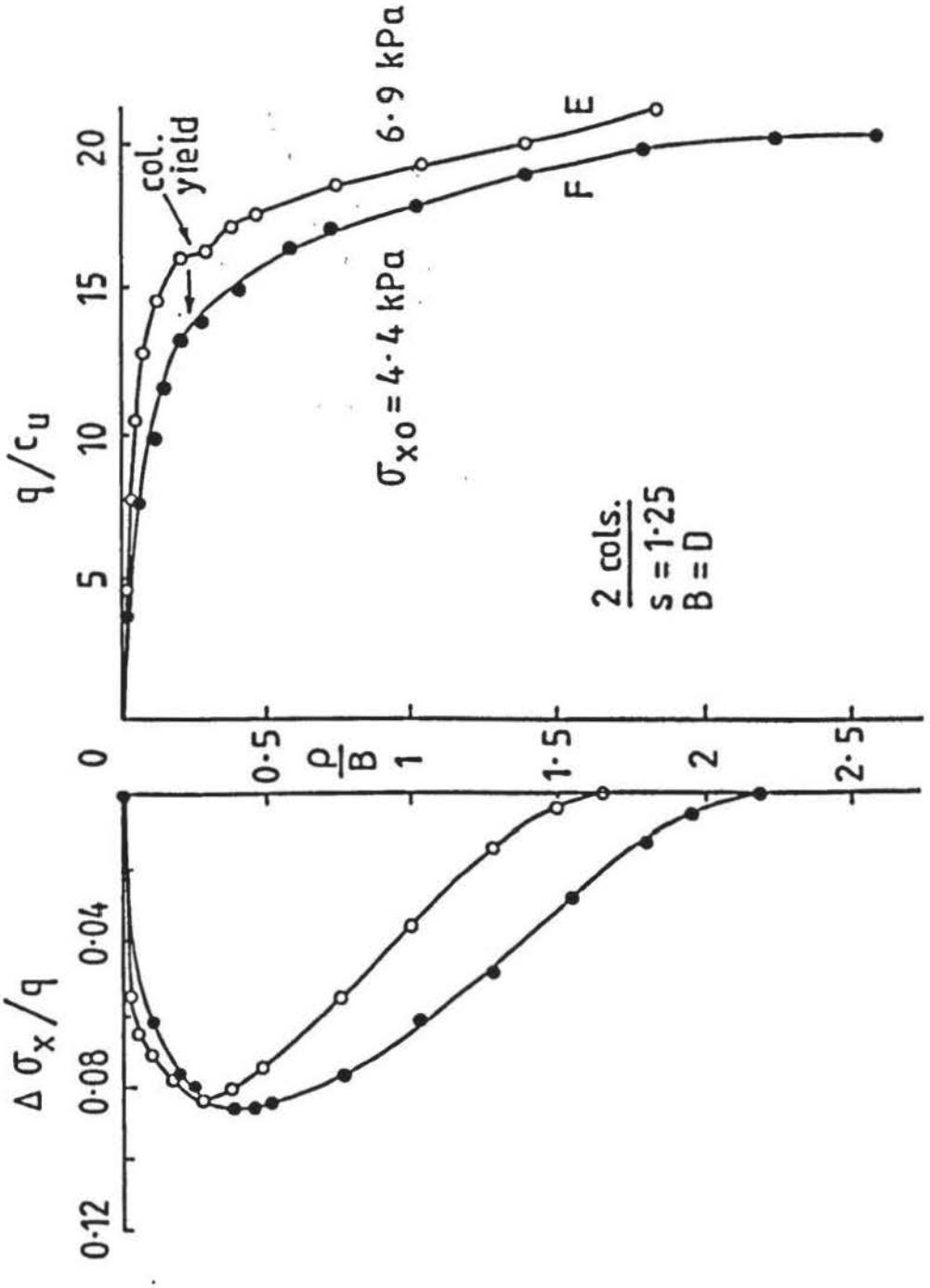

Typical variation of q/c_u and $\Delta\sigma_x/q$ against ρ/B when two columns are 1.25D apart for F and E conditions.

FIGURE 12.24

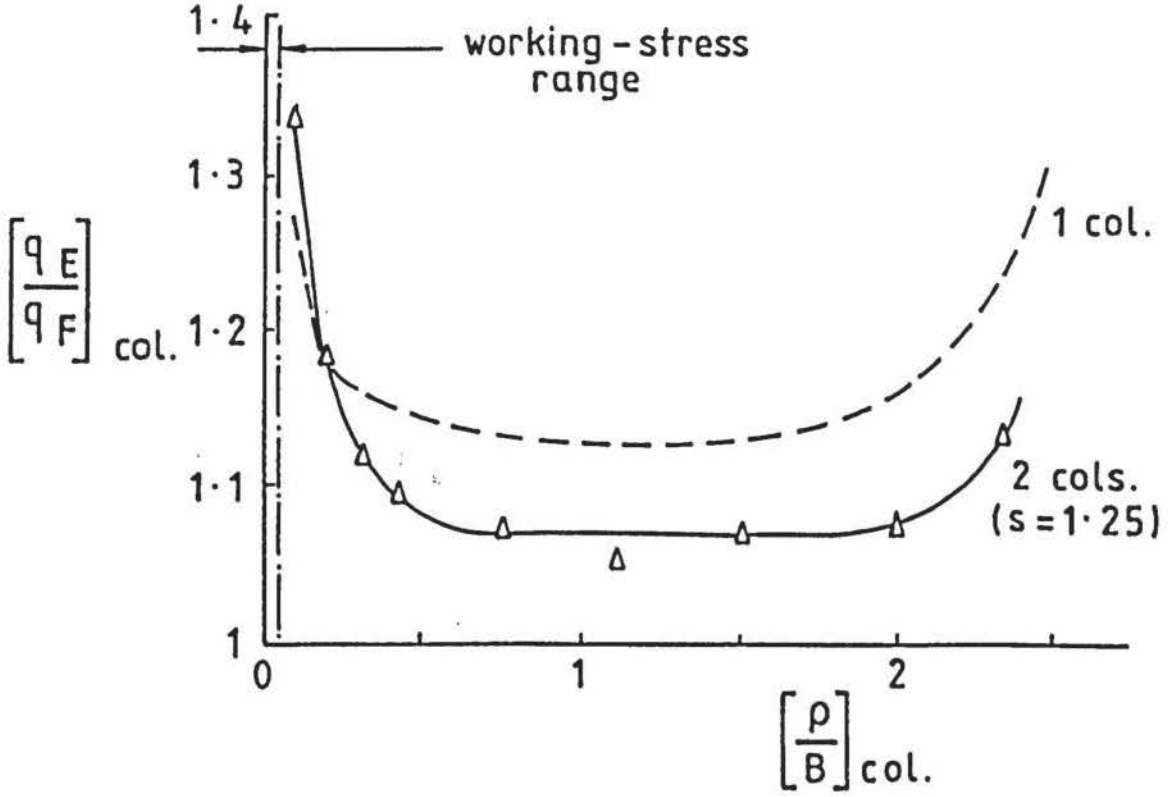

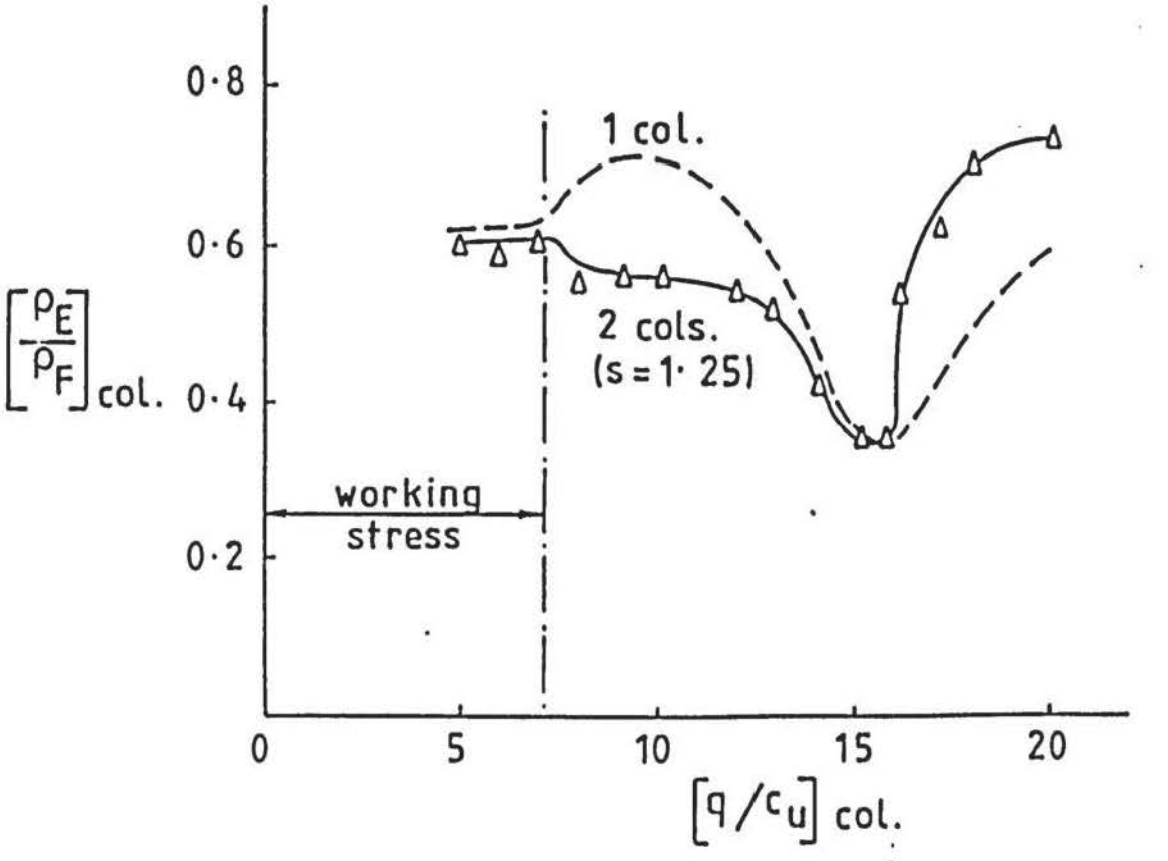

Typical variation of q_E/q_F with ρ/B and ρ_E/ρ_F with q/c_u for two columns at 1.25D compared to a single column.

FIGURE 12.25

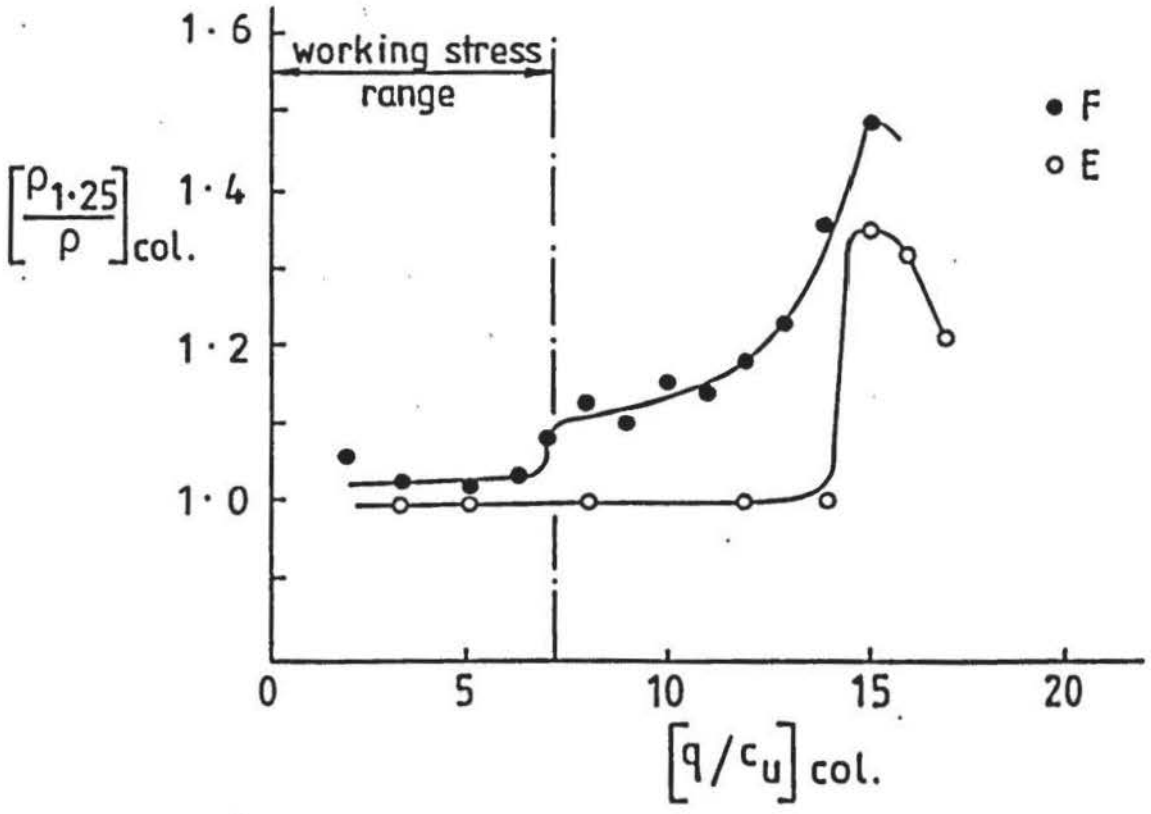

Variation of $\rho_{1.25}/\rho$ with q/c_u for F and E columns (average of three tests).

FIGURE 12.26

q/c_u for both E and F conditions. An average of three tests was taken. Up to q/c_u ≈/5 the ratio $\rho_{1.25}/\rho$ is almost unity for the E column, so there is virtually no change in the charcteristics whether the columns are close or widely spaced. For the F column, however, the pattern is different. Almost up to working stress levels the settlement is within a few percent of the E column, after which the settlment of the closely spaced columns progressively increases relative to that of a single F column.

12.4.2 Interaction

The effects shown in Figure 12.25 and 12.26 can be explained by column interaction. In considering the action of a conventional rigid pile, Cooke et al (1980) explained that axial loading was almost wholly supported by shaft resistance which transferred loads away from the shaft to create shear stress in the supporting soil. At working-loads pile-soil slip is negligible and so settlement in this range is almost wholly due to vertical (ε_y) and engineering shear strains (γ_{xy}) induced by the transferred loading. This effect has been shown to apply directly to a granular column in the previous section.

Cooke et al (1979) showed the radial zone of influence of induced settlement to be at least 12D (D was the pile diameter) at 50% of ultimate load. On this basis Cooke et al (1980) proposed that unloaded piles adjacent to a loaded one would be displaced downwards due to pile interaction and showed by field tests that the principle of superposition applied up to 50% of ultimate load.

Using a similar principle to that of Cooke et al (1980), the action of one loaded column (A) on another unloaded 'passive' column (B) at spacings from 1.25D to 3D was determined for F (Test Nos. IC1 to IC5) and E (Test Nos. IC1E to IC5E) up to $q/c_u \approx 22$ and is shown in Figure 12.27. For the F case, the vertical deflection δ_B at the top of the passive column to $q/c_u \approx 15$ (about twice the working-stress) at first shows settlement, after which the passive column (B) rises. The magnitudes of δ_B at conjugate q/c_u values are smaller as spacing increases. Settlement is almost zero when the columns are 3D apart. In the E case induced settlement is almost zero at

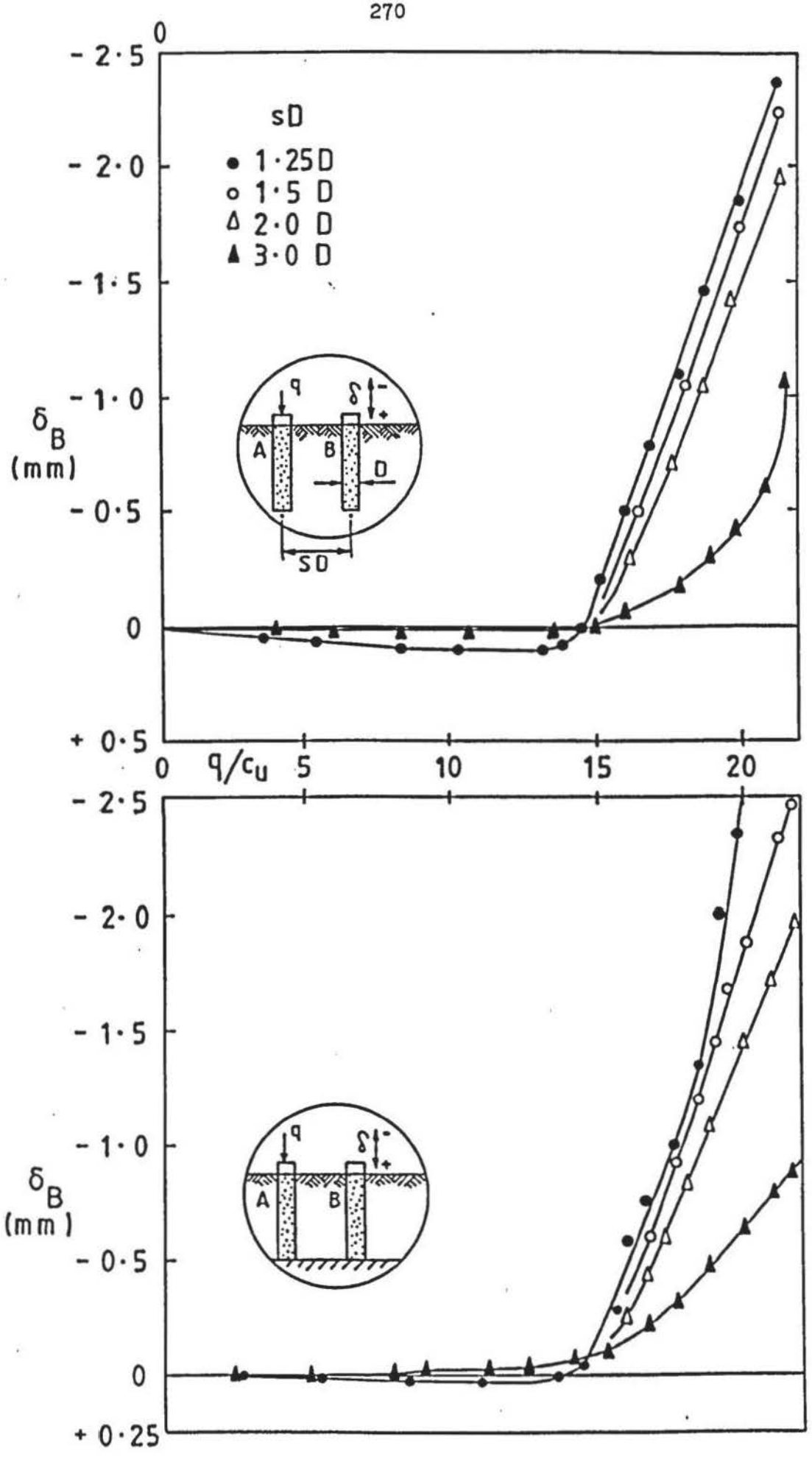

Typical variations of vertical surface displacement of a passive column δ_B against q/c_u of an adjacent loaded column at various spacings for F and E conditions.

FIGURE 12.27

any spacing. The cross-over point from settlement to uplift for all spacings and column bearing conditions is about the same. The cross-over point corresponds to $\rho/B \approx 0.2$ to 0.3, up to which point vertical distortions shown in Figure 12.6 and 12.8 predominate over lateral distortions in affecting the passive column. As progressive bulging and yield of the loaded column occurs, a point is reached where sufficient lateral distortion of the clay causes volume change of the sand forming the passive column. Movement of the sand takes the least line of resistance and hence upward movement at the column surface occurs. This effect is enhanced by the upward plastic flow of the clay shown by the displacement fields in Figure 12.13 and 12.14.

By plotting δ_B against ρ_A for both F and E conditions, shown in Figure 12.28, the relative vertical displacement characteristics are emphasised. Over the working-stress range interactive displacement occurs as settlement (i.e. vertical displacement is downwards). Cooke et al (1980) re-defined the interaction factor of Poulos (1968) as :

$$\Omega = \frac{\delta_B}{\rho_A} \qquad (12.5)$$

and also defined the settlement ratio R_S, as:

$$R_s = \frac{\text{Mean settlement of pile group}}{\text{settlement of single pile carrying a load equal to the mean load carried by the piles of the group}} \qquad (12.6)$$

By applying these definitions to two similar equally loaded granular columns, the additional interactive settlements for both columns are the same. Therefore:

$$R_s = 1 + \Omega_s \qquad (12.7)$$

where s is the column spacing factor. This gives the total settlement for either column as:

$$\left[\rho_s\right]_{E,F} = \left[\rho\,(1 + \Omega_s)\right]_{E,F} \qquad (12.8)$$

The range of R_S at working-stress levels for s = 1.25 to 3.0 for F and E columns obtained from the laboratory tests are tabulated in Figure 12.29.

Using Eqn. 12.8 and values of R_S when s = 1.25, the difference between $\rho_{1.25}/\rho$ for the F and E columns is about 3% up to about twice working-stress levels ($q/c_u \approx 15$). Whilst this

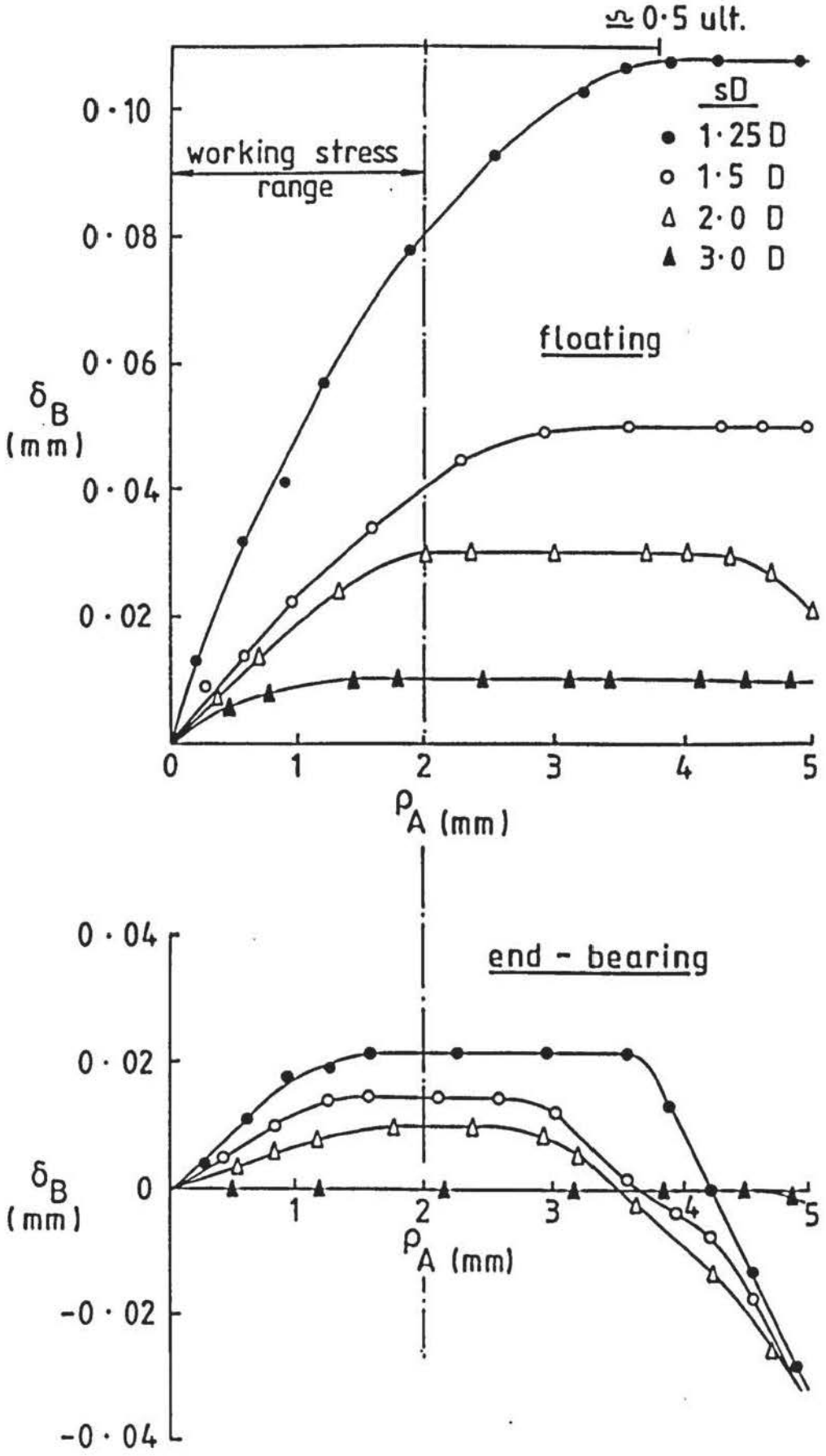

Typical variation of δ_B against surface settlement of a loaded pile ρ_A at various spacings for F and E conditions.

FIGURE 12.28

Column spacing factor s	VALUES OF SETTLEMENT RATIO R_s			
	Working Stress		0.5 ult.	
	F	E	F	E
1.25	1.04	1.011	1.03	1.05
1.5	1.02	1.0075	1.015	-
2.0	1.015	1.005	1.01	-
3.0	1.005	0	1.003	-

Typical values of settlement ratio R_s for F and E columns at various spacings.

FIGURE 12.29

difference gives excellent agreement over the working stress range, there is no correlation once this level is exceeded. It was concluded that when both the columns are loaded beyond the working stress additional interactions predominate and, as a result, the principle of superposition cannot be applied to granular columns in the same way as to conventional piles using only the results from loaded/passive column tests.

A minimum column spacing of 2.5D was proposed by Hughes and Withers (1974) on the basis of the maximum lateral extent of significant horizontal strains (i.e. less than 1%) occurring in the clay due to bulging of the column. At up to about twice working-stress ($\rho/B \approx 0.2$) the author's results, shown in Figure 12.17, support this. In the working-stress range this distance is conservative although at higher applied stress levels the influence of vertical strain and shear strain on adjacent-pile settlement suggests column spacings of over 3.0D.

For comparison, settlement of the clay surface adjacent to a loaded column was also measured at various spacings upt to 3.0D (Test Nos. IC1 TO IC5 and IC1E to IC5E). The maximum vertical displacement ($+\delta_B$) of the surface of the clay and passive column are compared at the same increasing radial distance (sD) in Figure 12.30. Apparently settlement is reduced by the presence of the column alone.

12.4.3 Column-clay distortion

Lateral distortions of a column at 1.5D from a similar column when both are loaded simultaneously at $\rho/B = 0.2$, 0.66 and 1.5, for F and E conditions, are shown in Figure 12.31.

On the clay side of the columns, the magnitude and distribution of the lateral distortions are the same as for the single isolated column (Figure 12.6), in F and E conditions, for all three vertical dispalcement stages. On the adjacent column side, the lateral distortion down the column length is suppressed. This effect becomes more apparent as ρ/B increases, and is due to the approach of the sides of the bulging columns. Since bulging starts at the top of each column, this suggests that the clay between them is deformed downwards, causing the additional settlement of each column that would not exist when one of the columns is passive.

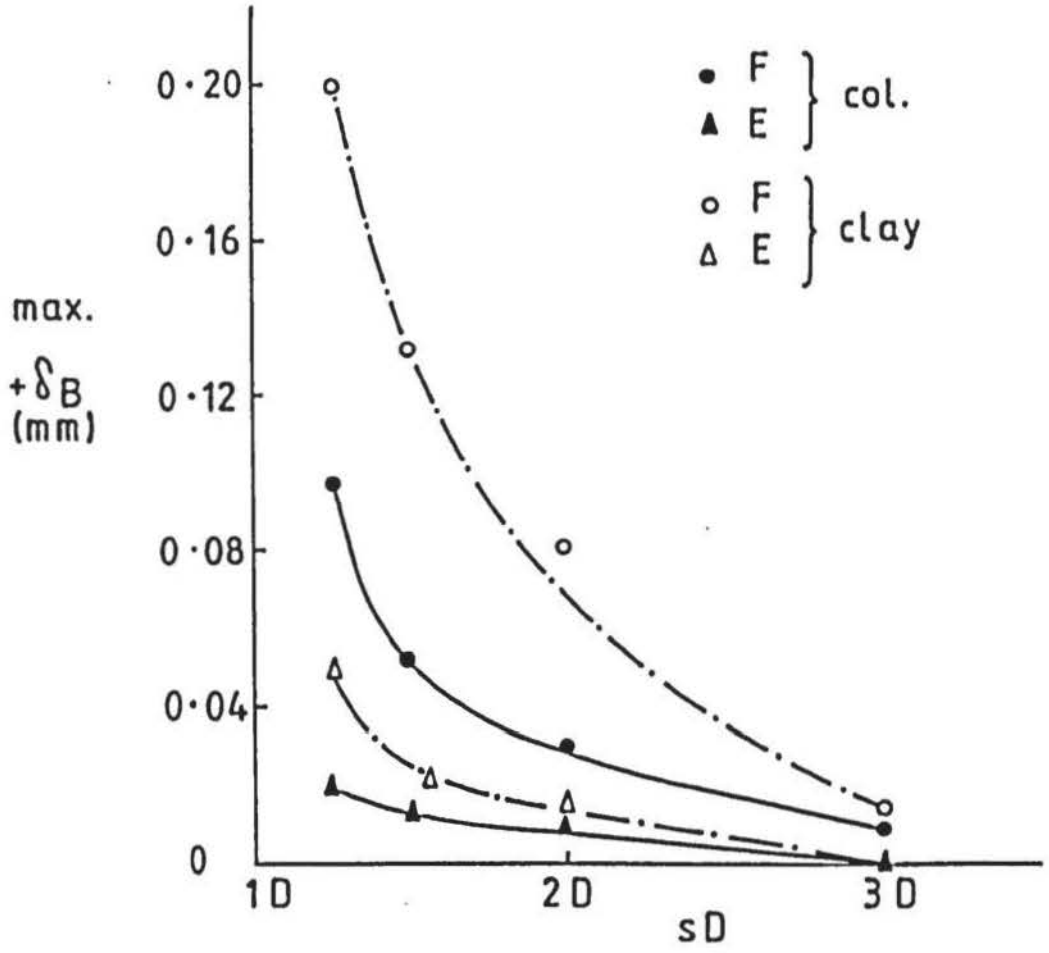

Typical variation of maximum settlement $+\delta_B$ of clay and column surface at increasing distance sD from a loaded column.

FIGURE 12.30

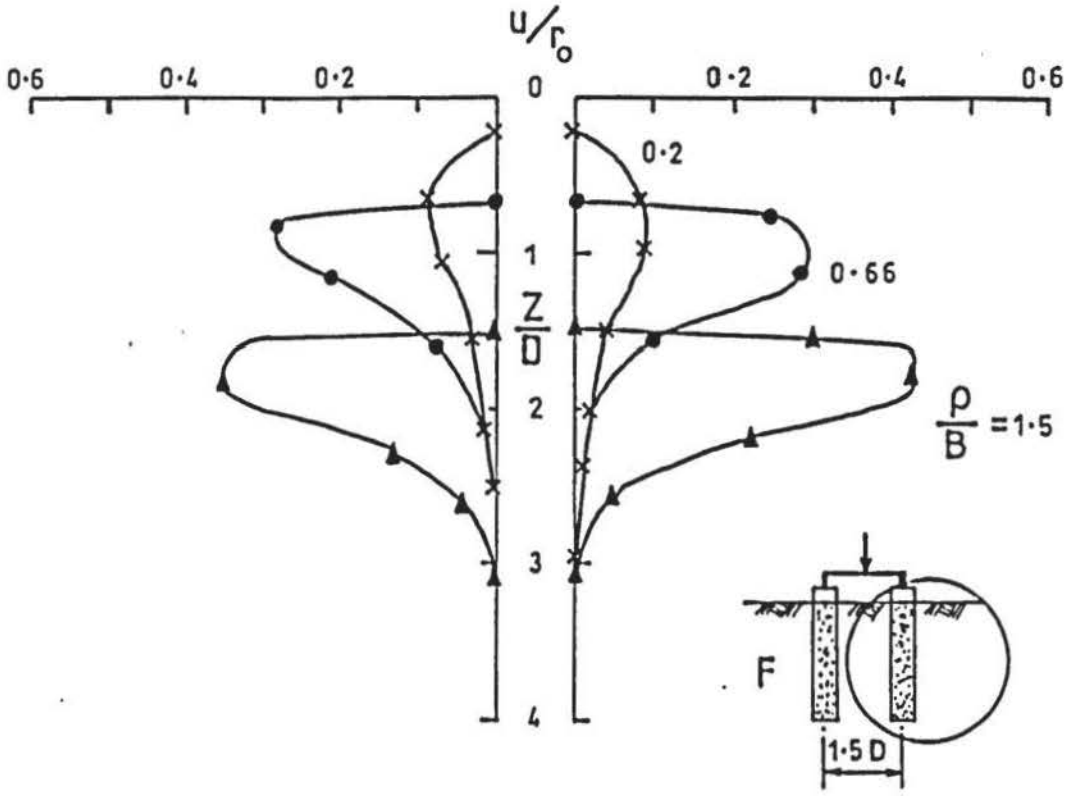

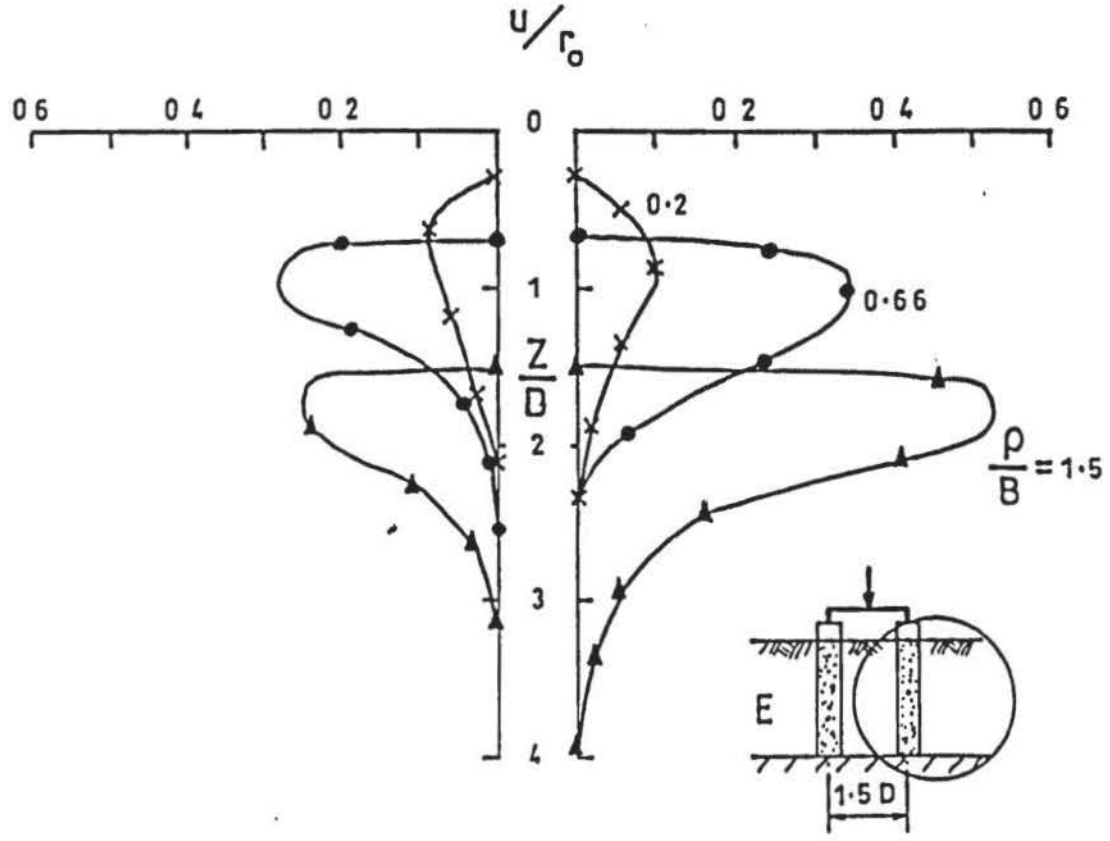

Lateral distortions of a column at 1.5D from a similar column when both are loaded simultaneously, for F and E conditions.

FIGURE 12.31

Continuation Page.....

The corresponding relative vertical distortions within the columns and adjacent clay are shown in Figures 12.32 to 12.34. The characteristics are largely similar to a single isolated column in that distortion within the column increases with increasing ρ/B, and at $\rho/B \geq 0.66$ the distortions within the column are greater than those in the clay. Strain reversal is also shown by the F column at $\rho/B = 1.5$.

On the column side, the vertical distortion in the adjacent clay is greater than at the opposite side of the column, which becomes more apparent as ρ/B increases. This gives some support to the idea of downward squeezing of the clay between the columns inducing additional interactive settlement. Also on the column side, relative distortions between the column and clay, and within the column, are almost totally suppressed at the lower portion of the column. As these distortions still occur at the opposite side, this suggests that the columns and the clay between them are acting as a composite system. This would cause a larger volume of clay near and beneath the column toe to be stressed resulting in greater vertical strain, and hence greater settlement.

12.4.4 Clay displacement fields

The downward squeezing effect in the clay is immediately apparent in Figures 12.35 to 12.37. There is also movement indicated at the base of the F columns, which is both downward and lateral, commencing at the first strain increment ($\rho/B = 0.2$). With a single F column, vertical displacement at the column toe was not observed at this stage. Displacement trajectories along the length of the F column, on the clay side, also differ by having a larger vertical component than with the single F column. These effects are more apparent at the second strain increment ($\rho/B = 0.66$).

It is considered, therefore, that the additional interactive settlement is due to the downward deformation of the clay between the columns which is induced by the progressive growth of the bulging zones from the top of each column. With the F columns, the effect is magnified by movement at the abse of the columns.

The displacement trajectories indicate that the columns and the clay between them act as a single unit from at least $\rho/B = 0.2$.

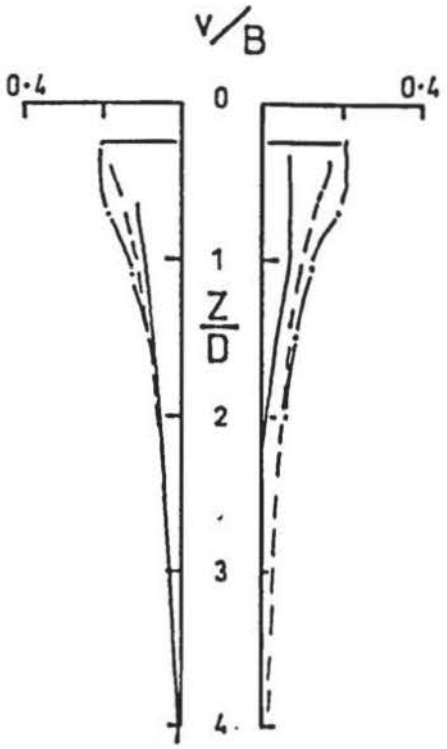

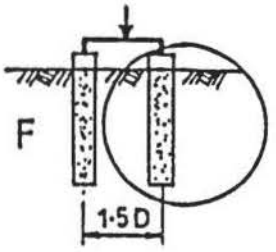

$\frac{\rho}{B} = 0{\cdot}2$

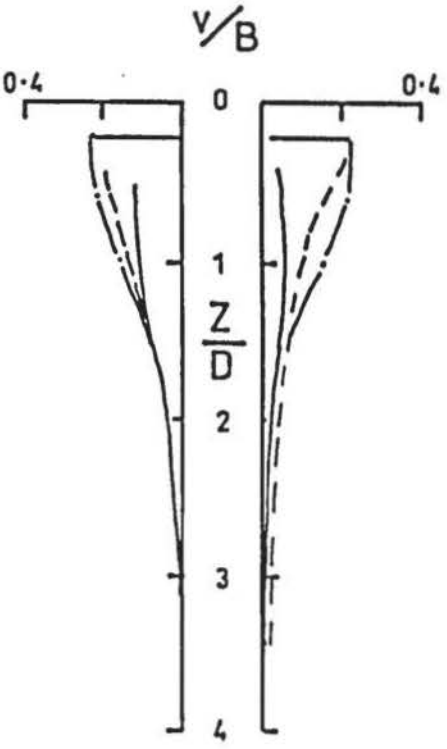

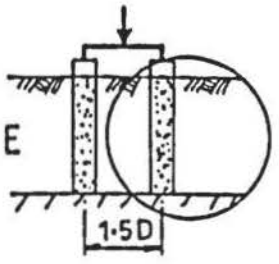

Relative vertical distortions within a column at 1.5D ($\rho/B = 0.2$).

FIGURE 12.32

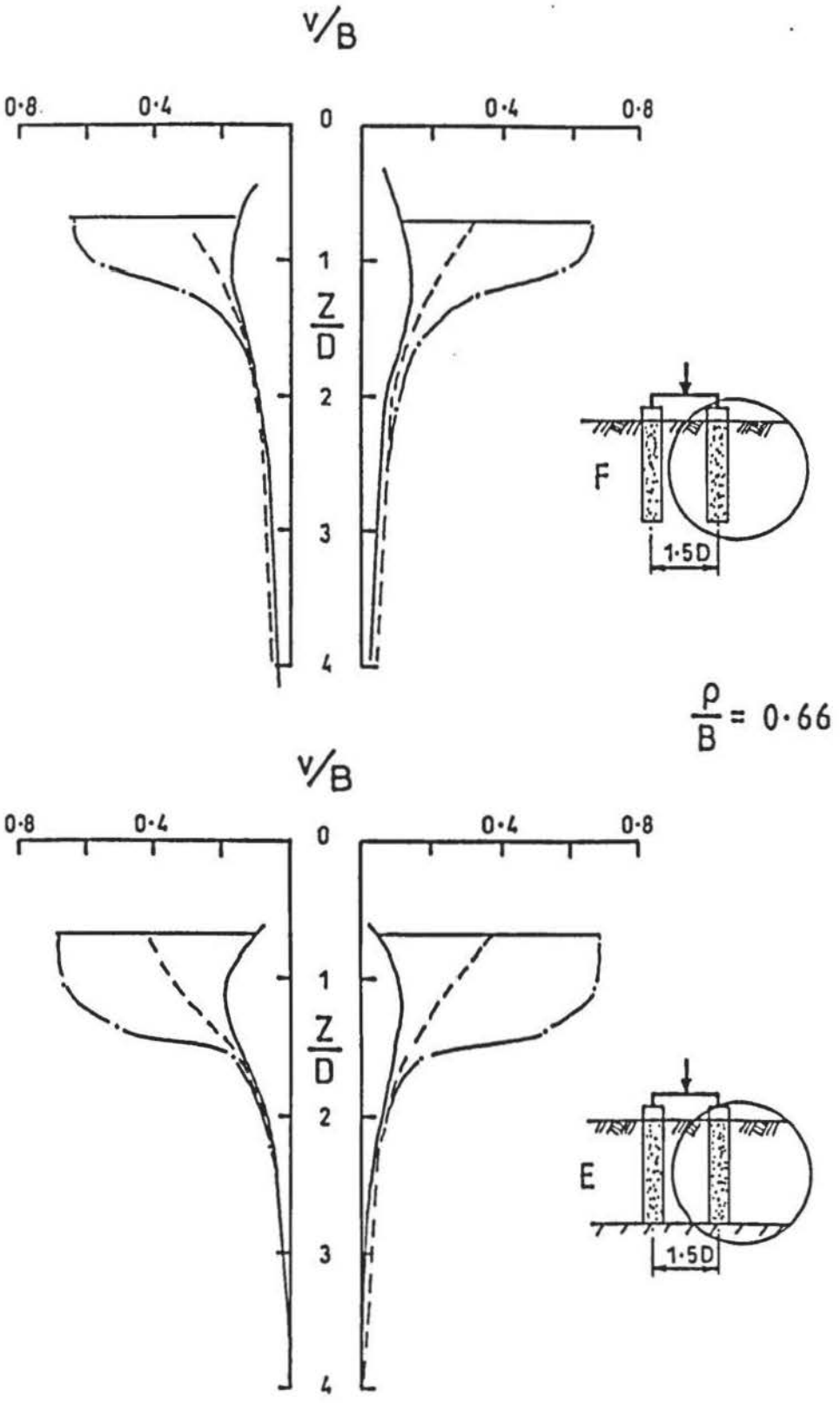

Relative vertical distortions within a column at 1.5D ($\rho/B = 0.66$).

FIGURE 12.33

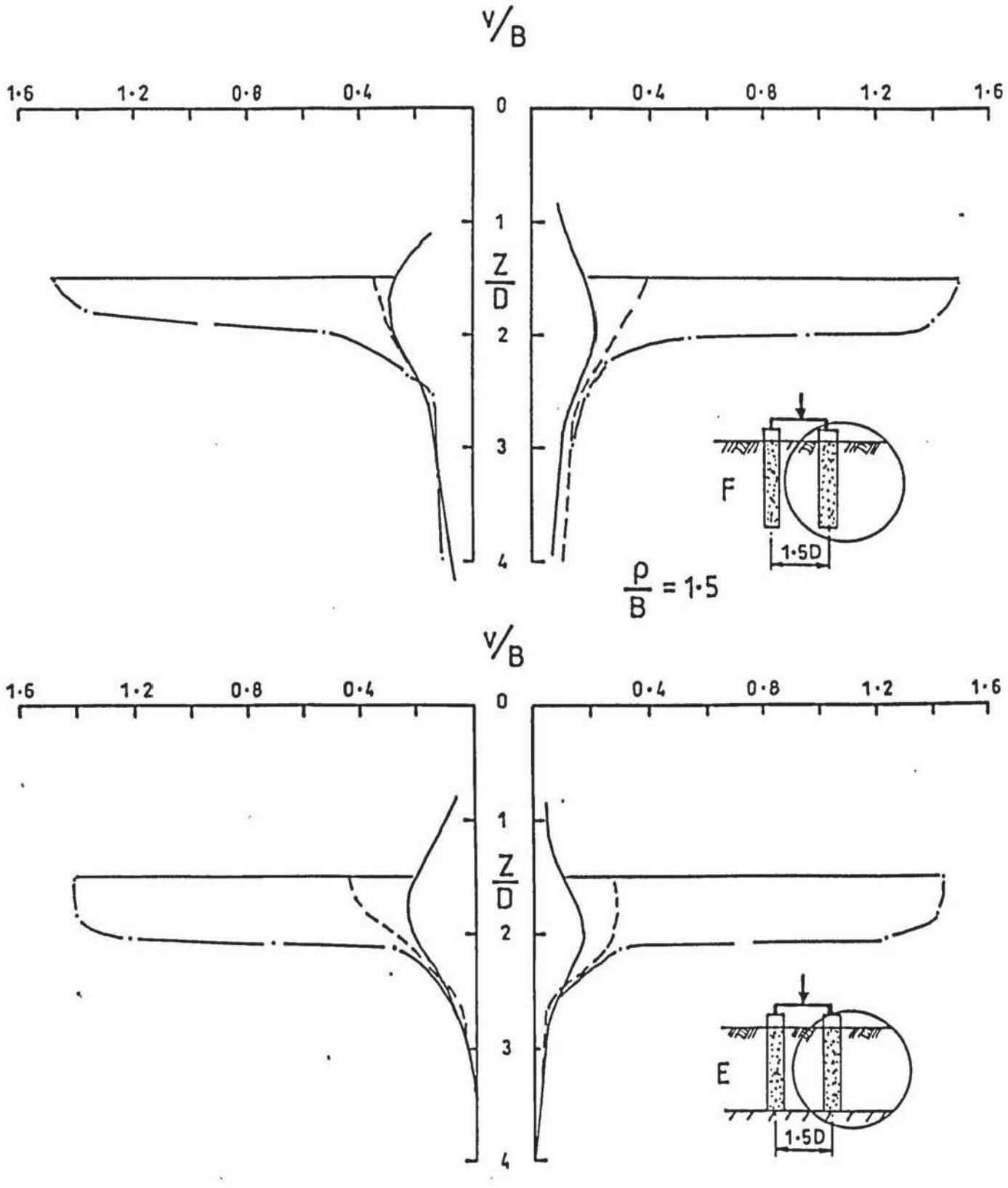

Relative vertical distortions within a column at 1.5D (ρ/B = 1.5).

FIGURE 12.34

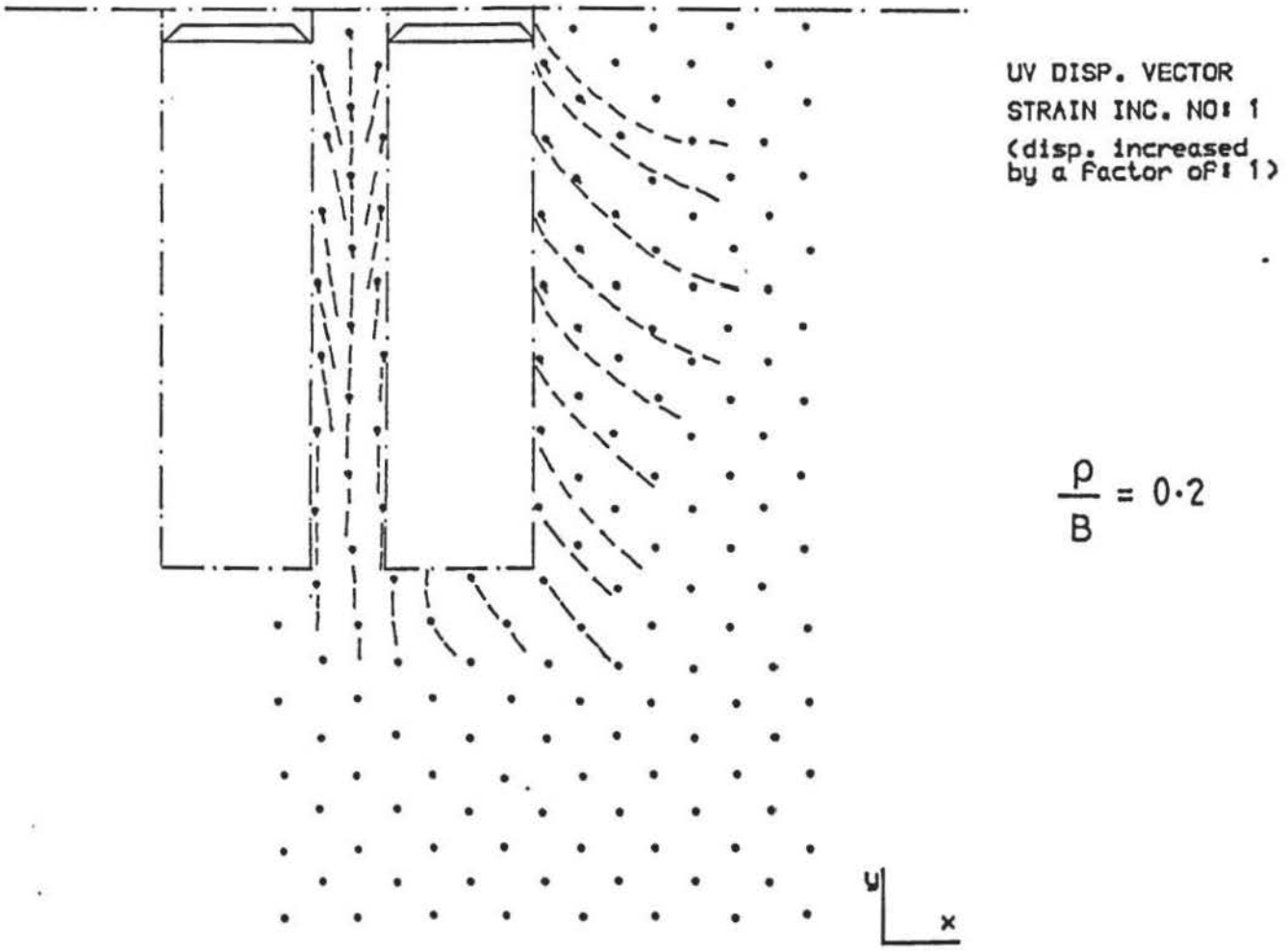

Clay displacement fields at ρ/B = 0.2, due to two columns at 1.5D, for F and E conditions.

FIGURE 12.35

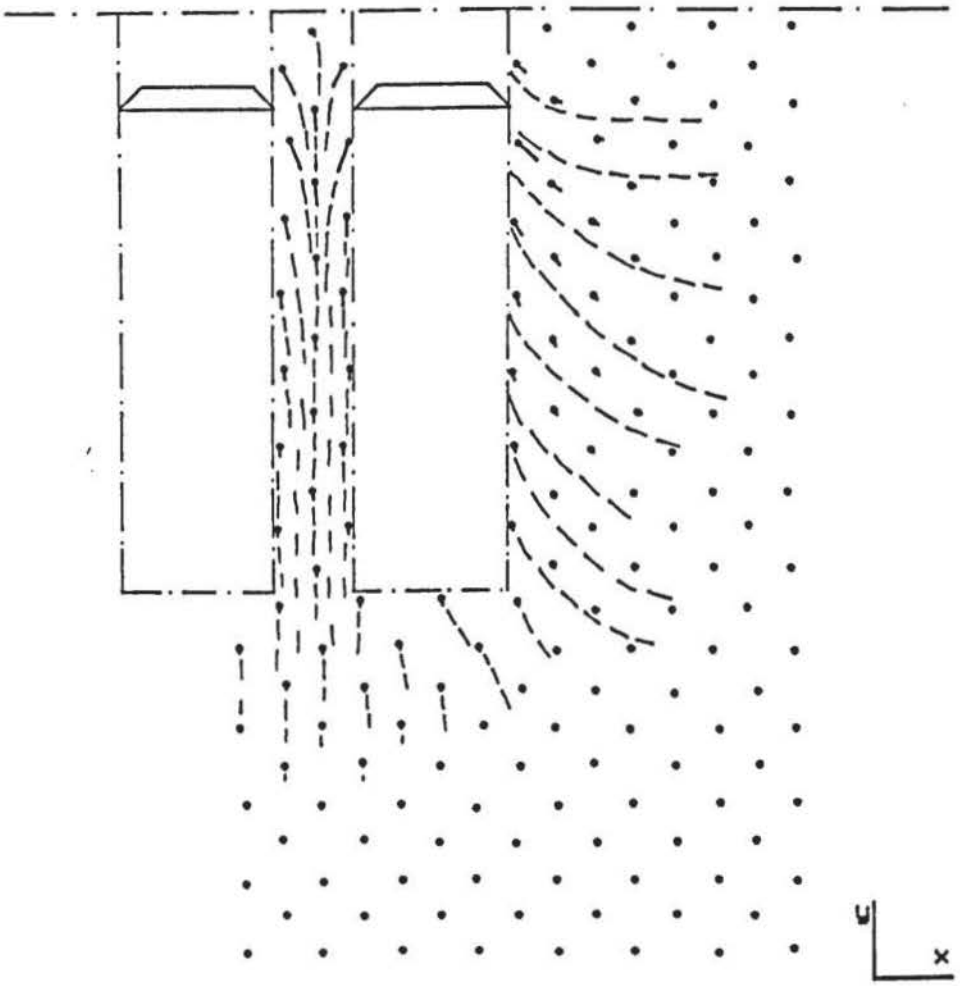

Clay displacement fields at ρ/B = 0.66, due to two columns at 1.5D, for F and E conditions.

FIGURE 12.36

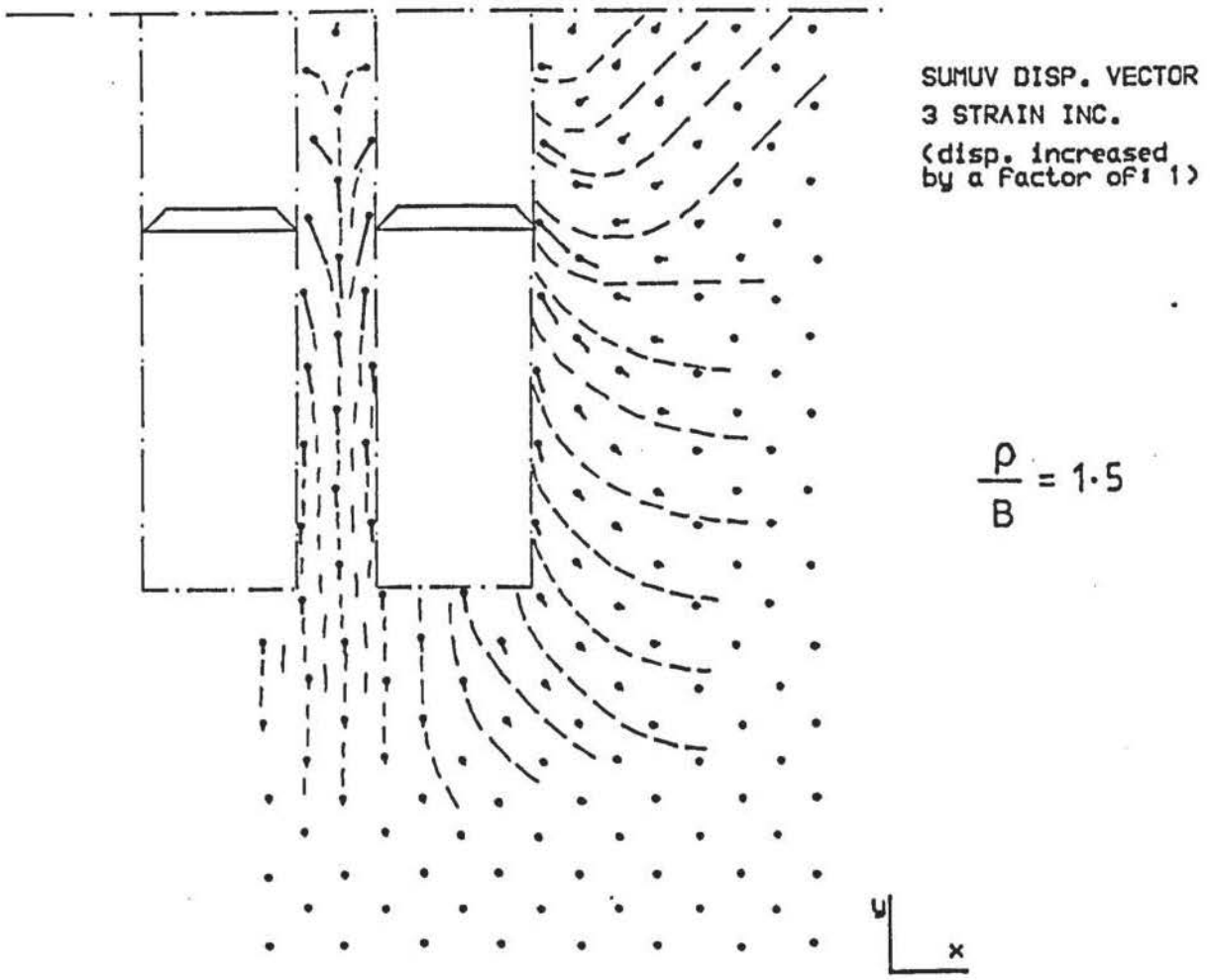

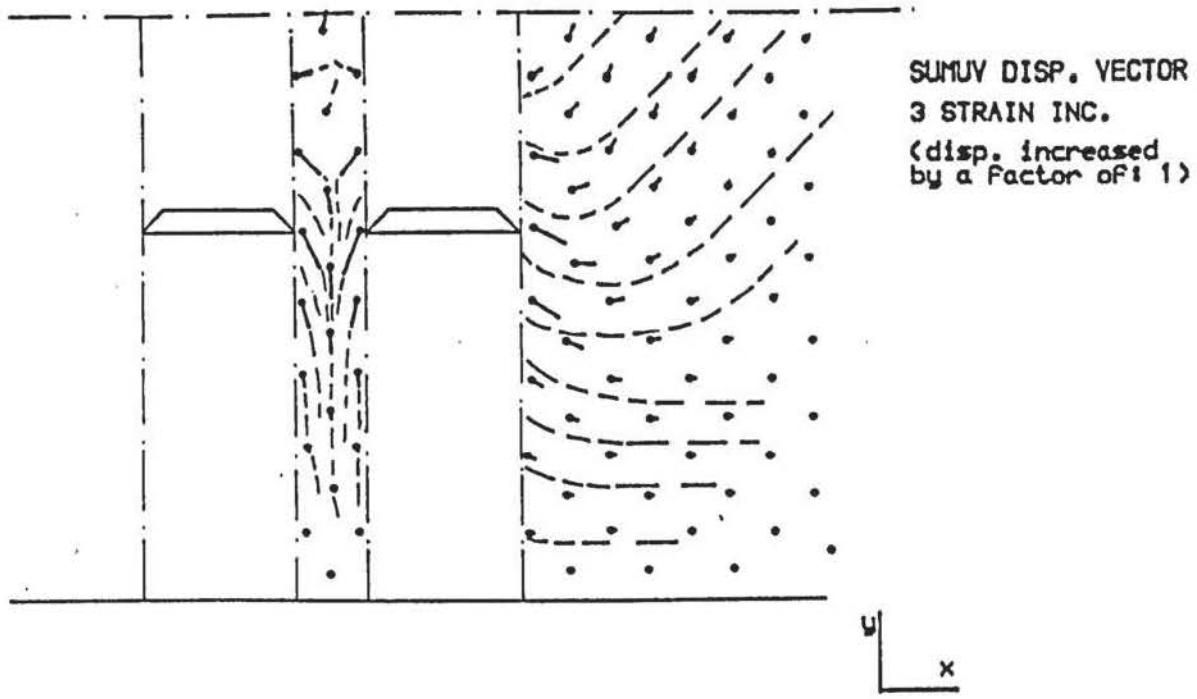

Clay displacement fields at ρ/B = 1.5, due to two columns at 1.5D, for F and E conditions.

FIGURE 12.37

12.4.5 Column-soil strains

Strains ε_x and ε_y, ε_1 and ε_3, γ_{xy} for two similar simultaneously loaded columns at 1.5D spacing (Test Nos.: XTC2 and XTC2E) are shown in Figures 12.38 and 12.39 for strain increment number 1 ($\rho/B = 0.2$), Figures 12.40 to 12.41 for strain increment No. 2 ($\rho/B = 0.66$) and Figures 12.42 to 12.43 for stain increment number 3 ($\rho/B = 1.5$).

Because of the unsymmetrical boundary conditions to which the columns are subject, strains are shown on either side of the centre-line of one column. However, in the E case intermmediate lead-shot were inadvertently omitted during the test, on the adjacent column side, and so strains for that case are not shown. In the F case ε_x, ε_y and ε_1, ε_3 reveal almost complete symmetry about the column axis for all the strain increments, and are similar to those of a single column.

A significant distribution of vertical strains (ε_y) is shown in the clay, between the F and E columns. Their magnitude and depth of influence, from the bulging zone, increase with each strain increment and are more than in the clay surrounding the columns. This further supports the view of the squeezing effect. Indeed, just above the bulging zone ε_y is shown to be tensile as clay is squeezed upwards. There is less engineering shear strain in the clay between the columns and consequently rotation of principal planes is less than in the surrounding clay. By the second and third strain increments the major principal strains are almost horizontal in the bulging zone and near vertical beneath it. This supports the observation that shear deformations are suppressed within the clay, previously shown in Figures 12.32 to 12.34.

A greater zone of clay beneath the column bases becomes strained with increasing ρ/B. At the third strain increment it is apparent that the columns and intermediate clay are acting as a unit, in terms of vertical displacement.

12.4.6 Zero extension

As with a single column, the zero extension lines show a well-defined zone of plastic deformation on the clay side of the column by the first strain increment, and also within the

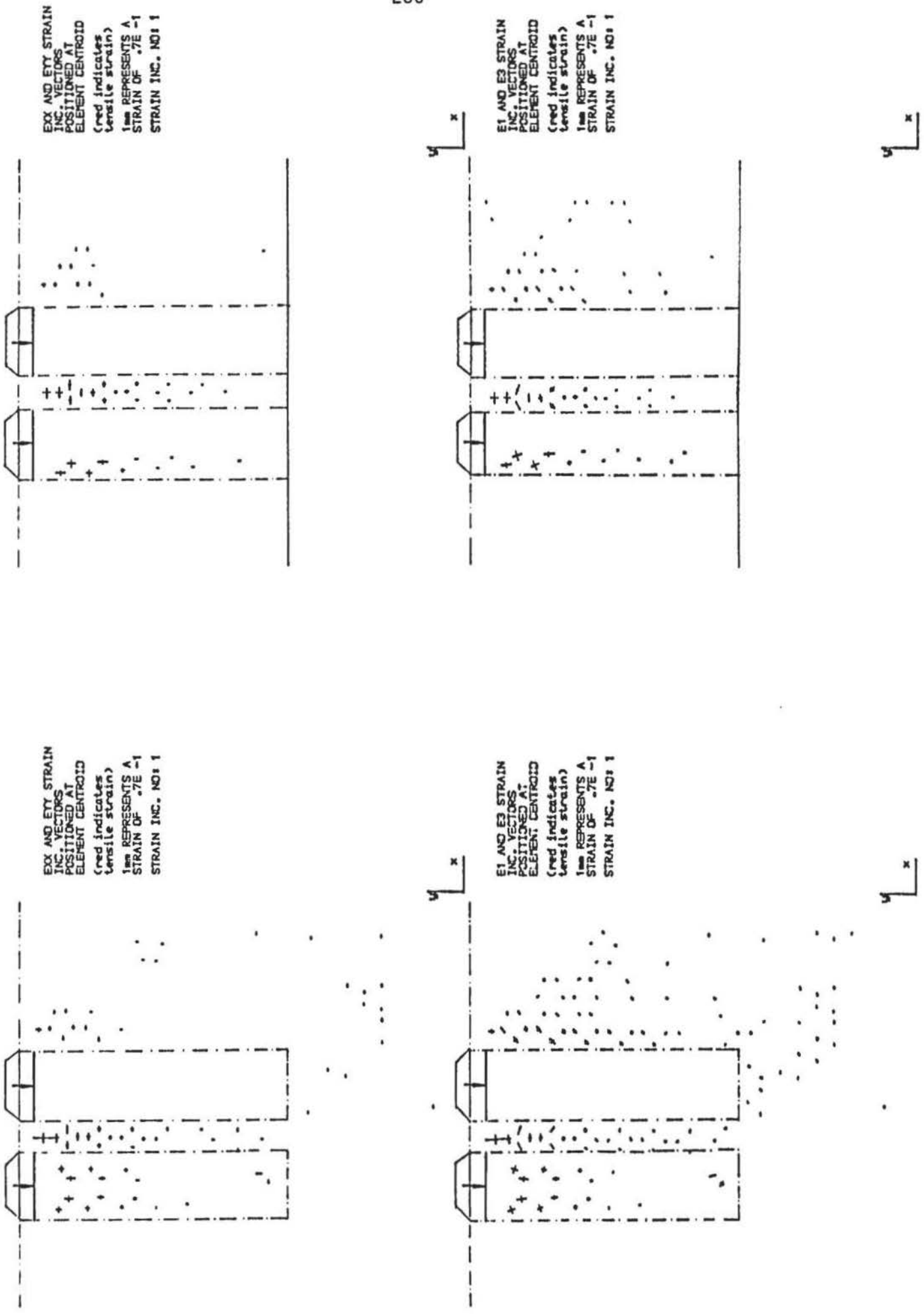

ε_x and ε_y, ε_1 and ε_3 vectors for F and E columns at $\rho/B = 0.2$.

FIGURE 12.38

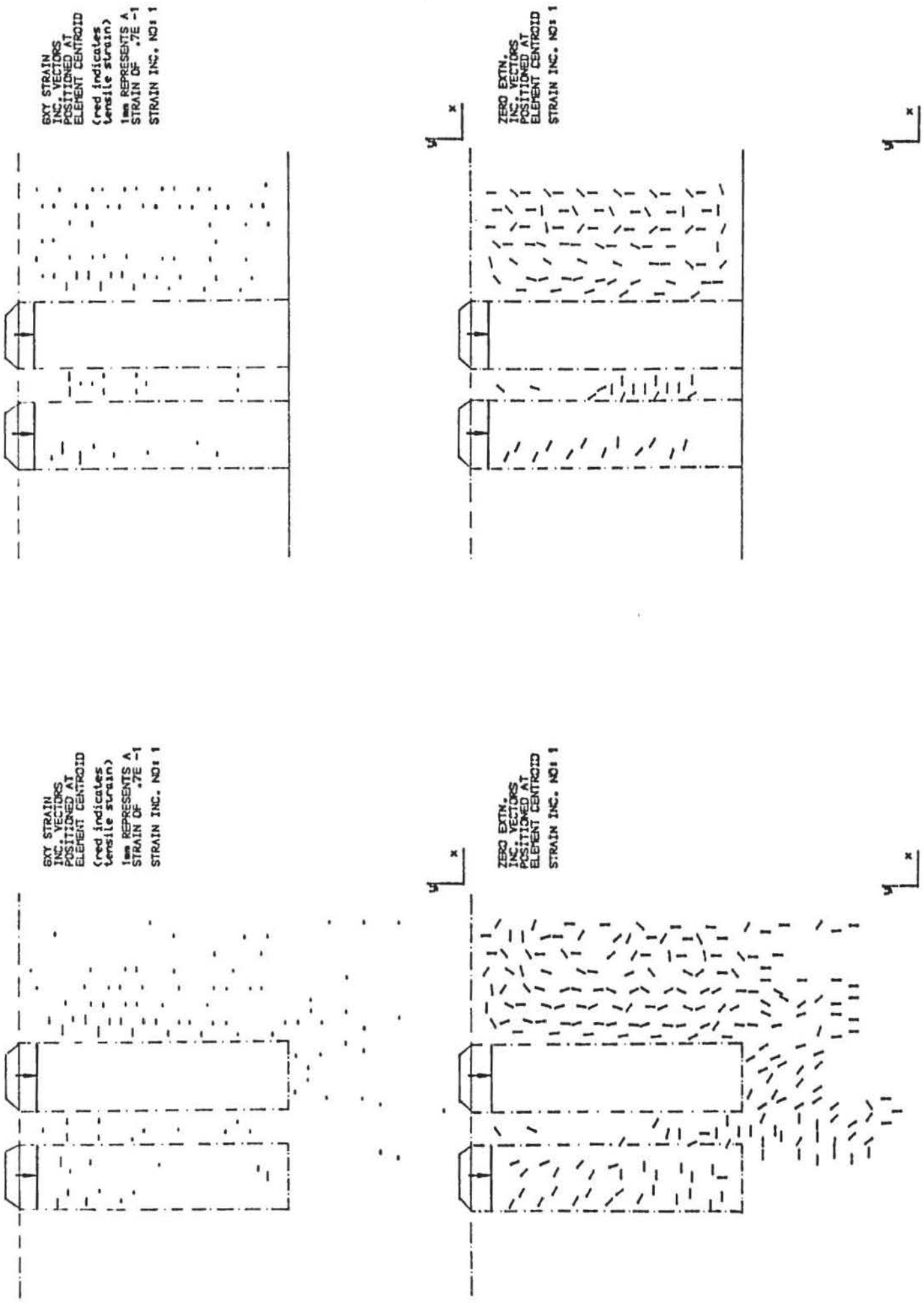

γ_{xy} and zero extension lines for F and E columns at $\rho/B = 0.2$

FIGURE 12.30

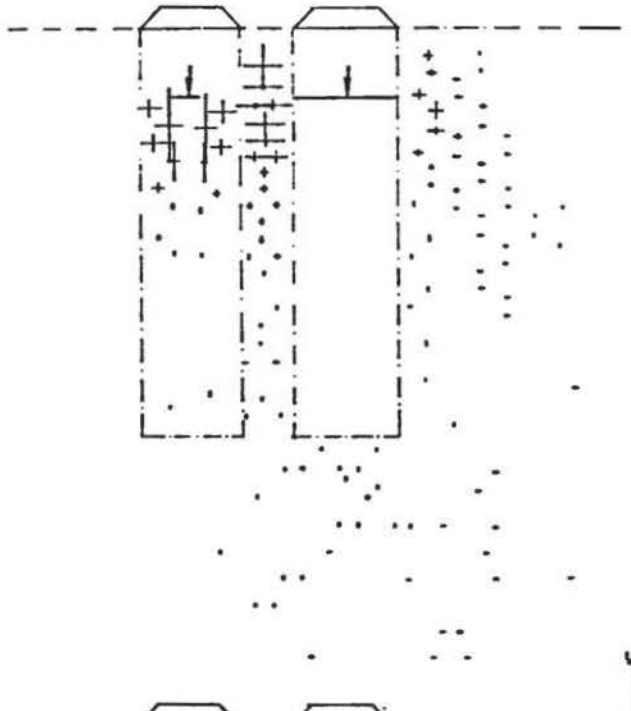

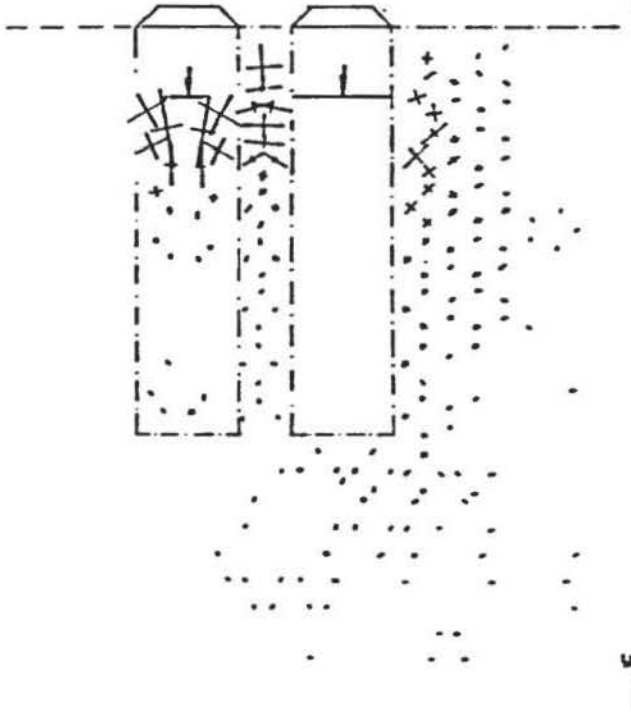

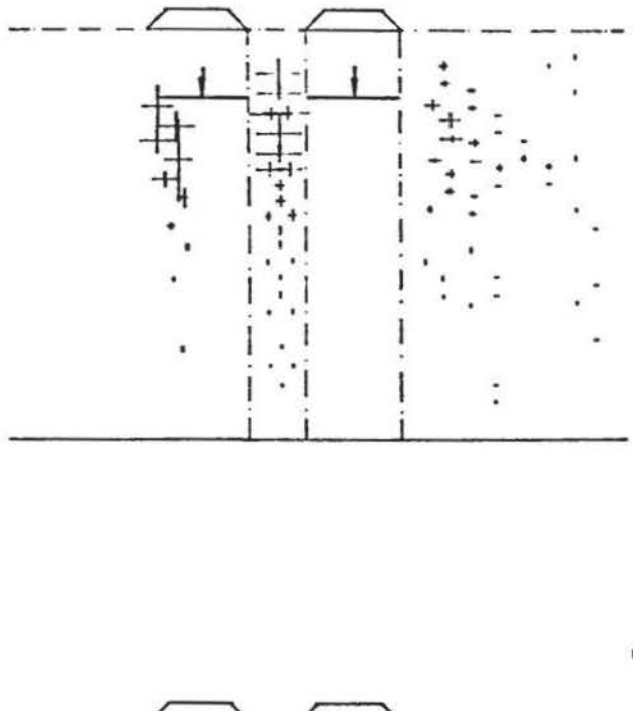

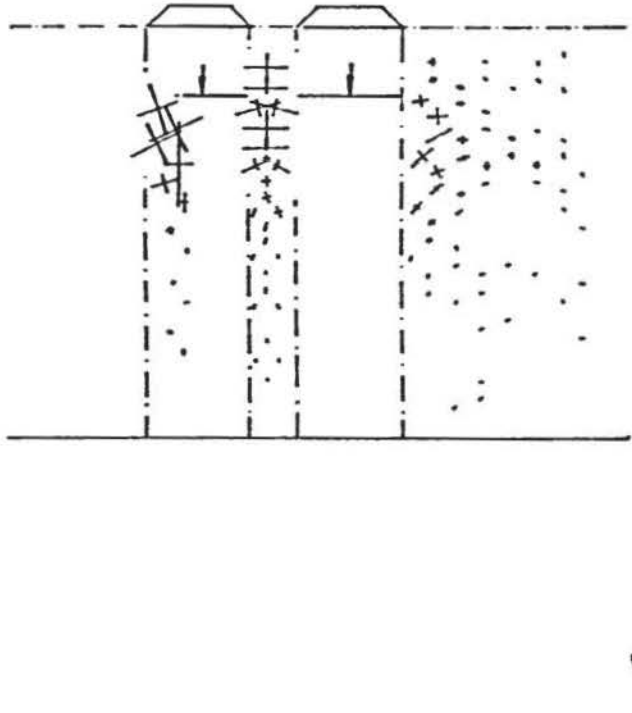

ε_x and ε_y, ε_1 and ε_3 vectors for F and E columns at $\rho/D = 0.66$.

FIGURE 12.40

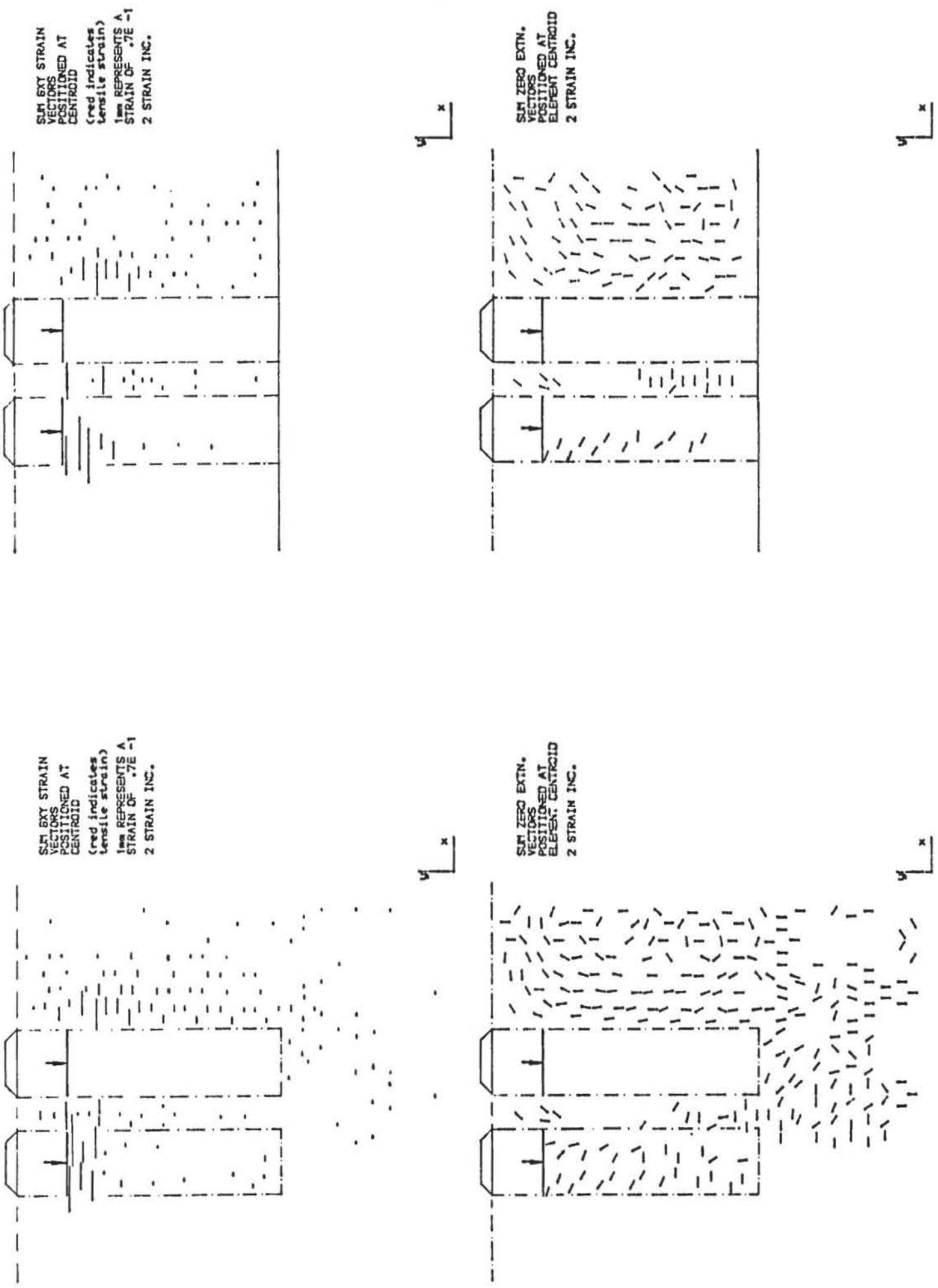

γ_{xy} and zero extension lines for F and E columns at $\rho/B = 0.66$.

FIGURE 12.41

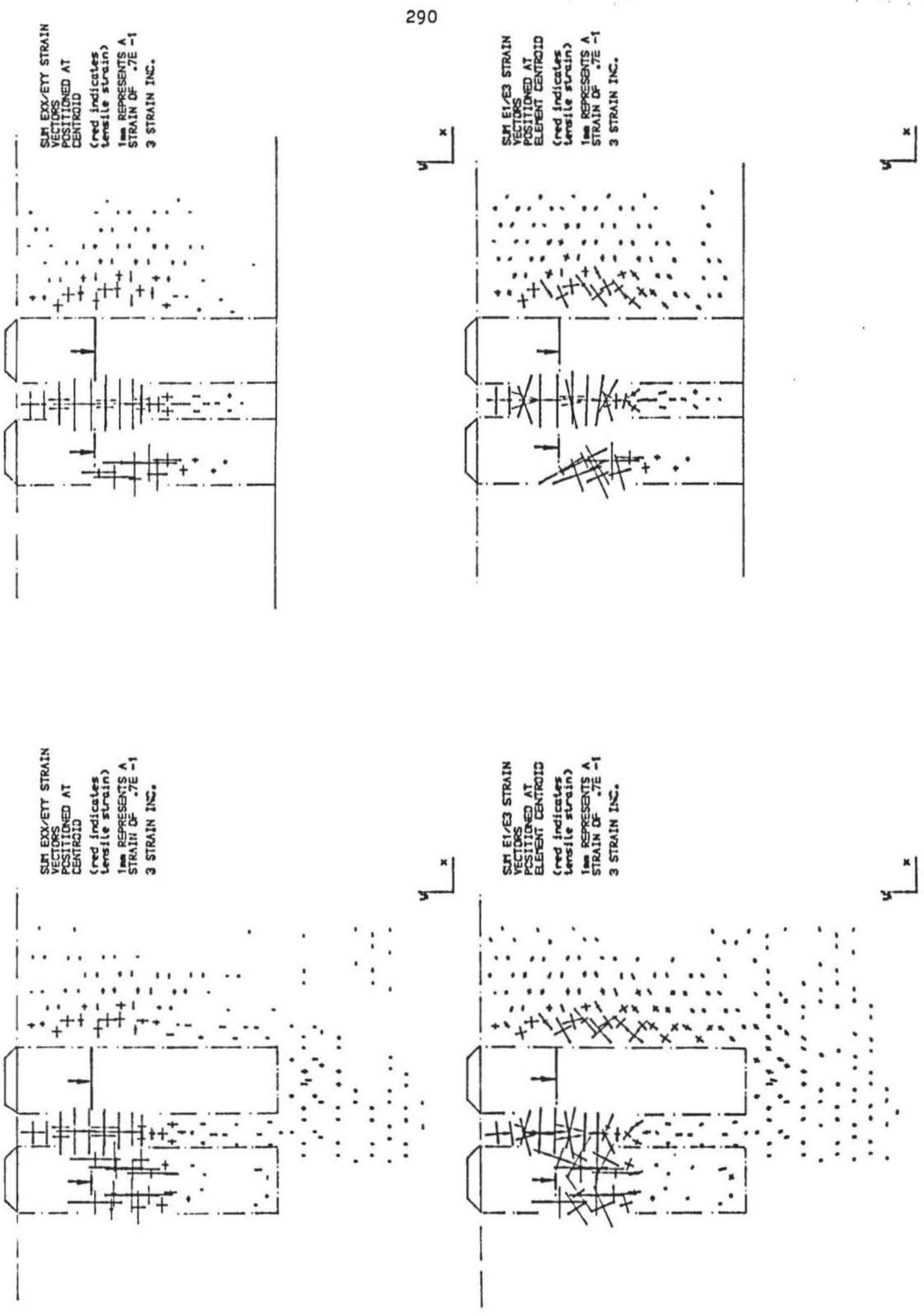

ε_x and ε_y, ε_1 and ε_3 vectors for F and E columns at $\rho/B = 1.5$.

FIGURE 12.42

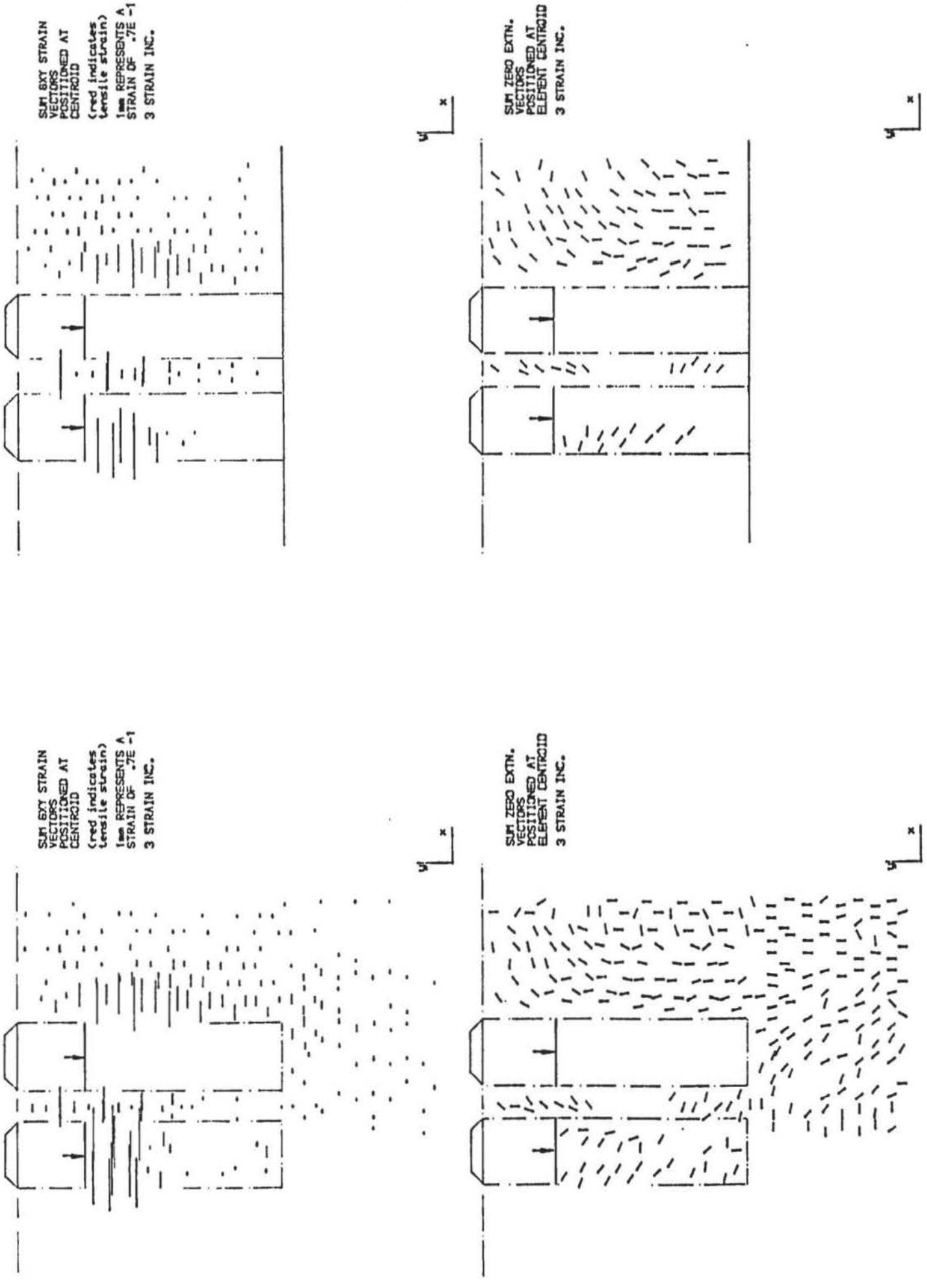

γ_{xy} and zero extension lines for F and E columns at $\rho/B = 1.5$.

FIGURE 12.43

column.

Where there are no zero extension lines within the clay between the columns, this is because the areal strain ($\varepsilon_x+\varepsilon_y$) is greater than the maximum engineering shear strain (γ_m).

12.5 FOUNDATIONS ON SINGLE COLUMNS

12.5.1 Boundary stresses and settlement

Single columns, in F and E conditions, were subject to loading by circular and square foundations of various sizes (Test Nos.: C1 to C1E and SQ1 to SQ1E) and also by a rectangular foundation (Test Nos.: R and RE) that had the same width as the column. Typical examples of the variations of q/c_u and $\Delta\sigma_x/q$ with ρ/B for single F columns are shown in Figure 12.44. The replacement ratio (a_c), defined previously by Equation 1.21 as the initial area of the column ($\pi D^2/4$) divided by the area of the foundation, relating to each test is shown adjacent to the corresponding q/c_u - ρ/B curve. Peak $\Delta\sigma_x/q$ typically occurred at ρ/B = 0.2 to 0.35, with its magnitude increasing as a_c decreased. The latter decreased the distance between the edge of the foundation and the horizontal stress transducer and so higher stresses were recorded.

The variation of applied pressure with settlement is strongly dependent on a_c. For a given ρ/B, the value of q/c_u decreases with a_c for the square and circular foundations. The results obtained from the rectangular (a_c = 0.2) and the largest square foundation (a_c = 0.05) are out of sequence, in relation to the a_c values, with the other curves. This may be explained in terms of the bearing capacity factor N_c which relates undrained cohesion to the ultimate bearing pressure. For circular and square foundations N_c is the same, where N_c for a rectangular foundation is less by an amount depending on the relative sizes of its width and length (e.g. Skempton, 1951). Consequently, a rectangular foundation having the same area as a square or circular foundation will sustain smaller bearing pressures. Also, as the square foundation becomes larger the boundary effects of the clay container become more significant and result in slightly higher bearing pressures.

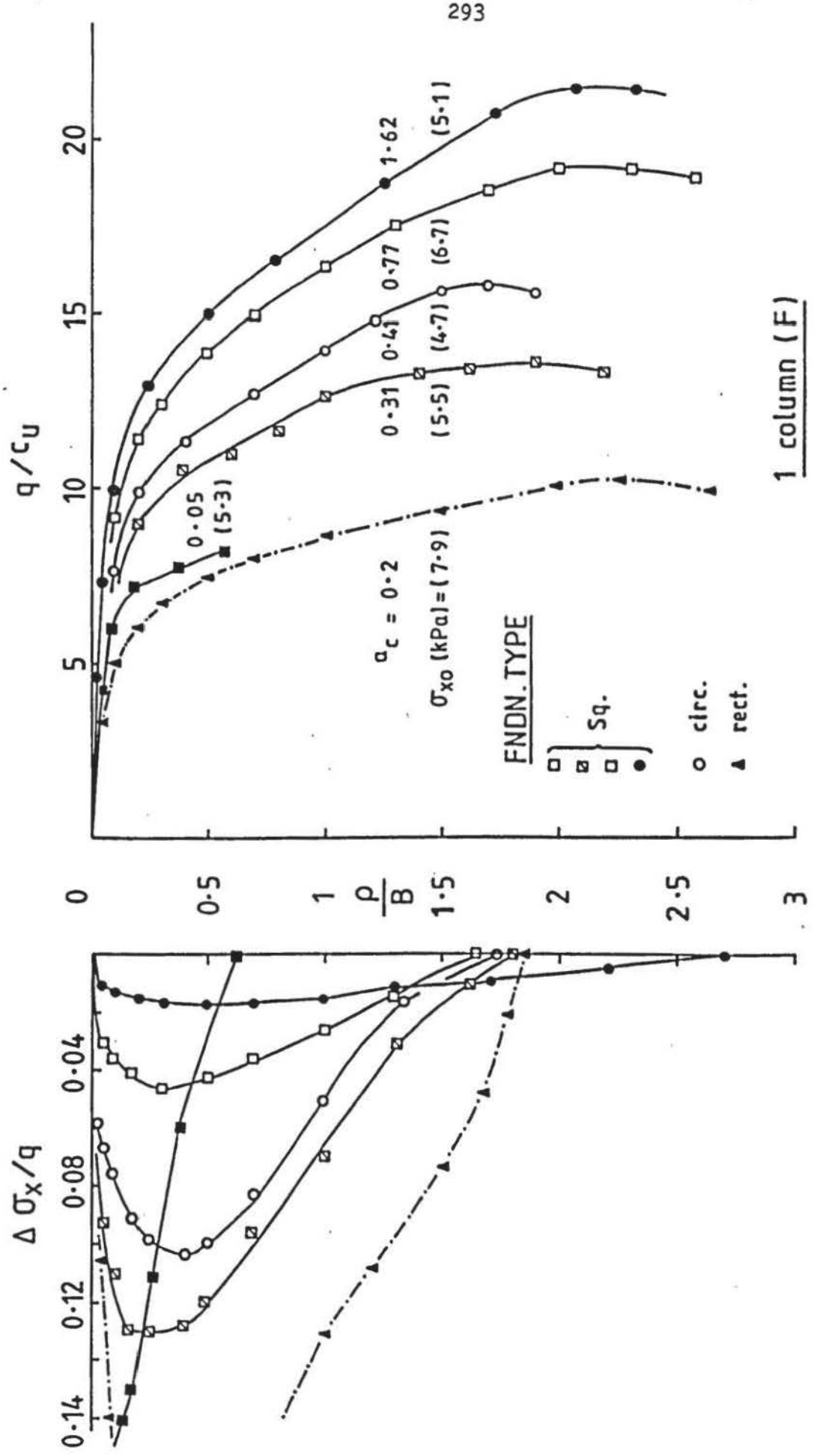

Typical variations of q/c_u and $\Delta\sigma_x/q$ against ρ/B for single columns loaded by foundations of various geometries.

FIGURE 12.44

Ultimate values of q/c_u were obtained in all the tests with the exception of the largest square foundation ($a_c = 0.05$; B = L ≈ 150 mm) because of the limitations of the upward travel of the platen of the compression machine. Ultimate q/c_u when $a_c = 0.31$, was almost half of that obtained when $a_c = 2.48$. Similarly, working stresses are also affected. A table of ultimate and working q/c_u with the corresponding magnitude of a_c are shown in Figure 12.45. It is also shown that ρ/B at working stresses is generally the same, which on average gives $\rho/B \approx 0.054$.

Using q/c_u values at ρ/B = 0.05, 0.2, 0.66 and 1.5 a formal relationship was established between q/c_u and $1/a_c$, for the square and circular foundations, which is given in Figure 12.46 for the F case. Curves for the E case were similar with slightly higher q/c_u for the same $1/a_c$. In essence, the relationship shows the bearing capacity of the foundations increases as the column cross-sectional area beneath them becomes larger and decreases at the clay area increases relative to the column area.

This effect may be explained by considering two extreme cases. When the area of a column is infinitesimal compared to the size of the foundation, the bearing pressure will be limited to the bearing capacity of the clay (q_{CLAY}). Conversely, when the column area is many times greater than the foundation the bearing pressure will be governed by the bearing capacity (q_{GRAN}) of the granular material forming the column. From the engineering characteristics of the soft clay and the high ϕ' and density of the column material, then $q_{GRAN} >> q_{CLAY}$, which defines the upper and lower limits of available bearing capacity. Consequently, as a foundation size increases relative to the column, its bearing capacity tends to q_{CLAY}. To maximise the bearing capacity, a_c needs to be as large as practicable for a given column specification and performance.

Foundation type	a_c	Ultimate stress $[q/c_u]^{ult}$	Working stress $[q/c_u]^{ult}/3$	ρ/B at working stress
Circ.	2.48	26.1	8.7	0.054
Sq.	1.62	22.6	7.5	0.057
Circ.	1.0	21.5	7.2	0.053
Sq.	0.77	19.3	6.4	0.065
Circ.	0.59	17.6	5.9	0.052
Sq.	0.47	16.0	5.3	0.048
Circ.	0.41	15.9	5.3	0.058
Sq.	0.31	13.68	4.6	0.048
Average ρ/B at working stress :				≈0.054

Table of ultimate and corresponding working stresses and the ρ/B at which they occur for single F columns loaded by square and circular foundations of various sizes.

FIGURE 12.45

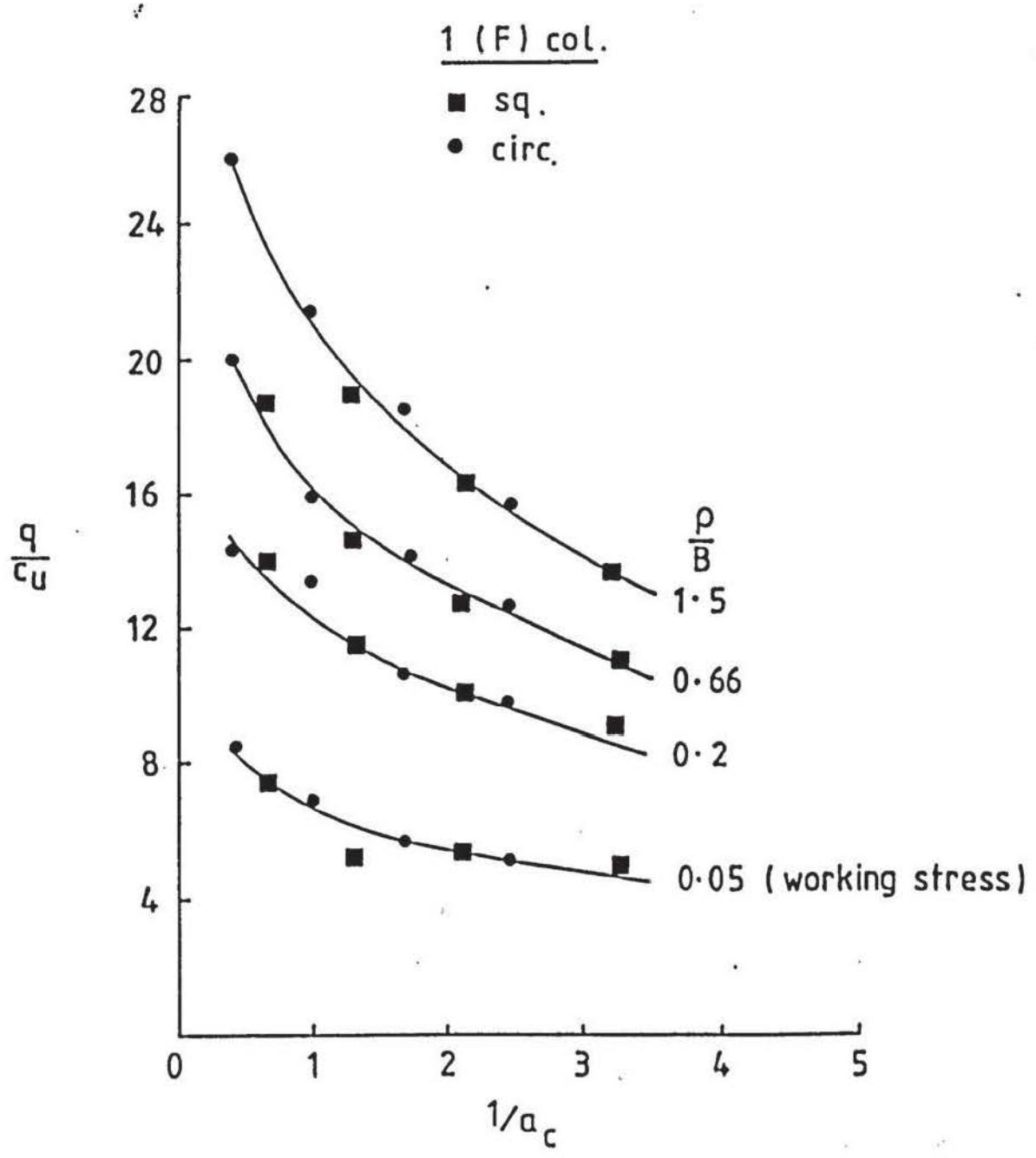

Typical variation of q/c_u with $1/a_c$ for a single F column loaded by circular and square foundations.

FIGURE 12.46

12.5.2 Improvement

Typical bearing capacity improvement curves of I_q against ρ/B are shown in Figure 12.47. Potential improvement decreases as the foundation size increases with respect to the column (i.e. a_c decreases) and becomes almost negligible when $a_c \leq 0.05$. I_q for the rectangular foundation (represented by shaded triangular symbols in Figure 12.47) now lies in sequence, in terms of a_c, since I_q is a measure of the increased bearing capacity (q) relative to the bearing capacity for the same foundation on the clay (q_{CLAY}).

When a_c is less than 0.77, peak values of I_q are not apparent which suggests that column yield is suppressed as a greater proportion of the total load is taken by clay.

Typical settlement improvement curves of m against q/c_u are given in Figure 12.48. These show that potential improvement in settlement is also strongly dependent on a_c, with no improvement being shown up to working stress when $a_c \leq 0.05$. This effect may be similarly explained by considering again the two extreme cases of foundation size relative to the column area, discussed in the previous Section. Compressibility of the column material will be substantially less than for the clay (i.e. $\rho_{GRAN} << \rho_{CLAY}$) and also will not be subject to any long-term settlement, although consolidation settlement does not form any part of the present study.

So, as with the case of bearing capacity, when the foundation size increases relative to the column area, settlement characteristics of the clay will become more predominant.

The relationships shown in Figure 12.49 were established between working stress values of I_q ($[I_q]^{WS}$) and m ($[m]^{WS}$) with $1/a_c$ for the square, circular and rectangular foundations in F and E conditions. The magnitude, and rate of decrease, of $[I_q]^{WS}$ decreases with $1/a_c$ based on a logarithmic scale. This is attributable to an increasing proportion of the applied load being taken by the clay as the foundation area increases relative to that of the column. For the same reason, the rate of increase in m reduces as a_c decreases. For maximum improvement in

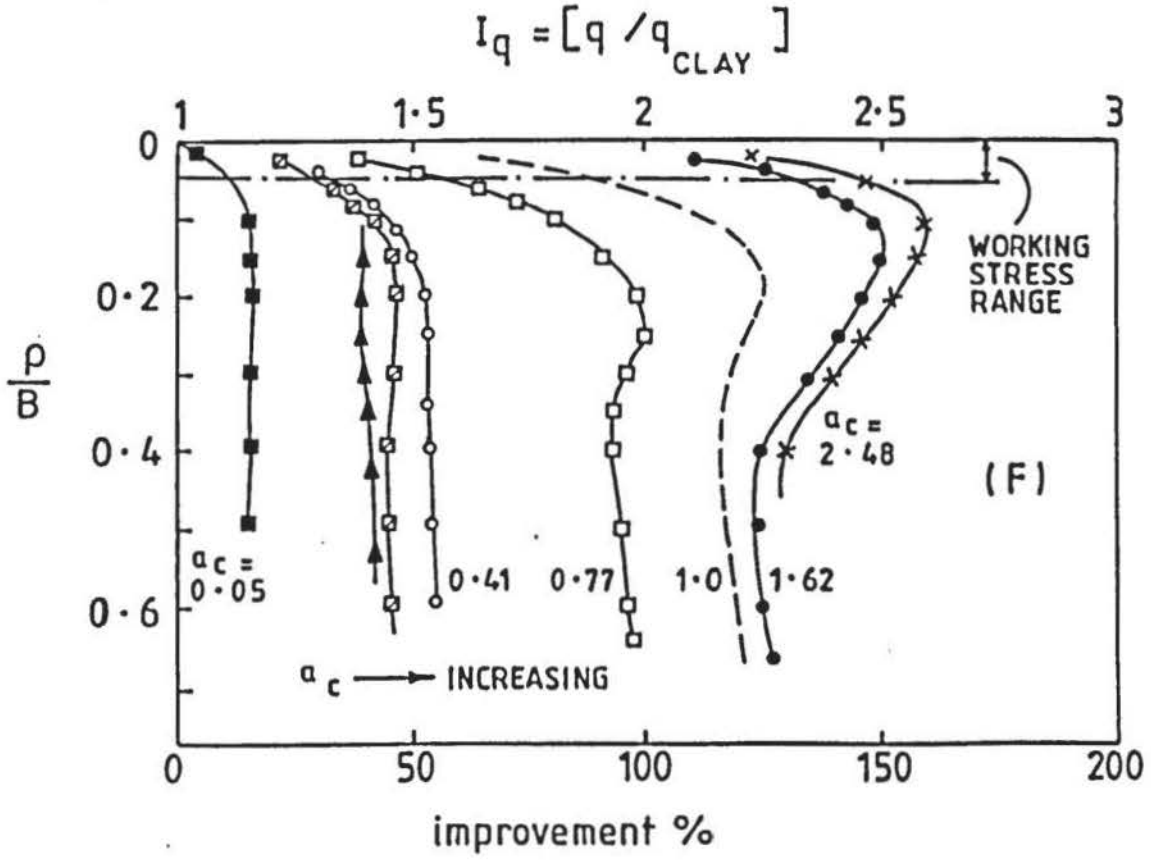

Typical bearing capacity improvement curves for a single F column loaded by foundations of various sizes and geometries.

FIGURE 12.47

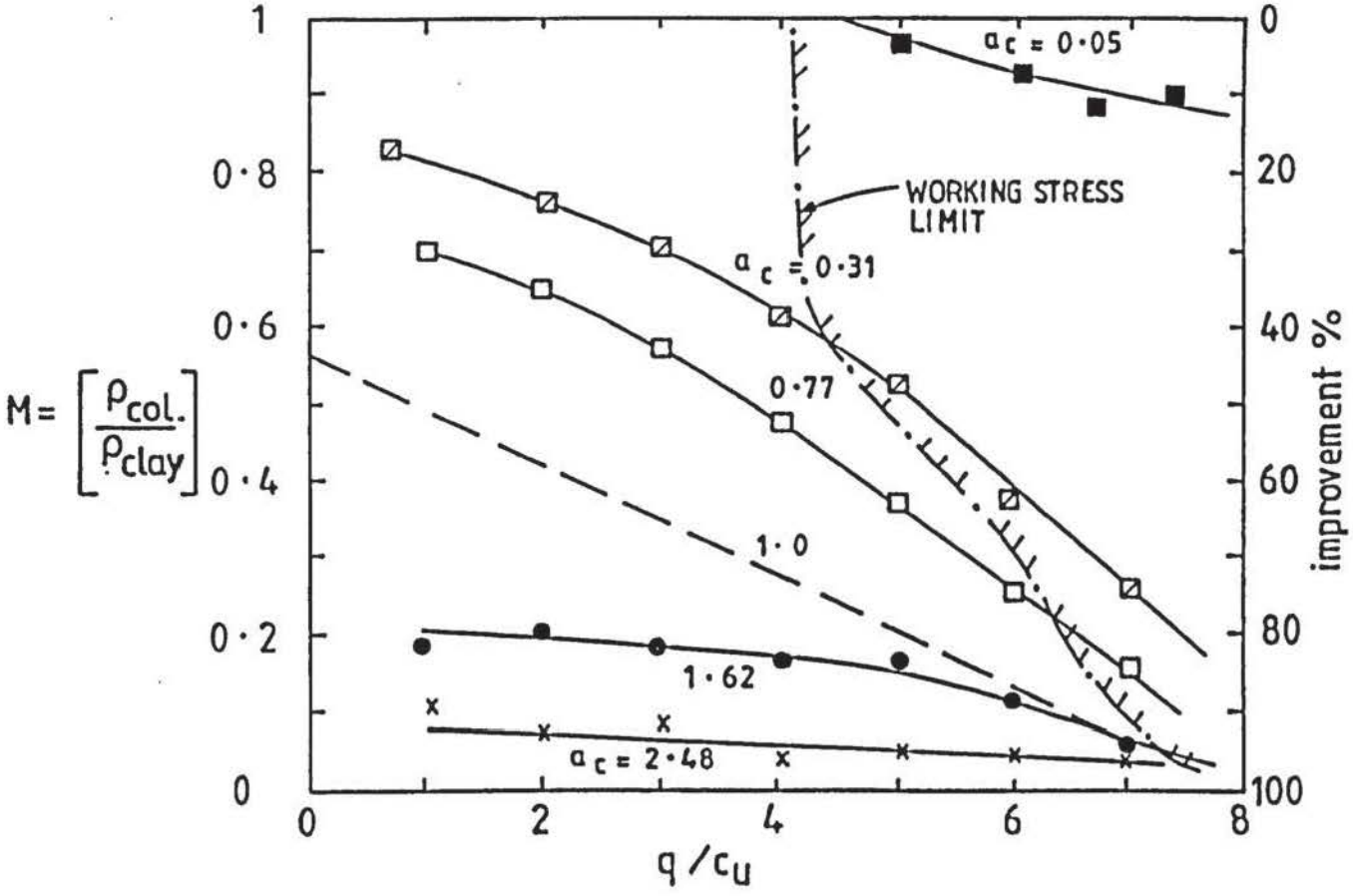

Typical settlement improvement curves for a single F column loaded by foundations of various sizes and geometries.

FIGURE 12.48

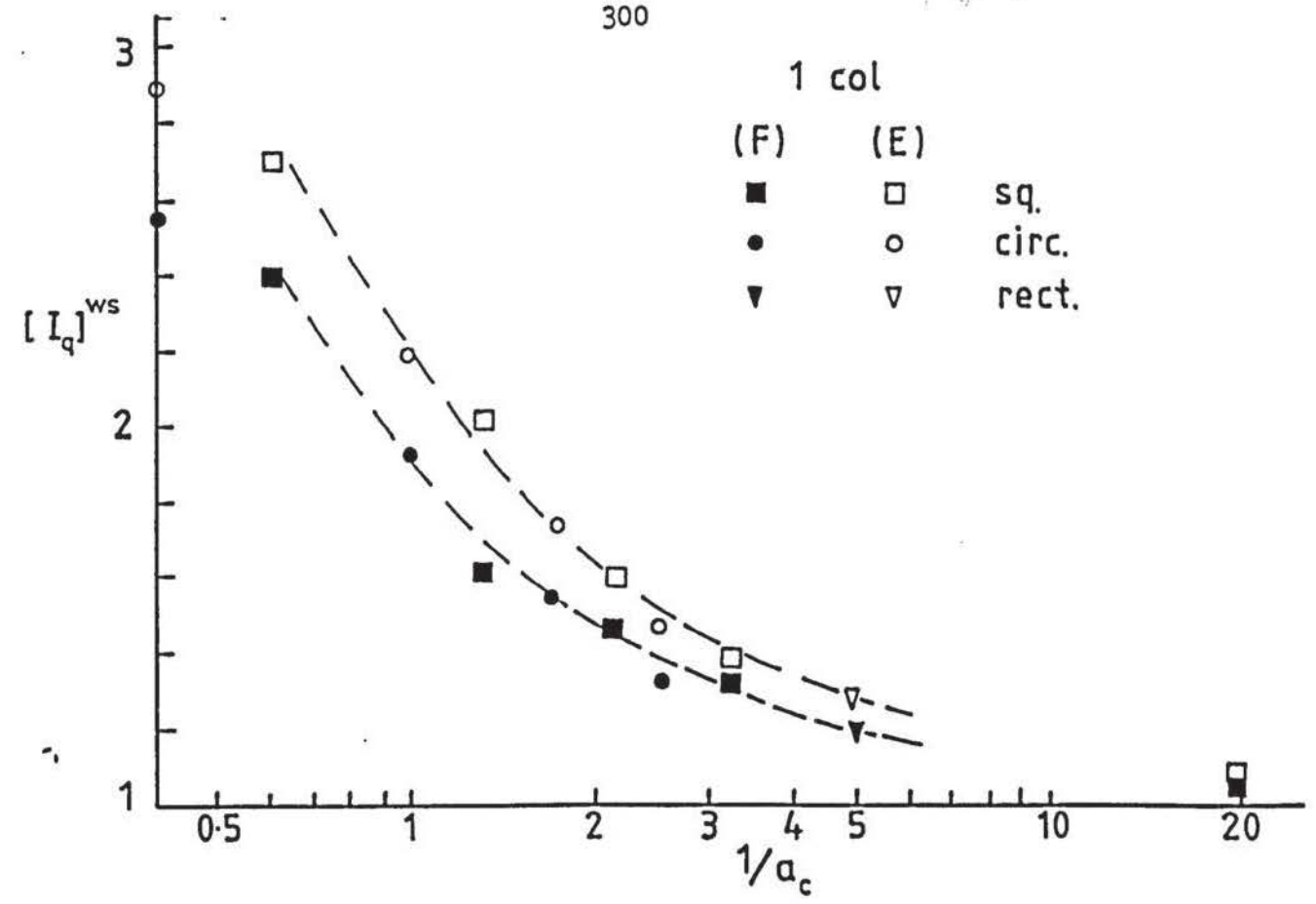

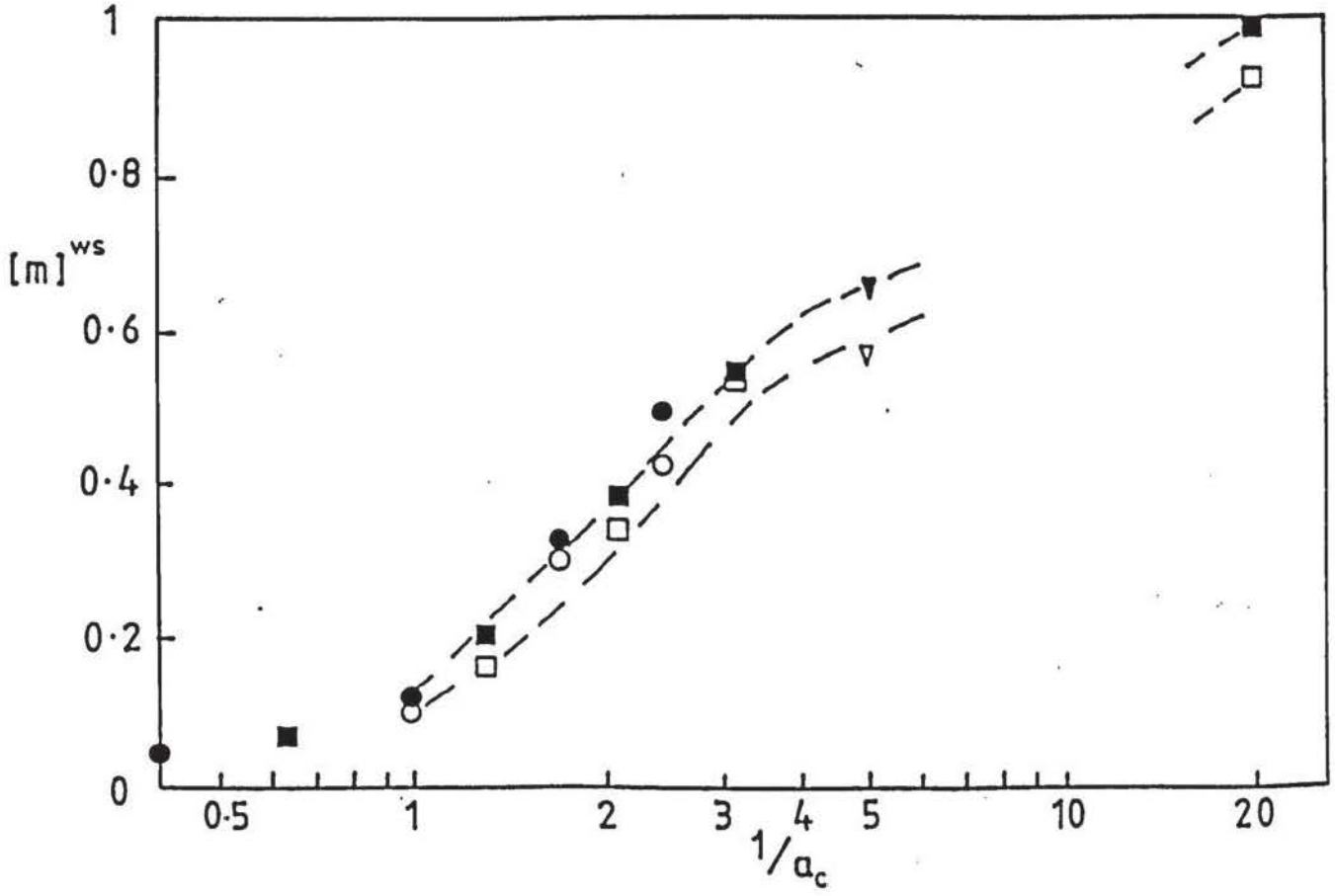

Typical variation of I_q and m at working stress with $1/a_c$ for single F and E columns loaded.

FIGURE 12.49

settlement, the foundation area also needs to be as small as possible with respect to the column area.

The improvement parameters for the E cases are signficantly better than for the F case. This applies particularly to the improvement in bearing capacity.

12.5.3 Column yield

As the foundation size increased relative to the column area, column yield was apparently suppressed and the severity of the yield plateau on the q/c_u - ρ/B curve progressively diminshed as a_c decreased. The effect is shown in Figure 12.50 for the E column.

Commencement of the yield plateau was found to be almost coincident with the peak value of I_q for any given value of a_c.

12.5.4 Column-clay distortion

The pattern of radial and vertical distortions for a single column loaded by a circular foundation (Test Nos.: XC4 and XC4E) with a diameter 1.58 times the column diameter (B = 1.58 D; $a_c = 0.41$) are shown in Figures 12.51 to 12.52.

Radial distortions for both the F and E columns are signficiantly larger than when B=D, at all three loading stages, by about 20%, 40% and 100% at ρ/B = 0.2, 0.66 and 1.5 respectively. The length of column affected by these distortions is also greater. In the F case, a rigid-pile failure mode is evident from vertical movement of the lowest lead-shot marker at the third loading stage. At the top of the column, for both cases, radial distortion is suppressed over a length of about one column diameter. The degree of suppression increases closer to the foundation. Even with such relatively large radial displacements no ultimate applied stress was reached by the E column, but was achieved by the F column due to the rigid-pile failure.

The vertical distortions, in Figure 12.52, show no relative movement within the column, or with the clay, over 0.5D column length beneath the foundation and indicate suppression of shear strains. Over the remaining column length, vertical distortions appear marginally larger than when B = D, for both the F and E cases, but there is considerably less distortion within the

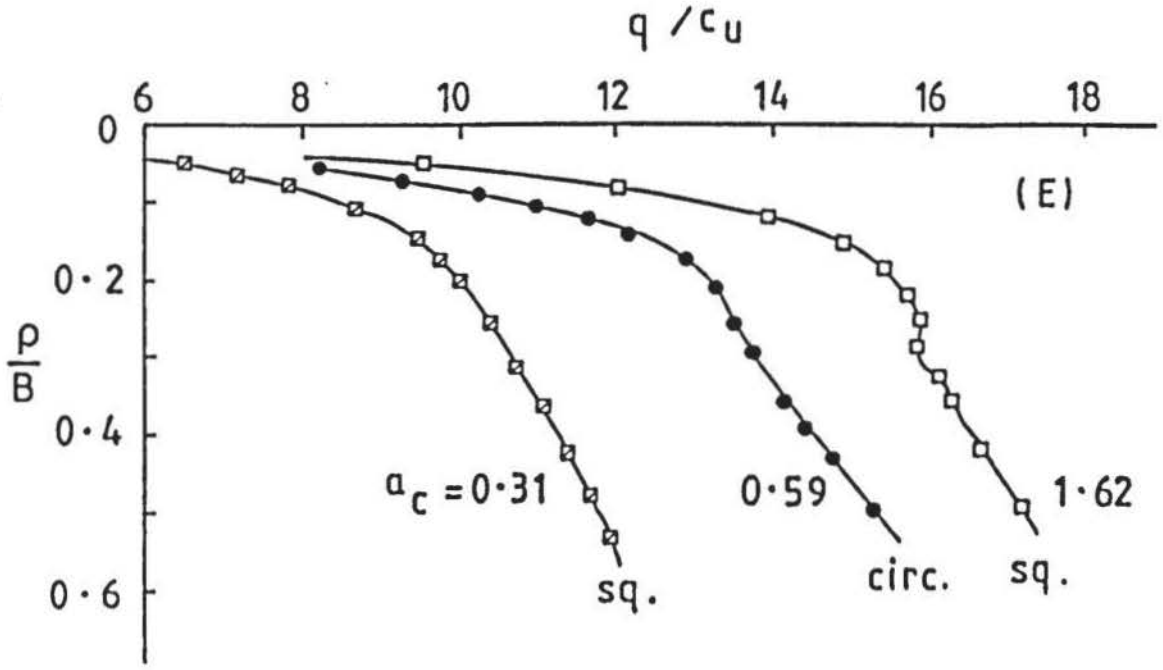

Typical diminishing yield plateau as a_c decreses for E column.

FIGURE 12.50

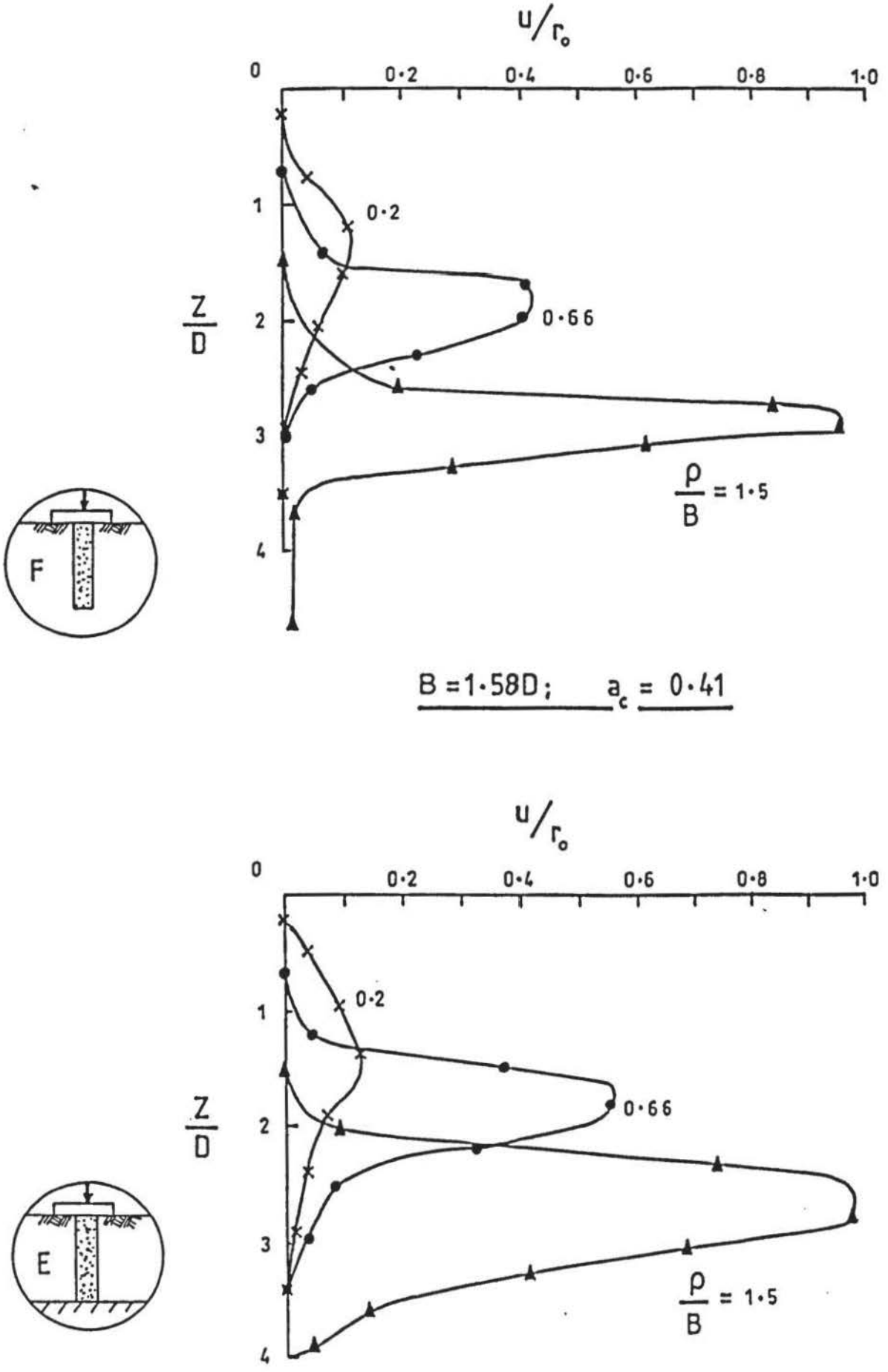

Lateral distortion of F and E columns (B = 1.58D; a_c = 0.41) at three stages of vertical deformation.

FIGURE 12.51

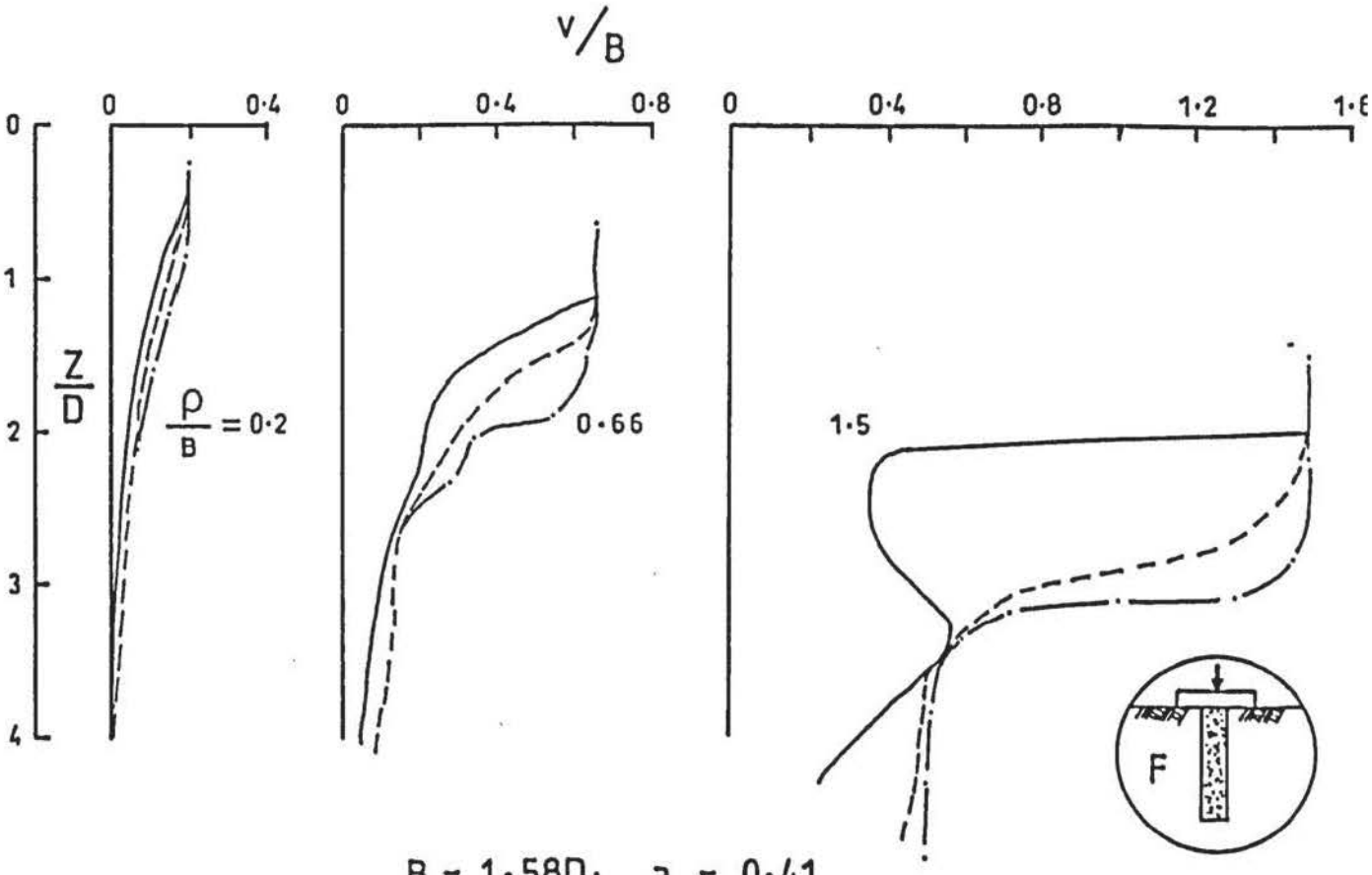

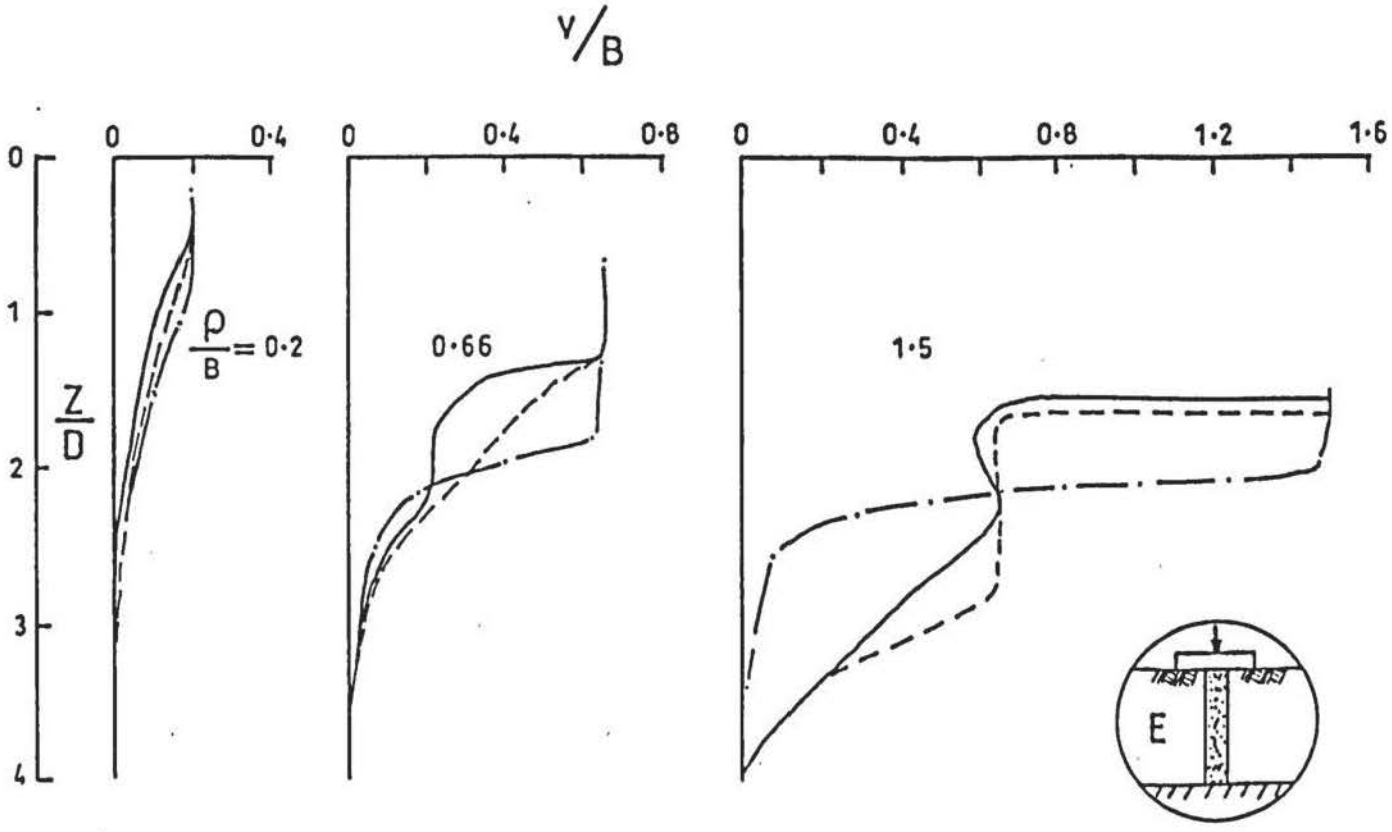

Relative vertical distortions within F and E columns and at the column-clay boundary (B = 1.58D; $a_c = 0.41$).

FIGURE 12.52

column with the larger foundation. In the E case strain reversal is evident from $\rho/B = 0.66$, as is pile failure mode in the F case.

12.5.5 Column-foundation deformation

Additionally to the main test programme, a number of the column compression tests were repeated to allow casts of the deformed columns to be made after a nominal applied vertical displacement of about 40 mm. This was achieved using Kaffir-D as the casting material, after removal of the sand. Drawings of the casts are given in Figure 12.53 and 12.54, on a scale of 1:2.

For the circular and square foundations, the length (L_s) of column over which radial expansion was suppressed increased with foundation size. An empirical relationship is given in Figure 12.55, based on the observation that this length is roughly concident with a line drawn at 45^o to the horizontal from the extremity of the foundation. With the E columns, when $B \approx 4D$, actual L_s became constant and extended to $\approx 1.7D$ from beneath the foundation. With the F column, this distance increased until no radial expansion occurred at any point along the column length when $B = 4.6D$. For rectangular foundations, the length of column not affected by bulging reached a maximum of $\approx 0.8D$ when the foundation length (L) $\geq 2.75D$ and occurred along the longitudinal axis. The mechanism of column deformation is shown to be like a granular 'plug' inducing the largest lateral movement at 90^o to the longitudinal axis of the foundation by a 'wedge' action shown by 'view A' in Figure 12.54. This mode of failure is largely the same as the theoretical model proposed by Madhav and Vitkar (1978) for a granular trench.

It would seem that in all cases, suppression of radial expansion at the top of the column is due to a combination of restraining shear stresses at the foundation face, on both the column and the clay, at the base of the foundation and confinement by lateral stresses in the clay induced by the bearing pressure. The length of column affected becomes redundant as far as column load capacity is concerned by reducing the effective column length. In the F case this results in a pile failure mode occurring at smaller values of ρ/B. As a general guide, where $B > D$ and F column needs to be extended by amount relative to the foundation size shown in Figure 12.55.

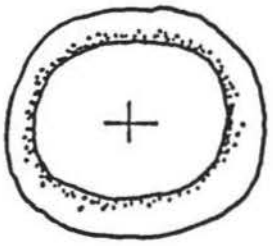

Scale 1:2

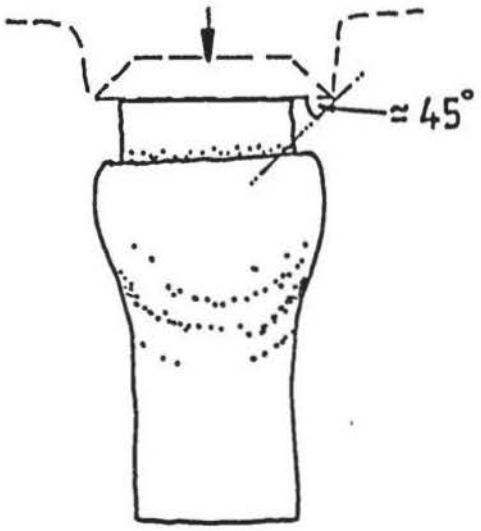

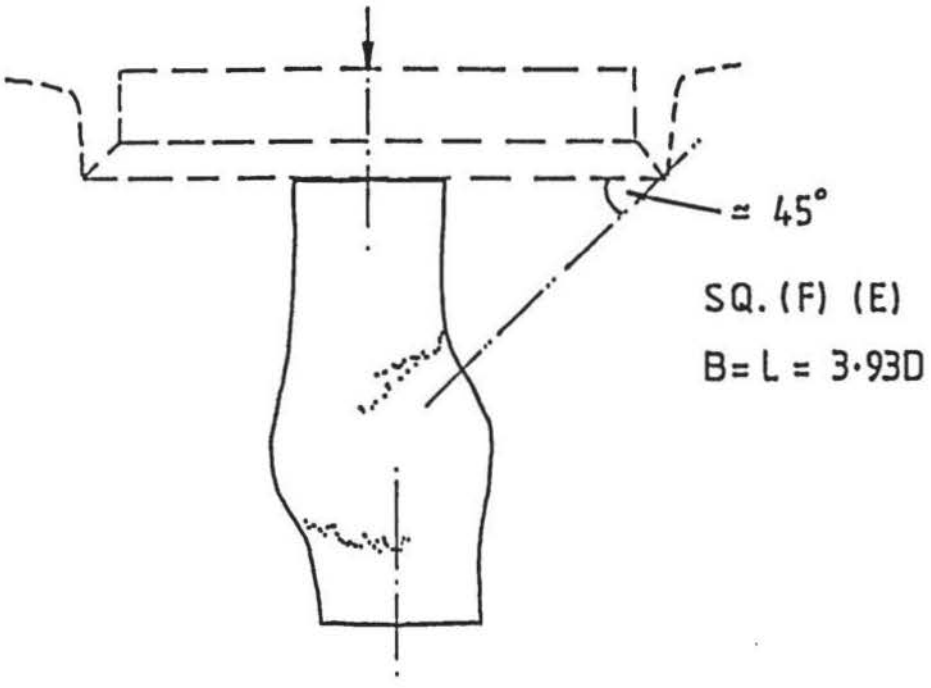

Column deformation under circular and square foundations.

FIGURE 12.53

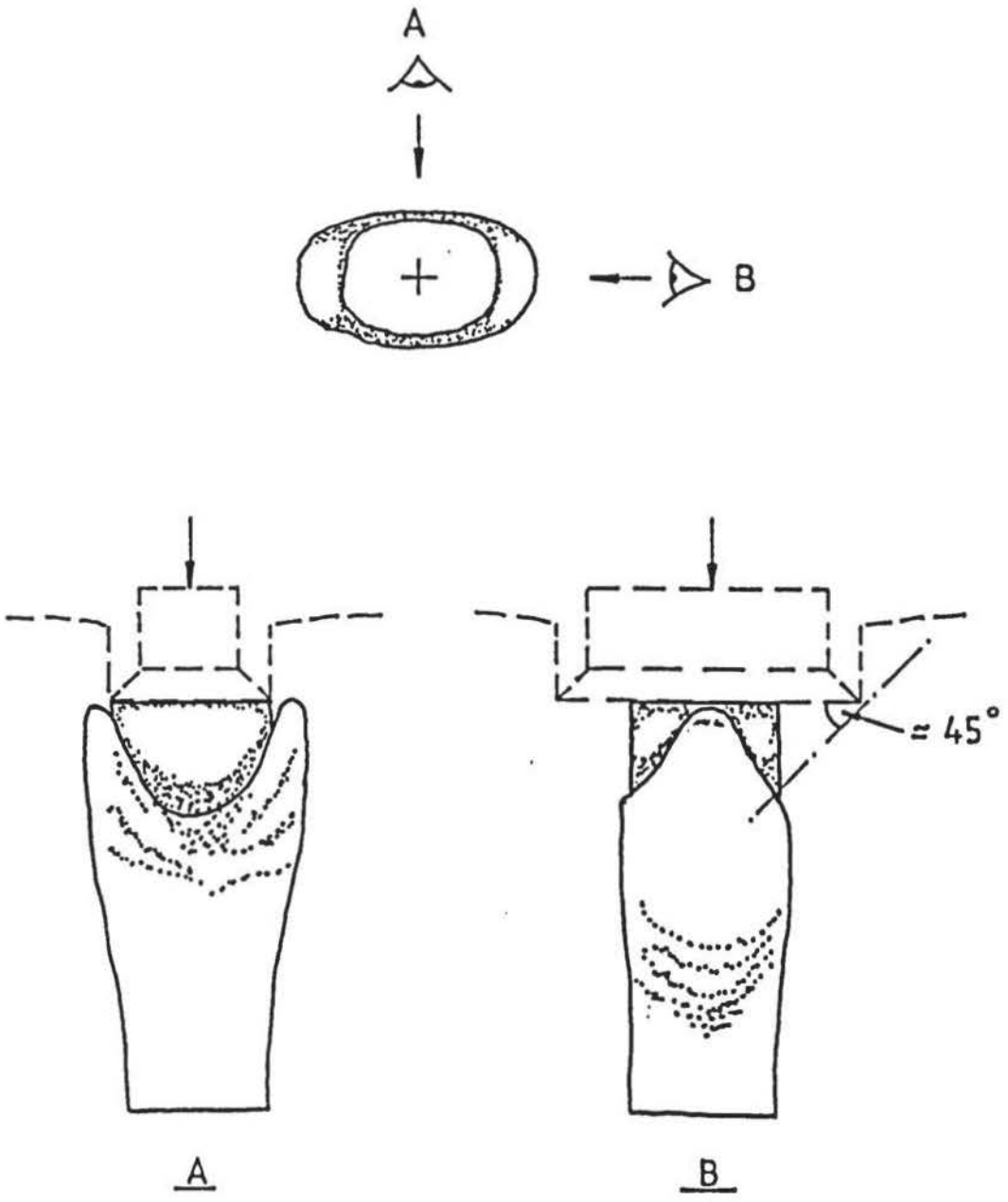

Column deformation under a rectangular foundation.

FIGURE 12.54

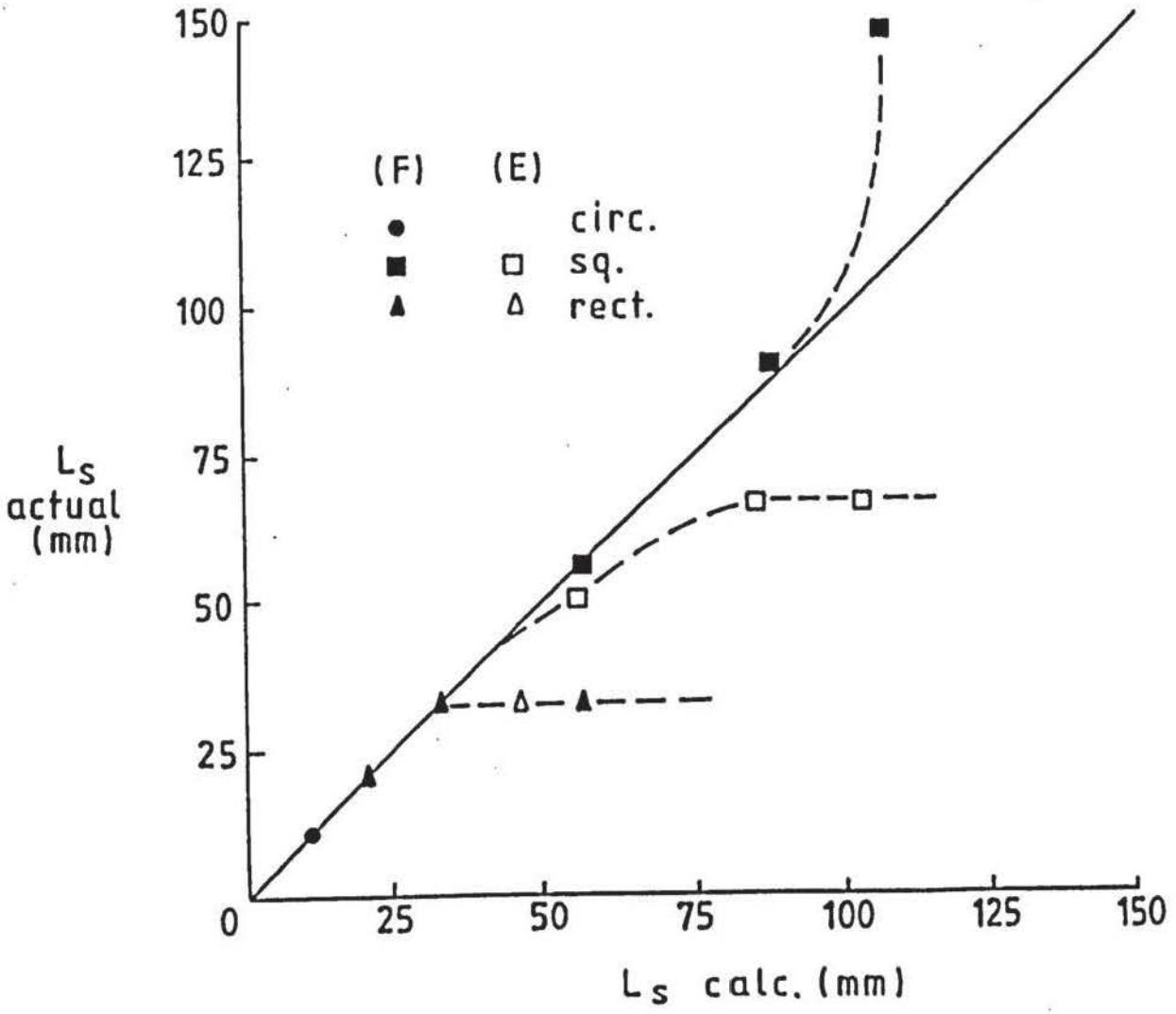

circ. $L_s \triangleq (B - D)/2$

sq. $L_s \triangleq \sqrt{0{\cdot}25\,B^2} - D/2$

rect. $L_s \triangleq (L - D)/2$

Observed and calculated lengths of columns in which lateral displacement has been suppressed by the action of a foundation.

FIGURE 12.55

Column deformation is affected by the proximity to other columns and also by the size and shape of the foundation carried.

12.5.6 Clay displacement fields

Displacement fields in the clay when a F and E column is loaded by a circular foundation B = 1.58D are shown in Figures 12.56 and 12.57 for $\rho/B = 0.2$ and 0.66, respectively.

The displacement trajectories from the first strain increment ($\rho/B = 0.2$) correspond largely to those when two columns are closely spaced. With the F column, vertical and horizontal displacements are almost equally important. Movement at the base of the column is indicated, with pile failure mode occurring at a smaller value of ρ/B than when B=D, but at about the same ρ/B when two columns are closely spaced.

12.5.7 Column-soil strains

Strains in the column and soil when loading F and E columns by a circular foundation (B = 1.58 D; $a_c = 0.41$) are shown in Figures 12.58 to 12.61 for ρ/B 0.2 and 0.66.

The pattern of tensile and compressive strains in the column and clay is similar to when B=D, but their magnitudes and distribution are larger. Only marginally so in the column, but more so in the clay. The horizontal strains (ε_x) within the clay adjacent to the foundation are tensile (those affected by the bulging zone are compressive) and show the restraining influence at the top of the column. Consequently, ε_x in the top of the column is significantly suppressed. Orientation of the principal strains (ε_1 and ε_3) in this region is towards the centre of the column, while those below are oriented towards the clay and show a change in the direction of the shear strains. This is confirmed by the changes in sign of γ_{xy}. The effect is more apparent when $\rho/B = 0.66$.

For both the F and E cases, strains occur along the full length of the column, and in the former, at the column base from $\rho/B = 0.2$. By inspection, vertical strain is more predominant in the clay when B > D.

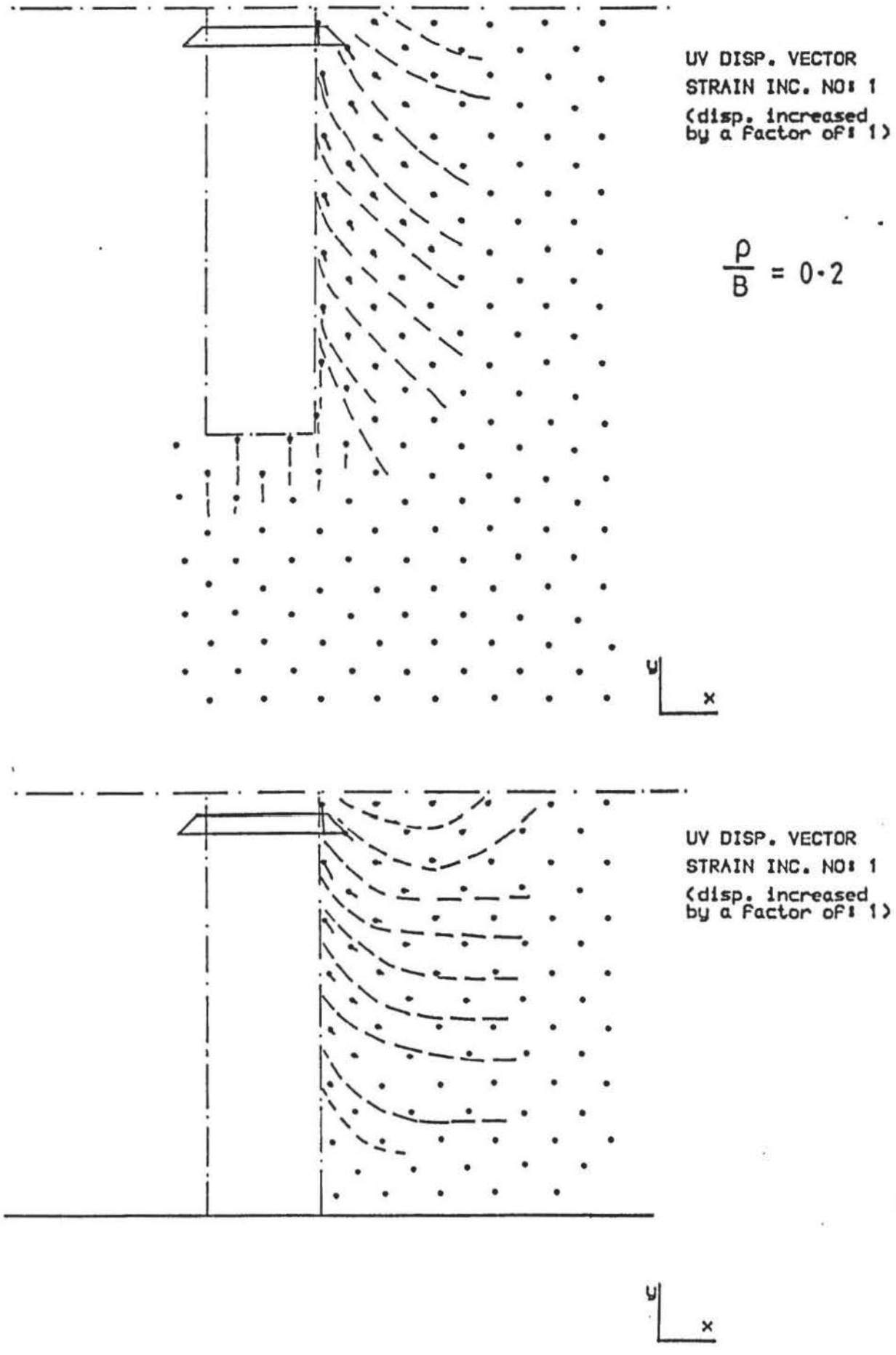

Clay displacement fields at ρ/B = 0.2 for F and E columns (B = 1.58D; $a_c = 0.41$).

FIGURE 12.56

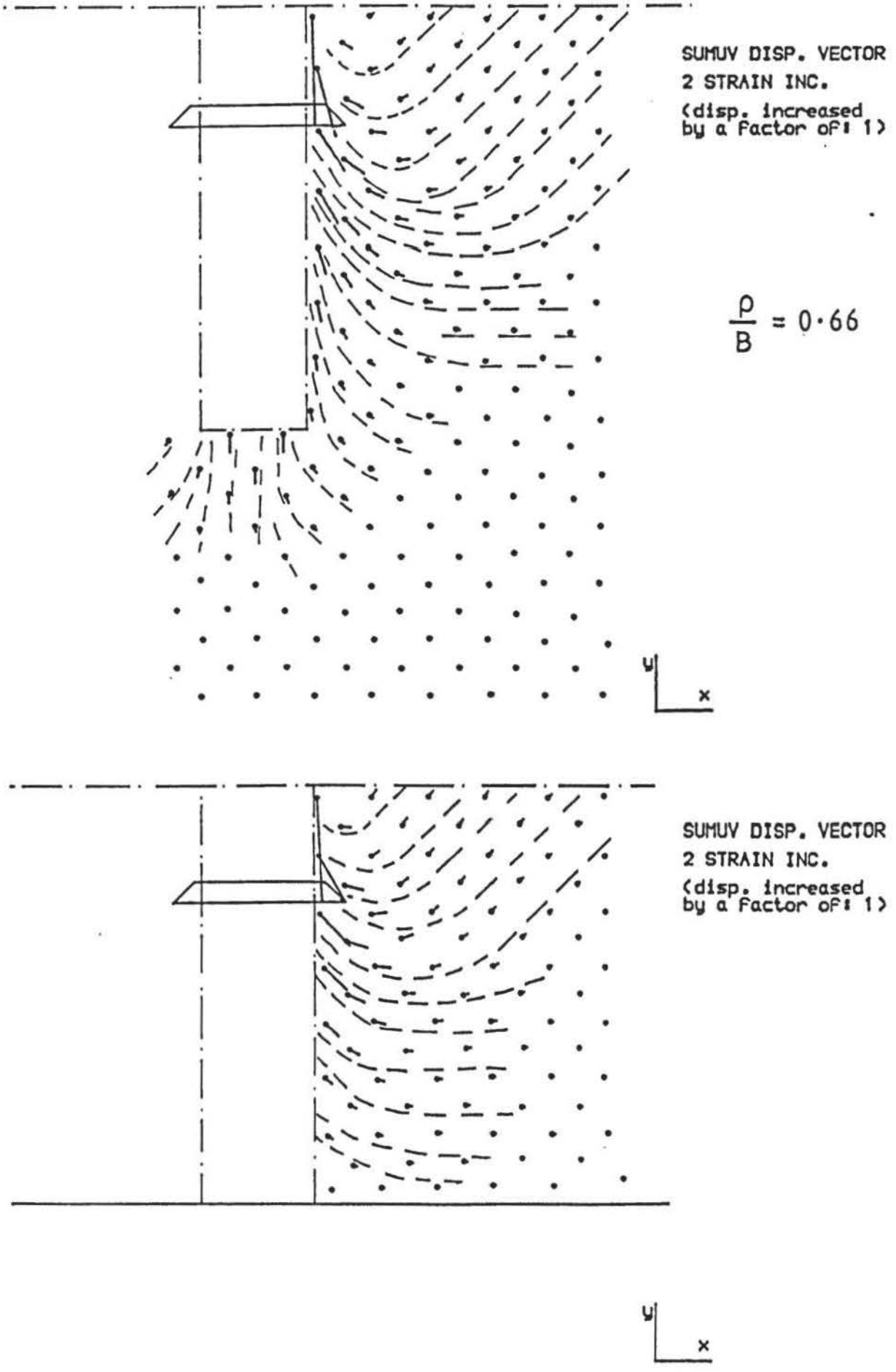

Clay displacement fields at $\rho/B = 0.66$ for F and E columns ($B = 1.58D$; $a_c = 0.41$).

FIGURE 12.57

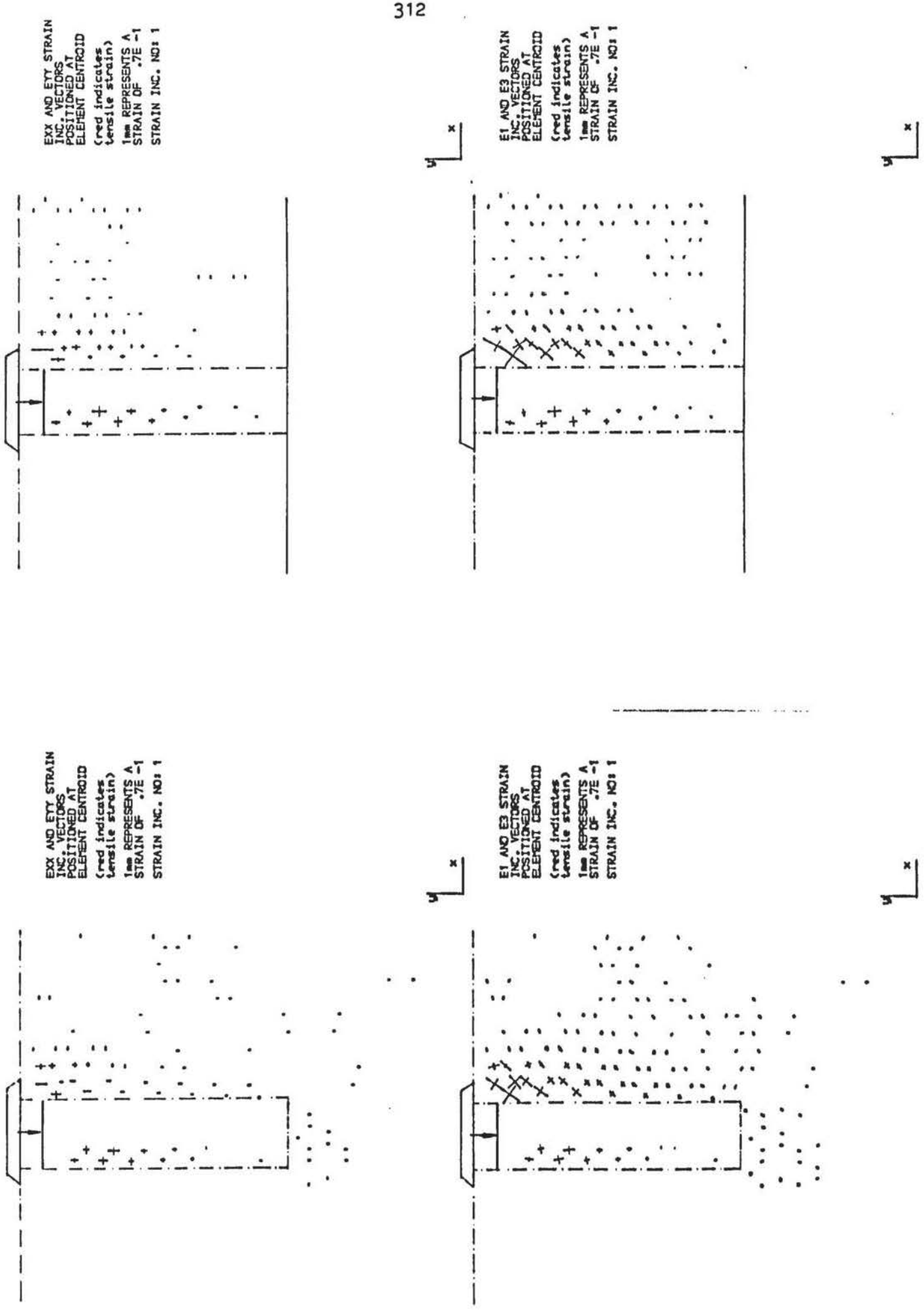

ε_x and ε_y, ε_1 and ε_3 vectors for F and E columns (B = 1.58D; a_c = 0.41) at ρ/B = 0.2.

FIGURE 12.58

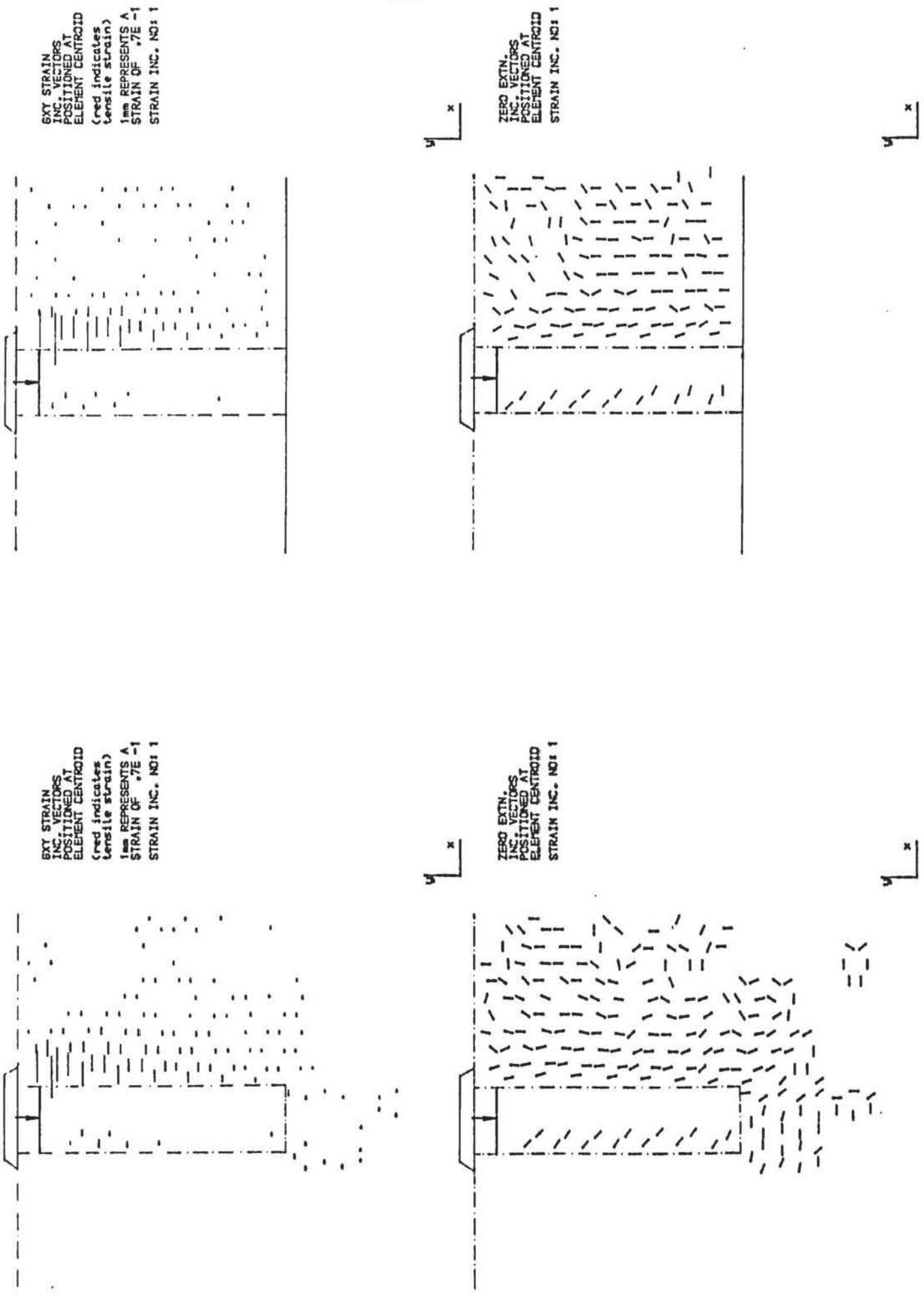

γ_{xy} and zero extension lines for F and E columns (B = 1.58D; a_c = 0.41) at ρ/B = 0.2.

FIGURE 12.59

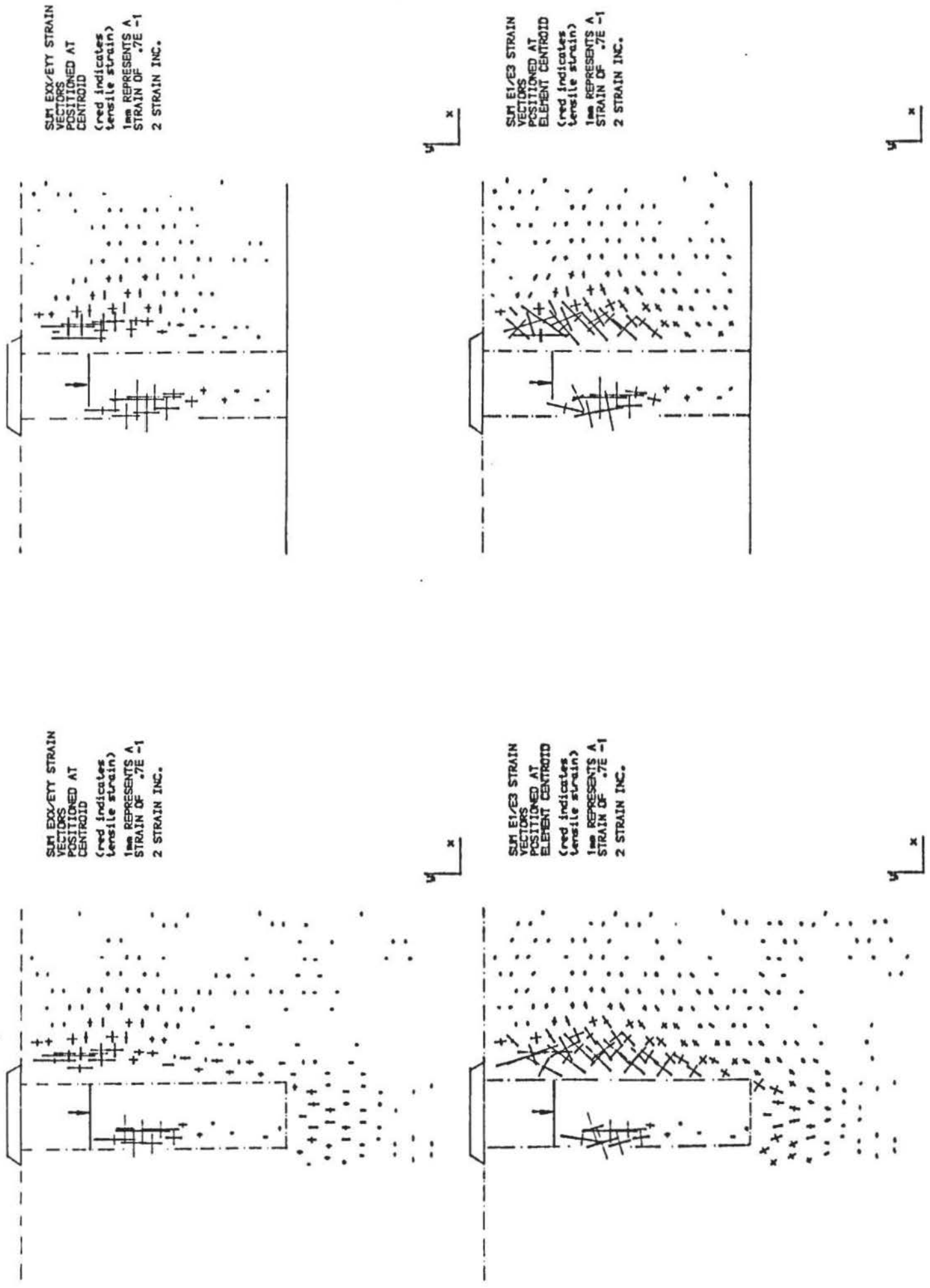

ε_x and ε_y, ε_1 and ε_3 vectors for F and E columns (B = 1.58D; a_c = 0.41) at ρ/B = 0.66.

FIGURE 12.60

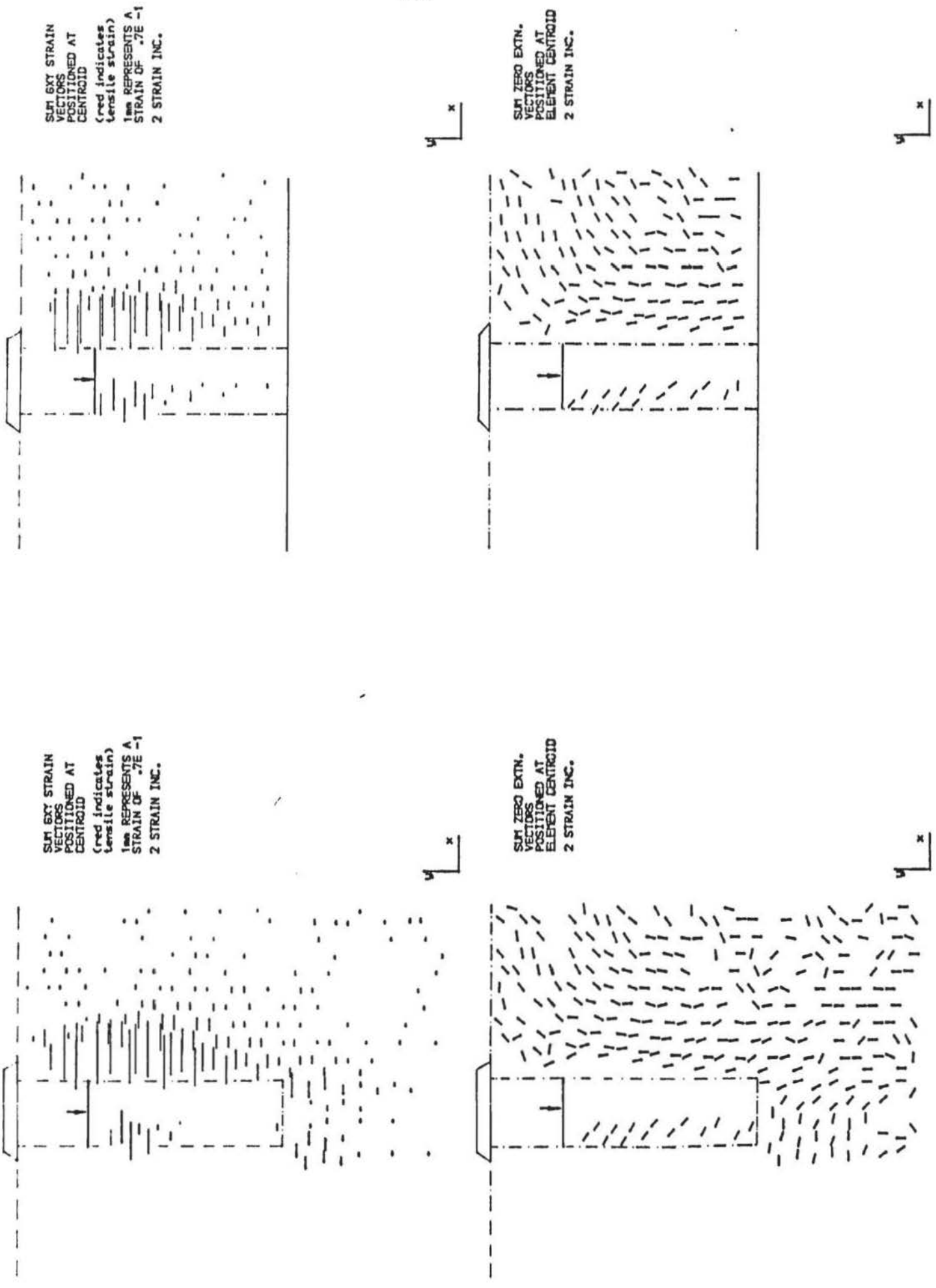

γ_{xy} and zero extension lines for F and E columns (B = 1.58D; a_c = 0.41) at ρ/B = 0.66.

FIGURE 12.61

Extending this further, when the column area is infinitesimal compared to the foundation size, then vertical displacement will be the sum of the shear strains and vertical strains in the clay.

Attention is drawn to the ε_x and γ_{xy} at the base of the column in strain increment number 2 ($\rho/B = 0.66$). At the centre-line of the column ε_x is zero and becomes tensile towards the base perimeter. Also, γ_{xy} is zero at the centre-line. The magnitudes of ε_x decrease almost along a 45^o line drawn from the base perimeter. Considering this effect on a surface foundation, with a column beneath it, explains the phenomenon in the previous section. That is, expansive ε_x acting from the perimeter of the foundation suppress radial expansion of the column to lower depths. Also, zero or little γ_{xy} in the clay immediately beneath the foundation will cause no relative distortion between itself and the column and so they act as a combined unit. That part of column signficiantly affected by these conditions will be strain-neutral in the x-direction and in terms of shear strains.

12.5.8 Zero extension

The pattern of the zero extension lines are similar to those when B=D although in the present case (B = 1.58D) potential slip planes running parallel to the shaft of the column in the adjacent clay are clearer defined at the first strain increment ($\rho/B = 0.2$). This is indicative of a greater growth of the zone of plastic deformation which in the F case leads to general shear failure occurring as a rigid pile action. Slip planes within the upper part of the column lay at about 46-48^o to the horizontal at the first strain increment, and 42^o - 45^o by the second increment. However, the potential slip planes further down the column become more inclined to the horizontal ($\approx$46 - 48^o) and indicate progressive mobilisation of shear strength even after column yield has occurred.

12.6 RECTANGULAR FOUNDATIONS ON A NUMBER OF COLUMNS

12.6.1 Boundary stresses and settlement

Two columns, in F and E conditions, at various spacings, related to the initial column diameter, (sD) were loaded by rectangular foundations (Test Nos.: R0 to R7 and R0E to R7E) which had the same width as the columns (i.e. B=D). Tests were also carried out using three columns at a spacing of 1.25D (Test Nos.: R8 and R8E).

Similarly to the test results in the previous Section, the variation of the applied foundation pressure (expressed as q/c_u) with settlement (expressed as ρ/B) was also found to be strongly dependent on a_c. Peak $\Delta\sigma_x/q$ typically occurred at $\rho/B = 0.3 - 0.4$ with the magnitude decreasing as a_c decreased. The longitudinal axis of each foundation lay at 90^o to the horizontal stress transducer and their distance was the same for each test.

Ultimate values of q/c_u were obtained in all the F case tests and a Table of ultimate and working q/c_u with the corresponding magnitude of sD and a_c is given in Figure 12.62. The ρ/B at working stresses varied between 0.05 and 0.064, which on average gave $\rho/B \approx 0.056$. For all practical purposes, this is the same as the average $\rho/B \approx 0.054$ obtained for the square and circular foundations.

The relationship between q/c_u and $1/a_c$ is shown in Figure 12.63 for the F case and it is evident that q/c_u decreases as a_c decreases. Curves for the circular and square foundations are indicated by a broken line and lie at higher stress levels. This effect has been previously discussed in Section 12.5.1 as being due to :

$$N_c \text{ rect.} < N_c \text{ circ.} \qquad (12.9)$$

for the same area of foundation. So when B=L, then the curves for both the rectangular, circular and square foundations should coincide when a_c is unity.

To maximise bearing capacity, a_c needs to be as large as practicable. Expressed in terms of column spacing, for B=D, the spacing factor (s) needs to be a minimum.

Spacing sD	a_c	Ultimate stress $[q/c_u]^{ult}$	Working stress $[q/c_u]^{ult}/3$	ρ/B at working stress
*0	0.2	10.8	3.6	0.050
1.25D	0.7	17.3	5.8	0.053
1.5D	0.63	16.8	5.6	0.055
2.0D	0.57	14.9	5.0	0.060
2.5D	0.45	14.1	4.7	0.058
3.0D	0.40	13.5	4.5	0.064
4.0D	0.32	11.9	4.0	0.058
**1.5D	0.59	15.2	5.1	0.053
Average ρ/B at working stress :				≈0.056

* 1 column
** 3 columns at 1.5D

Table of typical ultimate and corresponding working stresses and ρ/B at which they occur for two F columns (one and three columns where shown) at various spacings, loaded by rectangular foundations with B = D

FIGURE 12.62

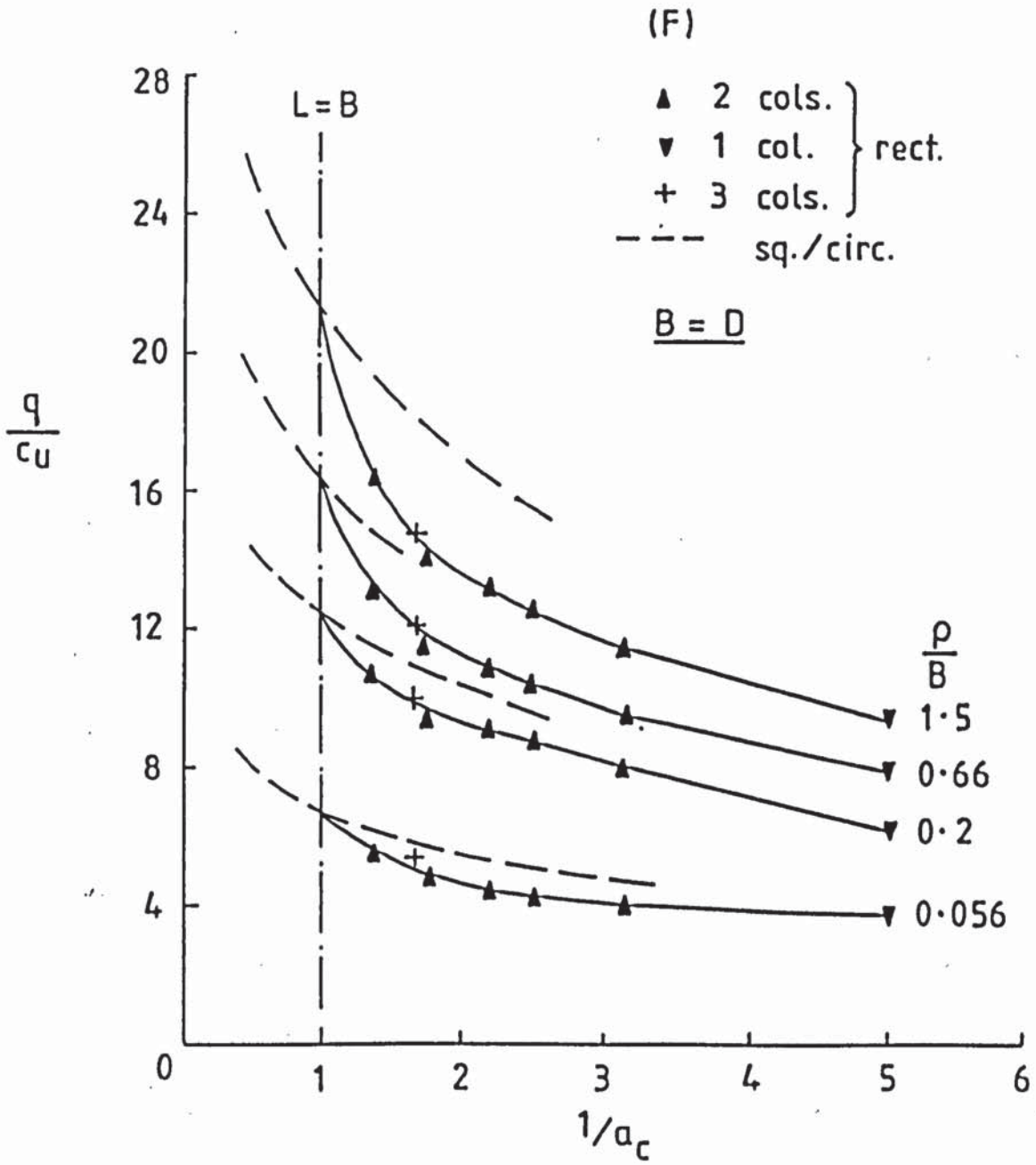

Typical variation of q/c_u with $1/a_c$ for one, two and three F columns loaded by a rectangular foundation with B = D.

FIGURE 12.63

12.6.2 Improvement

By plotting I_q achieved at the working stress ($[I_q]^{WS}$) for the respective foundation against $1/a_c$ (logarithmic scale), an excellent correlation with the previous curve (Figure 12.49) was obtained for both the F and E conditions and is shown in Figure 12.64. Good agreement was obtained when m was plotted against $1/a_c$ (logarithmic scale), although obtaining this parameter from large scale plots of q/c_u against ρ/B was found to be more critical than for bearing pressures. This further supports the observations discussed in Section 12.4, that column interaction even at close spacing is negligible at working stresses, and also that the effect of the foundation does not appear to alter this situation by any significant amount.

12.6.3 Column yield

As with the case of square and circular foundations loading a single column, the effect of column yield diminished as a_c decreased (column spacing increased). When two columns were immediately adjacent (sD = 1D; $a_c = 0.7$) the yield plateau was most evident, shown in Figure 12.65 for the E case, and almost unoticeable, on the q/c_u against ρ/B curve, when the columns were at a spacing of 4.0D ($a_c = 0.32$).

The effect was generally less pronounced in the F columns. Similarly to the cases discussed in the previous sections, q/c_u at which column yield became evident was consequently higher with the E columns than the F columns. But for both cases q/c_u at column yield became less in magnitude as a_c decreased. This effect is clearly shown in the table given in Figure 12.66 when the results obtained from using the rectangular foundations on one, two and three columns are compared to those using the square and circular foundations on a single granular column.

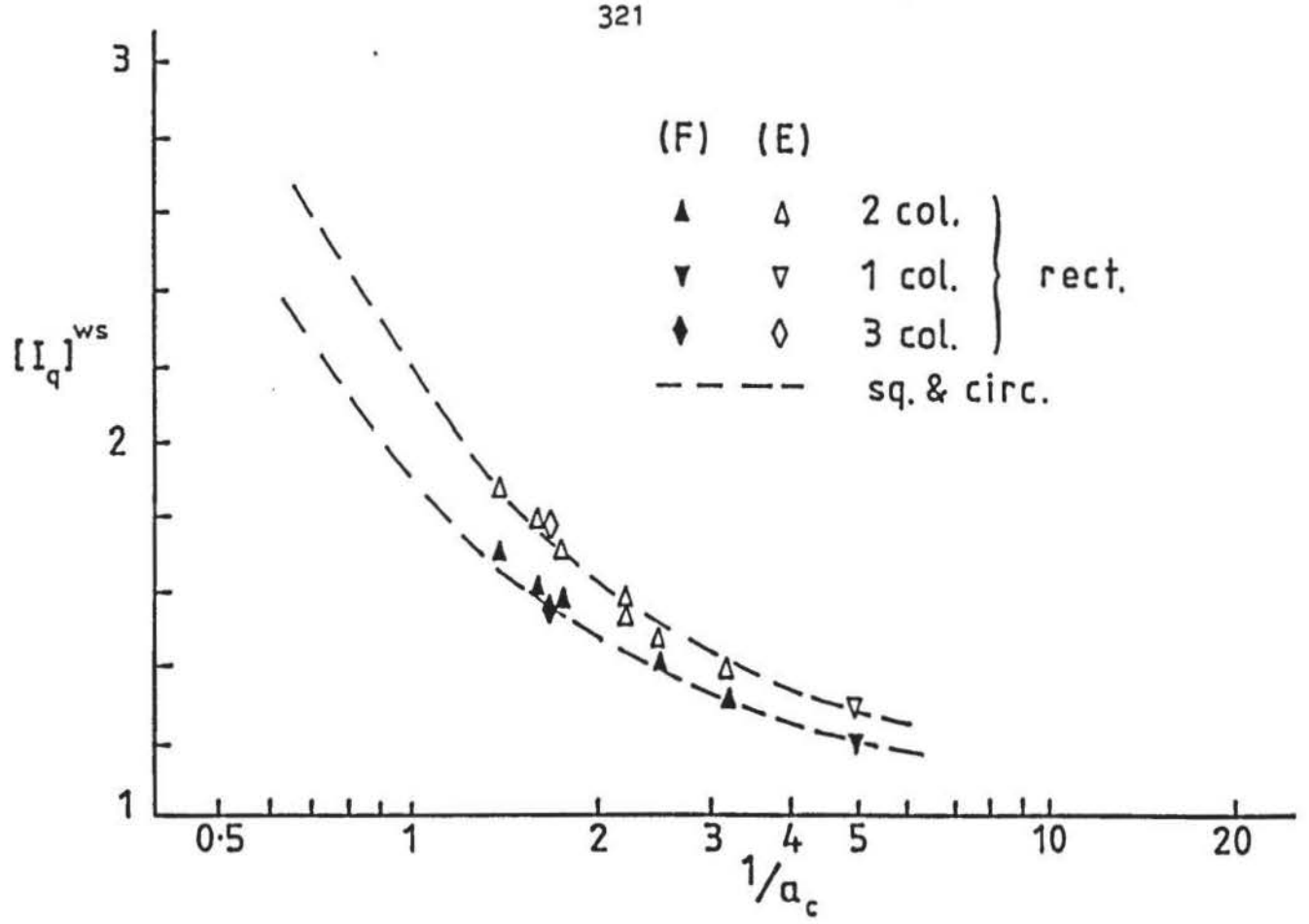

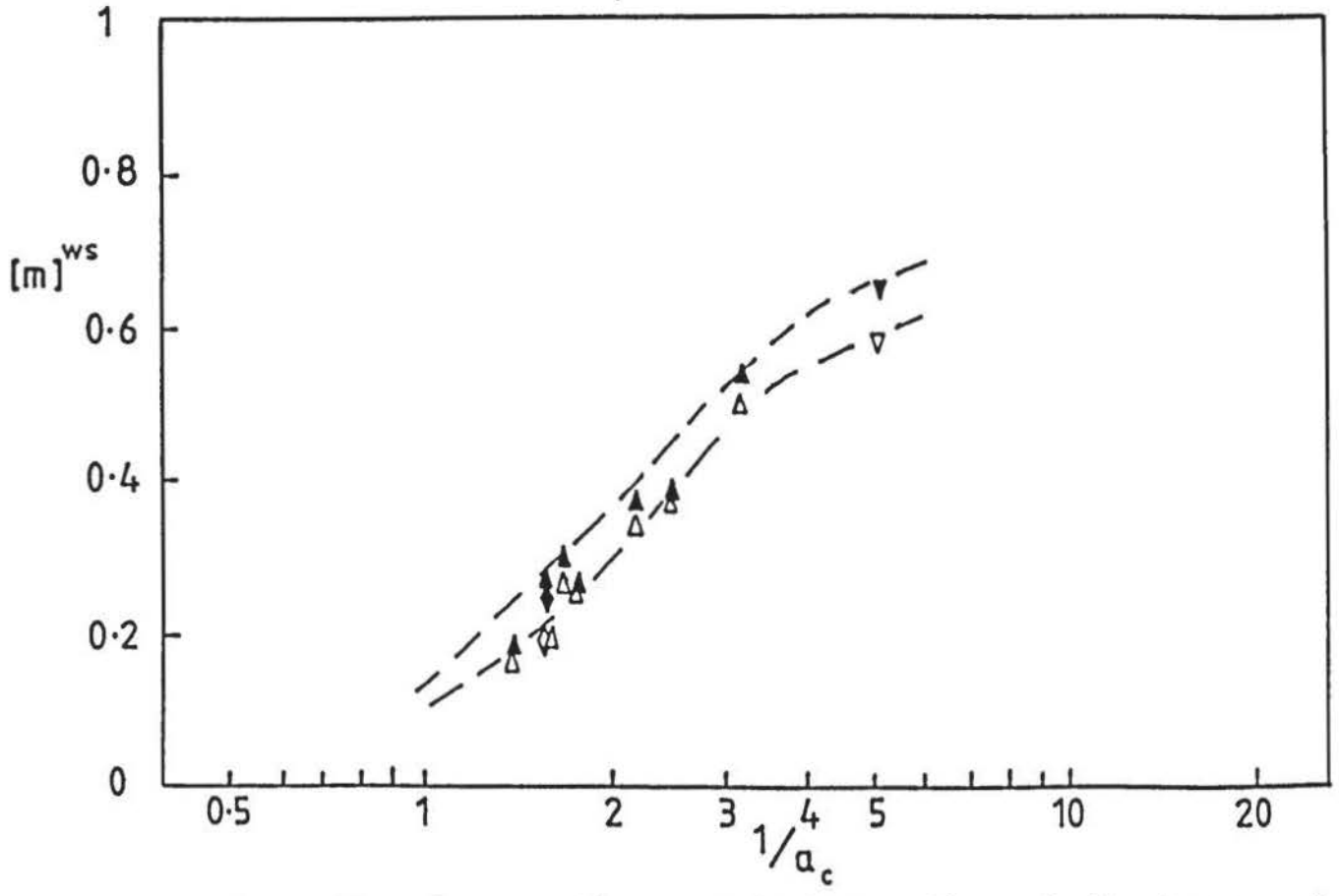

Typical variaton of I_q and m at working stress of columns subject to loading by rectangular columns.

FIGURE 12.64

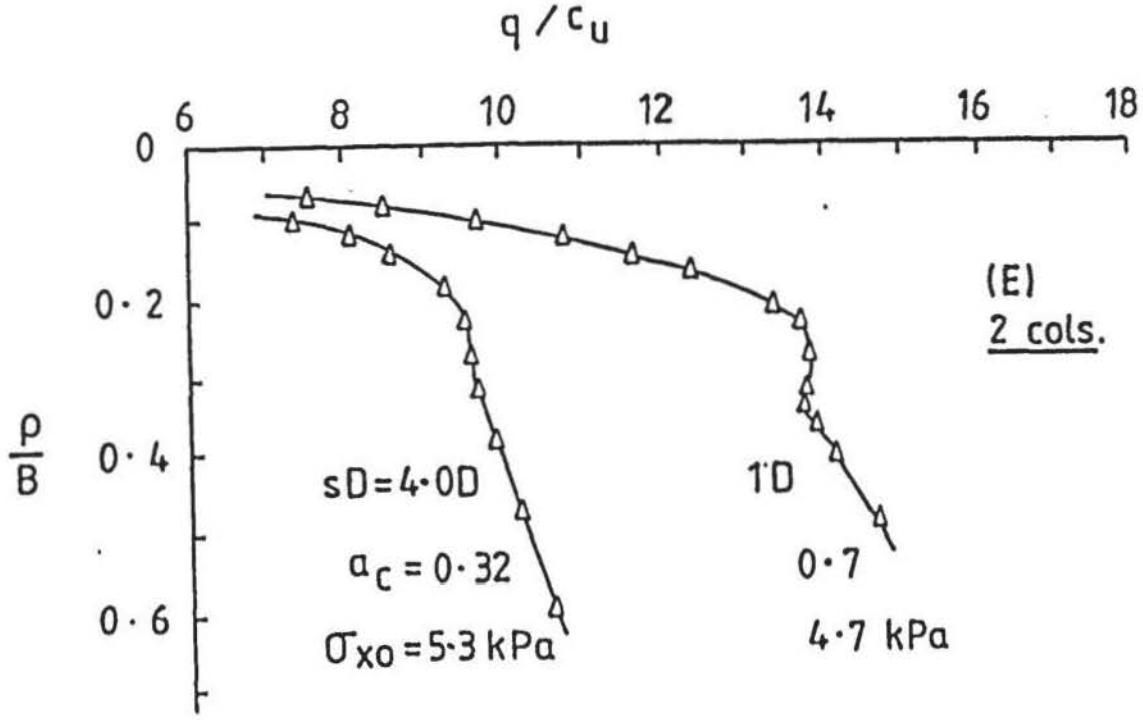

Typical diminishing yield plateau as spacing increases (a_c decreases), for E column.

FIGURE 12.65

Fndn.	s	a_c	q/c_u at point of column yield. (F)	(E)
Rect.	1.0	0.7	11.1	12.1
2 cols.	1.25	0.7	11.5	12.8
	1.5	0.63	10.2	12.0
	2.0	0.57	10.0	11.2
	2.5	0.45	9.2	10.0
	3.0	0.39	9.3	9.4
	4.0	0.32	8.4	8.7
3 cols.	1.5	0.59	10.7	11.6
1 col.	-	0.2	7.8	8.6
Sq.	-	0.77	12.2	13.2
	-	0.47	10.0	10.7
	-	0.31	8.5	9.4
Circ.	-	1.0	13.5	16.0
	-	0.59	10.8	12.4
	-	0.4	9.1	11.0

Table showing q/c_u at column yield for numbers of columns loaded by square, circular and rectangular columns.

FIGURE 12.66

12.6.4 Column-clay distortion

Lateral distortions of one of the two columns, subject to rectangular foundation loading, when spaced at distances of 3.0D (a_c = 0.39) and 1.5D (a_c = 0.63) for F and E conditions are shown in Figure 12.67 and 12.68 respectively (Test Nos.: XTC4, XTC4E and XTC2 and XTC2E).

For the F case, lateral distortions on the foundation side of the column are less than those on the clay side. The magnitude of the former are generally 30 to 40% smaller than those, shown previously in Figures 12.6 and 12.31, when the columns were loaded independently by circular foundations (B=D). The foundation, therefore, restricts lateral growth of the bulging zone and no lateral distortion is noticeable immediately beneath the foundation. At the last loading stage when $\rho/B = 1.5$ and the columns are closely spaced, the lateral distortion is greater than when two columns are loaded independently and occurs through, or as a result of, lateral shift of the column away from the foundation side. Lateral shift of the column is also apparent at wider spacing but occurs to a smaller extent.

In the E case, no lateral shift of the column is evident and this is attributed to the restraining action of shear stresses acting at the base of the column. Lateral distrotion is more suppressed at the foundation side of the column than in the F case, but is generally greater on the soil side. For all the boundary conditions, however, restriction of lateral distortion in one direction is compensated by greater lateral distortion in other directions. Whilst Figures 12.67 and 12.68 only reveal the events in a single plane it seems plausible that additional lateral displacement will also occur around that sector of the column perimeter which is not subject to the confining stress induced by the foundation.

Over a depth, below the foundation, of between 0.5D to 2D a small degree of vertical distortion is indicated within the column and with the clay in Figures 12.69 to 12.70. This occurs at the foundation side of the column, and is attributed to the lateral distoriton of the bulging zone.

The remaining length of column is unaffected and shows the clay and column beneath the foundation to undergo the same vertical distoriton. That is, the clay and column act together in the same way as two closely spaced independently loaded columns. The present case, however, is

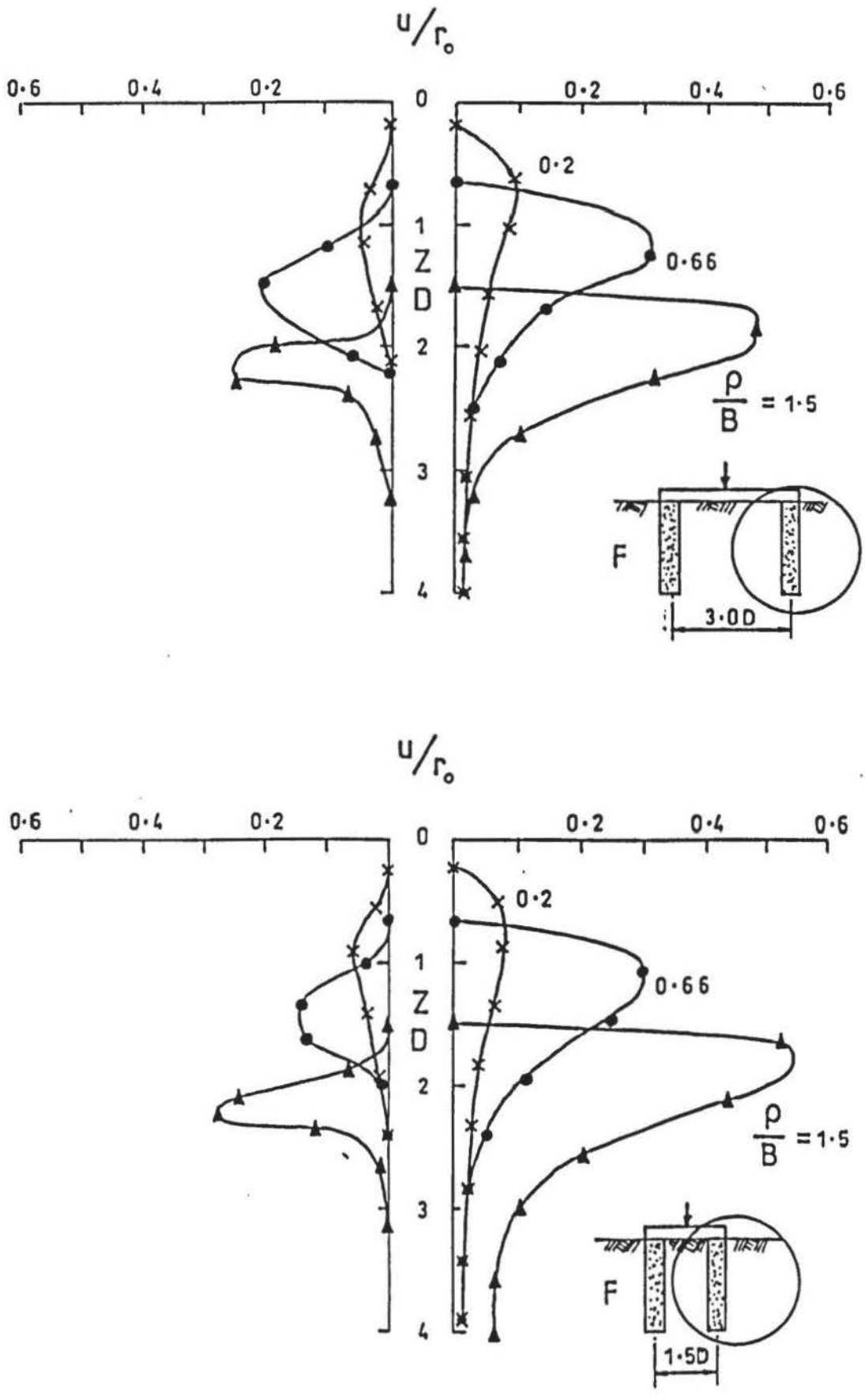

Lateral distortion of one of the two F columns spaced at 3.0D (a_c = 0.4) and 1.5D (a_c = 0.63) loaded by a rectangular foundation.

FIGURE 12.67

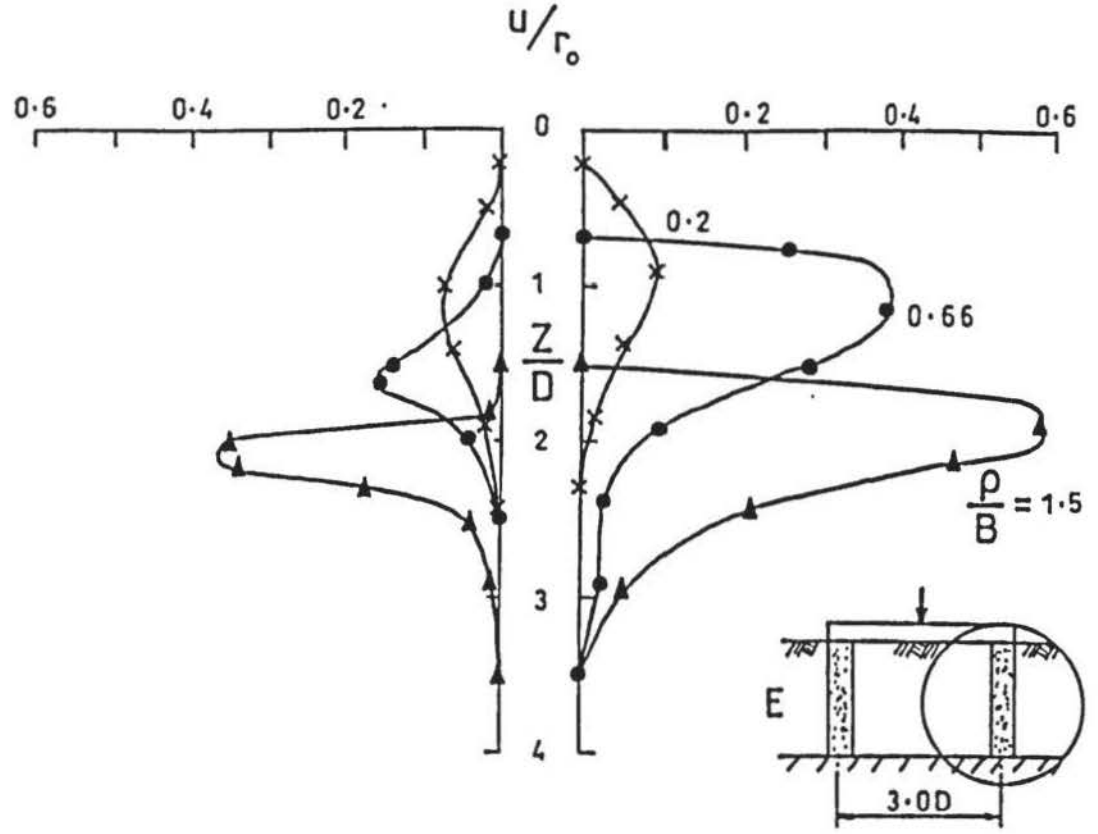

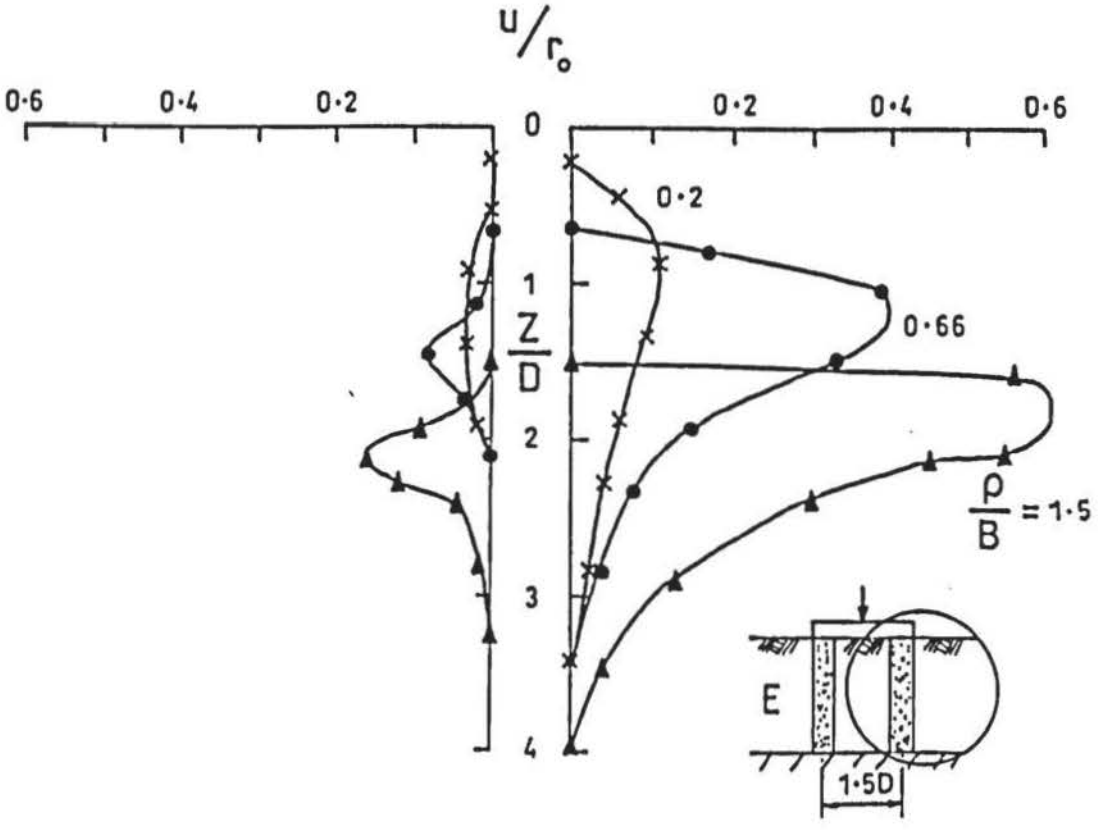

Lateral distortion of one of the two E columns spaced at 3.0D (a_c = 0.4) and 1.5D (a_c = 0.63) loaded by a rectangular foundation.

FIGURE 12.68

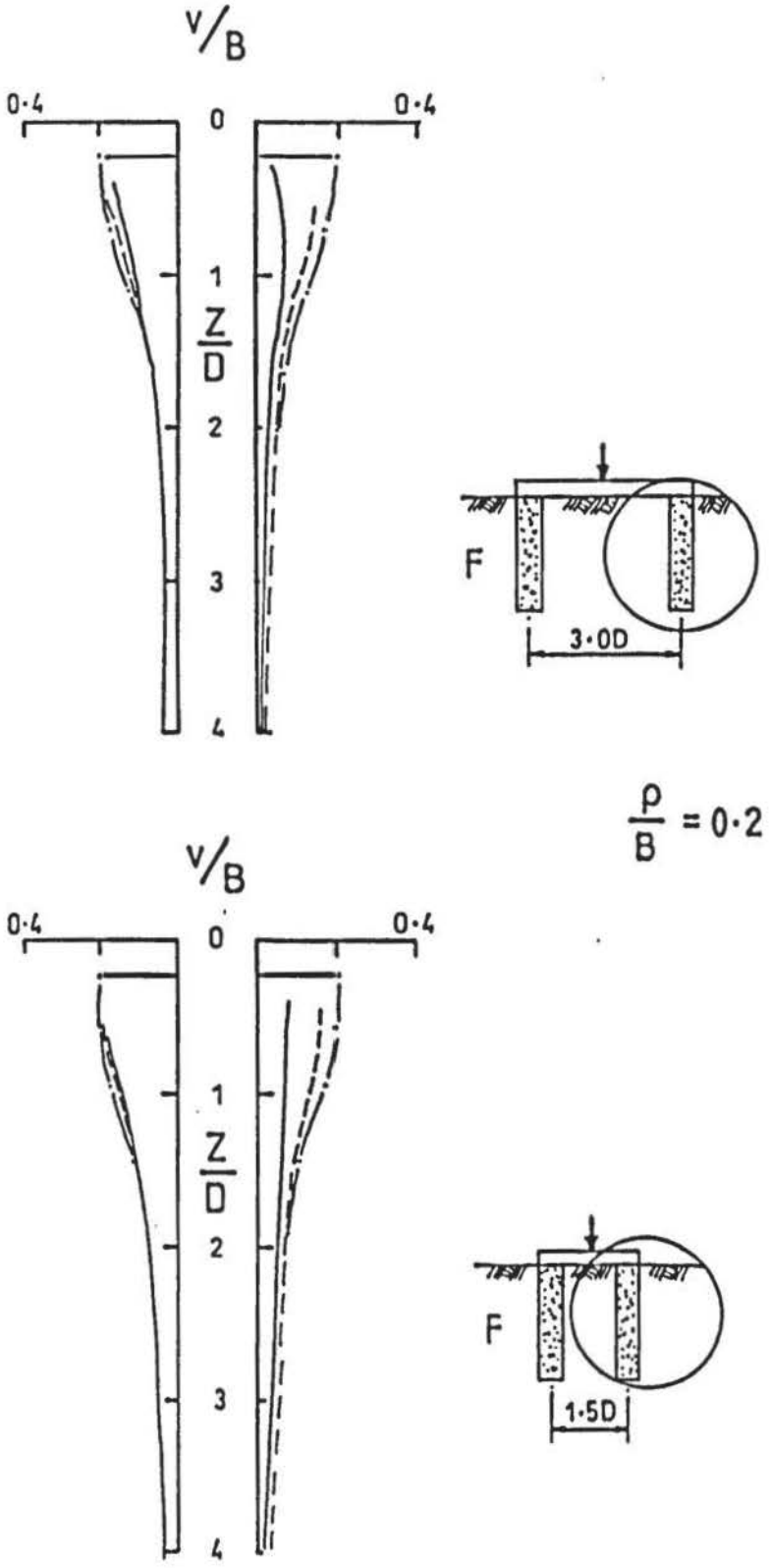

Relative vertical distortions within one of the two F columns and at the column-clay boundary, spaced at 3.0D ($a_c = 0.4$) and 1.5D ($a_c = 0.63$), at $\rho/B = 0.2$.

FIGURE 12.69

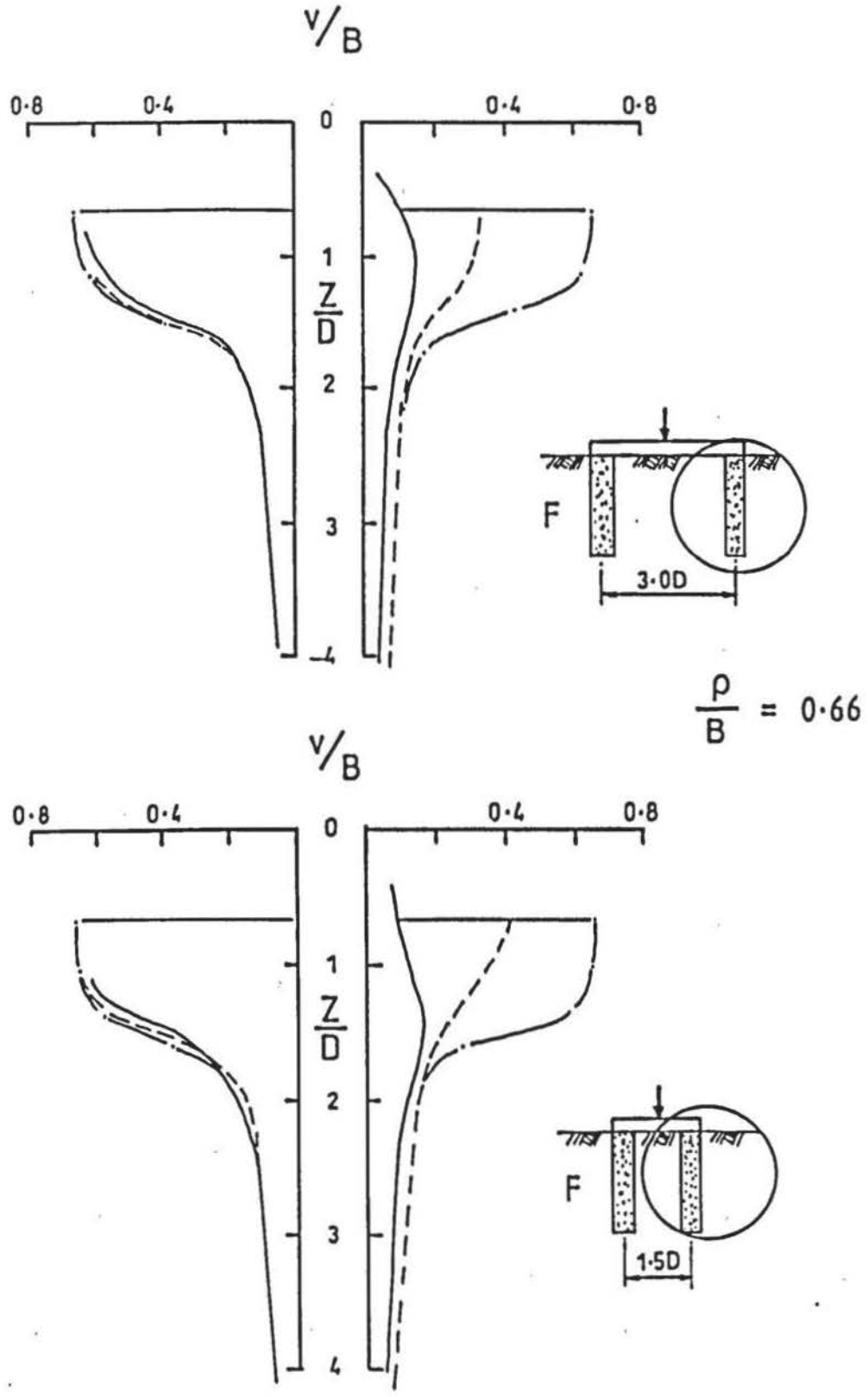

Relative vertical distortions within one of the two E columns and at the column-clay boundary, spaced at 3.0D ($a_c = 0.4$) and 1.5D ($a_c = 0.63$), at $\rho/B = 0.66$.

FIGURE 12.70

independent of spacing and the vertical displacement group effect is due to the action of the foundation. On the clay side of the column, vertical distortions are almost identical to those of a single column shown previously in Figure 12.8.

Vertical distortions of the E columns were found to be essentially the same as those of the F column, with the exception of vertical movement at the base of the column in the latter.

12.6.5 Column-foundation deformation

A drawing of a Kaffir-D cast of one of the two columns is shown in Figure 12.71, on a scale of 1:2. The general shape of the deformed column was found to be the same irrespective of spacing or column end-bearing condition.

The deformed geometry is a combination of that shown by a single isolated column (B=D) and the single column loaded centrally by a rectangular foundation, in Figure 12.54. In all cases, lateral displacement was predominant at 90^{o} to the longitudinal axis of the foundation. View 'A' in Figure 12.71 graphically illustrates the effect a foundation has on increasing the depth to the position of maximum bulging of the column.

By inspection, maximum bulging of the column occurs at right angles to the longitudinal axis of the rectangular foundation (view B in Figure 12.71) with the benefit of this result, the effect seems obvious since the general shear failure mechanism of a rectangular foundation, on a homogeneous soil, occurs in this plane.

12.6.6 Clay displacement fields

Displacement fields in the clay for close (1.5D) and large (3.0D) spacing of the columns, in F and E conditions, at $\rho/B = 0.2$ and 0.66 are given in Figures 12.72 to 12.75.

The overall patterns of the displacement trajectories for all the cases and strain increments largely correspond to those when two closely spaced columns are loaded independently (B=D), shown previously in Figures 12.35 to 12.37.

In the F cases vertical displacement is more pronounced than in the E case, at the clay side of the column. Group action by the columns and clay between them is just evident from $\rho/B = 0.2$, and becomes more apparent when the columns are closely spaced. The result also suggests

Deformation of one of two columns under a rectangular foundation.

FIGURE 12.71

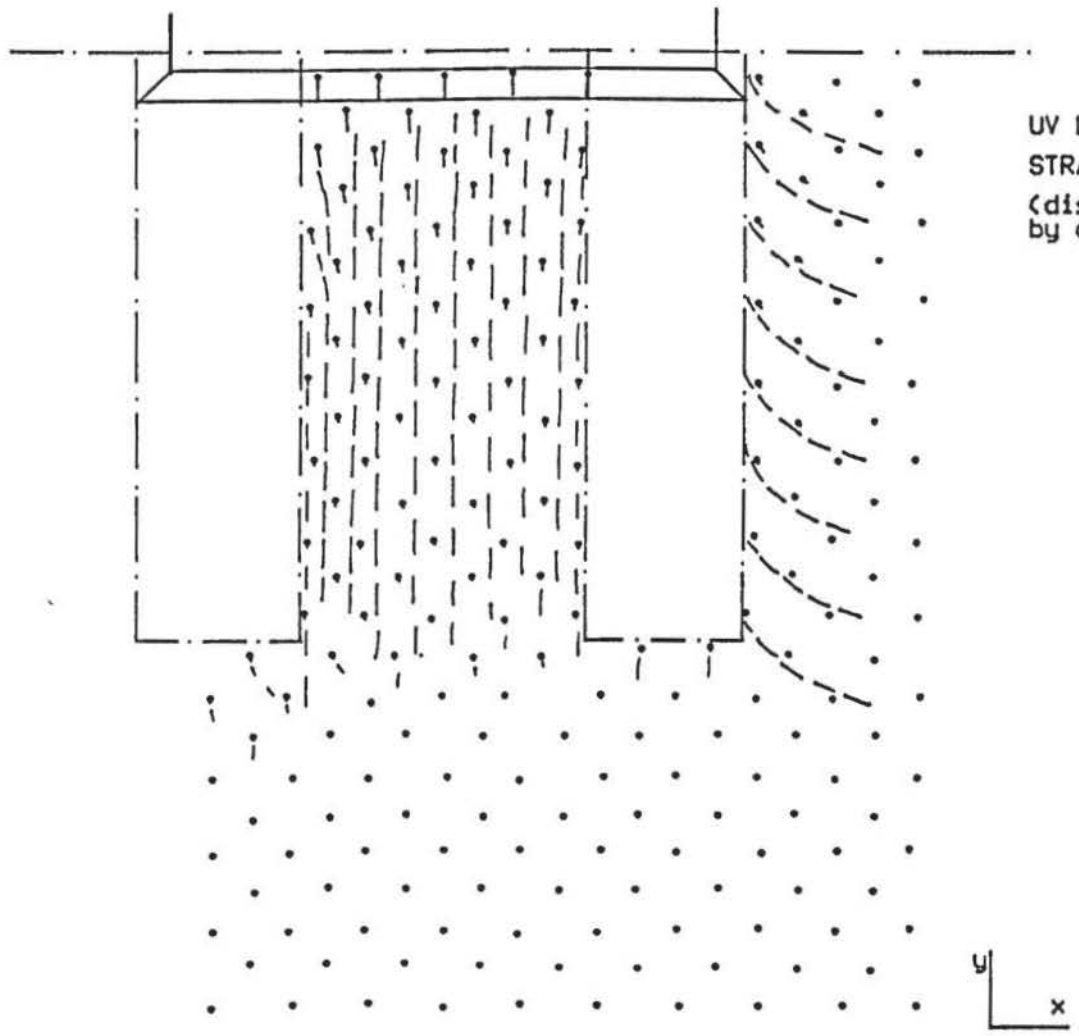

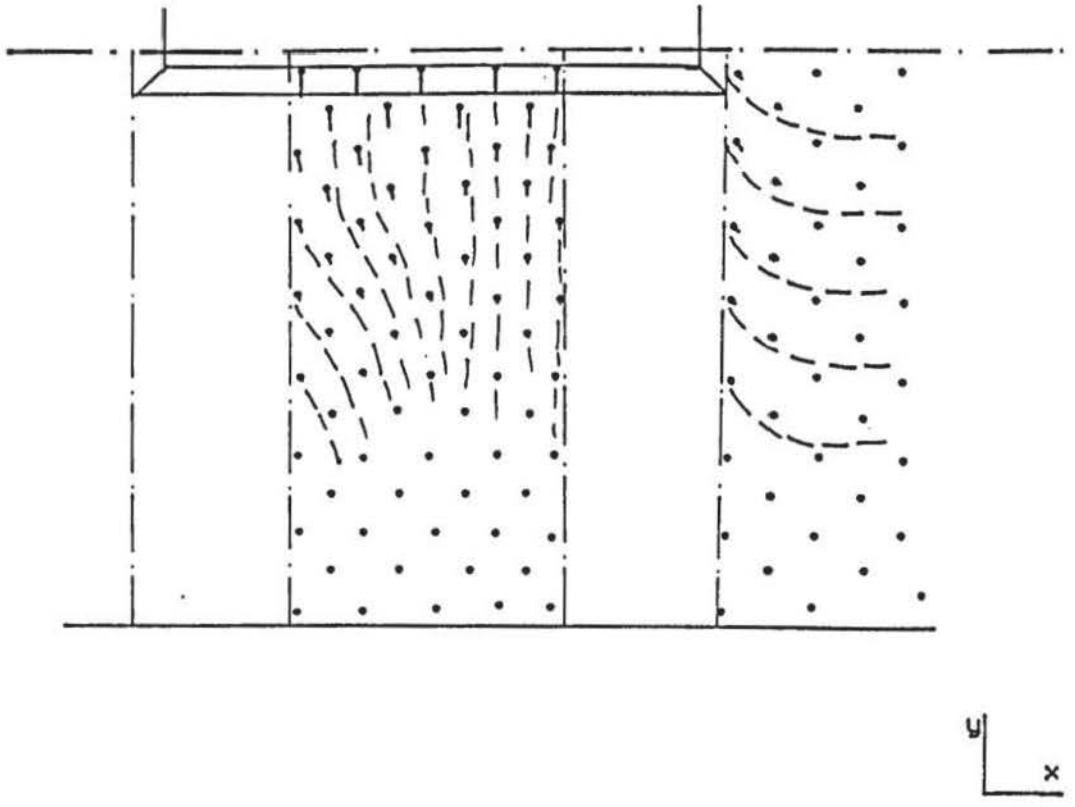

Clay displacement fields at $\rho/B = 0.2$ for F and E columns ($s = 3.0$; $a_c = 0.4$).

FIGURE 12.72

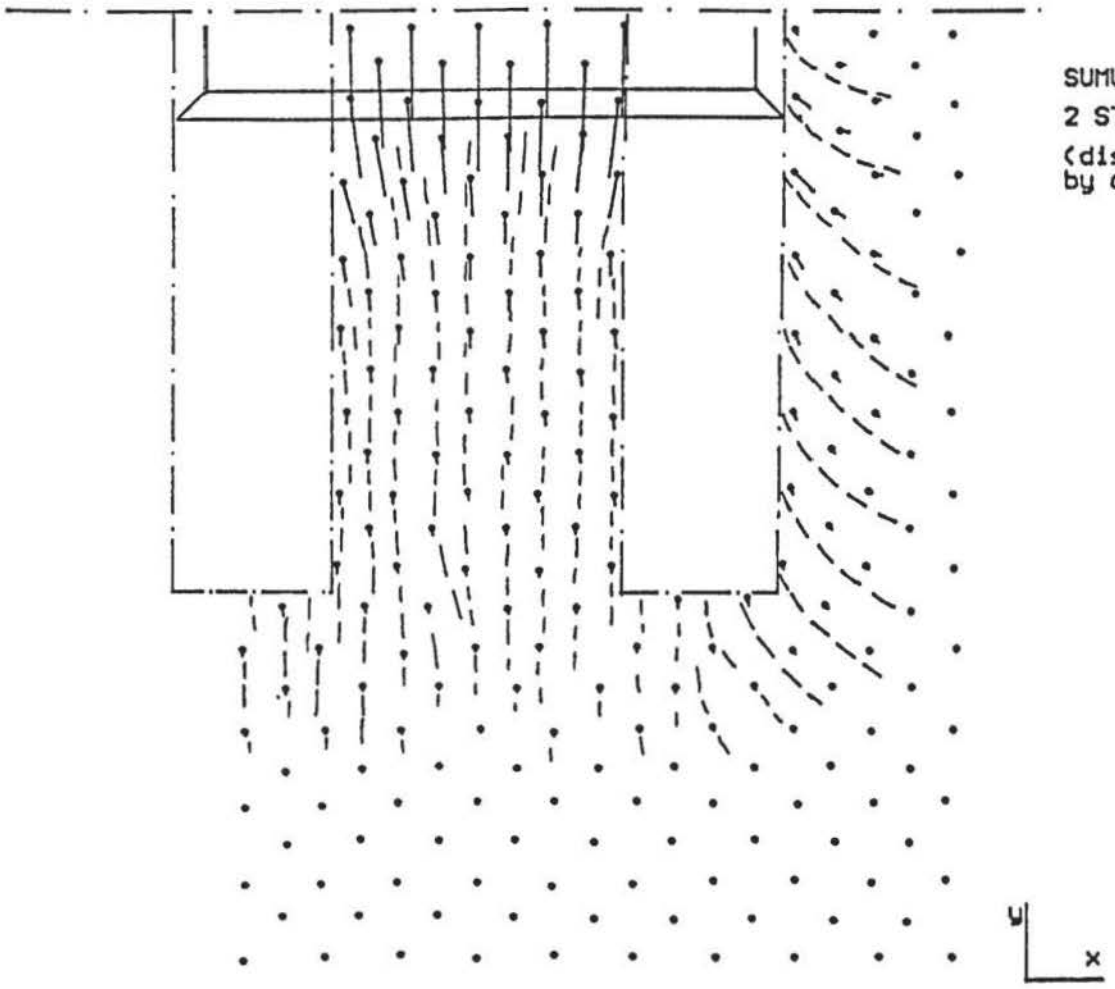

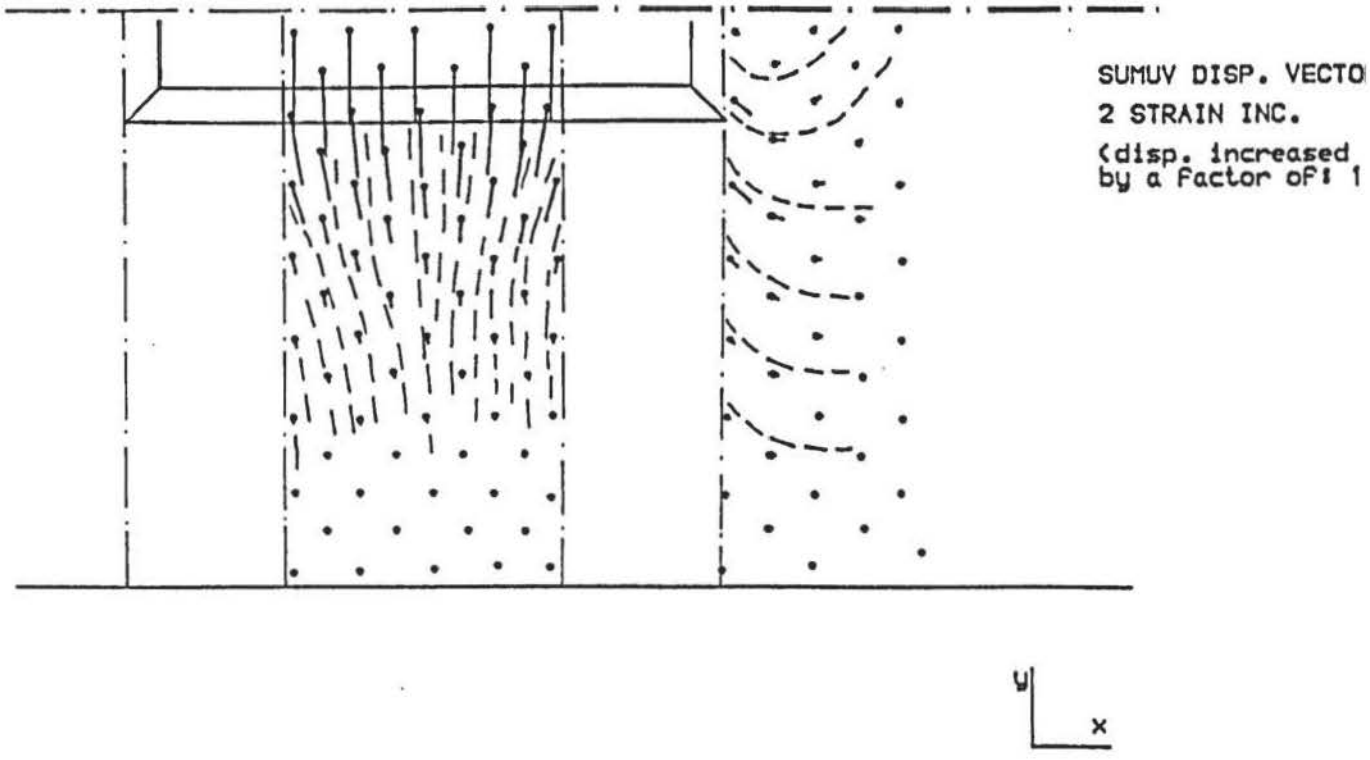

Clay displacement fileds at $\rho/B = 0.66$ for F and E columns ($s = 3.0$; $a_c = 0.4$).

FIGURE 12.73

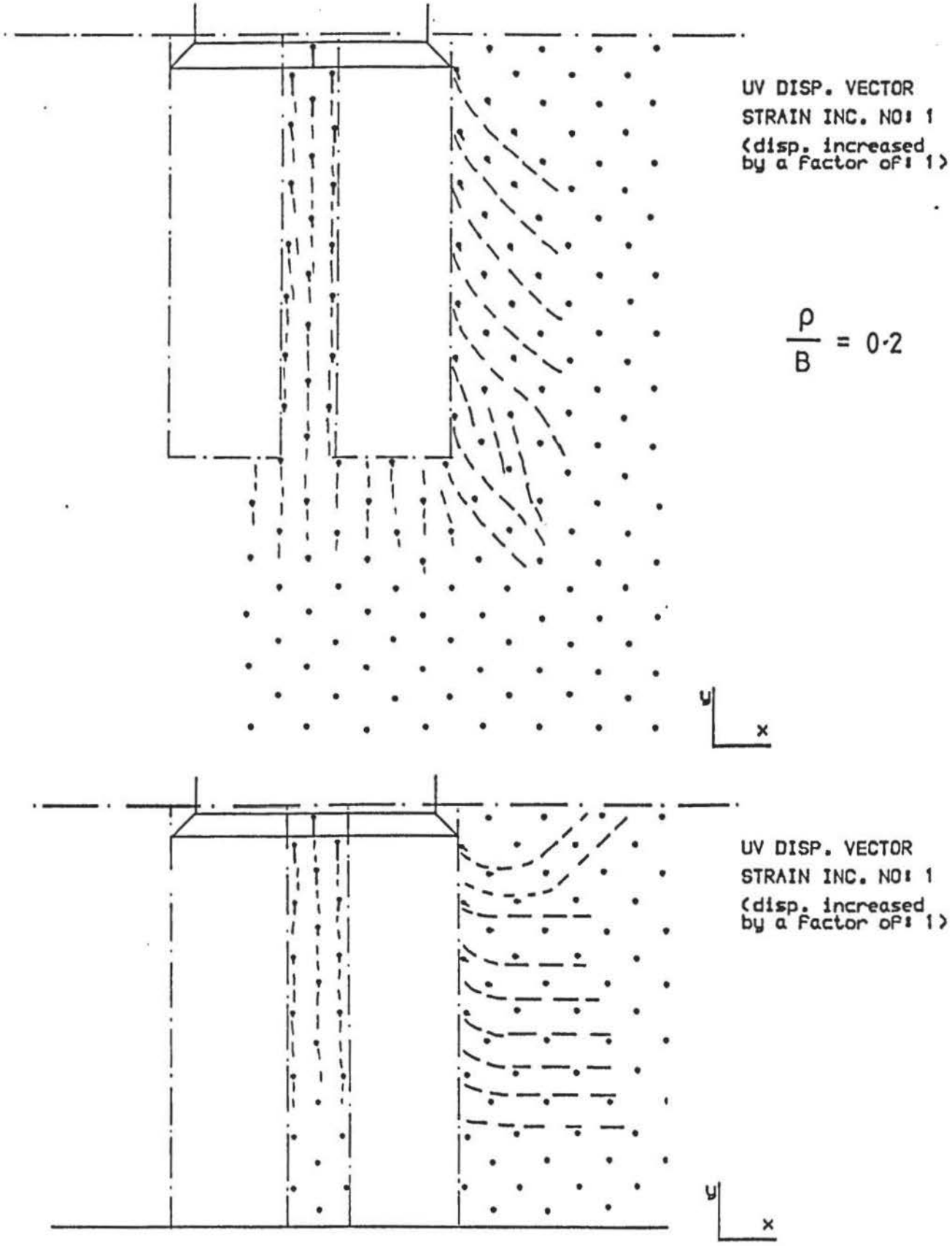

Clay displacement fields at $\rho/B = 0.2$ for F an E columns ($s = 1.5$; $a_c = 0.63$)

FIGURE 12.74

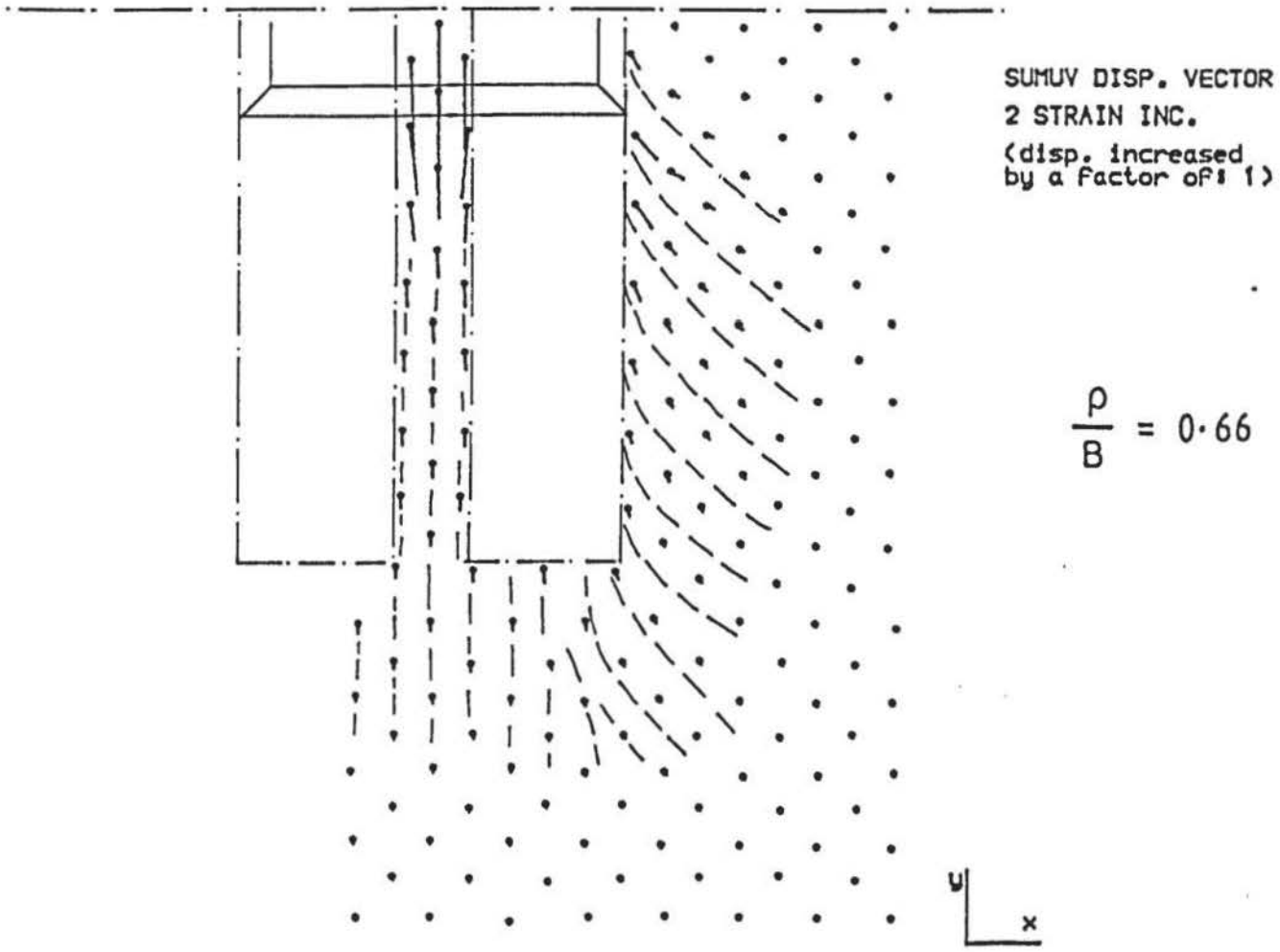

Clay displacement fields at $\rho/B = 0.66$ for F and E columns ($s = 1.5$; $a_c = 0.63$)

FIGURE 12.75

that the displacement fields, on this plane, are largely unaffected by foundation action on the soil between the columns. However, as the previous Section 12.6.5 has shown, the overall picture of clay displacement is incomplete because more signficant displacement behaviour may occur in the plane at right angles to the longitudinal axis of the foundation. This plane of clay displacement was not subject to radiography since at that stage of understanding column-foundation behaviour, it was considered more appropriate to observe the interaction between the two columns and the clay-foundation reaction between them.

12.6.7 Column-soil strains

The column and clay strains when two columns were loaded by a rectangular foundation at $\rho/B = 0.2$ and 0.66 are given in Figures 12.76 to 12.83. The results of two tests are shown when columns were spaced at 1.5D (Test Nos.: XR2 and XR2E) and 3.0D (Test Nos.: XR6 and XR6E).

When the columns are closely spaced (1.5D), direct comparison can be made with the results in Figures 12.38 to 12.41 when two columns were loaded independently by circular foundations having the same diameter as the columns.

At the first strain increment ($\rho/B = 0.2$) the influence of the rectangular foundation is to induce a predominance of ε_y in the clay between the columns and produce relatively negligible ε_x. It is considered, however, that signficiant horizontal strains occurred perpendicular to this plane by a squeezing action as column bulging developed. The ε_x and ε_y are both shown to be compressive. Inclination of ε_1 in the present case is inclined by about 10-20^o to the vertical. When the columns were loaded independently, ε_1 was inclined to the horizontal. This indicates that γ_{xy} has been suppressed vertically and acts in the horizontal plane, although the magnitude remains small.

In the columns, strain patterns of tensile ε_x and comprssive ε_y remain the same and

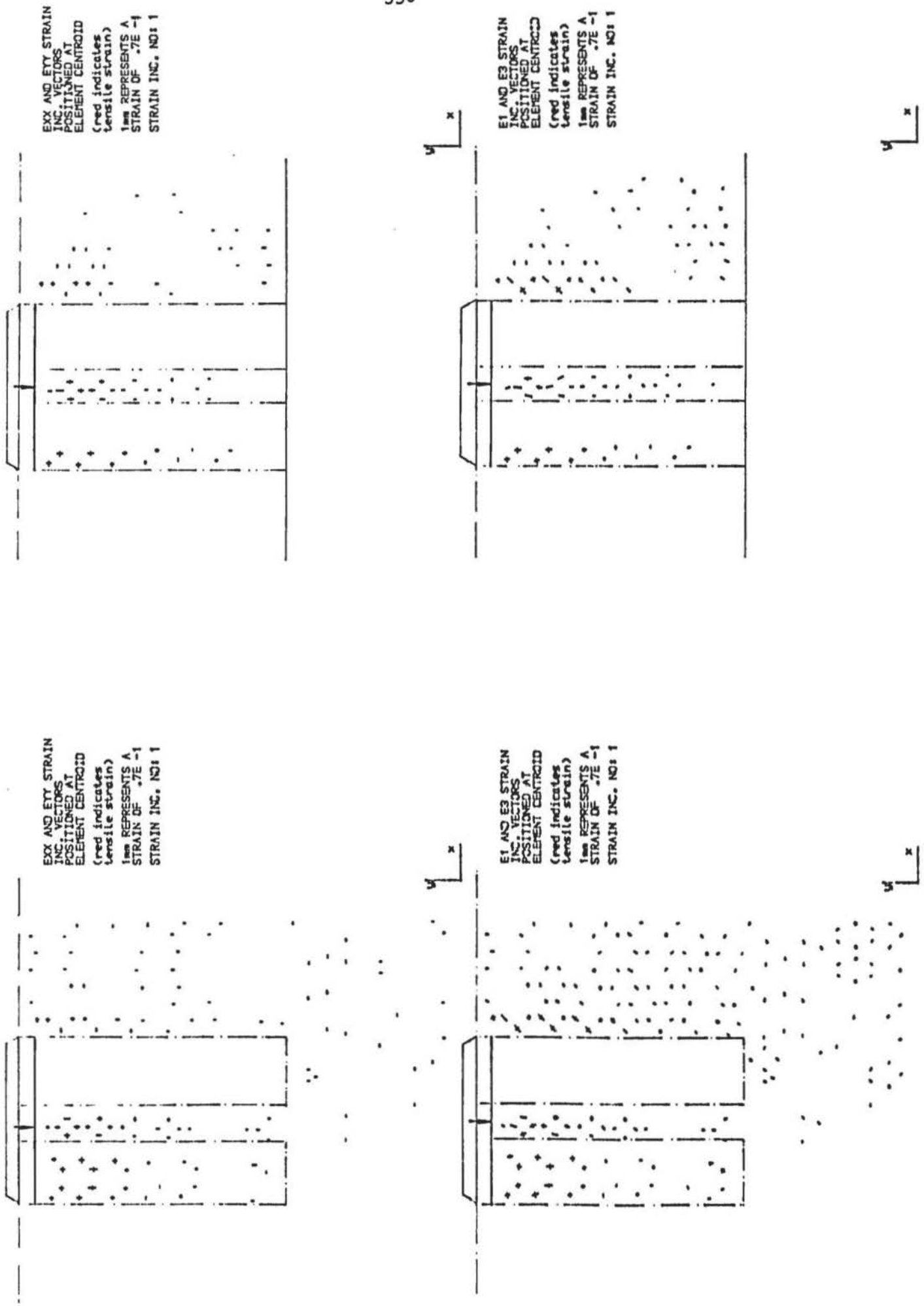

ε_x and ε_y, ε_1 and ε_3 vectors for F and E columns. ($s = 1.5$; $a_c = 0.63$) at $\rho/B = 0.2$.

FIGURE 12.76

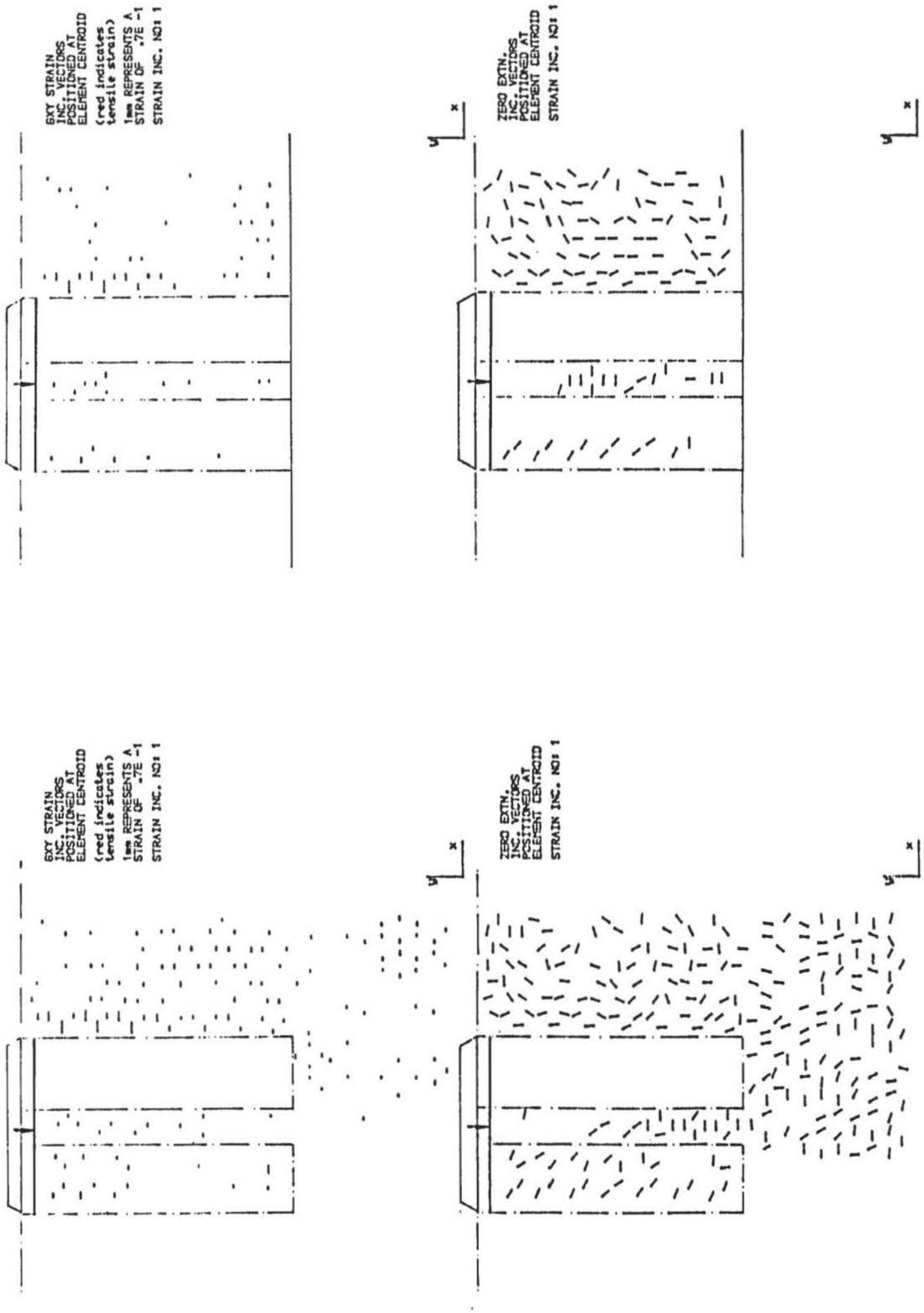

γ_{xy} and zero extension lines for F and E columns ($s = 1.5$; $a_c = 0.63$) at $\rho/B = 0.2$.

FIGURE 12.77

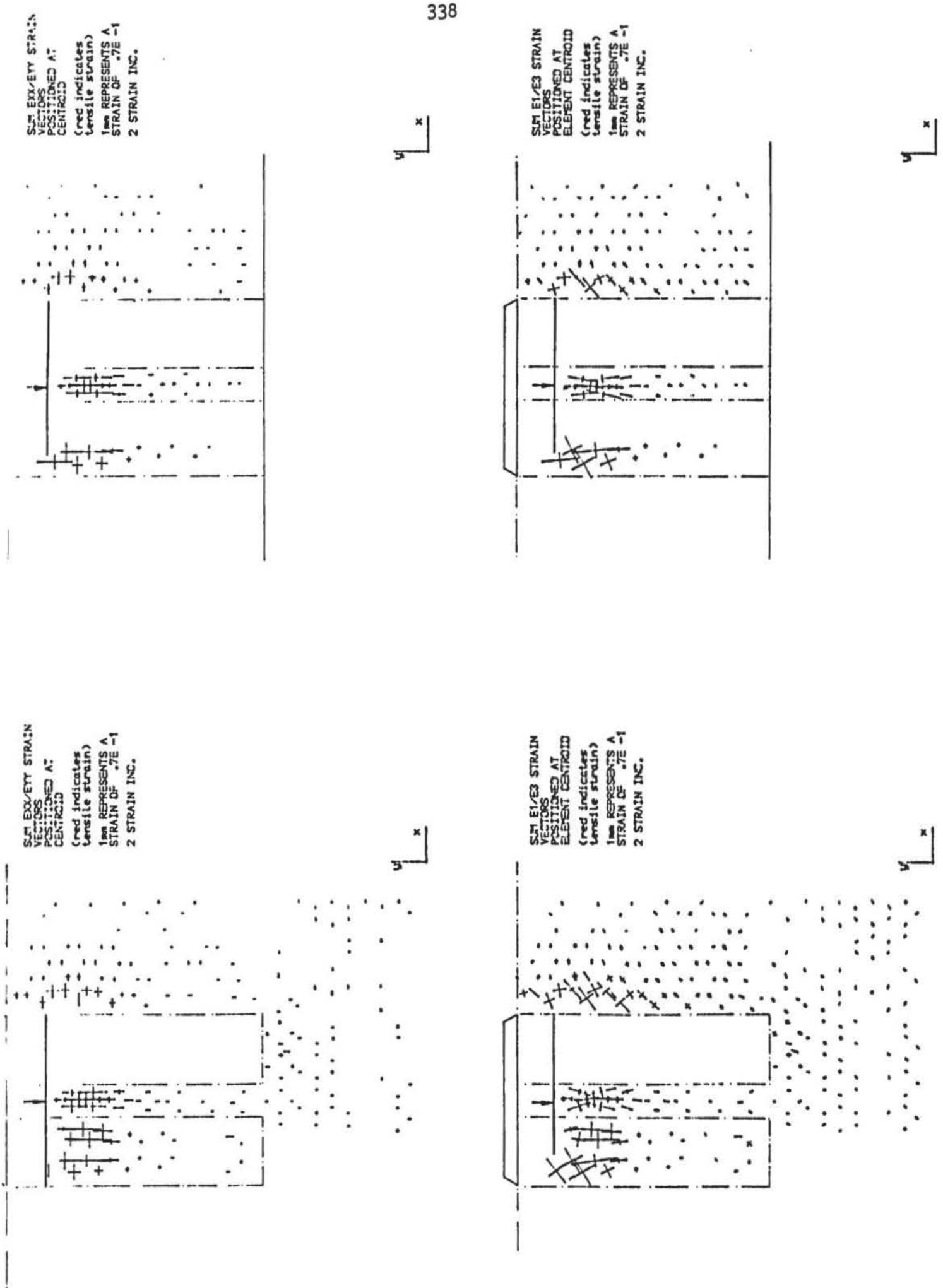

ε_x and ε_y, ε_1 and ε_3 vectors for F and E columns ($s = 1.5$; $a_c = 0.63$) at $\rho/B = 0.66$.

FIGURE 12.78

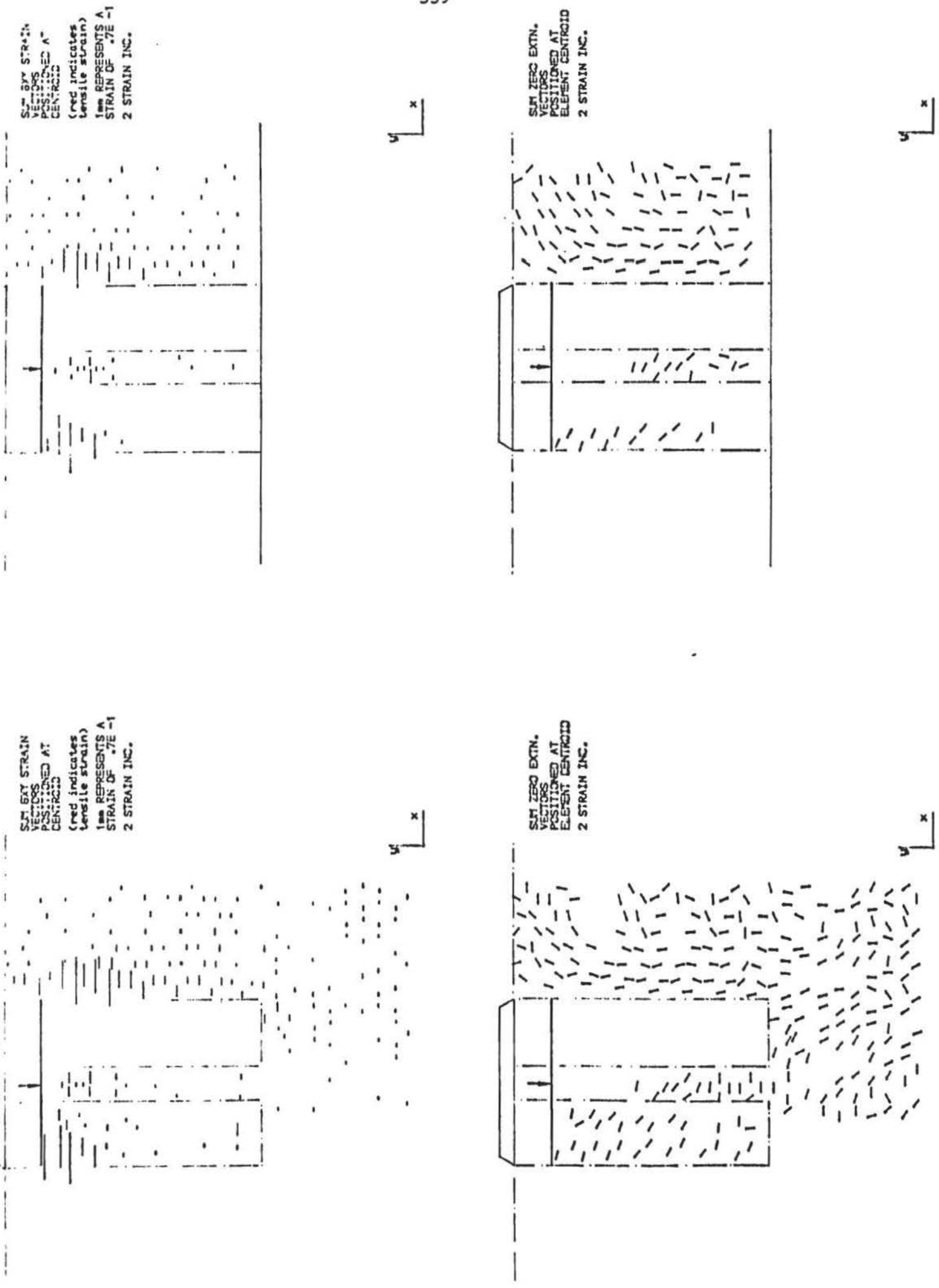

γ_{xy} and zero extension lines for F and E columns ($s = 1.5$; $a_c = 0.63$) at $\rho/B = 0.66$.

FIGURE 12.79

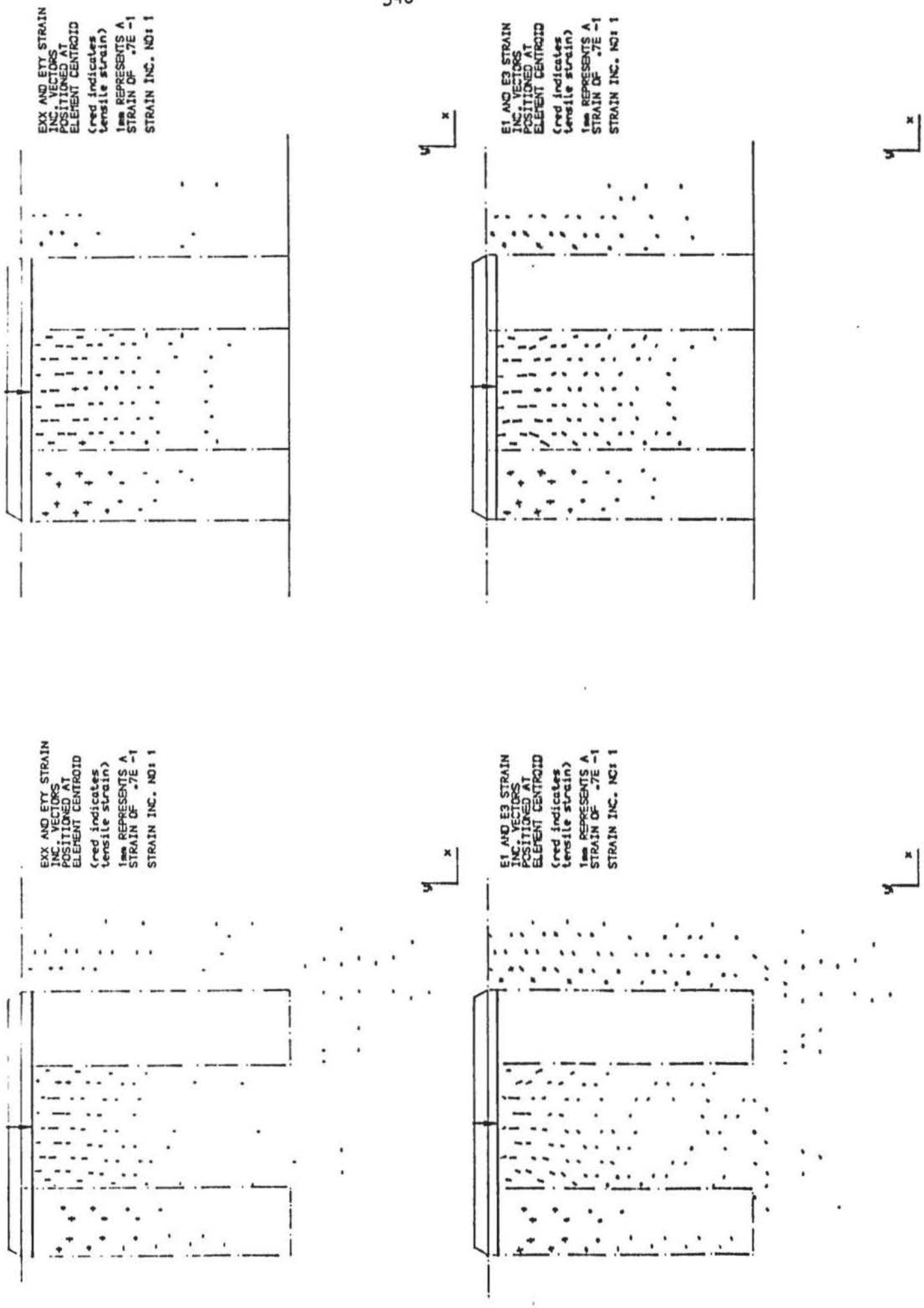

ϵ_x and ϵ_y, ϵ_1 and ϵ_3 vectors for F and E columns ($s = 3.0$; $a_c = 0.4$) at $\rho/B = 0.2$.

FIGURE 12.80

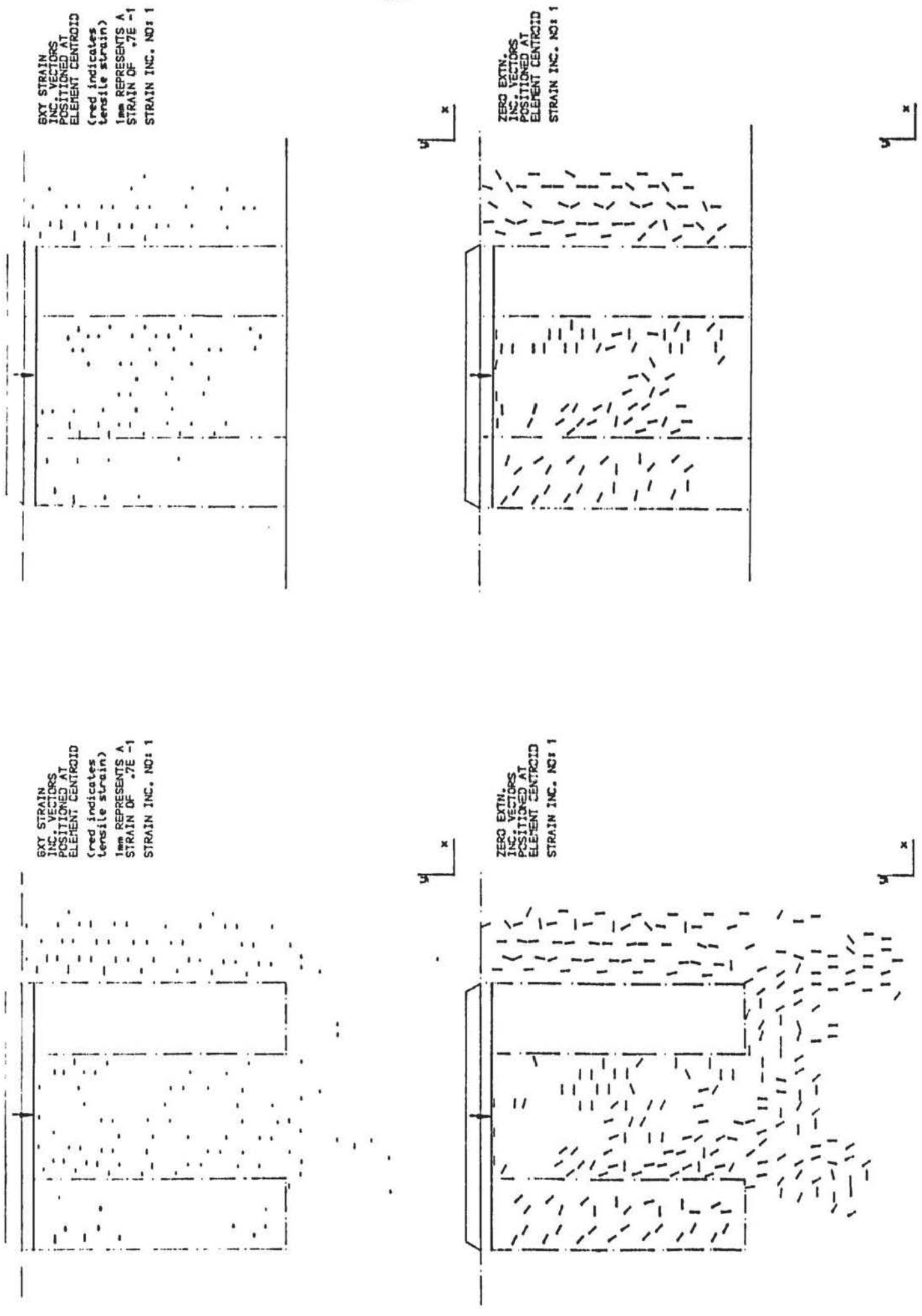

γ_{xy} and zero extension lines for F and E columns ($s = 3.0$; $a_c = 0.4$) at $\rho/B = 0.2$.

FIGURE 12.81

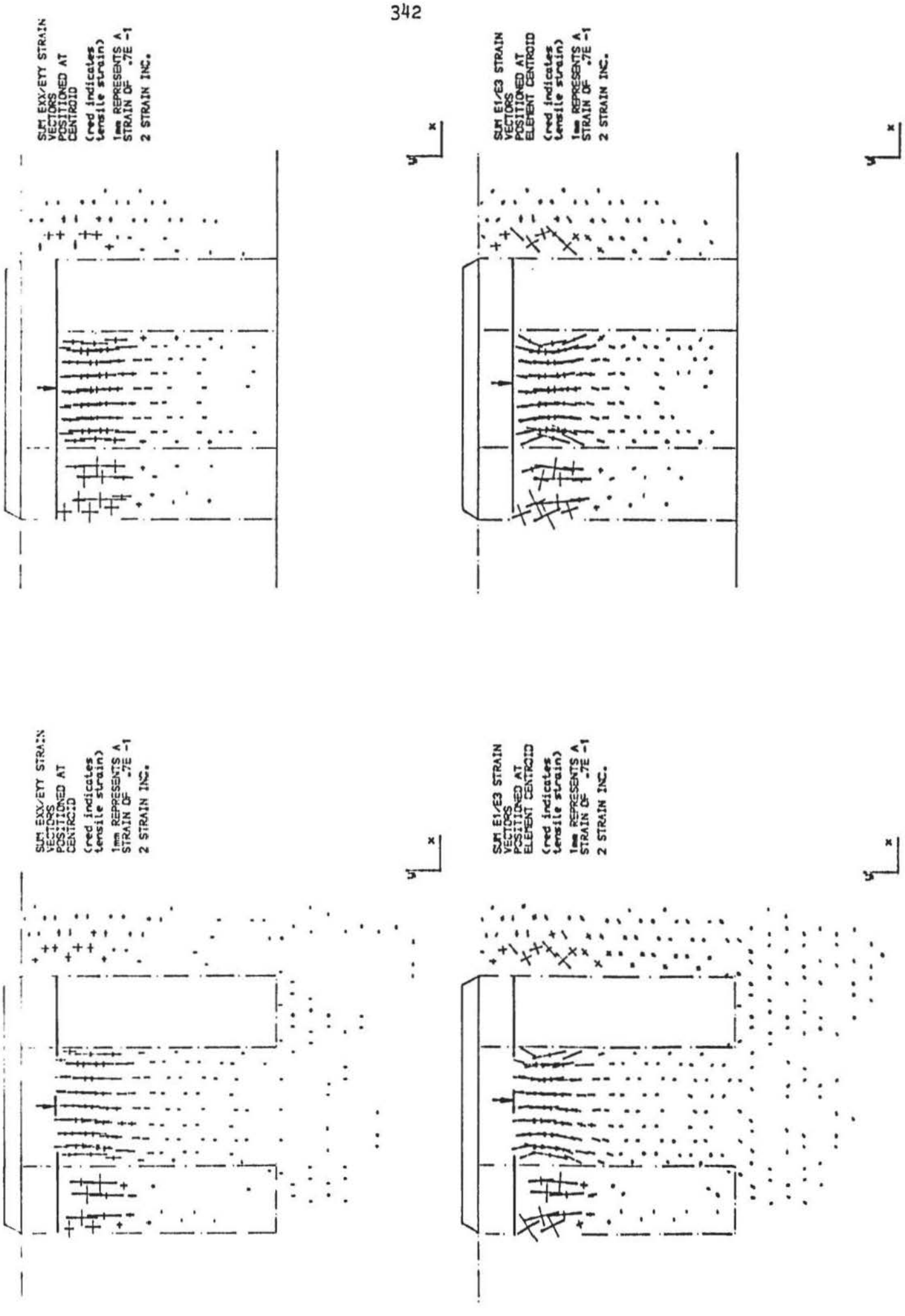

ε_x and ε_y, ε_1 and ε_3 vectors for F and E columns ($s = 3.0$; $a_c = 0.4$) at $\rho/B = 0.66$.

FIGURE 12.82

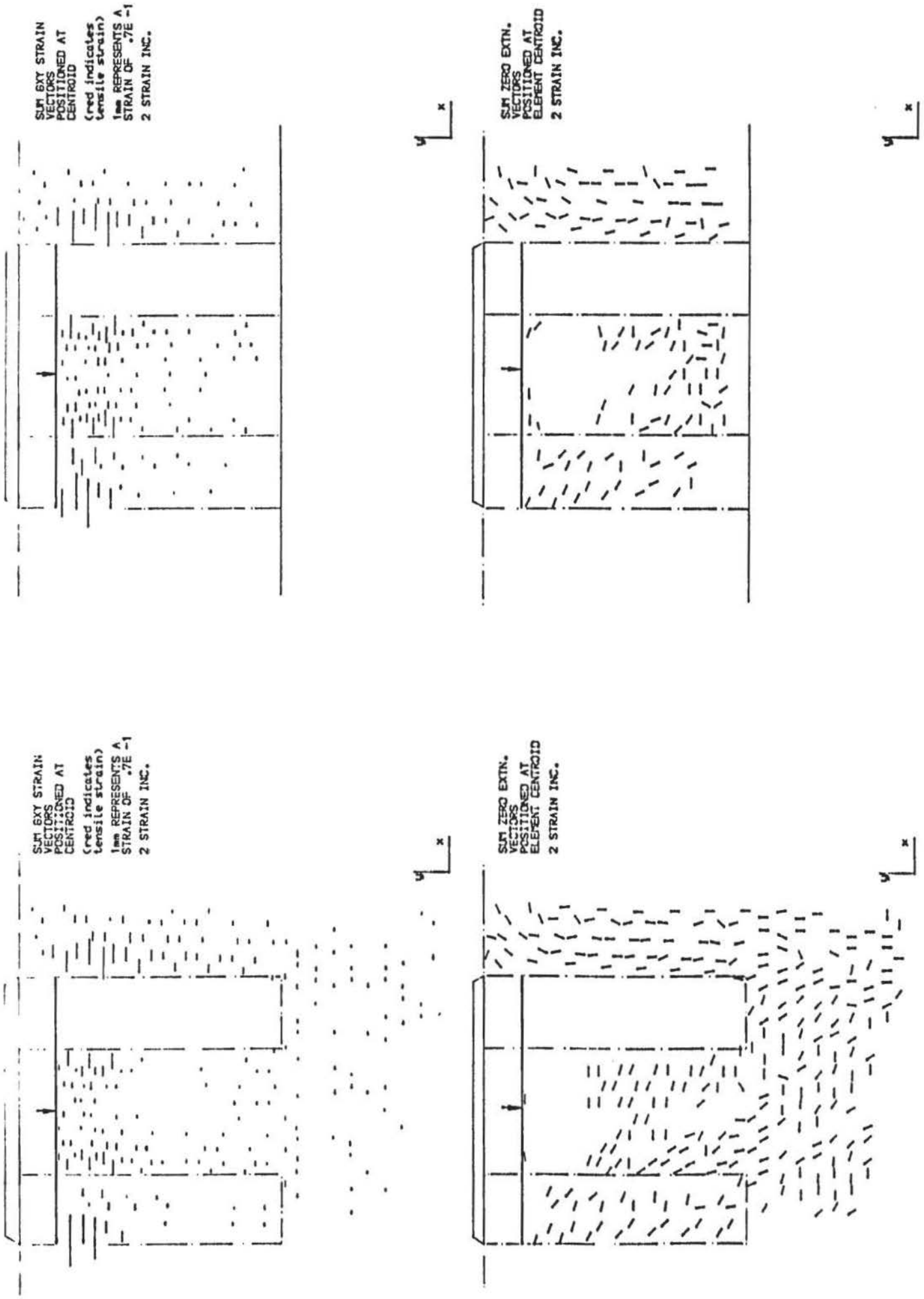

γ_{xy} and zero extensions lines for F and E columns ($s = 3.0$; $a_c = 0.4$) at $\rho/B = 0.66$.

FIGURE 12.83

within about a depth of one column diameter ε_y is suppressed. Almost all the length of the column, however, is affected by strain. This indicates that a greater penetration by the surface loading has occurred which may be attributed to the suppression of the vertical distribution γ_{xy}. This is supported by closer inspection of ε_y in the columns and clay between them, which shows that their magnitudes are almost identical.

These effects become more apparent at the second strain increment ($\rho/B = 0.66$), at which point, pile mode group failure has started to develop. Strains in the clay around the column are of a similar magnitude and distribution to those when the columns were loaded independently.

When the columns were at a spacing of 3.0D, ε_x and ε_y, and the principal strain patterns are similar to those at 1.5D but obviously a larger amount of clay between the columns becomes affected. In this zone, with the occasional exception, ε_x is insignificant when $\rho/B = 0.2$ although it develops within about a depth of one column diameter beneath the foundation when $\rho/B = 0.66$. At either stage there is almost no inclination of the principal axes and ε_1 is vertical. Also, the effect of the foundation is to produce the same magnitudes of ε_1 and ε_y at equal depths, in the clay and columns. The principle of equal strain in materials of different stiffness or compressibility subject to foundation loadings has been assumed by a number of researchers referred to in the first Chapter.

12.6.8 Zero extension

The patterns of zero extension largely correspond to those when two columns were loaded independently although potential slip planes within the column occur to the full depth of the column in the present case. This further supports the previous observation that the applied surface load has penetrated to the base of the column.

12.7 SQUARE FOUNDATIONS ON A NUMBER OF COLUMNS

12.7.1 Boundary stresses and settlement

Four columns, in F and E conditions, at various spacings, related to the initial column diameter, (sD) were loaded by square foundations (Test Nos.: PSQ6 to PSQ9 and PSQ6E to PSQ9E). Tests were also performed with a fifth column placed central to the group of four columns (Test Nos.: PSQ2 to PSQ5 and PSQ2E to PSQ5E). The distance (s'D) of the central column to each of the other columns may be calculated from:

$$s'D = 0.5\sqrt{2}.\,sD \qquad (12.10)$$

where s is the spacing factor relating to the four columns.

The replacement ratio a_c ranged form 0.43 to 0.15.

Similarly to the test results in the previous two Sections, the variation in the applied foundation pressure (expressed a q/c_u) with settlement (expressed as ρ/B) was found to be related to a_c. No ultimate q/c_u was obtained for the F case due to the restriction in platen travel of the compression machine. In any case, vertical displacement of those larger foundations needed to be restricted to minimise the influence of the proximity of the container base in relation to the foundation width. Working stress for the F and E cases was determined as the value of q/c_u when $\rho/B = 0.054$. The ρ/B value was chosen since this was the average obtained for the circular and square foundations in Figure 12.45.

Peak $\Delta\sigma_x/q$ typically occurred at $\rho/B \approx 0.02$ to 0.03 (ten times less in value than the previous tests) with the magnitude increasing with foundation size. The increasing distance of the edge of foundation to the horizontal stress transducer also contributed to higher recorded stress levels.

The relationship between q/c_u and $1/a_c$ is shown in Figure 12.84 for the F case and good agreement with the curves for the circular and square foundations loading a single column is obtained. Corresponding agreement was also obtained for the E case with q/c_u having higher

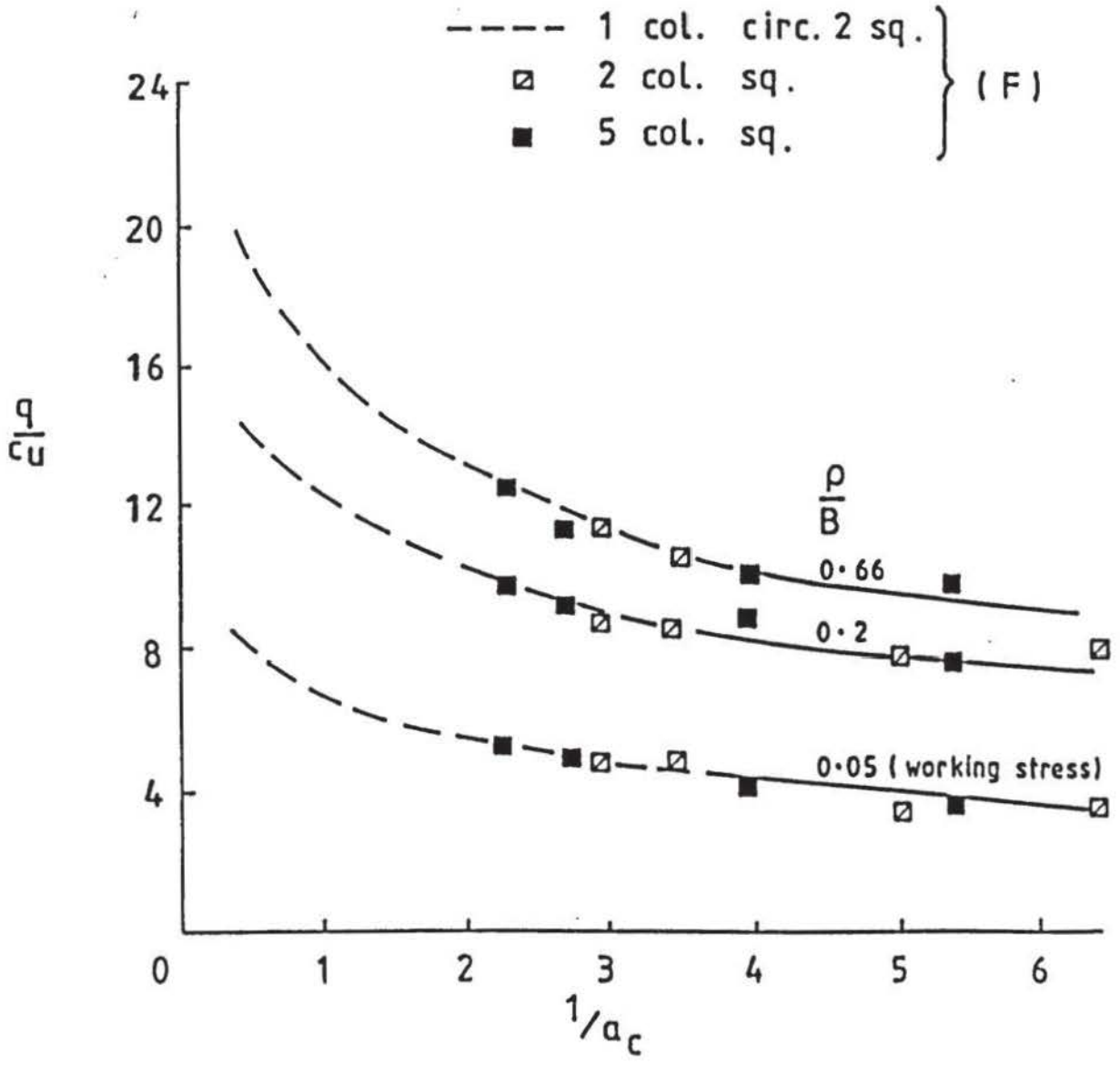

Typical variation of q/c_u with $1/a_c$ for five and four F columns loaded by square foundations.

FIGURE 12.84

values for the same ρ/B.

It is concluded that the bearing capacity of clay containing granular columns (of a given specification) is directly related to the ratio of their respective initial areas contained within the boundary of a foundation. The relationship between bearing capacity and column spacing may be deduced from geometric considerations, but this will only be valid providing the spatial relations between the columns and the foundation sizes are constant. For example, the bearing capacity available for a column spacing of, say, 1.5D and a foundation width B = 2.5D will be greater than if B > 2.5D, since a_c will be smaller for the latter case.

12.7.2 Improvement

It has been demonstrated that the improvement of bearing capacity using granular columns is dependent upon the applied bearing pressure level and that its magnitude expressed as the improvement coefficient I_q is also dependent on the relative surface areas of the columns and clay within the foundation perimeter. These characteristics were exhibited by the square foundations loading groups of four and five columns in F and E conditions. In practice, the improvement in bearing capacity and settlement are of most concern at working stresses particularly where structural foundations are concerned.

The improvement and settlement coefficients at working stresses $[I_q]^{WS}$ and $[m]^{WS}$ respectively, for groups of four and five columns are shown against $1/a_c$ (logarithmic scale) in Figure 12.85 together with the results presented in the previous sections for both F and E cases. Columns in the E condition give higher improvement than the latter for the same ratio of vertical displacement to foundation width. When $a_c = 0.05$ almost no improvement is obtained for either bearing condition. In terms of settlement, the E columns give the larger reduction in settlement for the same working stress levels as the F columns. When $a_c = 0.05$ settlement reduction is negligible.

12.7.3 Column yield

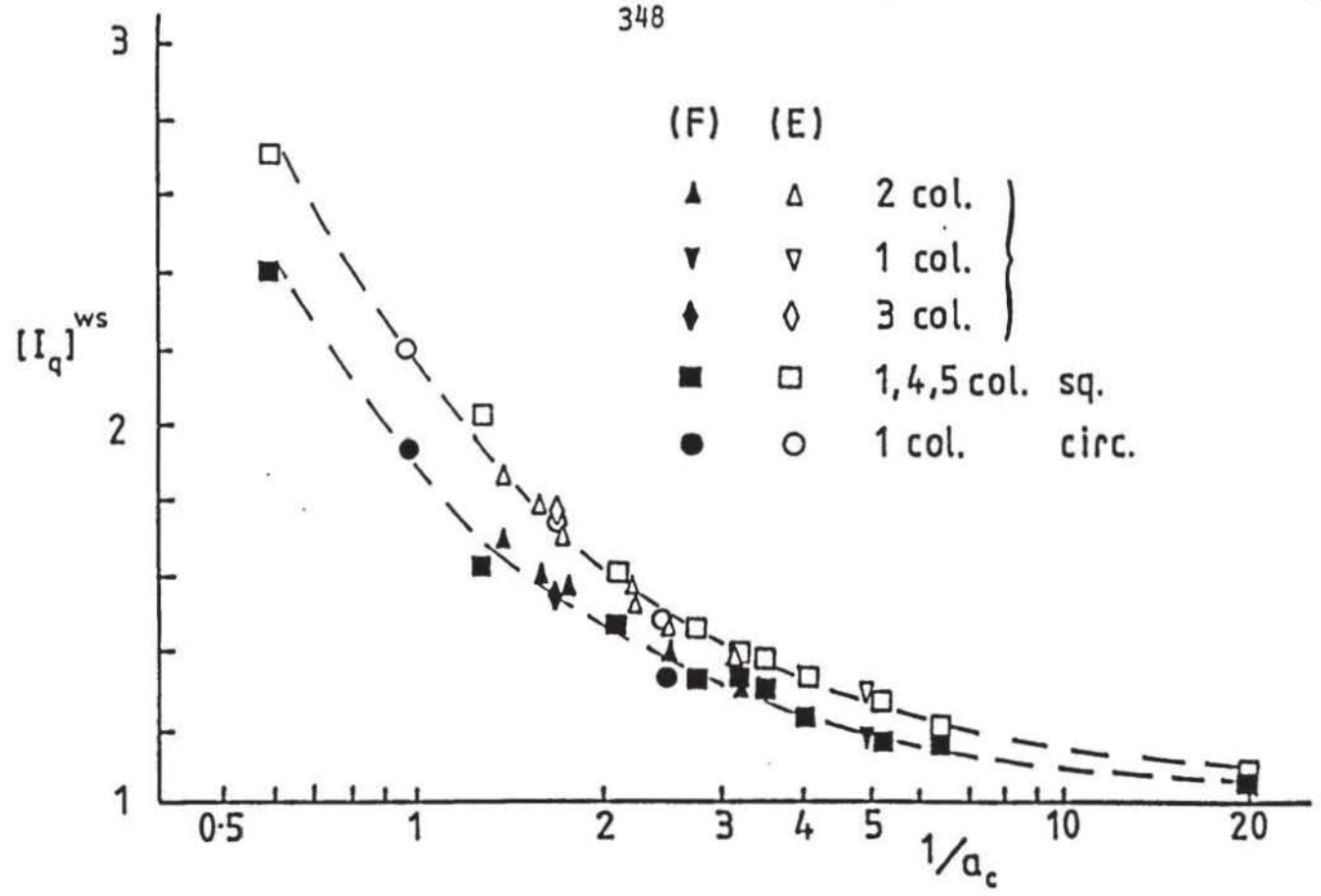

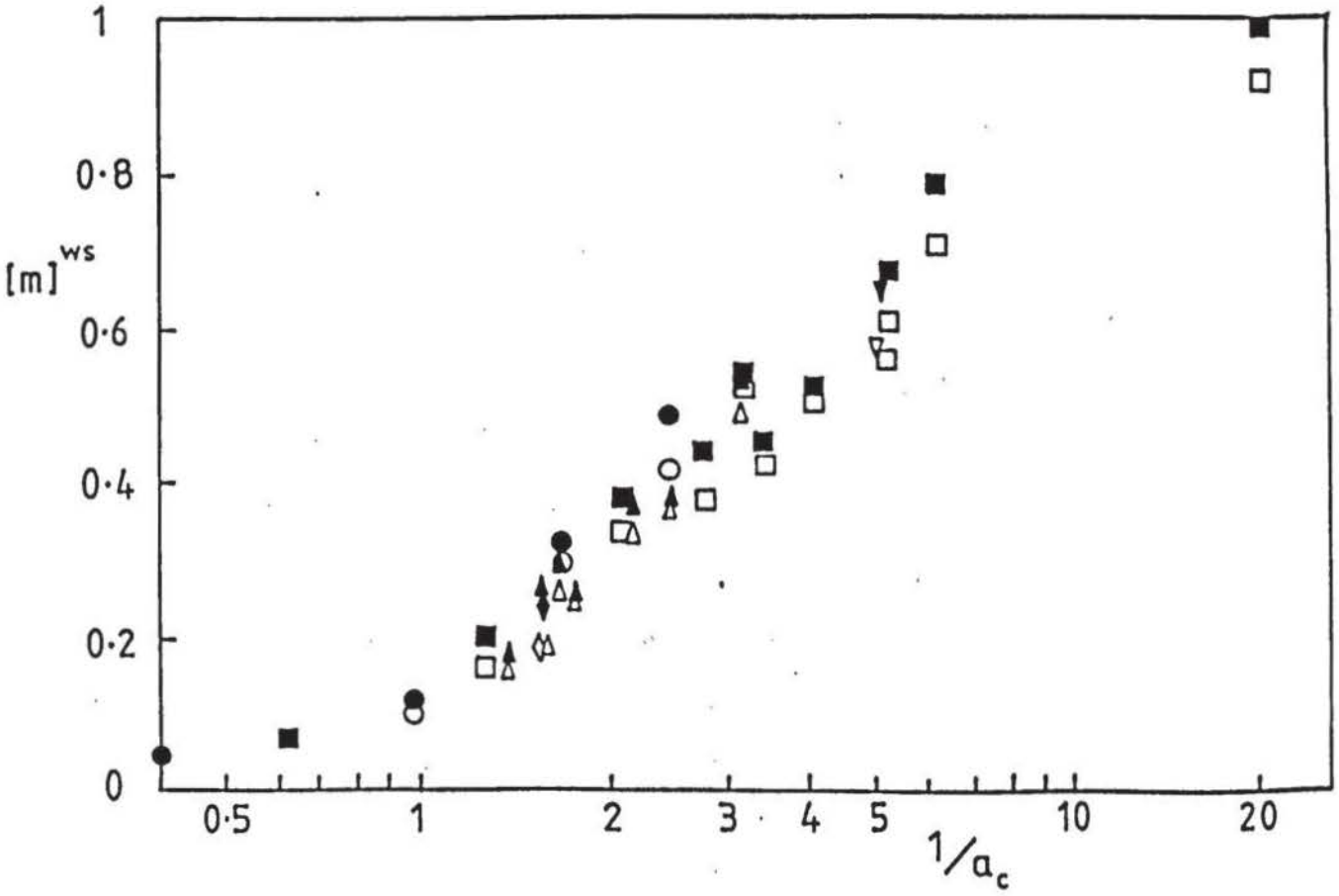

Typical variation of I_q and m at working stress of columns subject to loading by circular, square and rectangular foundations.

FIGURE 12.85

In the same manner as the previous column-foundation configurations, column yield was less noticeable on the q/c_u against ρ/B curves as a_c decreased. The value of q/c_u, at yield, also became less with smaller values of a_c.

It has been previously identified that peak values of I_q correspond to the start of the yield plateau on the q/c_u against ρ/B curve. Peak I_q, therefore, is considered to be representative of the point at which column yield commences. From this, the value of q/c_u at column yield ($[q/c_u]_{yield}$) can be accurately determined. The values of $[q/c_u]_{yield}$ are shown plotted against $1/a_c$ (logarithmic scale) in Figure 12.86 along with the results from all the previous tests. Since, in practice, foundation sizes will be larger than one column diameter, the range $1/a_c = 1$ to 20 is shown. The E cases consistently achieved a higher q/c_u at yield than the F cases.

12.7.4 Column-foundation deformation

Deformation of the columns at the corners of the square foundations showed a more spectacular mode of deformation than the previous cases. In the F condition, Kaffir-D casts showed the upper third of the column to have sheared along a plane at about 46-48° to the horizontal in the direction of the foundation diagonal. The lower portion of the column was displaced away from the foundation as vertical compression proceeded. The effect is shown by the drawing on a scale of 1:2 in Figure 12.87. This mode of failure is commensurate with that proposed by Brauns (1978).

With the E columns, the same failure mode was exhibited but occurred in a compound fashion with shearing taking palce in two planes. The angle, to the horizontal, of these planes was about 46-48°. Bending of the column was evident in the E case and was attributed to the end restraint on the column acting against a general bodily movement aways from the foundation in the direction of its diagonal.

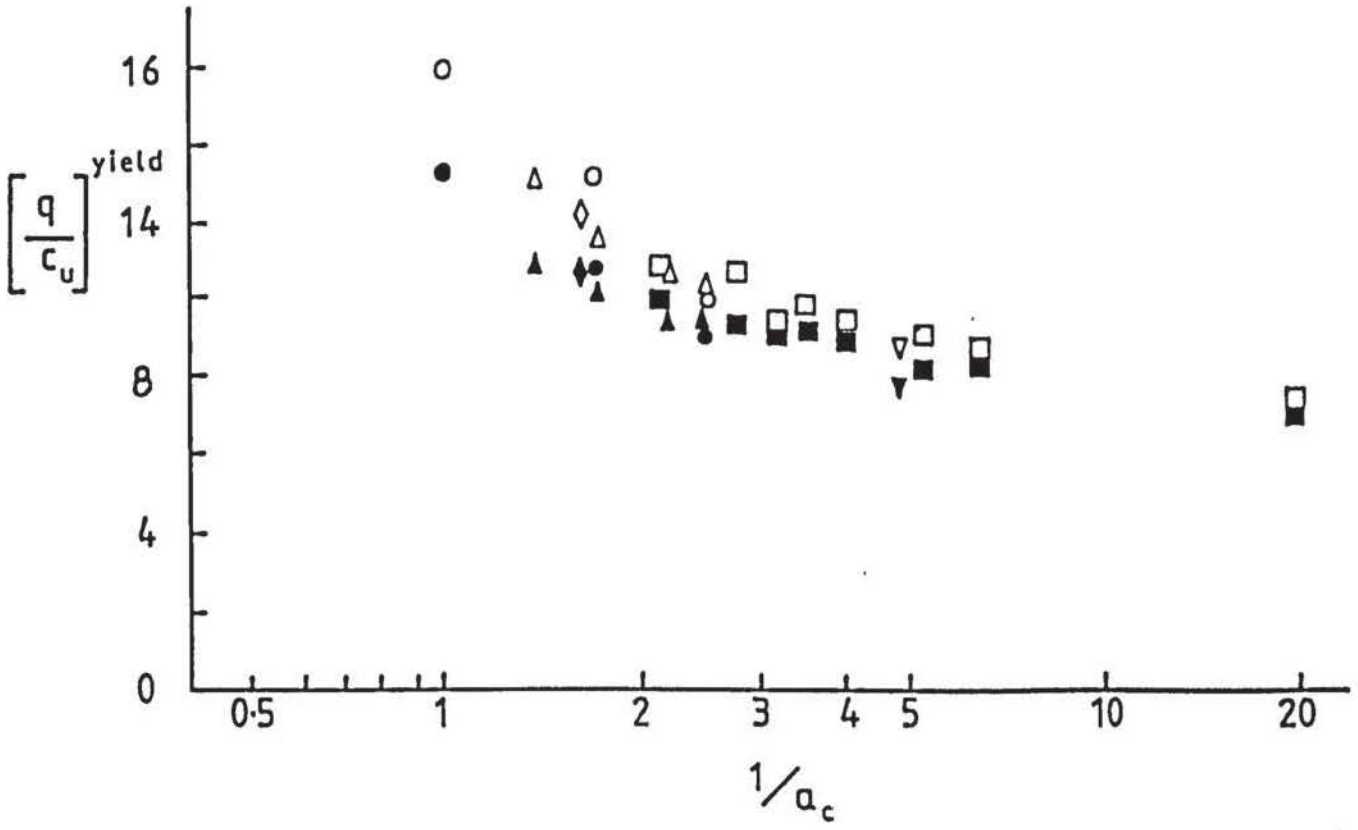

Typical variation of q/c_u at column yield with $1/a_c$ for columns subject to loading by circular, square and rectangular foundations.

FIGURE 12.86

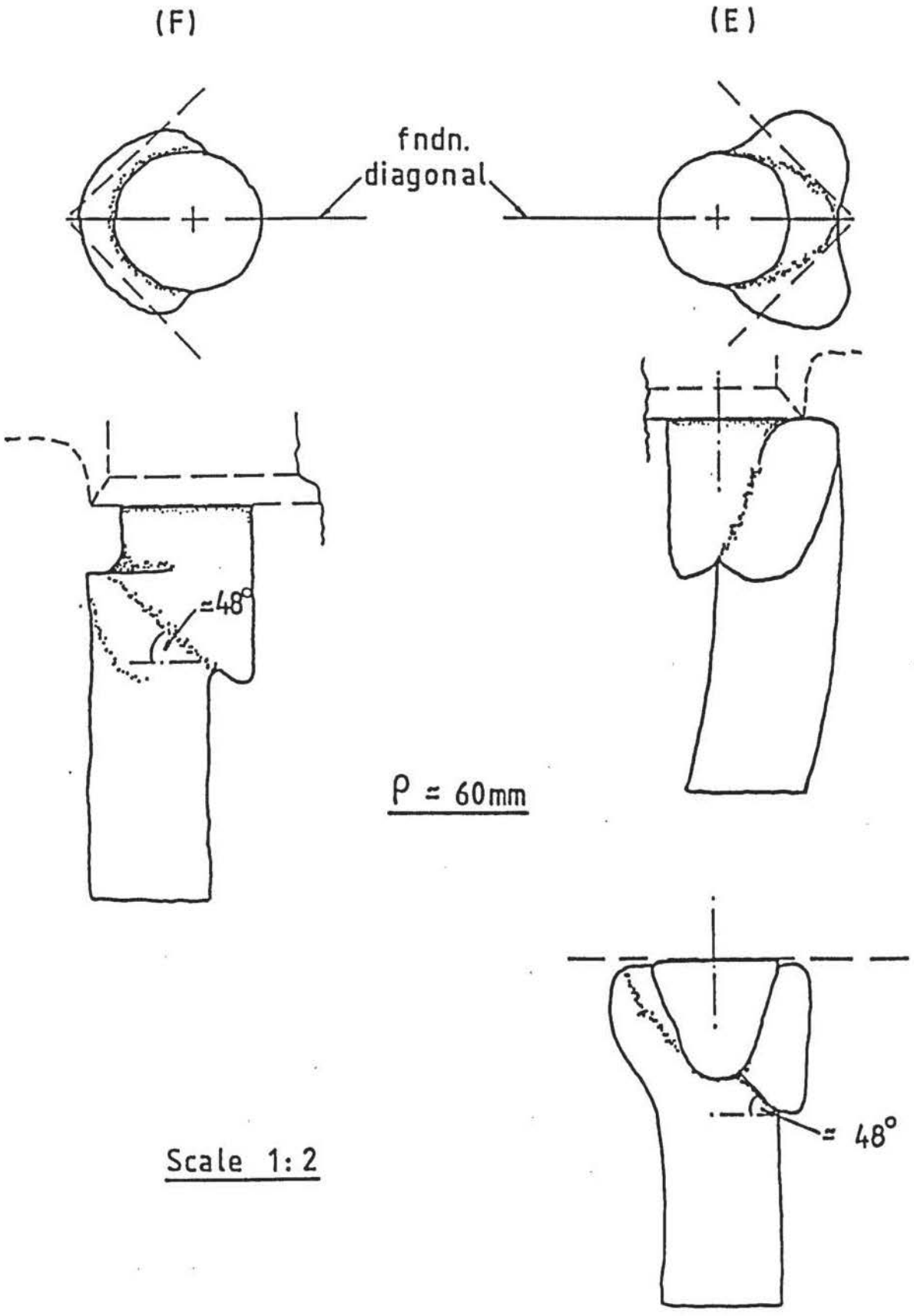

Deformation of F and E columns at the corner of a square foundation (group of four or five columns).

FIGURE 12.87

Figure 12.88 illustrates the effect of the corner columns and foundation on bulging of a central fifth column. Whilst the effect of foundation width is to increase the depth to the bulging zone, the mode of shear by the corner columns compounds the effect. This behaviour occurred in both F and E conditions, although when B = 4.6D no bulging of the central column occurred in the F condition.

It is considered that this mode of column failure is due to plastic deformation of the clay beneath the foundation tending to displace the columns laterally whilst the upper loaded portion of the column is being restrained by confining stresses induced by the foundation and column-foundation shear stresses.

12.7.5 Internal strains and displacements

Internal strains and displacements for the four and five column configurations were not obtained because their size precluded the use of radiography.

Use of a smaller scale was considered but this presented a number of practical difficulties and incompatibility of dimensional similitude.

To maintain radiographic quality, the lead-shot size would have had to remain the same and correspondingly their presence would have had a greater influence on the clay, and particularly, the column behaviour. The major problem, however, was one of achieiving the same levels of accuracy of the results. To obtain comparable strain patterns and coverage, the lead-shot mesh would have had to be reduced in direct proportion to the scale used. Displacements of the lead-shot would also be less. Due to the limitations in measurement accuracy, it was concluded that the potential levels of error that would arise were unacceptable.

It is worthy of note that Hughes and Withers (1974) mentioned using a range of column diameters from 12.5 mm to 38 mm in their laboratory programme. In their presentation of internal displacements a 38 mm diameter column was shown. This was interpreted by the author that the smaller scale results were not as acceptable for presentation as the larger scale used.

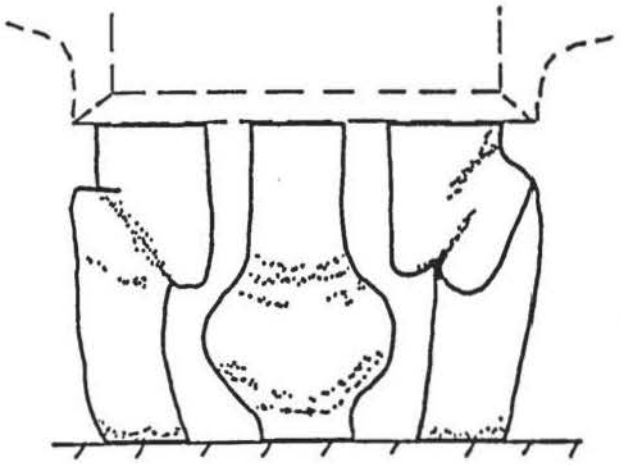

NOT TO SCALE

(E)

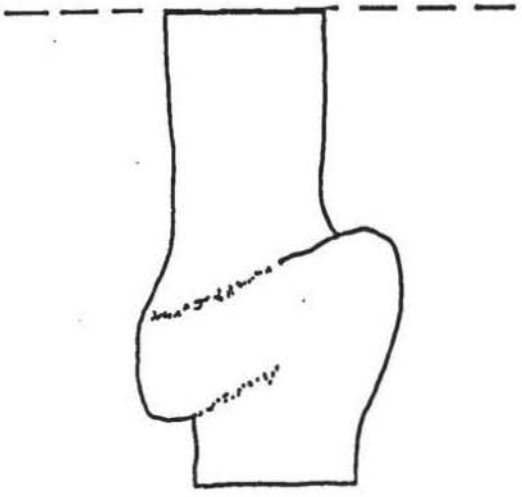

Scale 1:2

(F) & (E)

Deformation of the central column in a group of five columns loaded by a square foundation

FIGURE 12.88

12.8 FOUNDATION-COLUMN-CLAY CONTACT STRESSES

12.8.1 Preliminary

The contact pressure transducers were used in foundations loading one, two, four and five column configurations (Test Nos.: PC1, PC2, PC1E, PC2E, PSQ1, PSQ1E, PR1 to PR3, PR1E to PR3E, PSQ3 to PSQ10, PSQ3E to PSQ10E).

To minimise the recording of ficticious normal stress caused by shear stresses acting across the measuring face, each transducer was positioned so the 'passive' strain gauges were coincident with the anticipated direction of maximum nett shear stress across the foundation face. This corresponded to the diagonal of a square foundation (corner columns) and the longitudinal axis of a rectangular foundation (columns at opposite ends). As a result, fictitious normal stresses were not found to be significant.

At the design stage, initial concern was centred on achieving an even contact between the foundation base and the clay-column surfaces, at zero displacement. During the main laboratory programme, this potential difficulty was not found to arise providing sufficient time and care was taken during the preparation stages.

The PTFE casing was originally conceived to allow ease of debonding and removal from the Kaffir-D, in which the transducers were cast, without risk of damage. It was found, however, that PTFE was unecessary since the conical shape of the casing achieved the same result.

The total average vertical stress measured at the top of the column is an effective stress (σ'_{vc}). Effective stress and total stress notation has been used for the column (σ'_{vc}) and the clay soil (σ_{vs}), respectively.

For each test, a check of load equilibrium was made to ensure the sum of the measured vertical loads taken by the clay ($L_s = \sigma_{vs}.A_s$ - where A_s is the clay area) and the columns ($L_c = \sigma'_{vc}.A_c$ - where A_c is the total column area) was equal to the total vertical applied load ($L = q.A$ - where A is the area of the foundation). Typical load equilibrium characteristics are shown in Figure

12.89. After column yield, an over-registration of load measured by the contact pressure transducers was generally observed. This was attributed largely to the column transducers since it seemed more probable that their sensitivity would be affected by physical changes of the sand at the measuring face.

12.8.2 Stress concentration ratio

A typical relationship between the stress concentration ratio $n = \sigma'_{VC}/\sigma_{VS}$ and ρ/B is shown in Figure 12.90, and was found to be dependent on column end-bearing condition. The general trend of n decreasing with ρ/B agrees with that reported by Aboshi et al (1970) and the results from full-scale field tests (Greenwood, 1972; Wong, 1973). Using data given by Wong, the field test results are shown in Figure 12.90. The replacement ratio (a_c) and column-foundation configuration was similiar to the example used by the author. Because events in the field differ from those in the laboratory, due to similitude and other factors, the ρ/B scales vary by a factor of about one hundred. It is emphasised, therefore, that the comparison is one of a trend and not of specific values.

Figure 12.91 gives the variation of the components of n, σ'_{VC} and σ_{VS} divided by the average bearing pressure q, with ρ/B. Clearly, σ'_{VC} shows a decreasing contribution to q and σ_{VS} an increasing one as vertical displacement proceeds. The relationship between σ'_{VC}/q and σ_{VS}/q is one of vertical load equilibrium, such that:

$$qA = \sigma'_{vc}.A_c + \sigma_{vs}.A_s$$

$$\text{therefore} \qquad q = \sigma'_{vc}.a_c + \sigma_{vs}(1-a_c)$$

$$\text{giving} \qquad 1 = \frac{\sigma'_{vc}}{q}.a_c + \frac{\sigma_{vs}}{q}(1-a_c) \qquad (12.10)$$

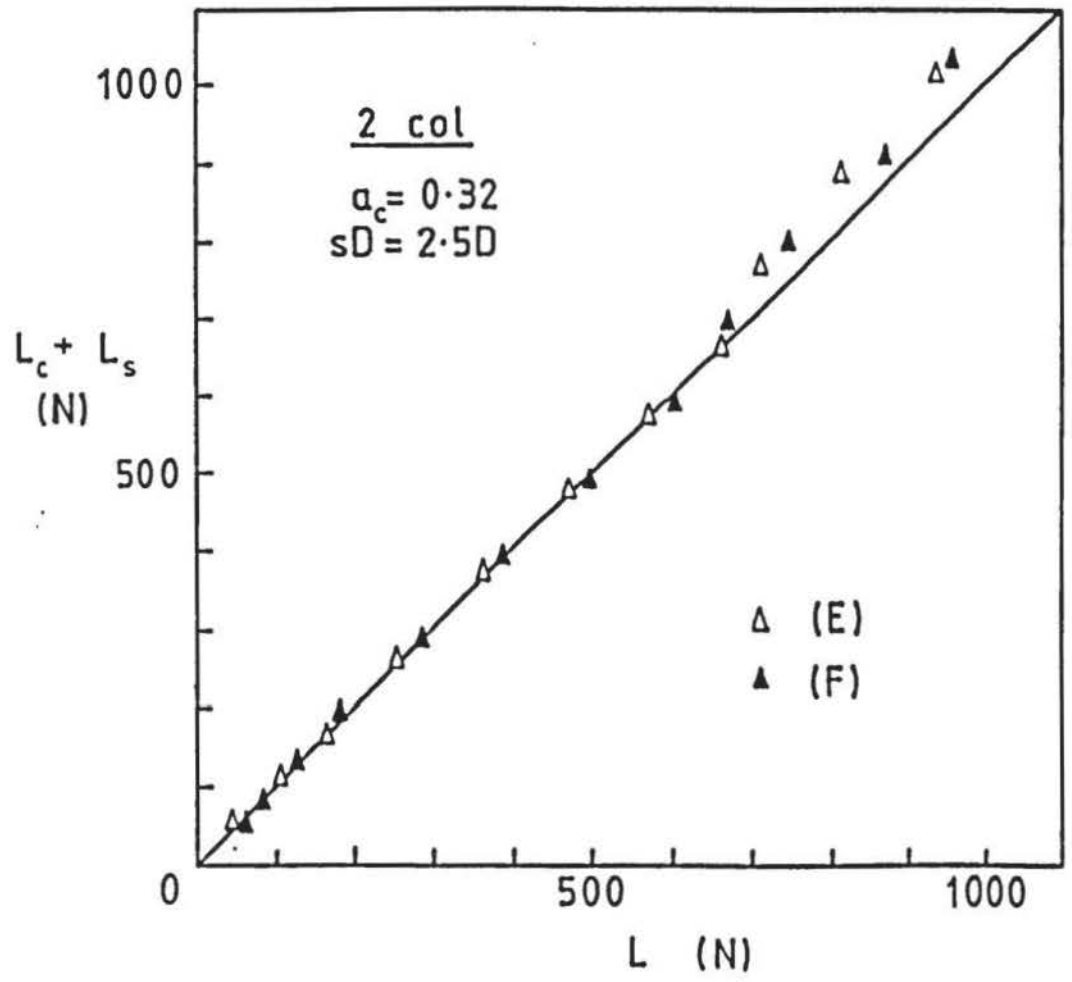

Typical vertical load equilibrium characteristics

FIGURE 12.89

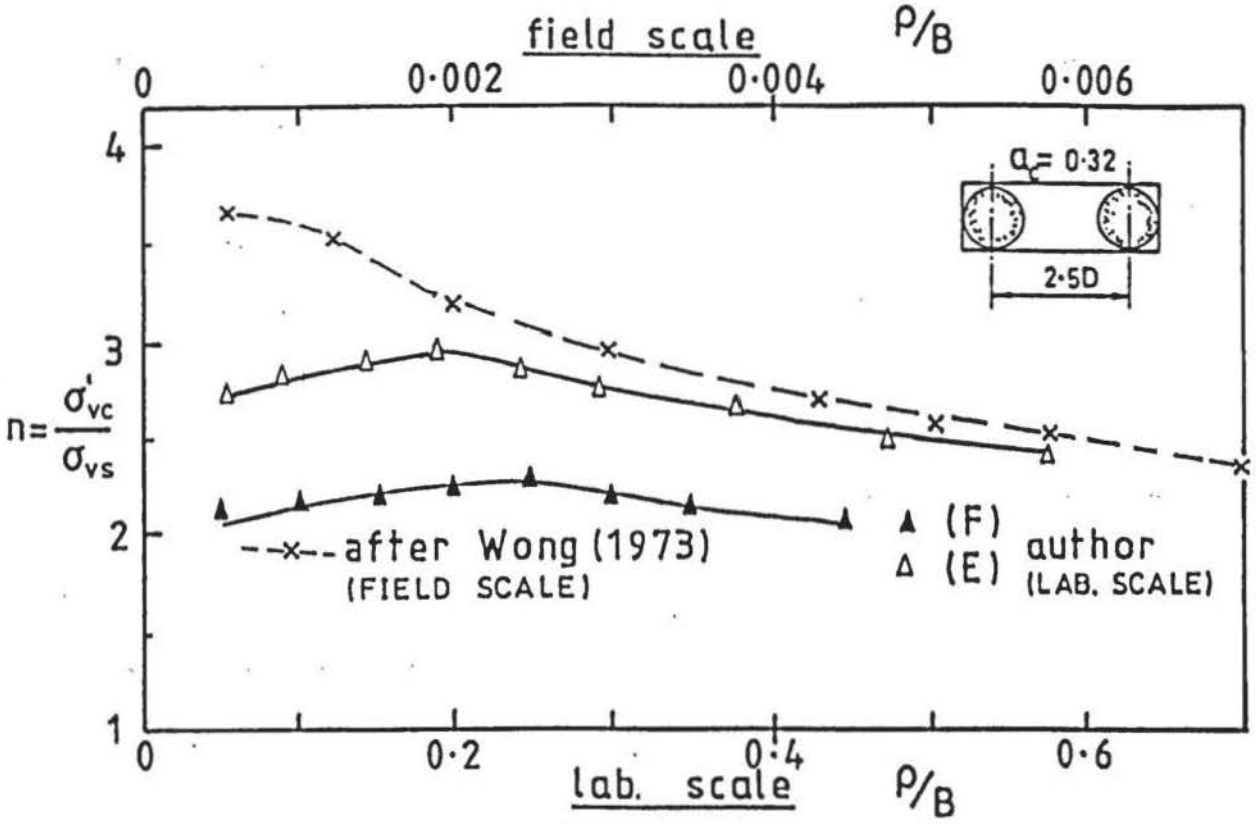

Typical variation of n with ρ/B (a_c = 0.32) including a comparison with Greenwood (1970) and Wong (1973).

FIGURE 12.90

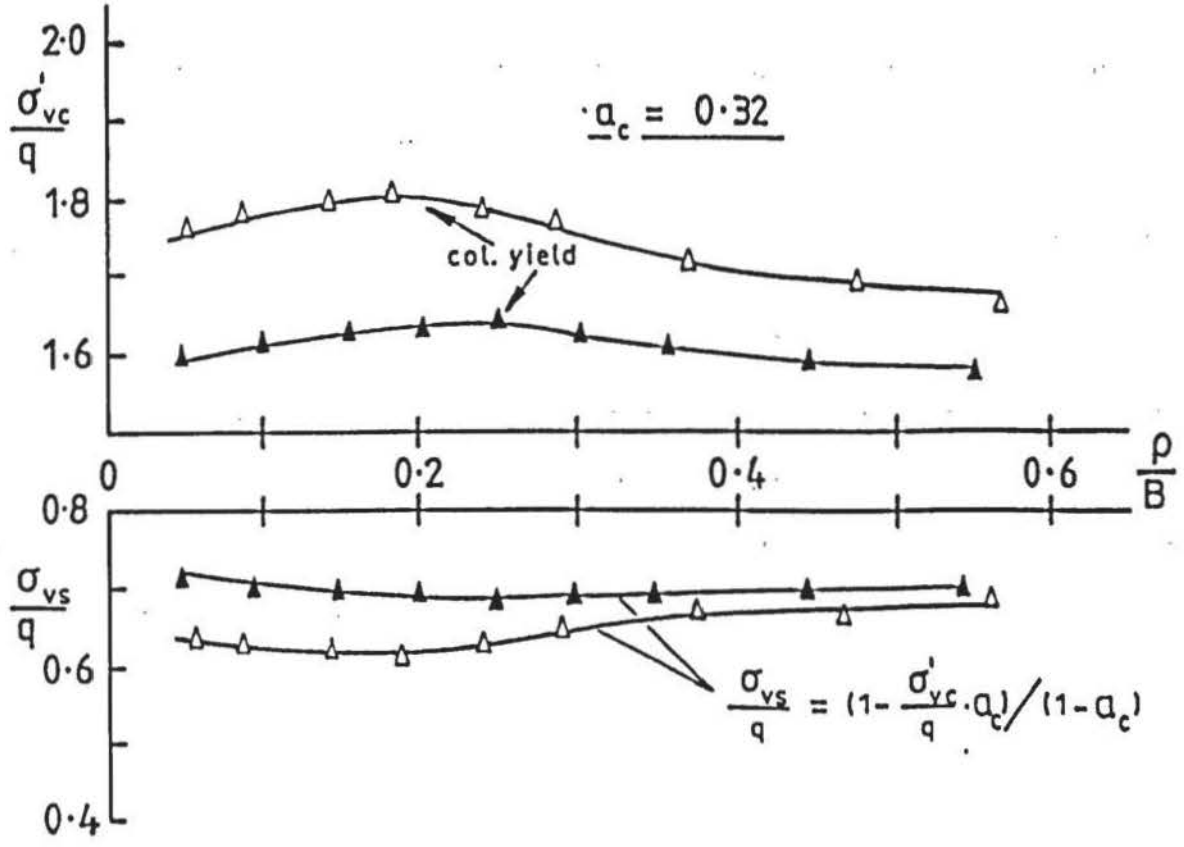

Variation of σ'_{vc}/q and σ_{vs}/q with ρ/B (a_c = 0.32).

FIGURE 12.91

The sand forming the columns develops a higher shear strength than the clay and it is achieved more rapidly. This allows the columns to develop a proportionately higher capacity for bearing stress. This is shown by the variation of σ'_{vc}/c_u and σ_{vs}/c_u with ρ/B in Figure 12.92. The curves are similar to the q - ρ/B characteristics obtained for a single isolated column and for the foundation on the clay only.

Initially, a larger proportion of the applied bearing pressure is taken by the column. As the clay shear strength becomes progressively mobilised it will sustain an increasing share of the total applied load. As a result, σ'_{vc} will correspondingly be reduced as a proportion of q to maintain vertical load equilibrium expressed by Eqn. 2.10.

The magnitude of the components of n were also found to be dependent upon a_c. Figure 12.93 shows the variation of σ'_{vc}/q and σ_{vs}/q with $1/a_c$ at column yield. A largely linear relationship is shown by the former with the complimentary σ_{vs}/q curve derived from the equation:

$$\frac{\sigma_{vs}}{q} = \frac{(1 - \sigma'_{vc}.a_c/q)}{(1 - a_c)} \qquad (12.11)$$

giving good agreement with the recorded measurements. Eqn. 12.11 was transposed from Eqn. 12.10. A family of curves is produced at varying displacement, illustrated by Figure 12.94. As a_c decreases, σ_{vs} tends to q_{CLAY} (previously defined as the foundation bearing pressure on the clay only). The magnitude of σ_{vs} relative to q_{CLAY} varies between 1.2 (a_c = 0.59) and 1.05 (a_c = 0.05) and decreases as vertical compression proceeds as shown in Figure 12.95. This is attributed to changes in the stress distribution beneath the foundation due to the presence of the granular column(s). At the initial stage of loading a column central to a foundation (B > D), it is suggested that the clay contact stress is modified in a similar manner to that shown in Figure 12.96 to produce a higher value of average stress. In the case of rectangular foundations, closely spaced columns

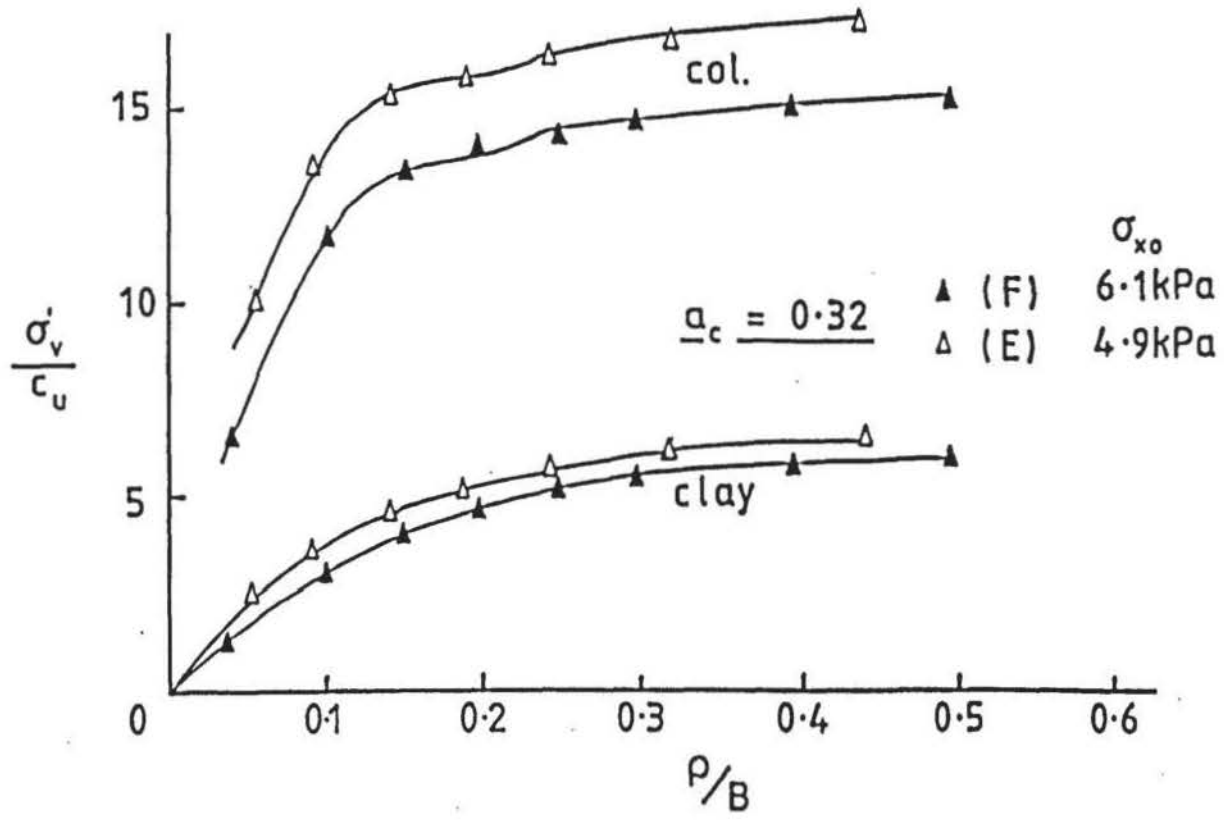

Variation of σ'_{vc}/c_u and σ_{vs}/c_u with ρ/B ($a_c = 0.32$).

FIGURE 12.92

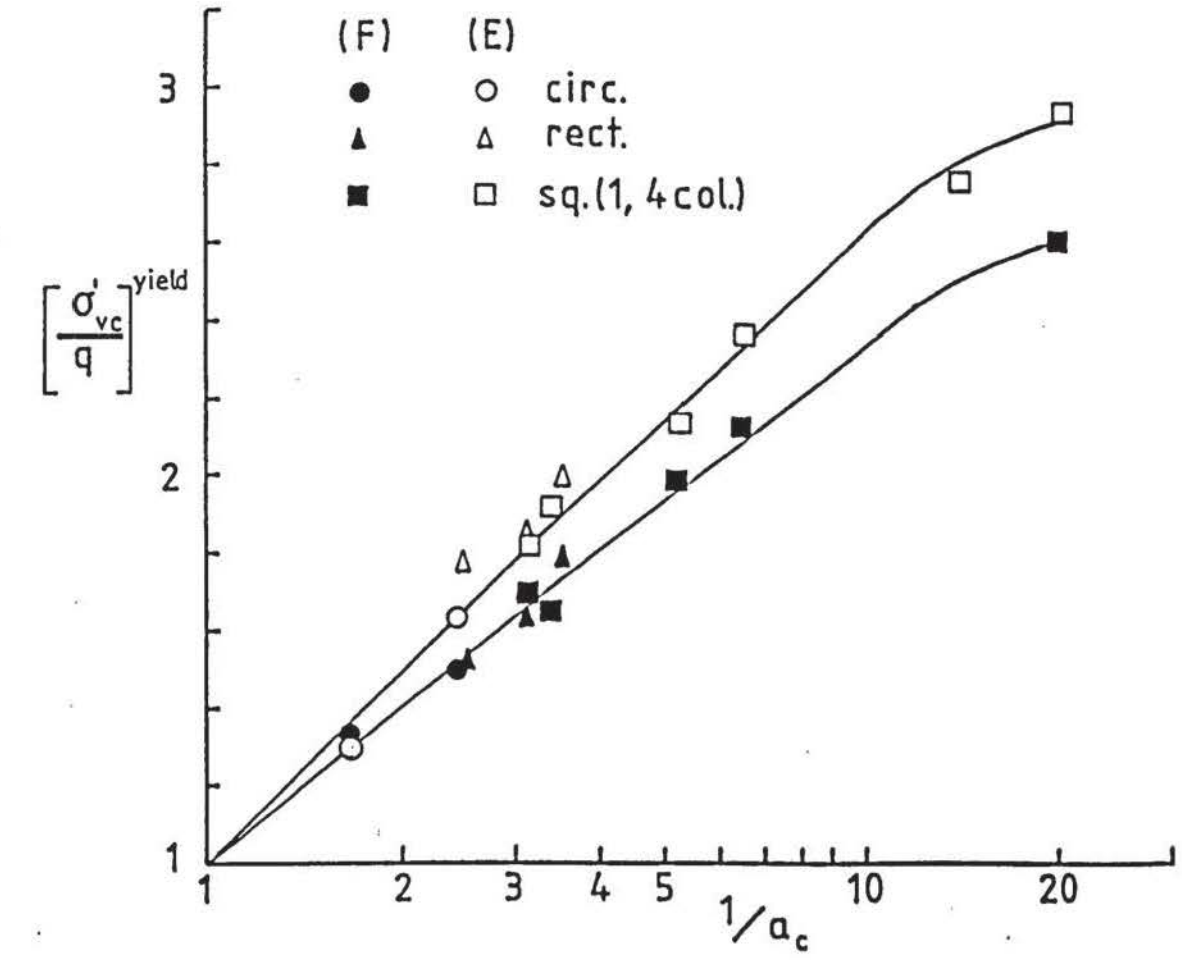

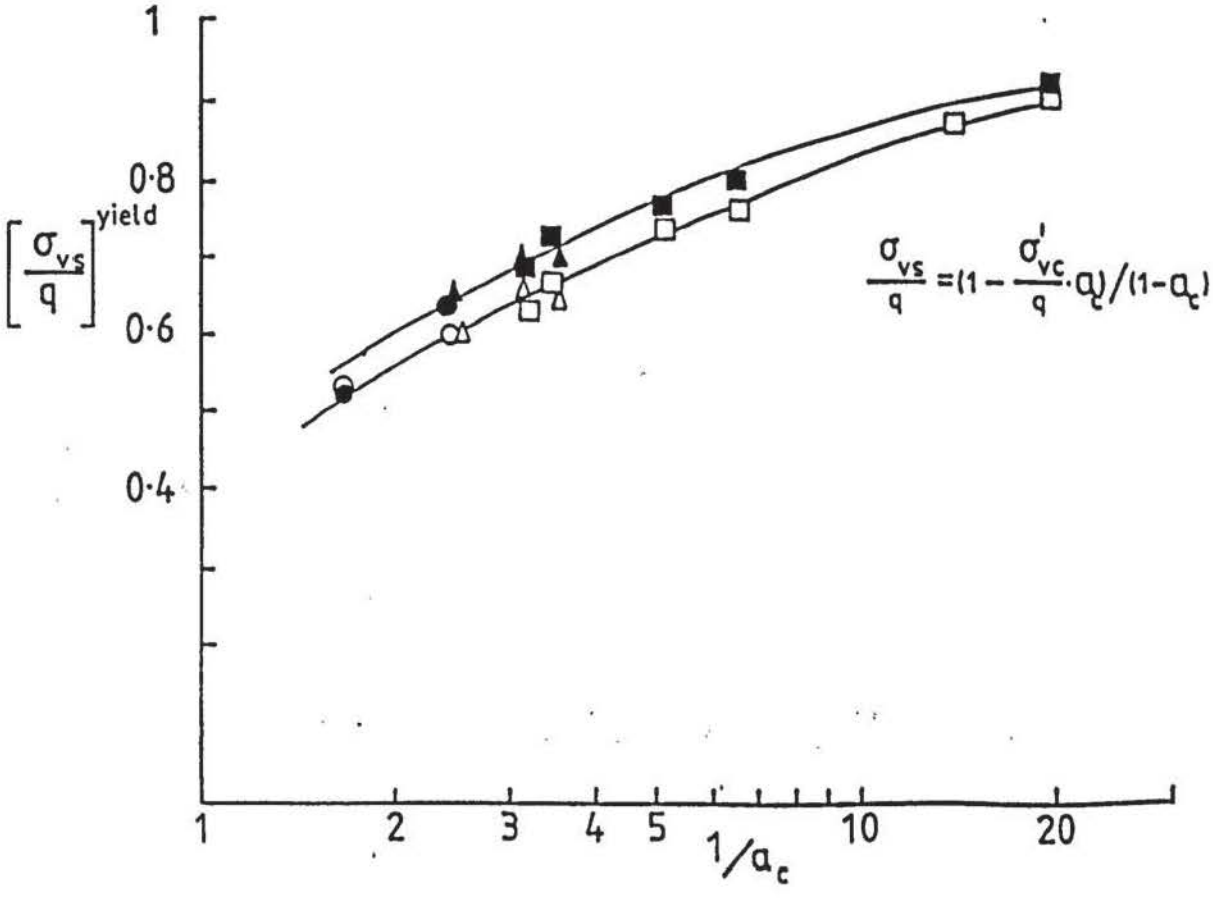

Variation of σ'_{vc}/q and σ_{vs}/q at column yield with $1/a_c$.

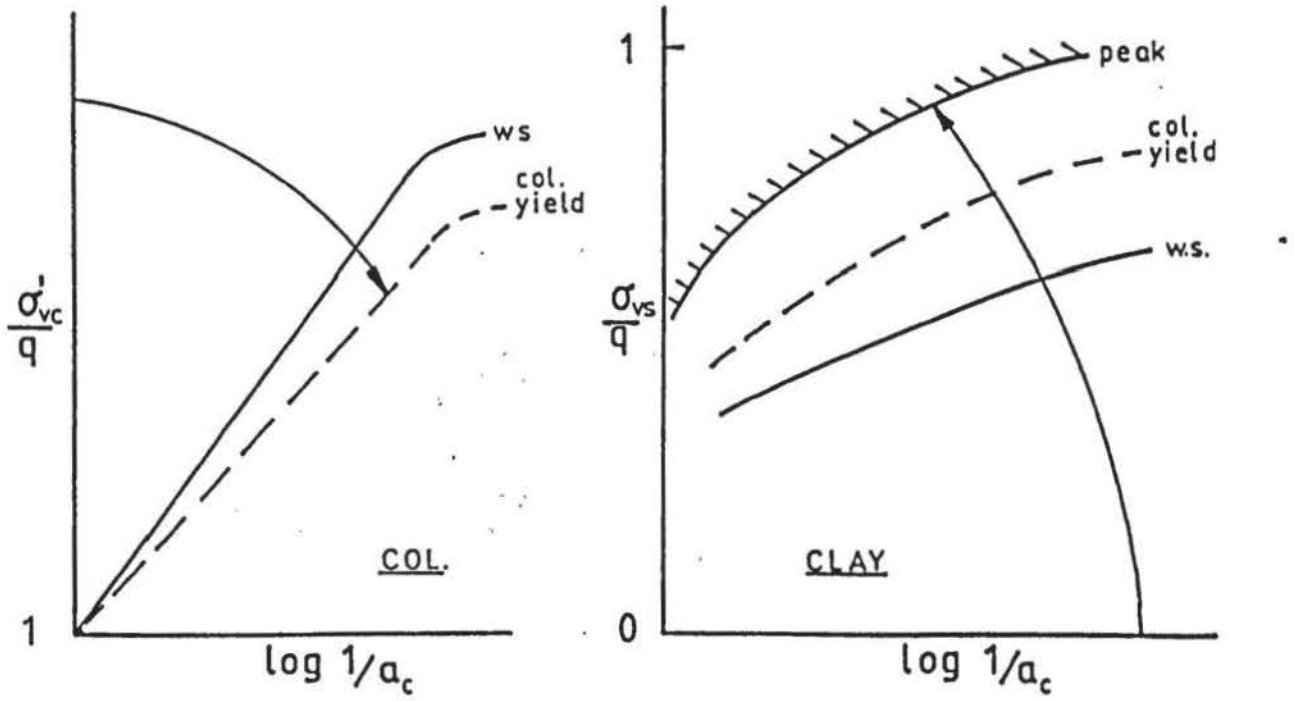

Illustrating family of σ'_{vc}/q and σ_{vs}/q curves with $1/a_c$.

FIGURE 12.94

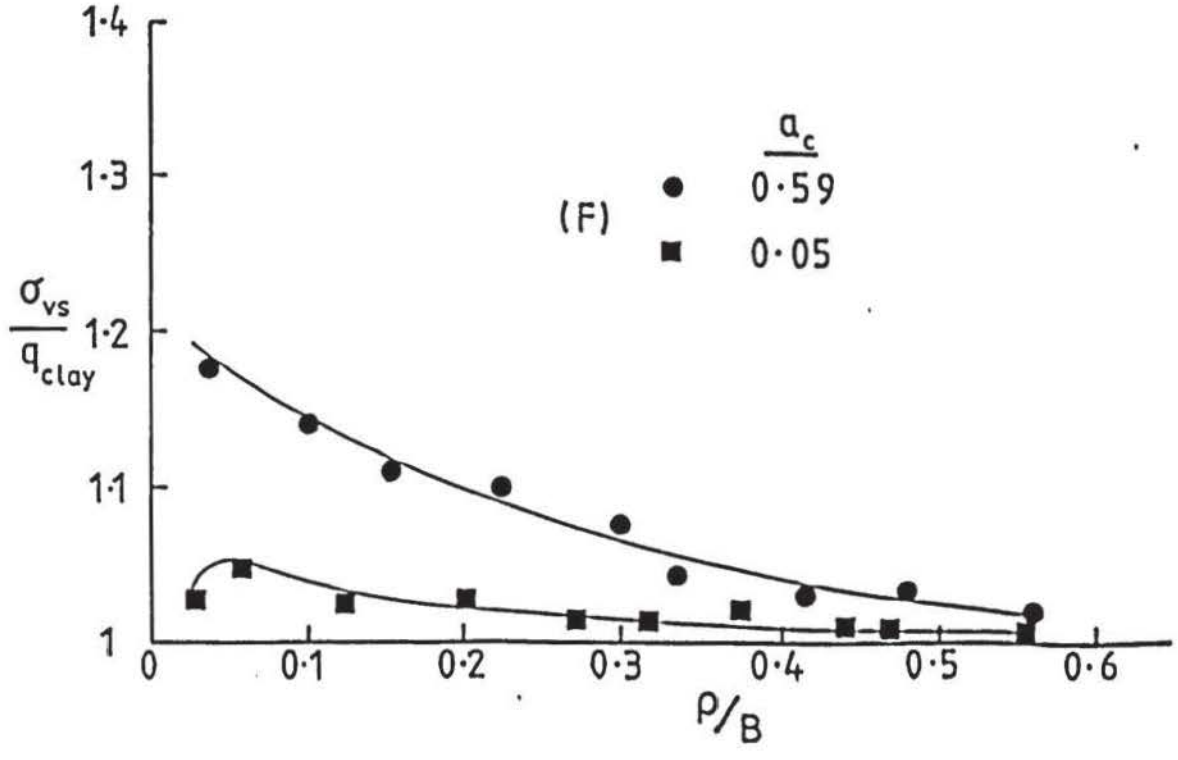

Typical variation of σ_{vs}/q_{CLAY} with ρ/B.

FIGURE 12.95

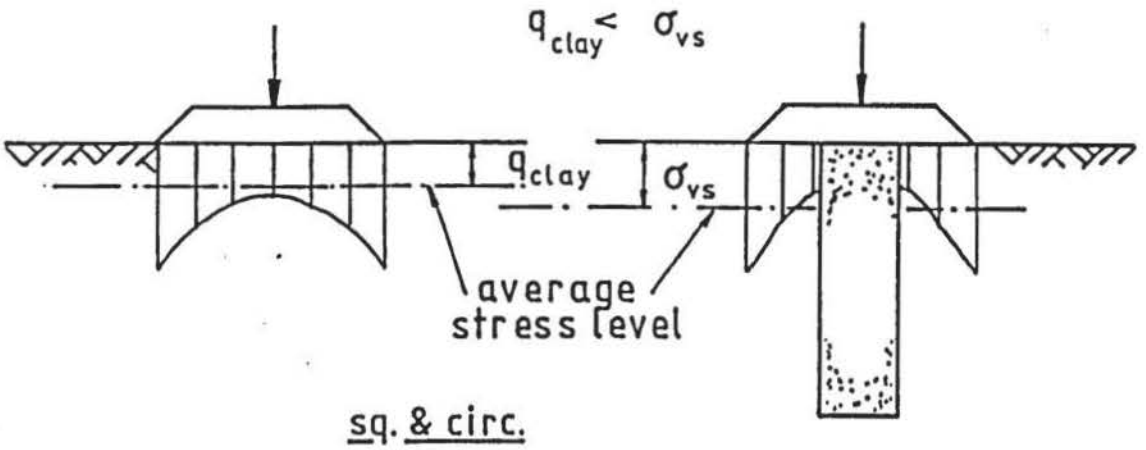

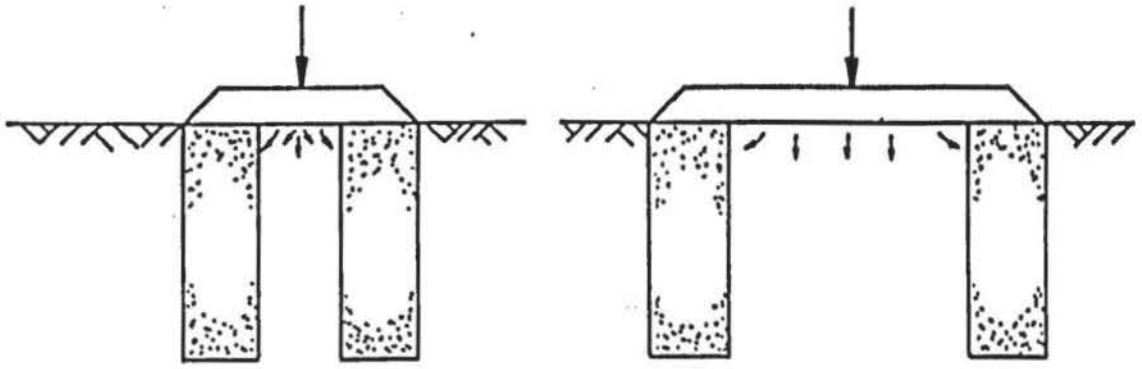

Illustration of changes to average clay stress due to the presence of a granular column.

FIGURE 12.96

will give an added resistance to the movement of clay beneath the foundation with the effect becoming less predominant as the column distance increases (a_c increases). With increasing vertical displacement, and for reasons not presently understood, the column-clay-foundation interaction causes modification to the stress distribution with the nett result of σ_{VS} tending to q_{CLAY}.

12.8.3 Five column configuration

The results obtained when five columns were loaded by square foundations gave an unexpected result. In all cases, σ'_{VC} at the middle column ($\sigma^{m'}_{VC}$) was significantly higher than the average of the four corner columns ($\sigma^{c'}_{VC}$). The variation of $\sigma^{m'}_{VC}$ with $\sigma^{c'}_{VC}$ at increasing vertical displacement is shown in Figure 12.97, from which it is evident that vertical stresses on the central column relative the corner columns increase with decreasing a_c.

The result was unexpected since in the case of conventional piles in a group beneath a pile-cap, loads are less at the centre than at the corners (Banerjee, 1969; Cooke, 1974). Also, when the foundations loaded the clay without the columns, the transducers at the corners recorded σ_{VS} as nominally 10-20% greater than the central transducer.

It was also found, however, that the average vertical stress on all five columns gave good agreement with the σ'_{VC}/q against $1/a_c$ curves obtained from the other foundation-column configurations. The result is shown in Figure 12.98.

In the case of conventional piles, the strength of any pile within the group is the same. For practical purposes they are also dimensionally stable. In the case of columns, it seems probable that the bearing capacity of the corner columns is reduced due to the severity of the asymmetric loading and the resulting shear-plane failure mode (Figure 12.87). The centre column, however, is subjected to higher confining pressures due to the foundation and inward movement of the corner columns. As a result, the strength of the central column is increased.

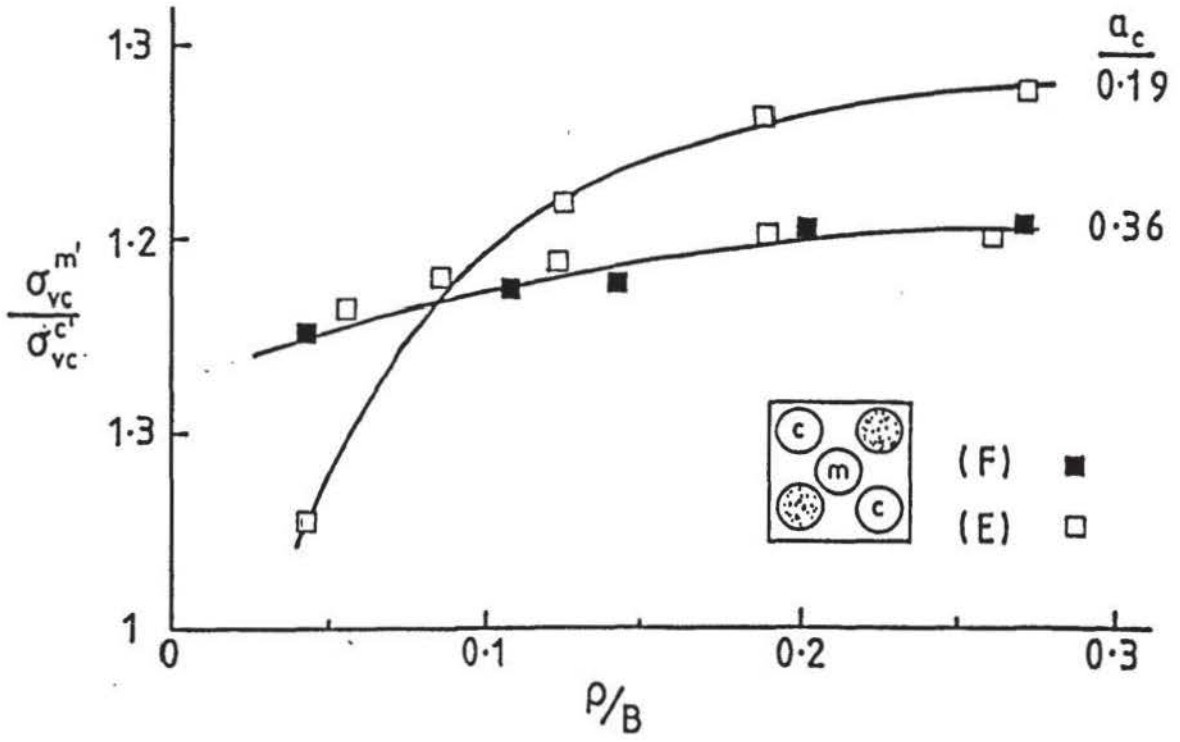

Variation of σ'_{vc} for centre and corner columns

FIGURE 12.97

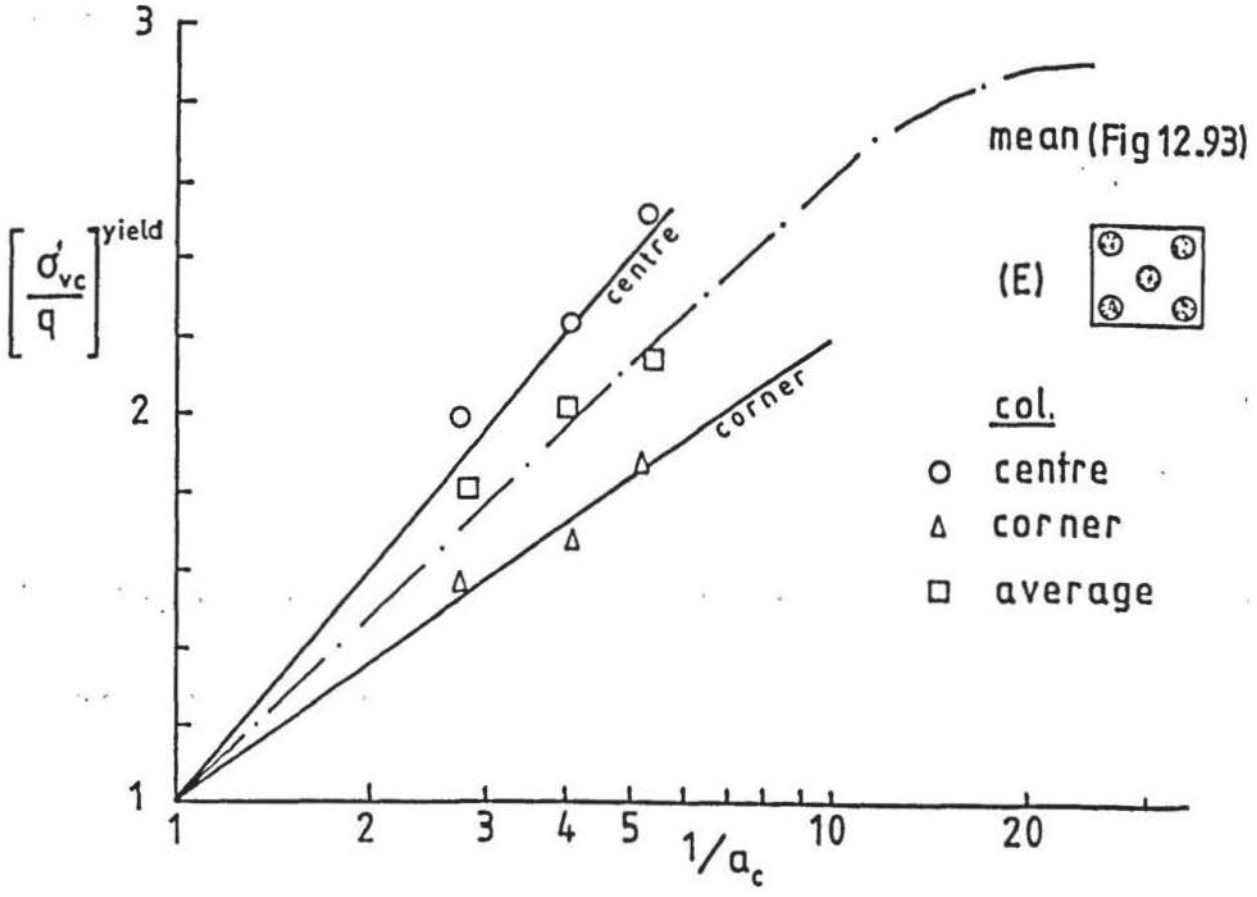

Variation of σ'_v/q with $1/a_c$ for five column configuration.

FIGURE 12.98

CHAPTER 13

CONCLUSION

13.1 INTRODUCTION

This Chapter describes a number of fundamental conclusions drawn from the experimental work and comparisons are made with relevant existing analyses, discussed previously in the first Chapter.

13.2 IMPROVEMENT

The vibroreplacement method is used to achieve an increase in bearing capacity and a reduction in potential settlement of foundations. The improvement coefficients I_q and m are, therefore, of primary importance.

It is to be realised that the stress concentration ratio $n = \sigma'_{vc}/\sigma_{vs}$ is not a direct measure of bearing capacity improvement. By definition :

$$I_q = q/q_{CLAY}$$

Since the foundation size is the same for both, then:

$$I_q = (L_c + L_s)/L_{CLAY} \qquad (13.1)$$

By comparison:

$$n = \frac{L_c}{A_c} \cdot \frac{A_s}{L_s}$$
$$= \frac{L_c}{L_s} \frac{(1 - a_c)}{a_c} \qquad (13.2)$$

It is possible, however, to relate I_q approximately to n by assuming an average relationship between σ_{vs} and q_{clay} up to column yield, of $\sigma_{vs} \approx 1.08\ q_{clay}$. Using Eqn. 12.10 it is easily shown that:

$$I_q \approx 1.08\left[n\, a_c + (1 - a_c)\right] \qquad (13.3)$$

Values of n were calculated using Eqn. 1.28 (after Priebe, 1976) with $K_{ac} = 0.22$ ($\phi' = 40^o$) and $\nu = 0.49$. The latter was chosen since it makes n a minimum. Using Eqn. 13.3, I_q was calculated for $a_c = 1$ to 0.05 and is shown plotted in Figure 13.1 with the experimental results of maximum I_q. The latter is shown for the F and E cases. The calculated values seriously over estimate I_q up to about $1/a_c = 4$ and thereafter show some correlation with the F case.

Values of n obtained from Eqn. 1.27, dervied by Bauman and Bauer (1979), lay in the range 10 to 20 using $K_c = 0.36 - 0.22$ and $E_c / E_s = 10 - 25$. Consequently, further application of this expression was not pursued.

It can also be shown from Eqn. 12.10, that:

$$I_q = \frac{q}{q_{clay}} = \frac{\sigma'_{vc}}{q_{clay}} \cdot a_c + \frac{\sigma_{vs}}{q_{clay}} (1 - a_c) \qquad (13.4)$$

when $a_c = 1$, then σ'_{vc}/q_{clay} is equal to I_q for a single isolated column. Puting $\sigma_{vs}/q_{clay} = 1.08$ and substituting into Eqn. 13.4:

$$I_q = \left[I_q\right]^{a_c = 1} a_c + 1.08 (1 - a_c) \qquad (13.5)$$

Using the experimental values of maximum $[I_q]^{a_c=1}$ from the F and E cases, I_q was determined for $a_c = 1$ to 0.05 and is also shown in Figure 13.1. An excellent correlation was obtained with the observed values. The process was repeated for I_q at working stress and is shown in Figure 13.2.

The inference is that the improvement in bearing capacity of small groups of columns, up to column yield, may be estimated from the bearing pressure - settlement characteristics of a foundation (where $a_c=1$) loading a single column and clay without the column.

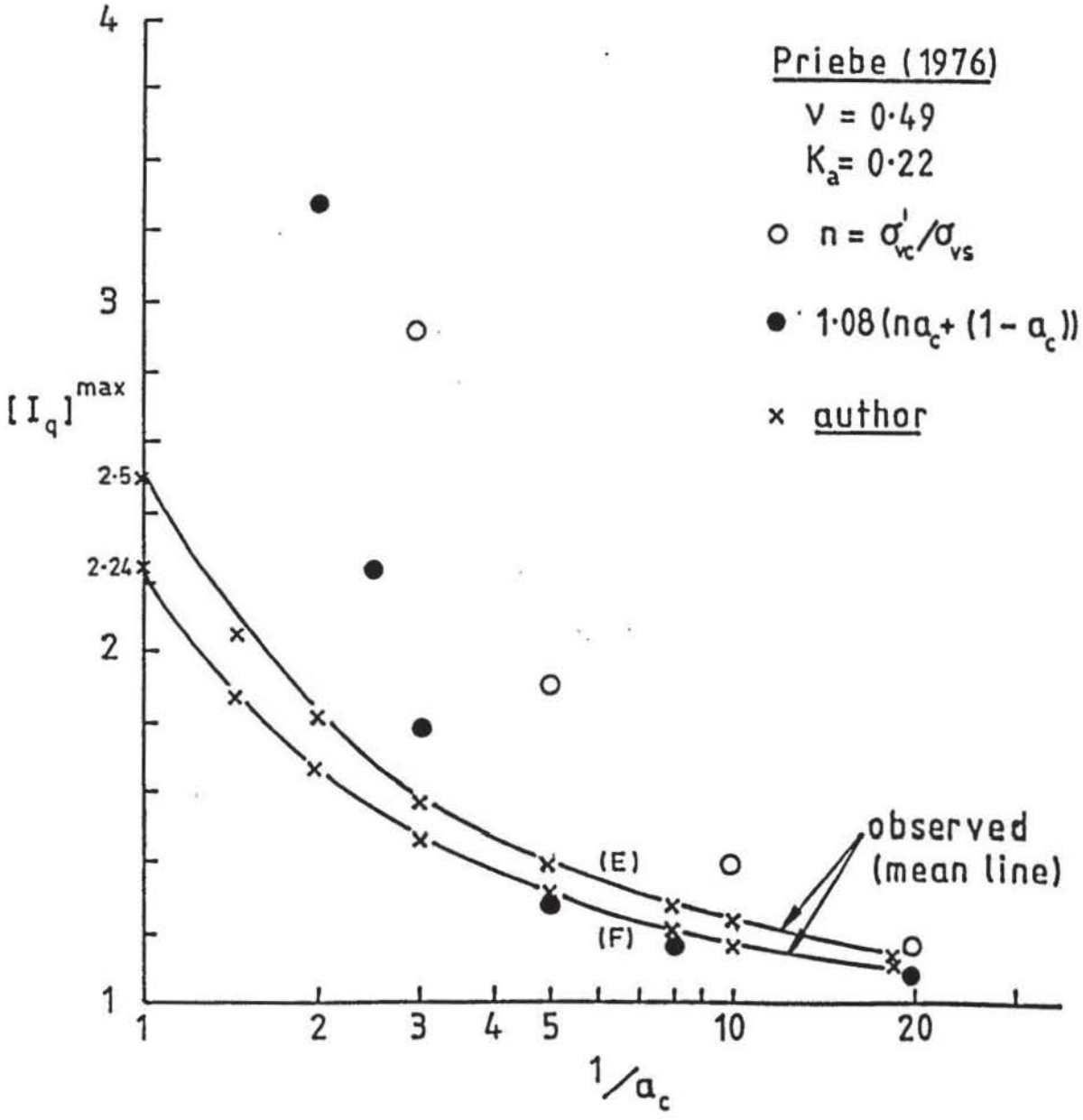

$$[I_q]^{max} = [I_q]^{yield}$$

Comparisons of calculated and observed maximum I_q for F and E conditions.

FIGURE 13.1

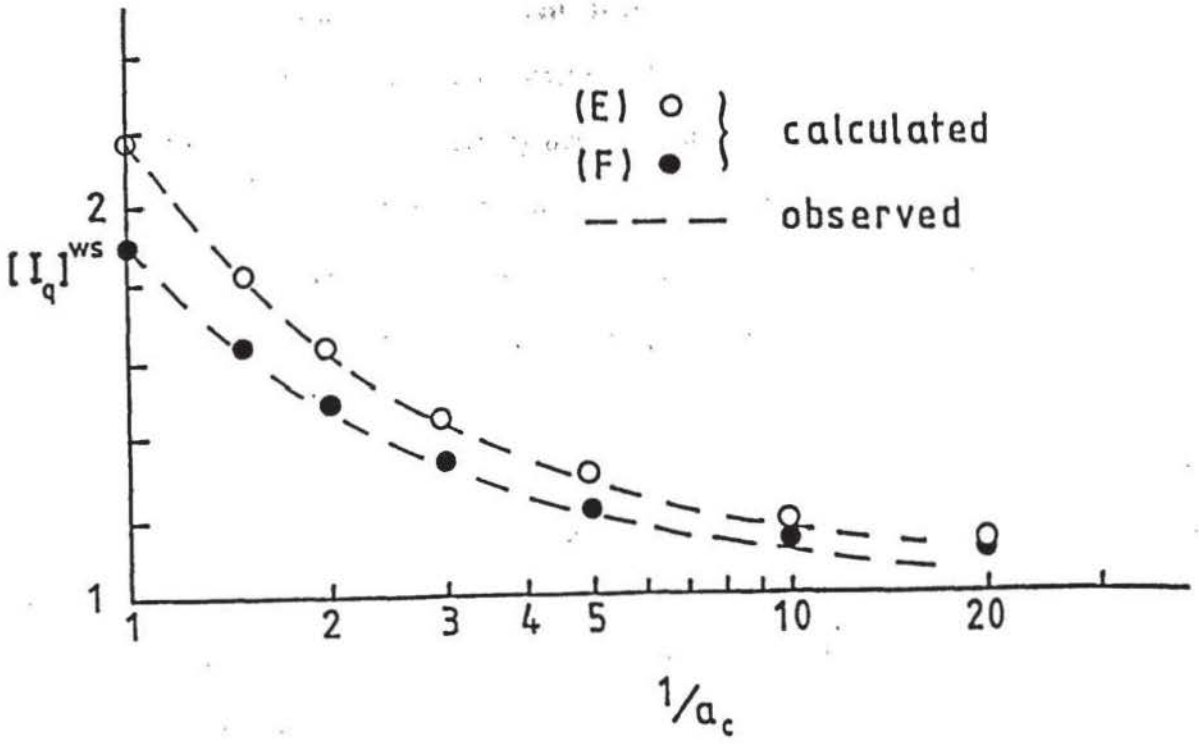

Comparisons of calculated and observed I_q at working stress levels for F and E conditions.

FIGURE 13.2

13.3 COLUMN BEARING CAPACITY

The results obtained from methods proposed by a number of authors of calculating the ultimate bearing capacity of a single granular column are summarised in Figure 13.3. The failure modes on which the analyses are based are also given. In the experimental work, F columns showed an ultimate $q/c_u \approx 20 - 21.5$ in a rigid-pile mode, whilst the E columns showed no ultima condition. Apart from the Greenwood (1970) and Poteur (1973) approaches, there is good numerical agreement between the remaining methods and with the observed ultimate bearing stress.

When columns were subject to foundation loading in the experimental work, the following trends of column deformation were observed:

1. For symmetrical loading, column bulging was predominant with the depth to the bulging zone increasing with foundation size.
2. Columns loaded by a rectangular foundation exhibited asymmetric bulging conmensurate with a 'trench' failure mechanism.
3. Columns beneath the corners of a square foundation developed a shear plane which was inclined at approximately 46^o-48^o to the horizontal.

It was evident that the mechanism of column deformation was dependent upon the boundary conditions with (1) having compatability with the Hughes and Withers (1974) analysis, (2) with that of Brauns (1978) and (3) with the theoretical model proposed by Madhav and Vitkar. Although these mechanisms were not observed as an ultimate bearing capacity failure, they did, however, result in column yield.

13.4 COLUMN YIELD

The ability of a granular material to support load increases with the level of confining pressure. In the case of a column, the limit of the confinement is a function of the clay strength (c_u) and the existing horizontal stress (σ_{xo}). Vibroreplacement is applied to cohesive soils with low shear strength and are usually normally consolidated. As a result, column yield may become the limiting criterion. In large scale field trials Vautrain (1978) reported column yield occurring

Method	Failure Mode	Calculated ult. q/c_u
Greenwood (1970)	Passive earth pressure	11.3
Poteur (1973)	Triaxial	11.2
Hughes and Withers (1974)	Radial expansion (Bulging)	20.5
Brauns (1978)	Shear Plane	22.2
Madhav and Vitkar (1978)	Trench	15.4
-	Rigid pile	24.7

CONSTANTS

$\phi' = 40^o$ $\sigma_{xo} = 5.1$ kPa

$c_u = 11.35$ kPa $\gamma_b = 16.2$ kPa

Comparison of methods for determining ultimate bearing capacity of a single column.

FIGURE 13.3

without an ultimate failure, but the large settlements produced were unacceptable for structural foundations.

If yield of the column occurs at peak ϕ' when σ'_{vc}/σ_h is a maximum, where σ_h is the limiting lateral confining stress, then the maximum load a column will take will be governed by the magnitude of σ_h.

From the results obtained by Labrue (1981) in investigating the stress-strain behaviour of glyben using a small scale pressuremeter, it can be deduced that:

$$\sigma_h \approx \sigma_{xo} + 3\,c_u \qquad (13.6)$$

It may be noted that this result is mid-way between that suggested by Poteur (1973) in Eqn. 1.14, and by Hughes and Withers (1974) in Eqn. 1.3.

The relationship given by Eqn. 13.6 does not, however, take into account any adverse effects due to shear strain in the clay immediately surrounding the column. Substituting $\sigma_{xo} = 5.1$ kPa (average) and $c_u = 11.35$ kPa gives the limiting lateral stress $\sigma_h = 39.2$ kPa. The lateral distortion (u/r_o) at which σ_h was achieved by Labrue was typically 0.08 to 0.12. This gives excellent agreement with u/r_o obtained radiographically for a single column (Figure 12.6) at $\rho/B = 0.2$, which corresponded to the position of column yield. This supports the calculated value of σ_h.

Because of shear stress at the column perimeter $\sigma'_{vz} < \sigma'_{vc}$, where σ'_{vz} is the effective vertical stress at depth z in the column. Peripheral shear stress has been shown by Hughes et al (1975) to significantly reduce vertical stress within the column. This effect is also evident from the radiographic results which have shown vertical strain within the column to rapidly decay with depth. As a_c decreases, average σ'_{vc} on each column within a group increases for a given ρ/B. The average load ($\overline{L_c}$) taken at the top of each column in a group will also vary.

By inspection, it was found that the diameter at the top of the columns, up to $\rho/B = 0.2$ - 0.3, was nominally the same as the initial diameter. This was attributed to confining stresses at the foundation face. This enabled, however, $\bar{L}_c$ to be determined. The variation of L_c with $1/a_c$ is shown in Figure 13.4. When $a_c = 0.5$, $\bar{L}_c$ is about 50% greater than when $a_c = 1$. Column loads are relatively constant for the rectangular foundations.

If yield of the column material is assumed to occur within the bulging zone, σ'_{vz} can be estimated for single columns loaded by the smaller foundations. The rotation of the principal planes, shown by the radiographic results, indicate that maximum shear strength within the clay, adjacent to the column, is fully mobilised down to the bulging zone. Therefore, the reduction in vertical load due to shear (S) is:

$$S \approx c_u \pi D_a z \qquad (13.7)$$

where D_a is the average column diameter over depth z to the bulging zone.

The estimated values of σ'_{vz} tabulated in Figure 13.5 show good agreement with an average value of $\sigma'_{vz} = 120$ kPa.

If σ'_{vz} and σ_h are principal stresses then :

$$K_{pc} = \frac{(1 + \sin \phi')}{(1 - \sin \phi')} = \frac{120}{40} = 3 \qquad (13.8)$$

where K_{pc} is the coefficient of passive pressure. From the triaxial test results shown in Figure 2.4 $[\sigma_1'/\sigma_3'] = 4.6$ ($\phi' = 40°$), when $\sigma_3' = 40$ kPa, and gives poor agreement with the result obtained. Wong (1975) has suggested that for granular columns the earth pressure coefficient lies between the active and passive values.

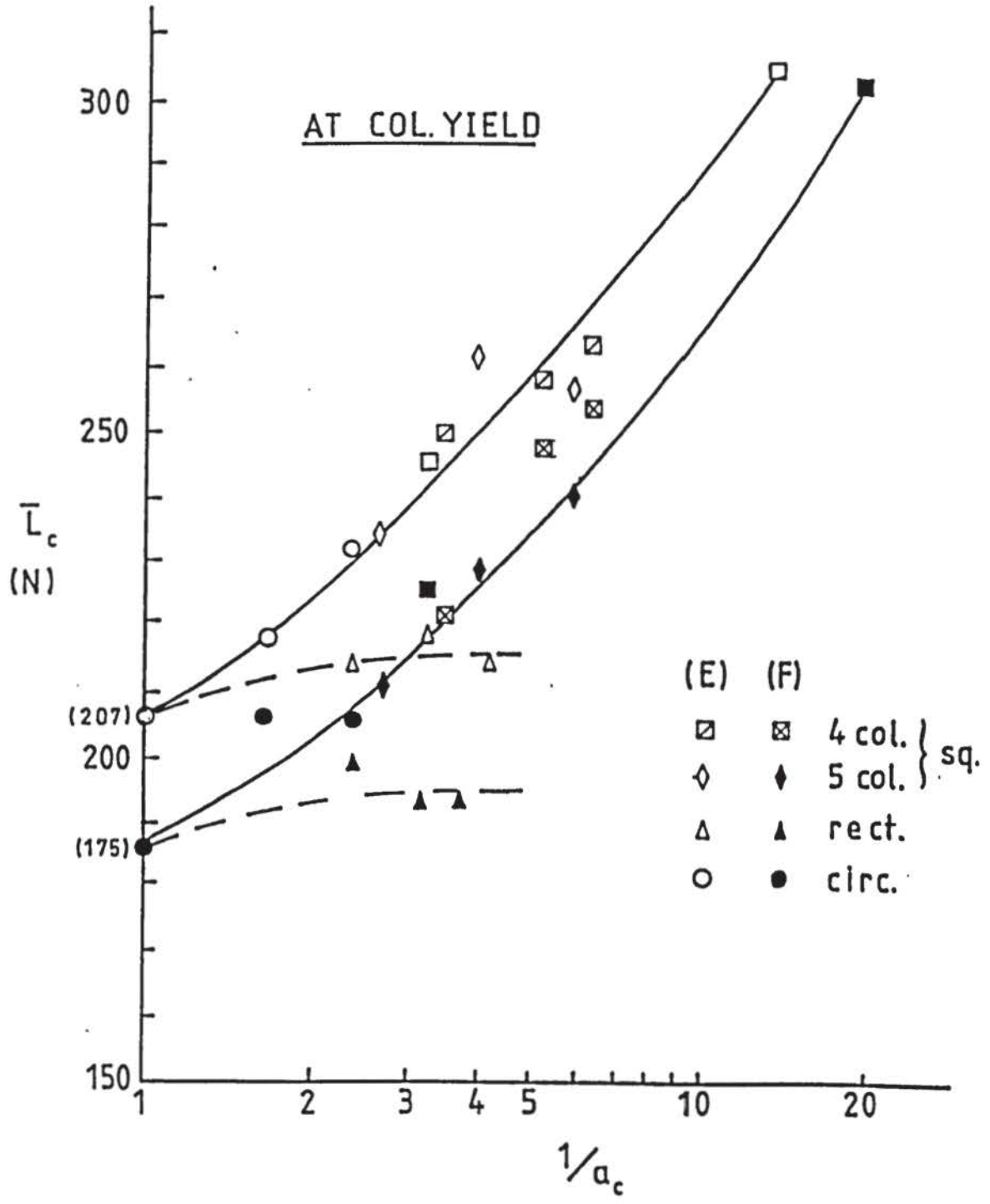

Variation of load (L_c) at the top of a column with $1/a_c$.

FIGURE 13.4

	B = D $1/a_c = 1$		B = 1.58 D $1/a_c = 2.48$	
	F	E	F	E
L_c (N)	175	207	210	220
u/r_o	0.08	1.12	1.12	1.15
D_b (col. diam. at bulging zone) (mm)	41.1	42.1	42.7	43.9
S (N)	-40	-41	-56	-56
L_c at bulging zone (N)	125	166	154	164
σ'_{vz} (kPa)	112	130	121	125

Initial diameter of column (D) = 38.1 mm.

$D_a \approx (D + D_b)/2$

$c_u = 11.35$ kPa.

Estimation of vertical stress (σ'_{vz}) at the bulging zone for single columns.

FIGURE 13.5

Considering the position of the yield plateau indicated on the re-drawn curve of Hughes and Withers (1974) results in Figure 12.11, using their analysis, gives $K_{pc} = 1.4$. Because of the small vertical displacement at which this value occurs ($\rho/B \approx 0.02$) it is unlikely that the result is valid.

For rectangular foundations, peripheral shear forces are generally similar when $a_c > 0.59$ and a relatively constant column load for increasing a_c may be expected. Determination of σ_{vz} in the case of the other foundation-column configurations is considered too complex to be undertaken at this stage. This is because of asymmetric shear stress distributions down the shaft of the column (in some cases) and the unknown magnitudes and influence of lateral stresses induced by the foundation (particularly at small values of a_c) on the shear strength of the sand. Where the depth to the zone of column yield increases (in the case of central columns beneath the larger foundations) higher loads will be needed at the top of the column to overcome the increased peripheral shear load, if σ_1/σ_3 were to be constant.

It has been shown that the effect of column yield on the q/c_u - ρ/B curve becomes less apparent as a_c decreases. Soil beneath a foundation is affected by shear stresses which grow progressively from the position of loading until the formation of potential planes of failure. The bearing capacity of a soil mass may be considered as having two phases (Lambe and Whitman, 1969):

1. Local shear failure, which occurs when peak shear strength is reached locally in a zone immediately beneath the surface load but not beyond this zone.

2. General shear failure, which is the ultimate stage of bearing capacity failure when distinct failure wedges are formed and peak shear strength is mobilised along all slip planes.

So when a_c is large, yield of the column will be exhibited as a general shear failure of the sand. As a_c decreases, column yield will tend to a local shear failure as the contribution of the columns to the overall bearing capacity becomes less.

13.5 SETTLEMENT

Calculated results of the settlement ratio m, using the method proposed by Billam (1981) given by Eqn. 1.31, are compared with the observed values in Figure 13.6. The ratio E_c/E_s was determined as 8.3 and 10.0 for the F and E cases respectively, on the following basis. For vertical load equilibrium :

$$qA = \sigma_{vc}.A_c + \sigma_{vs}.A$$

for equal vertical strain in the column and clay :

$$\sigma'_{vc} = \sigma_{vs}\frac{E_c}{E_s} \quad ; \quad q = \sigma_{vs}\frac{E}{E_s}$$

where E_c is Young's Modulus for the column.

E_s is Young's Modulus for the clay.

E is the nett Young's Modulus for the composite clay and columns beneath a foundation applying a bearing pressure q.

by substitution :

$$\frac{E}{E_s} = \frac{E_c}{E_s}.a_c + (1 - a_c) \qquad (13.9)$$

Settlement of the composite is :

$$\rho = q/E$$

Settlement of the clay without columns:

$$\rho_o = q_{CLAY}/E_s$$

giving

$$m = \frac{\rho}{\rho_o} = E/E_s$$

when $a_c = 1$.

$$\frac{E_c}{E_s} = \frac{1}{m} = R_m \qquad (13.10)$$

From Figure 13.6, m = 0.12 which gives R_m= 8.3.

The result is the same for Billam's Eqn. 1.31 since the principle used in the derivation was the same.

This method of establishing R_m was considered more applicable than using secant moduli from the triaxial test results since E_c of the column is also some function of E_s. This is because displacement at the top of the column includes a component of vertical strains and engineering shear strains from the clay around the column perimeter, due to the foundation loading.

The correlation between the calculated and observed results, however, is poor. Plotting the observed results on a log-log scale, shown in Figure 13.7, and comparing it with curves for a range of R_m = 5 to 25, it is evident that R_m in the observed case is not constant. Using Billam's equation actual R_m was determined using the observed values of m for a range of a_c and is shown in Figure 13.8. This result is largely explained by Figure 13.9 which shows the variation of the ratio of the secant moduli of the sand and clay with vertical strain, obtained from the triaxial test results. It is apparent that there is a signficant decrease of E_{SAND}/E_{CLAY} (which corresponds to E_c/E_s) as vertical strain increases. In the case of the columns, for a given ρ/B, the sand forming the column experiences increasing magnitudes of strain as a_c decreases.

On the basis of the results shown in Figure 13.8, a modification to Billam's equation is proposed in the form of

$$m = 1/\left[R_m.a_c + (1 - a_c)\right]$$

where

$$\log R_m = \log\left[\frac{1}{m}\right]^{a_c = 1} - 0.5 \log (1/a_c) \qquad (13.11)$$

Calculated values of m, using Eqn. 13.11, are compared to the observed results in Figure 13.10.

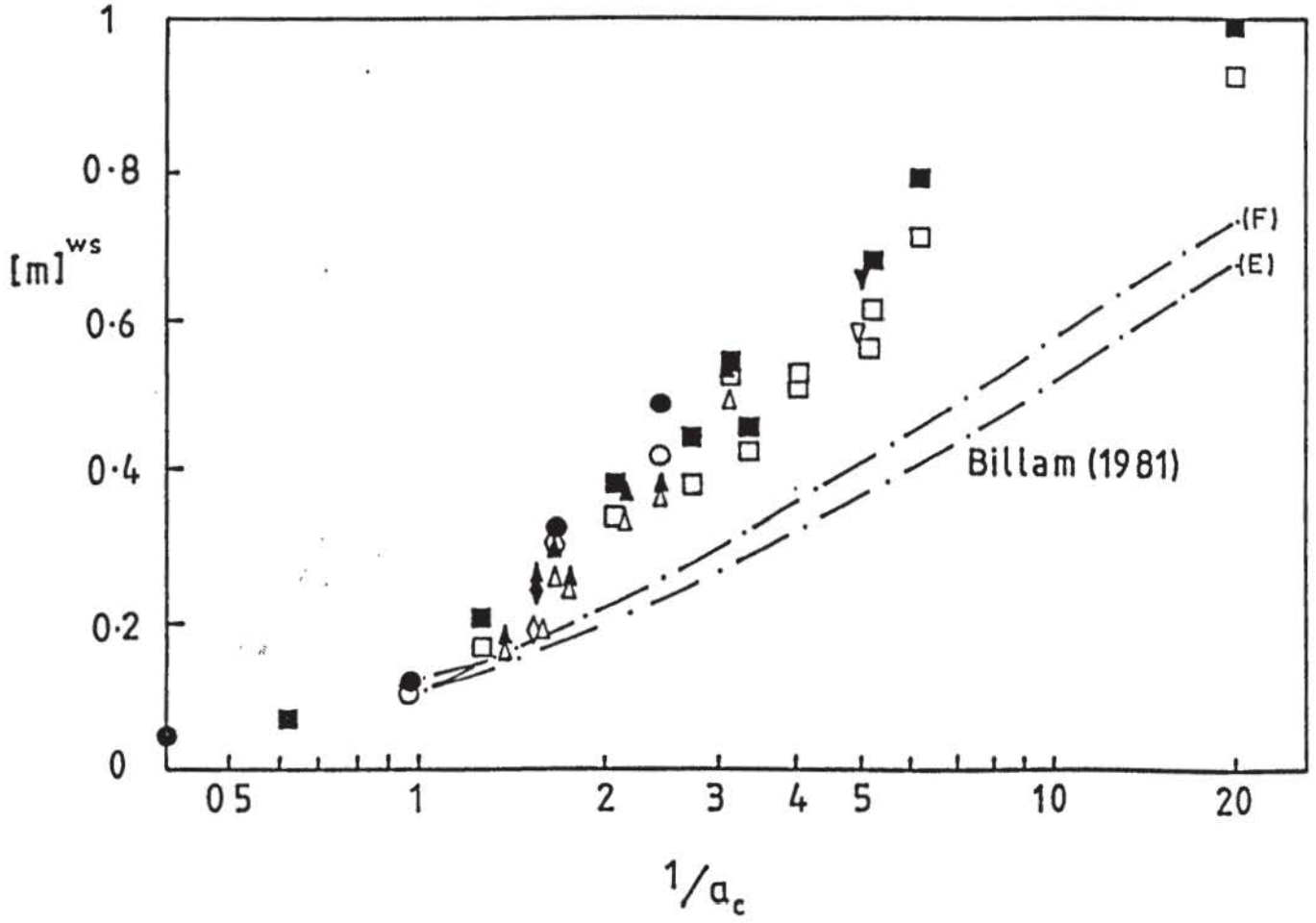

Calculated and observed values of settlement ratio m.

FIGURE 13.6

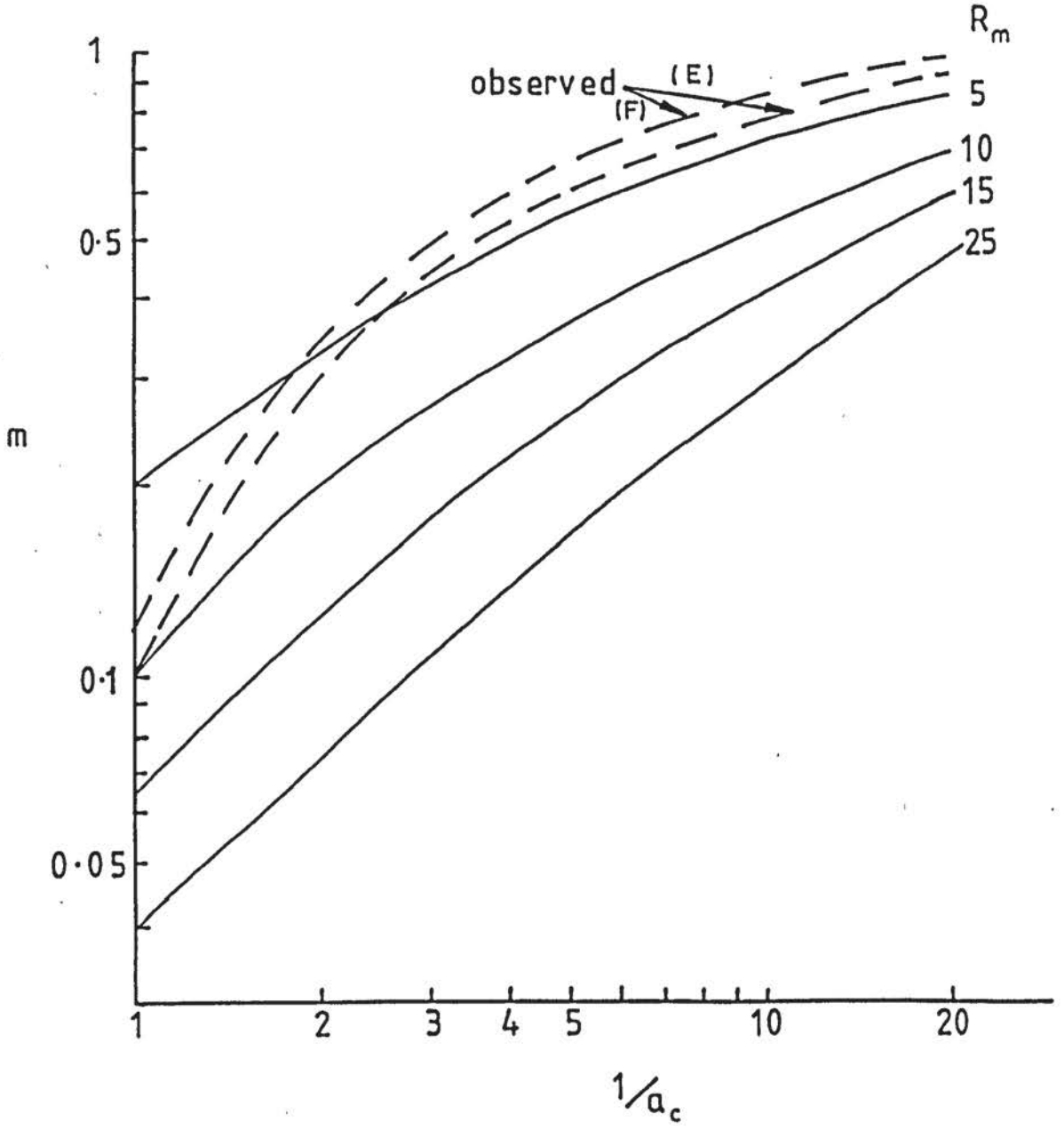

Calculated and observed values of m (log-log scale).

FIGURE 13.7

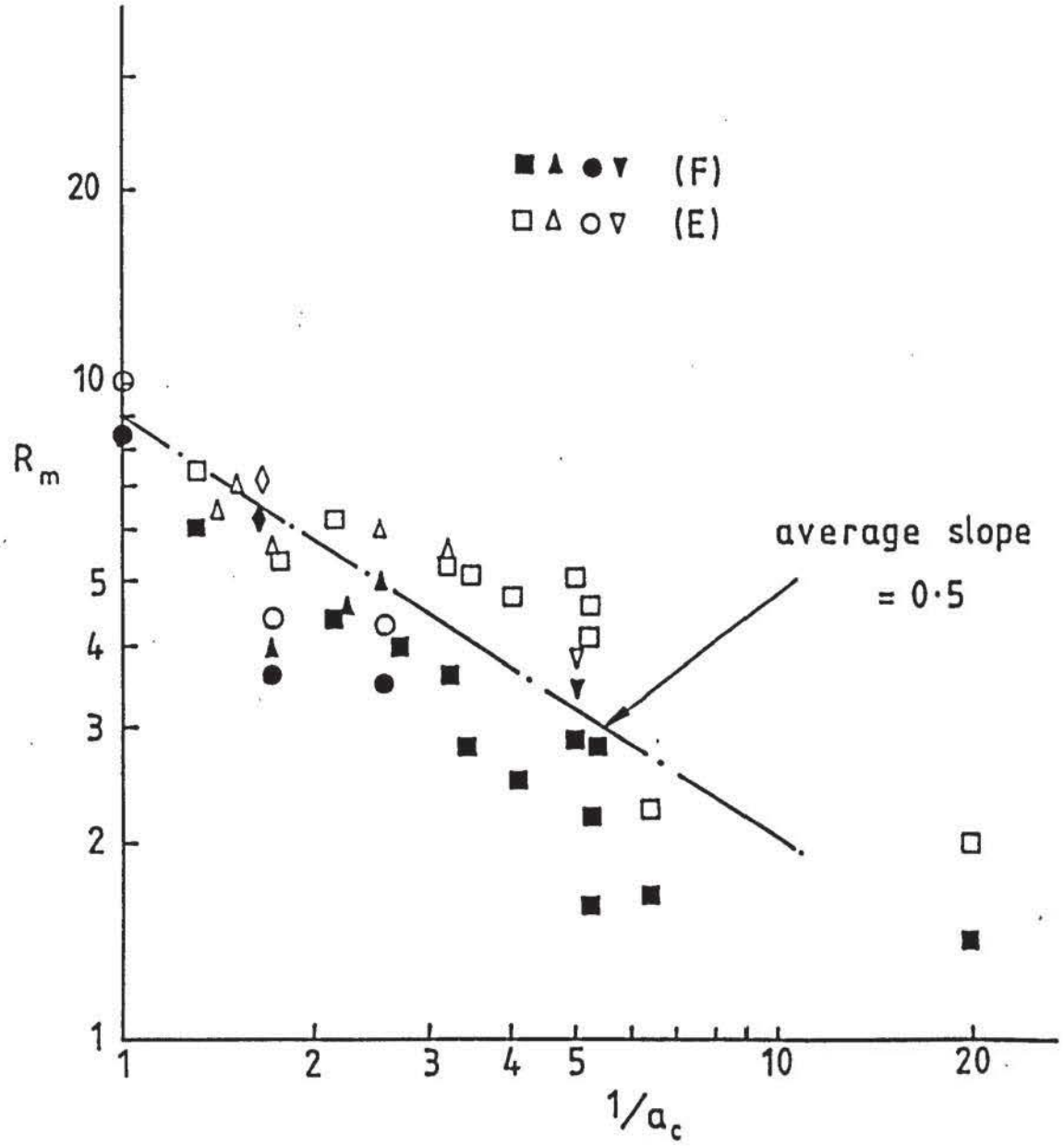

$$\log R_m = -0{\cdot}5 \log(1/a_c) + \log[R_m]^{a_c=1}$$

Variation of R_m with a_c.

FIGURE 13.8

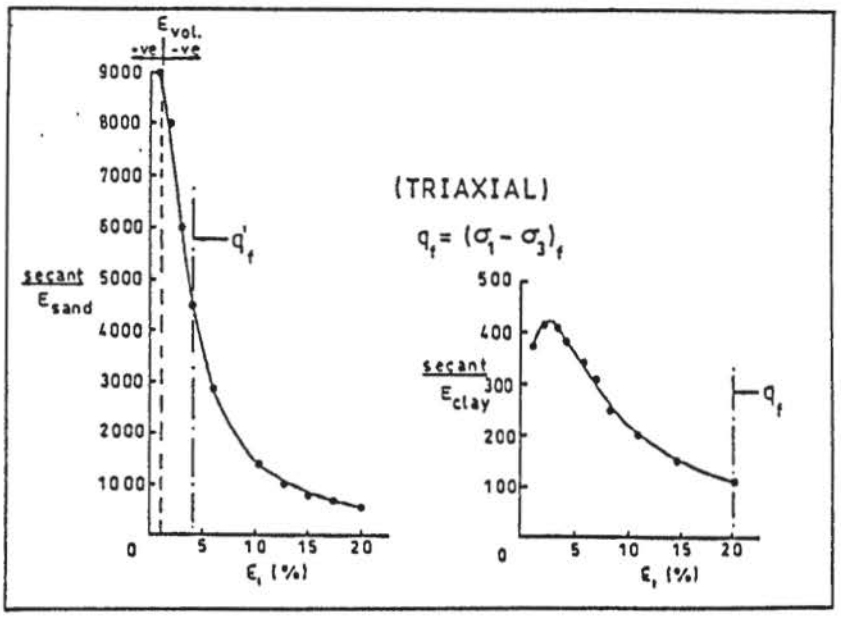

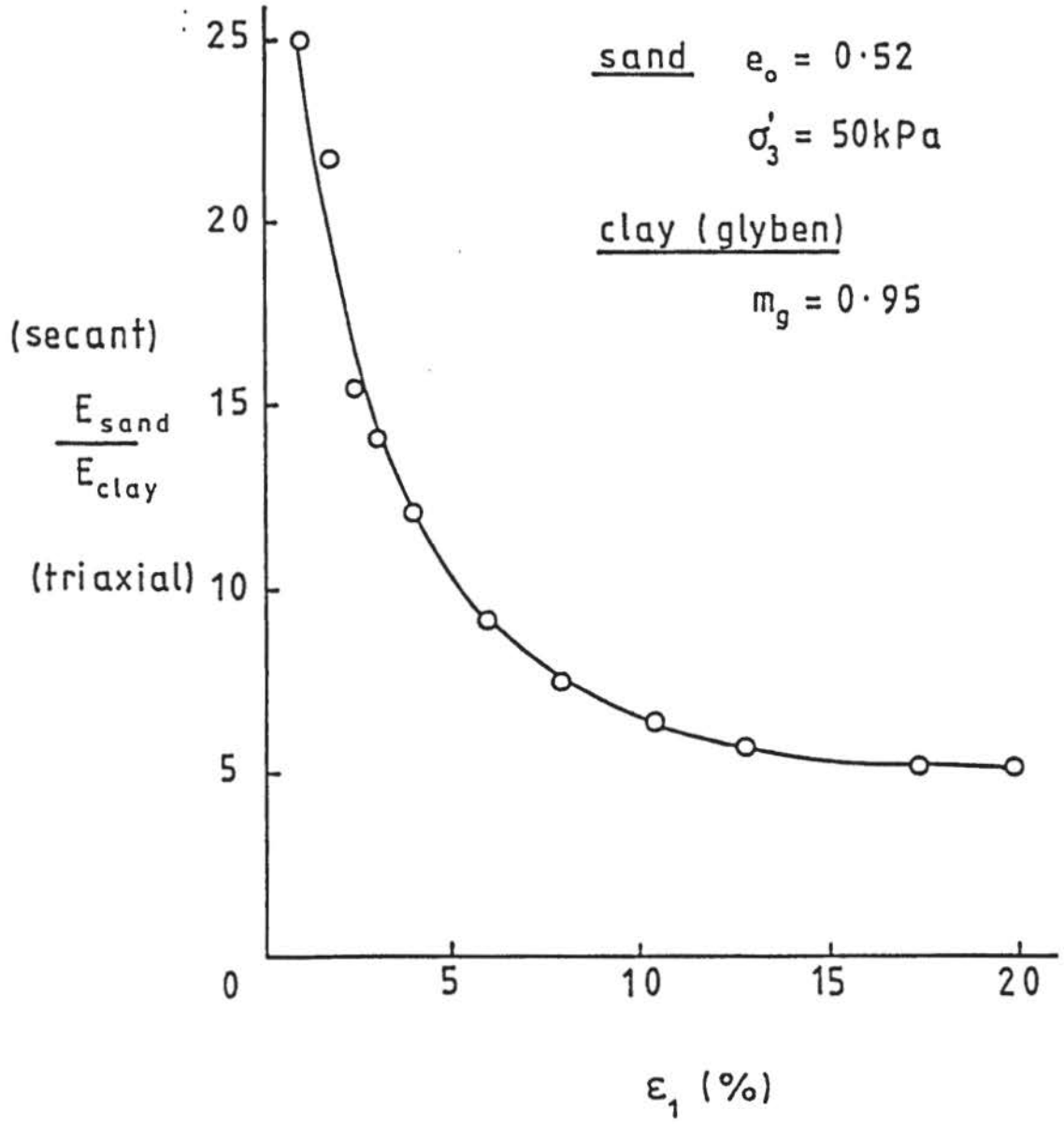

Variation of triaxial E_{sand}/E_{clay} with vertical strain.

FIGURE 13.9

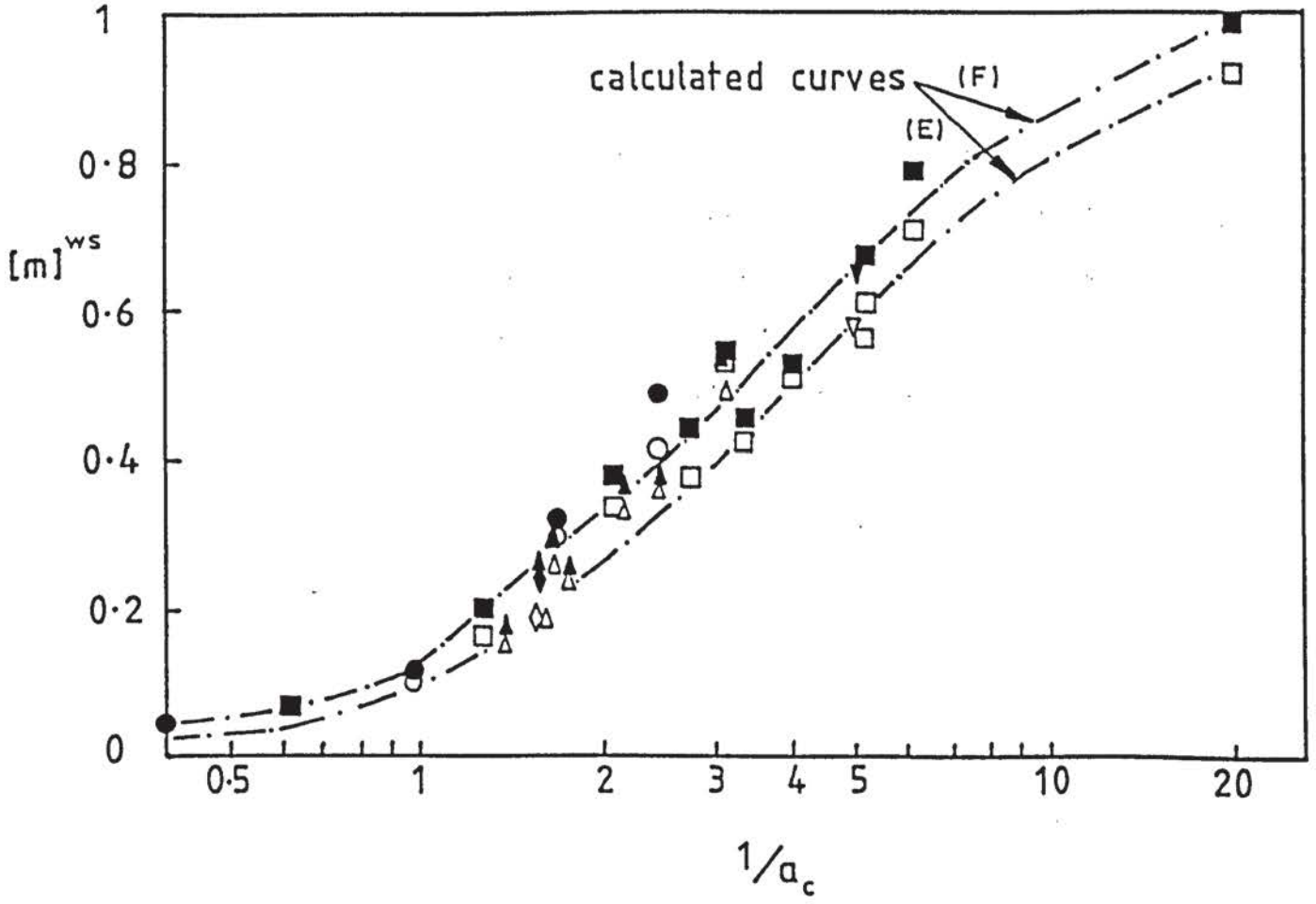

Comparison of observed and calculated m using the modified version of the equation by Billam (1981)

FIGURE 13.10

APPENDICES

APPENDIX A

Derivation of Eqn. 2.5.

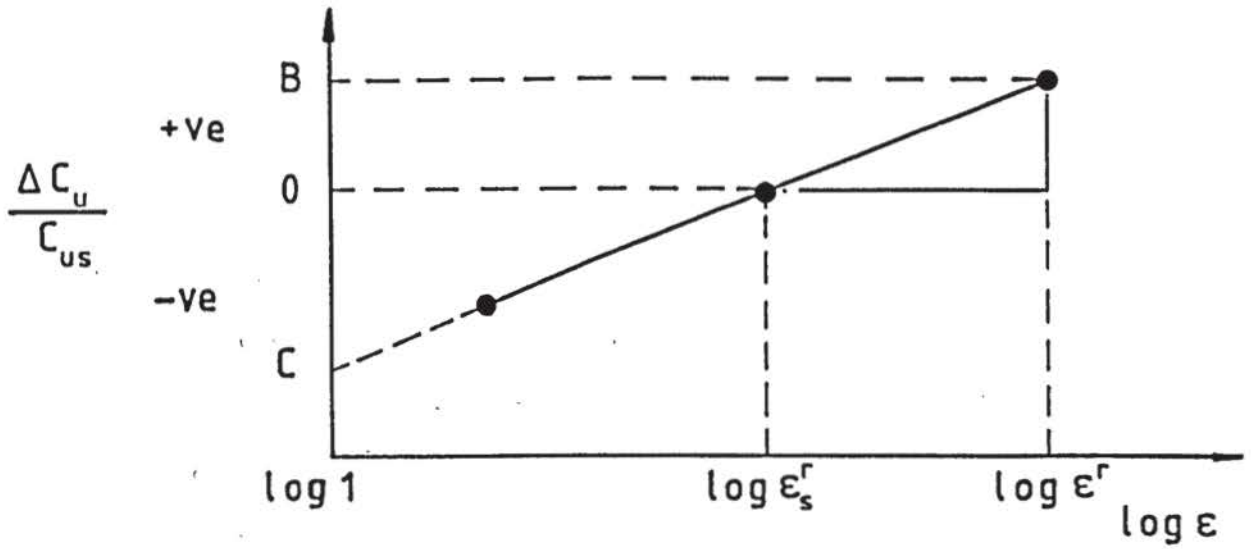

ε_s^r = standard rate of strain

ε^r = actual rate of strain

$$\frac{\Delta c_u}{c_{us}} = \left[\frac{B}{\log \varepsilon^r - \log \varepsilon_s^r}\right] \log \varepsilon + C \qquad (1)$$

from experimental results shown in Figure 2.11:

$$\frac{\Delta c_u}{c_u} = \left[\frac{0.206}{(\log 0.713 - \log 0.335)}\right] \log \varepsilon + C$$

$$= 0.067 \log \varepsilon + C \qquad (2)$$

by substitution:

$$0 = 0.067 \log \varepsilon_s^r + C$$

$$C = -0.067 \log \varepsilon_s^r$$

Substituting into Eqn. (2):

$$\frac{\Delta c_u}{c_{us}} = 0.067 \log \varepsilon^r - 0.067 \log \varepsilon_s^r$$

$$\Delta c_u = c_{us}\left[0.067 \log (\varepsilon^r/\varepsilon_s^r)\right] \qquad (3)$$

APPENDIX B

Transducer Amplifier Specification

1. Manufacturer

CIL Electronics Limited,
14, Willowbrook Road,
Worthing,
Sussex.

2. Specification (Model SGA 100)

Input offset voltage (Max)	1 mV
Temperature variation of input offset voltage (Max)	1μV/°C
Input impedence	>2.5MΩ
Input noise up to 1kHz	<1μV pk-pk
Bandwidth	0.4Mhz
Output voltage span	$\pm(V_s-3)$
Output current	5 mA
Output impedence	<1Ω
Closed-loop gain	5 to 10 000
Open-loop gain	>100 dB
Bridge supply voltage	approx. $2V_{ref}$
Supply voltage	±2 to ± 18 volts
Supply current	12 mA
Power dissipation	0.5 watt
Operating temperature	-25°C to 85°C
Storage temperature	-40°C to + 85°C
Common-mode rejection	>100 dB (temperature independant)

APPENDIX C

KAFFIR-D Industrial Plaster

Manufacturer:

British Gypsum Limited,
Ferguson House,
15/17 Marlybourne Road,
LONDON,
NW1 5JE.

Physical Properties:

Plaster/water ratio for plastic consistency	3.34 kg/litre.
Approximate setting time	10 minutes
Percentage expansion	0.23%
2 hour compressive strength	23.4 MPa.

APPENDIX D

Determination of the angle of a principal strain with respect to the horizontal, in the physical plane. (after Horsington, 1981).

Derivation

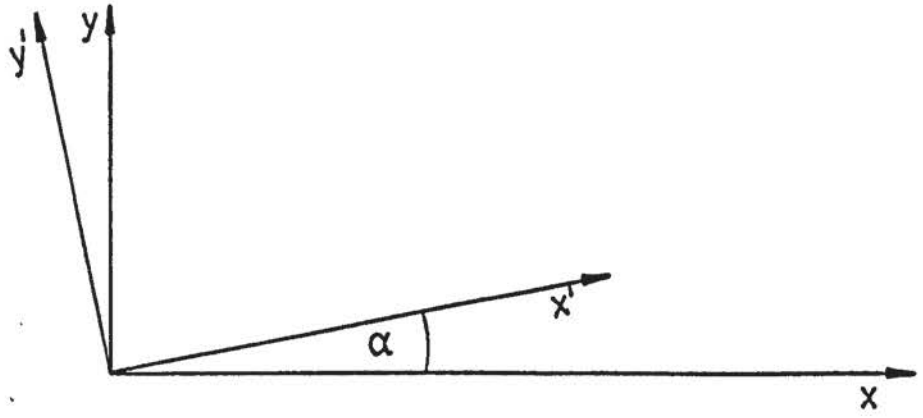

The strain increment components $\delta\varepsilon_x$, $\delta\varepsilon_y$, $\delta\gamma_{xy}$ relative to the x-y axes are known. Consider an alternative pair of axes x'-y', making an anti-clockwise angle α with the original pair. Strain increments relative to these new axes are given by the transformation equations (Graves-Smith, 1974):

$$\begin{matrix}\delta\varepsilon_{x'} \\ \delta\varepsilon_{y'}\end{matrix} = 0.5\,(\delta\varepsilon_x+\delta\varepsilon_y) \pm 0.5\,(\delta\varepsilon_x-\delta\varepsilon_y)\cos 2\alpha \pm 0.5\,\delta\gamma_{xy}\sin 2\alpha$$

$$\delta\gamma_{x'y'} = -(\delta\varepsilon_x-\delta\varepsilon_y)\sin 2\alpha + \delta\gamma_{xy}\cos 2\alpha$$

If an angle 2θ is defined, such that:

$$\sin 2\theta = \frac{\delta\gamma_{xy}}{S}$$

$$\cos 2\theta = \frac{(\delta\varepsilon_x - \delta\varepsilon_y)}{S}$$

$$\text{where} \quad S = +\sqrt{\left[(\delta\varepsilon_x - \delta\varepsilon_y)^2 + \delta\gamma_{xy}^2\right]}$$

Then 2θ is uniquely defined in the range 0 to 2π. (i.e. there is only one angle 2θ for which the sine or cosine will be of the correct sign.)

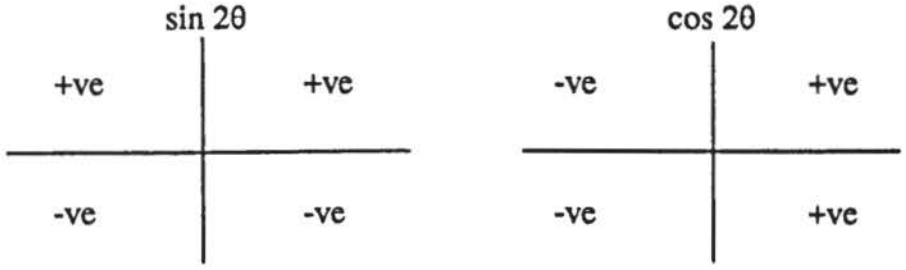

Thus, the value of θ in the physical plane is uniquely defined in the range of 0 to π.

It is easy to verify that the transformation equations may be re-written as:

$$\begin{matrix} \delta\varepsilon_{x'} \\ \delta\varepsilon_{y'} \end{matrix} = 0.5\,(\delta\varepsilon_x + \delta\varepsilon_y) \pm 0.5.S.\cos(2\theta - 2\alpha)$$

$$\delta\gamma_{x'y'} = S.\sin(2\theta - 2\alpha)$$

If the axes x'-y' are to be principal axes, then by definition:

$$\delta\gamma_{xy} = 0$$

therefore $\quad \sin(2\theta - 2\alpha) = 0$

and $\quad \alpha = 0$

Thus, the directions of the principal axes (anti-clockwise to the original axes) are defined by :

$$\alpha = 0.5 \arcsin\left[\frac{\delta\gamma_{xy}}{S}\right]$$

and $\quad \alpha = 0.5 \arccos\left[\frac{\delta\varepsilon_x - \delta\varepsilon_y}{S}\right]$

Each of these equations will yield two values of α in the range 0 to π. Only one of these values will satisfy both of the equations.

Application

Calculate the values of :

$$\sin 2\theta = \delta\gamma_{xy}/S$$

and $$\cos 2\theta = (\delta\varepsilon_x - \delta\varepsilon_y)/S$$

Using the sign (i.e. +ve or - ve) from each, determine the quadrant from:

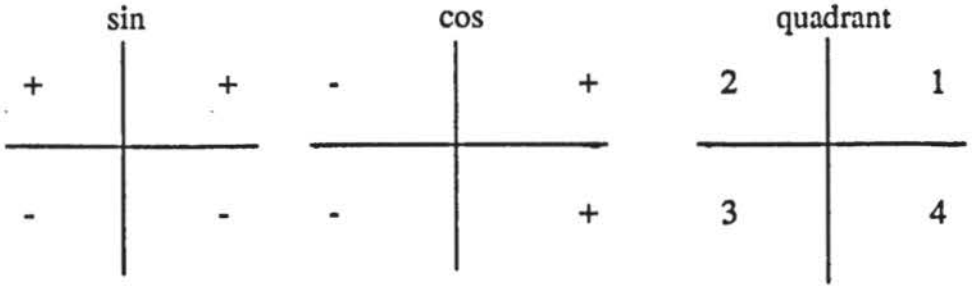

and use the angle from sin 2θ to find angle α from:

$$A = |\text{arc } \sin 2\theta|$$

Sine	Cosine	Quadrant	2α	α
+	+	1	A	(360^o-A)
+	-	2	(180^o-A)	(180^o+A)
-	-	3	(180^o+A)	(180^o-A)
-	+	4	(360^o-A)	A

(e.g. for sin 2θ (+ve) and cos 2θ (-ve) then $\alpha = (180^o\text{-A})$)

APPENDIX E

Determination of true x-y co-ordinates of lead-shot from radiographs (after Stroud, 1971)

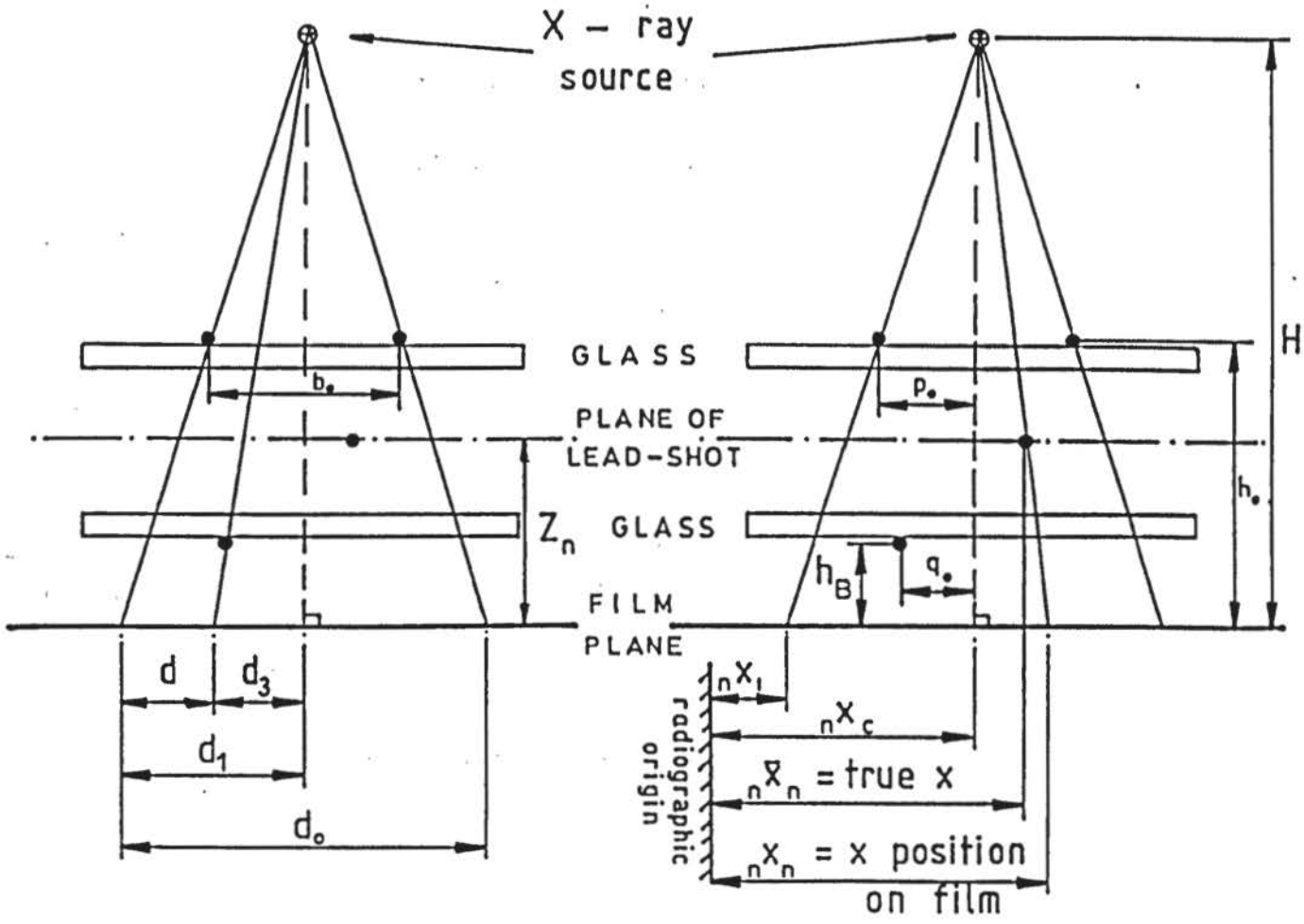

Relative positions of X-Ray source, film, material within glass boundaries and lead-shot.

FIGURE E1.

by similar triangles :

$$\frac{{}_nx_n - {}_nx_c}{H} = \frac{{}_nx_n - {}_n\bar{x}_n}{Z_n}$$

hence

$${}_n\bar{x}_n = {}_nx_n + \frac{Z_o}{H}({}_nx_c - {}_nx_n) \qquad (1)$$

Z_n and H are known, and ${}_nx_n$ may be measured on the digitiser.

${}_nx_c$ is obtained as follows:

by similar triangles:

$$\frac{{}_nx_c - {}_nx_1}{H} = \frac{p_o}{(H - h_o)}$$

therefore

$${}_nx_c = {}_nx_1 + \frac{H}{(H - h_o)} p_o \qquad (2)$$

h_o may be directly measured and p_o is obtained as follows:

Determine d and d_o by digitiser measurement. The magnitudes of b_o, $b = (p_o - q_o)$ and $w = (h_o - h_B)$ may also be obtained by direct measurement.

$$q_o = \frac{(H - h_B)\, d_3}{H}$$

$$p_o - b = \frac{(H - h_o + w)}{H} \cdot d_3 \qquad (3)$$

$$p_o = \frac{(H - h_o)}{H} \cdot d_1 \qquad (4)$$

$$d = d_1 - d_3 \qquad (5)$$

from Eqn. 4

$$d_1 = \frac{H \cdot p_o}{(H - h_o)} \qquad (6)$$

from Eqn. 3

$$d_3 = \frac{(p_o - b)\,H}{(H - h_o + w)} \tag{7}$$

Substituting Eqn's. 6 and 7 into Eqn. 5:

$$d = \frac{H.p_o}{(H - h_o)} - \frac{(p_o - b)\,H}{(H - h_o + w)}$$

transposing for p_o gives :

$$p_o = \frac{d\,(H - h_o)\,(H - h_o + w)}{H.w + H.b\,(H - h_o)} \tag{8}$$

The method is similarly applied to the y-ordinates.

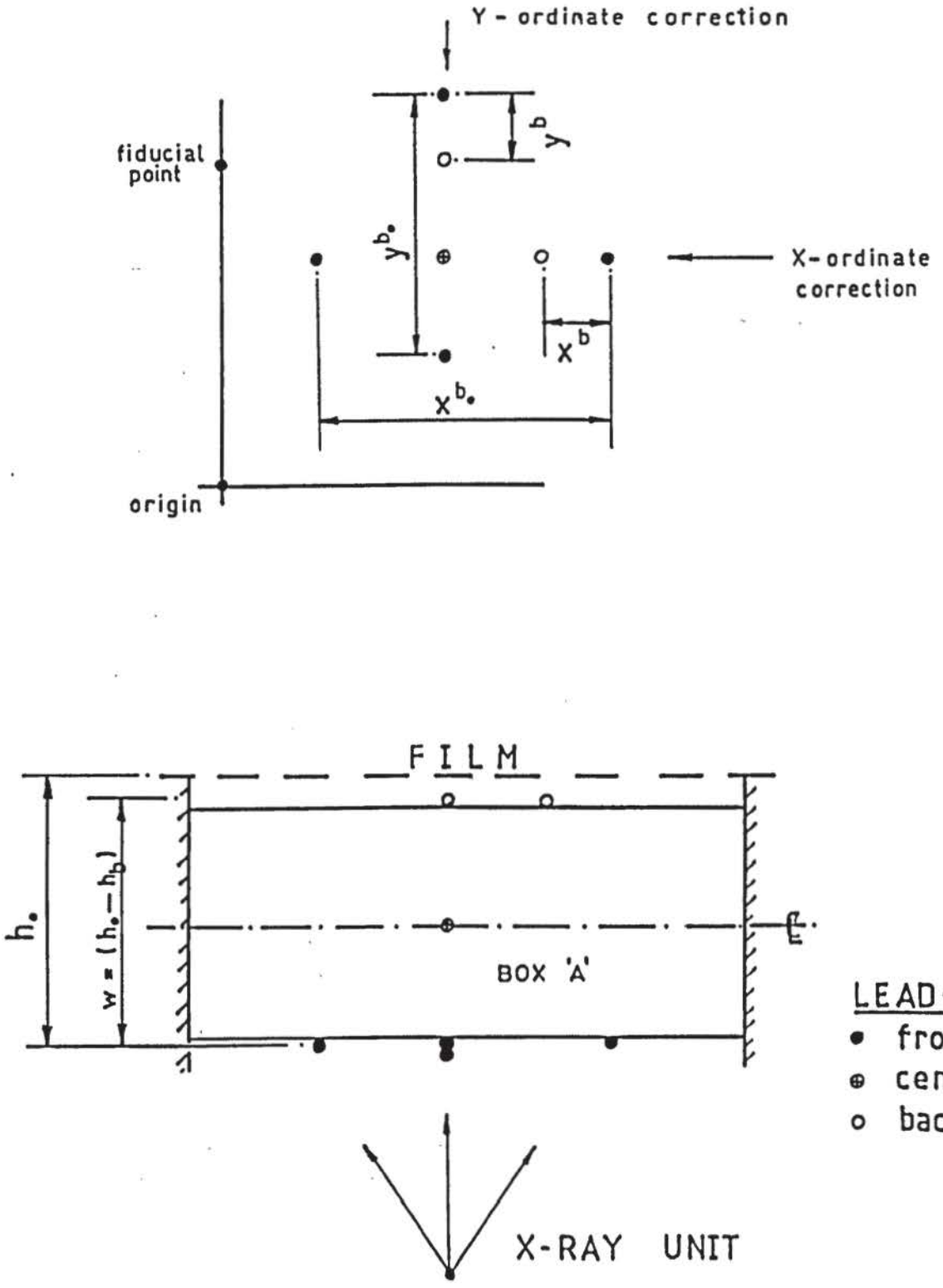

Positions of lead-shot to obtain a radiograph for the determination of correction factors to obtain the true x-y co-ordinates of the lead-shot images.

FIGURE E2

APPENDIX F

Large strain equations.

Natural strain

In general form :

$$\varepsilon^L = \ln (1+\varepsilon) \qquad \text{based on original co-ordinates}$$

Hence

$$\varepsilon_x^L = \ln (1+\varepsilon_x)$$
$$\varepsilon_y^L = \ln (1+\varepsilon_y)$$
$$\gamma_{xy}^L = \ln (1+\gamma_{xy})$$

Principal strains obtained from results.

Green's strain tensor

Based on original co-ordinates :

$$\varepsilon_x^L = \frac{\partial u}{\partial x} + 0.5 \left[\left(\frac{\partial u}{\partial x}\right)^2 + \left(\frac{\partial v}{\partial x}\right)^2 \right]$$

$$\varepsilon_y^L = \frac{\partial v}{\partial y} + 0.5 \left[\left(\frac{\partial v}{\partial y}\right)^2 + \left(\frac{\partial u}{\partial y}\right)^2 \right]$$

$$\gamma_{xy}^L = \frac{\partial u}{\partial y} + \frac{\partial v}{\partial x} + \left[\frac{\partial u}{\partial x}.\frac{\partial u}{\partial y} + \frac{\partial v}{\partial x}.\frac{\partial v}{\partial y} \right]$$

using polynomials (Eqn. 7.1) given in Section 7.5:

$$\varepsilon_x^L = - b + 0.5 (b^2 + f^2)$$
$$\varepsilon_y^L = - f + 0.5 (f^2 + c^2)$$
$$\gamma_{xy}^L = - c + e + (b.c + e.f)$$

Principal strains obtained from results.

APPENDIX G

Reading and writing alphanumerical information in a FORTRAN program using a DEC PDP-11 or VAX SYSTEM

Programming

```
            BYTE    TESTNO(100)
            DIMENSION statements
            READ (1, 500) IBC, (TESTNO(N), N=1, IBC)
500         FORMAT (Q, 100A1)
              }
            WRITE (2, 600)(TESTNO(N), N=1, IBC)
600         FORMAT (100A1)
              }
            END
```

Data (100 alphanumeric characters maximum)

e.g. TRIAXIAL TEST No: A5/6 (undrained) 20.7.88

APPENDIX H

Producing element identification tables using a computer program

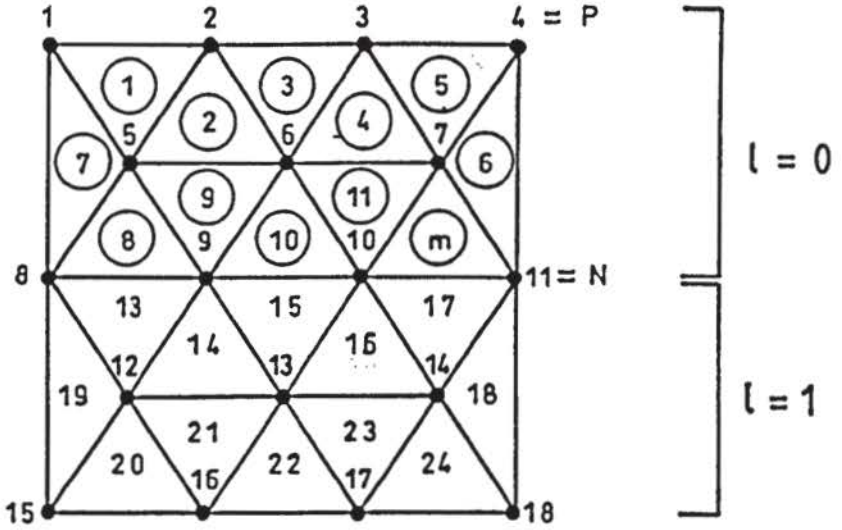

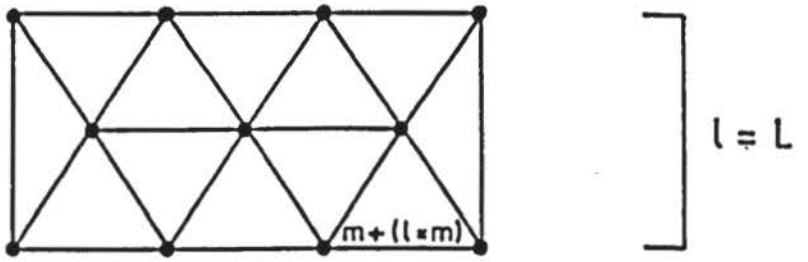

element number m	nI(m)	node number nJ(m)	nK(m)
1	1	2	5
2	2	6	5
3	2	3	6
4	3	7	6
5	3	4	7
6	4	11	7
7	1	5	8
8	5	9	8
9	5	6	9
10	6	10	9
11	6	7	10
M	7	11	10
.	.	.	.
.	.	.	.
.	.	.	.
m+(lxm)	nI(m)+(lxD)	nJ(m)+(lxD)	nk(m)+(lxD)

PROGRAM FLOW CHART

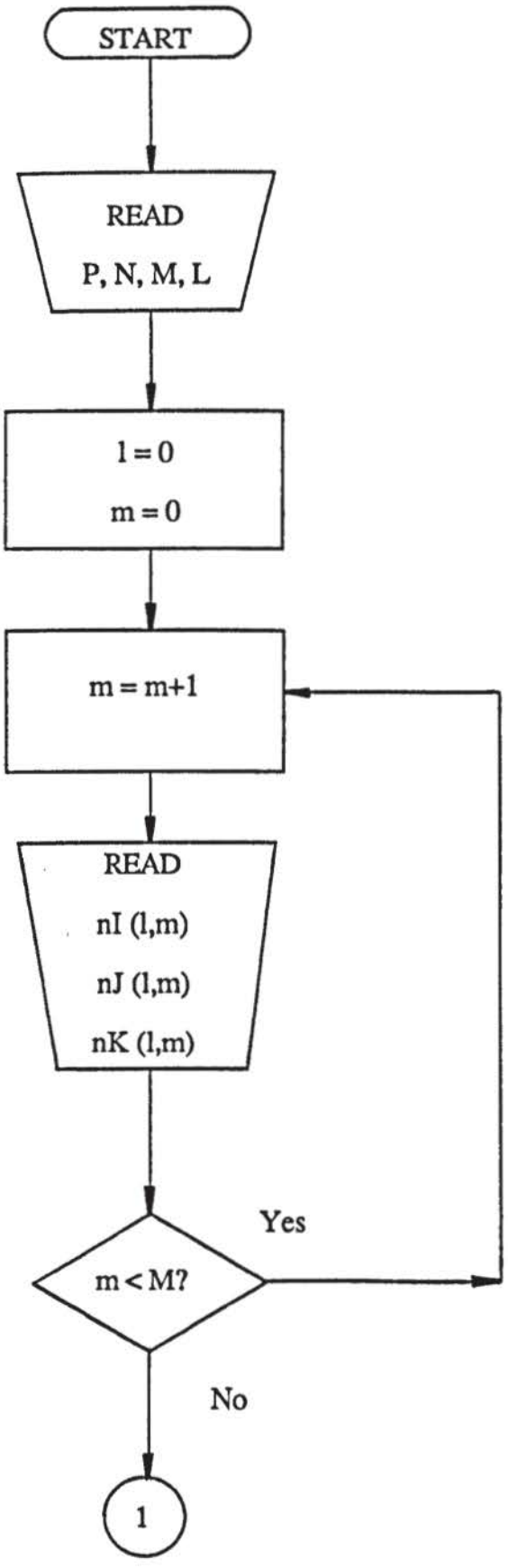

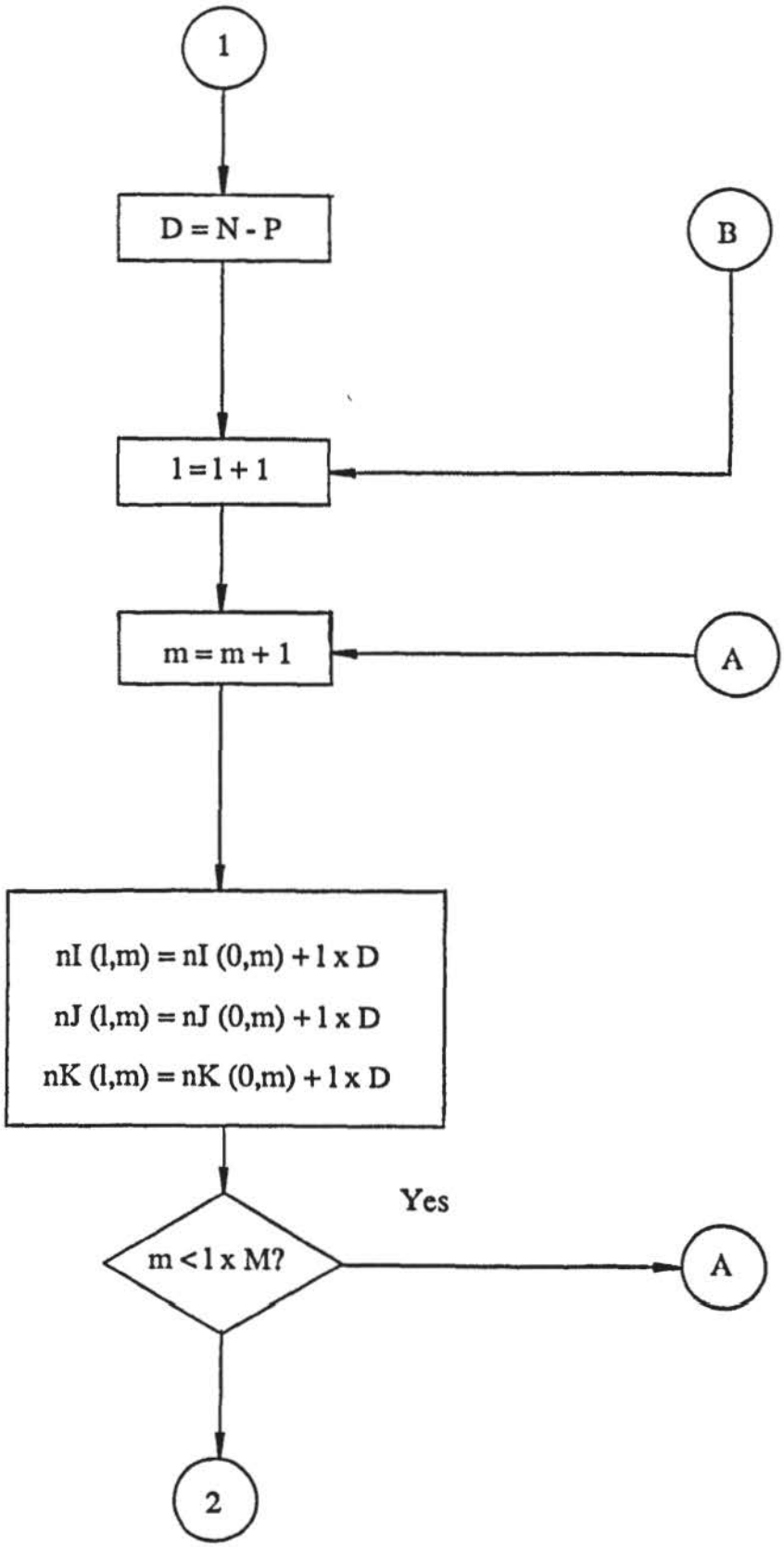
1
D = N - P
B
l = l + 1
m = m + 1
A
nI (l,m) = nI (0,m) + l x D
nJ (l,m) = nJ (0,m) + l x D
nK (l,m) = nK (0,m) + l x D
Yes
m < l x M?
A
2

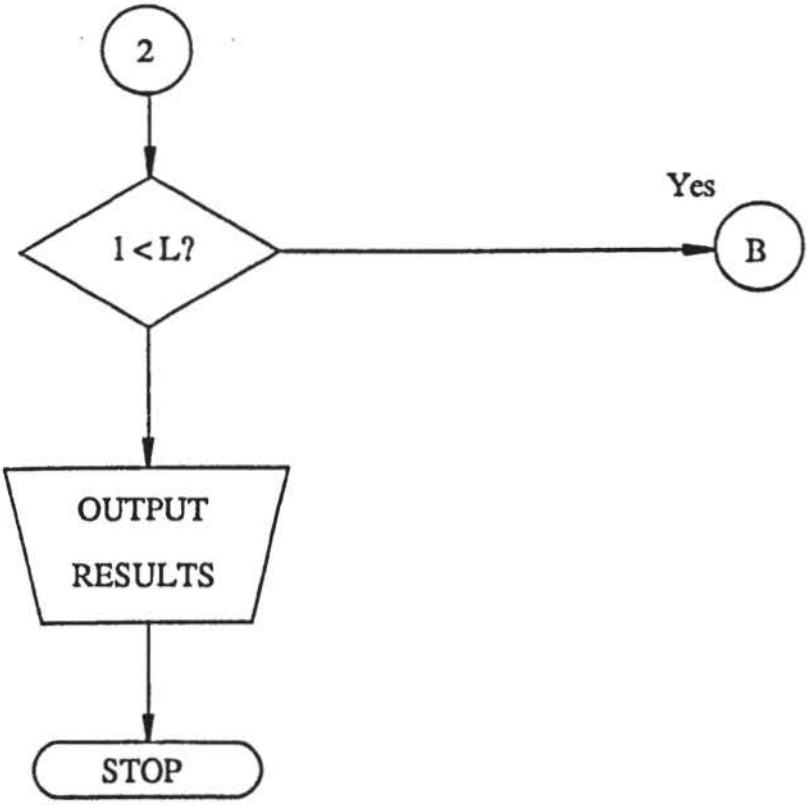
2
I<L?
Yes
B
OUTPUT
RESULTS
STOP

APPENDIX I

Examples of presentation of numerical results.

RESULTS OF SMALL SCALE FOOTING TESTS

TESTNO: STA4/1.4 2.0D

footing width = 25.00mm
footing length = 114.80mm
Cu(20) = 13.00kN/sq.m
Cu(corrected) = 13.27kN/sq.m
SIGXO = 1.61kN/sq.m

TIME	Q	RO	Q/CU	RO/WID	Q/Cfmx	RW/Q	Cf	Nc	SIGX	SIGX/Q
0 0 0	0.00	0.00	0.00	0.0000	0.00	0.000000	0.00	0.00	0.00	0.000
0 0 0	3.65	0.00	0.28	0.0000	0.27	0.000000	0.68	5.37	0.23	0.063
13530	31.22	1.04	2.40	0.0416	2.34	0.001333	5.72	5.46	1.89	0.061
13540	43.16	1.81	3.32	0.0723	3.23	0.001676	7.81	5.53	2.82	0.065
13550	51.34	2.63	3.95	0.1051	3.84	0.002046	9.17	5.60	3.69	0.072

RESULTS OF ONE COLUMN TEST

TEST NO: PC4SU 1.6 LAPGE-BOX(4 COLS)

column diameter = 38.20mm
footing width = 152.50mm
footing length = 152.50mm
Cu(20) = 13.00kN/sq.m
Cu(corrected) = 12.28kN/sq.m
SIGXO = 3.60kN/sq.m

TIME	Q	RO	Q/Cu	RO/WID	Q/Qfg	Q/Qmx	SIGX	SIGX/Q	normQ/Cu	RW/Q	Qn
0 0 0	0.00	0.00	0.00	0.000	0.000	0.000	0.00	0.0000	0.00	0.000000	0.00
0 0 0	2.55	0.00	0.20	0.000	0.025	0.023	0.03	0.0111	-0.97	0.000000	-12.58
643 0	47.95	5.51	3.69	0.036	0.479	0.433	2.71	0.0566	2.53	0.000754	32.83
644 0	84.14	10.78	6.47	0.071	0.841	0.760	6.40	0.0761	5.31	0.000840	69.01

RESULTS OF TWO COLUMN INTERACTION(ONE LOADED)

TEST NO: ICOL 1.5

column diameter = 38.20mm
footing diameter = 38.02mm
Cu(23) = 11.30kN/sq.m
Cu(corrected) = 11.50kN/sq.m
SIGXO = 5.49kN/sq.m

TIME	Q	Qnorm	RO	Q/Cu	Qn/Cu	RO/WID	DELTA	DEL/DIA	FACTOR	SIGX	SIGX/Q	
0 0 0	0.00	0.00	0.0000	0.00	0.00	0.0000	0.0000	0.00000	0.0000	0.00	0.000	0.
0 0 0	4.56	-18.49	0.0000	0.40	-1.64	0.0000	0.0000	0.00000	0.0000	0.06	1.203	0.
13458	21.22	-1.93	0.1799	1.88	-0.16	0.0047	0.0268	0.00070	0.1490	0.26	0.012	0.

RESULTS OF TWO COLUMN TEST

TEST NO: STC 2.7

column diameter = 38.20mm
footing width = 38.10mm
footing length = 189.70mm
Cu(20) = 11.50kN/sq.m
Cu(corrected) = 10.92kN/sq.m
SIGXO = 4.41kN/sq.m

TIME	Q	RO	Q/Cu	RO/WID	Q/Qfg	Q/Qmx	SIGX	SIGX/Q	normQ/Cu	RW/Q	Qn
0 0 0	0.00	0.00	0.00	0.000	0.000	0.000	0.00	0.0000	0.00	0.000000	0.00
0 0 0	1.02	0.00	0.09	0.000	0.010	0.008	0.15	0.1427	-1.55	0.000000	-17.51
2 616	10.38	0.39	0.92	0.010	0.101	0.077	1.06	0.1022	-0.72	0.000984	-8.16
2 620	16.96	0.71	1.50	0.019	0.165	0.127	1.65	0.0973	-0.14	0.001101	-1.57
2 624	23.12	0.99	2.05	0.026	0.224	0.172	2.17	0.0940	0.41	0.001125	4.59
2 628	29.27	1.31	2.59	0.034	0.284	0.218	2.75	0.0940	0.95	0.001174	10.74
2 632	35.14	1.62	3.11	0.043	0.341	0.262	3.32	0.0944	1.47	0.001212	16.61

APPENDIX J

Assessment of Column Length

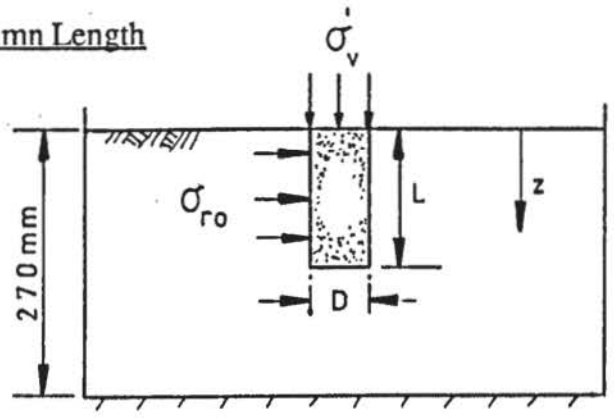

Clay γ_b = 16.2 kN/m^3 ; c_u = 11.36 kPa

Column ϕ' = 40°

σ_{xo} (horizontal stress transducer) = 5.1 kPa (average)

Bulging Failure - Hughes and Withers (1974)

$$\frac{\sigma'_v}{\sigma'_r} = \left[\frac{\sigma'_1}{\sigma'_3}\right] = \frac{1 + \sin\phi'}{1 - \sin\phi'} = K_p = \underline{4.6}$$

$$\sigma'_v = K_p (\sigma_{ro} + 4\, c_u)$$

If spreading allowed at z = 1.5 D, then:

$$\text{max. } \sigma'_v = K_p\left[(\sigma_{xo} + 1.5\, D\, \gamma_b) + 4\, c_u\right]$$

$$= 4.6\left[(5.1 + 1.5 \times 0.0381 \times 16.2) + (4 \times 11.36)\right] \text{kPa}$$

$$= \underline{236.7 \text{ kPa}} \qquad (1)$$

Rigid Pile Mode

$$\text{max. } \sigma'_V = c_u\,(9 + 4\, L/D)$$

$$= 11.36\,(9 + 4L/0.0381) \text{ kPa}$$

$$= (102.2 + 1192.7\, L) \quad \text{kPa} \qquad (2)$$

For equal likelihood of failure, equating (1) and (2)

$$236.7 = 102.2 + 1192.7\,L$$

$$\text{min.}L = 134.5/1192.7 \text{ m}$$

$$= \underline{113 \text{ mm}}$$

Allow for say 35 mm displacement at top of column :

$$L \approx \underline{\mathbf{150 \text{ mm}}}$$

APPENDIX K

Derivation of Eqn. 10.1

Viscosity correction after Meigh (1950)

Determining which rate of foundation loading corresponds to the standard rate of strain used in the triaxial test is done by equating the time taken to failure in a loading test to the time taken to reach failure in a footing test.

From triaxial test results in Figure 2.6(a):

Strain at failure	= 18 - 20%, say 19%
Average sample length	= 75 mm
Standard test rate	= 2.5 mm per minute
Average compression of triaxial sample at failure	= 19% x 75 mm/100
	= 14.25 mm
Time taken to reach failure	= 14.25 mm/2.5 mm per min.
	= 5.7 min.

If a foundation is assumed to reach general shear failure at a settlement of 0.5B (Meigh stated that the correction for viscosity was insensitive to this assumption), then the rate of loading corresponding to the triaxial test :

	0.5 B in 5.7 minutes
or	1 B in 11.4 minutes
gives	B/11.4 in 1 minute

where B is the foundation width.

So, the standard rate of strain in a foundation test corresponding to the standard rate of strain in the triaxial test:

$$\varepsilon_s^r = B \times 100/(11.4 \times 75)\ \% \qquad (1)$$

and the actual rate of strain corresponding to the triaxial test :

$$\varepsilon^r = \text{rate of loading (R)} \times 100/75\ \text{mm}\ \%$$

$$= 100R/75\ \% \qquad (2)$$

From Eqn. 2.5

$$\Delta c_u = c_{us}\left[0.067 \ln (\varepsilon^r/\varepsilon_s^r)\right]$$

substituting (1) and (2)

$$\Delta c_u = c_{us}\left[0.067 \ln (11.4\ R/B)\right]$$

giving

$$\mathbf{c_u = c_{us}\left[1 + 0.067 \ln (11.4\ R/B)\right]} \qquad (3)$$

REFERENCES

Aboshi, H., Ichimoto, E., Enoki, M. and Harada, K. (1979). The 'compozer' - a method to improve characteristics of soft clays by inclusion of large diameter sand columns. Int. Symp. on Soil Reinf. (Paris), Vol. 1, pp 211-216.

Arthur, J.R.F. (1962). Strains and lateral force in sand. Ph.D thesis, University of Cambridge (unpublished).

Arthur, J.R.F. and Roscoe, K.H. (1961). An earth pressure cell for the measurement of normal and shear stresses. Civ. Engng. Publ.Wks. Review, Vol. 56, No. 569, pp 765-770.

Baguelin, F., Jezequel, J.F. and Shield, G.H. (1978). The pressuremeter and foundation engineering, (1st Ed.). Trans. Tech. Publications : Germany.

Balaam, N.P. and Booker, J.R. (1981). Analysis of rigid rafts supported by granular piles. Int. Jnl. Numerical and Analytical Methods in Geomech., Vol. 5, pp 379-403.

Balaam, N., Booker, J.R. and Poulos, H.G. (1976). Analysis of granular pile behaviour using Finite Elements. Proc. Int. Conf. on Finite Element Methods in Engng. (Adelaide, Australia), pp 29.1-13.

Balaam, N.P. and Poulos, H.G. (1978). Methods of analysis of single stone columns. Proc. Symp. on Reinf. and Stabilising Techniques in Engrg. Practice. (Sydney, Australia), Vol. 1, pp 497-512.

Banerjee, P.K. (1969). A contribution to the study of pile foundations. PhD Thesis, University of Southampton (unpublished).

Bauman, V. and Bauer, G.E.A. (1974). The performance of foundations on various soils stabilised by the vibro-compaction method. Can.Geotech. Jnl., Vol. 11, pp 509-530.

Bell, A..L. (1915). The lateral pressure and resistance of clay and the supporting power of clay foundations. Proc. Instn. Civ.Engrs., Vol. 199, pp 233.

Billam, J. (1965). A preliminary study of the response of a new earth pressure cell. MSc thesis (laboratory project report), University of Birmingham (unpublished).

Billam, J. (1981). Vibroflotation and Vibroreplacement. Notes for a Seminar at McClelland Engineers (Harrow, Middlesex) (unpublished).

Bishop, A.W. and Henkel, D.J. (1962). The measurement of soil properties in the triaxial test. Edward Arnold; London.

Bransby, P.L. (1968). Stresses and strain in sand caused by rotation of a model wall. Ph.D thesis, University of Cambridge (unpublished).

Bransby, P..L. (1973). Cambridge contact stress transducers. Internal Report No. CUED/D - Soils/LN2, Department of Engineering, University of Cambridge (unpublished).

Brauns, J. (1978). Initial bearing capacity of stone columns and sand piles. Proc. Symp. on Reinf. and Stabilizing Techniques in Engineering Practice (Sydney, Australia), Vol. 1, pp 477-496.

Brown, R.E., Jones, J.S., Mayne, P.W. and Dimaggio, J.A. (1979). A parametric study of stone column behaviour. Int. Symp. on Soil Reinf. (Paris), Vol. 3, pp. 175-178.

Brown, S.F. (1971). The performance of earth pressure cells for use in road research. Civ.Engng. Publ. Wks. Review, Vol. 66, No. 775, pp 160-165.

Burland, J.B. (1967). Deformation of soft clay. Ph.D thesis, University of Cambridge (unpublished).

Burland, J.B. and Roscoe, K.H. (1969). Local strains and pore pressures in a normally consolidated clay layer during one-dimensional consolidation. Géotechnique, Vol. 19, No. 3, pp 336-356.

Burn, K.N. (1973). A transducer to measure porewater pressures in soil tests. Symp. on Laboratory shear testing of soils. ASTM Special Tech.Publ., No. 361, pp 390-395.

Button, S.J. (1953). The bearing capacity of footings on a two-layer cohesive sub-soil. Proc. 3rd. Int. Conf. Soil Mech. Fndn. Engng., Vol. 1, pp 332-335.

Cole, E.R. (1967). The behaviour of soils in the simple-shear apparatus. Ph.D thesis, University of Cambridge (unpublished).

Case, J. and Chilver, A.H. (1975). Strength of Materials. Edward Arnold : London.

Cooke, R.W. (1974). Piled foundations: A survey of research at the building research station. BRE Current Paper, CP24/74.

Cooke, R.W., Price, G. and Tarr, K. (1979). Jacked piles in London clay : A study of load transfer and settlement under working conditions. Géotechnique, Vol. 29, No. 4, pp 461-468.

Cooke, R.W., Price, G. and Tarr, K. (1980). Jacked piles on London clay : interaction and group behaviour under working conditions. Géotechnique, Vol. 30, No. 2, pp 97-136.

Cornforth, D.H. (1964). Some experiments on the influence of strain conditions on the strength of sand. Géotechnique, Vol. 16, No. 2, pp 143-167.

Coumoulos, D.G. (1967). A radiography study of soils. Ph.D thesis, University of Cambridge (unpublished).

Coyle, H.M. and Shiffert, J.B. (1968). Manufactured soil samples for laboratory research. ASTM Jnl. of Mat., Vol. 3, No. 2, pp 272-293.

Cuckson, J. (1975). A new radiographic method of laboratory strain measurement in clays. Géotechnique 25, No. 1, Tech. Note, pp 137-141.

Davie, J.R. and Sutherland, H.B. (1977). Uplift resistance of cohesive soils. Jnl. Geotech. Engng. Div. Am.Soc.Civ.Engrs., Vol. 103, No. GT9, pp 935-952.

Davis, H.E. and Woodward, R.J. (1949). Some laboratory studies of factors pertaining to the bearing capacity of soils. Proc. Highways Research Board, Vol. 29, pp 467-476.

Dodd, M.W. (1979). Model tests on isolated stone columns in soft clay to confirm predicted ultimate loads. MSc thesis (Laboratory project report), University of Birmingham (unpublished).

Dullage, C.R. (1969). An investigation into the feasibility of small-scale tests on granular piles in clay. MSc thesis, University of Wales, Swansea (unpublished).

Dunn, C.S. and Billam, J. (1966). A study of the response characteristics of a new minature earth pressure cell. Civ.Engng. Publ.Wks. Review, Vol. 61, No. 715, pp 181-186.

Gerber, E. (1929). Untersuchungen ueber die Druckverteiling im Oerlich Belasteten Sand. Dissertation, Techische Hochschule, Zurich (unpublished).

Gibson, R.E. and Anderson, W.F. (1961). In-situ measurement of soil properties with the pressuremeter. Civ.Engng. Publ.Wks. Review, Vol. 56, No. 658, pp 615-618.

Goughnour, R.R. and Bayuk, A.A. (1979a). Analysis of stone column-soil matrix action under vertical load. Int.Symp. on Soil Reinf. (Paris), Vol. 1, pp 271-277.

Goughnour, R.R. and Bayuk, A.A. (1979b). A field study of long term settlements of loads supported by stone columns in soft ground. Int. Symp. on Soil Reinf., (Paris), Vol. 1, pp 270-285.

Graves-Smith, T.R. (1974). Stress and Strain. (Modular Textbooks in Engng. - Ed. A.C. Walker), Chatto and Windus : London.

Greenwood, D.A. (1970). Mechanical improvement of soils below ground surface. Proc. Conf. Ground Engng., Paper 2, ICE : London, pp 11-22.

Greenwood, D.A. (1972). Vibroflotation - rationale for design and treatment. Symp. on Methods of Treatment of Unstable Ground (Sheffield Polytechnic). pp 189-205.

Hambly, E.C. (1969). Plane-strain fields in sand. Ph.D thesis, University of Cambridge (unpublished).

Hanna, T.H. (1973). Foundation instrumentation. (1st Ed.), Trans.Tech. Publications : Cleveland.

Hansen, B. (1958). Line ruptures regarded as narrow rupture zones. Basic equations based on kinematic considerations. Proc. Conf.Earth Press. Problems (Brussels), Vol. 1, pp 39-48.

Hope, D. (1979). A preliminary investigation into the characteristics of a new plane-strain apparatus. MSc thesis (Laboratory project report), University of Birmingham. (unpublished).

Horsington, R.W. (1981). Private Communication.

Hughes, J.M.O. and Withers, N.J. (1974). Reinforcing of soft cohesive soils with stone columns. Ground Engng., Vol. 7, No. 3, pp 42-49.

Hughes, J.M.O., Withers, N.J. and Greenwood, D.A. (1975). A field trial of the reinforcing effect of a stone column in soil. Geotechnique, Vol. 25, No. 1, pp 31-44.

James, R.G. (1965). Stress and strain fields in sand. Ph.D thesis, University of Cambridge (unpublished).

James, R.G. (1973a). Radiographic techniques. Int. Report No. CUED.C-soils LN1(b), Department of Engineering, University of Cambridge (unpublished).

James, R.G. (1973b). Determination of strains in soils by radiography. Int.Report No. CUED/C-soils/LN1(a). Department of Engineering, University of Cambridge (unpublished).

James, R.G. (1980). Private communication.

Jones, J.S. (1972). Bearing capacity of cylindrical aggregate piles. MSc thesis, University of Virginia (unpublished).

Kallstenius, T. and Bergau, W. (1956). Investigations of soil pressure measuring by means of cells. Proc. Swedish Geotech. Inst., No. 12.

Kodak (1980). Radiography in Modern Industry (4th Edition). Eastman Kodak Co.: New York.

Kolbuszewski, J.J. (1948a) An experimental study of the maximum and minimum porosity of sands. Proc. 2nd Int. Conf. Soil Mech. Fdn.Engng. (Rotterdam), Vol. 1, pp 158-165.

Kolbuszewski, J.J. (1948b). General investigation of the fundamental factors controlling loose packing of sands. Proc. 2nd. Int. Conf. Soil Mech. Fdn. Engng. (Rotterdam), Vol. 7, pp 47-49.

Kolbuszewski, J.J. (1958). Fundamental factors affecting experimental procedures dealing with pressure distribution in sands. Proc. Conf. on Earth Press. Problems (Brussels), Vol. 1, pp 71-83.

Labrue, J.F. (1981). An investigation of glyben with a pressuremeter. MSc project (Laboratory project report), University of Birmingham (unpublished).

Lambe, T.W. and Whitman, R.V. (1969). Soil Mechanics. John Wiley and Sons Inc.: London.

Lewin, P.I. and Burland, J.B. (1970). Stress-probe experiments on saturated normally consolidated clay. Geotechnique, Vol. 20, No. 1, pp 38-56.

Lippiatt, A.G. (1979). The architecture of small computer systems. Prentice Hall International : London.

Lord, J.A. (1969). Stresses and strains in an earth pressure problem. Ph.D thesis, University of Cambridge (unpublished).

Lubking, P., Jekel, J.W. and Brons, K.F. (1976). Discussion. Proc. Symp. Ground Treatment by Deep Compaction, ICE: London, p 144.

Madhav, M.R. and Vitkar, P.P. (1978). Strip footing on weak clay stabilised with a granular trench or pile. Can. Geotech. Jnl., Vol. 156, pp 605-609.

Mattes, N.S. and Poulos, H.G. (1969). Settlement of a single compressible pile. Jnl. Soil Mech. Fdn.Div.Am.Soc.Civ.Engrs., Vol. 95, SM2, pp 189-207.

Mayfield, B. (1963). The performance of a rigid wheel moving in a circular path through a clay. Ph.D thesis, University of Nottingham (unpublished).

Meigh, A.C. (1950). Model footing tests on clay. MSc thesis, University of London (unpublished).

Metzger, G.V. and Koerner, R.M. (1975). Modelling of soil densification by vibroflotation. Jnl. Geotech.Engng.Div.Am.Soc.Civ.Engrs., Vol. 101, No. GT4, Technical Note, pp 417-421.

Meyerhof, G.G. (1951). The ultimate bearing capacity of foundations. Geotechnique, Vol. 2, No. 4, pp 301-332.

Monfore, G.E. (1950). An analysis of stress distribution in and near strain gauges in elastic solids. U.S. Bureau of Reclaimation, Report SP-26.

Murray, W.M. and Stein, P.K. (1958). Lectures and laboratory exercises on strain gauge techniques. Department of Engineering, University of California.

Nahrgang, E. (1976). Untersuchung des Tragverhaltens von eigerüttelten Schottersäulen and Hand von Modellversuchen. Baumaschine und Bautechnik, Heft 8.

Lubking, P., Jekel, J.W. and Brons, K.F. (1976). Discussion. Proc. Symp. Ground Treatment by Deep Compaction, ICE: London, p 144.

Madhav, M.R. and Vitkar, P.P. (1978). Strip footing on weak clay stabilised with a granular trench or pile. Can. Geotech. Jnl., Vol. 156, pp 605-609.

Mattes, N.S. and Poulos, H.G. (1969). Settlement of a single compressible pile. Jnl. Soil Mech. Fdn.Div.Am.Soc.Civ.Engrs., Vol. 95, SM2, pp 189-207.

Mayfield, B. (1963). The performance of a rigid wheel moving in a circular path through a clay. Ph.D thesis, University of Nottingham (unpublished).

Meigh, A.C. (1950). Model footing tests on clay. MSc thesis, University of London (unpublished).

Metzger, G.V. and Koerner, R.M. (1975). Modelling of soil densification by vibroflotation. Jnl. Geotech.Engng.Div.Am.Soc.Civ.Engrs., Vol. 101, No. GT4, Technical Note, pp 417-421.

Meyerhof, G.G. (1951). The ultimate bearing capacity of foundations. Geotechnique, Vol. 2, No. 4, pp 301-332.

Monfore, G.E. (1950). An analysis of stress distribution in and near strain gauges in elastic solids. U.S. Bureau of Reclaimation, Report SP-26.

Murray, W.M. and Stein, P.K. (1958). Lectures and laboratory exercises on strain gauge techniques. Department of Engineering, University of California.

Nahrgang, E. (1976). Untersuchung des Tragverhaltens von eigerüttelten Schottersäulen and Hand von Modellversuchen. Baumaschine und Bautechnik, Heft 8.

Northey, R.D. (1950). The sensitivity of clays. Ph.D thesis, University of London (unpublished).

Pilot, G. (1977). Methods of improving the geotechnial properties of soft clays. Proc. 5th Southeast Asian Conf. on Soil Engineering. (Bangkok), pp 92-101.

Peattie, K.R. and Sparrow, R.W. (1955). A review of the design of earth pressure cells. Civ.Engng. Pub.Wks. Review, Vol. 50, No. 590, pp 872.

Plantema, G. (1953). A soil pressure cell and calibration equipment. Proc. 3rd Int. Conf. Soil Mech. Fdn.Engng., Vol. 1, pp 283-288.

Poteur, M. (1973). Die Verbesserunger der Tragfahigkeit bindiger Böden durch reine Tauchruttelung. Baumaschine und Bautechnick, Vol. 20, No. 10, pp 385-393.

Poulos, H.G. (1968). Analysis of the settlement of pile groups. Géotechnique, Vol. 18, No. 4, pp 449-471.

Priebe, H. (1976). An evaluation of settlement reduction in a soil improved by vibroreplacement of settlement reduction in a soil improved by vibroreplacement. (translated from German). Die Bautechnic., Vol. 53, No. 5, pp 160-162.

Reddy, A.S. and Srinivason, R.J. (1967). Bearing capacity of footings on layered clays. Jnl. Soil Mech. Fndn. Div. Am. Soc. Civ. Engrs., Vol. 93, SM2, pp 83-99.

Redshaw, S.C. (1954). A miniture earth pressure cell. Jnl. Scientific Instr., Vol. 31, pp 467-469.

Roscoe, K.H. (1957). A comparison of tied and free pier foundations, Proc. 4th Int. Conf. Soil Mech. Fndn. Engng., Vol. 1, pp 419-423.

Roscoe, K.H. Arthur, J.R.F. and James, R.G. (1963). The determination of strains in soils by an X-ray method. Civ.Engng. Pub.Wks. Review, Vol. 58, pp 873-876 and 1009-1012.

Roscoe, K.H. and Schofield, A.N. (1956). The stability of short pier foundatons in sand. Symp. Plastic Theory of Struct. (Cambridge), British Welding Jnl., Vol. 3, No. 8, pp 343-354.

Rowe, R.K., Booker, J.R. and Balaam, N.P. (1977). Application of the initial stress method to soil structure interaction. Int. Jnl.Num.Meth. in Engng., Vol. 3, pp 291-296.

Saffery, M. and Tate, A.P.K. (1961). Model tests on pile groups in a clay soil with particular reference to the behaviour of the group when it is eccentricially loaded. Proc. 5th Int. Conf. Soil Mech. and Fdn.Engng. (Paris), Vol. 2, pp 129.

Schofield, A.N. (1961). The development of lateral force of sand against the vertical face of a rotating model foundation. Proc. 5th Int. Conf. Soil Mech. (Paris), Vol. 2, pp 479-484.

Seed, H.B. and Chan, C.K. (1959). Structure and strength characteristics of compacted clays. Jnl. Soil Mech. Fdn. Div.Am.Soc.Engrs., Vol. 85, No. SM5, pp 31-47.

Selig, E.T. and Vey, E. (1965). Shock induced stress wave propagation in sand. Jnl. Soil Mech. Div. Am.Soc.Civ.Engrs., Vol. 91, SM3, pp 19-49.

Sherif, M.M. (1975). Pressure exerted by soil on retaining structures. Ph.D. thesis, University of Leeds (unpublished).

Skempton, A.W. (1951). The bearing capacity of clays. Proc. Building Research Congress, Vol. 1, pp 180-189.

Stroud, M.A. (1971). The behaviour of sand at low stress levels in the simple shear apparatus. Ph.D. thesis, Unviersity of Cambridge (unpublished).

Steinfield, K. (1953). Über den räumlichen Erdwiderstand. Mitteilungen der Hannoverschen Versuchsanstalt fur Grundbau und Wasserbau, Heft 3, 5.51 ff.

Suen, Y.C. (1981). Private communication.

Suen, Y.C. (1982). Lateral pressure on retaining walls due to surcharge. Ph.D thesis, University of Birmingham (unpublished).

Tanimoto, K. (1973). Introduction to the sand compaction pile method as applied to stabilisation of soft ground. Div. Appl. Geomech., Tech. Rep. No. 16, Commonwealth Scientific and Indust. Research Org. (Australia).

Taylor, D.W. (1939). A comparison of results of direct shear and cylindrical compression tests. Proc. ASTM, Vol. 39, pp 1058-1070.

Taylor, D.W. (1943). Cylindircal compression research programme on stress deformation and strength characteristics of soils. 9th Progress Report, Section 4, Soil Mech. Lab. Massachusetts Institute of Technology.

Taylor, D.W. (1947). Review of pressure distribution theories, earth pressure cell investigations and pressure distribution data. U.S. Waterways Experimental Station, Soil Mech. Fact Finding Survey, Part 2.

Thomas, H.S.H. and Ward, W.H. (1969). The design, construction and performance of a vibrating-wire earth pressure cell. Géotechnique, Vol. 19, No. 1, pp 39-51.

Thorburn, S. (1975). Building structures supported by stablised ground. Géotechnique, Vol. 25, No. 1, pp 83-94.

Thorburn, S. and MacVicar, R.S.L. (1968). Soil stabilisation employing surface and depth vibrators. Struct. Engr., Vol. 46(10), pp 309-316.

Tory, A.C. and Sparrow, R.W. (1967). The influence of diaphragm flexibility on the performance of an earth pressure cell. Jnl. of Scientific Inst., Vol. 44, pp 781-785.

Trollope, D.H. and Currie, D.T. (1960). Small embedded earth pressure cells - their design and calibration. Proc. 3rd. Aust. - N.Z. Conf. Soil Mech. Fdn.Engng., pp 145-151.

Trollope, D.H. and Lee, I.K. (1961). The measurement of soil pressures. Proc. 5th Int. Conf. Soil Mech. Fdn. Engng. (Paris), Vol. 2, pp 493-499.

U.S. Corps of Engineers (1944). Soil pressure cell investigation. U.S. Waterways Experimental Station, Tech. Memo. No. 210-1.

Vautrain, J. (1978). Reinforced earth wall on stone columns in soil. Bull. Liaison Labo. P. et Ch., Special Issue, VIE, pp 188-194.

Wadell, C. (1933). Sphericity and roundness of rock particles. Jnl. Geol., Vol. 41, pp 310-331.

Watt, A.J., Boer, B.B. de, Greenwood, D.A. (1967). Loading tests on structures founded on soft cohesive soils strengthened by compacted granular columns. Proc. 3rd. Asian Reg. Conf. Soil Mech. Fdn. Engng. (Haifa), pp 248-251.

Whittaker, T. (1960). Some experiments on model pile foundations in clay. Proc. Symp. on Pile Fdns., 6th Congress Int. Assoc. Bridge and Struct. Engng. (Stockholm), pp 124-139.

Whittaker, T. (1963). The constant rate of penetration test for the determination of the ultimate bearing capacity of a pile. Proc. Instn. Civ. Engrs., No. 26, pp 119-123.

Whitman, R.V. and Healy, K.A. (1963). Shear strength of sands during rapid loadings. Trans.Am.Soc.Civ.Engrs., Vol. 128, pp 1553-1594.

Williams, J.D.G. (1969). Small tests on granular piles in soft clay. BSc dissertation, University of Wales, Swansea (unpublished).

Wong, H.Y. (1973). Field instrumentation of vibroflotation foundation. Symp. Field Instr. Geotech.Engng. (London), Pt. 1, pp 475-487.

Wong, H.Y. (1974). Some design and performance considerations of diaphragm type pressure cells using strain gauges. Géotechnique, Vol. 24, No. 1, Tech. Note, pp 93-99.

Wong, H.Y. (1975). Vibroflotation - its effect on weak cohesive soils. Civ.Engng., Vol. 70, No. 824, pp 44-49.

Wroth, C.P. and Hughes, J.M.O. (1973). An instrument for the in-situ testing of soft soils. Proc. 8th Int. Conf. Soil Mech. Fdn.Engng. (Moscow), Vol. 1, pp 487-494.

Zienkiewicz, O.C. (1977). The Finite Element Method. McGraw-Hill: London.